2.5 × 3.3 × 40 mm for the small composite
the larger composite samples.

Room-temperature flexure strengths we
bending method, with a support span of 25.
6.4 mm, and a crosshead speed of 0.0085 mm

ORNL/FMP--90/1

DE91 001158

PROCEEDINGS OF THE FOURTH ANNUAL CONFERENCE ON FOSSIL ENERGY MATERIALS

Compiled by
R. R. Judkins and D. N. Braski

Date Published: August 1990

Compiled for
Department of Energy
Fossil Energy Office of Technical Coordination
and
Oak Ridge Operations
AA 15 10 10 0

Compiled by
OAK RIDGE NATIONAL LABORATORY
Oak Ridge, Tennessee 37831-6285
operated by
MARTIN MARIETTA ENERGY SYSTEMS, INC.
for the
U.S. DEPARTMENT OF ENERGY
under Contract DE-AC05-84OR21400

PREFACE

The Fourth Annual Conference on Fossil Energy Materials was held in Oak Ridge, Tennessee, on May 15-17, 1990. The meeting was sponsored by the U.S. Department of Energy's Office of Fossil Energy through the Advanced Research and Technology Development (AR&TD) Materials Program, and ASM International. The objective of the AR&TD Materials Program is to conduct research and development on materials for longer-term fossil energy applications as well as for generic needs of various fossil fuel technologies. The management of the Program has been decentralized to the DOE Oak Ridge Operations Office with Oak Ridge National Laboratory (ORNL) as the technical support contractor. The research is performed by staff members at ORNL and by a substantial number of researchers at other national laboratories, universities, and in private industry. The work is divided into the following categories: (1) Ceramics, (2) New Alloys, (3) Corrosion and Erosion, and (4) Technology Assessment and Technology Transfer.

This conference is held every year to review the work on all of the projects of the Program. Although not a participant in the AR&TD Materials Program, Ceramatec, Inc. was invited to take part in the conference because of the relevance of its project involving ceramic composites. The Ceramatec project is sponsored by the Small Business Innovation Research (SBIR) Program. The agenda for the meeting is given in Appendix A, and a list of attendees is presented in Appendix B.

These proceedings have been published from camera-ready masters supplied by the authors. All of the contributions have been checked for errors but have not been subjected to peer reviews. However, most of the papers had already undergone technical review within the individual organizations before submission to the Program Office.

The successful completion of the conference and publication of the proceedings has required help from a number of dedicated people. The organizers wish to thank Gail Beyersdorf for her superb coordination work; Carolyn Wells for her assistance with preparations for the conference and excellent work at the registration desk; Bonnie Reesor and the ORNL Conference Office for their help in the many arrangements;

Susie Kirk for her invaluable assistance in the financial aspects of the conference; and the numerous staff and support personnel associated with the conference. ASM International cosponsored the conference, for which we are especially grateful. Finally, we express our sincere appreciation to the authors themselves whose efforts are the very basis of the conference.

TABLE OF CONTENTS

SESSION I - CERAMICS

MECHANICAL PROPERTY CHARACTERIZATION OF FIBER-REINFORCED SiC MATRIX COMPOSITES

D. P. Stinton, R. A. Lowden, and R. H. Krabill

Oak Ridge National Laboratory
P.O. Box 2008
Oak Ridge, TN 37831-6084

ABSTRACT

Mechanical properties of Nicalon-fiber-reinforced silicon carbide (SiC) matrix composites fabricated by a forced chemical vapor infiltration (CVI) process have been measured and compared with properties of composites fabricated by a conventional isothermal process. The mechanical properties are nearly identical for composites fabricated by the two processes provided that hot-face temperatures <1200°C are used for the forced CVI process. Composites reinforced with more stable Tyranno fibers were fabricated by forced CVI and exhibited room temperature mechanical properties similar to those of Nicalon-reinforced composites and improved high-temperature strengths.

INTRODUCTION

Composites consisting of silicon carbide (SiC) matrices reinforced with continuous silicon-carbide-oxygen (Si-C-O) fibers are being developed for many high-temperature structural applications. Chemical vapor infiltration (CVI) is an attractive process for fabricating these fiber-reinforced composites because continuous ceramic fibers can be processed without strength degradation. The great potential use of ceramic matrix composite materials has prompted in-depth investigations of these materials.

Fiber-reinforced ceramic-matrix composites have been fabricated by two distinctly different CVI processes. The first, by which most CVI composites are fabricated, is the isothermal process in which reactant gases diffuse into freestanding preforms (Fig. 1).[1-3] The second process, developed at Oak Ridge National Laboratory (ORNL), simultaneously uses a thermal gradient and a pressure gradient in which the reactant

gases are forced into the cool side of the fibrous preform. Densification in the isothermal process is relatively slow in comparison with the forced-flow process because of the use of diffusive transport of gaseous reactants and reaction by-products. The reduced infiltration times offered by the forced-flow process make the ORNL process especially attractive for densifying thick-walled, simple shapes.

Unfortunately, the properties of the Nicalon fibers routinely used in both CVI processes degrade at elevated temperatures. Composites fabricated by the isothermal process are exposed to a lower processing temperature than are composites fabricated by forced CVI. Therefore, this investigation compares the mechanical properties of composites fabricated by the two processes. In addition, the mechanical properties of composites reinforced with reportedly more stable Tyranno fibers were compared with those of Nicalon-reinforced composites.

BACKGROUND

Comparison of CVI Processes

The economical densification of composites by the isothermal process requires large furnaces. To ensure uniform infiltration throughout the furnace, the isothermal process must be slowed by combinations of low-temperature, low-reactant concentrations and low pressures to avoid coating and sealing the outer surface of the preform and depleting the reactants before they reach the inner volume. The Societe Europeenne de Propulsion (SEP) has successfully commercialized this process and has licensed it to E. I. du Pont de Nemours and Company in the United States. Although the process is proprietary and specific processing conditions are unknown, the processing temperature is assumed to be ~1000°C. The composite shapes are exposed to this temperature for relatively long periods (weeks to months) during which the fibers are thought to lose some fraction (30 to 50%) of their strength.

In the forced CVI process[4-6] fibrous preforms are retained within a cylindrical graphite holder that contacts a water-cooled, metal gas distributor that cools the bottom and side surfaces of the substrate

(Fig. 2). The top of the fibrous preform is exposed to the hot zone of the furnace (normally 1200°C), which creates a steep temperature gradient through the thickness of the preform. The reactant gases are forced under pressure into the cooled side of the fibrous preform but, because of the low temperature, do not initially react. The gases flow from the cooled portion of the preform into the hot portion, where they react-depositing the matrix on the fibers. Deposition of matrix material within the hot region of the preform increases the density and thermal conductivity of the preform; therefore, the deposition zone moves progressively from the hotter regions toward the cooler regions. Composites fabricated by the forced CVI process are thus exposed to higher temperatures (1200°C compared to 1000°C) than in the conventional CVI process but for much shorter times (~24 h vs weeks or months).

Comparison of Fiber Reinforcements

The baseline fiber used by SEP for isothermal CVI processing has been ceramic-grade Nicalon, a polymer-derived Si-C-O fiber.[7-8] The fiber consists primarily of SiC, which makes it attractive for elevated temperature reinforcement. During the development of the forced CVI process, plain-weave ceramic-grade Nicalon cloth was used almost exclusively for the fabrication of composites. The strength of the fiber reinforcement in ceramic matrix composites can be directly correlated with the overall mechanical properties of the composite. Because of grain growth and the formation of large pores, the strength of the Nicalon is degraded when it is heated above 1000°C.[9-10]

As a result of the reported higher stability of Tyranno over Nicalon, Tyranno reinforcing fibers are of great interest.[11] Nippon Carbon Company reported the strengths of Nicalon to be 2900 MPa; however, strengths are reduced to about 1000 MPa by carbon coating, weaving into fabric, and annealing at 1200°C. Tow testing of Tyranno fibers determined the as-received strength to be 3500 MPa.[12] After the Tyranno fibers were carbon coated, woven into fabric and annealed to temperatures as high as 1400°C, a tensile strength of 2000 MPa was maintained.

Control of Fiber-Matrix Bonding

The mechanical properties of Nicalon-reinforced SiC composites are controlled by the strength of the bond between the fibers and the matrix. Deposition of the SiC matrix directly onto the Nicalon fibers results in a strong interfacial bond that produces brittle behavior. An intermediate coating applied to the fibers before infiltration is needed to weaken the fiber-matrix bond and produce crack deflection and fiber pullout that contribute to the "toughening" of the composite. Deposition of a carbon or boron nitride layer has been shown to produce appropriate fiber-matrix bonding to enhance fiber pullout and slip with a resultant increase in the toughness and the ultimate strength of the composite material.[12-16]

EXPERIMENTAL PROCEDURES

Preform Assembly

Fibrous preforms were assembled for the forced CVI process by stacking multiple layers of Nicalon plain-weave fabric rotated in a $0° \pm 30°$ sequence within the cavity of a graphite holder. The layers were compressed by hand to produce a preform with a nominal loading of 40 vol % fiber and were held in place by a perforated graphite lid. Two sizes of fibrous preforms were constructed, small disks (45 mm diam, 12.5 mm thick) and larger disks (75 mm diam, 16 mm thick). After assembly, preforms were precoated with thin layers (0.2 to 0.3 μm) of carbon from an argon/propylene mixture. Boron nitride coatings (0.2 to 0.3 μm thick) were applied from a mixture of boron trichloride, ammonia, and hydrogen to a few 45-mm-diam preforms.

Composite Infiltration

Preforms were infiltrated with SiC produced by the decomposition of methyltrichlorosilane (MTS) in hydrogen at elevated temperature and atmospheric pressure. A series of disk-shaped composite specimens was fabricated for our investigation of the effect of top surface

temperature on the mechanical properties of the material. Composite specimens with hot-face temperatures ranging from 1100 to 1400°C were investigated, and the processing conditions are detailed in Table 1.

Table 1. Composite specimens fabricated for investigation of the effect of hot-face temperature on mechanical properties

Run	Fiber content (%)	Processing temperature (°C)	Processing time (h)
351	41.7	1100	36.0
249	39.8	1175	27.5
346	41.8	1200	19.0
247	40.9	1225	17.1
248	41.0	1275	18.0
353	41.2	1300	20.5
354	41.7	1400	9.0

Notes: All composites were fabricated from plain-weave, ceramic-grade Nicalon fabric that had been coated with a carbon interface. All samples were 45 mm diam and 12 mm thick.

A second series of composite specimens was fabricated to evaluate the effect of elevated temperatures on the mechanical properties of composite materials. Preforms consisting of carbon coated Nicalon (run 255), boron nitride coated Nicalon (run 268) and carbon coated Tyranno (run 258) were infiltrated with SiC for this investigation.

A third series of composites was fabricated from Tyranno fabric to determine their room-temperature mechanical properties. Three 45 mm diam. preforms containing ~42% carbon coated Nicalon fibers were infiltrated with SiC at 1200°C.

Flexure Testing

Flexure bars were cut with a diamond saw from the samples parallel to the 0° orientation of the top layer of cloth. Tensile and compression surfaces were ground parallel to the long axis of the specimen. The average dimensions of the test bars from the composite samples were

2.5 × 3.3 × 40 mm for the small composite samples and 3 × 4 × 55 mm for the larger composite samples.

Room-temperature flexure strengths were determined by a four-point bending method, with a support span of 25.4 mm, a loading span of 6.4 mm, and a crosshead speed of 0.0085 mm/s. Bend bars used for elevated-temperature flexure testing were first coated with a 35-μm layer of SiC to prevent oxidation of the carbon or boron nitride interlayers exposed during cutting and grinding. The elevated-temperature flexure strengths were determined by four-point bending, with a support span of 40 mm, a loading span of 20 mm, and a crosshead speed of ~0.009 mm/s. All specimens were loaded perpendicular to the layers of cloth.

The apparent fracture toughness of composites reinforced with carbon-coated Nicalon and Tyranno fibers were measured by the single-edge, notched-beam (SENB) technique. Notches were cut with a 0.25-mm blade across the width and at the center of flexure specimens (3 × 4 × 55 mm) to a depth 30% of the 3-mm thickness. The flexure bars were loaded in four-point bending (support span of 25.4 mm and a loading span of 6.4 mm).

RESULTS AND DISCUSSION

Room-temperature flexure strengths have been measured on composites fabricated by the forced CVI process.[17] The difficulties in interpreting flexure-test results for continuous fiber-reinforced composites are recognized, and the results are reported only for comparison of composites fabricated under different processing conditions. Composites fabricated before 1989 with a top or maximum temperature of 1200°C by the forced CVI process had an average flexure strength of 320 MPa. Flexure strength values were generally consistent within each composite sample (i.e., no apparent effect of location of the specimen existed with respect to the hot face of the composite).[17] These values are nearly identical to those reported by Lamicq et al.[18] for Nicalon-reinforced SiC matrix composites infiltrated at SEP by the isothermal CVI process.

Flexure strengths of typical composites fabricated more recently increased to about 380 MPa (Table 2). A slight decrease in density is observed from the top (or hot face) of the composite toward the bottom (or cold face). The reduced density of the flexure bars from the middle and bottom layers of the composite appears to decrease the flexure

Table 2. Characterization of Nicalon-reinforced composites

Sample	Fiber content (vol %)	Sample location	Composite density (% theoretical)	Flexure strength (MPa)
21	41	Top	87.2 ± 0.3	417 ± 18
		Middle	85.5 ± 0.7	406 ± 30
		Bottom	84.4 ± 0.7	390 ± 14
23	41	Top	88.2 ± 1.0	396 ± 30
		Middle	87.8 ± 0.4	354 ± 44
		Bottom	85.4 ± 1.0	308 ± 26
364	37	Top	91.8 ± 0.6	407 ± 23
		Middle	88.1 ± 0.8	345 ± 27
		Bottom	91.0 ± 1.0	339 ± 19

strength. When large numbers of samples were examined in a previous study,[17] strength was related to density but significant scatter in the data indicated that other factors also affect strength.

Apparent fracture toughness measured for composites fabricated from Nicalon cloth by the forced CVI process is 23.5 ± 2.9 $MPa \cdot m^{1/2}$, which is nearly identical to the room-temperature value reported by Du Pont or SEP[17] (25 $MPa \cdot m^{1/2}$) for isothermally produced composites. Because of the similar mechanical properties for composites fabricated by different CVI techniques, processing of composites at 1200°C by the forced CVI method must cause no greater degradation of fiber strength than processing at 1000°C by the isothermal method. Slightly higher flexure strengths (380 vs 320 MPa) reported by the forced CVI process may be the result of different cloth weaves.

Unusually low flexure strengths have been observed for composites processed at temperatures higher than 1200°C by the forced CVI technique. To investigate the effect of processing temperature on the strength of Nicalon/SiC composites prepared by forced CVI, disk-shaped samples were fabricated at top (hot) surface temperatures ranging from 1100 to 1400°C. A plot of the average flexure strengths of specimens cut from the uppermost portion (the volume that experienced the highest processing temperatures for the longest time) clearly illustrates the strength loss above 1200°C (Fig. 3). Similar attempts to correlate strengths with processing time or density, both of which spanned a narrow range, indicated no strong relationship.

During this investigation, a limited number of SiC-matrix composites were fabricated with Tyranno fibers precoated with ~0.2 μm of pyrolytic carbon (Table 3). Although composites fabricated with Tyranno fibers were not as dense as those fabricated with Nicalon fibers, the mechanical properties were approximately equal. Forced CVI processing has been optimized for the relatively open weave used at ORNL. Tyranno fibers have a diameter of 8 to 10 μm and are available in only 1500-filament tows. The smaller diameter flexible fibers form a tight bundle with little porosity, which makes them difficult to infiltrate. Optimized processing conditions would reduce the wide variation in density within the samples described in Table 3.

The mechanical properties of composites reinforced with Tyranno fibers were encouraging. Despite the somewhat less than optimum density of the fabricated composites, strengths >350 MPa were obtained for samples from the top, middle, and bottom of the composite (Table 3). Tyranno-reinforced composites exhibit "toughening" by fiber pullout. Although the fracture toughness values are similar, the fracture appears to be slightly more brittle than that of Nicalon composites.

The effect of testing temperature on the flexure strength of carbon-coated Nicalon and Tyranno fibers in a SiC matrix was investigated. The results of the elevated temperature tests are summarized in Fig. 4. A gradual increase in the strength of the Nicalon/SiC composites produced by forced CVI was observed up to a temperature of 1000°C.

Table 3. Characterization of composites reinforced with Tyranno fibers

Sample	Fiber content (vol %)	Sample location	Composite density (% theoretical)	Flexure strength (MPa)	Apparent fracture toughness ($MPa \cdot m^{1/2}$)
242	43	Top	79.4 ± 1.8	395.4 ± 18.4	20.9 ± 2.0
		Middle	75.6 ± 0.2	395.0 ± 7.5	20.6 ± 1.9
		Bottom	72.5 ± 0.5	351.9 ± 11.0	
243	42	Top	81.0 ± 0.7	368.9 ± 7.7	19.6 ± 1.0
		Middle	75.3 ± 0.1	364.2 ± 2.4	18.4 ± 1.8
		Bottom	64.4 ± 0.8	216.1 ± 36.5	
258[a]	40	Top	85.5 ± 0.7	388.3 ± 19.2	

[a]The middle and bottom of sample 258 used in other tests.

The composites exhibited good strengths and gradual failure in all tests. A decrease in the strength of the composites was noted above 1200°C, most likely due to the degradation of fiber properties at this temperature. These results are nearly identical to those reported by Lamicq et al. for composites produced at SEP by the isothermal CVI process.[18] The strengths of the Tyranno-reinforced composites were higher than those of the Nicalon/SiC composites at all test temperatures, and no significant decrease in flexure strength was observed above 1200°C. Additional tests at elevated temperatures and after long-term heat treatments are being performed to further characterize the high-temperature properties and the stability of the two fibers.

CONCLUSIONS

Silicon carbide matrix composites fabricated by the forced CVI process have been characterized for room-temperature flexure strength, room-temperature fracture toughness, and high-temperature flexure strength. Forced CVI composites fabricated at hot-face temperatures $\leq$1200°C exhibit an average flexure strength of ~380 MPa and an apparent fracture toughness of ~23 $MPa \cdot m^{1/2}$. Because these values are nearly

identical to those reported by SEP and Du Pont for composites fabricated by the isothermal CVI process, apparently no additional fiber degradation results from the higher processing temperature (1200°C) used by the forced CVI process. Hot-face temperatures >1200°C were shown to cause significantly greater fiber degradation.

Silicon carbide matrix composites reinforced with Tyranno fibers were also fabricated by the forced CVI process. The room-temperature flexure strength of the material is at least as high as Nicalon-containing composites of similar density with similar strain tolerance. Improvement is noticeable in the strength of the Tyranno-reinforced composites over that of Nicalon-reinforced composites tested at temperatures up to 1200°C. The dependence of the strength of Nicalon-reinforced composites on processing temperature will provide an impetus to further investigate Tyranno fibers.

ACKNOWLEDGMENTS

The authors are indebted to M. K. Ferber and M. G. Jenkins, whose interest and valuable suggestions helped carry this work to completion. The authors are grateful for the assistance of C. A. Valentine for draft manuscript preparation manuscript and H. D. Neu for final manuscript preparation.

REFERENCES

1. F. Christin et al., "In-Depth Chemical Vapor Deposition of SiC Within Porous Carbon-Carbon Materials," *Proc. 3rd European Conf. Chem. Vapor Dep.*, 154 (1980).

2. J. W. Warren, "Fiber- and Grain-Reinforced CVI Silicon Carbide Matrix Composites," *Ceram. Eng. Sci. Proc.* **6**(7-8), 64 (1985).

3. P. J. Lamicq et al., "SiC/SiC Composite Ceramics," *Ceram. Eng. Sci. Proc.* **6**(7-8), 336-38 (1985).

4. D. P. Stinton, A. J. Caputo, and R. A. Lowden, "Synthesis of Fiber-Reinforced SiC Composites by Chemical Vapor Infiltration," *Am. Ceram. Soc. Bull.* **65**(2), 347-50 (1986).

5. D. P. Stinton, "Ceramic Composites by Chemical Vapor Infiltration," pp. 1028-40 in *Proc. Tenth Intl. Conf. Chem. Vapor Dep.*, ed. G. W. Cullen, Electrochemical Society, Pennington, N.J., 1987.

6. D. P. Stinton, T. M. Besmann, and R. A. Lowden, "Advanced Ceramics by Chemical Vapor Deposition Techniques," *Am. Ceram. Soc. Bull.* **67**(2), 350-55 (1988).

7. S. Yajima et al., "Systhesis of Continuous SiC Fibers with High Tensile Strength," *J. Am. Ceram. Soc.* **59**(7-8), 324-27 (1976).

8. S. Yajima et al., "Anomalous Characteristics of the Microcrystalline State of SiC Fibers," *Nature* **27**(21), 706-7 (1979).

9. T. Mah et al., "Thermal Stability of SiC (Nicalon)," *J. Mater. Sci.* **19**, 1191-201 (1984).

10. G. Simon and A. R. Bunsell, "Creep Behavior and Structural Characterization at High Temperatures of Nicalon SiC Fibers," *J. Mater. Sci.* **19**, 3658-70 (1984).

11. T. Yamamura et al., "Compatibility of New Continuous Si-Ti-C-O Fiber for Composites," pp. 19-28 in *Looking Ahead for Materials and Processes*, ed. J. deBossou, G. Briens, and P. Lissac, Elsevier, Amsterdam, 1987.

12. B. A. Bender, J. S. Wallace, and D. J. Schrode, "Effects of Thermochemical Treatments on the Strength and Microstructure of SiC Fibers," *J. Mater. Sci.*, accepted for publication.

13. R. A. Lowden, *Characterization and Control of the Fiber-Matrix Interface in Fiber-Reinforced Ceramic Composites*, ORNL/TM-11039, Oak Ridge National Laboratory, Oak Ridge, Tenn., March 1989.

14. R. W. Rice et al., "The Effect of Ceramic Fiber Coatings on the Room-Temperature Behavior of Ceramic-Fiber Composites," *Ceram. Eng. Sci. Proc.* 2(7-8), 661-701 (1981).

15. B. Bender et al., "Effect of Fiber Coatings and Composite Processing of Properties of Zirconia-Based Matrix SiC Fiber Composites," *Am. Ceram. Soc. Bull.* **65**(2), 363-9 (1986).

16. A. J. Caputo, D. P. Stinton, R. A. Lowden, and T. M. Besmann, "Fiber-Reinforced SiC Composites with Improved Mechanical Properties," *Am. Ceram. Soc. Bull.* **66**(2), 268-72 (1987).

17. A. J. Caputo, D. P. Stinton, R. A. Lowden, and T. M. Besmann, "Fiber-Reinforced SiC Composites with Improved Mechanical Properties," *Am. Ceram. Soc. Bull* **66**(2), 368-72 (1987).

18. P. J. Lamicq et al., "SiC/SiC Composite Ceramics," *Am. Ceram. Soc. Bull.* **65**(2), 336-38 (1986).

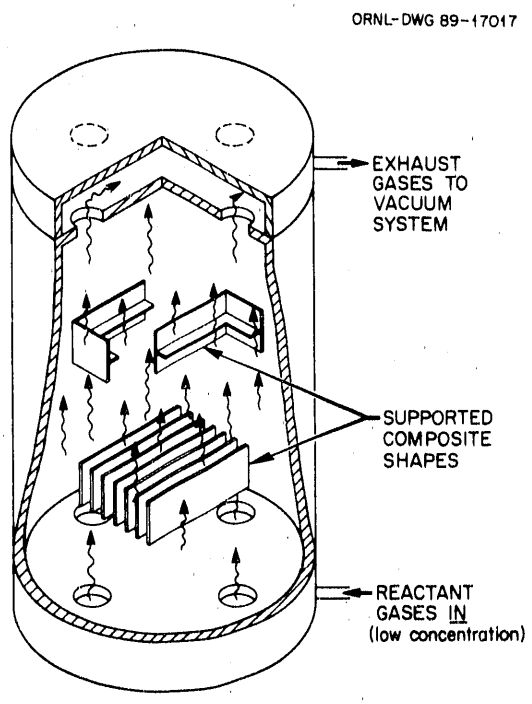

Fig. 1. Schematic representation of the isothermal CVI process. Reactant gases, as they flow through the furnace at a reduced pressure, diffuse into fibrous preforms and effluents diffuse back to the preform surface.

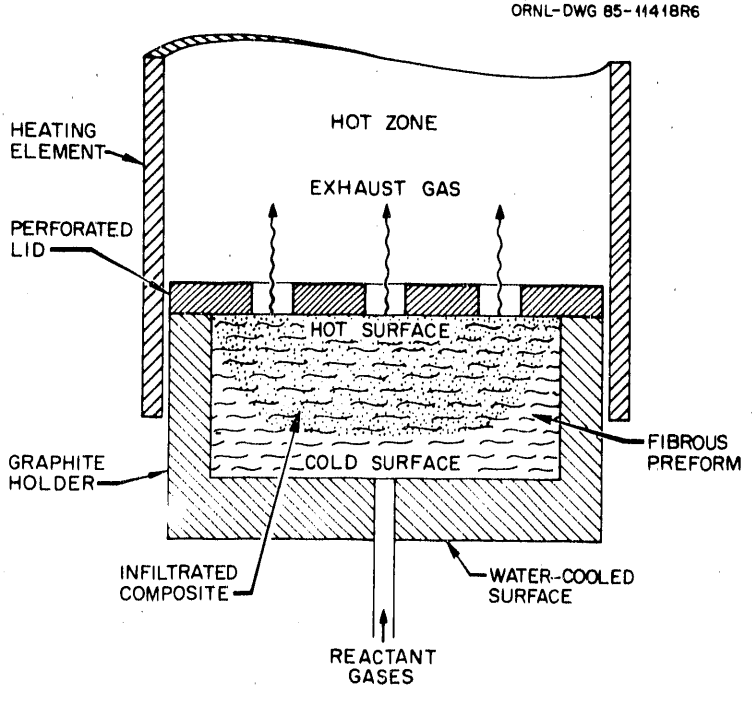

Fig. 2. Schematic representation of the forced flow-thermal gradient CVI process. Reactant gases are forced under pressure into the cooled side of the fibrous preform and flow toward the hot side, where SiC is readily deposited on the fibers.

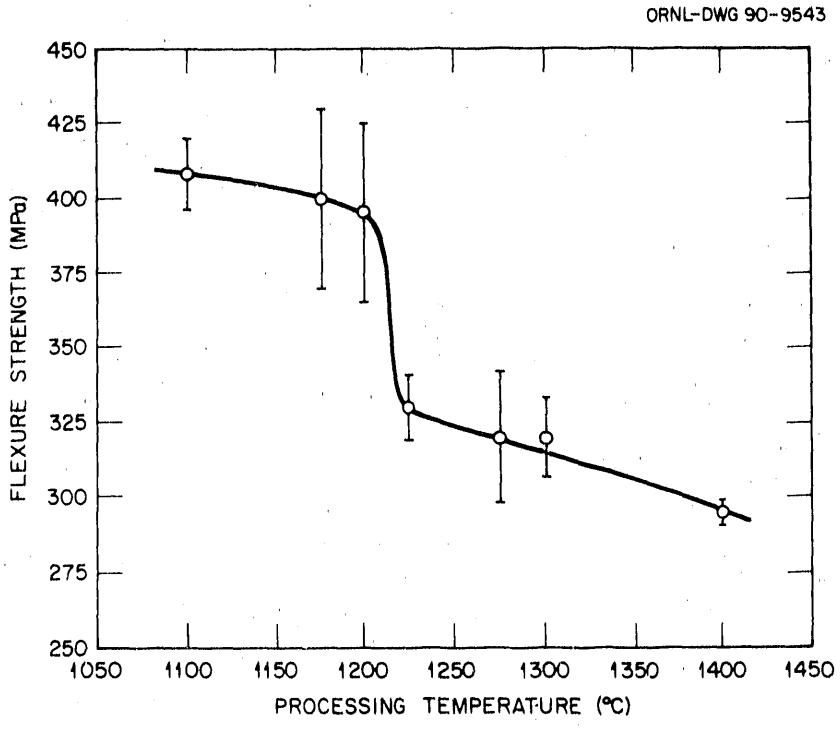

Fig. 3. Correlation of room-temperature flexure strength with processing temperature as measured on the hot face of the Nicalon-reinforced SiC matrix composite.

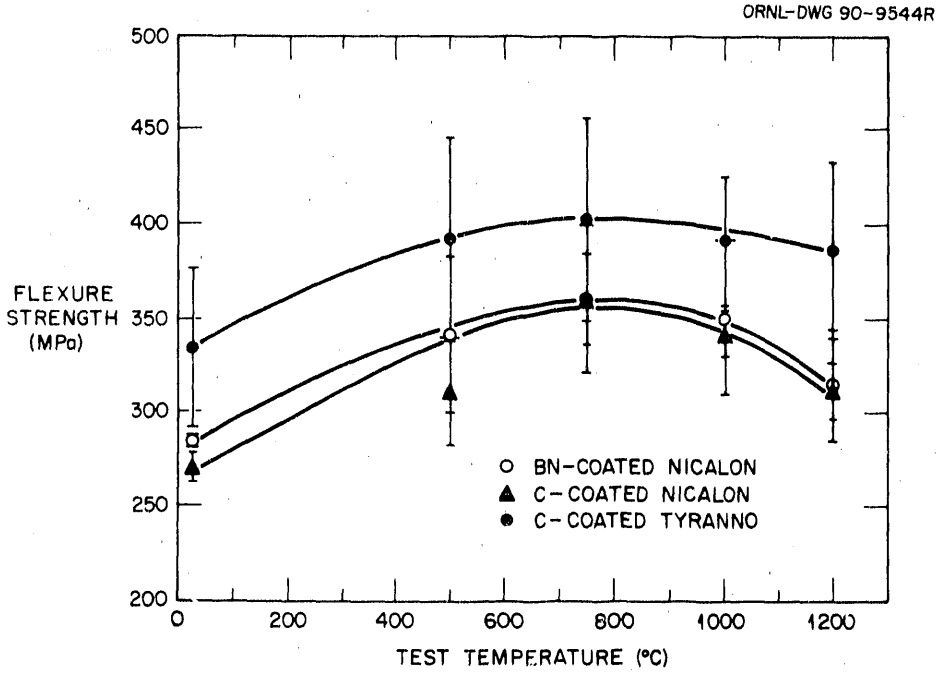

Fig. 4. Correlation of flexure strength with testing temperature for fiber-reinforced SiC matrix composites. Tyranno fibers with a carbon interface exhibit higher strengths at all temperatures than do Nicalon fibers with carbon or boron nitride interfaces.

3-D MODELING OF FORCED-FLOW THERMAL-GRADIENT CVI FOR CERAMIC COMPOSITE FABRICATION

T. L. Starr, A. W. Smith, G. F. Vinyard,
G. B. Freeman and T. C. Elston
Georgia Tech Research Institute
Georgia Institute of Technology
Atlanta, GA 30332

A 3-D model for forced-flow thermal-gradient chemical vapor infiltration (FCVI) has been developed using a "finite volume" formulation. A steady-state solution for heat conduction and Darcy's law permeation produces temperature and gas flow distributions within the fiber preform. These are used to generated matrix deposition rates within each volume element. By "marching" through time, a complete simulation of the densification process is obtained.

The model includes anisotropic transport properties (gas permeability and thermal conductivity) for cloth lay-up composites. These are calculated, as a function of density, from a two layer model using "series" and "parallel" combining laws. Model calculations are compared to experimental measurements for gas permeability.

The model is demonstrated for a FCVI system with cylindrical symmetry, matching the experimental configuration at the Oak Ridge National Laboratory. The model results suggest a self-optimizing feature of the force flow/thermal gradient CVI process that produces uniform density in the final composite over a range of infiltration conditions. This matches experimental observation where good uniformity has been achieved over a wide range of gas flows, pressure and temperature.

INTRODUCTION

Chemical vapor infiltration (CVI) is an effective and versatile technique for fabrication of ceramic matrix composites. The forced-flow thermal-gradient CVI technique (FCVI) yields reduced infiltration time and uniform densification of thick preforms. An analytical model for this process is being developed in order to optimize infiltration conditions and to design processing for large and complex shapes.

MODEL DEVELOPMENT

Earlier work with a one-dimensional CVI model was successful in matching experimental results for simple disc shapes. This model, however, is fundamentally unsuitable for more complex components. The three-dimensional FCVI model, now being developed, is based on conservation of mass or energy within finite volume elements which are defined by an orthogonal mesh of grid points (Figure 1)[1]. The difference between flow into and out of a volume element is set equal to any source or depletion contribution that is present. Overall balance of the flux terms between the volume elements and match to the imposed boundary conditions constitutes a steady-state solution.

The FCVI process involves heat transport, bulk flow of the reactant gas mixture, and convection, diffusion and reaction of chemical species. Within the preform, all of these terms depend on the material microstructure, which is anisotropic for cloth lay-up preforms, and which changes as densification proceeds.

The thermal model for the disc shaped preforms assumes constant temperatures at the hot face and at the water cooled injector equal to the setpoint values of the process control system. Internal temperatures depend on the thermal conductivities of the materials between these points. For SiC/Nicalon cloth lay-up composite a logarithmic relationship with density matches experimental measurements[2].

Gas flow through the preform is assumed to follow Darcy's law. The Darcy permeability depends in a complex way on the material microstructure and determination of this parameter for cloth lay-up composites is discussed below.

The mass balance for the reactant includes convection and diffusion as flux terms and reaction as a source (depletion) term. The diffusion flux is calculated assuming ordinary diffusion. (Knudsen flow is negligible at near ambient pressure which is used in the FCVI process.) The effective diffusion coefficient within the composite is calculated from the free space binary diffusion coefficient, the fractional porosity of the volume element and a "tortuosity" parameter. For SiC

deposited from methyltrichlorosilane (MTS), fiber coating experiments yield a rate law that appears first order in the reagent partial pressure[3]. Estimating the surface area of the internal porosity, this rate is used directly as a source term in the finite volume method.

PERMEABILITY MEASUREMENTS

Experimental permeability measurements were made in two directions on cubic test samples (ca. 2.5 mm on edge) cut from partially densified composite disks. Optical examination of the cubes reveals the very different microstructures parallel to the preform fabric weave as compared to perpendicular to the fabric weave as shown in Figure 2. Gas permeability was determined by measuring the flow rate and pressure drop across opposite faces of a cube. Although, as expected, the permeability decreases with increasing density and is higher parallel to the cloth layers, there is a great deal of scatter about these trends. Since the size of the large, interlaminar porosity is similar to the size of the cubes (see Figure 2), this likely is due to variation in the pore connectivity within individual cubes. Permeability values are fit to a two layer model. Anisotropic permeability, parallel and perpendicular to the cloth, is calculated from the density dependent permeability of each layer.

MODEL RESULTS

The FCVI system used at Oak Ridge National Laboratory has cylindrical symmetry and is effectively two dimensional. It is modeled using an 18 x 22 orthogonal grid of volume elements as shown in Figure 3. Steady-state solutions of the temperature (heat flow), pressure (gas flow) and concentration (reactant flow) problems are obtained sequentially for given values of the composite density distribution. The steady-state reaction rate then can be used to update the densities of each volume element for a small increment of time. Iteration yields a series of solutions showing the spatial evolution of composite density as the process proceeds. These solutions also show the changing gas

flow pattern and temperature distribution as density increases. These are determined by the density-dependent gas permeability and thermal conductivity of the composite.

CONCLUSION

The model results outlined above suggest a self-optimizing feature of the force flow/thermal gradient CVI process that has not been recognized previously. As regions of the preform increase in density the deposition rate there decreases, and, conversely, increases in those regions where the density is lower. This tends to produce uniform density in the final composite over a range of infiltration conditions, which matches experimental observation of good uniformity over a wide range of gas flows, pressure and temperature.

REFERENCES

1. S. V. Patankar, Numerical Heat Transfer and Fluid Flow (Hemisphere Publishing Corporation, New York, 1980).

2. H. Tawil, L. D. Bentsen, S. Baskaran, D. P. H. Hasselman, J. Mat. Sci. 20, 3201-3212 (1985).

3. Brennfleck, E. Fitzer, B. Schoch, M. Dietrich in Proc. of 9th Int. Conf. on Chemical Vapor Deposition, edited by G. W. Cullen (The Electrochemical Society, Pennington, New Jersey, 1984) pp. 649-662 .

4. R. A. Lowden, et al., Oak Ridge National Laboratory report ORNL/TM-10403, May 1987.

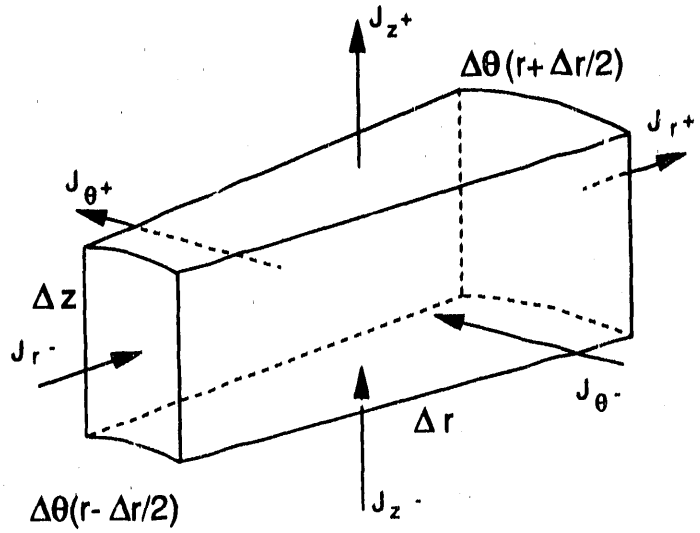

Figure 1. The finite volume method balances heat or mass fluxes through the faces of a discrete volume element with any source (or sink) term within the volume.

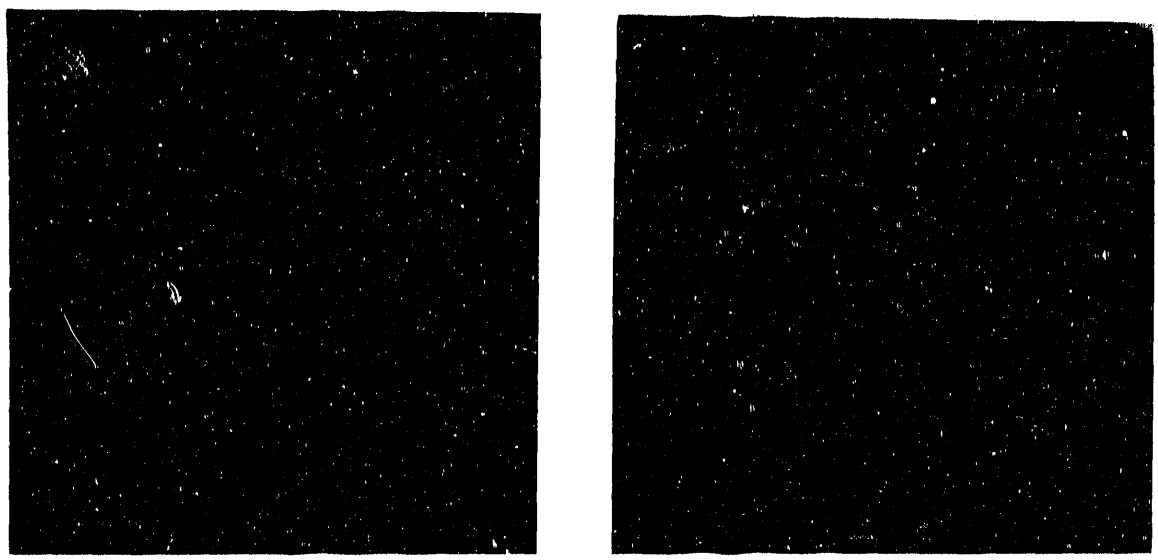

Figure 2. Cloth lay-up preform produces composite with anisotropic microstructure. Transport properties (gas permeability and thermal conductivity) are different parallel and perpendicular to cloth.

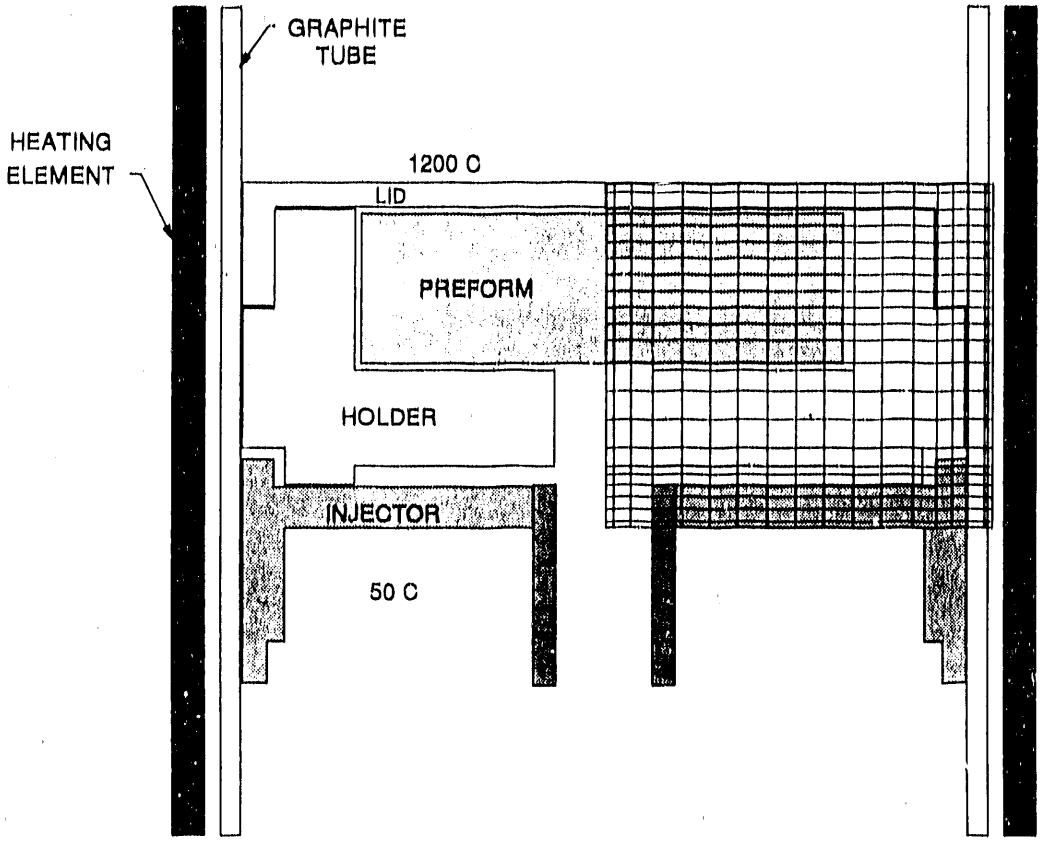

Figure 3. Finite volume element grid for modeling of ORNL FCVI process. With cylindrical symmetry, model is effectively 2-D. Numerical model includes preform, holder and furnace components.

FABRICATION OF FULL-SIZE FIBER-REINFORCED HOT GAS FILTERS BY CHEMICAL VAPOR INFILTRATION (CVI)

L. R. White

3M Company
3M Center/218-3S-03
St. Paul, MN 55144-1000

ABSTRACT

This project began August 1, 1989 and has a two-year performance period. The goal is to develop filters for separating particulates from dusty gases at high temperature. Applications could be in the utility industry and process industries in both environmental control and product recovery. The filter will be a rigid, porous, ceramic structure shaped like a large test tube about 60-75 mm diameter and 1.5-2 meters long. Dusty gas would enter the outside surface and clean gas would be exhausted from the interior. Filters would be mounted vertically with an array suspended from a support which also separates the "clean" and "dirty" sides of the filter. Periodically dust would be removed from the filter surfaces by back-pulsing with air. The technique being used to make filters involves three steps, making a preform of ceramic fibers, coating it with an interface, and coating it again with a ceramic using chemical vapor infiltration (CVI). The result will be a fiber-reinforced composite with good thermal and mechanical shock tolerance. Progress to date has been that the processes for making fibrous preforms and CVI coating have been shaken down, the permeability of filters has been measured, and directions for future work have been set.

INTRODUCTION

The specific objective of this project is to develop a hot gas filter for application in pressurized fluidized bed combustion (PFBC) and integrated coal gasification combined cycle (IGCC) systems.

Such filters would be used in PFBC to filter combustion products from coal upstream of a gas turbine and in IGCC to filter fuel gas before it is burned. PFBC and IGCC technologies are not yet fully developed so that success in hot gas filter development per se does not guarantee success overall, but it is an important ingredient.

PFBC and IGCC will be more efficient than conventional coal-burning technology and in-bed sulfur capture and reduced NO_x due to low combustion temperature make PFBC environmentally attractive as

well. Therefore, the economics of power generation could be improved and less pollution generated if this project were successful.

Since the oil crisis of 1973, more efficient coal to energy processes have been sought and PFBC and IGCC are attractive technologies. Hot gas cleanup is needed for both PFBC and IGCC and filtration using rigid, ceramic structures called candles shows promise. Dust removal has been achieved at very high efficiency and at an acceptable pressure loss. The resistance to attack by alkali vapor and coal ash has been good. Major concerns have been thermal shock caused by pulse-cleaning and cleanability.

Parallel development has occurred in the area of ceramic/ceramic composites. As engineering materials, composites which have brittle matrices are very old but mechanical behavior is less well understood than is the behavior of materials like fiberglass reinforced plastic (FRP).

Composites such as FRP or alumina fiber reinforced aluminum are characterized by

- the matrix (plastic or aluminum) being much less stiff than the reinforcement (fiberglass or alumina fiber)
- the bond between matrix and reinforcement being strong
- and, the strength of the composite being determined by the strength of the reinforcement.

Rules for making tough ceramic/ceramic composites differ from those for materials like FRP. Frequently, both matrix and reinforcement have similar values of tensile strength and modulus of elasticity. Hence mechanical properties are not dominated by properties of the reinforcement alone. Also, the bond between reinforcement and matrix must be loose. Decoupling the matrix from the reinforcement is essential or the composite will be brittle.

Conventional ceramics processing techniques such as hot pressing mixtures of ceramic particles and fibers cannot be expected to produce good composites because the fibers are likely to be damaged by the pressures and temperatures required in processing. Also, it is not clear how one would decouple the matrix from the reinforcement. Chemical vapor infiltration (CVI)[1] is a technique which avoids these problems, and it was recognized by the AR&TD Materials Program at ORNL that high temperature filters produced by CVI of fibrous substrates would be a good application.[2]

CVI is a method for filling and coating a porous structure with a

---

[1] Vapor Deposition, edited by Powell, C. F., J. H. Oxley, & J. M. Blocher, Wiley, New York, (1966)

[2] Stinton, D. P., R. A. Lowden, Ramsey Chang, Ceramic Engineering & Science Proceedings, vol. 9, no. 9-10, p. 1233-1244, 1988

layer of material which is uniform in thickness and of well-controlled composition. A structure called SICONEX™ is similar to the filters to be developed on this project. SICONEX™ is made by depositing silicon carbide on a ceramic fabric preform, the fabric being constructed of alumina-silica-boria fibers. Substantial experience has been gained making SICONEX™ and it can be applied directly to constructing candles via CVI of fibrous substrates.

DISCUSSION

The CVI candle-making process consists of the following steps:

- making a fibrous preform
- coating the preform with a suitable interface, and
- coating the preform with silicon carbide using CVI.

Both the strength and openness or permeability of the structure can be controlled by varying the permeability of the preform and the amount of silicon carbide deposited.

To understand the advantages which this technology offers to the making of filters, it is helpful to review experience with candles.

Candle filters used in endurance testing at a PFBC test facility in Grimethorpe, UK are shown in Figure 1[3]. They are constructed of large-grained silicon carbide particles bonded with a glassy phase. The filtering surface is the outside of the tube and is a thin, porous layer of much finer-grained material reinforced with silica-alumina fibers. Thus the filter consists of an outer layer of fine pores over a structural support having much larger pores. From the standpoint of filtration, this is a desirable structure. It fosters cake filtration where dust forms a layer on the surface. Depth filtration, where dust is captured within the filter itself is undesirable since such filters are difficult to clean.
During cleaning, a pulse of high pressure air is introduced into the center of the candle and the dust cake is removed by reverse flow. Pulse air is not heated and the candles are exposed to thermal shock. Cleaning is required about every two minutes and a large number of cleaning pulses must be endured if filters are to last thousands of hours. Economics require filters to last in the neighborhood of 10,000 hours.

---

[3]This figure was taken from a paper by: Morrell, R., D. M. Butterfield, D. J. Clinton, P. G. Barrat, J. E. Oakey, G. P. Reed, M. Durst, and G. K. Burnard, "The Mechanical Performance of Ceramic Dust Filter Elements in the Tertiary Dust Capture Filter of the Grimethorpe Pressurised Fluidised Bed Combustor (PFBC)", presented at The First International Conference on Ceramics in Energy Applications, April 9-11, 1990, Sheffield City Polytechnic, Sheffield, UK. 3M was given an advance copy of this paper. It is a post-test analysis of candle filters tested at Grimethorpe and is an excellent source of information on what candle filters need to be able to do.

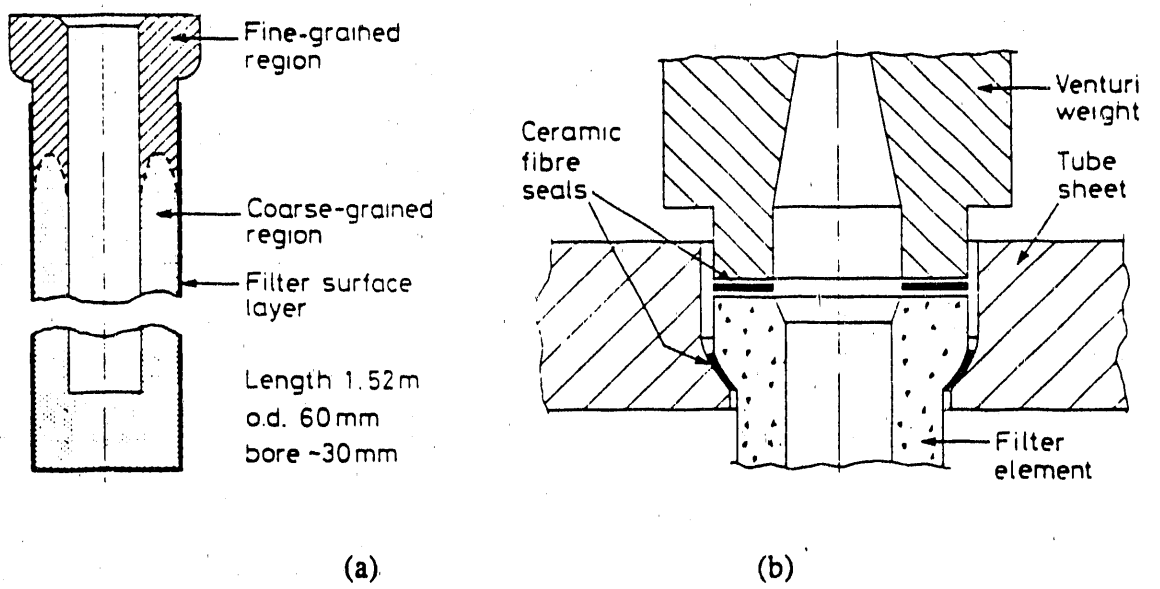

Figure 1. Silicon carbide filter element showing (a) its construction and dimensions, and (b) how it is mounted.

Examination of candles after 790 hours of PFBC service showed cracks due to thermal shock and tests showed significant loss in strength, at least for some of the candles.

A goal of this program is to develop a more shock-tolerant candle by incorporating fiber-reinforcement into its structure.

Work done to date can be summarized as follows. Eight preforms have been fabricated and coated with an interface and of those eight, four have been CVIed. See Table 1 for details.

The most important results are:

- Ceramic felt preforms were made by vacuum-forming. Silica binders were used to consolidate the felts.
- Ceramic felt preforms were CVIed
- Fiberfrax fibers are not "clean" enough and shrink too much during CVI processing. Shot and debris which are made with the fibers in the fiber manufacturing process reduce the openness of the felt and lead to low permeability. Shrinkage causes cracks and warpage in the CVIed structure.
- Chopped Nextel continuous filament yarn mixed with Saffil can be vacuum-formed; so can chopped Nicalon mixed with Saffil. Saffil/Nicalon can be CVIed to a crack-free structure. Saffil/Nextel has not been CVIed yet.

Table 1 CVI Processing Conditions for Candle Filters and Observations of CVIed Parts

Preform ID	Run no.	Date	MTS SLM	H2 SLM	T C	P Torr	Time Hours	SiC/sub. Wt. ratio	Yield %	Rate g/hr	Observations
F'frax 1	3A-176	2-8-90	2.5	2.2	975	5	1	0.048	10.	28.8	Part bowed and cracked
F'frax 1	3A-176B	2-13-90	2.5	2.2	1020	10	1	0.102	6.3	19.1	Part bowed a little more
F'frax 2	3B-178	2-22-90	1.89	2	1050	15	8.58	0.42	10.	20.8	Some cracks, very slight bow
F'frax 2	3B-178A	2-23-90	2.45	2	1050	25	6.43	0.675	10	26.3	Part is strong
Fabric 1	3B-180	3-5-90	2.59	2.1	1050	16	6.83	1.79	8.3	23	Part is weak, uniform coat
Saf/Nic 1	3B-181	3-14-90	2	2	1050	15	1	----	----	----	Non-uniform coating, soot on outside, no cracks, part is
Saf/Nic 1	3B-181	3-14-90	2	6	1125	50	7.54	0.684	17.	42	strong

- Permeability of CVIed felts is in the same range as sintered ceramic candle filters and based on their appearance they should be excellent filters provided they can be pulse-cleaned. The filtering surface is uniform and has fine pores.

- Permeability of the CVIed structure depends on permeability of the preform and the amount of silicon carbide deposited in the CVI process, results which confirm expectations.

- Based on experience with SICONEX™, the weight of CVI silicon carbide which is needed to confer adequate strength to the filter is about equal to the weight of the preform itself.

- Woven fabric preforms can be made and CVIed but lack strength and are too permeable.

- A pulse tester which will expose filters to repeated thermal shocks has been built.

The only characterization of preforms and CVIed parts which has been done so far has been measurement of permeability. This is non-destructive and can be applied to preforms before they are CVIed and to the part after coating. Strength tests are destructive and when more samples are available, "C" ring crush tests will be done and compared with data on candle filters[4].

Figure 2 is a sketch of a pulse tester. A filter specimen will be mounted in an enclosure and air heated to 500 C will be passed through it from outside in, as would occur in filtration. Periodically, the filter will be pulsed with cold air. Temperature and the number of pulses will be recorded. Frequency of pulsing will be determined by how rapidly the filter will be reheated after a pulse and should be as frequent as once every 10-15 seconds. After tens of thousands of pulses have been accumulated the strength of the specimen will be measured and compared with a sample that has not endured pulse testing.

Table 2 is a summary of fiber properties for materials used so far. Permeability data for preforms and CVIed parts are in Table 3.

---

[4]Morrell, R. ibid. "C" ring crush and tensile data are given and correlated with Ultrasonic time-of-flight measurements on specimens from Grimethorpe. Ultrasonic time-of-flight measurements are non-destructive and attractive for that reason.

HIGH TEMPERATURE FILTER BAG PULSE TESTER

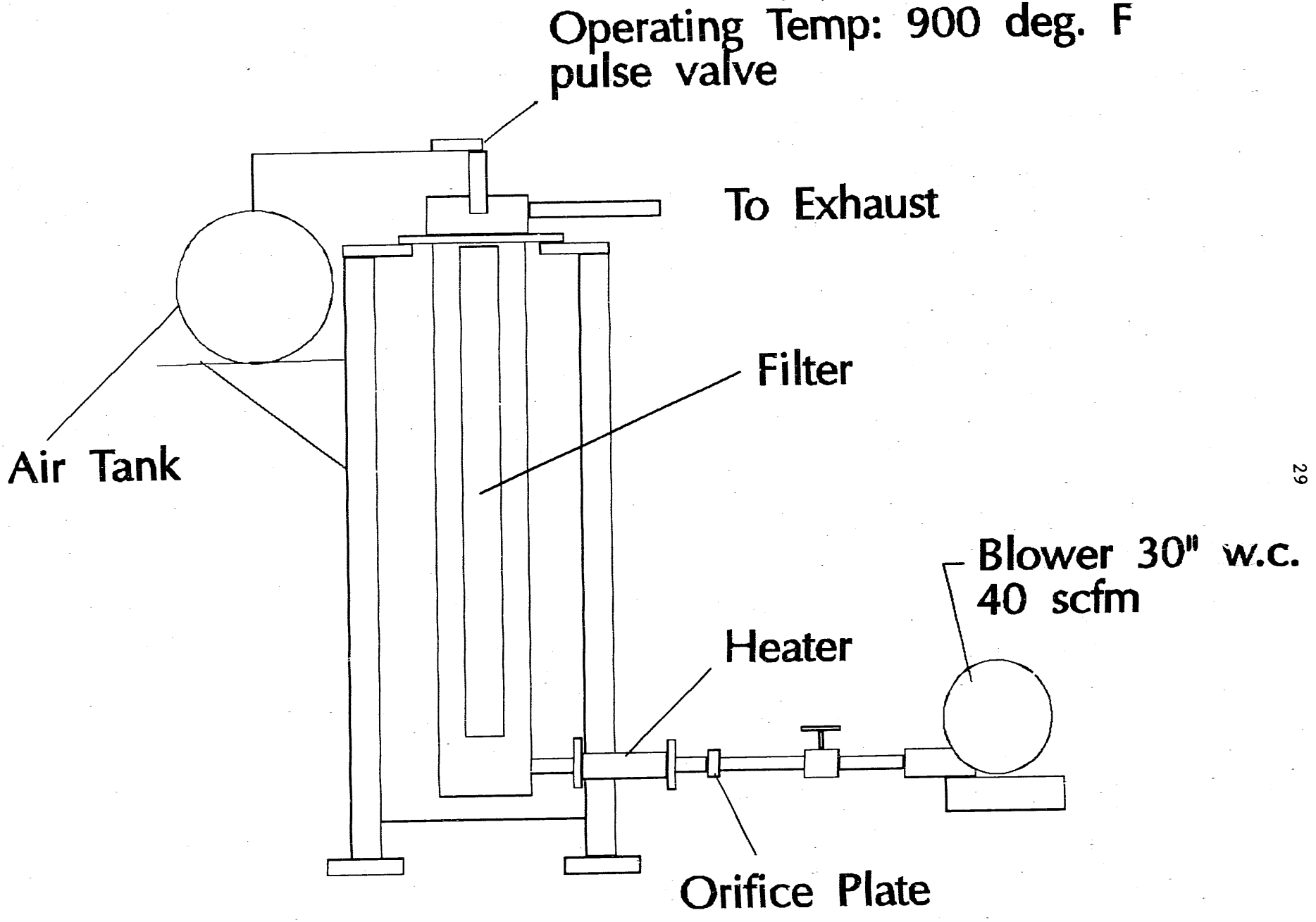

Table 2. Properties of fibers used to make preforms

Property	Fiberfrax	Nextel 312 chopped	Nicalon chopped	Saffil
Composition, % by wt.				
Al2O3	51.9	62		96-97
B2O3		14		
SiO2	47.9	24		3-4
Si			54.3	
O			11.8	
C			30	
Density, g/cc	2.73	2.75	2.55	3.3
Diameter, micrometer	2-3	11	10-15	3
Fiber length, inches	NA	0.125	0.12	NA
Use temp., C	1260	1200	1200	1600

Table 3 Permeability of preforms, CVIed parts and candle filters

Specimen ID	Permeability/pressure drop feet per minute/inches of water
Schumacher'sche (new)	2.2
Schumacher'sche (conditioned)	0.15
Fiberfrax preform NPD 90031-1	3.6
CVI Fiberfrax NPD 90031-1	0.5
Saffil/Nicalon preform	11.0
CVI Saffil/Nicalon felt	4.3
CVI Nextel fabric	78

SCIENTIFIC/TECHNICAL ISSUES

When this project was proposed, it was thought that a woven structure could be CVIed to produce a rigid filter, but early results do not confirm that and we believe slurry-formed ceramic fiber felts offer more promise.

Full-scale filter dimensions have been set at 1.5 meters long with an outside diameter of 75 mm. Candle filters which have been tested up to now have had an outside diameter of 60 mm. We have proposed changing to 60 mm. in order to facilitate testing in facilities such as Grimethorpe, UK and the Tidd, Ohio demo plant. Strength tests have not been run because we have been sample-poor and current methods are destructive. A non-destructive test is needed and ultrasonic time-of-flight measurements are being considered. For the near-term, destructive tests will be used and more samples are needed. To have more samples we must conduct CVI with multiple preforms and fixtures for making four filters at a time have already been made. SICONEX™ has been made in multiples and applying that experience to making filters will be straightforward.

RESULTS

The following results have been achieved:

- The process for making preforms has been shaken down.
- The CVI process for making filters has been shaken down.
- A test device has been built for simulating the thermal shock which filters will experience.
- Permeability of CVIed preforms is in the range of commercial candles.
- Candidates for future preforms have been identified.

Materials have been ordered for making preforms and plans made for future CVI runs. The pulse tester is being installed.

MICROWAVE SINTERING OF FUEL CELL MATERIALS

M. A. Janney and H. D. Kimrey

Oak Ridge National Laboratory
P.O. Box 2008
Oak Ridge, Tennessee 37831-6087

ABSTRACT

Microwave processing of $LaCrO_3$-based ceramics for the interconnect layer in the solid oxide fuel cell is reviewed. The characteristics of an inexpensive microwave furnace are detailed. $(La_{0.79}Ca_{0.2})(Cr_{0.9}Co_{0.1})O_3$ was shown to sinter at ≈ 150°C lower in the microwave furnace than in a conventional furnace.

INTRODUCTION

Microwave and conventional sintering experiments on $LaCrO_3$ - based interconnect materials has been initiated. Our initial experiments have been conducted using a modified home microwave oven, designated GE1*, which has been outfitted with a microprocessor-based programmable controller†, a platinum-sheathed Type-S thermocouple‡, and a 3-pen chart recorder§ to monitor sample temperature, exterior insulation temperature, and microwave power input.

Our first experiments used a Mg-doped $LaCrO_3$ material. Our insulation package consisted of bulk zirconia fiber¶ inside of an alumina fiber board cylinder¶. The Pt-sheathed type-S thermocouple was inserted in the sample to monitor and control temperature. A peak temperature of 1500°C, using a heating rate of 5°C/min, was achieved in several repeat runs using this setup. None of the parts were cracked after microwave firing, which indicates that the temperature was reasonably uniform within the parts. The particular composition that was used, $La_{0.99}Mg_{0.1}Cr_{0.9}O_3$, is not a particularly sinterable one under conventional firing conditions; hence, little densification was observed in our initial microwave experiments. Our main set of sintering experiments has been conducted using a more sinterable composition, $(La_{0.79}Ca_{0.2})(Cr_{0.9}Co_{0.1})O_3$**. That composition can also be readily heated in the microwave furnace, at heating rates as high as 40°C/min without cracking.

MICROWAVE FURNACE CHARACTERISTICS

The characteristics of heating $(La_{0.79}Ca_{0.2})(Cr_{0.9}Co_{0.1})O_3$ in the GE1 microwave furnace were studied. The sample soak temperature and the rate of heating were varied; the microwave power required to produce those conditions was monitored. Figure 1 shows two typical heating curves for a fast (R1) and a slow (R2) heating rate (schematic). The peak ramp power is defined as the maximum power used during the ramp up to temperature. The soak power is defined as the power level required to maintain a given temperature. P1, P2, S1, and S2 refer to peak and soak power levels for heating rates 1 and 2, with rate 1 > rate 2.

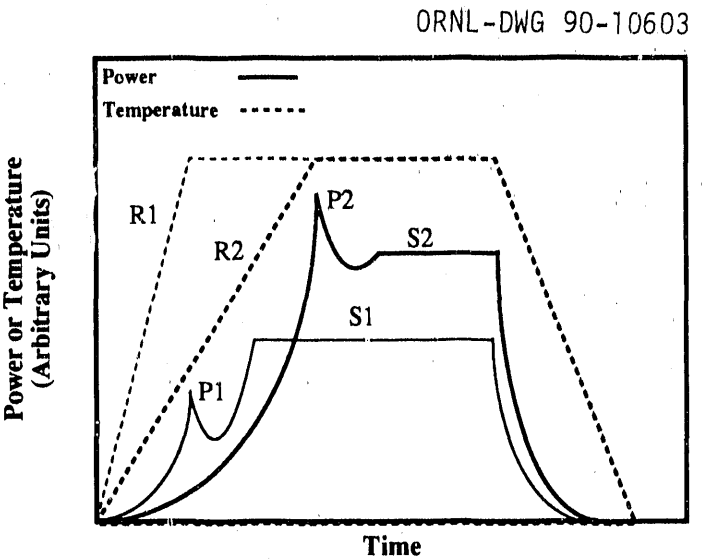

Note: P1, P2, S1, and S2 refer to peak and soak power levels, respectively, for heating rates 1 and 2, with rate 1 > rate 2.

Figure 1. Power and temperature profiles for the processing of $LaCrO_3$-based ceramics depended on the heating rate (schematic).

As one would predict based on conventional thermal processing, the soak power increased as the firing temperature increased (Fig. 2). Note that for the present system, with a sample weight of ≈20g, only 412 watts of microwave power was needed to maintain the temperature at 1400°C. This is much lower than would be required in a conventional furnace capable of 1400°C. It reflects the fact that in microwave heating the part is heated internally, and not by radiation from a heating element, which also heats the furnace walls, setters, etc.

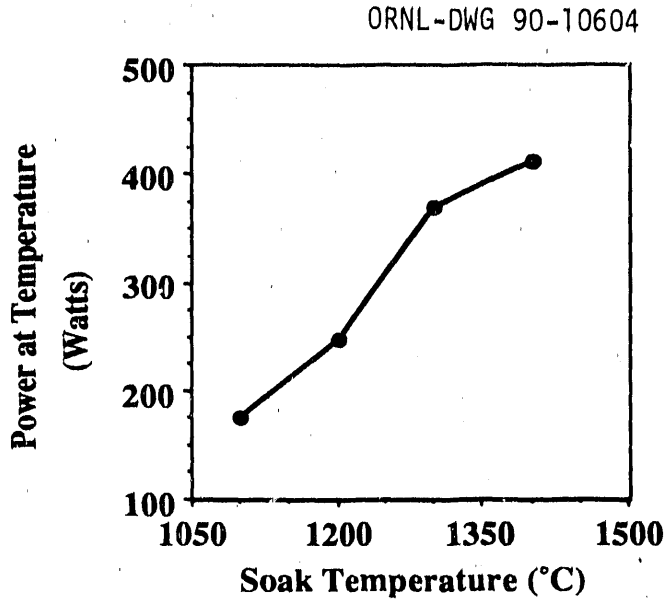

Figure 2. The power required to maintain a given temperature increased with increasing temperature for the GE1 furnace when firing $LaCrO_3$-based ceramics.x

The variation of peak and soak power with heating rate was not what was expected. Fig. 3 shows that the peak power and the soak power both decreased as the heating rate increased. One

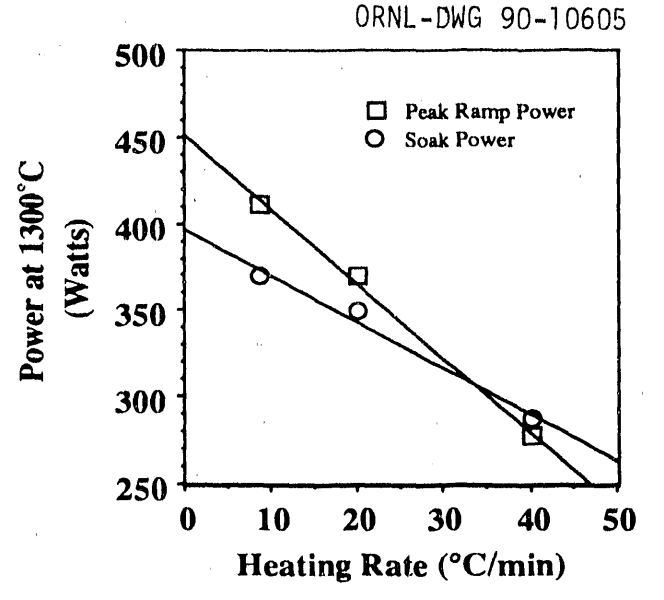

Figure 3. The peak ramp power and the soak power decreased with increasing heating rate for firing $LaCrO_3$-based ceramics in the GE1 microwave furnace.

would predict, based on conventional heating practice, that the peak power should increase as the heating rate increases; furthermore, one would predict that the soak power should be essentially independent of the heating rate. Also notice that the peak power level is higher than the soak power level for the slow heating rate, R2, but the peak power level is lower than the soak power level for the fast heating rate, R1.

The effects noted above can be explained as follows. In the microwave furnace, the sample is heated by dielectric heating within the sample; i.e., the part is self-heating. The sample, in turn, heats the insulation around it. At low temperature, the insulation does not interact with the microwaves in the furnace. As the insulation is heated by the sample, it starts to absorb some of the microwave power in the furnace and becomes part of the furnace load, in addition to the sample. As the furnace run proceeds, more of the insulation is heated by the sample, and consequently the load in the furnace increases. At a slow heating rate, a large portion of the insulation is heated by the time the soak temperature is reached because the insulation has been heated for a long time. Consequently, the microwave load in the furnace is large, and power required to heat the sample and insulation is high. At a fast heating rate, a smaller amount of the insulation is heated, the microwave load in the furnace is smaller, and the amount of power required to heat the sample and insulation is smaller.

SINTERING OF $LaCrO_3$-BASED CERAMICS

Sintering of $LaCrO_3$-based interconnect materials has shown promise. Figure 4 is a preliminary sintering curve for the composition $(La_{0.79}Ca_{0.2})(Cr_{0.9}Co_{0.1})O_3$. The nominal sintering temperature of this material is 1425 to 1450 °C under conventional conditions according to the manufacturer (HUA Assoc., Rolla, MO.). Under conventional conditions this material shows a terminal density of 93-94% td, which is what we observed in our microwave sintering tests, except at ≈150°C lower temperature, i.e., at 1300°C. This material shows tremendous promise for microwave sintering both in terms of the enhanced sintering and in terms of the ease with which we can fire it in the microwave furnace.

The microstructure of microwave-fired $(La_{0.79}Ca_{0.2})(Cr_{0.9}Co_{0.1})O_3$ consisted of a major phase of primary idiomorphic grains (primarily rectangular prisms) surrounded by an intergranular liquid phase, together with ≈6% porosity. The primary grains contained mainly La and Cr, as one would expect from a $LaCrO_3$ composition, with a small amount of Ca and Co. However, there was an interesting

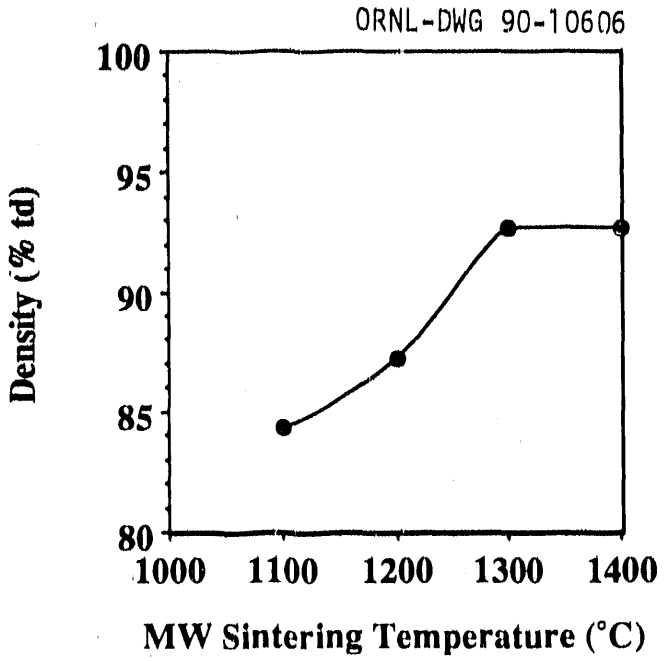

Figure 4. $(La_{0.79}Ca_{0.2})(Cr_{0.9}Co_{0.1})O_3$ sintered well in the GE1 microwave furnace. A nominal sintering temperature of 1300°C was observed, with a terminal density of ≈93% td.

feature to these grains. Most of them were "cored"; i.e., the center of the grains was rich in La and Cr, Table 1. The intergranular liquid phase was high in Co and Cr. Actually, there appear to be two different liquid phase compositions, as shown in Table 2. Composition 1, designated as areas 1 and 4,

Table 1. Electron Microprobe Analysis of Primary Grains in Microwave-Fired $(La_{0.79}Ca_{0.2})(Cr_{0.9}Co_{0.1})O_3$.

Element	Core (Counts)	Periphery (Counts)
La	12,100	10,000
Cr	12,000	11,000
Ca	2000	4000
Co	1000	1800

Table 2. Electron Microprobe Analysis of Intergranular Phases in Microwave-Fired $(La_{0.79}Ca_{0.2})(Cr_{0.9}Co_{0.1})O_3$

Area	Cobalt (Counts)	Chromium (Counts)
1	***2400***	***4600***
2	5300	1200
3	6000	800
4	***2300***	***5300***
5	6000	800

is high in Cr and low in Co. Composition 2, designated as areas 2,3, and 5, is high in Co and low in Cr. Calcium was relatively uniformly distributed across the microstructure, as determined from X-ray fluorescence maps. It was, however, specifically excluded from pockets of liquid phase that were high in Co. Additional detailed microprobe analyses are needed to determine the full extent of segregation of the elements during processing.

---

* Model Jet 342G-001, General Electric Co., Louisville, Kentucky.

† Micristar Model 828, Research Incorporated, Minneapolis, Minnesota.

‡ ARI, Inds. Inc., Addison, Illinois.

§ Yokagowa, Corp. of America, Newnan, Georgia.

¶ Zircar Products, Inc., Florida, N.Y.

** HUA Assoc., Rolla, Missouri.

INVESTIGATION OF PROPERTIES AND PERFORMANCE OF CERAMIC COMPOSITE COMPONENTS

K.L. Reifsnider, W.W. Stinchcomb, T.J. Dunyak

Materials Response Group
Engineering Science and Mechanics Department
Virginia Polytechnic Institute and State University
Blacksburg, Virginia 24061
(703) 961-5316

INTRODUCTION

The anticipated use of ceramic composites in high temperature structural applications requires the technical community to make the transition from properties of materials to the performance of engineering components. Making this transition requires comprehensive characterization and understanding (i.e., philosophy and rigorous modeling) of long-term behavior. For example, information from quasi-static tests, modulus of rupture tests, and fracture toughness tests is not sufficient to design a complex component such as a heat exchanger tube fabricated from anisotropic, fiber reinforced materials which may experience multiaxial stresses and elevated temperatures. The present research effort provides an experimental and analytical basis for the transition from properties to performance. In general, the program is a pioneering effort to make a first step beyond the limited characterization of small samples and coupons to the comprehensive mechanical characterization of complex engineering components such as ceramic composite tubes subjected to static and cyclic multiaxial loading and elevated temperature over various time periods.

OBJECTIVES AND APPROACH

The central objective of the present program is to develop an understanding of the mechanical behavior of advanced ceramic composites subjected to elevated temperature and dynamic (cyclic) loading, to develop a test system and test methods to obtain the properties and

performance information required to design engineering components made from ceramic composite materials, and to provide critical and comprehensive evaluations of such materials to material synthesizers and developers to support and enhance progress in ceramic composite material development. Specific objectives are given in Reference 1.

The approach to the program is designed to meet the objectives of the program through a series of four coordinated and complimentary tasks outlined in Table 1. Specific details of each task are given in Reference 1.

Table 1. Program Plan.

Schedule (Months)	1 (12 Months)	2 (12 Months)		3 (6 Months)
Task	1	2	3	4
Contruction of Test Device	Purchase of Test Frame; Design of Test Chamber and Grips	Construction of Room Temperature Device; Design of High Temp Equipment	Construction of High Temperature Device	Testing and Refinement
Quasi-static Room Temperature Characterization		Uniaxial Tension Tests	Tension-Compression Tests; Damage Analysis	Damage Analysis
Cyclic Room Temperature Characterization			Uniaxial Tension; Damage Analysis	Tension-Compression; Damage Analysis
High Temperature Characterization			Preliminary Tests; Quasi-static	Uniaxial Cyclic Damage Analysis Multiaxial Cyclic Tests *
Modeling	Literature Review	Identification of Failure Modes	Nondestructive Identification of Damage Modes	Formulations and Predictions
Planning of Investigations	Quasi-static Uniaxial Test Series	Uniaxial Cyclic Test Series	High Temperature Test Series	Verification Series; Future Work **

* Demonstration of multiaxial tests will be conducted during Task 4.

** Future work will include multiaxial, high temperature tests if the program is continued into Phase II.

DISCUSSION OF PREVIOUS WORK

Tasks 1 and 2 and portions of Task 3 were completed at the conclusion of the work period ending March 30, 1990. These tasks included:

- design, construction, installation, and acceptance testing of an Instron computer controlled, high stiffness biaxial test frame with hydraulic grips,
- design, fabrication, and evaluation of chopped graphite fiber (Hercules HMU-PVA-3k) / glass matrix (Corning CGW-7070) composite tubes,
- extensive literature reviews in the areas of test methods, nondestructive evaluation, failure mechanisms, and modeling of ceramic composites,
- investigation and application of nondestructive test methods to monitor the damage development process (Reference 2),
- completion of the room temperature, monotonic axial load test series, and planning of the room temperature, cyclic test series,
- development of a high temperature damage model based on the critical element concept.
- identification of future needs.

Each of these activities is discussed in detail in References 1, 3, 4, and 5.

DISCUSSION OF CURRENT ACTIVITIES

Current activities address the following topics:

- design of a second ceramic composite tube configuration,
- selection of a second ceramic composite material system,
- initiation of the room temperature, cyclic axial load test series,

- continued development and refinement of models to predict performance of ceramic composite components.

Each of these areas will be discussed in the following sections.

Specimen Design

The initial specimen consists of an eight inch long, dog bone shaped tube with an inside diameter of 1.0 inches. The length of the specimen is divided into five distinct regions: upstream and downstream uniform grip regions with a 1.5 inch outside diameter, a uniform gage section with a 1.2 inch outside diameter, and two transitions sections where the outside diameter tapers from 1.5 inches to 1.2 inches. The terms upstream and downstream refer to the axial flow direction of the injection molding compound relative to the gage section. The material flows into the upstream grip and transition sections, through the gage section, and into the downstream grip and transition sections. Different material states, particularly fiber orientations, were observed between the upstream and downstream regions. Therefore, the upstream and downstream orientations must be noted.

X-ray radiography was used to determine the state of the as-fabricated tubes. The results indicate that the fibers in the upstream and the test sections were oriented approximately parallel to the axis of the tubes. However, fibers in the downstream transition region were swirled to give a predominately off-axis orientation (Reference 2). In addition, regions of highly aligned fibers in the axial direction (termed knit lines) were observed in the upstream regions of the tube. Some knit lines extended through the gage section and contributed to the swirled fibers in the downstream transition region. The failure locations and failure surfaces of the tubes loaded in monotonic tension closely coincide with the structural details of the material in the downstream transition region. The critical failure modes consist of a combination of matrix cracks

transverse to the swirled fibers, shear failure parallel to the fibers, fiber pullouts and some fiber failures.

Two designs for a second generation tubular specimen have been proposed to eliminate the swirled fibers and transition section failures. The first design is an eight inch long, continuous fiber tube with a 1.5 inch outside diameter. Preforms will be filament wound with lay-ups of $[+\theta/-\theta/90]_s$ and $[+54_2/-54_2]_s$ where θ is the minimum angle that can be reliably wound. The second design is a tapered tube of the same length. A detailed finite element analysis will be conducted to decrease stress concentrations and enhance the potential for gage section failures.

Material Selection

The material system for the second generation ceramic composite tube is being changed to SiC/SiC to satisfy the requirements for many high performance, high temperature applications. The second generation continuously reinforced SiC/SiC tubular specimens will be fabricated by Oak Ridge National Laboratory using their filament winding and CVD processes.

Cyclic Test Series

The three graphite/glass tubes loaded in monotonic tension to failure had a tensile strength of 12.3 ± 0.5 ksi.

Four constant amplitude, cyclic axial load controlled tests will be conducted at $R = \sigma_{min}/\sigma_{max} = 0$ with maximum cyclic stresses (σ_{max}) of 50, 60, 70, and 80 percent of the monotonic tensile strength. Cyclic strains will be monitored using a 1.0 inch extensometer attached to the tubular specimens.

The computer controlled tests will be run at a cyclic frequency of 5 Hz using a block loading program. However, at pre-selected intervals, the cyclic frequency will be reduced to 0.05 Hz to acquire load and strain data for two continuous cycles. The 5 Hz loading will then

be automatically resumed. The load-strain data is processed, plotted, and stored for analysis.

Nondestructive evaluation (NDE) methods such as thermal/elastic stress imaging and acoustic emissions monitoring will be used to acquire damage related data during the cyclic tests.

The tubular specimen cycled at 60 percent of mean tensile strength survived 250k cycles. At approximately 150k cycles, a circumferencial crack was detected in the downstream transition region. The crack grew circumferentially with subsequent cycles. At 250k cycles, the crack extended approximately 120° around the circumference of the tube. The test has been halted and the specimen is being examined to characterize the damage. Cyclic loading will be resumed and will continue until fracture or one million cycles, whichever occurs first.

Modelling

Failure of composite materials due to monotonic and cyclic loading is a very complex and difficult problem to address. Unlike metals where failure is generally controlled by a single flaw, composite materials show a variety of failure modes and interaction between these modes which lead to failure. In addition, the internal stress state is highly dependent on the geometric configuration and the material. For injection molded components, such as ceramic composite tubes, the problem is further complicated by the highly non-uniform fiber distributions throughout the component.

Damage Development Model:

An approach is being developed to predict the damage development within an injection molded component and determine the effects of the damage on strength, stiffness and life of the component. Clearly, a progressive failure analysis is required in order to accurately model the progressive damage development. In addition, due to the complexity of the geometry and the nonuniform fiber orientations, the analysis must also be based on an approximation technique such as the finite element method. The solution technique parallels the ply

discount schemes developed for laminated polymeric composites except a failed element is discounted instead of a failed ply. The resulting approach can handle complex geometries, complex loadings, and local material property degradations. Although the methodology is developed for the general case of quasi-static and cyclic loading, the material data base to excercise or verify the cyclic loading applications is not yet available.

During execution, the stress state throughout the structure is determined via a finite element solution for each load step. The stress results are then checked for element failures using pre-selected criteria for monotonic and cyclic loadings. If element failures are predicted, the stiffness of the first failed element is degraded based on the predicted failure mode. The stress state is then re-calculated throughout the entire component, and the failure checks are repeated. Once the failure iteration procedure has been completed, the state of stress at the end of the load step is known. In addition, the change in the state of damage from the beginning of the load step to the end of the load step is also known.

The main advantage of this approach is the simplicity of a linear elastic analysis and the capability of the finite element method to handle complex problems. The same idea is being extended to consider the damage development and life prediction in layered composite materials. For the layered analyses, we degrade the ply properties of a failed ply as opposed to the properties of the entire element. In both cases, we can model the damage development throughout the life of the component.

Life Prediction Model:

Considerable progress has been made in the performance modeling using the "citical element concept" and the MRLife code developed by the Materials Response Group at Virginia Tech. It was decided to use the published data for a SiC/LAS-II composite, made by United Technologies, in an attempt to predict the remaining strength and life for several temperatures under cyclic tensile loading. The effort required the development of an improved scheme for the inclusion of

creep rupture effects on the material strength parameters that enter into the model, as a function of load level, temperture, and time. Although this model development effort is by no means complete, the effort was intended to demonstrate the feasibility of the modeling approach at this point of development.

For our high temperature application of the model, state of strength in the critical element is a function of the number of cycles (or of generalized time) since the degradation of strength will generally accompany sustained or cyclic long-term loading. A typical and important example of that type of degradation is the phenomenon generally called "creep rupture". In many instances, this kind of behavior is a "misnomer" in the sense that chemical and thermodynamic processes such as oxidation and chemical attack may be the physical source of such rupture events rather than creep in the classical sence. In particular, we choose our example for such a situation. We imagine that a creep-rupture test has been done on unidirectional material under conditions which correspond to service environments and service times. These data produce a measured strength reduction, ΔS_m, a reference time over which that reduction occured, τ_{ref}, and a stress which was applied over that period of time, σ_{ref}, for this choice of conditions. Then for other applied conditions of stress and time, we must determine the relationship shown below.

$$\Delta(\text{strength}) = f\left[\frac{\sigma}{\sigma_{ref}}\right] g\left[\frac{t}{\tau_{ref}}\right] \Delta S_m \qquad (1)$$

where the functions f and g which scale the applied conditions to those for which data were measured must be determined form laboratory experiments or from representations of the thermodynamic processes which occur. In addition, the degradation must be scaled to account for the influence of temperature on the creep rupture process. This scaling factor must also come from experimental data or from understandings established in the literature. As it happens, for many thermal activation processes, equations such as the following relationships can be used,

$$(\text{scale factor}) = A\left[\frac{T_1 - B}{C - T_1}\right] \qquad (2)$$

where the constants A, B, and C are material constants. The scale factor determined as indicated in equation (2) is then used to establish a strength reduction ratio (in normalized form) as shown in equation (3).

$$(\text{reduction ratio}) = 1 + (\Delta - 1) * (\text{scale factor}) \qquad (3)$$

This strength reduction ratio, in turn, multiples the appropiate material strength trensors, X_{ij}, that appear in the local strength function, S_u. In instances where strength reductions in different directions are different, several strength reduction ratios must be determined. However, if the strength in a given direction is known to be controlling (such as the strength in the fiber direction), and the strength reduction associated with creep rupture is measure in that direction to determine the constants in equations (1) and (2), then only one strength ratio may be necessary. For the calculations which have been made to date with the existing version of our citical element code, only one strength reduction has been used.

The demonstration example was run for an LAS-II glass-ceramic matrix material reinforced with silicon carbibe fibers (Nicalon), with a volume fraction of fibers between 45 and 50 percent, as reported by Prewo (Reference 6). Prewo reports somewhat scattered data for creep-rupture life at several temperatures, and limited data for residual strength at those temperatures under static loading. The creep-rupture data were used to estimate the parameters in equations (1) and (2). Prewo also reports some fatigue data at elevated temperatures. Our objective was to use the creep-rupture expression in our model, and attempt to predict the life of the materials under combined cyclic loading and creep-rupture conditions at several elevated temperatures. The properties used in our predictions are as follows:

Long. tensile str:	761 MPa	Trans. tensile str:	20 MPa
Trans. compressive str:	100 MPa	Shear strength:	100 MPa
Longitudinal modulus:	118 GPa	Transverse Modulus:	30 GPa
Shear Modulus:	20.9 GPa	Poisson's ratio:	0.28

A, B, C in equation (2): 0.0764, 298, and 1764 respectively.

The last experimental input required for our calculation of remaining strength using the critical element equations is a representation of the life, N. For this purpose, we used the room temperature, ply-level S-N fatigue strength-life equation for constant amplitude fatigue of unidirectional material loaded in the direction of the fibers. In normalized form, such as a relationship may take on the form

$$\frac{S_a}{S_u} = A_n - B_n (\log N)^{P_n} \qquad (4)$$

where S_a is the function which specifies the local stress state, S_u is the corresponding function which specifies the local strength state in the critical element, and the constants A_n, B_n, and P_n are material constants which express the rate of degradation associated with the unidirectional material under cyclic loading. N, the life of the element under constant conditions, can be solved for from equation (4) and entered into our strength reduction equation. Of course, the life of the critical element will not be constant because the state of stress, state of material, and possibly the material constants may be functions of the number of cycles of load applicacation or of the generalized time involved in the long-term behavior. However, relationships such as equation (4) may be easily determined in the laboratory, and may be used at the ply level as we are discussing for the current demonstrative example. For this application, the constants in equation (4) were found to be A_n=1.0128, B_n=0.04135, and P_n=0.7713.

Figure 1 presents results for the prediction of behavior of SiC-reinfroced LAS-II glass composites, at elevated temperatures which cause oxidation and degradation of the composites. The results for

600 and 900°C represent the combined effect of the temperature degradation and the damage caused by cyclic mechanical loading. Figure 1 shows a variety of predicted S-N curves for several temperatures above and below the 600 and 900°C results, for which some data are available. The predicted data agree remarkably well with the available data. Moreover, the other results allow the researcher and the engineer to anticipate behavior under a variety of other temperatures with some confidence. These data are very difficult (expensive and time consuming) to get. The present model, which is mechanistic, can provide guidance in the prediction of results under many such conditions, and can also provide guidance in the planning of tests to obtain data which may be critical for finalization of a design.

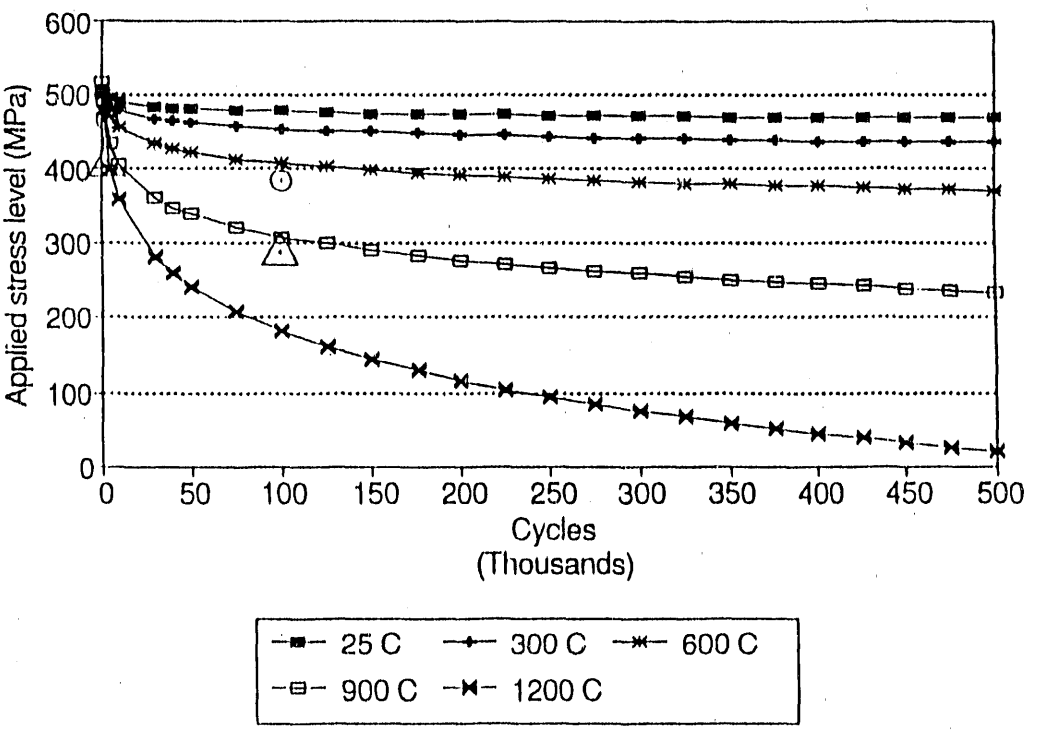

Figure 1. Predicted curves for fatigue strength vs. life for SiC-reinforced LAS-II glass composites under tension-tension cyclic loading for several different temperatures, compared with several different data points at 600°C (circles) and 900°C (triangles) [6].

REFERENCES

1. K. L. Reifsnider, W. W. Stinchcomb, and T. J. Dunyak; "VPI-1 - Investigation of Properties and Performance of Ceramic Composite Components"; ORNL/FMP-88/1 AR&TD Fossil Energy Material Program Semiannual Progress Report for Period Ending March 31, 1988.

2. T. J. Dunyak, K. L. Reifsnider, and W. W. Stinchcomb; Evaluation of NDE Methods as Applied to Ceramic Composite Tubes; ORNL/Sub/87-SA946/01; April, 1990.

3. K. L. Reifsnider, W. W. Stinchcomb, and T. J. Dunyak; "VPI-1 - Investigation of Properties and Performance of Ceramic Composite Components"; ORNL/FMP-88/2 AR&TD Fossil Energy Material Program Semiannual Progress Report for Period Ending September 30, 1988.

4. K. L. Reifsnider, W. W. Stinchcomb, and T. J. Dunyak; "VPI-1 - Investigation of Properties and Performance of Ceramic Composite Components"; ORNL/FMP-89/1 AR&TD Fossil Energy Material Program Semiannual Progress Report for Period Ending March 31, 1989.

5. K. L. Reifsnider, W. W. Stinchcomb, and T. J. Dunyak; "VPI-1 - Investigation of Properties and Performance of Ceramic Composite Components"; ORNL/FMP-89/2 AR&TD Fossil Energy Material Program Semiannual Progress Report for Period Ending September 30, 1989.

6. Prewo, K. M.; "Fatigue and Stress Rupture of Silicon Carbide Fibre-reinforced Glass-Ceramics", Journal of Materials Science; Vol 22 (1987), pp 2695-2701.

MECHANICAL PROPERTIES TESTING OF CERAMIC FIBER-CERAMIC MATRIX COMPOSITES

J. Sankar, A. D. Kelkar, and R. Vaidyanathan

Dept. Of Mechanical Engineering
North Carolina A & T State University
Greensboro, NC 27411

ABSTRACT

Ceramic fiber reinforced Ceramic matrix composites fabricated by forced chemical vapor infiltration (CVI) have recently received a lot of attention for use in high temperature structural applications because of their high strength and toughness. The effect of the reinforcement and the interfacial bond of SiC fiber reinforced SiC matrix systems on the tensile strength at temperatures up to 1000 °C are being investigated in this research program. Due to the short length and the short gage length of this sample, there is a need for precision alignment in tensile tests of this material. Some of the approaches that are presently considered for the tension testing of the SiC fiber SiC matrix composites are being presented in this paper. The laser telemetric system for measuring strain shows that it is stable at temperatures up to 1000 °C. The paper also presents the initial tension test results of the system at two different layups, namely $(0/90/\pm45)_{repeat}$ and $(0/30/60)_{repeat}$. Fractography analysis shows a lot of pull out for the fibers, showing strain tolerant behavior of this composite.

INTRODUCTION

Ceramic fiber-ceramic matrix composites fabricated by forced chemical vapor infiltration (CVI) are currently being developed as practical engineering materials because of their potential high strength and toughness, especially at elevated temperatures. The goals of this project are to expand the mechanical properties data base for composites fabricated by forced CVI. The infiltration method used in the current study has been developed at the Oak Ridge National Laboratory(ORNL) combining a thermal gradient and forced-flow approach. The details of the process and experimental procedures have been discussed in detail elsewhere[1]. The advantages of this technique is that it results in significantly reduced infiltration times, as compared with other systems which depend only on diffusion.

In this program, SiC fiber reinforced SiC matrix system developed through ORNL CVI process will be investigated. The effect of the reinforcement and the interfacial bond of the composite on the tensile strength, thermal shock resistance, oxidation resistance, and tensile strength during cyclic loading, at temperatures up to 1000 °C, shall be investigated in the proposed work.

The effort comprises of the following tasks:

Task 1 - Tensile Strength - The objective of this task is to determine the Uniaxial tensile strength of SiC Fiber-SiC Matrix composite from room temperature up to 1000 °C. Typical tensile stress-strain curves for this material shall be determined at the test temperatures.

Task 2 - Cyclic loading - The response of the SiC fiber-SiC matrix composite to cyclic loading is of considerable interest. The cyclic loading shall consist of loading the sample to about 10 % of the anticipated total load at failure and removing the load. A tensile curve shall be determined by loading the samples to about 10 % and relieve the stress, reload the sample to about 20 % and relieve the stress, etc. until failure.

Task 3 - Thermal Shock resistance - Fiber reinforced composites are exposed to thermal shock during service. Therefore, the response of the material to thermal shock shall be determined. The exact details of the test procedure shall be determined at a later date in consultation with the Program Manager after completing Tasks 1 and 2.

Task 4 - Oxidation Resistance - Fiber reinforced composites are exposed to extended service in oxidizing atmospheres. Therefore, the response of the material to oxidation shall be determined. The exact details of the test procedure here again shall be determined at a later date in consultation with the Program Manager after completing Tasks 1 and 2.

TENSILE STRENGTH CHARACTERIZATION

The tensile strength characterization consisted of the following areas of concentration.

1. Design of the specimen configuration for the SiC fiber - SiC matrix composite and the choice of a suitable laminate lay up to obtain an optimum strength and strain tolerant behavior.

2. Design of a gripping system for the above specimen configuration in the existing MTS 880 hydraulic testing machine at the N. C. A & T State University.

3. Laser extensometer characterization for strain measurements accuracy at elevated temperatures up to 1000 °C, and

4. Tensile testing and fractography using Scanning Electron Microscope (SEM).

Specimen Details

The details of the ORNL CVI process have been reported previously[1]. This process forms the matrix by a comparatively low-stress low-temperature chemical vapor deposition (CVD) process, avoiding many of the problems associated with conventional ceramic processing. Two types of fiber lay ups (orientations) have been tried out so far. Fibrous preforms in the shape of disks 76 to 78 mm in diameter by 13 mm thick were fabricated at ORNL. These were done by stacking and compressing multiple layers of a plain weave SiC cloth (Nicalon fibers) in a graphite holder (alternate layers oriented at 0° and 45° in the first case and alternate layers oriented at 0°-30°-60° intervals in the second case), yielding a body containing approximately 40 vol% fibers. The fibers in the preforms were then precoated with a thin (≅ 1 μm) layer of pyrolytic carbon to enhance fiber pull out, by infiltrating with propylene at 1100 °C for 2 h at ≅ 3 kPa. Following the carbon coating, the preforms were infiltrated with SiC to form the matrix phase of the composite. The resulting density for the two different lay ups were 75% and 85% respectively. Tensile specimens in the form of straight bars and with a simple neck as shown in Figure 1 were used for the tensile characterization. All tensile bar specimens were further over coated with 30 to 50 microns of SiC.

The lay up that is expected to give the best result is the $[0/90/\pm45]_{symmetric}$ lay up , from classical laminate theory, which gives

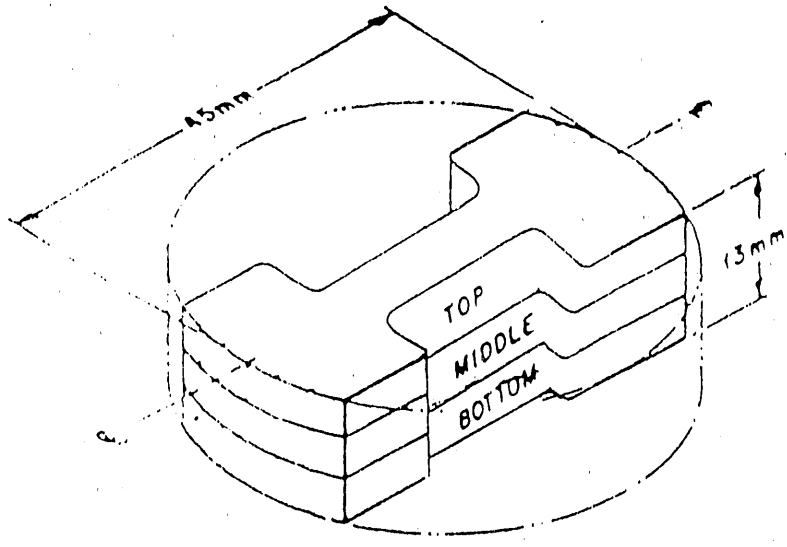

Figure 1. Tensile specimen configuration used (necked)

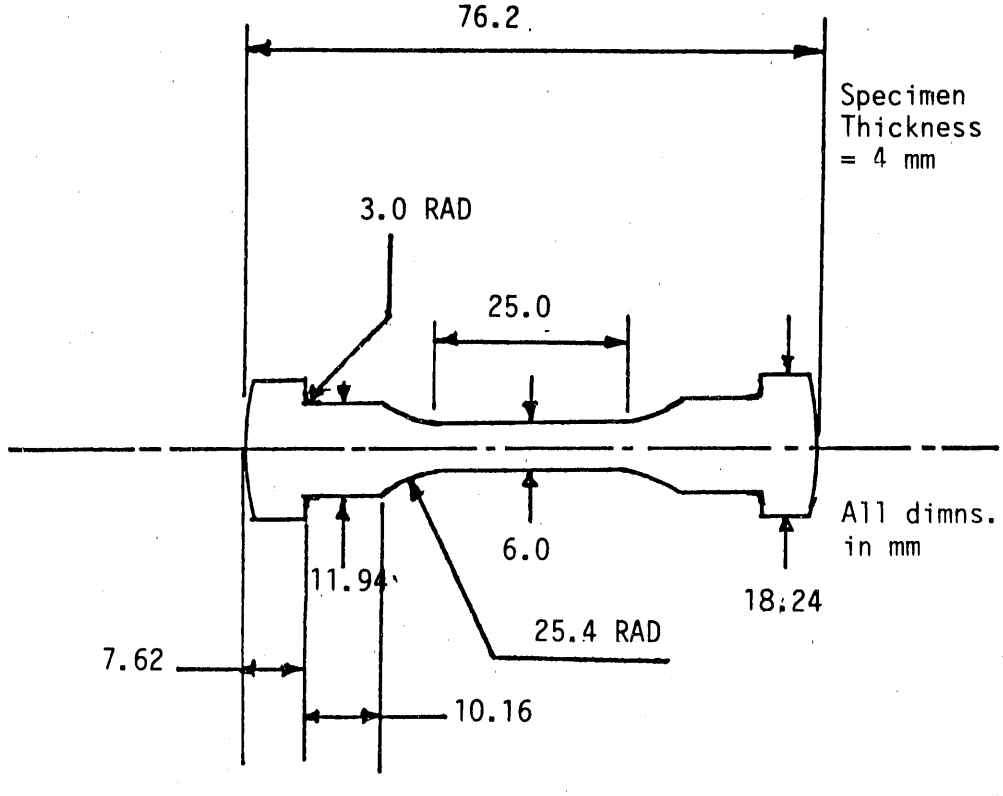

Figure 2. Suggested Specimen Configuration for $(0/90/\pm45)_s$ lay up sample

quasi-isotropic properties, so the sample can be necked. This design of the tensile test specimen configuration is shown in Figure 2 and will be tried in the future. This has been done considering the 3 inch dia disk shaped composite specimens fabricated by ORNL. The shape of the specimen was designed similar to the test specimen configuration used in an earlier work[2], where the radius change near the gage section resulted in avoiding a stress concentration near the gripping position. As may be observed from the figure, the tensile specimen has a gage section of 25 mm (.984 inches).

Gripping System

The gripping system used in an earlier work[2] is expected to be used to grip the composite tensile specimen. The only modification required is expected to be in the gripping wedges. As the cylindrical grip holder is threaded into the pull rod, two small tapered double split collar wedges inside will grip and hold the flat ends of the composite specimen. However, it is expected that tabs need to be attached to the samples, to prevent their crushing during the tensile testing. For room temperature tests, an available paste adhesive (Epon 828 Resin and Epon V-40 hardener from Shell Corporation in suitable mixes) will be used, which does not need any pressure to be applied during the attachment procedure. For high temperature tests, it is necessary to use a high temperature adhesive like Ceramabond.

Laser Extensometry

The accuracy of the laser extensometer for strain measurements from room temperature to very high temperatures was studied by comparing a gap measured by the laser extensometer against the same gap as measured by a standard micrometer which was located outside the furnace. A pair of alumina rods were used, one of which was held in the standard micrometer. The gap between the tips of the two rods could be increased or decreased by turning the micrometer wheel. Calibration of the laser system was done

at room temperature, 500, 800, 1000, and 1100 °C. Though the maximum test temperatures are expected to reach only 1000 °C, tests were conducted at higher temperatures also to evaluate the stability of the laser system over a long period of time above 1000 °C.

It was observed that the gaps measured simultaneously by the laser system and the standard micrometer matched up to a temperature of 1100 °C. Similar readings were obtained at 500, 800, and 1000 °C, indicating that the laser extensometer is an accurate strain measurement technique. Refer to the previous semi-annual report for further details.

Tensile Testing and Fractography Results

For obtaining an initial idea of the strength of the SiC fiber - SiC matrix composite, 3 samples with the (0/90/±45) fiber layup and 5 samples with the (0-30-60) fiber layup (3 straight and 2 necked samples) were tested in a MTS 810 machine, the samples being gripped by an available mechanical wedge grip. Due to the small size of the samples, it was impossible to attach an extensometer to the samples for the measurement of the strain. However, it was possible to observe the high amount of strain that the samples underwent before the final failure. The initial test results of these samples are given in Table 1. The (0/90/±45) lay up samples exhibited an average tensile strength of 136 MPa (19.72 Ksi) while the (0-30-60) lay up samples had a much higher average strength of 169 MPa (24.56 Ksi) for the straight tensile bars and 182 MPa (26.32 Ksi) for the necked samples. The average tensile strength of the (0-30-60) lay up samples is lower than the initial result of approximately 230 MPa obtained on one sample at ORNL previously[1]. The bending of the sample in the mechanical wedge grip in the current set up may have contributed to the reduction in the tensile strength. With the new gripping mechanism discussed previously along with the new tensile specimen configuration should help in avoiding this problem.

Initial fractography work using SEM done on the samples are given in Figures 3 through 7. Extensive amount of fiber pull out can be observed in Figure 4. Figure 5 shows the matrix infiltration process in the (0-30-60)

Lay Up	Average Tensile strength
(0/90/±45) repeat	136 MPa (19.72 Ksi)
(0-30-60) repeat (Flat samples)	169 MPa (24.56 Ksi)
(0-30-60) repeat (Necked samples)	182 MPa (26.32 Ksi)

Table 1. Preliminary Room Temperature tensile test results

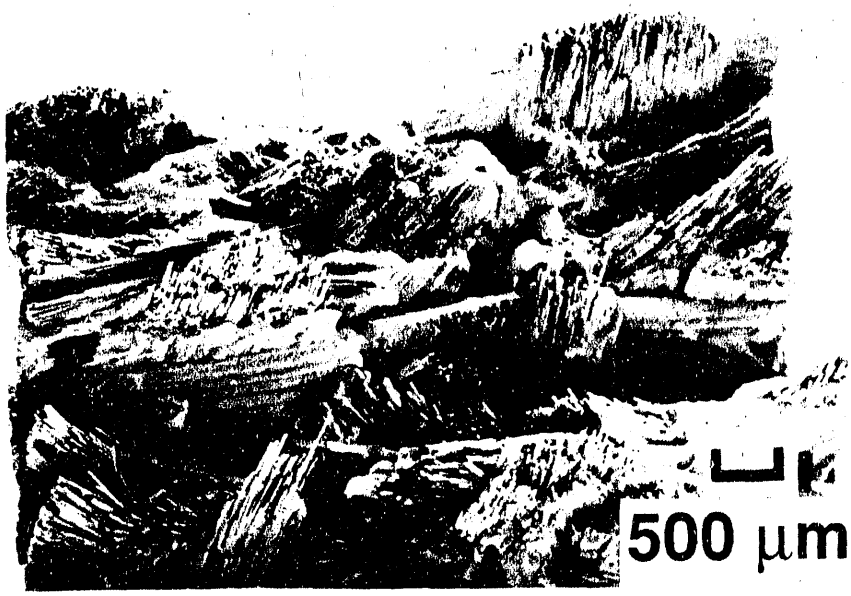

Figure 3. Overall fracture surface of (0-30-60) lay up sample.

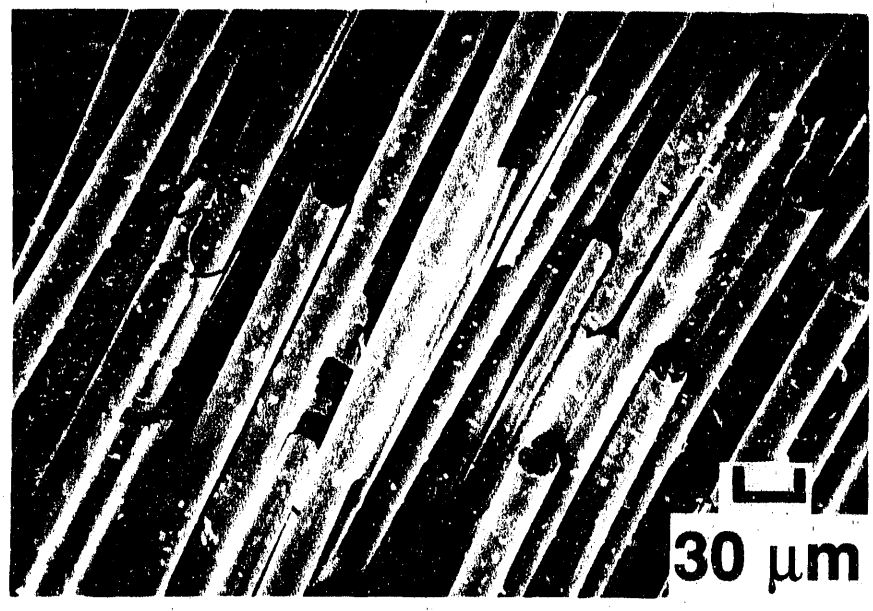

Figure 4. Fiber pull out in the 0° fiber orientation of the (0-30-60) lay up sample.

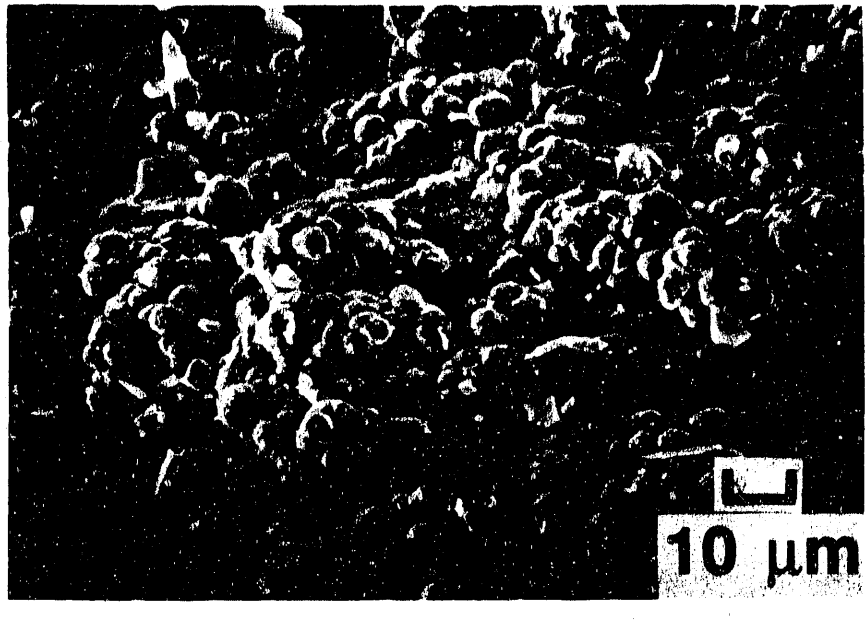

Figure 5. Matrix infiltration process in the (0-30-60) lay up sample.

lay up samples. Figure 6 shows the pyrolitic carbon coating on the surface of the fibers(shown by arrow), which contributes to the fiber pull out in this composite system, along with the high amount of strain tolerance. Figure 7 shows the matrix cracking in this material.

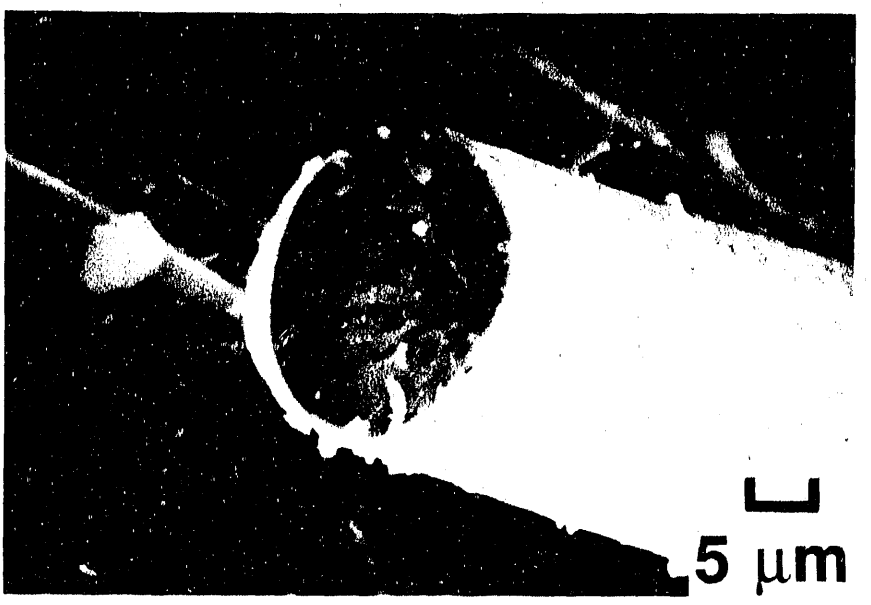

Figure 6. Pyrolitic carbon coating on the fiber surface (arrowed).

Figure 7. Matrix cracking in SiC-SiC material.

CONCLUSIONS

Based on the above results, the following could be concluded.

1. Initial studies indicate that the average room temperature tensile strength of (0-30-60) lay up composite samples are higher than the average tensile strength of the (0/90/±45) lay up composite samples.

2. All the composite samples showed high amount of strain tolerance.

3. Fractography studies indicate clean pull out of fibers oriented in all the directions.

4. Further tests for (0/90/±45) symmetric lay up composite samples are to be conducted, and the results are to be compared with the results obtained for the lay ups already tested.

REFERENCES

1. A. J. Caputo, D. P. Stinton, R. A. Lowden, and T. M. Besmann, "Fiber Reinforced SiC Composites with Improved Mechanical Properties", American Cer. Soc. Bull., 66 [2] 368-72 (1987).

2. J. Sankar, A. D. Kelkar, A. Sinha, and K. C. Liu, "Strength and Fatigue of Silicon Nitride in Uniaxial Tension", paper presented at the 26th Automotive Technology Development Contractor's Coordination meeting, Dearborn, Michigan, October 1988.

INTERFACIAL AND BULK PROPERTIES OF CONTINUOUS FIBER-REINFORCED CERAMIC MATRIX COMPOSITES

J. D. Bright, C. W. Griffin, S. Y. Limaye and D. W. Richerson

Ceramatec, Inc.
2425 South 900 West
Salt Lake City, Utah 84119

and

D. K. Shetty

Department of Materials Science and Engineering
University of Utah
Salt Lake City, Utah 84112

ABSTRACT

SiC monofilament was used to reinforce a modified NZP (sodium zirconium phosphate, $NaZr_2P_3O_{12}$) matrix optimized for moderate thermal expansion and high temperature stability. Unidirectional composites containing 23-33 v% SiC filaments were fabricated by filament winding, slurry coating and hot pressing. The composites were characterized by measuring elastic modulus and matrix-cracking stress in three-point bending and interface sliding friction stress in single-fiber pushout test. The matrix-cracking stress exhibited large variation (50-380 MPa) and was found to correlate with the sliding friction stress. The dependence of the matrix-cracking stress on the interfacial friction stress was compared to theoretical predictions for steady-state cracking for large cracks.

INTRODUCTION

Ceramic matrices reinforced with ceramic fibers can exhibit high matrix-cracking stresses and large inelastic strains before final failure. These pseudo-yield failure characteristics have been shown in several ceramic composites including SiC-reinforced LAS (lithium aluminosilicate) glass-ceramics[1,2] and SiC-reinforced RBSN (reaction-bonded Si_3N_4)[3]. Material requirements to achieve these composite failure characteristics

include high strength, modulus and volume fraction for the fibers, high fracture toughness, low elastic modulus and low coefficient of thermal expansion for the matrix and a fiber-matrix interface with preferably modest frictional bonding[2]. Thermochemical and thermomechanical compatibility to avoid excessive chemical and frictional bonding at the interface, modest processing temperatures to minimize degradation of fiber strength and oxidation resistance to maintain the integrity of the interface during high-temperature exposure in air are some of the key considerations in designing a ceramic-matrix composite.

Ceramatec Inc. has been involved in the development of a class of materials based on sodium zirconium phosphate (NZP, $NaZr_2P_3O_{12}$) and its crystal structure analogs to exploit their known low thermal expansion behavior. NZP and its crystal analogs have corner-linked polyhedral network structure that permits various ionic substitutions[4]. With appropriate ionic substitutions, it has been possible to produce NZP materials with an average coefficient of thermal expansion of 0.3×10^{-6} /C over 0 - 1200 C range. In addition to their low thermal expansion, NZP materials also exhibit low thermal expansion anisotropy, low thermal conductivity and high-temperature stability.

Proper matching of the thermal expansion of fibers and matrices is important to avoid high residual stresses that can lead to matrix cracking on cooling from the fabrication temperature (matrix thermal expansion, $\alpha_m > \alpha_f$, fiber thermal expansion) or to fiber-matrix debonding and a very low interfacial sliding friction ($\alpha_f > \alpha_m$). The ability to control the thermal expansion characteristics of NZP materials and their chemical compatibility with such refractory ceramic fibers as SiC stimulated the present study on SiC-reinforced NZP matrix composites. This paper focuses on the fabrication and bulk mechanical properties, matrix cracking stress (σ_c) and elastic modulus (E), and interfacial properties of these composites. A single fiber pushout test technique developed by Bright et al.[5] was used to evaluate interfacial sliding friction stress (τ_f). The matrix-cracking stress exhibited large variation and this variation was found to correlate with the interfacial sliding friction stress. The measured variation of the matrix cracking stress is compared with available theoretical predictions for frictionally-bonded interfaces. The variation of the interfacial sliding friction stress is examined in terms of the effect of thermal expansion mismatch between the SiC filament and the NZP matrix on the fiber clamping stress. Thermal expansion variation in the NZP matrices is also discussed with respect to the processing conditions and phase content of the matrices.

EXPERIMENTAL PROCEDURE

Unidirectional SiC-NZP composites were fabricated by first winding the SiC monofilament on a 20 cm diameter mandrel using the fiber winding apparatus designed at Ceramatec. A slurry consisting of the NZP powder and an organic binder was sprayed on the filament while it was still wrapped around the mandrel. After drying, the coated fiber tape was removed from the drum, cut into squares and stacked in a square graphite die, 44 x 44 mm, in dimensions. In addition to the fiber-reinforced composites, monolithic billets of the NZP were also hot pressed at the same time as the composite billets. The composite and the matrix billets were hot pressed at 1300 C for 20 minutes in argon atmosphere.

Densities of the hot-pressed billets were measured by the immersion technique§. The hot pressed billets were cut into bars, each approximately 3 x 4 x 44 mm, and surface ground. One pushout specimen, 5 mm in thickness, was cut from each composite bar prior to any mechanical testing of the composites. The fiber volume fraction was determined by counting the fibers in each bar and measuring the cross sectional area. The coefficients of thermal expansion for the matrix materials were measured using a high-temperature dilatometer.

The matrix-cracking stress and the elastic modulus of the composites were measured in three-point bending using strain gauges attached to the tensile surface of the bars. Matrix cracking was indicated by a discontinuous jump in strain in a load-strain record. Optical observations confirmed that this strain discontinuity was associated with the propagation of a crack in the matrix that was bridged by unbroken fibers. Matrix cracking was also indicated by a sharp decrease of the load on the load-time record. The two records were used to confirm the matrix-cracking load. Elastic modulus was determined from the linear portion of the load-strain record up to the matrix cracking load in the case of the composites or up to fracture for the matrix materials.

Pushout tests were carried out on a universal testing machine using micropositioners to support composite specimens and position individual filaments under a specially fabricated carbide tool mounted on the cross head of the machine. The test apparatus and procedure used have been discussed by Bright et al.[5]. The following linear approximations were employed to calculate shear strength and sliding friction stress from the respective pushout loads measured on single pushout specimens :

---

§ ASTM Standard C373-72.

$$\tau_d = \frac{P_d}{\pi d_f L} \quad (1)$$

$$\tau_f = \frac{P_{max}}{\pi d_f L} \quad (2)$$

In Equations 1 and 2, d_f and L are filament diameter and embedded filament length, respectively. P_d and P_{max} were identified after the method of Bright et al. Average values of τ_d and τ_f were calculated from pushout test results on at least five filaments and these average interfacial properties were then correlated with the matrix cracking stress and the elastic modulus measured on the same composite test bar. To examine the possible role of thermal expansion of the matrix material on the interfacial and composite properties, the coefficient of thermal expansion measured on the corresponding matrix billet was used to correlate with τ_d and τ_f or σ_c.

High temperature mechanical properties were measured on test bars in three point bending. Specimens were evaluated at temperatures of 25, 1000, 1200 and 1300°C in an air environment. Specimens were characterized for matrix cracking stress and ultimate strength.

EXPERIMENTAL RESULTS

Table 1 lists the average properties of the NZP matrix under the billet designation M. All the billets densified to near theoretical density (3.42 g/cc). The elastic modulus and the bend strengths did not vary significantly among the five billets. The average elastic modulus and three-point bend strength (listed under σ_c) were 97.4 GPa and 209 MPa, respectively. The numbers in parenthesis in Table 1 indicate the standard deviations for measurements on each billet. The average coefficient of linear thermal expansion over a temperature range of 100 - 1100 C varied from a low value of 2.7 to 4.7 x 10^{-6} /C.

Unlike the matrix monoliths, properties of the SiC-NZP composites varied significantly among the different billets (designated by C in Table 1). These property variations occurred despite using the same NZP composition for the matrix and nominally identical conditions for fabrication

Figure 1 shows two representative stress - displacement relations obtained in three-point bending on test bars sampled from a low strength (Billet # 228C) and a high strength

TABLE 1. Physical and Mechanical Properties of NZP Monoliths and SiC-NZP Composites

Billet	V_f	Density (g/cc)	α (10^{-6}/C)	E (GPa)	σ_c (MPa)	σ_u (MPa)	τ_d (MPa)	τ_f (MPa)
228M	0	3.40	3.0	104 (2)	208 (9)	-	-	-
228C	24.2	3.28	-	85 (19)	70 (18)	141 (43)	0.5 (0.3)	0.5 (0.4)
238M	0	3.40	3.5	93 (6)	205 (19)	-	-	-
238C	26.7	3.26	-	136 (5)	305 (13)	339 (51)	ND	0.74 (0.11)
242M	0	3.40	4.7	93 (4)	195 (31)	-	-	-
242C	22.9	3.26	-	127 (13)	340 (37)	489 (74)	1.53 (0.43)	1.23 (0.52)
245M	0	3.41	3.1	103 (8)	220 (23)	-	-	-
245C	30.0	3.21	-	90 (14)	74 (11)	194 (14)	0.58 (0.24)	0.17 (0.03)
251M	0	3.41	2.7	94 (4)	217 (10)	-	-	-
251C	32.8	3.28	-	140 (8)	144 (47)	211 (60)	ND	0.15 (0.05)

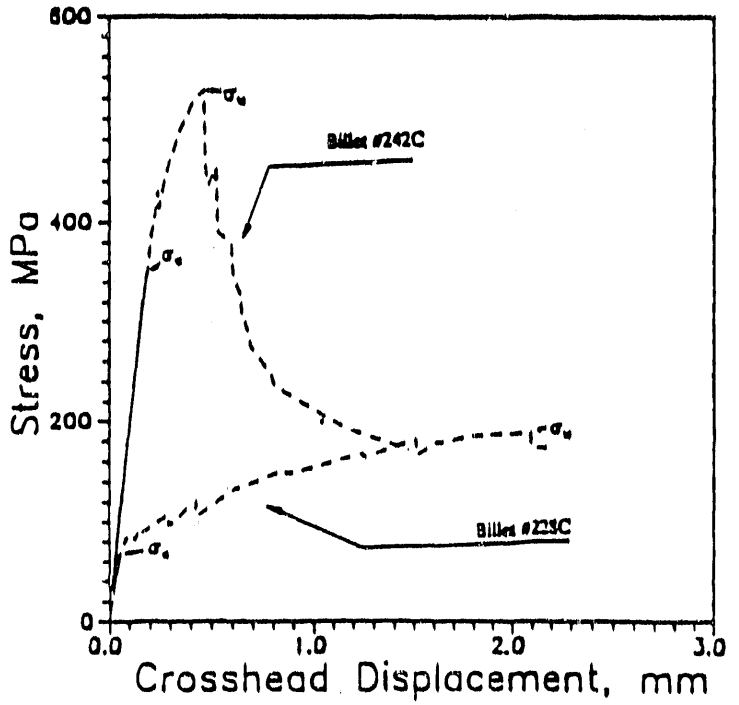

Figure 1. Representative Stress - Cross Head Displacement Plots Obtained in Three-Point Bending of SiC-NZP Composite Specimens Sampled From A High-Strength and A Low-Strength Billet.

composite billet (Billet # 242C). It should be noted in Figure 1 that the stresses plotted are the nominal elastic stresses for bending of beams. This is accurate up to the matrix cracking stress. Therefore, the stress-displacement lines are shown as solid lines up to σ_c. Above the matrix cracking stress, load redistribution occurs on account of damage in the tensile section of the beam in the form of matrix cracks and, therefore, the stresses calculated based on elastic bending formula are inaccurate[2]. For this reason, the stress-displacement plots are indicated by dotted lines and the ultimate strengths, σ_u, listed in Table 1 are nominal maximum stress values. It is evident from Figure 1 and Table 1 that the first matrix-cracking stress for the composite can be significantly higher (σ_c = 340 MPa) or lower (σ_c = 70 MPa) than the fracture stress of the unreinforced NZP matrix (σ_f ~ 200 MPa). Stress-displacement relations in Figure 1 also show other differences between the billets in addition to the marked difference in the matrix cracking stress. The low-strength billet showed a gradually rising load-displacement curve with the maximum load occurring at a large displacement (~ 2 mm). The load-displacement curve for the high strength billet showed a rapid rise, a peak load corresponding to σ_u and then a gradual but significant decrease in the load.

The elastic modulus of the composites varied from 85 to 140 GPa. All the measured values were less than the values expected from rule of mixtures for uniaxial composites. The measured values as fractions of the expected theoretical values ranged from 0.46 to 0.73. It is interesting to note in Table 1 that the low elastic moduli were obtained in composites that also showed low matrix-cracking stresses, while the high fractions were associated with the high-strength composites.

Interfacial Properties of the Composites

Table 1 lists the shear strengths and the sliding friction stresses estimated from the single fiber pushout tests. A clear debonding event was not always detected in the pushout tests and, therefore, shear strength is not listed for two billets. The measured sliding friction stress ranged from a low value of 0.15 to 1.23 MPa. These values are low compared to reported sliding friction stress measurements in some glass and glass-ceramic matrix composites[5,6]. Figure 2. shows that despite the low magnitude of the sliding friction stress, there is an approximate linear correlation with the linear coefficient of thermal expansion of the NZP matrix. The significance of this linear correlation and of the

extrapolated matrix thermal expansion at which the sliding friction stress approaches zero will be addressed in the discussion section.

Correlation Between Matrix-Cracking Stress and Sliding Friction Stress

Figure 3 shows a plot of the matrix-cracking stress versus the sliding friction stress for the SiC-NZP composites. Matrix-cracking stresses measured on individual composite test bars are plotted versus the average sliding friction stress measured on the pushout specimen sampled from the test bars. The different symbols correspond to different billets. The data points, therefore, illustrate the variation in the properties among the test bars from a given billet as well as the variation among the billets. Despite the large scatter Figure 3 does indicate a strong sensitivity of the matrix cracking stress to the interfacial sliding friction stress.

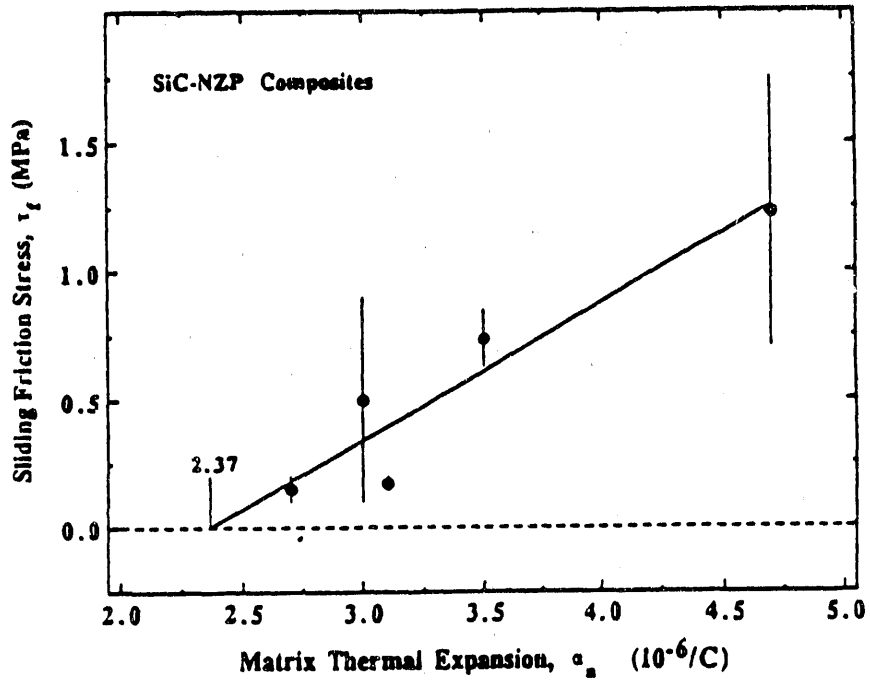

Figure 2. Linear Correlation Between Sliding Friction Stress (τ_f) and Coefficient of Thermal Expansion of the Matrix (α_m) in SiC-NZP Composites.

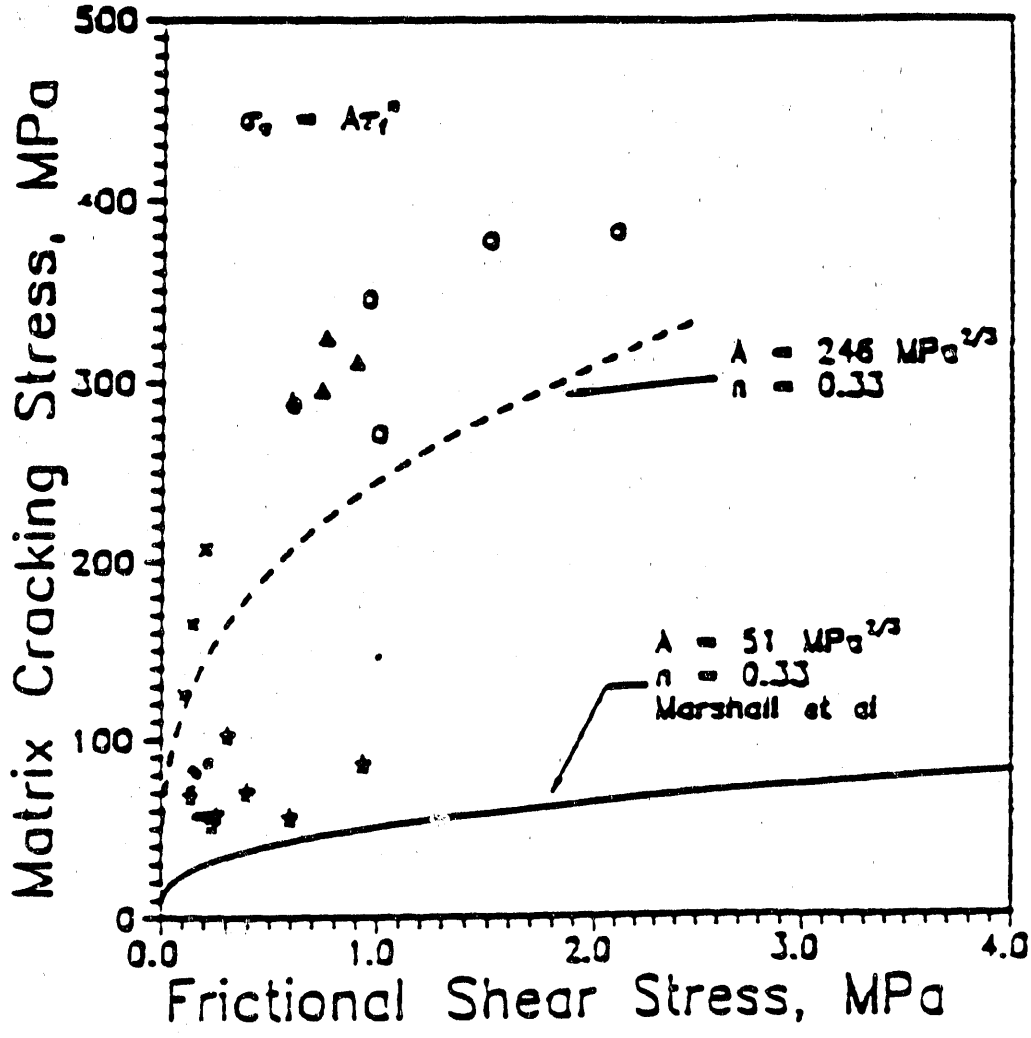

Figure 3. Correlation Between Matrix-Cracking Stress (σ_c) and Fiber-Matrix Sliding Friction Stress (τ_f) in SiC-NZP Composites.

Variation of Composite Properties with Temperature

Figure 4 shows the variations of the matrix-cracking stress and the ultimate strength of SiC-[NZP] composites with temperature. The SiC-[NZP] composite that exhibited high matrix-cracking stress and ultimate strength at ambient temperature showed some degradation at an elevated temperature (1200°C), while the composite with low strength at

ambient temperature showed some improvement at high temperatures. This trend is attributed to the variation of the clamping stress with temperature.

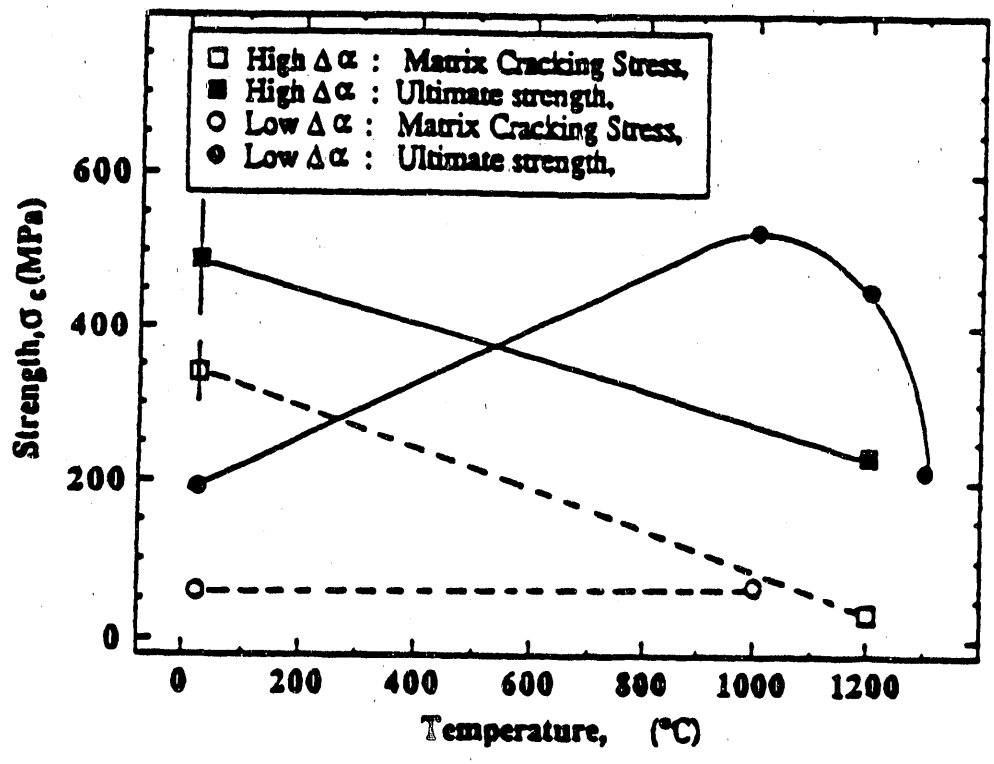

Figure 4. Variation of Matrix cracking stress and Ultimate Strength in Composites with High and Low Matrix Thermal Expansion

DISCUSSION

The large variation observed in the matrix cracking stress among SiC-NZP composites, fabricated under nominally identical conditions, is the most interesting result of the present study. As illustrated in Figure 3, the matrix cracking stress on individual test bars can range from a value as low as 50 MPa to as high as 380 MPa. In relation to the fracture stress of the unreinforced NZP matrix (~ 200 MPa), SiC reinforcement can result in severe strength degradation or significant strength enhancement with attendant composite

failure characteristics, such as load-bearing capability beyond the matrix-cracking stress and the large apparent strain to failure. It is clear that a basic understanding of the underlying causes for this variation is essential if SiC-NZP composites are to be viable as potential structural materials.

It is suggested here that the variation in the matrix cracking stress of SiC-NZP composites is largely due to the variation in the properties of the matrix NZP. Matrix properties that are known to affect matrix-cracking stress of a ceramic composite are matrix fracture toughness, elastic modulus and coefficient of thermal expansion[2,7]. Of these properties, variation in the thermal expansion of the matrix NZP and the consequent effect on sliding friction stress is the most likely cause for the variation of the matrix-cracking stress of the composites. The specific composition selected for the matrix NZP should ideally yield a single phase and a coefficient of thermal expansion of 2×10^{-6} /C. The measured coefficients of thermal expansion for the matrix NZP varied and were higher than this value. This variation could have been caused by the formation of a minor second phase which could change the parent phase composition and hence the thermal expansion. Indeed, there are many isostructural phases of varying compositions and thermal expansions in the NZP family which are not easily distinguished by x-ray diffraction. The experimental variable that could have caused this phase/composition variation is not firmly established. A potential candidate is that the temperature during hot pressing was insufficient to allow diffusion and generation of a single phase material.

Variation in the thermal expansion coefficient of the matrix can be expected to influence bulk mechanical properties of the composite via residual stresses and their effect on interfacial properties. The sliding friction stress at fiber-matrix interface, for example, has been modelled as a Coulomb friction[8] :

$$\tau_f = \mu \sigma_0 \qquad (3)$$

In Equation 3, μ is the coefficient of friction characteristic of the interface and σ_0 is a residual fiber clamping stress. In ceramic-matrix composites in which coefficient of thermal expansion for the matrix is greater than that of the fiber, the residual clamping stress is expected to be largely due to the thermal expansion mismatch[8] :

$$\sigma_0 = \frac{E_m(\alpha_m - \alpha_f)\,\Delta T}{(1+\nu_m) + \dfrac{E_m(1-\nu_f)}{E_f}} \qquad (4)$$

In Equation 4, E, α and ν are elastic modulus, thermal expansion coefficient and Poisson's ratio, respectively; subscripts m and f correspond to matrix and fiber and ΔT is the temperature range over which residual stress builds up. Equation 4 is an approximation for the residual clamping stress and it is strictly valid only for composites with low volume fraction of fibers. It is clear from Equations 3 and 4 that sliding friction stress τ_f should be proportional to $(\alpha_m - \alpha_f)$. The data shown in Figure 2 are qualitatively consistent with this interpretation of τ_f since α_f is a constant. In this connection, it is interesting to note the extrapolated value of the matrix thermal expansion coefficient in Figure 2 where the sliding friction stress is zero. This value, 2.37 x 10^{-6} /C, is close to the radial thermal expansion coefficient measured by Goettler and Faber[9] for the same SiC filament (2.53 x 10^{-6} /C). This agreement lends support to the interpretation of the effect of matrix thermal expansion on the interface friction stress.

Although the above interpretation is qualitatively correct, the low values of the sliding friction stress measured in the pushout experiments lead to quantitative difficulties in interpretation. For example, in order for the data of Figure 2 to be compatible with Equations 3 and 4, the coefficient of sliding friction would have to be of the order of 0.01. This is too low and unrealistic for a ceramic-matrix composite. Part of this discrepancy is due to Equation 4 which overestimates the clamping stress. Microscopic examination of partially-pushed filaments in a low-strength and a high-strength composite indicated that the interface in the low strength composite was smooth, while the interface in the high strength composite was granular. This suggests that the coefficient of friction may itself be changing for the different composites. One needs to assess the sliding friction load as a function of the embedded fiber length and analyze the data in terms of nonlinear shear-lag models to separate the effects of coefficient of friction and the clamping stress[5].

Finally, it is of interest to examine the variation of the matrix cracking stress with the interface friction stress quantitatively. Marshall et al.[7] have modelled matrix cracking in brittle-matrix composites by considering the crack-closure effects of the frictionally-bonded

bridging fibers. For large cracks, the matrix cracking stress is independent of crack size and a steady state matrix cracking stress is given by the following equation[7] :

$$\sigma_c = \left[\frac{6\,(1-\nu^2)\,K_{cm}^2\,\tau_f\,E_f\,V_f^2\,V_m(1+\eta)^2}{E_m\,R} \right]^{\frac{1}{3}} \qquad (5)$$

In Equation 5, ν is the composite Poisson's ratio, K_{cm} the matrix fracture toughness, V_f the fiber volume fraction, V_m the matrix volume fraction, R the fiber radius and η is given by $E_f V_f / E_m V_m$. The solid line in Figure 5 represents the prediction of Equation 5 with the following parameters : $\nu = 0.2$, $K_{cm} = 1$ MPa$\sqrt{m}$, $E_f = 427$ GPa, $V_f = 0.27$, $E_m = 97.4$ GPa, $V_m = 0.73$ and $R = 71$ μm. It is evident from Figure 3 that measured matrix cracking stresses are much higher than the prediction of Equation 5. It should be noted, however, that Equation 5 gives a lower-bound matrix-cracking stress at large crack lengths above a transition crack length. This transition crack length is of the order of 3.5 mm for the present SiC-NZP composites[7]. Thus, the matrix-cracking behavior in SiC-NZP composites is likely to be more representative of small cracks and accordingly stresses are higher and also they exhibit significant scatter.

The trends observed in the matrix cracking and ultimate strengths assessed in composites with high thermal expansion and low expansion matrices as a function of temperature can be related to the thermal expansion mismatch between fibers and matrix. In composites with $\alpha_m > \alpha_f$, the clamping stress, sliding friction stress and the matrix-cracking stress are all expected to decrease with temperature. This is a result of the high expansion matrix expanding in relation to the lower expansion fiber as temperature increases. The clamping stress at the fiber-matrix interface decreases as the matrix expands away from the fiber. In composites with $\alpha_m < \alpha_f$, these stress values are expected to increase with temperature as the higher expansion of the fiber generates pressure across the interface.

REFERENCES

1. J. J. Brennan and K. M. Prewo, " Silicon Carbide Fiber Reinforced Glass-Ceramic Matrix Composites Exhibiting High Strength and Toughness ", J. of Mat. Sci., 17, 2371-83 (1982)

2. D. B. Marshall and A. G. Evans, " Failure Mechanisms in Ceramic Matrix / Ceramic Fiber Composites ", *J. Am. Ceram. Soc.*, **68** [5] 225-31 (1985)

3. R. T. Bhatt, " Mechanical Properties of SiC Monofilament Reinforced Reaction-Bonded Si_3N_4 " pp. 675-86 in *Tailoring of Multiphase and Composite Ceramics*, Materials Science Research, Volume 20. R. E. Tressler, G. L. Messing, C. G. Pantano and R. E. Newnham (Eds.), Plenum Press, New York (1986)

4. S. Y. Limaye, D. K. Agrawal and H. A. McKinstry, " Synthesis and Characterization of Alkaline Earth Zirconium Phosphate Family ", *J. Am. Ceram. Soc.*, **70** [10] C-232 - C-236 (1987)

5. J. D. Bright, D. K. Shetty, C. W. Griffin and S. Y. Limaye, " Interfacial Bonding and Friction in Silicon Carbide (Filament)-Reinforced Ceramic and Glass-Matrix Composites ", *J. Am. Ceram. Soc.*, **72** [10] 1891-98 (1989)

6. D. H. Grande, J. F. Mandell and K. C. C. Hong, " Fiber-Matrix Bond Strength Studies of Glass, Ceramic and Metal Matrix Composites ", *J. of Mater. Sci.*, 23, 311-28 (1988)

7. D. B. Marshall, B. N. Cox and A. G. Evans, " The Mechanics of Matrix Cracking in Brittle Matrix Fiber Composites ", *Acta Metall.*, 33 [11] 2013-21 (1985)

8. D. K. Shetty, " Shear-Lag Analysis of Fiber Pushout (Indentation) Tests for Estimating Interfacial Friction Stress in Ceramic-Matrix Composites ", J. Am.Ceram. Soc., **71** [2] C-107-C-109 (1988)

9. R. W. Goettler and K. T. Faber, " Interfacial Shear Stresses in Fiber-Reinforced Glasses ", (In Press) Composites Science and Technology, December (1989)

ACKNOWLEDGEMENTS

This paper is based on research supported by the U. S. Department of Energy under Contract No. DE-AC05-87-ER80463 at Ceramatec Inc. Discussions with Prof. A.V. Virkar were valuable in the preparation of this paper.

DEVELOPMENT OF CONTINUOUS FIBER-REINFORCED SILICON NITRIDE

T. L. Starr, J. N. Harris, D.L. Mohr
and J. S. Lyons

ABSTRACT

Silicon nitride matrix composites have been fabricated using the reaction sintering process and five types of fiber reinforcement. Ceramic fiber cloths are impregnated with attritor milled silicon powder, stacked and compressed to form composite plates. The silicon is converted to nitride by heating in a nitrogen atmosphere at up to 1200°C over a period of approximately three hours, forming the composite matrix. These conditions are relatively mild, as compared to the standard nitriding process, and enhance fiber stability and retained strength. Composites range from 67 to 78% of full density with fiber loadings of 33 to 47% by volume. Good matrix density is observed between cloth layers but penetration within fiber tows needs to be improved. Flexure strengths range widely but all composites exhibit some non-brittle fracture behavior. Carbon coating does not enhance fiber pull-out. This net shape fabrication technique is suitable for large, complex components but improvement is needed in fiber coating and green forming methods.

INTRODUCTION

Ceramic composites continue to offer great promise for increasing the efficiency of fossil fuel utilization. One application is turbine components and vanes in the gas path which have to maintain their structural integrity at high temperatures and under aggressive chemical environments. These materials offer increased toughness and damage tolerance while maintaining the high temperature capability and chemical stability inherent in ceramics.

Fabricability is an important factor in such applications of ceramics composites, particularly for the relatively large and complex shapes used for fossil energy conversion systems. Near-net-shape fabrication methods are needed.

Silicon nitride matrix-composites can be formed by reaction sintering, wherein silicon powder is converted to nitride by reaction in a nitrogen atmosphere. This conversion process produces a fully crystalline

silicon nitride phase. Since the nitride occupies 23% greater volume than the silicon, densification occurs without reduction of the bulk volume. This feature makes reaction sintering an attractive process for near-net-shape fabrication of fiber-reinforced composites.

Two factors have limited prior application of this process in ceramic composite fabrication. Standard nitriding temperatures (1350-1400°C) and times (days) are too severe for the small diameter, polymer-derived ceramic fibers that have been developed. Also, typical silicon powders have a median particle diameter in the range of 5-10 μm which is too coarse to effectively infiltrate multifilament tows of 10-15 μm diameter fibers.

Previous results[1] with ultrafine silicon powder (less than 0.05 μm) indicate full conversion in a short time at dramatically lower temperatures. Other work with sub-micron silicon powders produced by thermal[2] or laser[3] decomposition of silane has shown rapid conversion to nitride at low temperatures. These powders, however, are high cost and yield low packing density, which results in low density in the ultimate nitride. Sub-micron powder prepared by attritor milling has been 90% converted to nitride at 1200°C[4]. In this case the nitriding time was long (40 hours) and no attempt was made to observe the nitriding kinetics with shorter schedules. This suggests that development of a fine, attritor milled silicon powder offers twofold advantages for composite fabrication. Lower temperature, shorter time processing conditions allows use of the small diameter, polymer-derived ceramic fibers and the smaller powder particles provide better infiltration of multifilament tows.

SILICON POWDER DEVELOPMENT

Silicon powder was prepared and characterized using ball milling, attritor milling and vapor decomposition. These processes produced materials of widely varying properties. Reference 5 gives a complete description of studies to determine the nitriding characteristics of coarse, fine and ultrafine silicon powders. The results confirmed the high reactivity of attritor milled silicon. Monitoring of the nitridation of this powder (Figure 1) shows near full conversion in less than two hours at a maximum temperature of 1250°C or less than four hours at 1200°C.

The attritor milled powder selected for fabrication of composites is considerably finer than the starting or the ball milled material. It has a relatively broad distribution of particle sizes with average particle diameter (mass average) of 1.5 μm and BET surface area of 19 m^2/g.

CONTINUOUS FIBER REINFORCED COMPOSITES

Composites were fabricated using five different fiber reinforcements, as shown in Table 1. Nicalon and Tyranno fibers are commercially available from Dow Corning and Textron Specialty Materials, respectively. The HPZ fiber is under advanced development and is available only in trial quantities at this time.

Carbon-coated Nicalon came from two sources. One (C1) was coated, as a cloth, using CVD at the Oak Ridge National Laboratory[6]. The second (C2) is a developmental material from Nippon Carbon Company with a carbon coating applied during the fiber manufacturing process, prior to weaving into cloth.

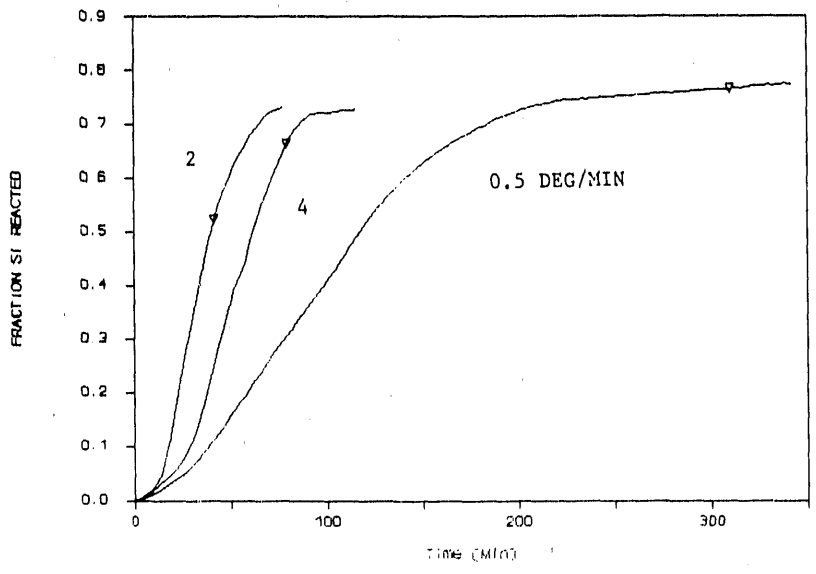

Figure 1. Nitridation of attritor milled silicon shows near full conversion after 200 minutes to a maximum temperature of 1200°C. Temperature was increased from 1100°C at indicated heating rates.

Table 1. Ceramic fiber cloths used for fabrication of reaction sintered silicon nitride composites.

Cloth	Fiber Diameter (μm)	Areal Density (mg/cm^2)	Weave	Manufacturer
Nicalon	12-18	37	8HS	Nippon Carbon
Tyranno	10-12	26	8HS	Ube Industries
HPZ	10-12	13	8HS	Dow Corning
Nicalon-C1	12-18	42	SQ	Nippon/ORNL
Nicalon-C2	12-18	37	8HS	Nippon Carbon

8HS = 8 harness satin weave SQ = square weave

Initial experimental composites were prepared with the Nicalon, 8-harness satin cloth. This Nicalon cloth is woven from a 500 filament tow, with individual filaments having a diameter of 10-15 μm. The areal weight of the cloth is 37 mg/cm^2. The woven cloth has an organic size that prevents proper wetting with the ethanol slurry of silicon powder and is removed by soaking in acetone prior to fabricating the composite specimens.

The procedure, adopted for preparation of the composites and used with each of the cloth materials in Table 1, was to dip the silicon cloth layers in a 30 percent silicon powder-ethanol slurry. The weight ratio of silicon to cloth was adjusted to 2:1 by subsequent additional dippings. The cloths were laid up in 0-90° alternating layers and pressed between aluminum plates under a pressure of 1270 psi (8.8 MPa). The pressed specimens were removed while still wet and placed between two perforated molybdenum plates (0.3 mm thick), backed up by two, 6.4 mm thick perforated silicon nitride plates. The assembly was clamped to restrain the specimen to its original pressed thickness during vacuum drying and nitridation. Nitriding was accomplished by sintering from 1100°C to 1200°C at a temperature increase of ½°C/minute in a 95% N_2-5% H_2 atmosphere. The specimens were held at 1200°C for 60 minutes.

CHARACTERIZATION

The composite materials were characterized by microscopy and by mechanical testing of bars cut from the composites. Microscopic examination of the composites generally showed good density between cloth layers but significant porosity within individual fiber tows. The mechanical testing consisted of measuring the modulus of rupture and static elastic modulus with the stress plane both parallel and perpendicular to the cloth layers using 4-point bending on specimens 3 x 4 x 45 mm.

Physical properties of the five composite materials are shown in Table 2 and strength values in Table 3.

All specimens showed some non-brittle fracture behavior, i.e., continued to carry load after initial crack generation. Except for a few cases, the bars remained intact throughout the test.

DISCUSSION AND CONCLUSIONS

Although fabrication techniques for the five composites were nominally identical, significant differences in physical and mechanical properties were obtained. Most of these can be attributed to differences in the fiber reinforcement. The three composites made with uncoated fiber are very similar in volume fraction fiber and in bulk density. All have fiber loading in the range 33-36%

Table 2. Composition and density of reaction sintered silicon nitride composites.

Composite	No. of Layers	Fiber Loading (%)	Density (g/cm^3)	Fraction Theor. Density (%)
Nicalon	7	32.9	2.06	69.0
Tyranno	11	34.0	1.99	66.5
HPZ	17	35.5	2.05	70.2
Nicalon-C1	8	47.2	2.03	70.8
Nicalon-C2	7	44.7	2.26	78.3

and residual porosity of 30-34%. However, microstructure examination and mechanical testing reveal significant differences. Of the three, the Nicalon reinforced material has the highest strength. Flexure testing (Figure 2) appears to exhibit "tough" behavior, gradual failure after reaching peak load. However, the fracture surface (Figure 3) does not show extensive fiber pull-out. Much of the "tough" fracture behavior can be attributed to interlaminar failure, crack branching and "tow pull-out" as intact bundles of fiber separate from the matrix. Fiber/matrix bonding appears to be too strong for optimum composite properties.

Table 3. Mechanical properties of reaction sintered silicon nitride composites.

Composite	Parallel		Perpendicular	
	Strength (MPa)	Modulus (GPa)	Strength (MPa)	Modulus (GPa)
Nicalon	72.3	27.8	85.3	51.7
Tyranno	31.0	13.5	39.9	19.8
HPZ	43.6	38.2	64.5	59.1
Nicalon-C1	36.8	17.8	41.9	23.0
Nicalon-C2	91.9	83.1	115.7	98.9

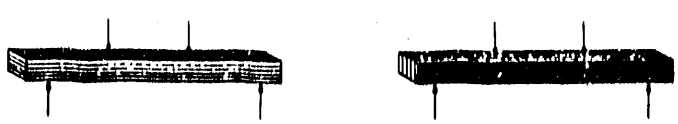

The Tyranno fiber reinforced composite is the weakest material tested. Micrographs of the fracture surface (Figure 4) show much fiber degradation. What appears to be fiber pull-out is really separation of fiber tows that were not infiltrated with matrix.

The microstructure of the HPZ material shows better matrix distribution and fiber pull-out than the other two composites. Although the volume of porosity is similar, it appears to be more evenly distributed between inter- and intralaminar regions.

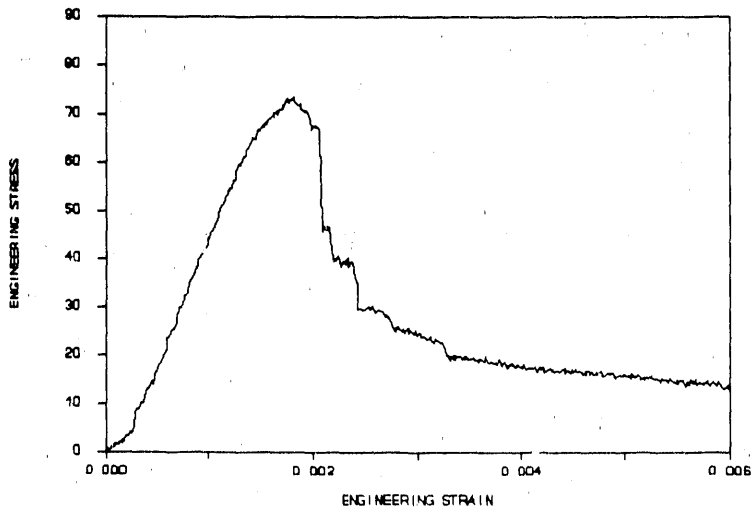

Figure 2. Stress-strain curve for flexure test of uncoated Nicalon composite shows "graceful" failure after reaching maximum load.

This likely is due to the looser, lower density weave of this cloth which allows better penetration of the silicon powder into individual fiber tows. Also, bonding between the fiber and the matrix appears to be weaker, with a number of areas exhibiting good pull-out (Figure 5). In spite of these desirable features, the strength of the HPZ material is less than that of the Nicalon composite. We attribute this to lower tensile strength of the HPZ fiber. Although recent reports give properties comparable to those of Nicalon, earlier batches of this developmental fiber were not as successful. In the absence of strength data for the specific material (we received a single 25cm x 25cm square of cloth), we can only suggest this explanation for the lower composite strength.

Due to unidentified processing variations, the composi-tions (fiber loading and residual porosity) of the two carbon-coated Nicalon composites are significantly different from those of the uncoated materials. The pyrocarbon-coated composite (C1) contains a similar amount of porosity (29%) but a much higher volume fraction of fiber. The result is a low fraction of matrix material (24%) in the composite. This, likely, is the cause of the low strength of this material.

The manufacturer-coated Nicalon composite has lower porosity (22%) and higher volume fraction fiber (45%) than the uncoated materials, and

exhibits the highest flexure strength of all. However, the fracture behavior of this material is the most brittle with several specimens fracturing completely after reaching the peak load. The fracture face of this composite (Figure 6) is relatively flat and shows no fiber pull-out. Strong bonding and, possibly, reaction between the coated fiber and the matrix is apparent.

This work suggests good potential for fabrication of successful silicon nitride matrix composites. Even though lower in density, flexure strengths of several of these materials are comparable to those of CVI composites when the fiber is uncoated or has a coating that gives strong matrix bonding[7]. Further development of composite fabrication techniques and fiber coating suitable for the reaction sintering environment can be expected to yield improved strength and toughness.

REFERENCES

1. T. L. Starr and J. N. Harris, "Development of Advanced Fiber Reinforced Ceramics", Georgia Tech Final Report for DOE Fossil Energy Materials Program, Oak Ridge National Laboratory Report ORNL/Sub/83-43369/01 (December 1986).

2. O. J. Gregory and S. B. Lee, "Reaction Sintering of Submicrometer Silicon Powder", J. Amer. Ceram. Soc., 70(3) C52-C55 (1987).

3. B. W. Sheldon and J. S. Haggerty, "The Nitridation of High Purity, Laser-Synthesized Silicon Powder to From Reaction Bonded Silicon Nitride", Ceram. Eng. Sci. Proc., 9(7-8), 1061-1072 (1988).

4. R. T. Bhatt, "Effects of Fabrication Conditions on the Properties of SiC Fiber Reinforced Reaction-Bonded Silicon Nitride Matrix Composites (SiC/RBSN)" in Metal Matrix, Carbon and Ceramic Matrix Composites, NASA Conf. pub. 2445, 277-295, (1986).

5. T. L. Starr, J. N. Harris and D. L. Mohr, "Low Temperature Processing of Reaction Sintered Silicon Nitride", Georgia Tech Topical Report for DOE Fossil Energy Materials Program, Oak Ridge National Laboratory Report ORNL/Sub/87-00184/01 (July 1989).

6. Pyrocarbon coated Nicalon cloth provided by R. A. Lowden, Oak Ridge National Laboratory.

7. R. A. Lowden and D. P. Stinton, "The Influence of the Fiber-Matrix Bond on the Mechanical Behavior of Nicalon/SiC Composites", Oak Ridge National Laboratory Report TM-10667, December 1987.

Figure 3. Fracture surface of Nicalon composite microstructure

Figure 4. Fracture surface of Tyranno composite microstructure

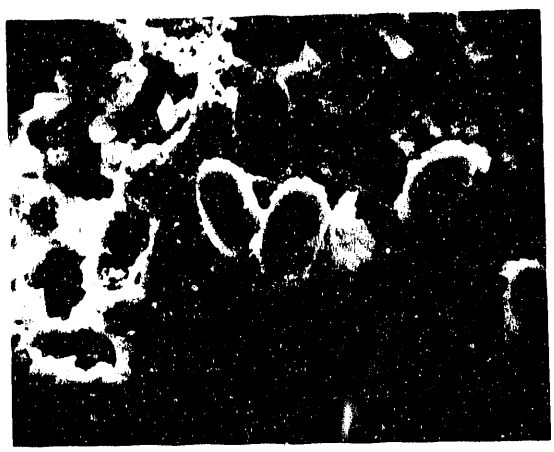

Figure 5. Fracture surface of HPZ composite microstructure

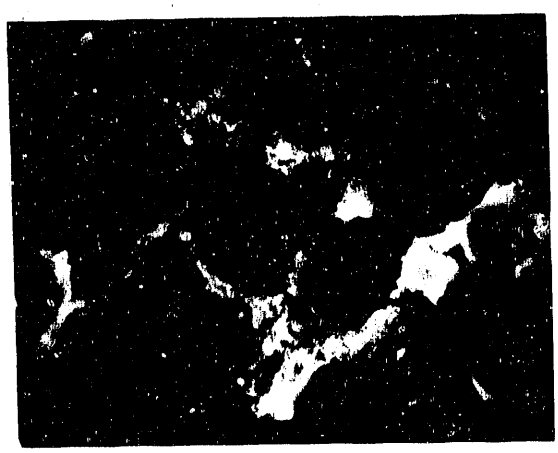

Figure 6. Fracture surface of carbon-coated Nicalon (C2) composite microstructure

JOINING OF FIBER-REINFORCED SILICON CARBIDE COMPOSITES

B. H. Rabin

Idaho National Engineering Laboratory
P.O. Box 1625
Idaho Falls, ID 83415-2218

ABSTRACT

This project is developing techniques for joining silicon carbide fiber-reinforced silicon carbide matrix composites for use in elevated temperature applications. In order to minimize property degradation of the composite caused by elevated temperature exposures during the joining process, new joining methods based on in situ reaction synthesis are under investigation. Two reaction systems have been selected for these studies; the first involves formation of a TiC+Ni cermet joining material from the reaction of titanium, carbon and nickel powders, and the second involves formation of SiC+Si joining materials by silicon infiltration of SiC+C powders or woven C cloth. When powder reactants are used, thin and uniform joining interlayers are fabricated using a modified tape casting procedure. In this paper, initial results concerning joint fabrication and microstructural characterization are presented.

INTRODUCTION

Silicon carbide fiber-reinforced silicon carbide matrix composites (SiC/SiC) produced by chemical vapor infiltration are under development for use in structural applications at temperatures approaching 1000°C [1-3]. These composites contain about 40 vol.% silicon carbide fibers (Nicalon®), and are infiltrated to about 85% of theoretical density with silicon carbide. In order to fully realize the advantages of these materials in fossil energy systems, practical joining techniques must be developed. Successful joining methods will permit the design and fabrication of components with complex shapes and the integration of component parts into larger structures. Joints must possess acceptable mechanical properties, and exhibit thermal and environmental stability comparable to that of the composite being joined.

Joining of silicon carbide has been accomplished by a variety of techniques including direct diffusion bonding [4, 5], co-densification of interlayer and green bodies [6], diffusion welding or brazing with boride, carbide and silicide interlayers [4], hot pressing of sinterable SiC powder [7], bonding with polymeric precursors [8], brazing with oxide [9] or oxynitride materials [10], reactive metal bonding [11], and active metal brazing [12]. Although varying degrees of success have been achieved, these joining methods are not generally applicable to the SiC/SiC composites presently under

investigation. For this material, reductions in strength have been shown to result from prolonged exposure to elevated temperatures. For example, strength losses are first observed above approximately 1000°C, and dramatic losses occur above 1200°C [2]. The reduction in properties has been attributed to degradation of the SiC fibers that occurs at these temperatures [13, 14]. Recent work has indicated that strength losses can be minimized to temperatures approaching 1400°C by coating the fibers with carbon and externally coating the composites with a protective layer of SiC [15]. Nevertheless, a successful joining method for these composites must minimize property degradation due to elevated temperature exposures during processing. This implies joining temperatures must be as low as possible, preferably below 1400°C, and processing should be performed in inert atmospheres. Considering that projected use temperatures for joined components are near 1000°C, this processing limitation poses a significant challenge for the development of reliable joining methods. Diffusion bonding and hot pressing, with or without interlayer materials, require temperatures exceeding 1650°C and therefore cannot be used. Metallic bonding or brazing is ruled out because currently available alloys cannot withstand the intended service temperatures.

In an effort to develop new joining methods applicable to SiC/SiC composites, approaches based on reaction synthesis techniques are under investigation. These approaches offer the possibility of synthesizing refractory joint materials, capable of meeting the 1000°C temperature requirement, using in-situ chemical reactions that are carried out at temperatures such that property degradation of the composite is minimized. The goals of the current research include identification of appropriate joining systems, establishing experimental procedures for fabricating joints, and characterizing the structure/property relationships of joined components. This paper presents the progress to date concerning development of the reaction joining methods. Joining procedures are described, and example microstructures of joined SiC/SiC composites are presented.

EXPERIMENTAL PROCEDURE

Initial studies identified two materials systems having potential for joining SiC/SiC composites by reaction methods. The compositions and characteristics of the reactant materials employed in these experiments are listed in Table I, and the two joining approaches are described below. In the first case, elemental titanium, carbon, and nickel powders are mixed according to the following reaction

$$Ti + C + 15\ wt.\%\ Ni \rightarrow TiC + Ni \qquad (1).$$

designation	element	description	particle size, μm	weight percent
TCN	Ti	-400 mesh, sponge[a]	~30	69.4
	C	acetylene black[b]	0.02	15.6
	Ni	carbonyl[c]	15-20	15
SiCC	SiC	-325 mesh, beta[a]	~7	67
	C	acetylene black[b]	0.02	33
	Si	lump[d]	--	--
CC	C	woven fabric[e]	0.28 mm (thickness)	--
	Si	lump[d]	--	--

Table I. Compositions and characteristics of the joining materials used in this study.

The Ti + C reaction is highly exothermic and readily proceeds to completion once initiated [16]. Nickel reduces the reaction initiation temperature from about 1600°C for pure Ti+C mixtures to about 1200°C, and also forms a liquid phase that aids densification [17]. The resulting microstructure is a cermet consisting of interconnected TiC grains surrounded by a nickel-rich matrix. The reaction was carried out under argon in a graphite resistance heated hot pressing furnace using applied pressures ranging from 20 to 50 MPa. The samples were heated at 20°C/min to a maximum furnace temperature of 1400°C, after which the furnace power was turned off.

The second joining method investigated employs different variations of the elemental silicon carbide reaction:

$$Si + C \rightarrow SiC \qquad (2).$$

The reaction is carried out by infiltrating carbonaceous material with molten silicon, and has been used commercially to produce various types of SiC+Si materials. In this study, the carbon source was either fine carbon powder that was mixed with SiC powder, or woven carbon cloth. When a mixture of SiC+C powders is used, the resultant microstructure consists of the original SiC grains bonded together by additional SiC reacted in situ, as well

[a] Cerac, Inc., Milwaukee, WI
[b] C-100, Chevron Chemical Co., Baytown, TX
[c] INCO type HDNP, Novamet, Wyckoff, NJ
[d] 99.999%, Johnsnon Matthey, Seabrook, NH
[e] Goodfellow, Malvern, PA

as free Si [18]. When carbon cloth is used, the resultant microstructure is a composite consisting of aligned SiC crystals that exhibit the distribution of the original carbon fibers, embedded in a Si matrix [19]. In both cases, silicon infiltration was carried out without pressure at 1480°C for 15 minutes under vacuum of about 4 Pa.

When powder reactants were employed, a thin uniform layer of powder was applied to both joining surfaces using the modified tape casting procedure shown in Figure 1, and described in detail elsewhere [20]. Tape casting involved milling the powders in a solvent, polymeric binder, and deflocculent in appropriate proportions to achieve the desired slip viscosity. The materials used to form the slip, as well as typical slip formulations, are listed in Table II. The slip was applied directly onto the joining surfaces using a moving doctor blade with height adjustment to allow control of layer thickness. Prior to joining, the binder was removed by slow heating (0.3°C/min.) in air to 400°C.

material	function	parts by weight
powder mixture	joint material	100
2-butanone (MEK)	solvent	90 to 120
poly(vinyl-chloride/vinyl-acetate)[f]	binder	5 to 15
menhaden fish oil[g]	deflocculent	2

Table II. Materials and typical slip formulations used for tape casting.

SiC/SiC composite specimens were fabricated at Oak Ridge National Laboratory by the chemical vapor infiltration process described elsewhere [1-3]. To provide improved thermal stability, the composites were first cut to the desired size and then externally coated with a protective layer of SiC approximately 30 μm thick. The specimens were rectangular bars having dimensions of approximately 6.4 mm x 8.9 mm x 22 mm. In most cases, the as-received surface finish was used for joining. Samples were carefully cleaned with acetone and ethanol prior to application of the joining materials.

[f] UCAR® VYNS-3, Union Carbide Corp., Danbury, CT
[g] type Z-3, Werner G. Smith, Inc., Cleveland, OH

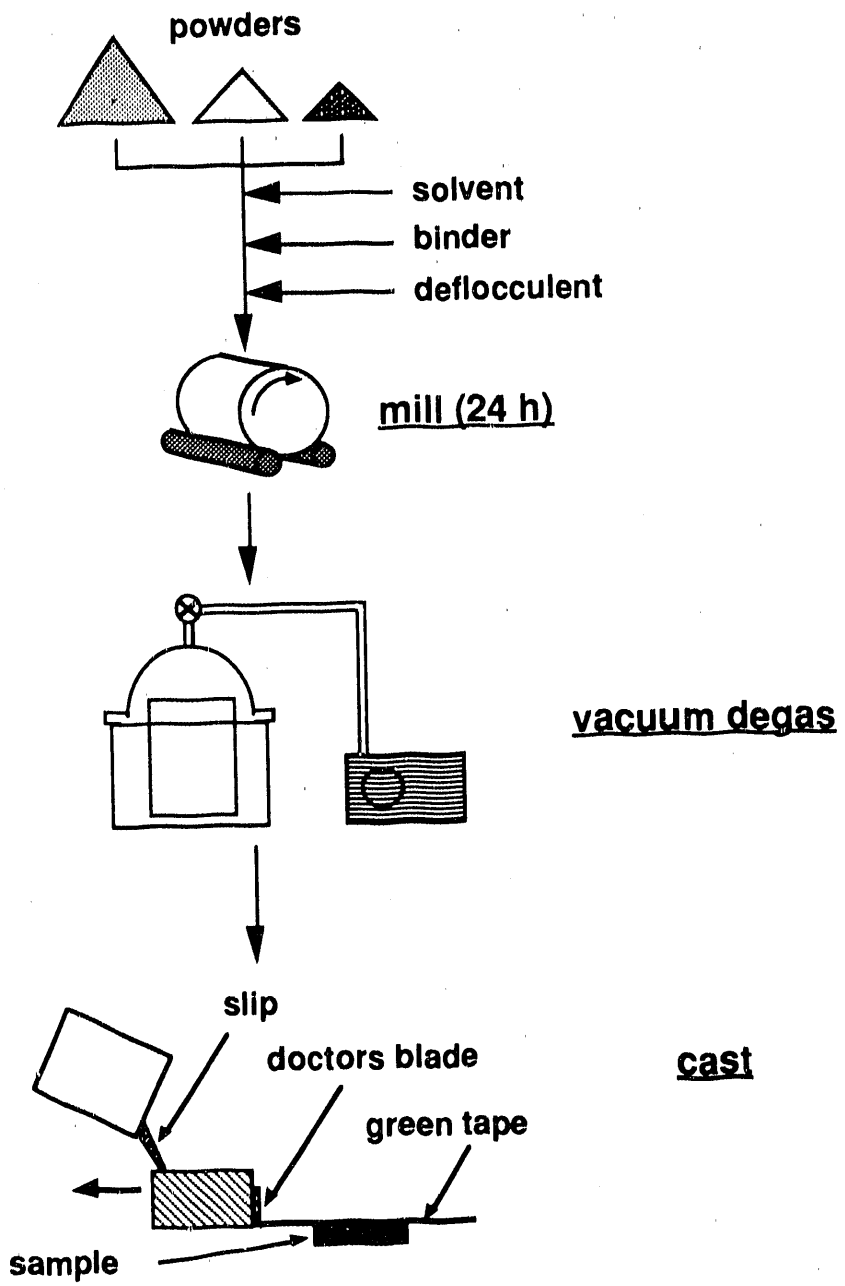

Figure 1. Schematic of the tape casting procedure used in this study.

RESULTS AND DISCUSSION

Figure 2 shows an optical micrograph of a SiC/SiC composite joint bonded with a TiC+Ni cermet interlayer produced according to Reaction 1. The dark phase within the joint interlayer is TiC and the light phase is the nickel-rich binder. Except for a few large

pores, the joint interlayer is relatively dense and exhibits a typical liquid phase sintered microstructure. The pores were believed to originate from binder defects within the original tape cast layer, and probably formed during binder burnout. Figure 2 also shows that there were some cracks within the joint that typically were perpendicular to the joint interface. This type of cracking pattern is characteristic of thermally induced stresses that result when the thermal expansion coefficient of the joint material is greater than that of the base material. The appearance of these cracks does not necessarily imply that low joint strengths will be achieved.

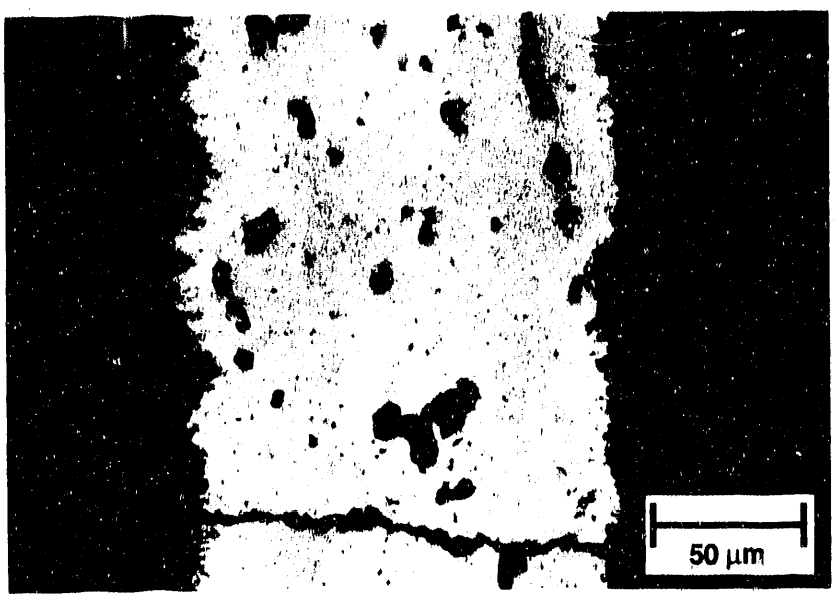

Figure 2. Optical micrograph of a SiC/SiC composite joined with a TiC+Ni interlayer that was formed according to Reaction 1 in text.

As can be seen in Figure 2, and also in the higher magnification SEM micrograph shown in Figure 3, it appears that the TiC+Ni cermet is well bonded to the SiC coated composite. It is apparent that some chemical interaction has taken place at the interface between the materials. This is evidenced by the small particles of SiC that are present within the joint material adjacent to the interface, as well as the fact that Si was detected within the nickel-rich regions of the TiC+Ni by energy dispersive x-ray mapping in the SEM. The details of the chemical interaction have not yet been studied, however, it is believed that localized dissolution of the silicon carbide has occurred during joining. These initial results are promising and suggest that good joint strengths may be achieved in this system.

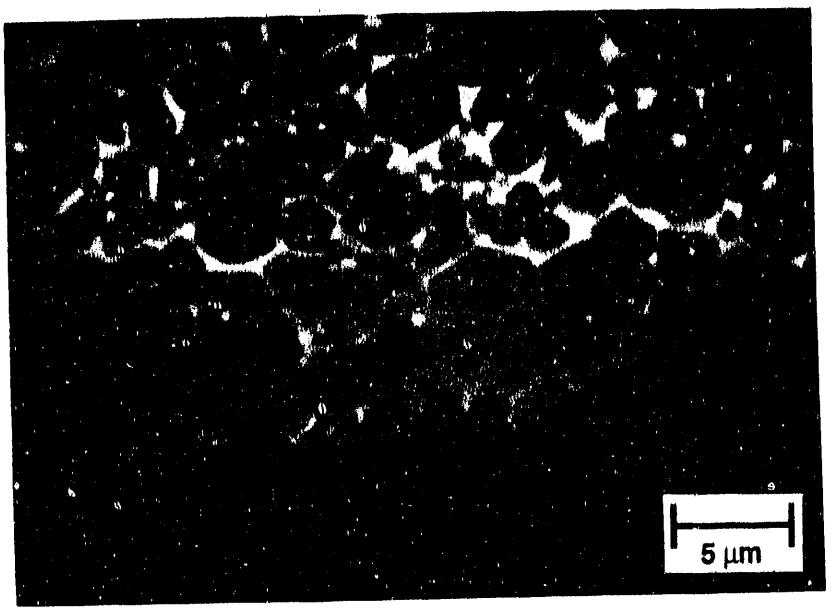

Figure 3. SEM micrograph of the interface region between the TiC+Ni joining material and the SiC coated composite. Note the apparent chemical interaction that has taken place during joining.

Figure 4 shows the microstructure of a SiC/SiC composite joined by silicon infiltration of a SiC+C mixture. The microstructure of the joint interlayer consists of SiCgrains (grey phase) within a Si matrix (light phase). Approximately 5 vol.% porosity (fine black areas) is present within the joint interlayer; this is typical of commercial reaction bonded silicon carbide (RBSC) materials [18]. The amount of SiC within the SiC+Si joint material is estimated to be about 50 vol.%. This quantity of SiC is considerably lower than what is typically found in commercial RBSC materials, which usually contain abut 80 vol.% SiC. This is believed to be a consequence of the relatively low green densities that were obtained in the tape cast layers. Further optimization of the starting SiC and C particle sizes must be carried out to improve particle packing within the green tapes, thereby increasing the SiC content within the joint interlayer.

During the infiltration joining process, molten Si completely wets the surface of the SiC/SiC composite resulting in a well bonded interface, as is apparent in the higher magnification SEM micrograph of the interface region shown in Figure 5. It is also interesting to note that there are a number of SiC grains within the joint interlayer that appear to have nucleated from, or grown into contact with, the SiC coating present on the surface of the composite. This result is promising and suggests that good mechanical properties may be achieved.

Figure 4. Optical micrograph of a SiC/SiC composite joint produced by infiltrating a SiC+C powder mixture with Si.

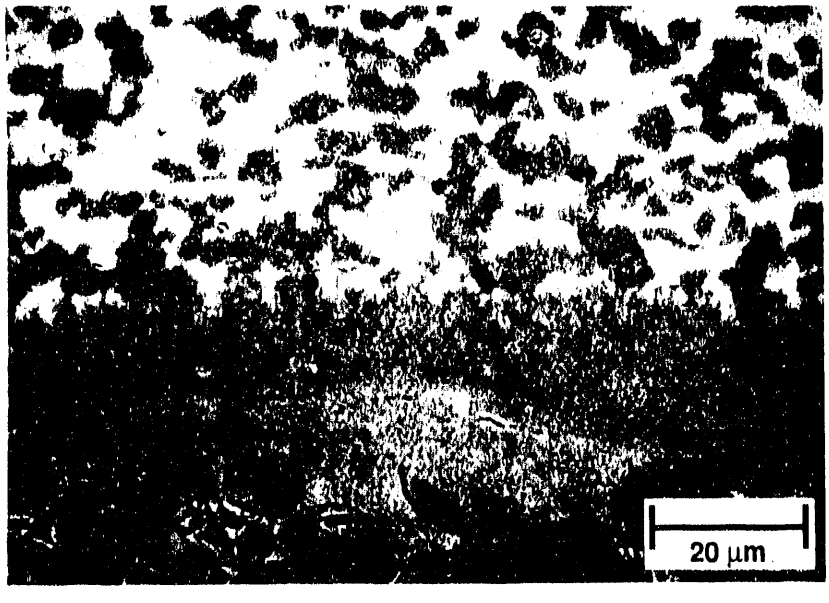

Figure 5. Higher magnification view of the interface between the SiC/SiC composite and the SiC+Si joint material produced by infiltrating a SiC+C powder mixture with Si.

Figure 6 shows a SiC/SiC composite joint produced by direct silicon infiltration of carbon cloth that was placed between the pieces to be joined. This microstructure also consists primarily of SiC and Si, however, the SiC crystals exhibit the aligned morphology of the original carbon fibers, and there is typically several percent of unreacted carbon present. As is evident in Figure 6, there was usually a layer of free Si present at the

composite/joint material interface. This is probably undesirable from a mechanical properties standpoint, since failure is likely to occur in this region. Nevertheless, since infiltration of carbon cloth is a considerably easier process to carry out compared to tape casting of SiC+C mixtures, this joining method deserves further investigation. By slurry coating the carbon cloth with carbon powder prior to infiltration, it may be possible to promote growth of SiC across the interface, similar to what was observed in Figure 5, and thereby produce a more desirable joint microstructure.

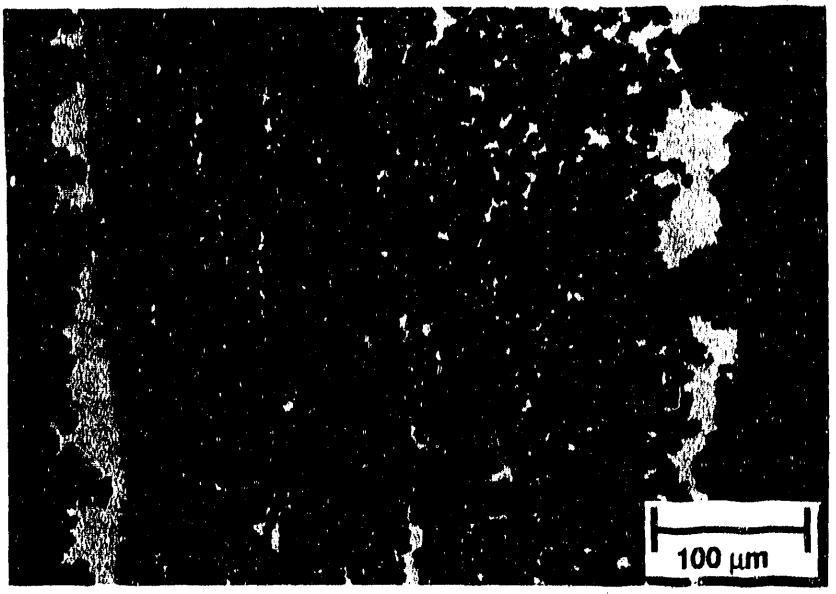

Figure 6. An optical micrograph of a SiC/SiC composite joint produced by direct silicon infiltration of carbon cloth placed between the pieces to be joined.

SUMMARY

In situ reaction methods have been developed and applied to join SiC/SiC composites under processing conditions expected to minimize property degradation of the composite, while providing joints capable of withstanding projected service temperatures approaching 1000°C. To date, joints have been produced using TiC+Ni and SiC+Si interlayers. The microstructures of joints fabricated to date have been characterized, and the results appear promising. Further work is needed to optimize joint microstructures, understand interfacial reactions, and to assess the mechanical properties of the joined components.

ACKNOWLEDGMENTS

The author would like to thank S. T. Schuetz and V. L. Smith-Wackerlie for their assistance with the experimental work. This research was performed under DOE Contract No. DE-AC07-76ID01570.

REFERENCES

1. A. J. Caputo and W. J. Lackey, "Fabrication of Fiber-Reinforced Ceramic Composites by Chemical Vapor Infiltration", ORNL/TM-9235, Oak Ridge National Laboratory, Oak Ridge, TN, 1984.

2. D. P. Stinton, A. J. Caputo and R. A. Lowden, "Synthesis of Fiber-Reinforced SiC Composites by Chemical Vapor Infiltration," *Amer. Ceram. Soc. Bull.*, 65(2), pp. 347-350, 1986.

3. A. J. Caputo, et al., "Fiber-Reinforced SiC Composites with Improved Mechanical Properties," *Amer. Ceram. Soc. Bull.*, 66(2), pp. 368-372, 1987.

4. T. J. Moore, "Feasibility Study of the Welding of SiC," *J. Amer. Ceram. Soc.*, 68(6), pp. C151-C153, 1985.

5. D. DeLeeuw, personal communication, Dow Corning Corporation, Midland MI, 1989.

6. C. H. Bates, et al., "Joining of Non-Oxide Ceramics for High-Temperature Applications," *Amer. Ceram. Soc. Bull.*, 69(3), pp. 350-356, 1990.

7. T. Iseki, K. Arakawa and H. Suzuki, "Joining of Dense Silicon Carbide by Hot Pressing," *J. Mater. Sci. Letters*, 15, pp. 1049-1050, 1980.

8. S. Yajima, et al., "Joining of SiC to SiC Using Polyborosiloxane," *Amer. Ceram. Soc. Bull.*, 60(2), pp. 253, 1981.

9. J. A. P. Gehris, "High Temperature Bonding of Silicon Carbide", M.S. Thesis, New Mexico Institute of Mining and Technology, Socorro, NM, 1989.

10. N. Tamari, et al., "Joining of Siliocn Carbide Ceramics with Si_3N_4-Y_2O_3-La_2O_3-MgO Mixture," *Yogyo-Kyokai-Shi*, 94(10), pp. 1087-1091, 1986.

11. S. Morozumi, et al., "Bonding Mechanism Between Silicon Carbide and Thin Foils of Reactive Metals," *J. Mater. Sci.*, 20, pp. 3976-3982, 1985.

12. J. K. Boadi, T. Yano and T. Iseki, "Brazing of Pressureless-Sintered SiC Using Ag-Cu-Ti Alloy," *J. Mater. Sci.*, 22, pp. 2431-2434, 1987.

13. T. Mah, et al., "Thermal Stability of SiC Fibres (Nicalon®)," *J. Mater. Sci.*, 19, pp. 1191-1201, 1984.

14. G. Simon and A. R. Bunsell, "Creep Behavior and Structural Characterization at High Temperatures of Nicalon SiC Fibers," *J. Mater. Sci.*, 19, pp. 3658-3670, 1984.

15. R. A. Lowden, personal communication, Oak Ridge National Laboratory, Oak Rideg, TN, March, 1990.

16. J. B. Holt and Z. A. Munir, "Combustion Synthesis of Titanium Carbide: Theory and Experiment," *J. Mater. Sci.*, 21, pp. 251-259, 1986.

17. S. D. Dunmead, et al., "Kinetics of Combustion Synthesis in the Ti-C and Ti-C-Ni Systems," *J. Amer. Ceram. Soc.*, 72(12), pp. 2318-2324, 1989.

18. C. W. Forrest, P. Kennedy and J. V. Shennan, "The Fabrication and Properties of Self-Bonded Silicon Carbide Bodies", in Special Ceramics 5, pp. 99-123, P. Popper (ed.), British Ceramic Research Association, Manchester, 1972.

19. W. B. Hillig, et al., "Silicon/Silicon Carbide Composites," *Amer. Ceram. Soc. Bull.*, 54(12), pp. 1054-1056, 1975.

20. B. H. Rabin, "A Modified Tape Casting Method for Ceramic Joining: Application to Joining of SiC," *J. Amer. Ceram. Soc.*, submitted for publication, 1990.

application of BN layers to the fibers prior to
composites with significantly improved strength
compared to those fabricated from untreated fib

The influence of interlayer thickness on
mechanical properties of fiber-reinforced ceram
received little attention. The influence of va

INTERFACE EFFECTS AND FRACTURE IN NICALON/SiC COMPOSITES

Richard A. Lowden

Oak Ridge National Laboratory
P. O. Box 2008
Oak Ridge, TN 37831-6063

ABSTRACT

Thin coatings deposited on ceramic fibers prior to densification employing chemical vapor infiltration techniques have been used to limit fiber-matrix bonding. This has resulted in improvements in strength and toughness for Nicalon® fiber-reinforced/SiC matrix composites. The properties of the composites are influenced by the thickness of the graphitic carbon interlayer. Matrix cracking, work of fracture, and ultimate strength are controlled by the nature of the interface. Interfacial forces were measured utilizing the indentation method in which a standard microhardness indentor is used to push on fibers embedded in the ceramic matrix. Correlations between interfacial phenomena and observed mechanical behavior have been made.

INTRODUCTION

A process to more efficiently fabricate ceramic matrix composites employing chemical vapor infiltration (CVI) has been developed at Oak Ridge National Laboratory (ORNL) [1-5] The ORNL process permits rapid fabrication of continuous fiber reinforced ceramic composites and simultaneously utilizes thermal and pressure gradients to reduce infiltration time. Densification times for centimeter-thick composites have been reduced from weeks to less than 20 h and thus the process has been termed "forced" chemical vapor infiltration (FCVI). Disk shapes up to 2.5 cm in thickness and one centimeter wall-thickness tubes[6,7] have been routinely infiltrated with a silicon carbide matrix using the FCVI technique.

The baseline reinforcement used in the development of the FCVI process has been the ceramic grade Nicalon fiber, a polymer-derived

---

Nicalon®, Nippon Carbon, Tokyo, Japan.

Si-C-O material.[8,9] The fiber consists primarily of SiC, which is well known for its exceptional high temperature properties and oxidation resistance, making it an excellent candidate as an elevated temperature reinforcement. Silicon carbide was also selected as the matrix to be investigated. The SiC matrix is deposited from the decomposition of methyltrichlorosilane (CH_3SiCl_3 or MTS) in hydrogen, typically at a hot surface temperature of 1473 K and atmospheric pressure. Uniformly infiltrated composites with good strengths and exceptional toughness have been fabricated using the FCVI process.[4,5]

Typically, a thin pyrolytic carbon layer is deposited on the fibrous preforms prior to densification to provide a uniform interface. The carbon is deposited from the decomposition of propylene in argon and deposition conditions were chosen to produce a graphitic coating with the basal planes parallel to the fibers.[10,11] The coatings were found to prevent chemical damage of the fibers during processing, as well as weaken the fiber-matrix interface, enhancing fiber debonding and slip.[12,13] Initially, there was little concern with regard to the thickness of the carbon coating, the strength of the fiber-matrix bond, or about excess slip. It was assumed that the fibers were long and entanglements in the fiber bundles would allow the tows to act like ropes thus providing sufficient reinforcement to carry the load at the onset of matrix failure.[14,15] Further examination of the interlayer revealed significant differences in mechanical properties that were strongly correlated with the thickness of the fiber coating.[12,13]

This report describes a study of the carbon coating used to alter the fiber-matrix bond and change the mechanical behavior of a ceramic fiber-reinforced ceramic matrix composite. The effects of the thickness of the carbon interlayer on the properties of the fiber-matrix interface and the resulting mechanical properties of the composites have been examined. The influence of interlayer thickness on interfacial forces, matrix cracking, work of fracture, and ultimate strength have been investigated. The strength of the fiber-matrix bond was determined using established indentation methods.[16] Room temperature flexure strengths were used to compare the effects of the various fiber pretreatments on the fracture behavior of the composites.

EXPERIMENTAL

Composite Fabrication

Fibrous preforms were fabricated by stacking multiple layers of Nicalon plain-weave fabric rotated in a 0° ± 30° sequence within the cavity of a graphite holder. The layers were hand compressed to produce a preform with a nominal loading of 40 vol % fiber and were held in place by a perforated graphite lid pinned to the holder. The cloth sizing was removed through multiple washings with acetone. The nominal size of the fibrous preforms was 45 mm in diameter and 12.5 mm thick.

Preforms were next precoated with thin layers of carbon. The coatings were deposited from an argon/propylene mixture at 1375 K and 3.3 kPa pressure. The thickness of the carbon layer was varied by changing deposition time and was measured from weight gains and using polarized-light optical microscopy of polished metallographic cross-sections. A control sample of uncoated fibers was prepared for comparison.

The preforms were densified with SiC produced by the decomposition of MTS in hydrogen at a hot-surface temperature of 1473 K and atmospheric pressure using the FCVI process. The densification of porous structures using the FCVI process has been previously described in detail.[1-5]

Mechanical Property Measurements

Bars were cut from the samples parallel to the 0° orientation of the top layer of cloth using a diamond saw, and tensile and compression surfaces were ground parallel to the long axis of the specimen. The average dimensions of the test bars from the composite samples were 2.5 × 3.3 × 40 mm and all specimens were measured and weighed to determine densities.

Bend bars prepared from a composite containing fibers with a 0.52 μm carbon coating were oxidized to remove the interlayer, thus producing a composite with no interfacial bonding or frictional

stresses. Specimens were placed in a furnace and heated treated at 873 K in flowing oxygen for 50 h. The low temperature minimized damage to the fibers and matrix but allowed oxidation of the carbon interlayer. Weight losses after heat treatment were measured to ensure complete burn-out of the carbon layer.

Room temperature flexural strengths were measured in four-point bending using a support span of 25.4 mm, a loading span of 6.4 mm, and a crosshead speed of 0.508 mm/min. All specimens were loaded perpendicular to the layers of cloth. Load-displacement curves were recorded to examine the fracture process and were used to determine the loads for matrix fracture and ultimate strength. In general, a single matrix crack was observed in the tests and was noted as the sudden drop in the load-displacement curve and/or deviation from linearity.

Work of fracture was measured for un-notched bend specimens that failed in a controlled manner and was determined from the area under the load-displacement curves and the area of the fracture surface approximated as twice the cross-sectional area of the bend specimen.[17,18] To obtain controlled failure of most materials, and thus measure the work of fracture, it is usually necessary to notch the bend specimens. As the fracture energy of a material increases, such as for fiber-reinforced composites, it becomes unnecessary to notch the specimens.[17,18]

The fracture surfaces of the specimens were examined using a Hitachi S-800 scanning electron microscope (SEM). Specimens that did not completely part during flexure testing were broken by hand so that the fracture surfaces could be examined.

Fiber-Matrix Bond Measurements

Several methods have been developed to quantify the strength of interfacial bonding in fiber-reinforced composites.[12,16,19] Such tests permit a semiquantitative determination of interfacial stresses derived from relatively simple load and displacement relationships. A common technique is the indentation method, which has been thoroughly examined.[16] This technique involves using a microhardness indentor to

apply a force to the end of a fiber embedded in a matrix. Interfacial shear stresses can be evaluated from the applied load and the displacement of the fiber.

A 6.0-mm-thick cross-sectional specimen was cut from each completed composite sample to be used for indentation testing. The specimens were cut along the 0° orientation of the top layer of cloth to ensure that a portion of the exposed fibers would be oriented perpendicular to the cut surface. This alignment is essential for proper implementation of the indentation mechanics. The specimens were mounted and polished using standard metallographic techniques. Loads were applied to fiber ends using a Vickers diamond indentor and a Shimadzu Type M instrument. Loading to the fiber ends was progressively increased until debonding was observed and continued until contact of the indentor with the edge of the fiber cavity was evident. Loads of up to 3.0 N were required to displace the fibers. Indents were also placed in longitudinally polished fibers to determine fiber hardness alues. The dimensions of the fibers and indent impressions we e measured using the ocular scale of the indentor.

RESULTS

Composite Fabrication

The fabric preforms contained a nominal 41.7 ± 0.9 vol % fiber. Carbon-layer deposition times were varied to produce coatings that ranged in thickness from 0.10 to ≈ 1.0 μm. The preforms were readily infiltrated with SiC to a maximum of 85 to 90% of theoretical density. The theoretical density is defined as the sum of the product of volume fraction and reported density of each component of the composite (fibers, interlayer, and infiltrated SiC). Infiltration of these preforms required 16 to 24 h. Individual composite specifications are summarized in Table 1.

Table 1. FCVI Nicalon/SiC composite specifications

Fiber Content (vol %)	Carbon Deposition Time (h)	Interlayer Thickness (μm)	Density (g/cm^3)	Average Porosity (%)
41.4	0.0	--	2.58 ± 0.08	11.6
41.8	0.3	0.10	2.48 ± 0.12	14.5
40.7	0.6	0.17	2.56 ± 0.11	12.3
41.3	1.0	0.26	2.61 ± 0.15	10.0
41.8	2.0	0.52	2.57 ± 0.17	10.0
40.9	3.3	0.99	2.47 ± 0.10	11.5

Fracture Behavior

Typical load-displacement curves for the Nicalon/SiC composites are shown in Figure 1. The composite prepared from uncoated fibers exhibited low flexure strength and displayed brittle failure, with no signs of toughening. The fracture surfaces were smooth and flat with no evidence of fiber debonding or pull-out. The oxidized specimens also had low strengths, but in contrast to the composites fabricated with uncoated fibers, the composites exhibited high strain to failure. A high degree of fiber pull-out at the fracture surfaces was observed.

The application of the carbon interlayer significantly altered the flexure behavior of the composites. In general, failure was gradual and the fracture surfaces of all composites fabricated with carbon-coated fiber displayed fiber pull-out. An increase in fiber pull-out length was observed with increasing interlayer thickness. The influence of the thickness of the carbon coating on the fracture behavior of the Nicalon/SiC composites is also displayed in the representative load-displacement curves in Figure 1.

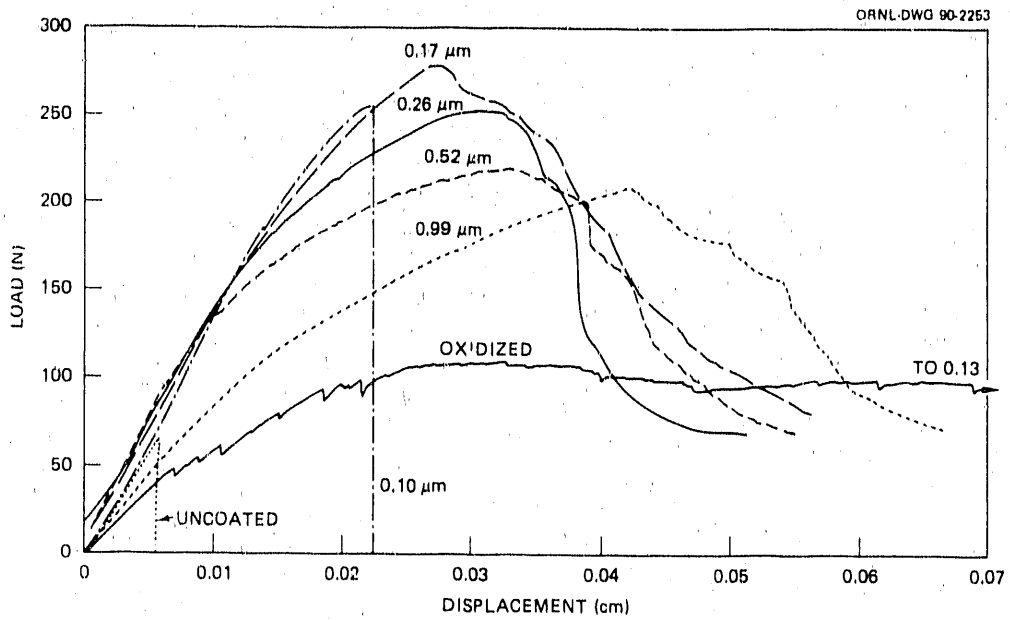

Figure 1. Representative flexure load-displacement curves for Nicalon/SiC composites with varying carbon interlayer thickness, thicknesses are shown on the curves in micrometers.

Composite Mechanical Properties

Mechanical property and interfacial shear stress measurements are summarized in Table 2. Matrix cracking stresses, work of fracture, and ultimate strength for the composites with varying interfacial pretreatments are listed. All mechanical properties were determined from the four-point flexure load-displacement curves. Shear stress was calculated from indented fibers using fiber radius and indent impressions measurements, a measured fiber hardness of 19.7 ± 0.9 GPa, and a fiber modulus of 110 GPa, as determined from previous tests and literature values.[8,9]

Interfacial Shear Stress

Composites with a broad range of interfacial shear strengths were fabricated. High interfacial shear stress was expected for the composite fabricated from uncoated fibers. A thin silica film forms at the surface of the fibers during exposure to the elevated temperatures of processing.[12,13] This layer bonds the fibers and matrix strongly and

Table 2. The influence of the fiber-matrix interface on the mechanical properties of Nicalon/SiC composites

Carbon Interlayer Thickness (μm)	Interfacial Shear Stress (MPa)	Matrix Cracking Stress (MPa)	Ultimate Flexure Strength (MPa)	Work of Fracture (J/m^2)
uncoated	762 ± 163	83 ± 10	83 ± 10	98 ± 24
0.10	385 ± 103	257 ± 29	343 ± 15	2590 ± 300
0.17	217 ± 48	238 ± 17	383 ± 35	4110 ± 880
0.26	127 ± 33	184 ± 22	379 ± 19	4990 ± 530
0.52	75 ± 26	122 ± 39	321 ± 25	4780 ± 300
0.99	39 ± 21	103 ± 6	293 ± 42	4530 ± 810
oxidized	0	40 ± 3	103 ± 39	4660 ± 630

does not allow for debonding and crack deflection at the interface, producing brittle fracture in the composites.

It was demonstrated that interfacial shear stresses were controllable through varying the thickness of a carbon interlayer. The relationship between interfacial shear stress and the thickness of the carbon interlayer is shown in Figure 2. The carbon interlayer reduced interfacial stresses and friction, thus required lower loads to displace the fibers within the matrix. The oxidation of the carbon layer produced a gap between the fibers and matrix resulting in no bonding or friction at the interface.

Matrix Cracking and Ultimate Strength

Provided the ratio of span to thickness ratio is high enough to minimize shear forces during testing, the determination of matrix fracture stress employing a flexure test is valid, for matrix cracking is the first damage to occur in the composite.[20] The oxidized specimens exhibited the lowest matrix fracture strengths. At this lower limit of interfacial bonding and friction, τ_i = 0 MPa, the matrix acts as a very porous material with no contribution from the fibers except to act as voids. Porosity reduces both strength and modulus in ceramics.[21] The matrix fracture stress for the oxidized composite specimens was

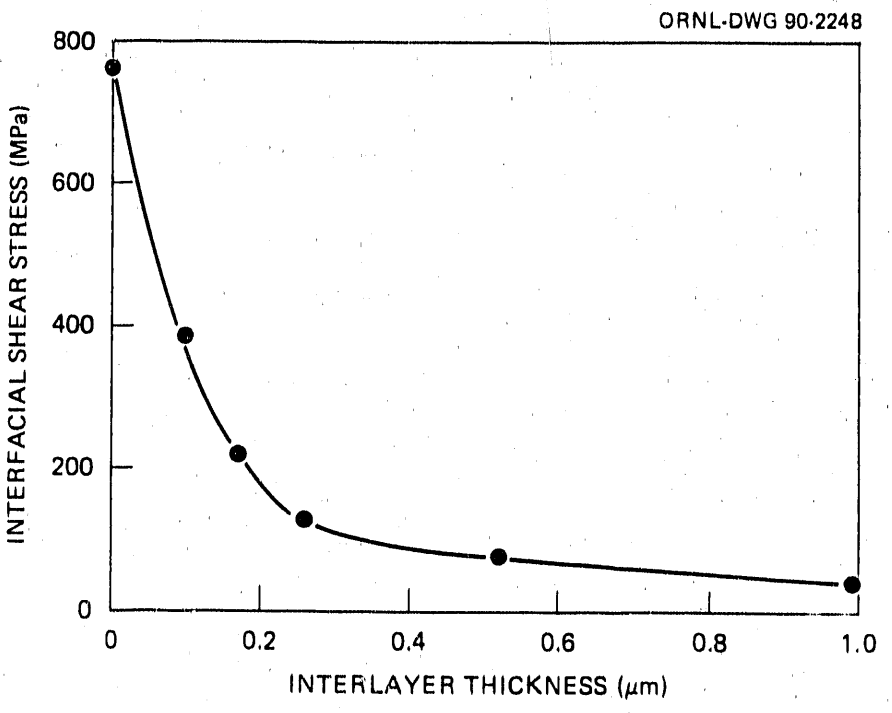

Figure 2. The influence of carbon coating thickness on interfacial frictional stress.

found to be 40 ± 3 MPa which agrees well with the strength of a CVD SiC body with 50% porosity calculated to be ≈ 40 MPa.

The relationship between carbon layer thickness and matrix cracking stress for the Nicalon/SiC composites is graphically depicted in Figure 3. Matrix fracture stress is improved by the application of the graphite interlayer, however, the value quickly decreases with increasing carbon layer thickness. As the thickness of the layer is increased, interfacial shear stress is decreased not allowing for adequate load transfer and thus utilization of the fiber properties to increase matrix cracking stress.

The ultimate flexure strength of Nicalon/SiC composites with varying fiber treatments is also depicted in Figure 3. The lowest strengths were obtained for the composite containing uncoated fibers. The low strength of the composites is due to the strong bonding of the fibers and matrix and fiber property deterioration during processing. The oxidized specimens, not shown in the figure, also exhibited low strength. The lack of interfacial bonding and friction did not allow for load transfer thus as the fibers fractured, they were easily pulled

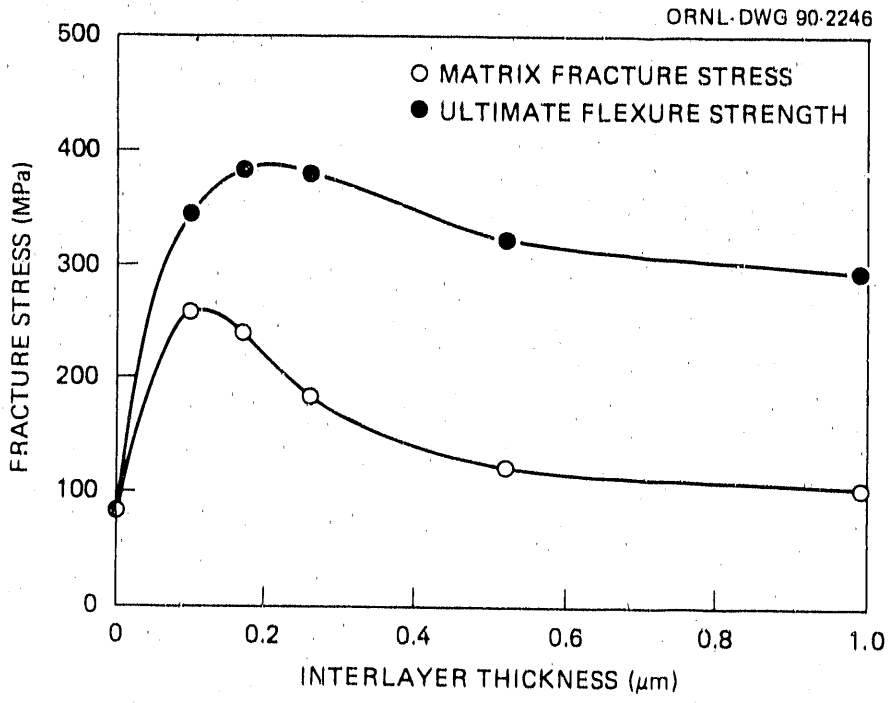

Figure 3. The effect of coating thickness on the matrix fracture stress and ultimate strength of the composites.

from the matrix. The flexure strength of the composites improved with the addition of a carbon fiber coating. An increase in strength was observed with increasing carbon layer thickness up to 0.26 μm, beyond which a degradation of strength was observed.

Work of Fracture

Work of fracture for the Nicalon/SiC composites was determined for un-notched specimens loaded in four-point bending and the results are displayed as a function of coating thickness in Figure 4. Although there was a measurable change in interfacial shear strength for the composites with the thicker interface layers, work of fracture was constant (Table 2). Upon examination of the fracture surfaces of the composites, a decrease in pull-out length with decreasing interlayer thickness was observed. Increasing interfacial shear stress results in a shorter critical length for load transfer thus a reduction in pull-out length. These concurrent changes in interfacial forces and pull-out length are equally offsetting therefore cause the work of fracture over

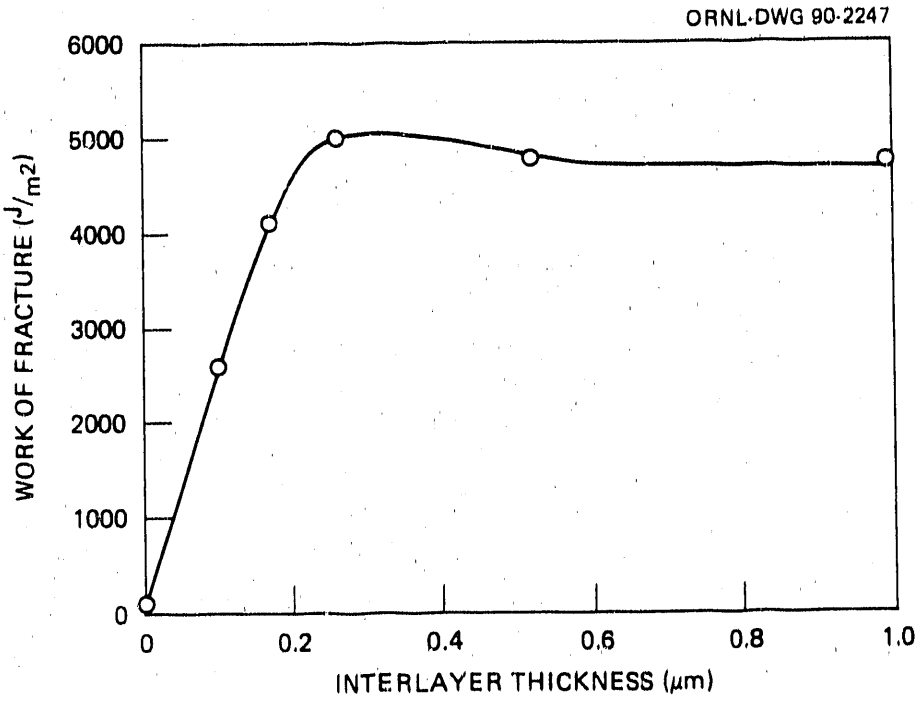

Figure 4. The influence of carbon interlayer thickness of the work of fracture for Nicalon/SiC composites.

the range of interfacial shear strengths to be constant (the same amount of energy is expended to pull a short fiber against high friction as for a longer fiber with lower friction).

The toughness of composites with thinner fiber coatings decreases with the decreasing layer thickness. As the thickness of the coating is decreased, the mechanisms of debonding and frictional sliding change. Fiber debonding and pull-out are more difficult as interfacial shear stress increases, and at a given stress, the mode of failure of the composite is changed. Fiber pull-out lengths becomes extremely short and/or fibers fracture in close proximity to the crack front, resulting in brittle failure and low toughness.

DISCUSSION

The mechanical properties of a fiber-reinforced composites are determined, to a large extent, by the degree of bonding and friction at

the fiber-matrix interface. In the case of uncoated Nicalon fibers in a SiC matrix, extensive chemical bonding and damage to the fibers during processing result in brittle failure of the composite. The application of a carbon interlayer protects the fibers and prevents chemical interaction at the fiber-matrix interface. The properties of the composites are thus influenced by the development of a mechanical bond at the fiber-matrix interface.

Interfacial shear stress in ceramic matrix composites has been described as a combination of the stress necessary to debond the interface, and the Coulomb frictional forces arising from the interaction of compressive stress acting on the fiber with the characteristic coefficient of friction of the interface.[22,23] The compressive stresses acting on the fiber can arise from a number of sources but characteristically arise from thermal expansion mismatch between the fiber and matrix. When the thermal expansion coefficient of the fibers is greater than that of the matrix ($\alpha_f > \alpha_m$), the fibers will shrink away from the matrix upon cooling. If there is poor bonding at the interface, the fiber will separate from the matrix in the radial direction, and neglecting debris or asperities at the debond surface, friction and shear stresses along the interface will be zero. When $\alpha_f < \alpha_m$, the matrix will contract more than the fibers upon cooling. The matrix will radially compress the fibers, increasing the degree of bonding and friction at the fiber-matrix interface.

Typically, thermal expansion mismatch effects, and thus interfacial shear stresses, have been modified by varying the composition of a matrix or by adjusting processing conditions.[16,24-27] Although these changes have a significant influence on the fiber-matrix interface and the mechanical properties of the composites, intercomparison of the influences of the interface is complicated by the consequential changes in matrix and fiber properties associated with altering compositions or processing conditions. Fiber coatings offer an alternative method of varying interfacial shear strength. Fiber coatings have been used to weaken interfacial bonding in a variety of fiber-reinforced ceramic matrix composites. Thin boron nitride coatings were found to control bonding and act as a diffusion barrier in ceramic fiber reinforced oxide matrix composites.[15,28] The

application of BN layers to the fibers prior to processing produced composites with significantly improved strength and toughness as compared to those fabricated from untreated fibers.

The influence of interlayer thickness on interfacial forces and mechanical properties of fiber-reinforced ceramic composites has received little attention. The influence of varying the thickness of a pyrocarbon fiber coating on the properties of Nicalon/LAS composites fabricated using a sol-gel/hot pressing technique has been examined.[29] Interlayer thicknesses up to 1 μm were investigated. An improvement in flexure strength was observed with increasing layer thickness up to a thickness of 0.4 μm beyond which strength decreased. Interfacial shear stresses were not measured and the variations in strength with respect to coating thickness were assumed to be due to mechanisms other than interfacial stresses.

The effects of a film at the interface on the stresses due to thermal contraction mismatch in whisker- and fiber-reinforced ceramic composites has been examined.[30] A reduction in thermomechanical stress is suggested only when a low modulus interfacial coating is present. For Nicalon/SiC composites, the matrix has a higher thermal expansion than the fiber thus upon cooling from processing temperatures, a clamping of the fibers occurs. The residual interfacial compressive stress for uncoated Nicalon fibers in a SiC matrix has been calculated to be $\approx$ 250 MPa, a significant residual compressive stress. The predicted influence of the graphitic carbon coating on the stresses at the fiber-coating-matrix interfaces in Nicalon/SiC composites is shown in Figure 5.

The presence of the carbon interlayer alters the compressive stresses at the interface. The carbon coating is able to deform and act as a buffer layer and thus is able to accommodate a large portion of the residual clamping stress of the matrix. The thickness of the carbon coating influences the clamping stress on the fiber and thus controls interfacial shear stress. Thicker coatings are able to absorb more of the stress caused by the thermal expansion mismatch of the components, therefore interfacial shear strength is inversely proportional to thickness (Figure 6).

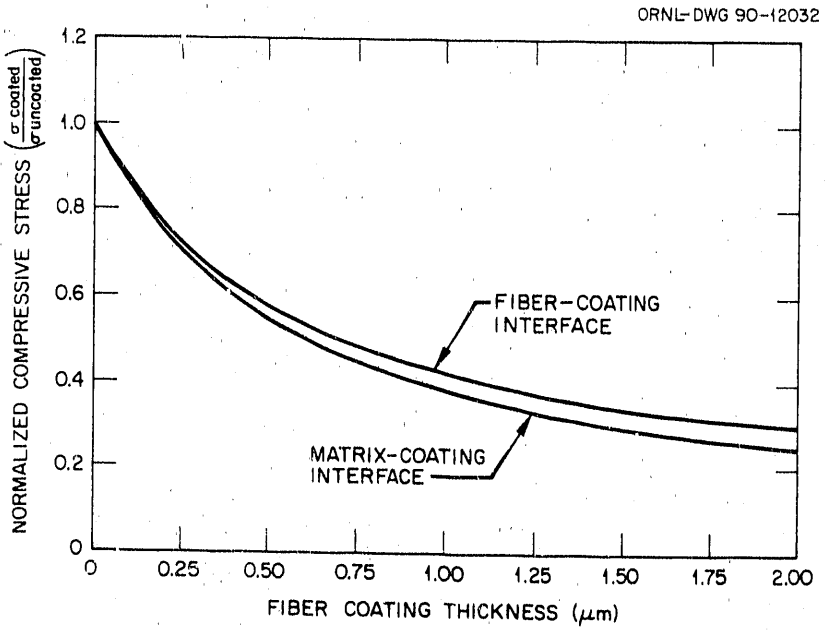

Figure 5. The predicted effects of the carbon interlayer on the compressive stresses at the fiber-matrix interface in Nicalon/SiC composites.

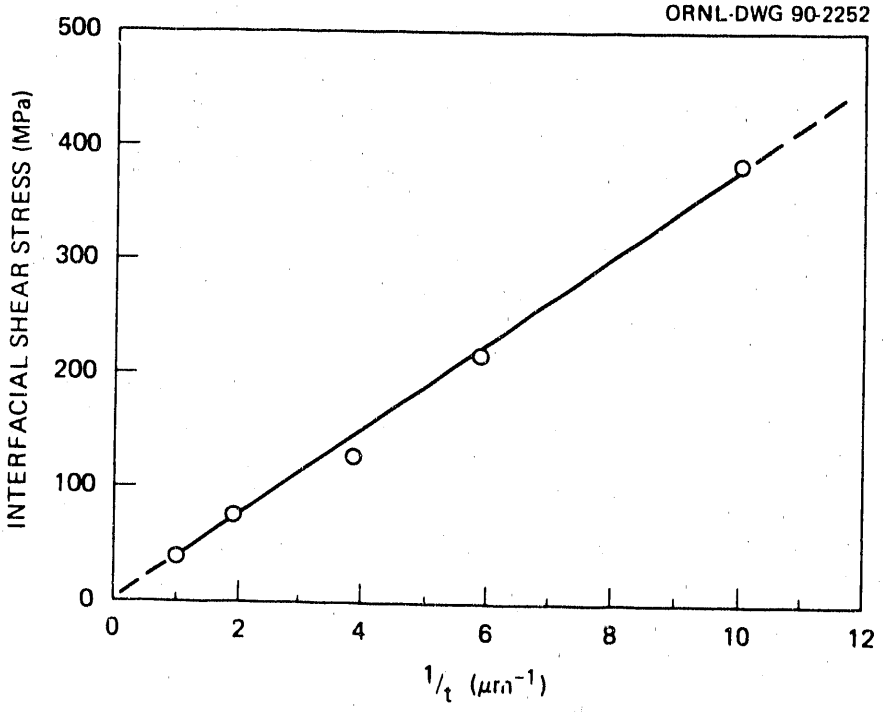

Figure 6. Interfacial shear stress was found to be inversely proportional to coating thickness.

As the thickness of the carbon layer is decreased, interfacial shear stress will increase and at some point exceed the maximum necessary for debonding and pull-out. Crack interaction at the fiber-matrix interface is altered and, in the extreme case corresponding to relatively high interfacial stresses, debonding and crack deflection do not occur, resulting in brittle failure. It may also be possible to compress the coating beyond its limit and thus change the mode of debonding and friction at the interface. In this case, excessive force must be applied to debond and slide the fibers, most likely inducing severe damage to the interlayer and possibly to the fiber and matrix contact surfaces. Interface morphology, thus sliding surface characteristics, would be changed and frictional sliding force would not vary linearly with respect to applied load. This would also result in brittle failure for the composite.

CONCLUSIONS

The fiber-matrix interface in fiber-reinforced ceramic composites controls the mechanical behavior of these materials. An extremely strong bond does not allow for crack deflection or debonding at the fiber-matrix interface therefore a crack propagating in the matrix simply passes through the fibers undisturbed resulting in brittle fracture. Conversely, an extremely weakened interface leads to a low matrix fracture stress and low ultimate strength, for as the composite is stressed, load is not transferred efficiently from the matrix to the fibers, thus the properties of the reinforcement are not utilized. Therefore, interfacial forces must be controlled to produce a composite material with good matrix failure stress and ultimate strength that also exhibits gradual composite failure through effective fiber pull-out.

Carbon has been shown to be an effective interfacial coating for the Nicalon/SiC system. The deposition of a graphitic carbon coating on the fibers prior to infiltration improved the ultimate strength and toughness of the material. The thickness of the coating affects the properties of the interface and thus can be varied to produce material with different mechanical properties. Interfacial shear stress is

inversely proportional to coating thickness. The carbon layer acts as a buffer to accommodate thermal expansion mismatch clamping stress at the fiber-matrix interface. At a thickness < 0.26 μm, the forces at the interface compress the coating beyond its limit and the failure mode of the composite becomes more brittle. This suggests interfacial shear strength, i.e., friction and debonding, is to high and does not permit crack deflection, fiber debonding, and fiber pull-out that are essential for strength and toughness in these brittle-brittle composite systems.

ACKNOWLEDGMENTS

This research is sponsored by the U.S. Department of Energy, Fossil Energy AR&TD Materials Program, under contract DE-AC05-840R21400 with Martin Marietta Energy Systems, Inc. The author would like to thank the ORNL High Temperature Materials Laboratory User Center for access to their mechanical property and analytical facilities. Appreciation is due P. F. Becher and M. K. Ferber for their review of the paper and for H. Neu for final manuscript preparation.

REFERENCES

1. Stinton, D. P., A. J. Caputo, and R. A. Lowden, "Synthesis of Fiber-Reinforced SiC Composites by Chemical Vapor Infiltration," *Am. Ceram. Soc. Bull.* **65**(2), 347-350 (1986).

2. Stinton, D. P., T. M. Besmann, and R. A. Lowden, "Advanced Ceramics by Chemical Vapor Deposition Techniques," *Am. Ceram. Soc. Bull.* **67**(2), 350-355 (1988).

3. Besmann, T. M., D. P. Stinton, and R. A. Lowden, "Chemical Vapor Deposition Techniques," *MRS Bull.* 13(11) 45-50 (1988).

4. Caputo, A. J., D. P. Stinton, R. A. Lowden, and T. M. Besmann, "Fiber-Reinforced SiC Composites with Improved Mechanical Properties," *Am. Ceram. Soc. Bull.* **66**(2), 268-272 (1987).

5. Besmann, T. M., R. A. Lowden, D. P. Stinton, and T. L. Starr, "A Method for the Rapid Chemical Vapor Infiltration of Ceramic Composites," *J. de Physique* 5(50), Colloque C5, 229-239 (1989).

6. Moeller, H. H., W. C. Long, A. J. Caputo, and R. A. Lowden, "Fiber-Reinforced Ceramic Composites," *Ceram. Eng. Sci. Proc.* 8(7-8), 977-984 (1987).

7. Moeller, H. H., W. C. Long, A. J. Caputo, and R. A. Lowden, "SiC Reinforced SiC Using Chemical Vaor Infiltration," *SAMPE Quart.* 17(3), 49-53 (1986).

8. Yajima, S., et al., "Synthesis of Continuous SiC Fibers with High Tensile Strength," *J. Am. Ceram. Soc.* 59(7-8), 324-327 (1976).

9. Yajima, S., et al., "Anomalous Characteristics of the Microcrystalline State of SiC Fibres," *Nature* 27(21), 706-707 (1979).

10. Kotlensky, W. V., "Deposition of Pyrolytic Carbon in Porous Solids," *Chem. Phys. Carbon* 9, 173-262 (1973).

11. Pierson, H. O., and M. L. Lieberman, "The Chemical Vapor Deposition of Carbon on Carbon Fibers," *Carbon* 13, 159-166 (1975).

12. Lowden, R. A., *Characterization and Control of the Fiber-Matrix Interface in Ceramic Matrxi Composites*, ORNL/TM-11039, Oak Ridge National Laboratory, Oak Ridge, TN (March 1989).

13. Lowden, R. A., and K. L. More, "The Effect of Fiber Coatings on Interfacial Shear Strength and the Mechanical Behavior of Ceramic Composites," *MRS Symposium Proceedings, Vol. 170, Tailoring Multiphase and Composite Ceramics* (March 1989).

14. Rice, R. W., "Mechanisms of Toughening in Ceramic Matrix Composites," *Ceram. Eng. Sc. Proc.* 2(7-8), 661-701 (1981).

15. Rice, R. W., et al., "The Effect of Ceramic Fiber Coatings on the Room-Temperature Behavior of Ceramic-Fiber Composites," *Ceram. Eng. Sci. Proc.* 2(7-8), 661-701 (1981).

16. Marshall, D. B., "An Indentation Method for Measuring Matrix-Fiber Frictional Stresses in Ceramic Components," *Comm. Am. Ceram. Soc.*, C259-260 (December 1984).

17. Phillips, D. C., "The Fracture Energy of Carbon-Fibre Reinforced Glass," *J. Mater. Sci.* 7, 1175-1191 (1972).

18. Phillips, D. C., "Interfacial Bonding and the Toughness of Carbon-Fibre Reinforced Glass and Glass-Ceramics," *J. Mater. Sci.* 9, 1847-1854 (1974).

19. Mandell, J. F., et al., "Modified Microdebonding Test for Direct In Situ Fiber/Matrix Bond Strength Determination in Fiber Composites," pp. 87-108 in *Composite Materials: Testing and Design (Seventh Conference)*, ASTM STP 893, ed. J. M. Whitney, American Society for Testing and Materials, Philadelphia (1986).

20. Marshall, D. B., and A. G. Evans, "Failure Mechanisms in Ceramic-Fiber/Ceramic-Matrix Composites," pp. 90-123 in *Ceramic Containing Systems*, ed. A. G. Evans, Noyes Publications, Park Ridge, NJ (1986).

21. Coble, R. L., and W. D. Kingery, "Effect of Porosity on Physical Properties of Sintered Alumina," *J. Am. Ceram. Soc.* 39(11), 377-385 (1956).

22. Bright, J., D. K. Shetty, C. W. Griffin, and S. Y. Limaye," *J. Am. Ceram. Soc.* 72(10), 1891-1898 (1989).

23. Shetty, D. K., "Shear-Lag Analysis of Fiber Push-Out (Indentation) Tests for Estimating Interfacial Frictional Stress in Ceramic Matrix Composites," *J. Am. Ceram. Soc.* 71(2), C107-C109 (1988).

24. Brennan, J. J., "Interfacial Characterization of Glass and Glass-Ceramic Matrix/Nicalon SiC Fiber Composites," *MRS Proceedings, Vol. 20, Tailoring Multiphase and Composite Ceramics*, ed. R. E. Tressler et al., Plenum Publishing Corporation, pp. 549-560 (1986).

25. Marshall, D. B., and W. C. Oliver, "Measurement of Interfacial Mechanical Properties in Fiber-Reinforced Ceramic Composites," *J. Am. Ceram. Soc.* 70(8), 542-548 (1987).

26. Grande, D. H., J. F. Mandell, and K. C. C. Hong, "Fibre-Matrix Bond Strength Studies of Glass, Ceramic, and Metal Matrix Composites," *J. Mater. Sci.* 23, 311-328 (1988).

27. Griffin, C. W., D. K. Shetty, and S. Y. Limaye, to be published in the Proceedings of the 14th Annual Conference on Composites and Advanced Ceramics, American Ceramic Society, Cocoa Beach, FL, January 1990.

28. Bender, B., D. Shadwell, C. Bulik, L. Incorvati, and D. Lewis III, "Effect of Fiber Coatings and Composite Processing on Properties of Zirconia-Based Matrix SiC Fiber Composites," *Am. Ceram. Soc. Bull.* 65(2), 363-369 (1986).

29. Menessier, E., et al., "Thermo-mechanical Characterization of Ceramic Composites Made of a LAS Galss-Ceramic Reinforced with Silicon Carbide Fibers," pp. 121-127 in *Proceeding of the Third European Conference on Composite Materials*, A. R. Bunsell, P. Lamicq, and A. Massiah, Elsevier Applied Science (1989).

30. Hsueh, C.-H., P. F. Becher, and P. Angelini, "Effects of Interfacial Films on Thermal Stresses in Whisker-Reinforced Ceramics," *J. Am. Ceram. Soc.* 71(11), 929-933 (1988).

DEVELOPMENT OF NONDESTRUCTIVE EVALUATION METHODS AND PREDICTION OF EFFECTS OF FLAWS ON THE FRACTURE BEHAVIOR OF STRUCTURAL CERAMICS

W. A. Ellingson, J. P. Singh, N. Gopalsami, S. L. Dieckman, C. –Y. Chu, T. Hentea, and P. Rizo

Materials and Components Technology Division
ARGONNE NATIONAL LABORATORY
Argonne, Illinois 60439

ABSTRACT

To establish predictive performance (i.e., fracture behavior) of structural ceramic composites, we undertook in combination (a) a study of flaws and material variations as they relate to mechanical properties and (b) development of nondestructive evaluation (NDE) methods suitable for obtaining data on flaws and material variations. Effects of whisker addition on development of flaw population and the resulting mechanical properties were evaluated in both green (cold-pressed) and dense (hot-pressed) Si_3N_4-whisker-reinforced Si_3N_4 matrix composites. To detect critical flaws in these composites, we used microfocus X-ray computed tomography and ultrasonic NDE methods. In addition, we designed a nuclear magnetic resonance (NMR) facility for use on composites.

Results to date suggest that failure in green Si_3N_4 composites initiates primarily from pores. Evaluation by mercury intrusion porosimetry of pore-size distribution indicated that average pore size and content increase with increasing whisker content.

Fracture toughness of hot-pressed composites increased from 6.5 to 8.8 with the addition of 5 vol.% whisker. Correspondingly, strength increased from 673 to 802 MPa. Further increases in whisker content resulted in decreased toughness and strength. This nonlinear dependence of strength and toughness is believed to be due to the combined effects of whisker reinforcement and grain size. Failures in these composites were observed to initiate from flaws such as pores, Si- and Al-rich inclusions, and whisker agglomerates. Critical flaw sizes calculated by fracture mechanics were larger than those observed by fractography (i.e., destructive evaluation); this suggests that the toughness measured in bulk specimens may be an overestimate of the local toughness that controls flaw propagation.

The spatial resolution required to detect variations in these ceramics has required significant improvements in NDE technologies. The microfocus radiography system, converted to a 3-D X-ray computed tomography (CT) system, was significantly modified

to improve spatial resolution. In addition, the ultrasonic system was modified, and data show sensitivities to variations in whisker content. The 3-D X-ray CT system now allows density variations of < 2% to be detected in green bodies and to a spatial resolution of 25-50 μm.

Preliminary results will also be presented on the correlation of critical flaw locations predicted by NDE and observed by fractography.

INTRODUCTION

Land-based turbines for electric power generation can be driven by direct-coal-fired systems, by gas produced by coal gasification, or—in the case of combined gas turbine/steam turbine systems—by fluidized bed systems.[1] Although gas turbines are usually used by domestic electric utilities to generate power during peak demands, it is anticipated that future demands will call for more turbine usage at high efficiencies, which will require higher turbine-inlet-temperatures (TIT).[1,2] Present turbines operate with a TIT of 760-1150°C without auxiliary cooling, and to 1260°C with auxiliary cooling.[1] Recent work by the U.S. Department of Energy (DOE) has focused on development of turbines with a TIT of 1430-1650°C. A high-performance turbine has reportedly operated at 1430°C[1], but in general, problems with fabrication and lack of material reliability has driven a development towards more reliable alternate materials.

Ceramic composites are a new class of structural ceramics that offer higher reliability and higher fracture toughness. However, ceramic composite development is a very immature technology, and significant improvements in processing technology are needed before these materials can be used reliably. New developments are also needed in nondestructive evaluation (NDE) methods.

The purpose of this paper is to present recent work on development of an understanding of the fracture behavior of Si_3N_4/Si_3N_4 ceramic/ceramic composites and on development of NDE methodologies (3-D microfocus X-ray computed tomography, nuclear magnetic resonance, and ultrasonic methods) that can detect nonuniformities in processed materials and that may generate data to be used as a precursor to failure prediction.

PREPARATION OF CERAMIC COMPOSITE SPECIMENS

Powders of monolithic Si_3N_4 and its composites with 5-35 vol.% Si_3N_4 whiskers (0.6 μm in diameter and 45 μm in length) were prepared by a conventional ceramic powder processing technique.[3] MgO was used as the sintering aid and polyethylene glycol was used as the binder.

Rectangular bar specimens were prepared by either uniaxial cold-pressing at ≈25,000 psi in a steel die or hot-pressing. Cold-pressed specimens were subsequently bisque-fired in a pure nitrogen atmosphere at 650°C for 2 h to evaluate the effects of binder burnout on the strength of the green specimens. Disk-shaped monolithic and composite specimens were made by hot-pressing in a BN-coated graphite die at 1750°C and 30 MPa for 2 h in an N_2 atmosphere. Density of the disks was as high as 99% of theoretical. The phase content of the hot-pressed disks was determined by X-ray diffraction using CuKα radiation. Modulus-of-rupture MOR bars, typically 35 x 4.5 x 3.0 mm, were cut from the disks with a high-speed saw fitted with a diamond-impregnated blade. Subsequently, the bars were surface-ground on a diamond-impregnated grinding wheel to a surface finish of 30 μm, and tensile edges were beveled. The green and dense bars were then used for NDE studies, mechanical property measurement, and fractographic studies. Results of the NDE testing and fractographic observations for critical flaw locations were subsequently correlated.

MECHANICAL PROPERTY MEASUREMENTS AND FRACTOGRAPHY

Flexural strength was measured by using a four-point bending mode with a support span of 19.0 mm, loading span of 9.5 mm, and a crosshead speed of 1.27 mm/min in a universal testing machine. Fracture surfaces of the broken bars were examined by optical and scanning electron microscopy to establish fracture modes and to locate failure-initiating critical flaws. The fracture toughness, K_{IC}, was measured by the Vickers indentation technique,[4] and elastic modulus was determined from ultrasonic velocity measurements made by a pulse-echo technique.[5]

The average value of the flexural strength was 1.89 ± 0.28, 1.62 ± 0.21, 1.49 ± 0.37, and 1.19 ± 0.24 MPa for green (cold-pressed) composites, and 3.87 ± 0.61, 4.00 ± 0.63, 4.14 ± 0.63, and 4.08 ± 0.49 MPa for bisque-fired composites with 0, 5, 15, and 20 vol.% Si_3N_4 whisker reinforcements, respectively.

Pore size distribution for both cold-pressed and bisque-fired specimens was evaluated by mercury intrusion porosimeter. The results indicated that the distributions shift towards a larger pore size with increasing whisker contents. Also, the bisque-fired specimens have a lower average pore size than the cold-pressed specimens. The strength of cold-pressed specimens with different whisker contents is believed to be controlled by total pore volume, which increases with increasing whisker content and results in decreased strength. On the other hand, the strength of bisque-fired specimens with different whisker contents is probably controlled by two competing factors; total pore volume and whisker reinforcement. For bisque-fired specimens, the strength of the composite is expected to increase with the reinforcing-whisker content. However, as observed for cold-pressed specimens, the increase in whisker content was associated with increase in total pore volume, resulting in a decrease in strength. Due to these two competing effects, the strength values of the bisque-fired specimen with different whisker contents remain nearly a constant. The increase of strength of the bisque-fired specimens relative to the cold-pressed specimens is believed due to the decreased pore size after bisque firing.

Strength data for composites with 0-20 vol.% whisker contents were used to construct Weibull plots to evaluate the flaw size distribution (strength distribution) in both the cold-pressed and bisque-fired specimens. From these plots, the values of Weibull modulus were calculated to be ≈ 5-7 for cold-pressed composites, and ≈ 7-9 for bisque-fired composites. The slightly higher values in the bisque-fired specimens may be due to a narrower distribution of pore sizes in these specimens. Strength distributions of the bisque-fired specimens will be compared with those of the corresponding dense specimens currently being fabricated by hot isostatic pressing of identical sets of cold-pressed and bisque-fired specimens. These comparisons will provide information on the correlation between flaw populations in green and corresponding densified specimens.

The measured values of strength (σ_f), fracture toughness (K_{IC}), and elastic modulus (E) for hot-pressed Si_3N_4 and its composites are summarized in Table 1.

Table 1. Mechanical Properties of Hot-pressed Si_3N_4 Composites

Vol.% of whisker	Strength, σ_f (MPa)	Fracture Toughness, K_{IC} (MPa$\sqrt{m}$)	Elastic Modulus, E(GPa)
0	673 ± 116	6.8 ± 0.2	314
5	814 ± 134	8.8 ± 0.4	316
10	802 ± 151	8.4 ± 0.5	318
15	740 ± 64	7.3 ± 0.3	311
20	688 ± 72	6.5 ± 0.4	312
35	721 ± 48	7.2 ± 0.4	311

The mechanical property data in Table 1 were used to calculate critical flaw size using the fracture mechanics approach,[6,7] which states that

$$\sigma_f = (1/1.35)\ K_{IC}/\sqrt{C_c}\ , \qquad (1)$$

where σ_f is strength, K_{IC} is fracture toughness, and C_c is the critical flaw size. The calculated values of critical flaw size (in μm) were 58-86, 33-77, 20-115, 54-89, and 53-105 for composites with 0, 5, 10, 15, and 35 vol.% whisker contents, re-spectively. The critical flaws were also located and their sizes were measured by fractographic observation of the fracture surfaces of the broken MOR bars, which indicated that pores, whisker agglomerates, and Si and Al-rich inclusions are the sites of failure origin (Fig. 1). The measured critical flaw sizes were generally independent of whisker loading. If so, as shown in Eq. 1, the strength of the composites should be proportional to fracture toughness if critical flaw size does not change with whisker loading. In agree–ment with this hypothesis, our data in Table 1 indicate that the strength variation with different whisker loadings was similar to that of the fracture toughness variation. This qualitatively confirms the validity of critical flaw size measurements.

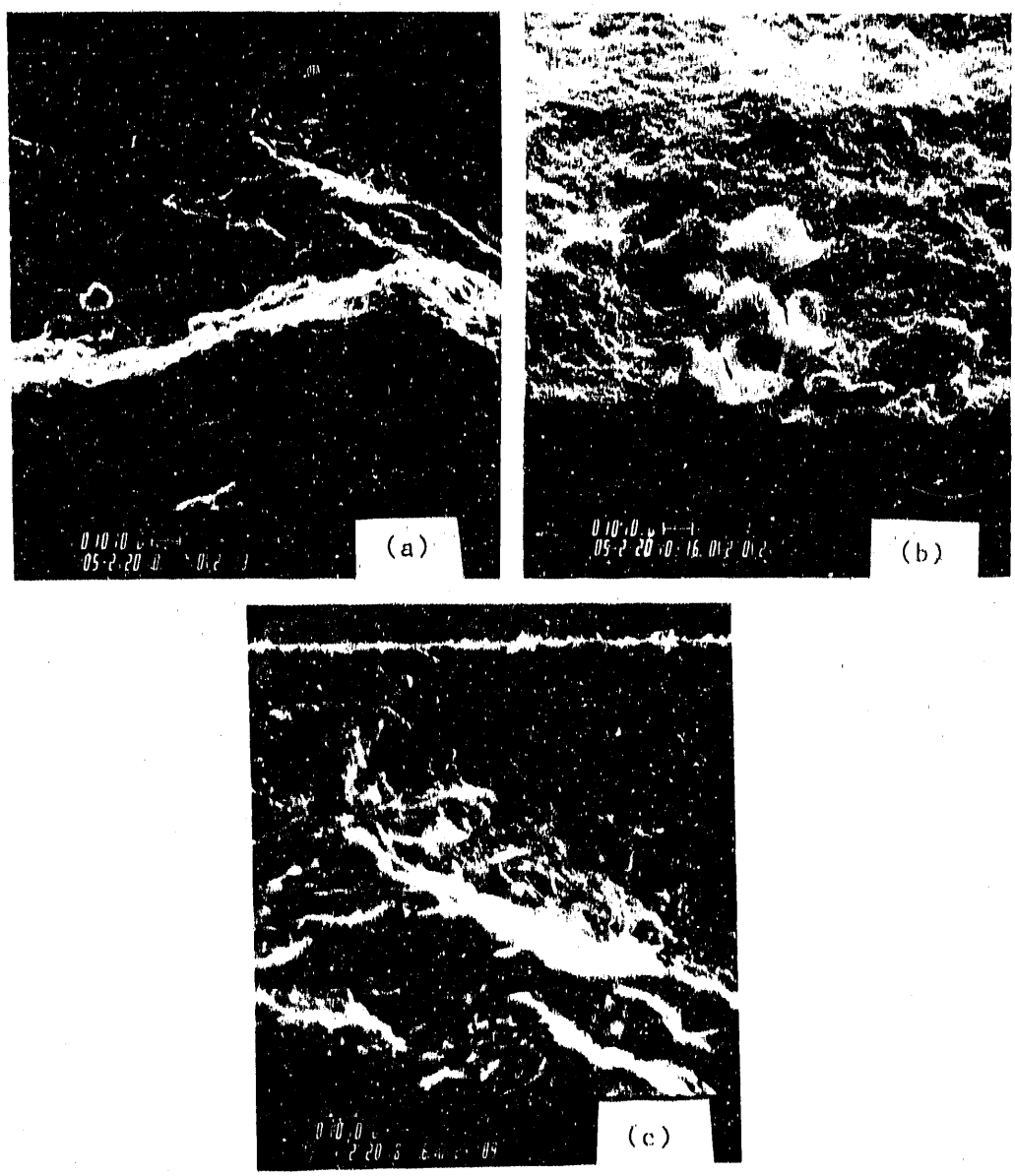

Fig. 1. Scanning electron micrographs of the fracture surface of a Si_3N_4-15% Si_3N_4 whisker composite showing critical flaws: (a) whisker agglomerate, (b) inclusion, and (c) pores.

Measured critical flaw sizes were observed to be smaller than those calculated by fracture mechanics; this affects the necessary NDE sensitivity. The ratio of the calculated and measured flaw size ranged from 1.6 to 2.1. This observation suggests that the K_{IC} measured in bulk specimens may not be applicable for local crack propagation and may be an overestimate of the local fracture toughness that controls the crack propagation. A comparison between fractographic observations and NDE (ultrasound) predictions of the critical flaw location indicated good agreement in 6 of 10 specimens evaluated.

CHARACTERIZATION OF Si_3N_4/Si_3N_4 COMPOSITES BY X-RAY MICROTOMOGRAPHY

Development of whisker/matrix ceramic/ceramic composites with uniform mechanical properties is difficult because preferential alignment of whiskers yields anisotropic behavior. In addition, clumping of whiskers (agglomeration) provides flaw sites for fracture initiation, as noted in the preceding section. Characterization of green bodies by destructive methods (in order to provide process development information) is difficult because of the "smearing" that occurs when attempting to "polish" the section. Thus, high-resolution NDE characterization methods can be highly useful for characterizing processing variables.[8]

Because of the variation of whisker/matrix parameters in all three dimensions, NDE characterization methods to provide 3-D information are needed. X-ray computed tomographic imaging is very sensitive to density variations, (typically less than 1% above noise) and, properly configured, e.g., 3-D with point X-ray source, can provide very high spatial resolution (< 25 μm) in all three dimensions.[9,10,11] A 3-D microfocus X-ray computed tomographic imaging facility has been developed, and initial data have been obtained on cold-pressed Si_3N_4/Si_3N_4 and hot-pressed Si_3N_4/Si_3N_4 composite materials.[11]

The 3-D microfocus scanner is shown schematically in Fig. 2. With the use of a microfocus source, very high spatial resolutions are achieved. Three-dimensional images are obtained via a two-dimensional detector. The detector is an image intensifier/CCD array (512 x 512) camera. The images are reconstructed on a VAX 8700 or an Alliant FX-8 Super Computer. The codes we use for the reconstruction are Feldkamp[9] and Radon.[11] The significant differences in these codes will be discussed in a future paper.[11]

Application of 3-D microfocus computed tomography to ceramic/ceramic composites for fracture behavior prediction began in calendar year 1989. An initial set of

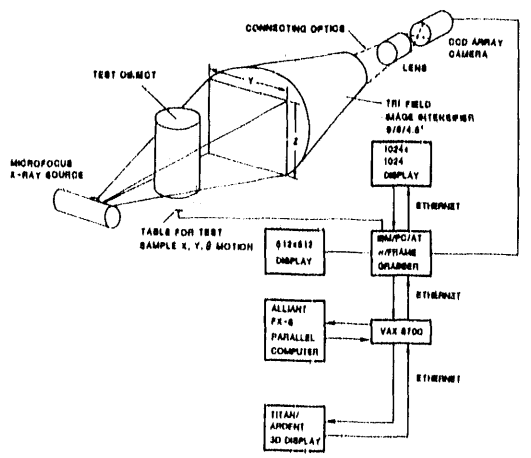

Fig. 2. Schematic of 3-D microfocus X-ray computed tomography system.

4 x 8 x 50 mm MOR bars was produced; their whisker loadings and bulk densities are listed in Table 2. For the microfocus X-ray CT studies, two specimens were used together during data acquisition. They were paired together as listed in Table 3.

Table 2. Si_3N_4/Si_3N_4 Composites for Computed Tomography

	Sample Identification	Whisker Loading (vol.%)	Bulk Density (g/cm^3)
COLD–PRESSED	1B	0	1.85
	1Y	0	1.86
	5U	10	1.83
	5V	10	1.80
HOT–PRESSED	250-6	0	3.201
	209-2	0	3.194
	249-6	20	3.195
	193	20	3.199

Table 3. Sample Pairs Used in Microfocus CT Tests

Test	Samples	Density (g/cm^3)
1	1Y/5U	1.86/1.83
2	1B/5V	1.85/1.80
3	250–6/193	3.201/3.199
4	209–2/249–6	3.194/3.195

RESULTS FOR GREEN COMPOSITES

The microfocus X-ray computed tomography data for green composites show a high sensitivity to density variation between samples, as well as detection of voids and apparent whisker stratification. In all cases, a 15-mm-long region in the MOR bars,

covering the 9.5-mm-long region used in fracture behavior, were studied. Because the data are acquired on a 3-D scanner, individual "cross sections" can be selected for display throughout this 15-mm section. We have chosen to use 1 mm thick "cross sections," which results in 15 sections to be analyzed for each test. Figure 3 shows four typical X-ray CT cross-sections obtained from test number 1. Clearly evident in each cross-section is the 1.5% difference in density. Figure 3a, shows cross-sections taken near the middle of the samples. In these cross-sections, a very clear low density region is noted in the section of sample 1Y (the uppermost sample in each case). Based on gray scale values, this appears to be ≈ 1.5 - 2% lower than the surrounding body. We were able to establish that this low density region extended over 5 of our cross-sections or approximately 5 mm. Since this is located in the constant-moment cross-section of the MOR bars, this would be expected to impact the green strength. Further, detection of apparent whisker stratification was detected in sample 5U. This is seen in Fig.3b. The dark regions parallel to the width of the specimen are normal to the pressing direction as has been observed in several destructive analysis in earlier work.

RESULTS FOR DENSE COMPOSITES

The microfocus X-ray CT data for dense Si_3N_4/Si_3N_4 composites show no variation in density between samples, as would be expected because the specimens were all of the same density. One small void (< 1 mm in diameter) was detected in one MOR bar. From the standpoint of data acquisition, the dynamic range of the detection system may be a limitation on detection sensitivity for dense composites. This is now being addressed.

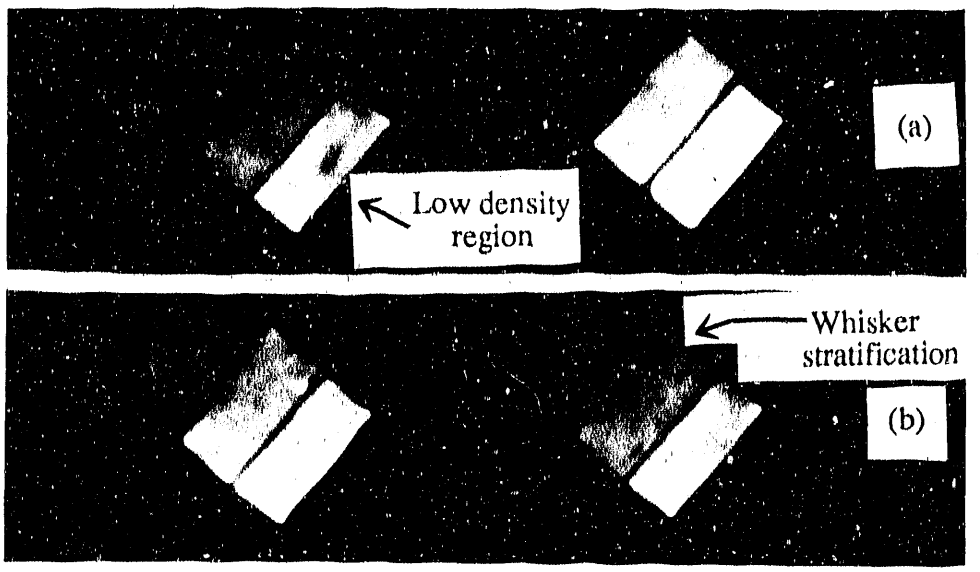

Fig. 3. Microfocus X-ray CT cross-section images of green Si_3N_4/Si_3N_4 composites showing density variation of < 1.5% between samples, low-density region in the higher-density sample and apparent whisker stratification. Sample cross section is 4 x 8 mm. (a) images showing low density inclusion, and (b) images showing apparent whisker stratification.

DEVELOPMENT OF NMR IMAGING SYSTEM FOR CERAMIC COMPOSITES

The chemical sensitivity of NMR suggests that this technique has a strong potential role relative to ceramic/ceramic composites. NMR imaging can detect poor whisker distribution (inhomogeneities in distribution, and agglomerization) and fibers or platelets in composites. Because NMR imaging is a quantitative technique, it is quite sensitive to density variations also, as manifested in concentration of NMR–active nuclei

Despite the advances in NMR imaging in the medical area, few effort[12,13] have been made to apply this technique to materials studies because of the need for special imaging systems and techniques. Because the spectral properties and the desired resolution are often material/sample-dependent, the specific hardware and software requirements vary greatly. They vary even among ceramic materials, as for instance, among slip-cast and injection-molded ceramics and composites.

Large proton spectral widths (approximately 2500 Hz) in green injection-molded ceramics require the application of high magnetic field gradient strengths to achieve reasonable desired spatial resolution. For example, the imaging of ceramics with a spatial resolution of 100 μm would require a gradient strength of 50 G/cm. Because these materials have short spin–spin relaxation times (T2), back-projection imaging is more suitable than the conventional spin–warp techniques. Narrow spectral linewidths possible in as-cast slip-cast composites will allow use of conventional (medical-type) multidimensional-slice selected spin-warp (or spin-echo) imaging techniques. However, the need to image whisker aggregates may require the ability to obtain very thin (< 0.4 mm) slices with 50 μm spatial resolution. We designed and built a flexible, modular–type NMR imaging system for characterization of injection-molded and slip-cast green ceramics and composites.

The Argonne NMR imaging system has been built around a Bruker CXP–100 spectrometer. The main imaging accessories needed to convert the spectrometer into an imaging system included a special imaging probe, an IBM-PC-based pulse programmer, and versatile image reconstruction software. The imaging probe is designed to be used in an 89–mm vertical bore, 2.35–T superconducting magnet in conjunction with the Bruker CXP–100 spectrometer. The probe includes an RF coil for excitation and detection of the nuclear signals, and a set of gradient coils to create orthogonal gradient fields, up to 50 G/cm, with respect to the x, y, and z spatial coordinates.[14] The probe can accommodate samples up to 28 mm in diameter to meet our present requirements. Using trigger pulses from the spectrometer, the pulse programmer provides control pulses for the x, y, and z gradient coils, as well as RF-wave-shaping pulses necessary for image slice selection. NMR data are acquired on the Bruker spectrometer and then transported from its Aspect 3000 computer to a VAX 8700 computer via Ethernet for image reconstruction and processing. Image reconstruction is performed by application of multidimensional FFT techniques or filtered back-projection image reconstruction techniques. Image processing and display are performed on a local PC clone.

The efficacy of the imaging system for injection-molded monolithic ceramic characterization was tested by imaging modulus-of-rupture (MOR) test bars made of injection-molded Si_3Ni_4 supplied by the Garrett Ceramic Components Division. A

resolution phantom was prepared by drilling holes of various sizes in a test bar see (Fig. 4). Back-projection images of protons from the organics in the bar were produced in the x–z plane (no slice selection was made along the thickness of the bar). A total of 90 projections and 128 averages were used for each image. Figure 5 shows two NMR images of the resolution phantom corresponding to gradient strengths of 3.6 and 7.2 G/cm. Adjacent to the resolution phantom is the image of an intensity standard (a small section of an MOR bar placed next to the test bar). Clearly, the holes in the phantom are well-resolved at 7.2 G/cm except for the smallest hole (1.02 mm) at the bottom, which is barely visible. The two upper holes are not in the field of view. Based on this test, projected resolution with 50-G/cm gradient strength is 175 μm.

CONCLUSIONS

This paper has addressed the role of flaw characterization in the prediction of fracture behavior of whisker-type ceramic/ceramic composites and the detection of flaws by nondestructive characterization methods. Si_3N_4/Si_3N_4 composites of 0-35 vol.% whiskers have been produced by cold-pressing and hot-pressing. Microfocus X-ray computed tomography has been developed and has been shown to be able to detect density variations in green bodies to less than 1.5%. Detection of small density variations, e.g., < 2%, in dense Si_3N_4/Si_3N_4 bodies will necessitate a higher-dynamic-range detector or a capability to shift the 7-8 bit dynamic range available. A nuclear magnetic resonance imaging system has been built to study ceramic/ceramic composites and will be used to study whisker/matrix chemical and physical variations.

ACKNOWLEDGMENTS

This work was supported by the U.S. Department of Energy, Office of Fossil Energy, Advanced Research and Technology Development Materials Program, work breakdown structure element ANL-1, under contract, W-31-109-Eng-38. M. Szuster, D. Lifka, and P. Bertoncinni of Argonne National Laboratory assisted with experimental data acquisition and computer software development.

REFERENCES

1. W. P. Parks, Jr., R. R. Ramey, D. C. Rawlins, J. R. Price and M. vanRoode, "Potential Applications of Structural Ceramic Composites in Gas Turbines," Oak Ridge National Laboratory Report ORNL/SUB/88–5A798/01 (September 1989).

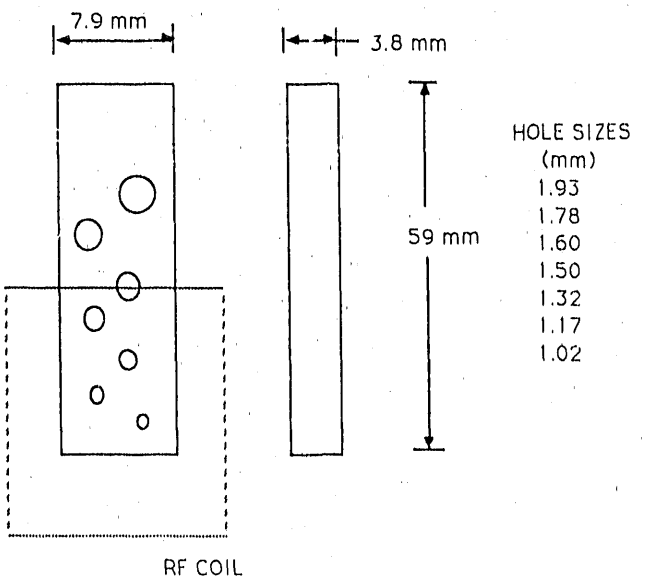

Fig. 4. NMRI imaging resolution phantom for injection-molding studies.

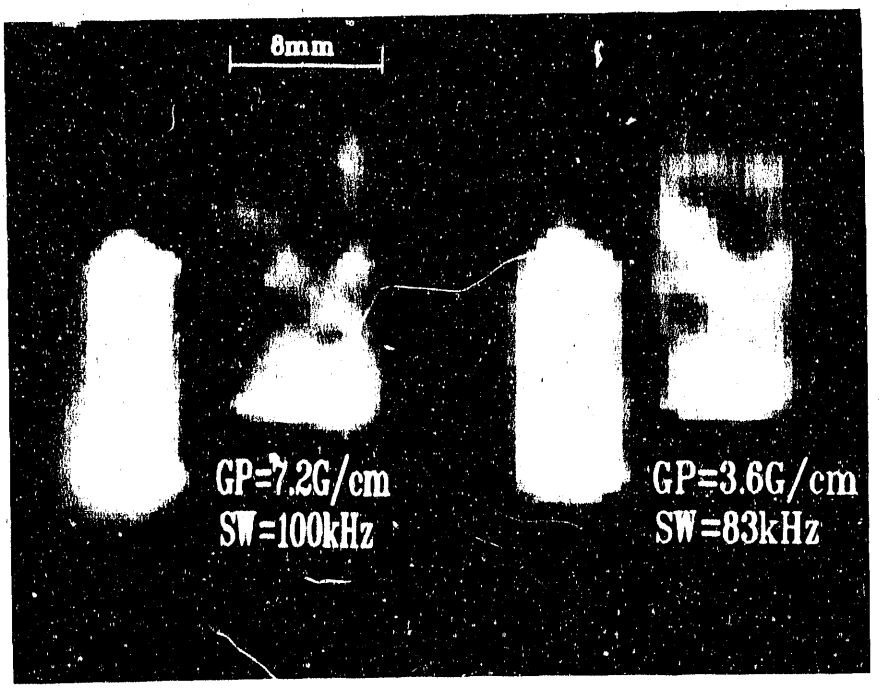

Fig. 5. NMR images showing impact of gradient strength. Current gradient strength of the system is more than 50 G/cm.

2. "Materials for Large Land-Based Gased Turbines," Electric Power Research Institute Report, EPRI APL-4476 (March 1986).

3. C. Y. Chu and J. P. Singh, "Mechanical Properties and Microstructure of Si_3N_4 -Whisker-Reinforced Si_3N_4 Matrix Composites," Proc. 14th Annual Conf. on Composites and Advanced Ceramics, Cocoa Beach, FL, Jan. 14-17, (1990).

4. A. G. Evans, "Fracture Toughness: The Role of Indentation Techniques," in Fracture Mechanics Applied to Brittle Materials, S. W. Freiman, ed., ASTM STP 678, pp. 112-135 (1979).

5. J. Krautkrämer and H. Krautkrämer, Ultrasonic Testing of Materials, Springer-Verlag, New York (1983).

6. A. S. Kobayashi, "Crack Opening Displacement in a Surface Flawed Plate Subjected to Tension or Plate Bending," in Proc. 2nd Intl Conf. on Mechanical Behavior of Materials, Boston, MA, pp. 1073-1077 (August 1976).

7. C. A. Anderson and R. J. Bratton, "Effect of Surface Finish on the Strength of Hot-Pressed Silicon Nitride," in Science of Ceramic Machining and Surface Finishing II, R. R. Hockey and R. W. Rice, eds., NBS Publication 562, pp. 463-476 (1979).

8. J. Minter, "The Role of NDE in Ceramic Turbine Engine Component Development," in Proc. of Third Intl. Symp. on Ceramic Materials and Components for Engines," V. J. Tennery, ed. Published by the Am. Ceram. Soc., pp. 1289-1298 (1988).

9. L. A. Feldkamp and G. Jesion, "3-D X-ray Computed Tomography," in Review of Progress in Quantitative Nondestructive Evaluation Vol. 5A, D. O. Thompson and D. E. Chimenti, eds. Plenum Press, pp. 555-565 (1985).

10. S. Webb, J. Sutcliffe, L. Burkinshaw and A. Horsman, "Tomographic Reconstruction from Experimentally Obtained Cone-beam Projections," IEEE Transactions on Medical Imaging Vol. MI-6, No. 1, pp. 67-73 (March 1987).

11. P. Rizo and W. A. Ellingson, "An Initial Comparison Between Two 3-D X-ray CT Algorithms," To be published in the Proc. Conf. on Nondestructive Evaluation of Modern Ceramics, Columbus, OH (July 1990).

12. J. M. Listerud, S. W. Sinton, and G. P. Drobny, "NMR Imaging of Materials," Analyt. Chem., 61, 23 (1989).

13. W. A. Ellingson, J. L. Ackerman, L. Garrido, P. S. Wong, and S. Gronmeyer, "Development of NMR Imaging Technology for Advanced Ceramics," Argonne National Laboratory Report ANL–87–53 (1988).

14. N. Gopalsami, G. A. Forster, S. L. Dieckman, W. A. Ellingson, and R. E. Botto, "Development of NMR Imaging Probes for Advanced Ceramics," Review of Progress in QNDE, D. O. Thompson and D. E. Chimenti, eds., Plenum Press, New York, Vol. 9A, pp. 861–868 (1990).

Vapor-Liquid-Solid SiC Whisker Process Development

P. D. Shalek and W. J. Parkinson

Materials Science and Technology Division
Los Alamos National Laboratory
Los Alamos, NM 87545

ABSTRACT

Los Alamos National Laboratory completed, at the end of fiscal year 1989, the laboratory-scale development of a process for growing VLS SiC whiskers. The DOE Office of Fossil Energy is sponsoring a transfer of this technology to industry.

PROGRAM STATUS

Los Alamos has worked, over the past seven years, on the laboratory-scale development of a batch process for producing very high quality beta-SiC whiskers of up to 3.5 inches long by the vapor-liquid-solid (VLS) process. These whiskers have some outstanding properties, being smooth-surfaced single crystals with relatively few internal defects, resulting in tensile strengths ranging up to 17 GPa (2.5 Msi) in conjunction with a high elastic modulus (580 GPa). Most of the Los Alamos effort has gone into optimizing a process designed to produce whiskers of up to about 1 inch long that can be chopped for short fiber composite reinforcement or used at the the as-grown length in the development of staple yarns, a more recent component of the program.

For the first time anywhere at the laboratory scale, Los Alamos was able to achieve reasonably-sized and reproducible, uniform yields of VLS SiC whiskers. This was done by identifying and controlling all the external whisker growth process parameters, the most important of which was found to be the uniform mixing of the process gases. Yields of up to 10 grams per run of prime whiskers were thus obtained in the 0.25 cubic foot developmental box reactor. Because of the complexity of the process chemistry, a gas chromatograph was installed to give real time process

gas monitoring and subsequent better understanding and control of the process. A very comprehensive and detailed report covering all of this VLS SiC whisker process development over the period March 1982 through September 1989 is scheduled to be issued at Los Alamos in June, 1990, as a joint DOE OAR&TD Topical Report/DARPA Final Report under the title, "Laboratory-Scale Development and Optimization of the VLS Growth Process for Beta-SiC Whiskers." (DARPA gave coordinated support over the period October 1983 through September 1986.)

The information obtained with the chromatograph, along with other parametric data, was incorporated into a relational database and used to develop rules for an expert artificial intelligence (AI) processing system. There are two parts to this system. A Whisker Growth Consultant provides the user with enough information to correctly set up the run to give the desired product. This set-up information, derived from the knowledge base, is then incorporated into the rules base used by the second part: the Control System. The control system responds to perturbations in the process conditions to ensure that the proper corrections will be made and the desired product obtained at the end of the run. Such a system was felt to offer the best means for transferring this expert-intense technology to industry. This control system has been described in detail in a very recent report.[1]

With the conclusion of the Los Alamos laboratory-scale process development, the DOE Office of Fossil Energy, through Martin Marietta Energy Systems, Inc., is sponsoring the engineering-scale development of the VLS SiC whisker process in industry via the RFP route. The goal for Phase I of this contract, which will run for two years, is to establish a process that is capable of producing 100-500 pounds of whiskers per year. Los Alamos has participated throughout the proposal process and will actively assist the sponsor and chosen contractor during the period of technology transfer.

---

[1] W. J. Parkinson, P. D. Shalek, E. J. Peterson, and G. F. Luger, "Designing an Expert System for the Production of Silicon Carbide Whiskers," in *TMS Annual Meeting Symposium on Expert Systems Applications in Materials Processing and Manufacturing*, M. Y. Demeri, Ed. (TMS, Warrendale, PA, 1989), pp.159-177.

DEVELOPMENT OF A USER-FRIENDLY SOFTWARE FOR THERMOMECHANICAL STRESS ANALYSIS OF REFRACTORY SYSTEMS

Oral Buyukozturk

Massachusetts Institute of Technology
Cambridge, MA 02139

En–Sheng Chen

Integrated Engineering Design, Inc.
515 North Belt, Suite 265
Houston, Tx. 77060

ABSTRACT

In this paper a user–friendly software IDEAL developed for an integrated design and analysis of refractory linings is described. The concept of the software is given and its capabilities are briefly described.

INTRODUCTION

Design of refractory linings presents an interactive and iterative process. In this process complexity exists in the integration of material and system related information, knowledge, the analysis capability, and the expertise in the interpretation of the results such that in the final step an optimum design can be achieved. Over the past ten years a substantial amount of knowledge on the thermomechanical behavior of refractories and quantitative information have been generated [1–5]. Various analysis methods have been developed for the prediction of stress–strain distribution, and progressive cracking effects in these systems. These development included complex nonlinear mechanics, numerical analysis, material modeling and behavioral knowledge of the refractory linings. However, the use of these available capabilities by the designers in a specific design project presents enormous difficulty due to the complexity of these systems.

A user–friendly computer program IDEAL has been developed to facilitate the use of these complex capabilities, namely, to perform thermomechanical finite element stress analysis and to provide an integrated design environment for layered

refractory lining systems. The concept and capabilities of this program is described in the following.

IDEAL SOFTWARE CONCEPT

The concept of the IDEAL computer program is based on a computer software system that integrates a common data base for data sharing, a material property library for data storage and transfer, a user–friendly interface for graphic modeling, a finite element analysis module for studying the system behavior, and a post processing capability for analysis result display, report, and interpretation.

A conceptual diagram showing the various modulus of the software system is shown below:

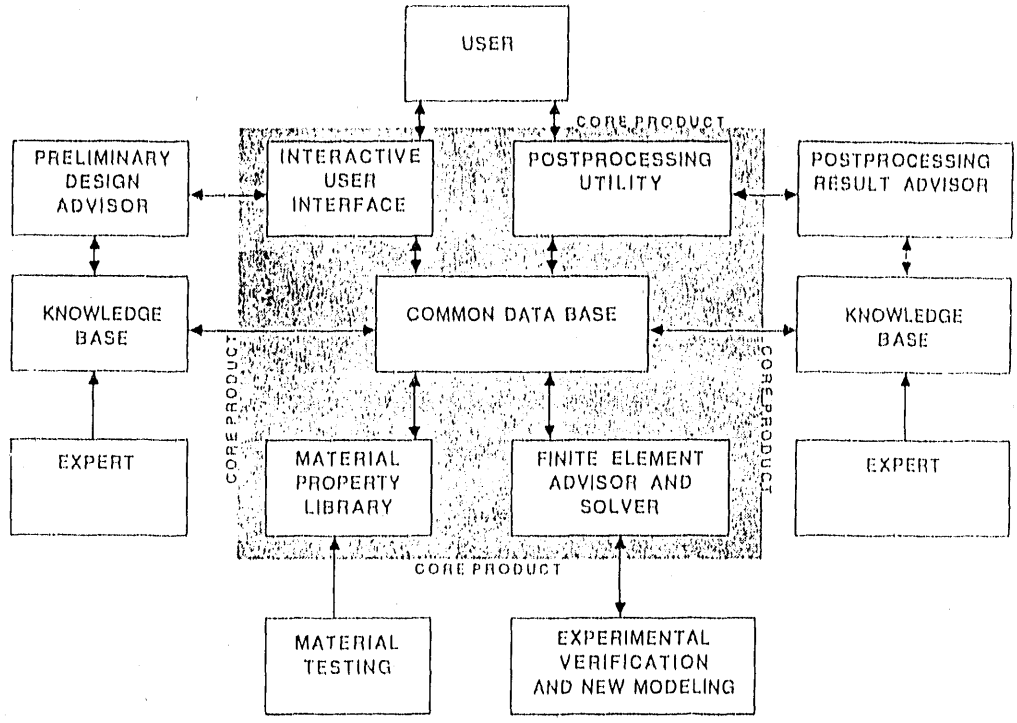

These modules are interconnected allowing automatic data flow throughout the system as needed. The system provides the use with design capabilities ranging from temperature dependent material storage and selection, through initial sizing, structural model setup, time dependent thermomechanical analysis, post processing, to design improvement and reanalyzing. It also provides a convenient way of data transfer between different groups of people involved in the design process.

CAPABILITIES OF THE SOFTWARE

The developed capabilities of the software are summarized below:

- User friendly
- Integrated material library
- Temperature dependent material constitutive models and model parameter fitting
- Steady state heat transfer (2D and 3D heat flow)
- Steady–state stress analysis
- Transient heat transfer analysis (2D and 3D heat flow)
- Transient linear stress analysis interacted with heat transfer
- Transient non–linear stress analysis interacted with heat transfer
- Cracking
- Creep
- Joint modeling and gap representation
- Automatic mesh generation
- Extensive display options and report generation

Examples of screen displays from the software obtained for a demonstration problem are given in Figures 1 to 4.

ACKNOWLEDGEMENT

IDEAL software has been developed by Integrated Engineering Design, Inc., under contract to Tennessee Center for Research and Development supported by an industry consortium and the Fossil Energy Materials Program of the U.S. Department of Energy.

REFERENCES

1. Chen, E.S., and Buyukozturk, O., "Methodology for Thermomechanical Analysis of Brittle Systems", American Ceramic Society Bulletin, 64, pp. 982–988, 1985.

2. Crowley, M.S., "Equation Helps Select Refractory Anchor System", Oil & gas Journal, pp. 122–125, 1982.

3. Potter, R.A., "Improvement of the Mechanical Reliability of Monolithic Refractory Linings for Coal Gasification Process Vessels", B & W report, 1981.

4. Chen, E.S., and Buyukozturk, O., "Thermomechanical Behavior and Design of Refractory linings in Slagging Gasifiers", American Ceramic Society Bulletin, 64, pp. 989–994, 1985.

5. Chen, E.S., Dicks, L.W. R., and Buyukozturk, O., "A Study to Optimize A Refractory Lining System", Shell Development Company Report, 1988.

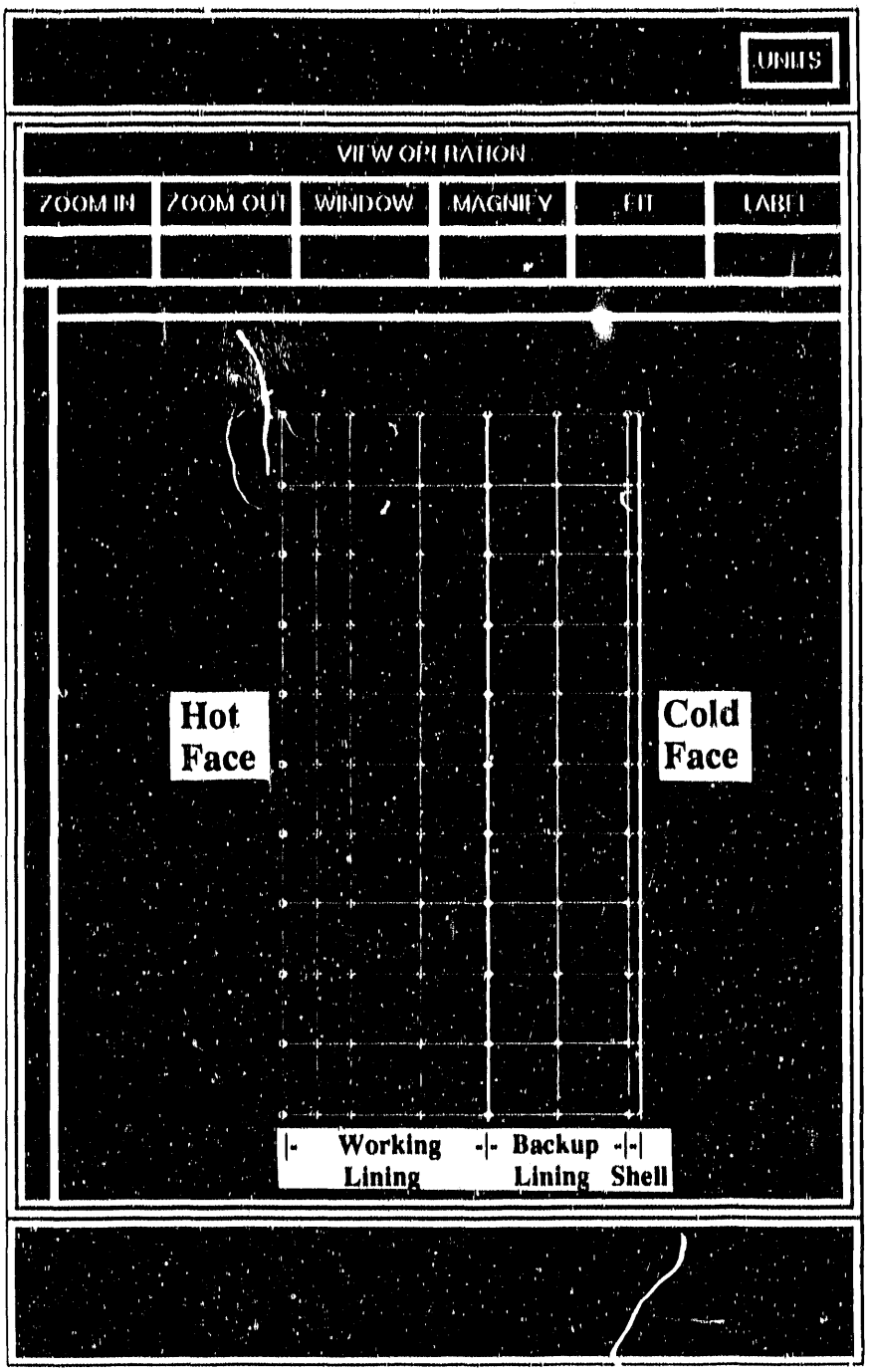

Figure 1. Example Model Generation

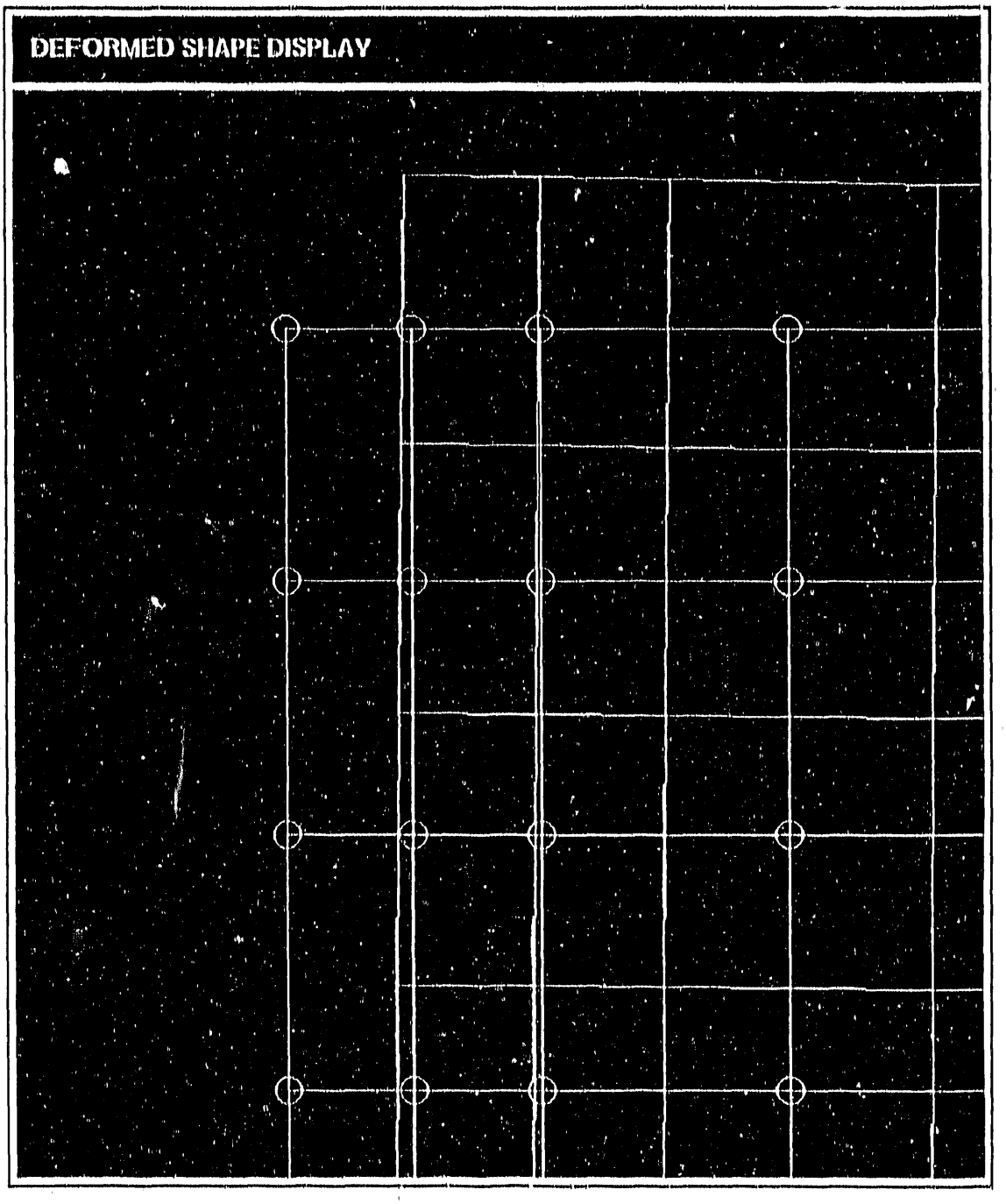

Figure 2. Deformed Shape

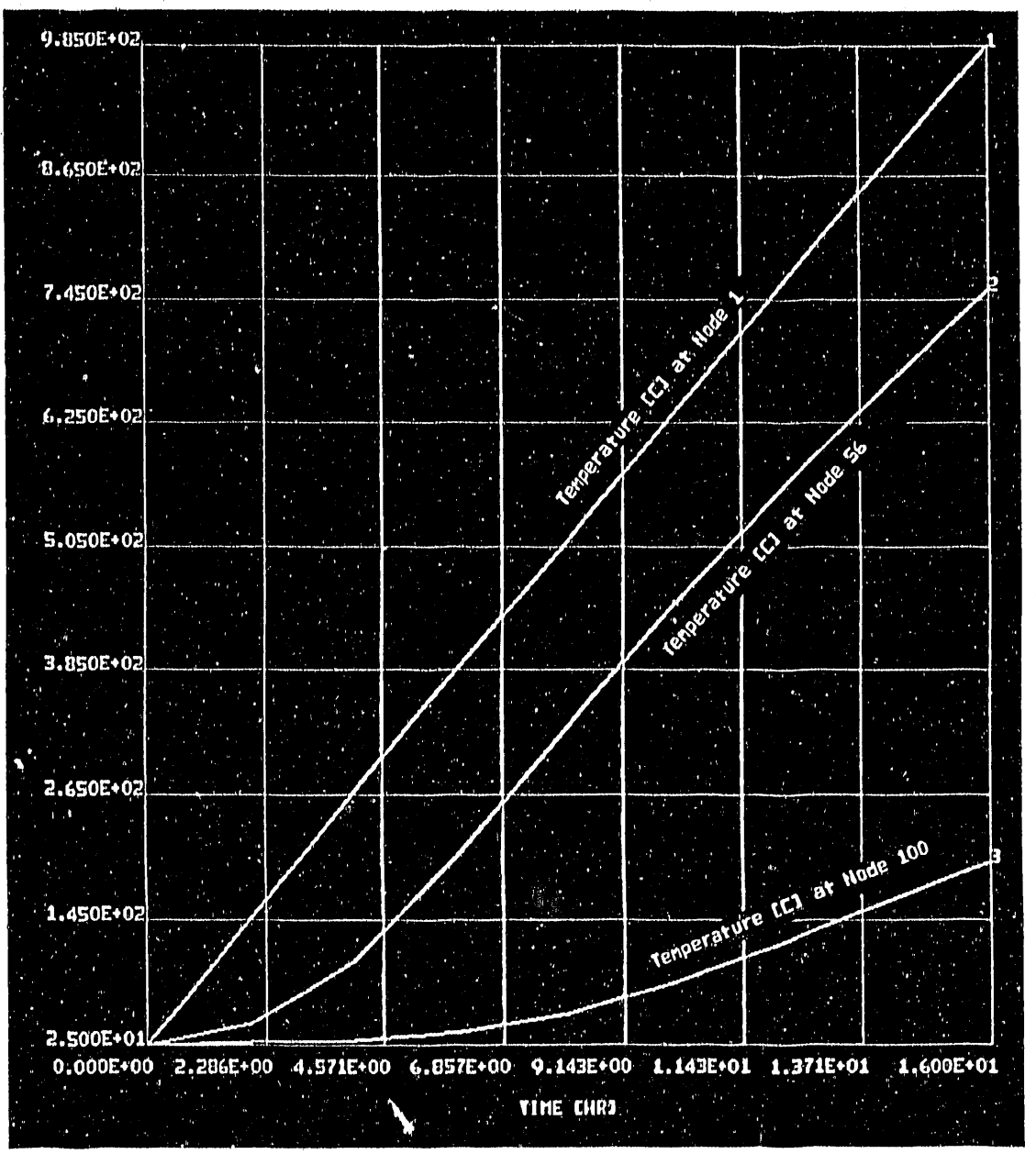

Figure 3. Temperature Prediction

IDEAL version 0.8 page 17

c20 May 1, 1990 13:24:16

ELEMENT NATIVE STRESS : time = 16.0000 HR

No.	stress-xx [NT/MM/MM]	stress-yy [NT/MM/MM]	stress-zz [NT/MM/MM]	stress-xy [NT/MM/MM]	stress-yz [NT/MM/MM]	stress-zx [NT/MM/MM]
1	-3.490e+00	-2.563e+01	-3.946e+01	-1.023e-02	0.000e+00	0.000e+00
2	-3.474e+00	-2.511e+01	-3.937e+01	-1.973e-01	0.000e+00	0.000e+00
3	-3.443e+00	-2.406e+01	-3.915e+01	-3.258e-01	0.000e+00	0.000e+00
4	-3.394e+00	-2.252e+01	-3.872e+01	-4.472e-01	0.000e+00	0.000e+00
5	-3.325e+00	-2.052e+01	-3.797e+01	-5.546e-01	0.000e+00	0.000e+00
6	-3.231e+00	-1.811e+01	-3.675e+01	-6.387e-01	0.000e+00	0.000e+00
7	-3.096e+00	-1.539e+01	-3.485e+01	-6.935e-01	0.000e+00	0.000e+00
8	-2.888e+00	-1.241e+01	-3.208e+01	-7.256e-01	0.000e+00	0.000e+00
9	-2.725e+00	-9.206e+00	-2.817e+01	-7.664e-01	0.000e+00	0.000e+00
10	-2.847e+00	-6.262e+00	-2.289e+01	-3.039e+00	0.000e+00	0.000e+00
11	-2.464e+00	-1.426e+01	-2.790e+01	-7.197e-02	0.000e+00	0.000e+00
12	-2.455e+00	-1.389e+01	-2.784e+01	-4.638e-01	0.000e+00	0.000e+00
13	-2.436e+00	-1.316e+01	-2.767e+01	-7.664e-01	0.000e+00	0.000e+00
14	-2.404e+00	-1.208e+01	-2.731e+01	-1.054e+00	0.000e+00	0.000e+00
15	-2.355e+00	-1.069e+01	-2.663e+01	-1.309e+00	0.000e+00	0.000e+00
16	-2.276e+00	-9.043e+00	-2.547e+01	-1.512e+00	0.000e+00	0.000e+00
17	-2.133e+00	-7.249e+00	-2.362e+01	-1.645e+00	0.000e+00	0.000e+00
18	-1.870e+00	-5.459e+00	-2.085e+01	-1.707e+00	0.000e+00	0.000e+00
19	-1.533e+00	-3.810e+00	-1.690e+01	-1.709e+00	0.000e+00	0.000e+00
20	-2.581e+00	-2.548e+00	-1.169e+01	-4.945e+00	0.000e+00	0.000e+00
21	-2.826e+00	5.364e-01	-1.277e+01	-1.239e-01	0.000e+00	0.000e+00
22	-2.817e+00	6.246e-01	-1.275e+01	-6.762e-01	0.000e+00	0.000e+00
23	-2.799e+00	8.005e-01	-1.267e+01	-1.117e+00	0.000e+00	0.000e+00
24	-2.768e+00	1.061e+00	-1.244e+01	-1.533e+00	0.000e+00	0.000e+00
25	-2.719e+00	1.397e+00	-1.191e+01	-1.898e+00	0.000e+00	0.000e+00
26	-2.639e+00	1.776e+00	-1.091e+01	-2.173e+00	0.000e+00	0.000e+00
27	-2.480e+00	2.115e+00	-9.229e+00	-2.302e+00	0.000e+00	0.000e+00
28	-2.191e+00	2.215e+00	-6.617e+00	-2.221e+00	0.000e+00	0.000e+00
29	-1.798e+00	1.695e+00	-2.861e+00	-1.862e+00	0.000e+00	0.000e+00
30	-3.792e+00	3.888e-01	1.912e+00	-3.872e+00	0.000e+00	0.000e+00
31	-1.233e+00	1.569e+01	2.491e+00	-6.768e-02	0.000e+00	0.000e+00
32	-1.264e+00	1.518e+01	2.416e+00	-4.917e-01	0.000e+00	0.000e+00
33	-1.327e+00	1.416e+01	2.311e+00	-8.152e-01	0.000e+00	0.000e+00
34	-1.418e+00	1.266e+01	2.268e+00	-1.125e+00	0.000e+00	0.000e+00
35	-1.532e+00	1.071e+01	2.431e+00	-1.400e+00	0.000e+00	0.000e+00
36	-1.653e+00	8.406e+00	2.994e+00	-1.599e+00	0.000e+00	0.000e+00
37	-1.738e+00	5.916e+00	4.214e+00	-1.648e+00	0.000e+00	0.000e+00
38	-1.703e+00	3.541e+00	6.405e+00	-1.432e+00	0.000e+00	0.000e+00
39	-1.447e+00	1.787e+00	9.917e+00	-8.555e-01	0.000e+00	0.000e+00
40	-2.936e+00	8.993e-01	1.468e+01	-1.510e+00	0.000e+00	0.000e+00
41	0.000e+00	0.000e+00	0.000e+00	0.000e+00	0.000e+00	0.000e+00
42	0.000e+00	0.000e+00	0.000e+00	0.000e+00	0.000e+00	0.000e+00
43	0.000e+00	0.000e+00	0.000e+00	0.000e+00	0.000e+00	0.000e+00
44	0.000e+00	0.000e+00	0.000e+00	0.000e+00	0.000e+00	0.000e+00
45	0.000e+00	0.000e+00	0.000e+00	0.000e+00	0.000e+00	0.000e+00
46	0.000e+00	0.000e+00	0.000e+00	0.000e+00	0.000e+00	0.000e+00
47	0.000e+00	0.000e+00	0.000e+00	0.000e+00	0.000e+00	0.000e+00

Figure 4. Stress Report

NONDESTRUCTIVE EVALUATION OF ADVANCED CERAMIC COMPOSITE MATERIALS

L. A. Lott and D. C. Kunerth

Idaho National Engineering Laboratory
EG&G Idaho, Inc.
P. O. Box 1625
Idaho Falls, ID 83415-2209

ABSTRACT

Nondestructive evaluation techniques are being developed to characterize performance degrading conditions in continuous fiber-reinforced silicon carbide/silicon carbide composites. These conditions include fiber-matrix interface bond strength, physical damage, and porosity. The material under study is formed by chemical vapor infiltration of the matrix material into a preform of woven reinforcing fibers. Acoustic, ultrasonic, and vibration response techniques are being studied. The fiber matrix interface bond is being studied because of its importance in determining the fracture toughness of the material. Correlations between interface bonding and acoustic and ultrasonic properties have been observed. These results are presented along with those obtained from acoustic and vibration response measurements on material samples subjected to mechanical impact damage.

INTRODUCTION

Nondestructive Evaluation techniques (NDE) are being developed for characterizing advanced ceramic composite materials. These high temperature structural materials are currently of great interest for fossil energy applications because they exhibit significantly higher fracture toughness than monolithic ceramics. The NDE techniques being developed are designed to detect and characterize those material conditions known to affect toughness and strength in continuous fiber-reinforced composites. Examples of known conditions include the degree of bonding between fiber and matrix, and physical damage such as fiber breakage and matrix cracking. Techniques under investigation include ultrasonic velocity and attenuation, acousto-ultrasonic (AU) response, and internal dynamic mechanical damping.

FIBER-MATRIX INTERFACE STUDY

The character of the fiber-matrix bond is critical to the performance of ceramic matrix composites because of its significant role in determining the fracture toughness of the material. Phenomena such as interface debonding, fiber slip, or pull-out, will improve material toughness by increasing the energy required to propagate a crack.[2] However, a bond which is too strong permits a crack to propagate directly through a fiber-matrix interface without being significantly impeded, resulting in brittle fracture. In a bond which is too weak, the toughening mechanisms are not significant. As a result, care is required in the manufacture of these materials to achieve optimum fiber-matrix bonding.[3] In support of efforts to develop ceramic matrix materials for fossil energy applications, the objective of this work is to develop and evaluate techniques to nondestructively characterize the fiber-matrix interface bonds. Acoustic, ultrasonic, and eddy current techniques are being investigated.

Description of Material and Test Samples

The samples used for this investigation were fabricated and supplied by Oak Ridge National Laboratory (ORNL). The testing material was comprised of a continuous fiber reinforced SiC matrix composite containing a 2-d weave Nicalon (Nippon Carbon Co., Tokyo, Japan) cloth layered in a 30-60-90 pattern. The matrix was formed using a chemical vapor infiltration (CVI) process. The samples are right cylinders 45 mm in diameter and 11.5 mm high with 40 vol% fiber and 85% of theoretical density.

Samples with strong (Sample 260), intermediate (Sample NS), and weak (Sample 265) interface bond strengths were fabricated at ORNL. The weak interface bond was produced by coating the Nicalon fibers with carbon prior to infiltration. Following infiltration, the sample was heat treated (850 C) for 2 hours in flowing oxygen to oxidize the carbon interlayer and effectively weaken the bond. The intermediate sample was

produced by coating the fibers with a carbon layer, but no heat treatment was done. The strong interface bond was produced by not applying any fiber precoat or subsequent heat treatment. Other samples prepared in similar fashions have been destructively tested by ORNL[4] to confirm the relationship between fabrication parameters and interfacial frictional stress.

Ultrasonic Properties

The velocity and attenuation of an ultrasonic wave are strongly influenced by the microstructure of the medium through which it propagates. For a ceramic matrix composite, the fiber-matrix interface contributes to both the amount of acoustic scatter and absorption. For composites using similar materials for both matrix and fibers, as is the case here, it is expected that, as the strength of the fiber matrix interface bond decreases, an increase in acoustic absorption and scatter should be observed. This would result in an increase in attenuation and a decrease in velocity.

Ultrasonic velocity measurements were made using a through-transmission technique. Because of the high attenuation in the material and difficulty in coupling contact transducers to the sample surfaces, ultrasonic measurements using conventional piezoelectric transducers were not repeatable. Reliable results were obtained using special noncontacting techniques. The beam from a pulsed Nd:YAG laser was directed onto one surface of the samples. This produces an acoustic pulse in the material by the thermo-elastic effect. The acoustic pulse propagates through the sample (in a direction perpendicular to the fiber plies in the geometry used) and strikes the opposite surface. The pulse was detected by a capacitive sensor placed in close proximity to the surface. The received signals were digitized and stored in a computer for subsequent processing. The ultrasonic velocities were calculated by measuring the sample thicknesses and the times required for the ultrasonic pulses to propagate through the samples.

Table 1 summarizes the longitudinal wave velocities measured in the

three samples. As can be seen, the expected decrease in velocity with decreasing fiber-matrix interface bond strength was observed. A significantly lower velocity is evident for Sample 265 (weakly bonded interface) when compared to Sample 260 (strongly bonded interface). The sample with the intermediate bond strength has an intermediate ultrasonic velocity.

Table 1. ULTRASONIC VELOCITIES MEASURED FOR STRONG AND WEAK BONDS

Sample	Ultrasonic Velocity
Strong Bond (260)	8.73 (mm/μs)
Intermediate Bond (NS)	6.90
Weak Bond (265)	2.35

Because the three samples are similar in density and fiber content, the measured differences in acoustic properties are attributed to the differences in interface bonding.

Acousto-Ultrasonic Response

Dynamic mechanical response measurements are also being used to characterize fiber-matrix interface bonds. One of the parameters directly measured by this technique is the internal damping of vibrational energy that can occur at the fiber-matrix interfaces of a composite. A measure of the internal damping can be obtained by the diffuse field decay rate method.[5] An advantage of the method is that samples of nearly any shape can be used. The analysis is based upon the premise that a diffuse ultrasonic field in an isolated sample will decay only from absorption mechanisms and that the contributions of damping by air, transducers, and fixturing are minimal. The damping is measured

through determination of the volume averaged decay rate of the ultrasonic field as a function of frequency and time. A greater decay rate indicates a greater amount of internal damping or energy absorption by internal friction.

The technique was implemented using an experimental setup similar to that commonly used for acousto-ultrasonic (AU) measurements. Two piezoelectric transducers are placed on the same side of a material sample. An excitation pulse to one transducer generates acoustic waves in the sample which are received by the other transducer, amplified, and recorded in a manner similar to conventional transmit-receive ultrasonics. The difference is that, instead of detecting a well-defined acoustic pulse traveling between the transducers, as is the case with conventional ultrasonics, a complicated superposition of wave modes and sample reverberations which resembles an acoustic emission signal is generated and detected. Mechanical isolation of the sample is accomplished by weakly coupling the transducers to the sample, which is set on point supports. Determination of the decay rate is accomplished by dividing the recorded waveform into a number of time windows after which Fourier transforms are performed. The resulting spectra are then broken into frequency bins and the mean square spectral amplitude is calculated for each bin. This provides a measure of the signal decay rate for individual frequency bins as a function of time.

Experimental measurements and diffuse decay rate analysis were performed on the three samples; the results are shown in Figure 1. The time decay rates of the measured signals are plotted as functions of frequency for the three composite samples. The general trend shown in the figure is increasing decay rates (increasing absorption) with increasing frequency. At any given frequency, except at the low frequency range, the composite samples exhibit increasing absorption of vibrational energy with decreasing bond strength. That is, more energy is absorbed by frictional motion at the poorly bonded interfaces.

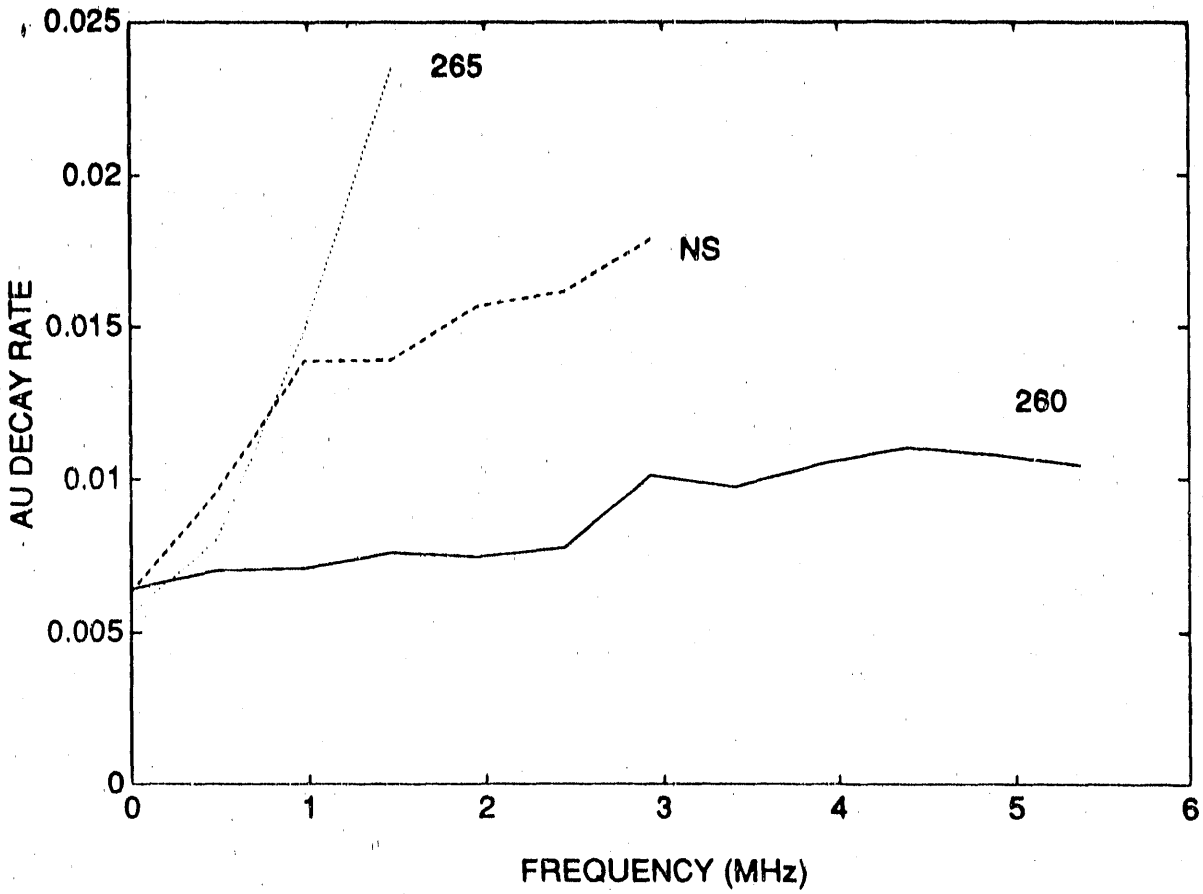

Figure 1. Diffuse field decay rates for SiC/SiC composite samples having different fiber-matrix interface bond characteristics.

MECHANICAL DAMAGE CHARACTERIZATION

A study of the ability of NDE techniques to characterize physical damage such as fiber breakage and matrix cracking is also being conducted. The acousto-ultrasonic technique and conventional vibration response/internal damping techniques are being used. The acousto-ultrasonic technique measures the acoustic response of samples of arbitrary shape at frequencies up to several Mhz, while the vibration response technique requires samples of certain geometry and measures the response at the natural mode frequencies of the sample.

Material Test Samples

The samples, obtained from Refractory Composites, Inc., Whittier, California, were in the form of plates measuring approximately 90 x 25 x 2.5 mm. They were fabricated from preforms of multiple layers of Nicalon SiC cloth with the SiC matrix added by chemical vapor infiltration. The samples tested had approximately 30 vol% fiber content.

Mechanical impact damage was produced in the samples by placing them on a solid backing plate and dropping a steel ball of known mass onto the samples from a measured height. This produced primarily cracking and crushing of the matrix at the impact energies used.

Acousto-Ultrasonic Measurements

Samples having different degrees of impact damage were characterized, both before and after impact, with the same acousto-ultrasonic technique described above. Figure 2 shows the result for a typical sample before and after damage of 0.6 J and 2.2 J energy.

Vibration Response Measurements

In addition to the diffuse field decay rate method, more conventional methods of taking vibration response measurements are being pursued. The method being used is the measurement of the flexural vibrations of a rectangular sample vibrating in the first fundamental mode. This is accomplished by supporting a sample on two knife-edge supports and giving it an impulsive excitation by a small mechanical impact at the center of the sample. The vibrations of the sample are measured with a magnetic or piezoelectric sensor located near one end. The separation of the knife edges is set to allow support of the sample at the nodes of the fundamental "free-free" vibration mode, namely 0.224L from each end, where L is the overall sample length.

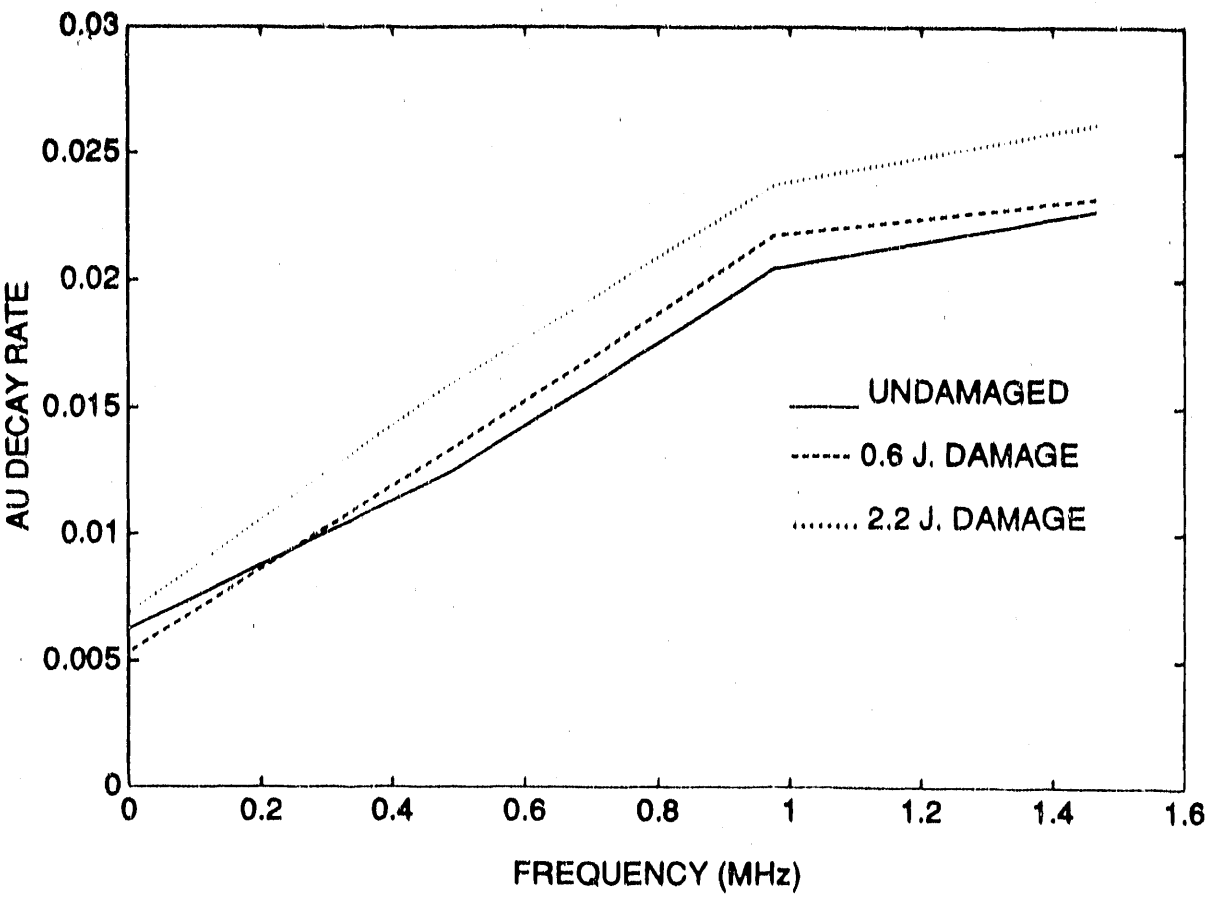

Figure 2. Diffuse field decay rates for SiC/SiC composite sample before and after impact damage energies of 0.6 J and 2.2 J.

The vibration signal is digitized and transformed to the frequency domain with a Fast-Fourier Transform (FFT). The absolute frequency of the observed resonance peak is related directly to the elastic modulus of the sample, while the width of the peak at half power, defined as the loss factor, is a measure of the internal damping[6]. The results of a vibration measurement and analysis are shown in Figure 3, in which the flexural vibration spectra of a sample, before and after impact damage of 3.9 J are shown. As can be seen, the damage changed both the modulus and damping of the sample.

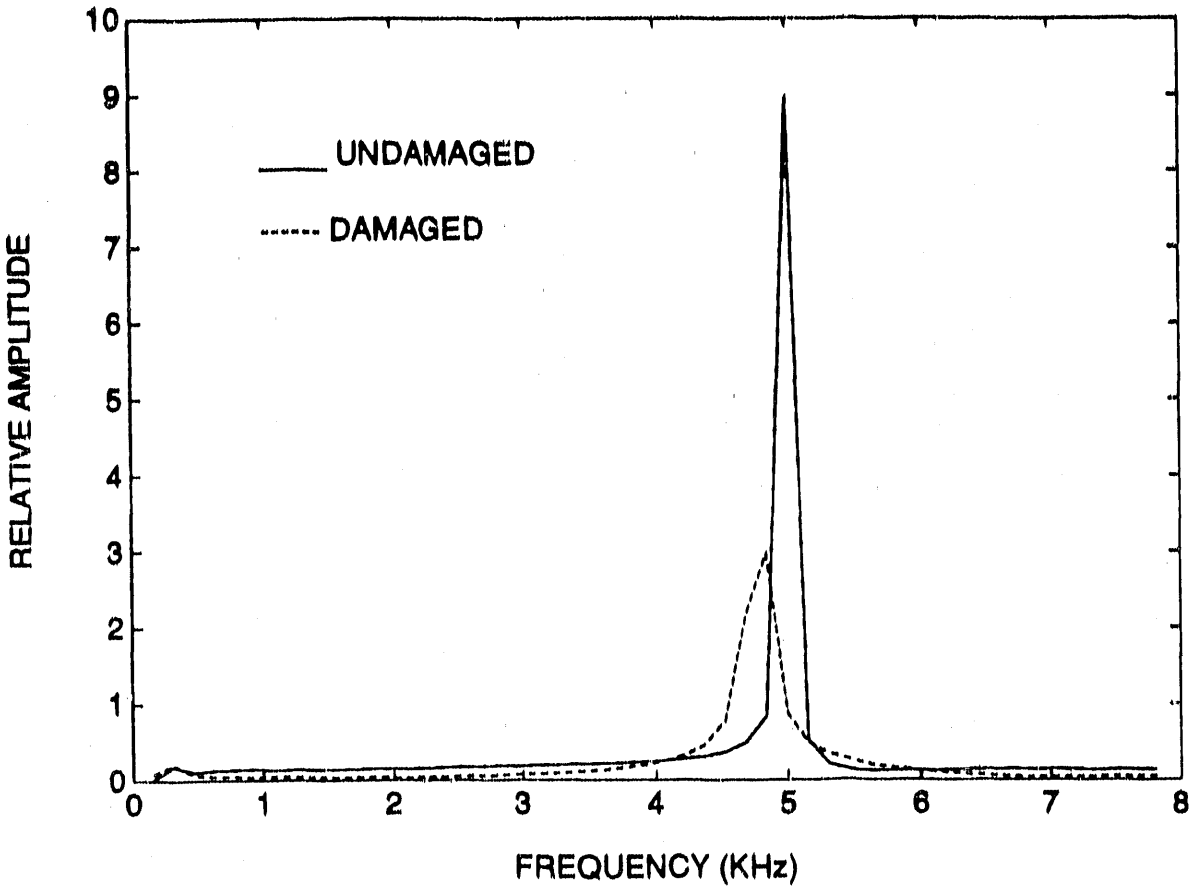

Figure 3. Vibration spectra of a SiC sample before and after impact damage of 3.9 J.

Summary and Conclusions

The feasibility of acoustic and dynamic mechanical techniques for characterizing the degree of performance degrading conditions in ceramic/ceramic composites has been demonstrated. Ultrasonic property measurements and acousto-ultrasonic measurements of internal damping have been shown to be capable of discriminating between differences in fiber-matrix interface conditions in otherwise identical samples. Similarly, preliminary studies of internal mechanical damping show this to be a promising technique for detecting and characterizing mechanical impact damage in the material. Measurements on a larger sample base

will be necessary to establish the correlations with some statistical confidence. All of the techniques considered can potentially be done with noncontacting laser based sensors, enabling NDE measurements to be done during processing, at high temperatures, and/or in service conditions.

REFERENCES

1. J. B. Walter, L. A. Lott, and K. L. Telschow, "Ultrasonic Characterization of Ceramic-Ceramic Composites," in Review of Progress in Quantitative Nondestructive Evaluation, Vol 7B, 1988, Plenum Publishing Co., pp. 971-978.

2. R. A. Lowden, D. P. Stinton, and T. M. Besmann, "Characterization of Fiber-Matrix Interfaces in Ceramic Composites," Whisker and Fiber-Toughened Ceramics, ASM Conference Proceedings, 1988, pp. 253-264.

3. A. J. Caputo, D. P. Stinton, R. A. Lowden, and T. M. Besmann, "Fiber-Reinforced SiC Composites with Improved Mechanical Properties," Am. Ceram. Soc. Bull., 66(2), (1987), pp. 368-372.

4. R. A. Lowden, "Characterization and Control of the Fiber-Matrix Interface in Ceramic Matrix Composites," ORNL/TM-11039 (March 1989).

5. R. L. Weaver, "Diffuse Field Decay Rates For Material Characterization," Solid Mechanics Research for Quantitative Non-destructive Evaluation, edited by J. D. Achenbach and Y. Rajapaskie (Martinus Nijhoff Publishers, 1987), p. 425.

6. S. A. Suarez, R. F. Gibson, and L. R. Deobald, "Random and Impulse Techniques for Measurement of Damping in Composite Materials", Experimental Techniques, Vol. 8, No. 10, October, 1984, pp. 19-24.

MEASUREMENT OF FIBER-MATRIX INTERFACIAL PROPERTIES AND THEIR RELATION TO CERAMIC COMPOSITE TOUGHENING

Edwin R. Fuller, Jr. and Elizabeth P. Butler

Ceramics Division, Room A256, Building 223
National Institute of Standards and Technology
Gaithersburg, MD 20899

ABSTRACT

An experimental approach was developed using single-fiber pull-out tests to measure intrinsic interface properties of ceramic composites. Interface properties are determined from a pull-out force-displacement curve, which is directly related to reinforcement toughening via fiber-matrix debonding and frictional pull-out. The properties were evaluated for a model composite system of continuous SiC fibers with various surface treatments in a borosilicate glass matrix. For the processing conditions used, the interface fracture toughness and the interface frictional shear resistance were found to be 1.0 ± 0.5 J/m^2 and 3.3 ± 0.6 MPa, respectively, for as-received fibers. Experiments conducted with long embedded fiber lengths allowed the frictional shear resistance to be deconvolved into an interface friction coefficient, 0.05 ± 0.01, and an initial fiber-clamping pressure, 65 ± 6 MPa. Nitric acid-washed fibers gave an increased interface toughness, 3.6 ± 0.1 J/m^2, and friction coefficient, 0.08 ± 0.02, but nearly the same initial clamping pressure, 72 ± 12 MPa. Independent evaluation of the clamping pressure from processing conditions and from stress birefringence measurements were in general agreement with this value.

INTRODUCTION

Major improvements in the fracture toughness of brittle ceramics have been made in the last decade by developing microstructures which lead to the phenomenon of crack shielding. In such systems, elements of the microstructure shield the crack tip from the applied mechanical load. A notable example is the incorporation of ceramic reinforcements into brittle matrices to enhance their toughness [1]. Advantages of reinforcement toughening over other shielding mechanisms are: a variety of reinforcements (fibers, whiskers, platelets, etc.) can be incorporated into a myriad of host materials; directional properties can be obtained; and shielding can be retained at elevated temperatures. However, basic understanding of reinforcement-toughening mechanisms has yet to be established. Furthermore, links

between ceramic processing, toughening mechanisms, and structural performance are equally vague. Such understanding is most readily be attained via a micromechanics description of reinforcement toughening, relating microstructure/interfacial properties to processing/structural performance.

Reinforcement toughening depends critically upon the properties of the fiber-matrix interface. The toughening increment via fiber bridging is simply the product of the volume fraction of fibers, V_f, and the integral of the force-displacement curve for fiber debonding and frictional pull-out. In terms of the J-integral [2], this toughening increment is:

$$J_T = V_f \cdot \int T(\delta)\, d\delta, \qquad (1)$$

where $T(\delta)$ is the force-displacement relation for a single-fiber pull-out. The important parameters for fiber toughening lie in this force-displacement relation. These parameters are amenable to direct experimental measurement via a single-fiber pull-out test. This test was initially developed for testing polymeric composites [3], but is now widely applied to all composite materials. Furthermore, this test provides a systematic way for investigating the influence of fiber-matrix properties and processing conditions on the toughness of the final manufactured composite.

THEORY

Single Fiber Pull-Out Test

Analysis of fiber debonding and subsequent frictional pull-out is treated here as an interfacial fracture problem [4,5] with frictional wake tractions [6,7]. A simplistic analysis [8,9], i.e., one with no Poisson's contractions, is illustrated schematically in Fig. 1. A cylindrical crack of radius R (also the fiber radius) is propagated down the fiber-matrix interface as a pure Mode II crack. The axial stress, σ, is transferred from the fiber to the matrix along the debonded-crack flanks by interfacial friction. The differential stress transfer with axial distance z is:

$$d\sigma/dz = -2\tau/R, \qquad (2)$$

where τ is the frictional shear stress on the interface. Assuming Coulomb

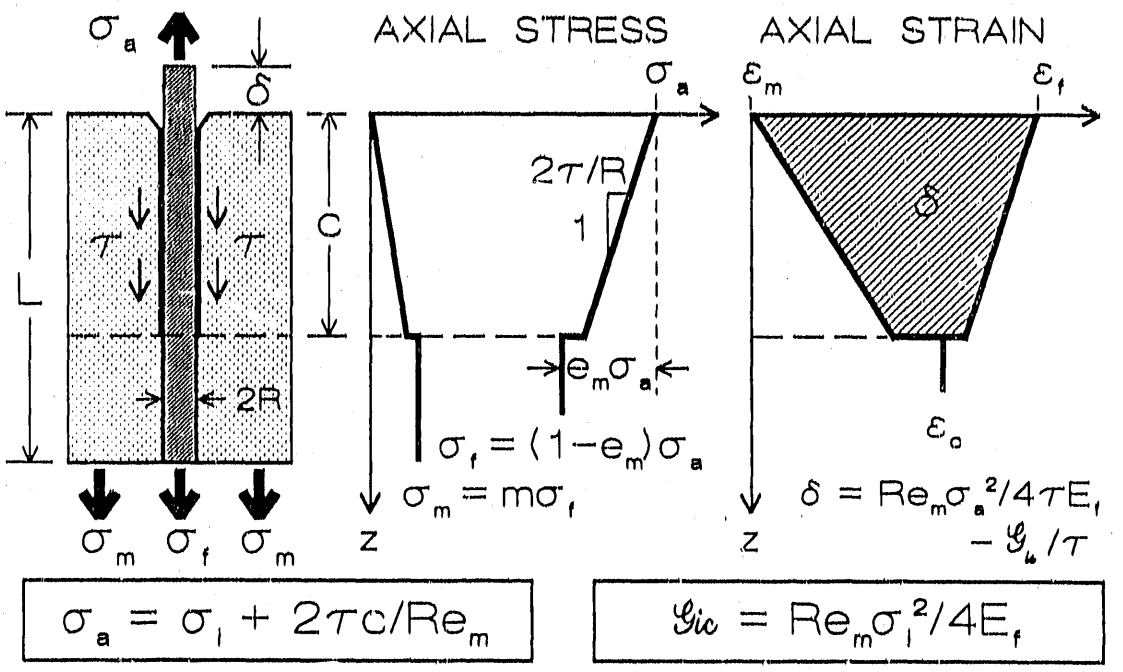

Fig. 1. Schematic drawing of a simplistic analysis of fiber debonding (i.e., one with no Poisson's contractions) and subsequent frictional fiber pull-out: an interfacial fracture problem with frictional wake tractions.

friction for τ with a friction coefficient, μ, this shear stress is:

$$\tau = \mu \cdot \sigma_{rr}, \tag{3}$$

where σ_{rr} is the radial matrix (clamping) stress. With no Poisson's contractions, σ_{rr} is only the initial clamping pressure, q_o, which results from the thermal expansion mismatch strains that occur during fabrication. The frictional shear stress, $\tau=\tau_o$, is accordingly independent of z, so that the axial fiber stress, as determined from Eqn. (2), decreases linearly in z, as depicted in Fig. 1, as this stress is transferred to the matrix.

The interface is presumed to be cohesively bonded at the crack tip. Accordingly, the axial fiber stress does not fall entirely to its average composite value, σ_f, at the crack tip, but rather has a stress discontinuity.[1] To determine the magnitude that this stress discontinuity can reach

---

1. A rigorous analysis should include the crack-tip stress singularity and a non-frictional shear-stress transfer to σ_f beyond the crack tip.

before equilibrium crack propagation ensues, we use a strain-energy-release-rate analysis similar to that of Marshall and Oliver [6] and Gao et al [7]. We first calculate the elastic strain energy, U_{SE}, the external work, W_{ext}, and the frictional work, W_{fric}, and then differentiate (U_{SE} - W_{ext} + W_{fric}) with respect to crack area, $2\pi Rc$, to obtain a strain-energy-release rate, G. Equating this G to a critical interface toughness, G_{ic}, we obtain the following relation between external stress, σ_a, and debond crack length, c, for equilibrium crack propagation:

$$\sigma_a = \sigma_i + 2\tau_o c/Re_m, \qquad (4)$$

where $e_m = m/(m+f)$, $m = E_m/E_f$ [the ratio of the Young's modulus of the matrix to that of the fiber], and $f = V_f/(1-V_f)$ [the volume fraction ratio]. The "frictionless debond" stress, σ_i, is related the interface toughness, G_{ic}, through the relation: $\sigma_i = [4E_f G_{ic}/Re_m]^{1/2}$.

Eqn. (4) is effectively a fracture resistance curve (R-curve) for the interfacial fracture problem. Multiplying Eqn. (4) by $[Re_m/4]^{1/2}$, puts it in units of stress intensity factor: $\sigma_i[Re_m/4]^{1/2} = [E_f G_{ic}]^{1/2}$ is the critical stress intensity factor for the interface and $\tau_o c/(Re_m)^{1/2}$ is the rising fracture resistance with crack extension that results from frictional tractions across the crack flanks. When Poisson's effects are included, the resulting contractions reduce the radial clamping pressure and accordingly the effective distance over which the frictional shear stresses are transferred for a given debond crack length.[2] This phenomenon results in an asymptotic, or steady-state value for the fracture resistance, and debond stress. An analysis that includes fiber-debonding, frictional pull-out, and Poisson's contractions is that of Gao et al. [7]. Although their treatment is a plane-strain approximation to the exact problem, it is fully analytical and expressed in terms of materials', interface and processing parameters. Their generalization of Eqn. (4), is:

$$\sigma_a = \sigma_i e^{-\lambda \cdot c} + \tilde{\sigma}(1 - e^{-\lambda \cdot c}), \qquad (5)$$

where λ is a reciprocal length giving the effective frictional shear-stress transfer distance and $\tilde{\sigma}$ is the asymptotic pull-out stress for long cracks.

---

2. Note: The applied stress must be reduced, since the larger stress cannot now be transferred over a shorter distance with reduced friction.

The experimentally determined parameters σ_i, λ, and $\tilde{\sigma}$ are related, respectively, to the interface fracture toughness, G_{ic}, the fiber-matrix friction coefficient, μ, and the initial fiber-clamping pressure, q_o, by:

$$\sigma_i = [(4E_f G_{ic}/R)[1+(f/m)\cdot(1-2k\nu_m)/(1-2k\nu_f)]/(1-2k\nu_f)]^{1/2} \quad (6)$$

$$\lambda = 2\mu k/R \quad (7)$$

$$\tilde{\sigma} = q_o\cdot[1 + (f/m)\cdot(\nu_m/\nu_f)]/k \quad (8)$$

where $k = (m\nu_f + f\nu_m)/[m(1-\nu_f) + 1+\nu_m + 2f]$, and ν_m and ν_f are the matrix and fiber Poisson's ratio, respectively. These results reduce to the simplistic analysis of Fig. 1, when $\nu_m = \nu_f = 0$.

Thermal Expansion Mismatch Stresses

When the thermal expansion coefficient of the matrix is greater than that of the fibers, the matrix contracts onto the fibers upon cooling from the fabrication temperature. The residual (biaxial) clamping pressure on the fiber, q_o, that results from a cooling differential of ΔT is [10]:

$$q_o = E_{eff}(\alpha_m - \alpha_f)\Delta T \quad (9)$$

where α_m is the thermal expansion coefficient of the matrix and α_f is the (axial) thermal expansion coefficient of the fiber. The effective elastic modulus, E_{eff}, is given by:

$$E_{eff} = E_m k[1 + (m+f)/(m\nu_f+f\nu_m)]/[m+f + 2kf(\nu_f-\nu_m)], \quad (10)$$

where the parameters m, f, and k are defined above.

EXPERIMENTAL PROCEDURE

Single Fiber Pull-Out Test

Specimens for the single-fiber pull-out test were fabricated from SiC fibers sandwiched between two plates of borosilicate glass.[3] The fibers

---

3. The SiC fibers (AVCO SCS-6) are 142 μm diameter monofilaments of chemically vapor-deposited SiC on a carbon core and have two carbon-rich surface layers. The matrix material is Corning borosilicate glass #7740.

were first degreased by washing them in 1,1,1-tri-chloroethelyne, followed by rinsing them in acetone and then ethanol. The sandwich assembly was diffusionally bonded by hot pressing in vacuo at a temperature of 725°C and under a stress of 3.4 MPa. The bonded assembly with fiber protruding from both ends was then cut to give two specimens of different embedded fiber lengths. To enhance fiber-matrix bonding, some fibers were washed with a 50 vol% nitric acid solution following the degreasing procedure to remove the carbon-rich surface layers [11].

Fibers were pulled from the matrix using an universal testing machine with a 5 kg load cell. The sample-grip arrangement is shown in Fig. 2. The crosshead displacement speed was 10 mm/min, a rate fast enough to prevent environmentally assisted fracture, but slow enough for the response

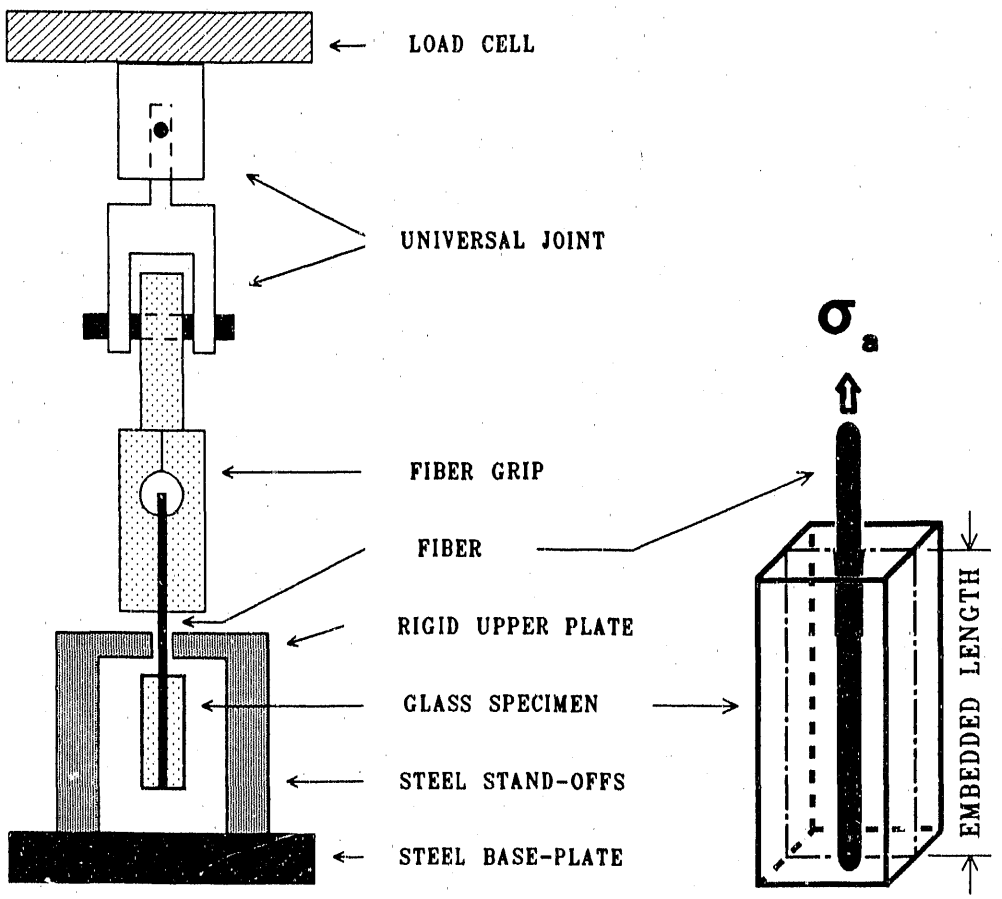

Fig. 2. Schematic diagram of the single-fiber pull-out test geometry.

time of the strip-chart recorder and load cell. Effects of system compliance on experimental results were evaluated and found to be negligible.

A principal experimental difficulty in many fracture mechanics measurements is the determination of the crack length. This difficulty is particularly pronounced for the fiber-matrix debond crack due to its three-dimensional nature. A simple stratagem was used in the current experiments to resolve this difficulty. The debond crack was propagated to the end of the specimen, at which point the crack length is known explicitly, namely the embedded fiber length, L. See Figs. 1 and 2. Since the applied stress, σ_a, increases with crack length, c, according to Eqn. (5), i.e., the "rising fracture resistance" behavior of the micromechanic pull-out problem, this "break-through" fracture condition corresponds to a maximum fiber-debond stress, σ_d:

$$\sigma_d = \sigma_i e^{-\lambda \cdot L} + \tilde{\sigma}(1 - e^{-\lambda \cdot L}), \tag{11}$$

After "break-through", the interface toughness no longer contributes to Eqn. (11), i.e., $\sigma_i=0$, and the applied stress drops to that of the maximum frictional stress, σ_f:

$$\sigma_f = \tilde{\sigma}(1 - e^{-\lambda \cdot L}). \tag{12}$$

Accordingly, by using specimens of varying embedded fiber lengths, empirical relations can be developed between σ_d and σ_f versus c=L. The stress drop upon "break-through" is an accurate way to determine, σ_i, or G_{ic}:

$$\Delta\sigma = (\sigma_d - \sigma_f) = \sigma_i e^{-\lambda \cdot L}. \tag{13}$$

Upon continued loading after the stress drop, the applied stress monotonically decreases to zero as the fiber pulls from the matrix. Theoretically this decrease should be represented by Eqn. (12) with L replaced by the remaining embedded length. Experimentally, a reverse curvature to that expected (i.e., positive rather than negative) is typically observed.

Clamping Pressure from Stress-Induced Birefringence

Under stress, glass becomes optically birefringent. This stress-induced retardation of light travelling through glass is directly proportional to the difference in principal stresses, $(\sigma_{rr} - \sigma_{\theta\theta})$, through the

stress optical law

$$\Delta = Ct(\sigma_{rr}-\sigma_{\theta\theta}), \tag{14}$$

where Δ is the relative phase shift of light waves polarized along the radial and tangential directions, C is the stress optic coefficient for the material, and t is the axial specimen thickness (and the optic path length). The principal stress difference in the matrix, $(\sigma_{rr} - \sigma_{\theta\theta})$, is related to the initial clamping pressure on the fiber, q_o, by the elasticity relation [7]

$$(\sigma_{rr}-\sigma_{\theta\theta}) = 2q_o\cdot(1+f)(R^2/r^2), \tag{15}$$

where R is the fiber radius, r is the polar coordinate measured from the fiber axis, and f is the volume fraction ratio, $V_f/(1-V_f)$. Thus, the initial clamping pressure is related to the relative phase shift, Δ, by

$$q_o = \Delta\cdot(r/R)^2/[2Ct(1+f)]. \tag{16}$$

The phase shift Δ was measured by the Tardy method [12] using a circular polariscope with both polarizer and analyzer and two quarter-wave plates in the crossed arrangement. The quarter-wave-plate wavelength was 546 nm.

RESULTS AND DISCUSSION

The maximum debond stress and the maximum frictional stress were both measured as a function of embedded fiber length. The results are presented in Fig. 3 for as-received fibers and nitric acid-washed fibers in a borosilicate glass matrix. For each fiber treatment, both the debond and frictional stress data show an initial linear behavior and then turn over into a common asymptotic stress, $\tilde{\sigma}$, at long embedded fiber lengths. The debond stress is always greater than the frictional stress at a given L. In the linear region of the debond curve, the initial gradient is equal to $\lambda(\tilde{\sigma} - \sigma_i)$ and the stress-axis intercept is the frictionless debond stress, σ_i.

The σ_d and σ_f data for each fiber treatment were fitted simultaneously to Eqns. (11) and (12), respectively, using a non-linear least squares analysis to determine the three independent parameters: σ_i, λ, and $\tilde{\sigma}$. Since the value for σ_i was typically very small, this simultaneous fit was not an accurate way to determine σ_i (i.e., this procedure occasionally gave

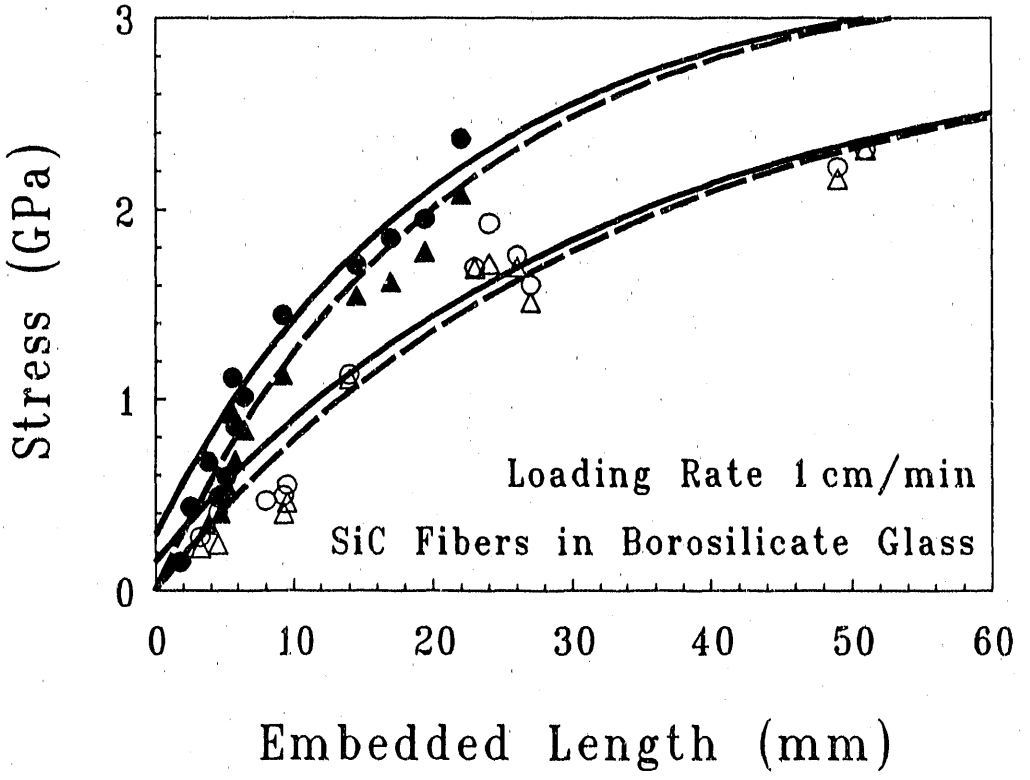

Fig. 3. Debond stress (circles) and maximum frictional stress (triangles) as a function of embedded fiber length for as-received fibers (open symbols) and nitric acid-washed fibers (filled symbols) in a borosilicate glass matrix. The solid and dashed lines are graphs of Eqns. (11) and (12), respectively, with the parameters σ_i, λ, and $\tilde{\sigma}$ determined from the least squares fit.

a negative value for σ_i, which is not physical, since experimentally the stress differences in Eqn. (13) were all greater than or equal to zero). Accordingly, both data sets were initially fit to Eqn. (12) to give a common value of λ and $\tilde{\sigma}$. The difference between the debond stress and the frictional stress at each value of L was then fit to Eqn. (13) with the known value of λ to determine σ_i. The values for the parameters thus determined are given in Table I for both the as-received and nitric acid-washed fibers. The error given for each parameter represents only that error resulting from the least squares fit. The intrinsic interface properties, G_{ic}, μ, and q_o, were calculated from these parameters using Eqns. (6), (7), and (8), respectively. These results are also given in

Table I. Pull-out measurements at long embedded lengths are required to deconvolve the interfacial shear resistance, τ_o, into its components, μ and q_o. However, τ_o by itself can be determined from the initial slope, $\lambda \cdot \tilde{\sigma}$, of frictional pull-out curve:

$$\tau_o = \mu \cdot q_o = (\lambda \tilde{\sigma} R/2)/[1 + (f/m) \cdot (\nu_m/\nu_f)]. \qquad (17)$$

The initial clamping stress on the fiber, as well as the stress in the matrix away from the interface, can be independently calculated from the known processing conditions. Using the coefficient of thermal expansion for borosilicate glass, 3.2 x 10^{-6}/°C, and the axial value for the fiber, 2.0 x 10^{-6}/°C from the manufacturer's data sheet [13], q_o was determined to be 47 MPa, in good general agreement with the value determined from the pull-out experiments. However, using the axial fiber coefficient of 2.63 x 10^{-6}/°C measured by Goettler and Faber [14], this value drops to 22 MPa.

The clamping stress can also be measured from the radial stress distribution in the borosilicate-glass matrix, since it has stress-induced birefringence properties. Using a circular polariscope, a fractional fringe order of 0.609 ± 0.003 was observed at a radial distance of 142 ± 7 μm. Literature values for the stress optical coefficient, C, of borosilicate glass are 2.8 TPa^{-1} [15] and 3.0 TPa^{-1} [16]. Using these values, we calculate the principal stress difference in the matrix to be 41.4 MPa

Table I. Single-fiber pull-out parameters and intrinsic interface properties of a SiC fiber-reinforced, borosilicate glass matrix composite system with varied fiber surface treatments.

SINGLE-FIBER PULL-OUT PARAMETERS AND INTRINSIC COMPOSITE INTERFACE PROPERTIES	Surface Treatment of SiC Fiber	
	As-Received	Acid-Washed
Frictionless Debond Stress, $\tilde{\sigma}_i$ (MPa)	149 ± 36	285 ± 52
Asymptotic Pull-Out Stress, $\tilde{\sigma}$ (GPa)	2.9 ± 0.3	3.3 ± 0.6
Inverse Stress Transfer Length, λ (m^{-1})	31 ± 5	48 ± 12
Interface Toughness, G_{ic} (J/m^2)	1.0 ± 0.5	3.6 ± 0.1
Frictional Shear Resistance, τ_o (MPa)	3.3 ± 0.6	5.5 ± 0.2
* Friction Coefficient, μ	0.05 ± 0.01	0.08 ± 0.02
* Initial Clamping Pressure, q_o (MPa)	65 ± 6	72 ± 12

± 0.2 MPa, or 38.6 ± 0.2 MPa, respectively. Corrected to the fiber-matrix interface, the value of q_o determined for the as-received fiber composite is 83 ± 8 MPa, or 77 ± 8 MPa, respectively. These values are in reasonable agreement, although slightly higher, with those for the pull-out results.

Comparing the results of the as-received and nitric acid-washed fiber pull-out tests, we observe that the fiber-matrix bond, as characterized by the interface toughness and friction coefficient, were both enhanced by the nitric acid treatment. Little change was observed in the initial clamping pressure within estimated errors. The acid wash facilitated the removal or etching of the outermost carbon layer(s) of the SCS-6 fibers [11]. These layers are important in two ways: as an interlayer to prevent strong fiber-glass bonding and as a frictional lubricant at the interface. Thus, removal of these layers would cause an increase in both interfacial bonding and interfacial friction. The initial clamping stress is only dependent on the processing temperature and difference in linear expansion coefficients between the fiber and matrix. As these parameters are not affected by the nitric acid wash, no change is expected in the clamping stress.

CONCLUSIONS

The single-fiber pull-out test is an excellent technique for determining fundamental interface properties and pull-out force-displacement relations. Long debond-crack lengths (embedded fiber lengths) are required to deconvolute the interfacial shear resistance into a friction coefficient and an initial fiber-clamping stress. Interfacial properties measured in this study for a model SiC fiber-borosilicate glass system are of similar magnitude to those reported by other authors working on similar systems.

The initial clamping stress on the fiber is amenable to determination by three different techniques which yield similar results. However, the stress birefringence measurements somewhat preliminary, as an experimental determination of the stress optical coefficient is needed.

The overall experimental procedure provides an effective way to determine micromechanical properties of composite interfaces, to infer composite toughening increments resulting from fiber reinforcement, and to monitor influences of processing variations on composite properties.

ACKNOWLEDGMENTS

Support of this research by the U. S. Dept. of Energy, Advanced Research and Technology Development (AR&TD) Fossil Energy Materials Program managed by Dr. R. R. Judkins of Oak Ridge National Laboratory, under the NIST-DOE interagency agreement DE-AI05-800R20679 is gratefully acknowledged.

REFERENCES

1. D. B. Marshall and J. E. Ritter, "Reliability of Advanced Structural Ceramics and Ceramic Matrix Composites," Am. Ceram. Soc. Bull., 66 [2], 309-317 (1987).

2. J. R. Rice, "A Path Independent Integral and the Approximate Analysis of Strain Concentration by Notches and Cracks," J. Appl. Mech., 35, 379-386 (1968).

3. L. J. Broutman, "Measurement of the Fiber-Polymer Matrix Interfacial Strength," in Interfaces in Composites, edited by M. J. Salkind, STP 452, Am. Soc. for Testing and Materials, Philadelphia, 1969, pp. 27-41.

4. C. Gurney and J. Hunt, Proc. Roy. Soc. (London), A299, 508 (1967).

5. H. Stang and S. P. Shah, J. Mater. Sci., 21, 953 (1986).

6. D. B. Marshall and W. C. Oliver, "Measurement of Interfacial Mechanical Properties in Fiber Reinforced Ceramic Composites," J. Am. Ceram. Soc., 70, [8], 542-48 (1987).

7. Y.-C. Gao, Y.-W. Mai and B. Cotterell, "Fracture of Fiber-Reinforced Materials," J. Appl. Math. and Phys. (ZAMP), 39, 550-572 (1988).

8. E. P. Butler, E. R. Fuller, Jr., and H. M. Chan, "Interface Properties for Ceramic Composites From a Single-Fiber Pull-Out Test," in Interfaces in Composites, edited by C. G. Pantano and E. J. H. Chen, MRS Symp. Proc., Vol. 170, (MRS, Pittsburgh, PA, 1990), pp. 17-24.

9. E. P. Butler and E. R. Fuller, Jr., to be published.

10. M. Vedula, R. N. Pangborn and R. A. Queeney, "Fiber Anisotropic Thermal Expansion and Residual Thermal Stress in a Graphite/Aluminum Composite," COMPOSITES, 19, [1], 55-60 (1988).

11. J. H. Cranmer, G. C. Tesoro, and D. R. Uhlmann, "Chemical Modification of Carbon Fiber Surfaces with Organic Polymer Coatings," Ind. Eng. Chem. Prod. Res. Dev., 21, 185-190 (1982).

12. Photoelastic Stress Analysis, by A. Kuske and G. Robertson, (John Wiley & Sons, New York, 1974), pp. 111-114.

13. Technical Data Sheet for Textron Silicon Carbide Fibers, TEXTRON Specialty Materials, Lowell, MA, March 1988.

14. R. W. Goettler and K. T. Faber, "Interfacial Shear Stresses in SiC and AL_2O_3 Fiber-Reinforced Glasses," Cer. Eng. Sci. Proc., 9, [7-8], 861-870 (1988).

15. W. Balmforth and A. J. Holland, "The Stress Optical Coefficient of Glasses," J. Soc. Glass Tech. 29, 111-123 (1945).

16. Roy M. Waxler and A. Napolitano, "Relative Stress-Optical Coefficients of Some NBS Optical Glasses," J. Res. NBS, 59 [2], 121-125 (1957).

ADVANCED MATERIALS FOR HIGH-TEMPERATURE SOLID ELECTROLYTE APPLICATIONS

J. L. Bates, L. A. Chick, W. J. Weber and G. E. Youngblood

Pacific Northwest Laboratory(a)
P.O. Box 999
Richland, WA 99352

ABSTRACT

Advanced materials for use as electrodes, interconnections, and electrolytes in high-temperature electrochemical applications are under investigation. The air sinterability of $La_{1-x}Sr_xCrO_3$ is highly dependent upon a synergistic relationship between the (La+Sr)/Cr ratio, cation volatility, and second phase formation and transformation. Electrical conductivity in the ZrO_2-Y_2O_3-CeO_2 and ZrO_2-Y_2O_3-TiO_2 systems is highly dependent on composition and atmosphere. The electrochemical processes that occur at the solid-solid-gas interfaces in La(Sr)MnO_3/ZrO_2(Y_2O_3) have been studied using an unbonded interface cell and impedance spectroscopy.

INTRODUCTION

Electrochemical technologies, such as solid oxide fuel cells (SOFCs), that utilize high-temperature solid electrolytes offer promise for the clean, efficient and broad utilization of this country's fossil energy resources. Other electrochemical technologies with significant potential include sensors, oxygen production, and chemical conversion, separation, purification and synthesis; however, with the exception of fuel cells and sensors, these technologies are only conceptual at this time. In these applications, the materials for electrodes, electrolytes and interconnections, as well as the solid-solid-gas interfaces in these systems, are all critical and integrally related to the electrochemical processes. Therefore, an understanding of both the electrochemical processes and the role of the materials and materials properties is needed to develop these technologies with favorable performance and economics for fossil energy applications. Since the SOFC is the most advanced of all high-temperature

---

(a) Operated by Battelle Memorial Institute for the U.S. Department of Energy under contract DE-AC06-76RLO 1830.

electrochemical technologies, it is upon this emerging SOFC technological base that advances for using high-temperature electrochemical processes can best be developed [1].

The objectives of this research are to 1) develop an understanding of high-temperature electrochemical processes employing solid electrolytes; 2) develop advanced materials for use as electrodes, electrolytes and interconnections; and 3) establish the roles that these materials and their properties have on the electrochemical processes. The scope of the research is initially directed to the materials, electrochemical processes and issues associated with the SOFC. This scope currently includes the major issues of air sinterability (below 1823 K) of the lanthanum chromite interconnection; development of a reduced oxide fuel electrode; and an understanding of the electrochemical processes that occur at the electrode-electrolyte-gas and electrode-interconnection interfaces.

Three studies are discussed in this paper: 1) mechanisms for the air-sintering of $La_{1-x}Sr_xCrO_3$; 2) electrical transport in ZrO_2-Y_2O_3-CeO_2 and ZrO_2-Y_2O_3-TiO_2; and 3) electrochemical processes at the solid-solid-gas, La(Sr)MnO_3-ZrO_2(Y_2O_3)-air, interface using an unbonded interface cell coupled with AC impedance spectroscopy.

SINTERING MECHANISMS OF La(Sr)CrO_3

The synthesis, via the Glycine-Nitrate Process (GNP) [1,2], of highly active La(Sr)CrO_3 powders with well-controlled stoichiometry that can be sintered in air at 1823 K has enabled the factors and mechanisms for air sintering to be studied. Composition, cation ratio, formation and interaction of minor second phases and Cr volatilization during sintering are the most significant factors affecting the air sinterability of La(Sr)CrO_3.

Powder Quality and Composition Control

The La(Sr)CrO_3 powders synthesized by GNP are highly active because of their small particle size, high surface area and exceptional homogeneity. These powders, which are formed during self-sustaining combustion with

flame temperatures near 1720 K, are crystalline with 20 to 40 nm particle sizes and surface areas ≥ 30 m^2/g. The GNP powders are homogeneous with no significant particle-to-particle compositional variability when compared with wide compositional variations in powders synthesized by the amorphous-citrate process, [3] as illustrated in Figure 1. The superior GNP powder characteristics result from the rapid, high-temperature combustion of a homogeneous liquid precursor directly to a crystalline oxide powder with soft agglomerates. In contrast, the amorphous-citrate combustion occurs in multiple steps from a solid, amorphous precursor with transformations over long periods with externally-supplied heat. In the amorphous-citrate process, several intermediate phases form and decompose during thermal treatments; these phases require solid-state diffusion of cations and oxygen diffusion to form the homogeneous $La(Sr)CrO_3$ perovskite phase. Hard agglomerates form during these extended thermal treatments.

Large variations in air sinterability of active and homogeneous GNP-synthesized powders result from relatively small changes in composition; consequently, precise control of synthesized $La(Sr)CrO_3$ compositions is required. An improved method for analysis of metal nitrate stock solutions, using EDTA titrations, results in compositions controlled to within ±0.5%. This compares with a precision of ±5% for inductively coupled plasma atomic emission spectroscopy (ICP), the method previously used. Figure 2 is a ternary plot of 24 $La(Sr)CrO_3$ compositions produced using EDTA control. The six-sided envelope represents the potential range of chromite compositions produced using ICP control. Within this envelope, the resulting sintered density can vary ≈50%. In contrast, the compositional envelope for EDTA titration falls within the circles.

Effects of Composition and Volatility

Compositions of $La(Sr)CrO_3$ indicated in Figure 2 were synthesized and sintered at 1823 K under varying conditions of air flow. Sample composition (cation ratio), second phase formation and volatilization during sintering were found to be important factors affecting the densities, porosities, and final phase composition of the sintered samples.

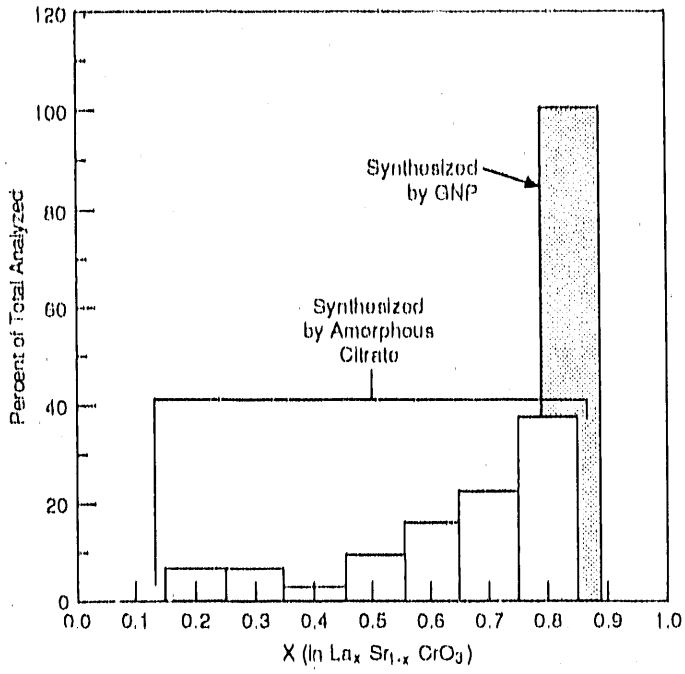

Fig. 1. Comparison of La(Sr)CrO_3 particle-to-particle homogeneity by EDS.

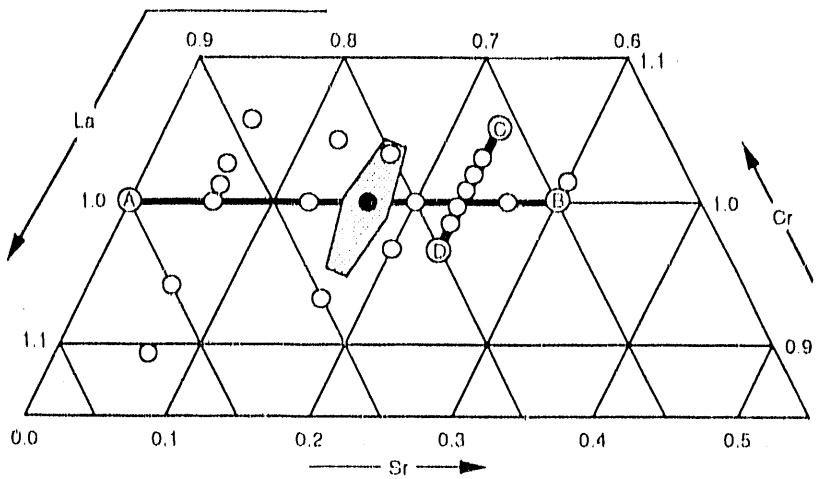

Fig. 2. Ternary La(Sr)CrO_3 compositions. Numbers on ternary refer to formulation: $La_wSr_xCr_yO_3$, where w+x+y = 2.0.

Strontium Content

The data in Figure 3 represent sintered densities for $La_{(1-x)}Sr_{(x)}CrO_3$ with (La+Sr)/Cr = 1.0 from the line A-B in Figure 2. These compositions

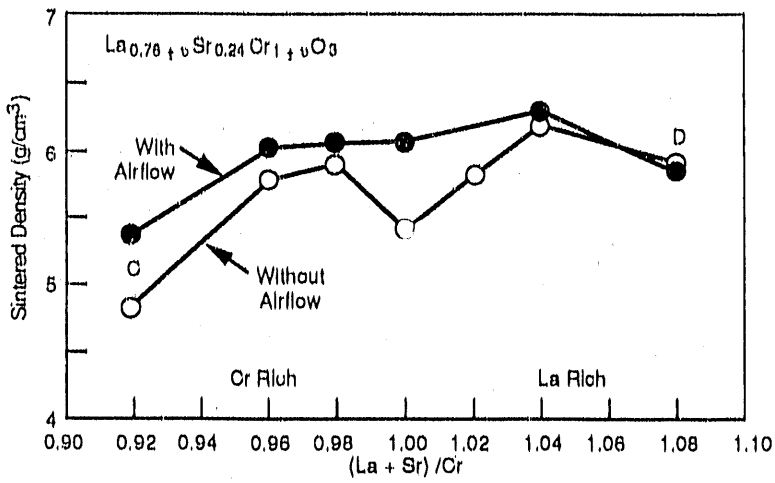

Fig. 3. Sintered density as function of Sr content with (La+Sr)/Cr = 1.00. Compositions represent line A-B, Figure 2.

were sintered at 1823 K for 8 hours in stagnant furnace air. Increased substitution of Sr for the La has little effect on the sintered density below x = 0.12. From x = 0.12 to 0.30, the sintered density increases by ≈50%. The sintered densities of three compositions were enhanced by introducing an airflow of 5 liters/min through the furnace, as also shown in Figure 3, with the 0.24 Sr composition showing the largest improvement. The effect of airflow was unaltered by changing from dry air to air saturated with water at 303 K.

(La+Sr)/Cr Ratio

In Figure 4, the sintered densities of $La_{(1-x)}Sr_{(x)}CrO_3$ with compositions along the line C-D in Figure 2 are shown. The initial Cr content in these samples is either enriched [(La+Sr)/Cr < 1] or depleted [(La+Sr)/Cr > 1]. In stagnant air, a minimum in the sintered density occurs for the composition at (La+Sr)/Cr=1.0, with slight enrichment or slight depletion of chromium improving sinterability. Sintering densities in 7 liters/min airflow eliminated the minimum. The sample with (La+Sr)/Cr=1.04 exhibited the highest density.

Figure 5 shows the weight lost during sintering of the same series of compositions as Figure 4. Chromium appears to be the major volatilizing cation as evidenced by a weight loss directly proportional to chromium

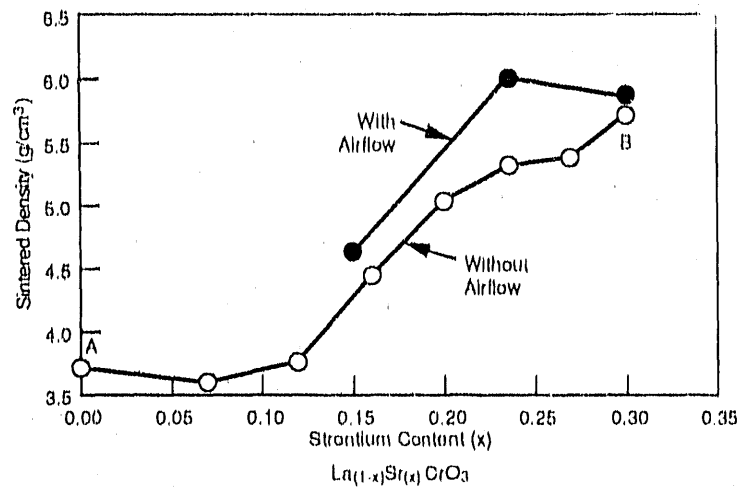

Fig. 4. Sintered density as function of (La+Sr)/Cr ratio for $La_{0.76-y}Sr_{0.24}Cr_{1.00+y}O_3$. Compositions represent line C-D, Figure 2.

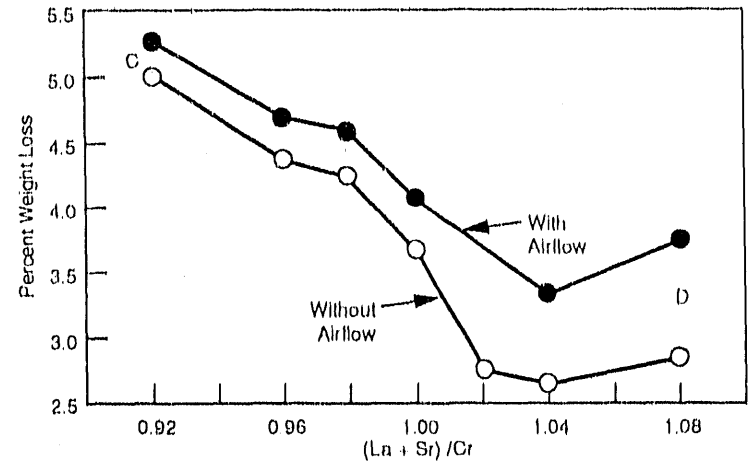

Fig. 5. Weight loss during sintering as function of (La+Sr)/Cr, corrected for 0.8 wt% loss adsorbed water. Compositions represent line C-D, Figure 2.

enrichment. Both of the weight loss curves exhibit minima that correspond to the maximum in the sintered density curve in Figure 4; however, airflow did increase the weight loss, with more pronounced effects on the compositions with depleted Cr.

Microstructure and Secondary Phases

In $La_{(0.78)}Sr_{(0.24)}Cr_{(0.98)}O_3$ that was sintered to the highest bulk density, a high-density surface layer, within about 100 μm of the surface, was observed that was almost devoid of pores and contained a second phase highly enriched in La, probably La_2O_3. The interior of this specimen had a higher porosity with less La-rich second phase but with another fine second phase that was rich in Sr. This observation suggests that the mechanisms of air sintering may involve pore closure during sintering with surface volatility creating a Cr concentration gradient. Since the $La(Sr)CrO_3$ perovskite matrix should have (La+Sr)/Cr = 1.0, depletion of Cr causes exsolution of La and formation of the La_2O_3 phase, leaving the perovskite phase enriched in Sr relative to the sample interior. The matrix phase near the surface thus contains higher Sr levels, which may be responsible for the enhanced sintering of the near-surface layer.

Although the starting $La(Sr)CrO_3$ powder is composed of single-phase perovskite, a minor secondary phase forms during calcination at 923 K [2]. During sintering, this secondary phase decomposes and/or transforms, thus affecting the sintering mechanisms. Strontium is highly soluble in the perovskite at high temperatures, and because the GNP combustion reaches flame temperatures near 1720 K, the resulting powder is single phase. However, during lower-temperature calcination and the early stages of sintering, Sr is exsoluted by the perovskite. Thus, during calcination of single-phase $La_{(1-x)}Sr_{(x)}CrO_3$ powder with $x > 0.07$, $SrCrO_4$ is formed.

Dynamic X-ray diffraction was used to observe these phase changes in $SrCrO_4$ heated at 5 K/min to 1520 K. The $SrCrO_4$ phase (A) began to decompose and an unidentified phase (B) began to form at 1100 K. At ≈1300 K, the $SrCrO_4$ (A) was gone. It was replaced by two unknown phases, (B) and (C), which subsequently disappeared (melted) at ≈1500 K. In single-phase $La_{(0.76)}Sr_{(0.24)}CrO_3$, the $SrCrO_4$ phase forms at ≈900 K, indicating Sr exsolution from the perovskite phase. The derivative phases of $SrCrO_4$, (B) and (C), were also detected and disappeared at ≈1500 K. The Sr-rich crystalline derivatives of $SrCrO_4$ are assumed to melt and form a Sr-rich liquid phase at ≈1500 K, which influences air sintering.

The effects of these phase transformations on sintering shrinkage of four $La(Sr)CrO_3$ compositions are shown in Figure 6. Significant shrinkage

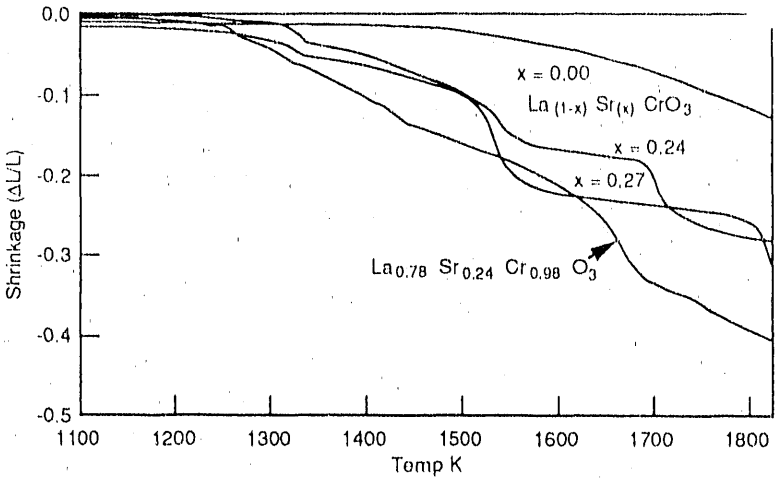

Fig. 6. Shrinkage during sintering at 100 K/h for $La_{(1-x)}Sr_{(x)}CrO_3$ three upper curves, and for $La_{0.78}Sr_{0.24}Cr_{0.98}O_3$ (lower curve).

begins for all compositions at temperatures between 1250 and 1300 K. At higher temperatures, $LaCrO_3$ (x=0.00) shrinks uniformly, indicating a simple sintering mechanism. The shrinkage of the other compositions, however, showed up to three inflections, indicating changes in sintering mechanisms during heating. The two samples with (La+Sr)/Cr=1.00, with x=0.24 and x=0.27, show a major inflection that begins just above 1500 K. This increase in shrinkage rate is attributed to melting of the Sr-rich phases and liquid-phase sintering. However, the other inflections are not yet understood. All Sr-containing compositions show a small inflection near 1330 K. The higher-temperature inflections appear strongly composition dependent, varying broadly with only minor changes in cation ratios. For example, the Cr-depleted $La_{(0.78)}Sr_{(0.24)}Cr_{(0.98)}O_3$ does not exhibit the inflection at 1500 K. This may explain the presence of the small quantity of Sr-rich phase in this sample after sintering. Chromium depletion may inhibit the formation of the liquid phase.

ELECTRICAL TRANSPORT IN ZrO_2-Y_2O_3-CeO_2 AND ZrO_2-Y_2O_3-TiO_2

The fuel electrode of SOFCs operates at very low oxygen partial pressures. Present state-of-the-art anodes are porous Ni/ZrO_2 composites bonded to the electrolyte and chromite interconnection. It is advantageous to replace the anode with an all ceramic electrode that can be sintered in air with in situ reduction by the fuel. Potential candidate

materials for the fuel electrode include complex oxides, such as Y_2O_3-ZrO_2-MO_x, where MO_x is an oxide addition that on reduction forms a complex oxide with high-electronic conductivity and that is compatible with the Y_2O_3-ZrO_2 electrolyte. For this study, CeO_2 and TiO_2 were added to $(0.1)Y_2O_3$-$(0.9)ZrO_2$.

The electrical conductivities of $(0.1)Y_2O_3$-$(0.9-x)ZrO_2$-$(x)TiO_2$ and $(0.1)Y_2O_3$-$(0.9-x)ZrO_2$-$(x)CeO_2$ with x = 0.0, 0.25, 0.45, 0.65 and 0.9, were determined in both air and Ar-4% H_2 (10^{-10} Pa oxygen pressure at 1373 K) using a four probe, dc pulse method. These results are shown in Figure 7. In air, the electrical conductivity of the $(0.1)Y_2O_3$-$(0.9-x)ZrO_2$-$(x)TiO_2$ system decreases with increasing mole fraction x, and the activation energy increases. In contrast, the electrical conductivity of $(0.1)Y_2O_3$-$(0.9-x)ZrO_2$-$(x)CeO_2$ in air decreases initially with x, then increases above x = 0.45. The activation energies increase slightly with x up to x = 0.45, then decrease.

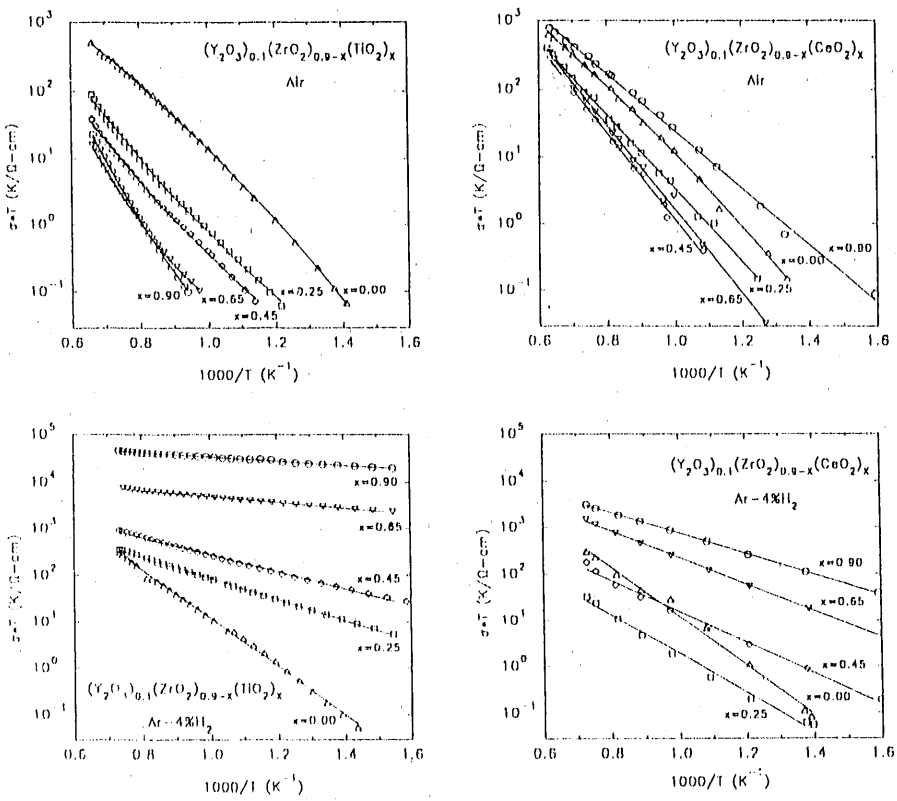

Figure 7. Log(σT) versus 1/T for the $(0.1)Y_2O_3$-$(0.9-x)ZrO_2$-$(x)TiO_2$ and the $(0.1)Y_2O_3$-$(0.9-x)ZrO_2$-$(x)CeO_2$ systems.

The electrical conductivities of both systems in air are assumed to be nearly 100% ionic and given by $\sigma_{ion} = (\sigma_o/T)\ \exp(E_m/kT)$, where σ_o is a charge carrier and material dependent constant. The continuing decrease in electrical conductivity of $(0.1)Y_2O_3$-$(0.9\text{-}x)ZrO_2$-$(x)TiO_2$ with increasing TiO_2 is indicative of the decreasing number of oxygen ion vacancies, since TiO_2 does not substitute for ZrO_2 or Y_2O_3 to retain the fluorite solid solution structure considered necessary for ionic conduction. The decreasing conductivity for $(0.1)Y_2O_3$-$(0.9\text{-}x)ZrO_2$-$(x)CeO_2$ with increasing CeO_2 content is indicative of the transition from a predominantly (Y_2O_3 + CeO_2)-stabilized ZrO_2 system to (Y_2O_3 + ZrO_2)-stabilized CeO_2. The higher conductivity for $x = 0.9$ results because Y_2O_3-stabilized CeO_2 has a higher ionic conductivity than Y_2O_3-stabilized ZrO_2.

In 4% H_2 the electrical conductivity, σ, of $(0.1)Y_2O_3$-$(0.9\text{-}x)ZrO_2$-$(x)TiO_2$ increases continuously with increasing x. In 4% H_2 the σ of $(0.1)Y_2O_3$-$(0.9\text{-}x)ZrO_2$-$(x)CeO_2$ shows an initial decrease with CeO_2 addition at $x = 0.25$, then a continuing increase with increasing CeO_2 content. The conductivity of $(0.1)Y_2O_3$-$(0.9)ZrO_2$ is the same in both air and 4% H_2. The increasing conductivities and smaller activation energies are consistent with changes from ionic conduction to predominantly electronic conduction. The data also suggest that between $x = 0.25$ and 0.45 the conductivity in 4% H_2 is mixed ionic\electronic; above 0.65 it is predominantly electronic in nature.

ELECTROCHEMICAL PROCESSES: UNBONDED INTERFACE CELL AND COMPLEX IMPEDANCE

The performance of high-temperature solid electrolyte systems, such as SOFCs, are often critically dependent upon the electrochemical processes that occur at solid-solid-gas interfaces. It is therefore important to understand these processes and the influence that the electrode and electrolyte materials and their transport properties exert on these processes. It is the purpose of this study to develop methods leading to an understanding of the roles of current, potential, temperature, environment and time on these processes.

To investigate the electrochemical reactions at cell interfaces without the influences of interface morphology variations, an unbonded interface cell (UIC) was developed and tested. The new cell design consists of a solid electrolyte disc pressed against a solid electrode disc. The interface comprises two ground surfaces in partial contact. Platinum is bonded to the outer surfaces of the electrode and electrolyte for electrical measurements. Although only a small fraction of the surfaces are in contact, the contact area can be calculated from the data. This design resolves the difficult problems of preparing reproducible virgin interfaces during cell fabrication by co-sintering of different high-temperature oxides. In addition, the relative ease of cell fabrication and assembly make reproducible and rapid measurements of the electrochemical processes at the materials interfaces possible. Similar cells can be made of electrode and interconnection materials.

The UIC is coupled with AC impedance spectroscopy (IS) to study materials properties, materials interaction and cell and interface performance. The IS [4] is used to measure the resistance and capacitance of materials interfaces and cells over a wide frequency range. This method potentially can separate a number of electrochemical and electrical processes such as polarization and charge transfer at the electrode/electrolyte interface, absorption reactions, defect generation and recombination, diffusion, degradation, and grain and grain boundary conductivity.

Impedance spectroscopy measurements were used to study the transport properties of Y_2O_3-stabilized ZrO_2 (YSZ) electrolyte up to 1273 K. The ionic bulk and grain boundary conductivity in the electrolyte were determined, and the results were in good agreement with data measured by the four-probe DC method. IS measurements on an UIC utilizing $La_{0.9}Sr_{0.1}MnO_3$ air electrode and YSZ electrolyte indicated that the inverse polarization resistance, R_p^{-1}, which is proportional to the reaction rates at the electrode-electrolyte interface, was very sensitive to changes in temperature, oxygen partial pressure and applied DC voltage bias. This interfacial reaction involves the adsorption of oxygen and charge transfer.

In air at 1173 K, the interfacial reaction rate decreases initially with a cathodic bias up to -200 mV, then increases at higher bias

voltages. In contrast, with an anodic bias, the reaction rate only increases with increasing bias. Both cathodic and anodic bias induce permanent changes in the interface characteristics and the reaction rates. The reaction rate characteristics agree with similar results obtained in air by Hammouche et al. [5] and by Takeda et al. [6] using a DC polarization technique.

In a reducing air-argon mixture (11 Pa oxygen partial pressure at 1173 K) the interfacial reaction rates change significantly with an external bias. With a cathodic bias, an initial decrease in reaction rate is followed by large increases in rates as the cathodic bias increases. With increasing anodic bias, the reaction rate continuously increases. These changes were much larger than those observed in air; however, no permanent changes in reaction rates were observed.

REFERENCES

1. J. L. Bates, "Solid Oxide Fuel Cells: A Materials Challenge". "Energy Progress and Environmental Protection," in Energy Technology XVI, Proceedings of Sixteenth Energy Technology Conference, February 28 - March 2, 1989, Washington, DC, 1989 pp. 205-219.

2. L. A. Chick, J. L. Bates, L. R. Pederson, and H. E. Kissinger, "Synthesis of Air-Sinterable Lanthanum Chromite Powders," in Proc. of First International Symposium on Solid Oxide Fuel Cells, Electrochemical Society, Pennington, NJ, 1989, pp. 170-179.

3. D. J. Anderton and F. R. Sale, "Production of Conducting Oxide Powders by Amorphous Citrate Process," *Powder Metallurgy* **22** (1979) pp. 14-21.

4. J. E. Bauerle, "Study of Solid Electrolyte Polarization by Complex Admittance Method," *J. Phys. Chem. Solids* **30** (1976) pp. 303-310.

5. A. Hammouche, E.J.L. Siebert and A. Hammon, "Crystallographic, Thermal and Electrochemical Properties of the System $La_{1-x}Sr_xMnO_3$ for High-Temperature Solid Electrolyte Fuel Cells," *Mat. Res. Bull.* **24** (1989) pp. 367-380.

6. Y. Takeda, R. Kanno, M. Noda, Y. Tomida and O. Yamamoto, "Cathodic Polarization Phenomena of Perovskite Oxide Electrodes With Stabilized Zirconia," *J. Electrochem. Soc.* **134** No. 11. (1987) pp. 2656-2661.

CERAMIC CATALYST MATERIALS: HYDROUS METAL OXIDE ION-EXCHANGE SUPPORTS OF DIRECT COAL LIQUEFACTION

C. H. F. Peden, B. C. Bunker, S. L. Martinez and D. H. Doughty

Sandia National Laboratories
Inorganic Materials Chemistry Division
Albuquerque, New Mexico 87185-5800

ABSTRACT

This presentation describes studies aimed at understanding how the activity of a catalyst is related to the concentration and dispersion of active metals on the catalyst supports. Such information is critical to designing materials having optimum catalytic properties. We have developed synthetic techniques for controlling both the concentration and dispersion of nickel on hydrous sodium titanate catalyst supports. The techniques require an understanding of the solution chemistry of both the support material and dissolved metal species. Characterization of the material and catalytic properties of Ni-loaded hydrous titanates will be presented. In addition, studies of the local molecular structure by Raman and solid-state ^{17}O NMR spectroscopies will be described.

INTRODUCTION

As an AR&TD project, we are exploring the synthesis and evaluation of new ceramic catalytic materials for efficient, direct conversion of coal to clean liquid fuels. In this way, we are obtaining a better understanding of these materials that will impact the long-term, generic needs of various fossil fuel technologies. However, sufficient testing of the nydrous metal oxide ion-exchange catalysts with coal and coal-derived feeds has been accomplished to demonstrate that they show great promise for end-use process applications.[1]

The specific materials under study in this AR&TD project are from a group of hydrous oxide ion-exchange compounds of Ti, Zr, Nb, and Ta developed at Sandia National Laboratories. These compounds have been used to prepare catalysts by a novel synthesis route involving the incorporation of active metals by ion exchange.[2] Catalysts prepared in this manner, even at low active metal loadings of 1%, are equally effective for conversion of coal to low molecular weight products as a commercial Ni-Mo/alumina catalyst containing 15% by weight active metals.[1] One possible reason for the improved performance of the catalysts prepared from the hydrous titanate materials may be that

active metals are dispersed more completely via the ion-exchange process than when loaded by traditional incipient wetness techniques. As such, these materials offer a method to prepare greatly improved heterogeneous catalysts for many applications, provided we understand the important variables in the synthesis.

Our goal is to develop a fundamental understanding of the preparation and properties of these unique materials. Specifically, we have been investigating the following areas:

1) molecular and extended macroscopic structure of the hydrous titanate;

2) mechanism of incorporation of catalytic metals; and

3) catalytic and reactivity studies of the metal-loaded catalysts.

Having developed this basic understanding, we envision being able to tailor catalyst properties for specific applications, as well as providing a foundation for further catalyst development. This report summarizes recent work on this project and represents much of our current understanding and developments of the hydrous titanate materials.

DISCUSSION OF CURRENT ACTIVITIES

Results and Discussion

To optimize the use of the amorphous sodium titanate powders as catalyst substrates, it is important to fully characterize the ion-exchange properties of the material. Further, the solution properties of the active metal to be loaded onto the support will be an important parameter in the control of the adsorption process. For example, exposure of sodium titanate to a nickel salt solution does not guarantee that nickel will be loaded onto the sodium titanate, or that the nickel, if loaded, will be dispersed on an atomic level. Sodium titanate only behaves as a cation exchange material under certain pH conditions. The solution pH also influences the hydrolysis and speciation of dissolved nickel ions,[3] which can form large polymeric clusters or colloidal particles which are not adsorbed by the sodium titanate via a simple ion-exchange process. Thus, in order to control the mechanism by which nickel is loaded onto sodium titanate and to control the degree of nickel dispersion, we need to understand the ion-exchange properties of the sodium titanate support, the hydrolysis chemistry of the dissolved nickel, and how the different nickel species are expected to interact with the titanate support. These studies are described first, followed by comparative reactivity and characterization measurements on Ni-loaded catalysts. Finally, we discuss spectroscopic determination of the local molecular structure of the ion-exchange sites on the hydrous titanates. The experimental procedures to prepare and characterize the hydrous titanate-supported catalysts have been described elsewhere.[1,4-6]

Ion-Exchange Behavior of Sodium Titanate

The ion-exchange characteristics of sodium titanate supports are summarized in Fig. 1.[1] In the figure, proton (H^+) consumption is plotted by the solid line as the $Na_{0.6}Ti$ is titrated from a basic pH (≈12) with HCl. Na^+ (+) loss from and Cl^- (-) adsorption onto the support are followed by analysis of the solutions by ICP. At pH values above the isoelectric point (iep) of sodium titanate (pH 5), the surfaces of the sodium titanate particles are covered with anionic surface sites that are charge compensated by cations such as sodium. Above pH 5, the titanate support can function as a cation exchanger. For example if Ca(II) ions are added to a sodium titanate slurry, solution analyses indicate that one calcium ion is adsorbed by the support for every two sodium ions released into solution. Below pH 5, surface sites on the titanate support are primarily cationic, and the support behaves as an anion rather than a cation exchanger. In the above example, neither Ca(II) or Na(I) ions are adsorbed by the titanate powder when the solution pH is highly acidic (below pH 4). Therefore, the solution chemistry of sodium titanate suggests that if the powder is exposed to Ni(II), and if the Ni(II) is to be loaded via an ion-exchange process, no Ni(II) adsorption is to be expected below pH 5. Also apparent in Fig. 1 (note the two regimes of H^+ consumption at nearly constant pH of about 8 and 12) and in surface charge measurements as a function of pH[4c] is the presence of at least two anionic surface sites above pH 5. The distribution of these two sites is controllable during the synthesis of the sodium titanate powder as will be shown

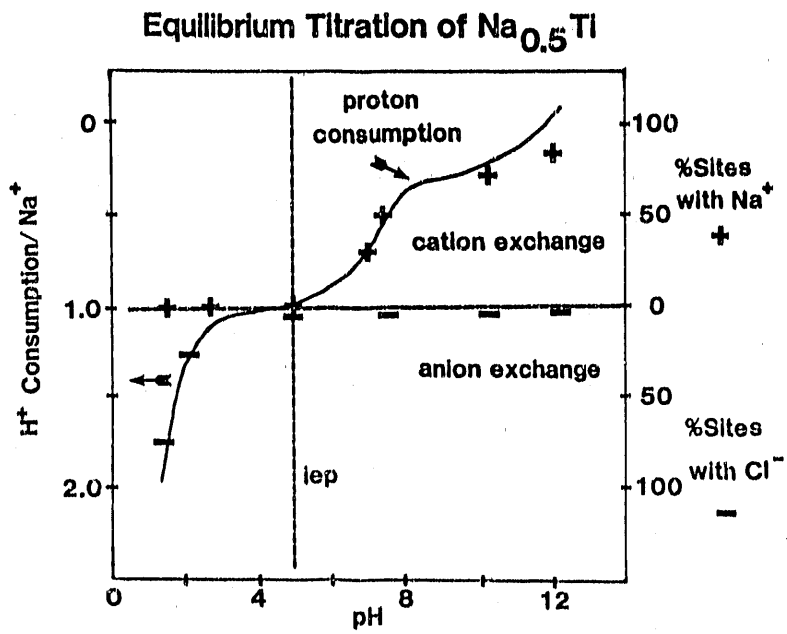

Figure 1: Plot of the H^+ (solid line) and Cl^- (-) consumption from solution, and Na^+ (+) depletion from a $Na_{0.6}Ti$ during titration with HCl (starting pH = 12).[1]

by our spectroscopic studies to be described below. It should be noted here that these latter studies will also show that the view of the titanate surface sites as strictly anionic above and cationic below the iep is naive.

Ni(II) Hydrolysis Chemistry and Loading Studies

Although Ni(II) exists in solution as a simple aquated cation in acidic solutions, increases in the solution pH can lead to the deprotonation of bound water molecules, leading to hydrolysis and condensation of Ni(II) to form polymeric clusters. The calculated hydrolysis diagram[3] for Ni(II), shows that for a 3 x 10^{-2} M nickel nitrate solution, hydrolysis and condensation should commence at a pH of approximately 6.5. Further increases in pH lead to the formation of larger insoluble polymeric species with Ni becoming less and less soluble as the pH is raised to pH 10. The hydrolysis diagram suggests that Ni(II) can only be loaded by a simple ion-exchange process at pH values below 6.5 where hydrolysis is negligible. Above pH 6.5, polymeric nickel clusters will be present which can either condense with surface sites on the titanate support via reactions such as:

$$\left\{\text{Ti-OH}\right\} + \text{Ni}_x(\text{OH})_y^{2x-y} \longrightarrow \left\{\text{Ti-O-Ni}_x(\text{OH})_{y-1}^{2x-y+1}\right\} + \text{H}_2\text{O}, \qquad (1)$$

or can condense with each other to form larger colloidal particles of nickel hydroxide. The relative amounts of nickel which are adsorbed as small clusters and as colloidal particles should be influenced by the relative availability of reactive sites on the support vs. the other clusters present in solution. In any case, the hydrolysis diagram predicts that above pH 6.5, Ni(II) adsorption should occur via hydrolysis and condensation rather than by ion exchange.

Combining the information obtained in our studies of the ion-exchange properties of sodium titanate with what is known concerning the hydrolysis characteristics of Ni(II), we would predict that below pH 4, Ni(II) is not adsorbed by sodium titanate, between pH 4 and pH 6.5, Ni(II) is adsorbed as a monomeric cation via an ion-exchange process, and that above pH 6.5, Ni(II) should be adsorbed as polymeric clusters and colloids via hydrolysis and condensation mechanisms. To check the above hypothesis, we have titrated acidic nickel nitrate solutions with sodium hydroxide in the absence and in the presence of sodium titanate and analyzed solution aliquots for Ni(II) as a function of pH (Fig. 2). The results obtained for nickel nitrate alone show that the hydrolysis of nickel leading to the formation of insoluble nickel hydroxide occurs between pH 7.5 and 8 (slightly higher than the pH of 6.5 predicted from simple hydrolysis diagrams, Ref. 3). Results obtained in the presence of sodium titanate suggest that as predicted, little Ni(II)

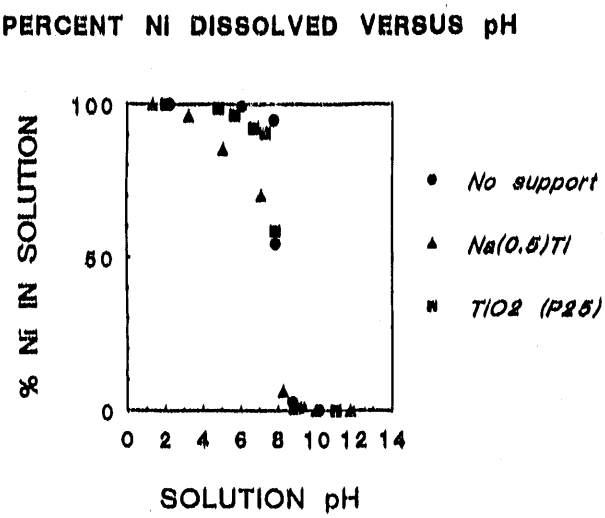

Figure 2: Plot of the amount of Ni in a 0.25M $Ni(NO_3)_2$ solution as a function of pH both in the presence and absence of a $Na_{0.5}Ti$ or a TiO_2 powder.

is adsorbed by the sodium titanate below pH 4. Between pH 4 and pH 7.5, Ni(II) is removed from solution via ion exchange, with more Ni(II) being adsorbed as the solution pH increases. Above pH 7.5, the precipitous drop in the dissolved Ni(II) concentration indicates that Ni(II) hydrolysis occurs at about the same pH in the presence of sodium titanate as in its absence. In this basic pH regime, Ni(II) adsorption should no longer occur via an ion-exchange reaction. Also plotted in Fig. 2 is a titration of a $Ni(NO_3)_2$ solution in the presence of a commercial TiO_2 powder (Degussa P-25). In this case, the behavior is very similar to that obtained without any powder demonstrating the lack of ion-exchange sites on this material.

Characterization and Reactivity Studies of Nickel-Loaded Catalysts

Because results from earlier catalytic studies[1] suggested that we have good metal dispersion even at high metal loadings (> 5%) on the sodium titanates relative to materials prepared by traditional methods, we investigated how the degree of nickel dispersion depends on the loading conditions. In this study, we compare two nickel-loaded catalysts prepared by ion exchange on the titanate powders or by impregnation on Degussa P-25 TiO_2. We have previously described characterization and reactivity studies of two very different Ni catalysts prepared on the titanates in which it was demonstrated that the ion-exchanged material showed characteristics of being highly dispersed, even at metal loadings of 5% or more.[4c,5]

A good test of the dispersion of the active metal is the activity and selectivity for the hydrogenolysis of n-butane. For example, it has been reported that highly dispersed

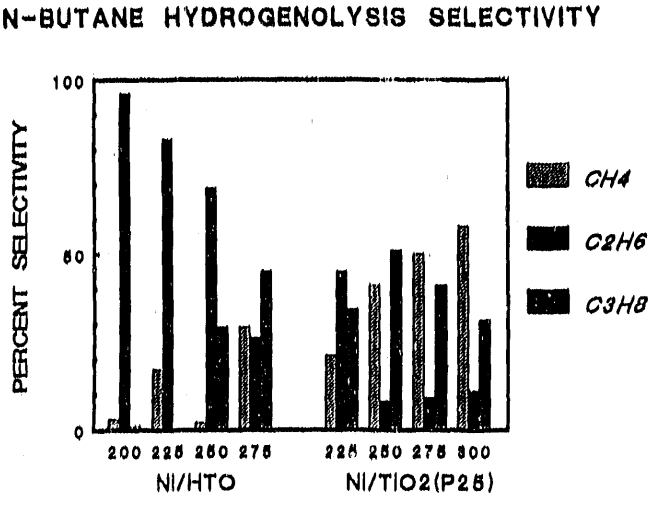

Figure 3: Selectivity for C_1 (CH_4), C_2 (C_2H_6), and C_3 (C_3H_8) hydrocarbon formation from the hydrogenolysis of butane over Ni/HTO and Ni/TiO_2 catalysts.

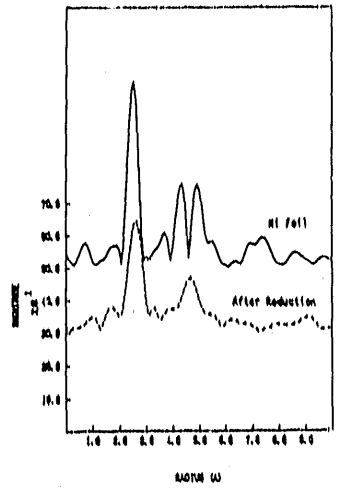

Figure 4: Ni EXAF spectra for a reduced HTO-supported catalysts. The spectrum of Ni foil is shown for comparison

Ir catalysts are particularly selective for ethane by preferential scission of the central C-C bond in n-butane.[7] Fig. 3 displays the results obtained for the selectivity for C_1, C_2 and C_3 paraffin hydrocarbons as a function of temperature on the two catalysts described above. It can be seen that the catalyst prepared by ion exchange on the hydrous titanate powders is very selective for C_2 hydrocarbons (ethane) at temperatures below 540 K. At higher temperatures (> 550 K), methane is the predominant product. In the case of the catalyst prepared by impregnation of TiO_2, methane and propane are the primary products for most temperatures studied. These results suggest that larger metal particles are present in the impregnated catalyst.

To confirm the highly dispersed nature of the ion-exchanged hydrous titanate supported Ni catalyst, we have obtained Ni K-edge EXAFS and XANES spectra of this catalyst in collaboration with Dr. Farrel Lytle of Boeing. The Ni K-edge EXAFS spectrum of the catalysts after H_2 reduction is shown in Figure 4 where the spectrum of a Ni foil is also shown for comparison. Significantly, there is a complete absence of the second, third and fourth nearest neighbor Ni peaks (at approximately 3.9, 4.5 and 5.2 Å, respectively) in the HTO-supported catalyst. There is a strong feature at approximately 4.8 Å which is unprecedented in supported-Ni catalysts. At the present time, we are not sure what this peak represents. However, a second nearest neighbor of Ni (or O) at such a long distance is very strong evidence that the Ni is highly dispersed.

Raman and ^{17}O NMR Spectroscopic Studies

In this section, we focus on ongoing studies of the local molecular structure of the hydrous titanate materials. As discussed above, the loading of active metals on sodium titanate supports by ion exchange leads to much more active and selective catalysts than can be obtained by other loading procedures. In addition, from the above described ion-exchange studies it appears that the concentrations and ion-exchange characteristics of active sites on the titanate supports are controlled by the coordination geometry of oxygens in the structure. We have utilized Raman spectroscopy and solid state NMR spectroscopy on ^{17}O labeled samples to determine the distribution of oxygen types and ion-exchange sites in amorphous titanates.

Crystalline titanates reported in the literature[8] exhibit a wide range of local structural environments. The titanium (IV) ions in the structures can be coordinated by either 4, 5, or 6 oxygens (designated Ti(4), Ti(5), and Ti(6)). The oxygens can be bonded to 1, 2, 3, or 4 titanium ions (designated O(1), O(2), O(3), and O(4)). To make definitive NMR peak assignments, we therefore prepared ^{17}O labeled crystalline compounds having as many possible combinations of O and Ti coordinations as possible to derive standards relating structure to the observed ^{17}O chemical shifts and Raman bands. The chemical shift information obtained for all model compounds is summarized in Fig. 5. (All chemical shifts are reported in ppm, with $H_2{}^{17}O$ serving as the 0 ppm reference.) While each type of oxygen does not always produce an NMR signal at exactly the same chemical shift, it appears that the chemical shifts tend to fall in the following ranges as illustrated in Fig. 5: O(4) = 600-700 ppm, O(3) = 400-600 ppm, O(2) = 330-450 ppm, and O(1) = 180-420 ppm. While the peaks associated with O(4) and O(3) are well separated from other ranges of chemical shift, there is considerable overlap in the ranges for O(2) and O(1). For an unknown compound, such as our amorphous titanates, peaks observed below 400 ppm could be attributed to either oxygen type. Fortunately, the presence of O(1) is easy to detect using Raman spectroscopy (see below), so we are confident that relative amounts of O(2) and O(1) can be obtained by combining NMR and Raman results.

The primary factor influencing the ^{17}O NMR chemical shift appears to be the electron density on the oxygen. One way to characterize the electron density on the oxygen is to use simple formal charge arguments (Fig. 6). For example, if Ti(IV) is bonded to six oxygens, the net charge which the titanium donates per oxygen is +4/6 = +0.67. The formal charge on oxygen is taken to be equal to -2. Therefore, if the oxygen is bonded to two Ti(6) ions, the net charge on the oxygen in this hypothetical structure is -2 + 2(0.67) = -0.67. Fig. 6 illustrates that similar arguments can be made to rationalize neutral and positively charged oxygen sites. We have demonstrated that there

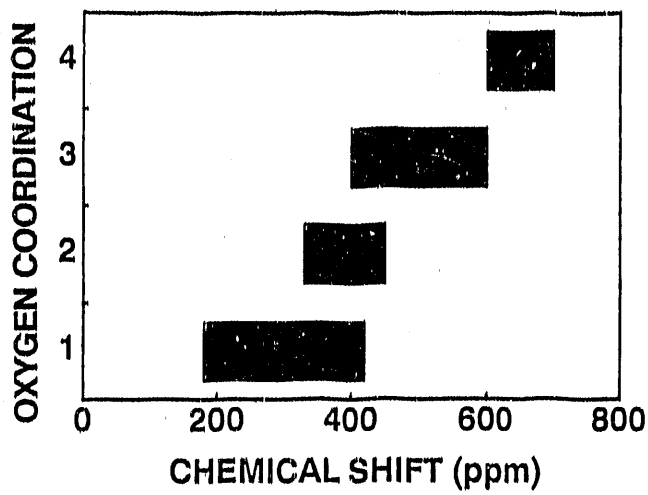

Figure 5: Approximate ranges observed for the ^{17}O chemical shifts of crystalline titanates as a function of oxygen coordination.

	Anionic	Neutral	Cationic
Charge	-2/3	0	+2/3
Species	Ti(6) — O — Ti(6)	Ti(6) Ti(6) O Ti(6)	Ti(6) Ti(6 O Ti(6 Ti(6)
Compound	$PbTiO_3$	TiO_2	$K_2Ti_4O_9$

Figure 6: Three examples of Ti-O coordination geometries which can give rise to variably charged sites in a titanate structure.

is a good correlation between the net charge on the oxygen and the observed chemical shift.[4d,4e]

Raman spectra have also been obtained for all model compounds investigated via NMR. The crystalline titanates exhibit rich Raman spectra below 1000 cm^{-1} associated with stretching and bending modes of different Ti-O bonding configurations. Definitive assignment of all modes is complicated and is not yet complete. However, one important

spectral region has been identified, and that is the region associated with non-bridging oxygens (nbo's). All compounds containing non-bridging oxygens exhibit a strong band (or bands) in the 700-900 cm^{-1} region of the Raman spectrum. Compounds which do not have non-bridging oxygens exhibit weak bands in this region, probably associated with impurities. Therefore, in those instances where the NMR results are ambiguous with regard to the presence of non-bridging oxygens, the Raman spectra can provide unambiguous proof that nbo's are present. In our recent spectroscopic studies, we have also focussed on 1) the effect of altering the Na/Ti stoichiometry in the amorphous powders, and 2) the effect of ion-exchange reactions in acid solution on the distribution of ion-exchange sites in the material.

Varying Na/Ti Stoichiometry. In the synthesis of the sodium hydrous titanate powders, the Na to Ti stoichiometry is easily controlled by varying the amount of NaOH used. This leads to altered ion-exchange properties as indicated by pH titrations and surface charge measurements.[9] From both the Raman and ^{17}O NMR spectra shown in Fig. 7, such altered properties can be rationalized. For example, the ^{17}O NMR spectra of $Na_{0.25}Ti$ and $Na_{0.5}Ti$ are both dominated by two features near 350 and 500 ppm that we assign to two-fold and three-fold oxygens respectively. However, the spectrum of $Na_{0.5}Ti$ also shows a peak at approximately 240 ppm, in the region expected for non-bridging oxygens. This assignment is reinforced by the Raman spectra of these two materials also shown in the figure. In this case, the spectrum of the $Na_{0.5}Ti$ powder contains a large scattering feature near 900 cm^{-1} while the $Na_{0.25}Ti$ sample shows little intensity in this region. On the basis of the formal charge arguments described earlier, we expect that the charged ion-exchange sites in the hydrous titanate materials will be the non-bridging and doubly-bridged oxygen sites. Such sites in the structure will be formally negative and charge-compensated by the Na cations. Thus, these results demonstrate that both the type and number of ion-exchange sites can be manipulated in a simple manner during the preparation of these materials.

Structural Rearrangement During Ion-Exchange Reactions. Previously, we showed that the ion-exchange properties of a $Na_{0.5}Ti$ powder can be irreversibly altered upon proton for sodium exchange in acidic solutions.[4a] On the basis of Raman spectra, we suggested[5] that this might arise from a reaction between doubly protonated non-bridging oxygens (O(1)'s) and doubly-bridged oxygens (O(2)'s) in the material. More recently, we have obtained ^{17}O NMR spectra of the $Na_{0.5}Ti$ starting material, and after it had been contacted with pH 7 and pH 2 solutions. The results, shown in Fig. 8, suggest that our previous conclusions were incomplete. Again the spectrum of the starting material (labeled pH 12 in the figure) shows spectral features at about 240, 350 and 500 ppm assigned above to nbo, O(2) and O(3) structural units, respectively. In agreement with the Raman results,[4e] we find that the nbo peak disappears at low pH. However, in

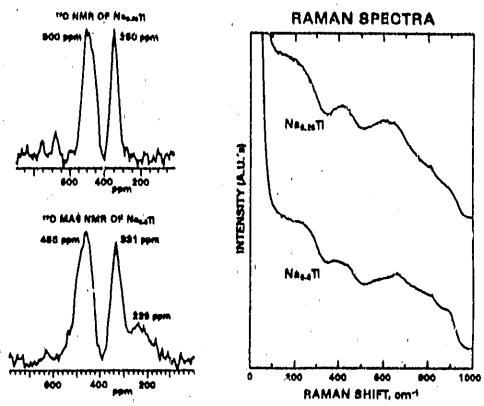

Figure 7: ^{17}O solid state NMR and Raman spectra of $Na_{0.25}Ti$ and $Na_{0.5}Ti$ amorphous hydrous titanate powders.

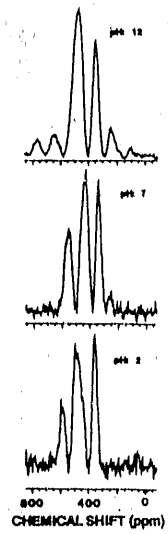

Figure 8: ^{17}O solid state NMR spectra of $Na_{0.5}Ti$ amorphous hydrous titanate powder as a function of solution pH.

addition to seeing changes in the relative populations of O(1), O(2), and O(3), we see a new NMR peak at about 600 ppm indicative of the presence of O(4). It now appears that network repolymerization at low pH is more complex than originally thought, involving formation of both O(3) and O(4) units from condensation reactions. The occurrence of reactions which convert mixtures of O(1), O(2), and O(3) into mixtures of O(2), O(3), and O(4) not only eliminates anionic oxygen sites available for cation exchange, but creates positively charged O(4) sites which are potential anion exchange sites (see Fig. 6). Notice that these sites begin to appear even at pH 7, above the iep of the sodium hydrous titanate material.[4c,6] The generation of sites available for ion-exchange of anions from solution (cationic sites) in this pH regime may explain why anions such as solvated Mo and V species adsorb onto the hydrous titanates above pH 5 (the iep). (These results will be reported in an upcoming semiannual report.) Similarly, that formally negatively charged O(2) sites persist at low pH may explain cation exchange (Ni(II) adsorption[4c,6]) below the iep.

ACKNOWLEDGMENTS

Sandia National Laboratories is supported by the U. S. Dept. of Energy under contract No. DE-AC04-76DP00789. The authors would like to thank D. R. Tallant

(Sandia National Laboratories) for the Raman spectra, G. L. Turner (Spectral Data Services) for performing the solid-state NMR measurements, F. L. Lytle (The Boeing Company) for EXAFS studies, and Prof. A. K. Datye and graduate student E. J. Braunschweig (University of New Mexico) who performed catalyst activity tests.

REFERENCES

1. (a) R. G. Dosch, H. P. Stephens, F. V. Stohl, B. C. Bunker and C. H. F. Peden, "Hydrous Metal Oxide-Supported Catalysts: Part I. - Preparation Chemistry and Physical and Chemical Properties," Sandia Report (SAND89-2399). (b) R. G. Dosch, H. P. Stephens and F. V. Stohl, "Hydrous Metal Oxide-Supported Catalysts: Part II. - Catalytic Properties and Applications," Sandia Report (SAND89-2400).

2. H. P. Stephens, R. G. Dosch and F. V. Stohl, "Catalysis Using Hydrous Metal Oxide Ion Exchangers," U. S. Patent No. 4,511,455; April 16, 1985.

3. C. F. Baes, Jr. and R. E. Mesmer, The Hydrolysis of Cations; John Wiley & Sons, 1976; New York.

4. (a) B. C. Bunker, C. H. F. Peden and S. L. Martinez, "Ceramic Catalyst Materials: Hydrous Metal Oxide Ion-Exchange Supports for Direct Coal Liquefaction," AR&TD Materials Semiannual Report, March-September, 1987; ORNL/FMP-87/2, p. 213. (b) C. H. F. Peden, B. C. Bunker and S. L. Martinez, ibid., October, 1987 - March, 1988; ORNL/FMP-88/1, p. 171. (c) C. H. F. Peden, B. C. Bunker and S. L. Martinez, ibid., April - September, 1988, p. 207. (d) B. C. Bunker, C. H. F. Peden and S. L. Martinez, ibid., October, 1988 - March, 1989, p. 183. (e) C. H. F. Peden, B. C. Bunker and S. L. Martinez, ibid., April - September, 1989, p. 179.

5. B. C. Bunker, C. H. F. Peden, S. L. Martinez, D. R. Tallant and G. L. Turner, "Raman and NMR Studies of Solution-Prepared Hydrous Titanium Oxide Ion-Exchange Materials," in Better Ceramics Through Chemistry III, edited by C. J. Brinker, D. E. Clark and D. R. Ulrich (MRS Symposium Proceedings, New York, 1988) p. 105.

6. B. C. Bunker, C. H. F. Peden, S. L. Martinez, E. J. Braunschweig and A. K. Datye, "Studies of Hydrous Sodium Titanate Ion-Exchange Materials for Use as Catalyst Supports," in Role of Characterization in Catalyst Development, edited by S. A. Bradley, M. J. Gattuso and R. J. Bertolacini (ACS Symposium Proceedings, New York, 1989) p. 65.

7. K. Foger and J. R. Anderson, "Hydrocarbon Reactions on Supported Iridium Catalysts," J. Catal. 59 (1979) 325.

8. (a) K. K. Wu and I. D. Brown, The Crystal Structure of β-Barium Orthotitanate, β-Ba_2TiO_4, and the Bond Strength-Bond Length Curve of Ti-O," Acta Cryst. B29 (1973) 2009. (b) S. Andersson and A. D. Wadsley, "The Structures of $Na_2Ti_6O_{13}$ and $Rb_2Ti_6O_{13}$ and the Alkali Metal Titanates," Acta Cryst. 15 (1962) 194. (c) T. Sasaki, M. Watanabe, Y. Komatsu and Y. Fujiki, "Layered Hydrous Titanium Dioxide: Potassium Ion Exchange and Structural Characterization," Inorg. Chem. 24 (1985) 2265. (d) S. Andersson and A. D. Wadsley, "The Crystal Structure of $K_2Ti_2O_5$," Acta Cryst. 15 (1961) 663. (e) C. E. Bamberger, G. E. Begun and C. S. MacDougall, Appl. Spectros. 44 (1990) 30.

9. S. L. Martinez, B. C. Bunker and C. H. F. Peden, unpublished data.

DEVELOPMENT OF CERAMIC MEMBRANES FOR GAS SEPARATION

D. E. Fain
G. E. Roettger

Oak Ridge Gaseous Diffusion Plant*
P. O. Box 2003
Oak Ridge, Tennessee 37831-7271

ABSTRACT

There is a great deal of optimism that ceramic membranes can be developed to separate gases at high temperatures or under highly corrosive conditions. Considerable progress has been made toward that end at the Oak Ridge Gaseous Diffusion Plant (ORGDP). The major initial emphasis is on developing a membrane for the separation of hydrogen from gasified coal at temperatures of 1000°F or higher. An analytical model is being developed and used to predict the membrane pore size that would be required to achieve high separation factors for various gas pairs. The model indicates that membranes having effective pore radii of less than 5Å will be required to achieve high separation factors. Improvements have been made in membrane fabrication methods that have reduced the mean pore radius of current ceramic membranes to 7 to 8Å. Characterization testing suggests that presently available fabrication methods should permit mean pore radii to be further reduced to less than 5Å. Pore size distributions and room temperature gas permeability data have been obtained on ceramic membranes having mean pore radii ranging from about 22 to 7Å. Separation factors have been calculated for several gas pairs from the pure gas permeabilities. Predictions from the theoretical model are compared with the empirical results, and predictions for smaller pore sizes are given.

INTRODUCTION

There is much interest today in developing ceramic membranes having pore diameters of a few angstroms. Such membranes should provide an efficient means of separating gases at high temperatures in corrosive environments. Development work being carried out at ORGDP has an initial objective of producing a ceramic membrane that will effectively separate hydrogen at high temperature and pressure from the synthetic gases produced by coal gasification processes. A key goal of this project during FY 1990 is to fabricate initial

*The Oak Ridge Gaseous Diffusion Plant is operated by Martin Marietta Energy Systems, Inc., for the U.S. Department of Energy.

ceramic membranes having an effective pore radius of less than 5Å. Another important goal is to evaluate the permeabilities of the small-pore-size developmental membranes to determine their separation factors. Concurrent with membrane development and characterization efforts, theoretical models of gas transport are being developed to provide guidance to the project and to aid in interpreting the empirical data.

MEMBRANE DEVELOPMENT

Experimental membranes that are currently being fabricated are tubular alumina membranes having a diameter of about 0.9 cm. Well over 100 such membranes have been fabricated and characterized during the first half of FY 1990, and very encouraging progress has been made in reducing pore size. Improvements that have been made in membrane fabrication methods have resulted in the mean pore radius of alumina membranes being reduced from about 15Å at the end of FY 1989 to 7 to 8Å currently. Pore size distributions as determined by the Dynamic Pore Size Test are shown for a late FY 1989 alumina membrane (Fig. 1) and for a recent alumina membrane (Fig. 2). Additional refinements of fabrication techniques have been identified that offer good potential for further reducing the mean pore size of alumina membranes to the near-term target of 5Å or smaller.

DYNAMIC PORE SIZE TEST

One of the key test systems that is being used to guide the membrane development effort is the Dynamic Pore Size (DPS) test, which is used to determine the pore size distribution. This system is used to measure the flow of nitrogen through the membrane pores with a controlled partial pressure of a condensible gas present. For any defined partial pressure, pores up to a given size (as determined by the Kelvin equation) are plugged with the condensible gas, while pores larger than that size are open and permit gas flow. By making such measurements over a wide range of partial pressures, the flow through each of many small increments of pore size can be determined and the pore size distribution defined. The DPS test provides a highly desirable flow-weighted pore size distribution, i.e., the fraction of total flow through the membrane that occurs in each small increment of pore size.

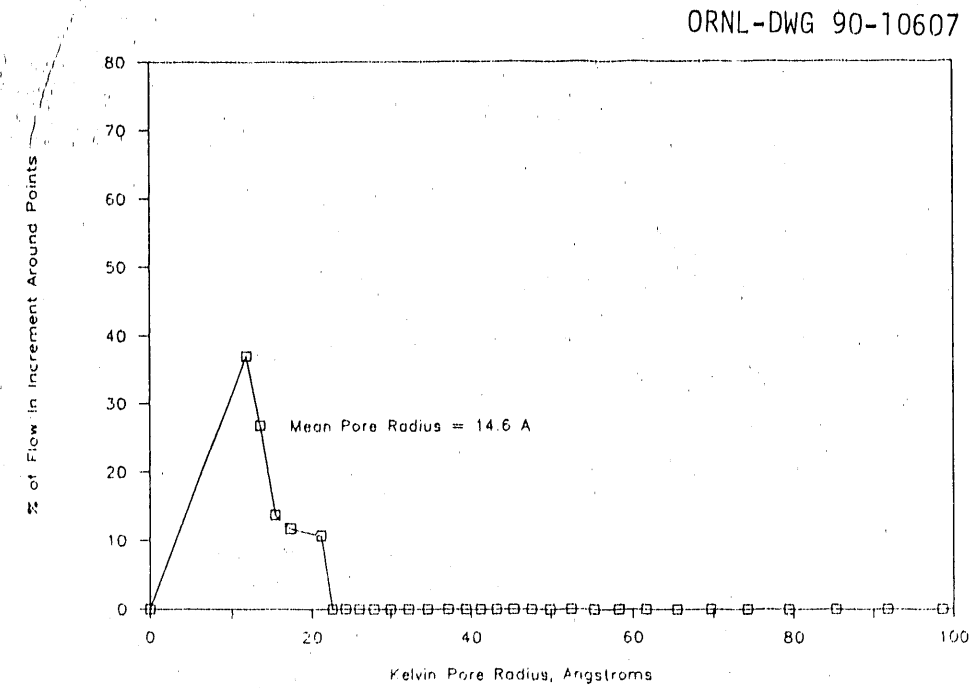

Fig. 1. Dynamic pore size distribution for late FY 1989 ORGDP alumina membrane.

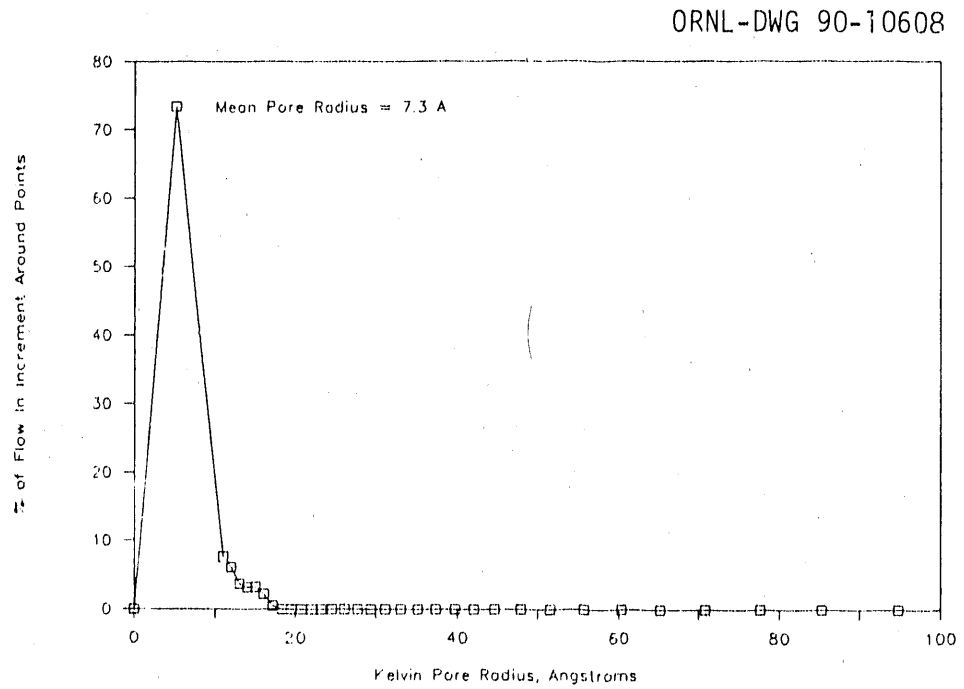

Fig. 2. Dynamic pore size distribution for recent ORGDP alumina membrane.

PURE GAS FLOW MEASUREMENTS

To initiate studies of the effects of membrane pore size on gas transport, pure gas flow measurements were made on two series of alumina membranes (13 total membranes) having mean pore radii ranging between about 7 and 22Å. The permeabilities of the membranes were measured at room temperature using helium, nitrogen, and carbon dioxide. Examples of the pure gas permeability data taken over a range of pressures are shown (Figs. 3 and 4) for two of the alumina membranes. The data clearly show substantially higher permeabilities for helium than for nitrogen or carbon dioxide. Separation factors were calculated for He/N_2 and He/CO_2 from the ratios of the pure gas permeabilities. A plot of separation factors versus mean pore radii is shown in Fig. 5 for the first series of membranes and in Fig. 6 for the second series of membranes, along with ideal separation factors calculated assuming a Knudsen transport mechanism. As expected for these small-pore-size membranes, the data indicate that other mechanisms in addition to Knudsen transport are active, especially in the case of carbon dioxide. The enhanced permeability of carbon dioxide, which is indicated by a lower He/CO_2 separation factor than predicted from Knudsen transport alone, probably results from adsorption and surface diffusion of carbon dioxide. Other gas transport mechanisms, such as molecular screening, should become important for pore sizes smaller than those evaluated in the current tests. That is, the separation factor on such a plot should go through a minimum and then increase sharply as the pore radius decreases.

MATHEMATICAL MODEL FOR CERAMIC MEMBRANES

In any development process, it is extremely helpful to have a model that can be used to predict behavior and guide the development process. In addition, the existence of a model can be helpful in determining the type of experimental data that is needed to provide additional insight into the mechanisms and functional dependencies of the model.

At this point in time, there necessarily must be a great deal of uncertainty associated with any model for very small pore size ceramic membranes. The major reason for the uncertainty is the lack of sufficient and appropriate experimental data on such membranes.

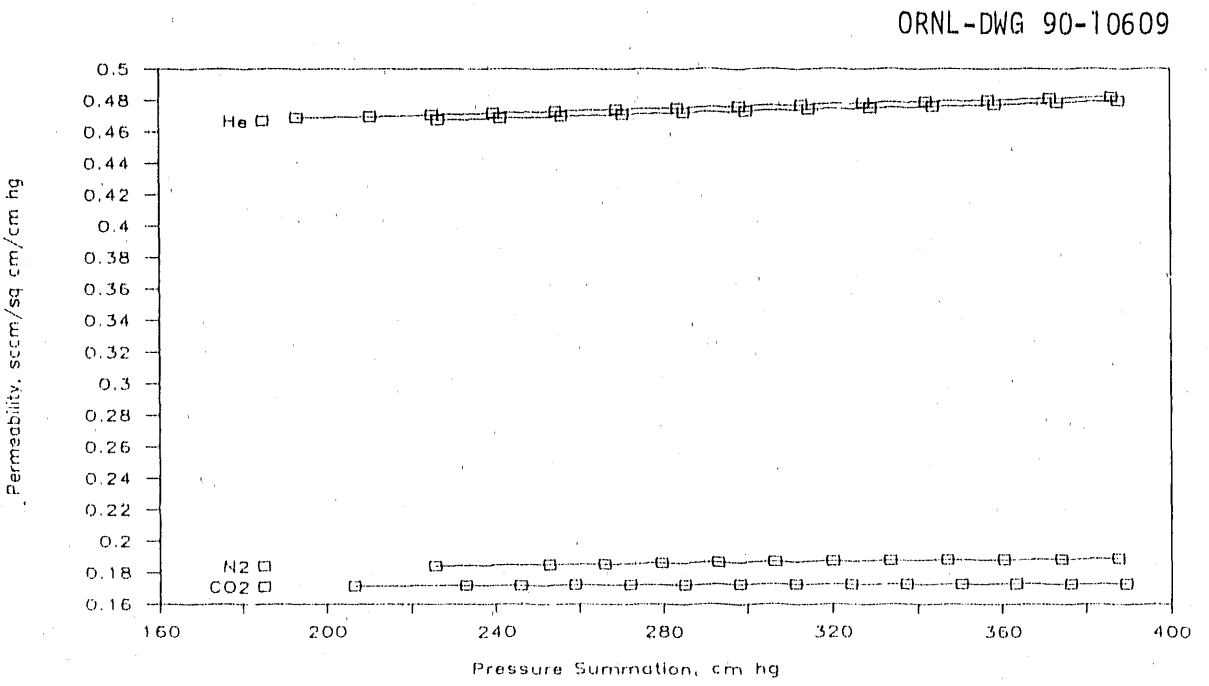

Fig. 3. Permeability of several gases measured with a 17.6Å mean pore radius alumina membrane

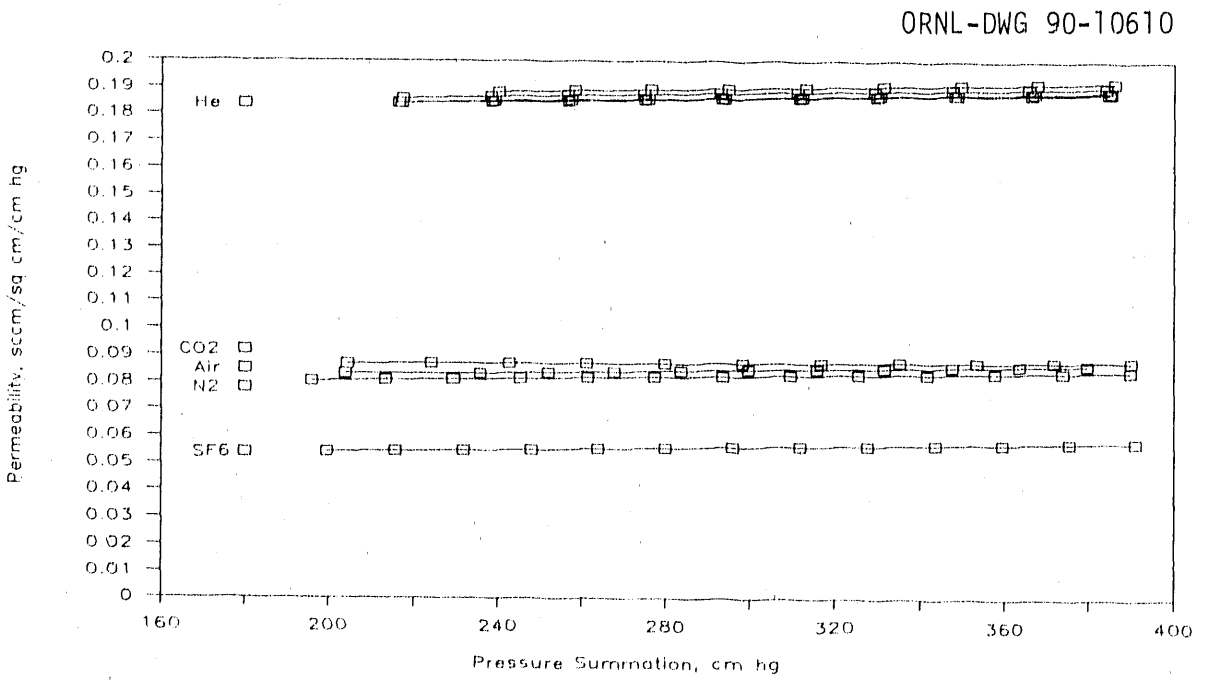

Fig. 4. Permeability of several gases measured with a 9.6Å mean pore radius alumina membrane.

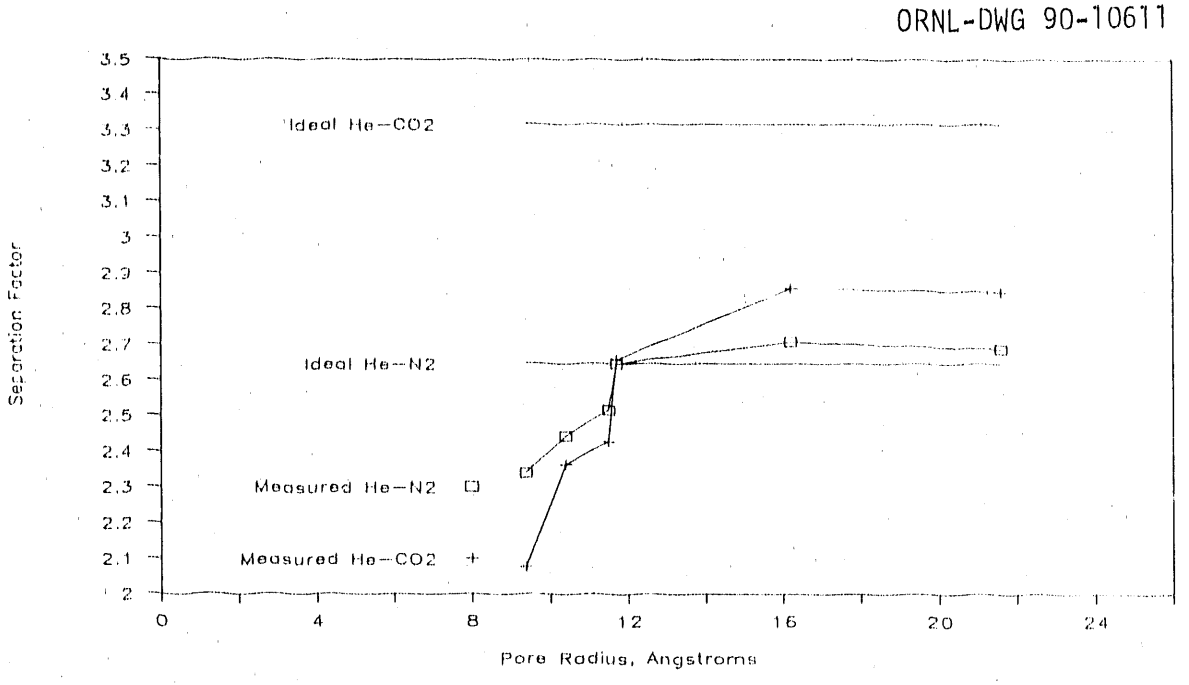

Fig. 5. Separation factors calculated from pure gas permeabilities measured on series A of alumina membranes with different mean pore radii.

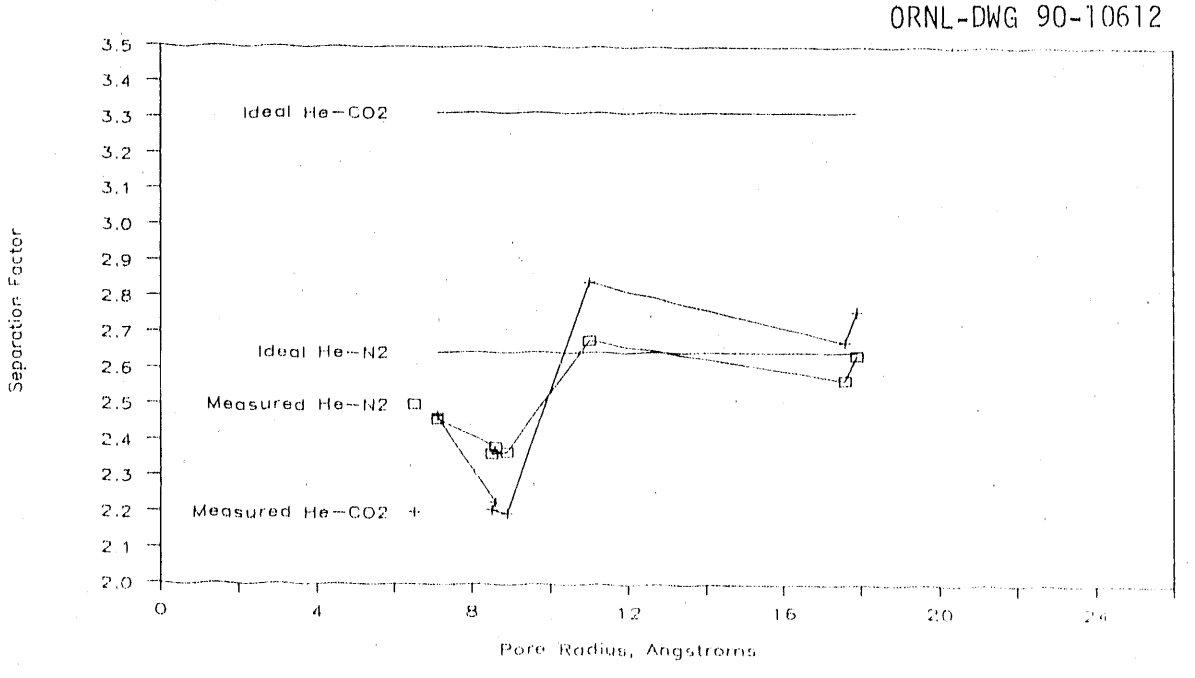

Fig. 6. Separation factors calculated from pure gas permeabilities measured on series B of alumina membranes with different mean pore radii.

But there is also uncertainty about the types of transport mechanisms that will be in effect. In fact, it is likely that there will be transport mechanisms that are currently not known or recognized.

The mathematical model that is currently being developed does show some significant ability to predict the qualitative behavior of the transport of some gases over a limited range of operating conditions where experimental data has been obtained. Predictions from the model have already suggested some significant experiments that are currently in progress and will be discussed briefly below.

Molecular Screening

One of the major interests in developing ceramic membranes for gas separation is the possibility of using molecular screening to achieve very large separation factors. Therefore, the first input to a model should be the effect of the size of the individual molecules on the transport mechanism. This can best be approached by starting with what is currently well known. In membranes or porous materials where the gas mean free path of the molecules is large in comparison to the mean distance between collisions with material walls, the transport is fairly well understood in terms of free molecule diffusion or Knudsen flow. The equation for free molecule flow in a circular capillary in terms of standard cubic centimeters per second (sccs) is given in Eq. (1).

$$F = 2/3\,\bar{v}\,\pi r^3\,\frac{T_o \Delta P}{T P_o \ell} \qquad (1)$$

where F is sccs, $\bar{v}$ is the mean molecular velocity, r is the mean pore radius, T_o and P_o are standard temperature and pressure, ΔP is the pressure difference across the capillary, and ℓ is the length of the capillary. The separation factor for a binary mixture is the ratio of the specific flows (the flow rate per unit pressure difference) of the individual gases. With free molecule diffusion, the separation factor for a binary mixture is equal to the ratio of the molecular velocities or the inverse ratio of the square root of the molecular weights.

Equation (1) governs the transport so long as the effective pore radius is large compared to the diameter of the molecules. As the effective pore radius approaches the size of the gas molecules, then the size of the gas molecule should be taken into account. As a first approximation, we can consider a circular capillary with rigid, smooth, walls as a

model. The distance of closest approach of the center of a gas molecule to a wall is the radius of the molecule. Therefore, the effective radius of the capillary for transport is the difference between the capillary radius and the molecule radius. Then Eq. (1) becomes

$$F_i = 2/3\,\bar{v}\pi\,(r - \delta_i)^3\,\frac{T_o \Delta P}{T P_o \ell} \qquad (2)$$

where δ_i is the effective radius of the molecule. Now the effective transport radius of the capillary is different for each gas species. The ideal separation factor is calculated from the ratio of Eq. (2) for each gas. The separation factor calculated from this ratio for several binary mixtures is shown in Fig. 7. Using this as a model, the separation factor becomes infinite when the capillary radius becomes smaller than the larger molecule but still larger than the smaller molecule. Under this condition, there is transport of the smaller molecule but no transport of the larger molecule. This may be a gross oversimplification, but at least it is a starting point.

The next level of approximation takes into account the fact that there is adsorption of molecules on the walls of the capillary. The adsorption of the molecules on the walls also decreases the effective pore radius of the capillary. Initially, at low effective relative pressures, the adsorption is very sparse. If we define a monolayer of adsorbed gas molecules in terms of a close packed single layer of molecules on the surface, then we may talk about adsorption in terms of a fraction of a monolayer. Small fractions of a monolayer can be described in terms of Henry's Law adsorption. The adsorption is simply proportional to the partial pressure of that gas.

$$\theta = kP \qquad (3)$$

where θ is the fraction of a monolayer adsorbed, k is the Henry's Law constant, and P is the pressure. With fractions of a monolayer, the molecules are randomly distributed on the surface, so that now the surface is bumpy. It is difficult to accurately and analytically take into account such a bumpy surface. However, statistically and as a first approximation, we may assume that the effect is equivalent to having a continuous layer with a thickness that is equal to the fraction of the thickness of a monolayer corresponding to the fraction of a monolayer adsorbed. This will cause the effective pore radius to change with changes in pressure. It should also be recognized that the presence of the adsorbed layer will change

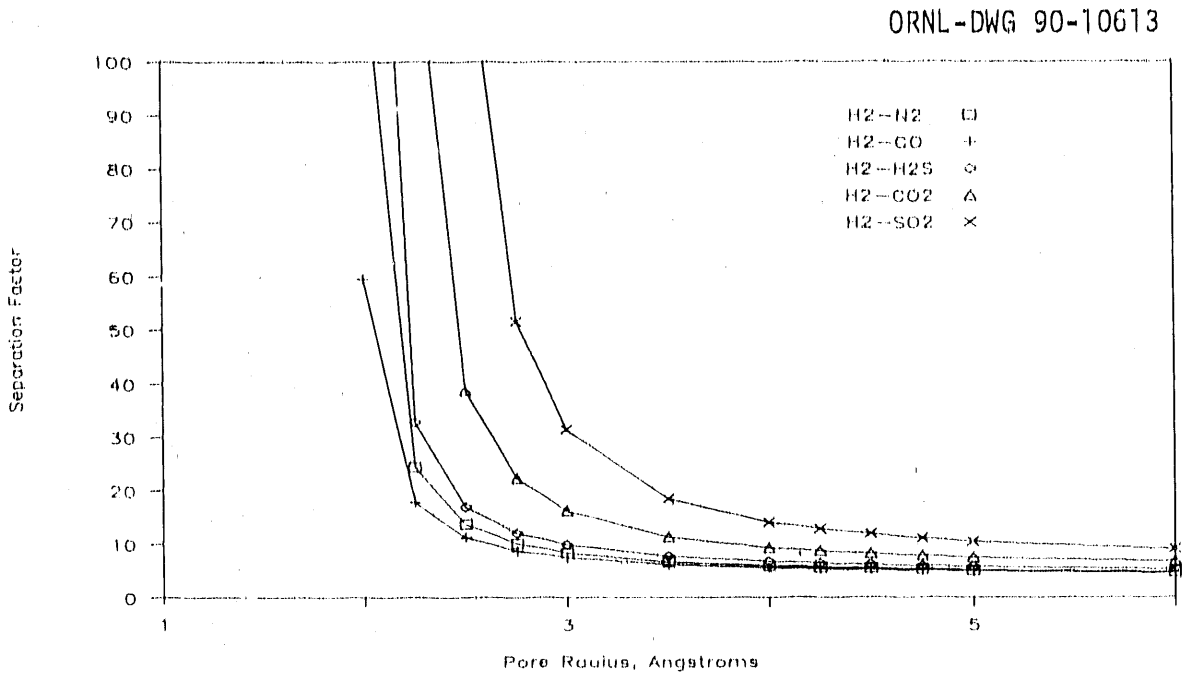

Fig. 7. Separation factors calculated for free molecule diffusion with correction for molecule size

the effective pore radius for both gases even though one of the gases may not exhibit any adsorption. The equation for the flow rate becomes

$$F_i = 2/3\,\bar{v}\pi(r - \delta_i - t_i - t_j)^3 \frac{T_o \Delta P}{T P_o \ell} \qquad (4)$$

where t_i and t_j are the effective thickness of the adsorbed layer of gas i and j. This effect makes the separation factor pressure dependent. One cannot necessarily assume that the separation factor calculated from the ratio of the measured pure gas permeabilities will be realized with the mixture. The model calculation of permeabilities for helium and carbon dioxide relative to pure Knudsen flow and correcting for molecule size with and without adsorption plugging for a membrane with pore radius of 8 A is shown in Fig. 8. The corresponding separation factors for the pure gases and the mixture are shown in Fig. 9 as a function of pore radius for several pressures. In this level of approximation, only Henry's Law adsorption is shown and, therefore, applies only to gases with relatively low adsorption. The model can easily be extended to take into account adsorption governed by Langmiur, BET, or other adsorption isotherms.

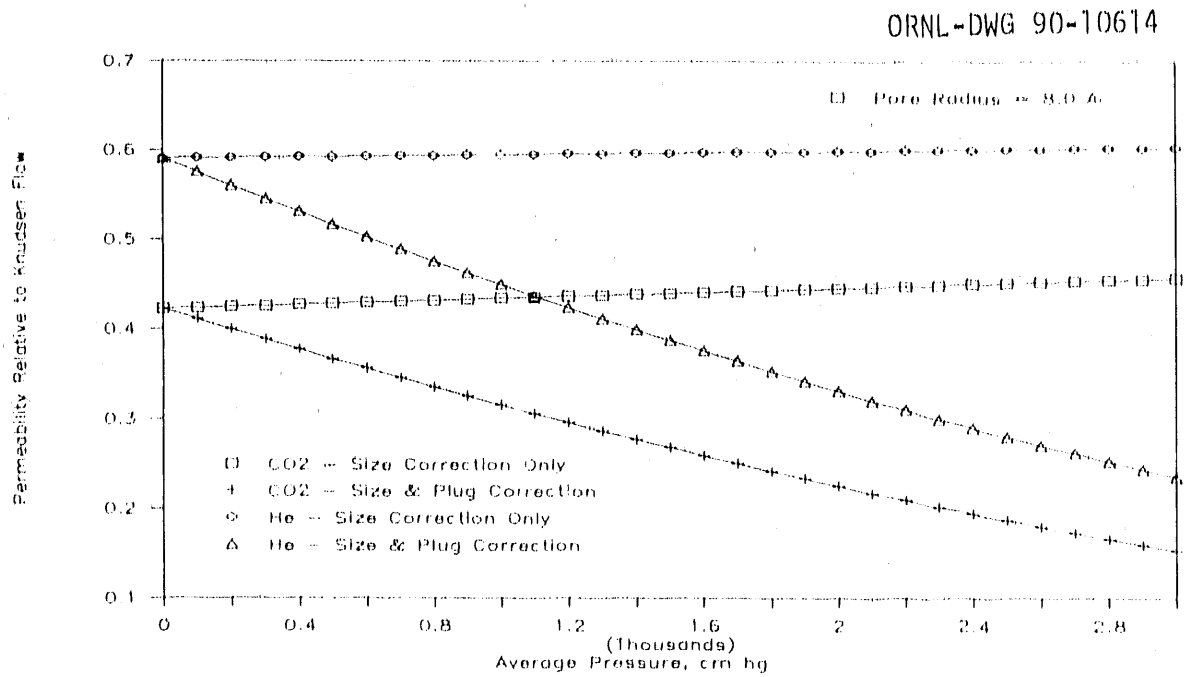

Fig. 8. Model calculations of He and CO_2 permeability relative to Knudsen permeability correcting for molecule size with and without adsorption plugging.

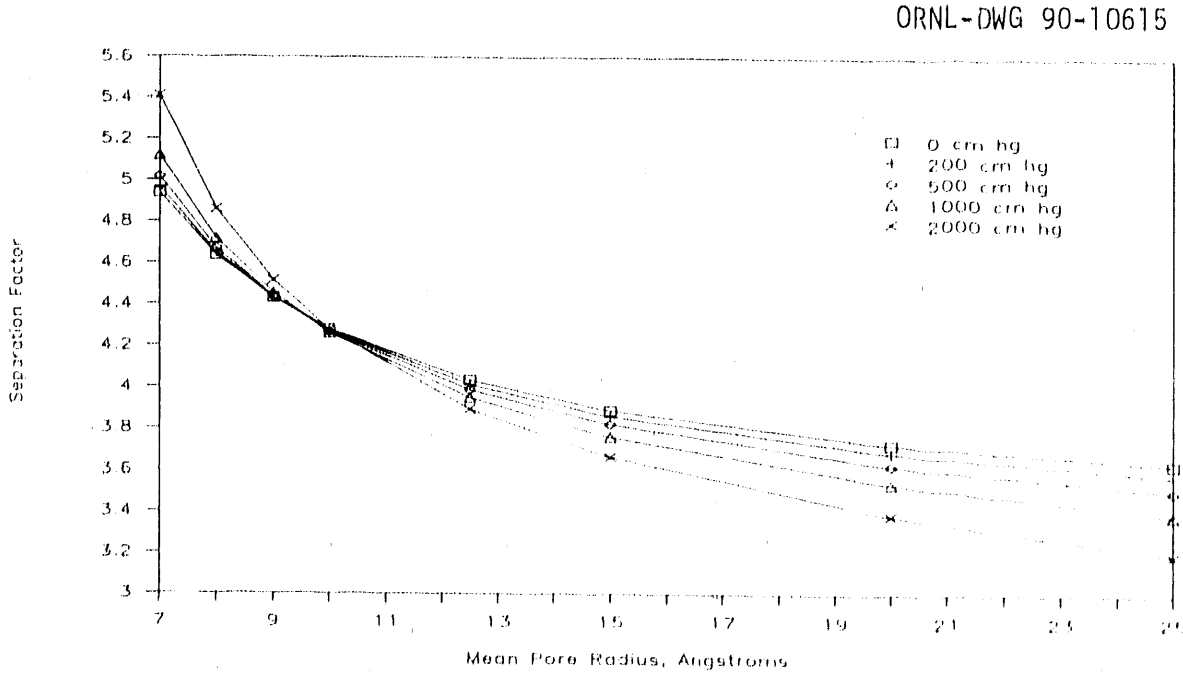

Fig. 9. Model calculation of He and CO_2 separation factors correcting for molecule size with adsorption plugging.

The next level of approximation takes into account the movement of molecules on the surface while in the adsorbed state. A reasonable assumption is that the adsorbed molecules diffuse on the surface by hopping between activation sites between the surface atoms. A detailed calculation of the diffusion coefficient will be left for a higher approximation and will be discussed in later reports. The important point to note at this level is that the driving force for the surface diffusion is the pressure gradient which is the same driving force as that for the gas phase diffusion. The equation for the transport is now given by

$$F_i = 2/3\bar{v}\pi(r - \delta_i - t_i - t_j)^3 \left(1 + \frac{A}{(r - \delta_i)^2}\right) \frac{T_o \Delta P}{T P_o \ell} \qquad (5)$$

where A is a constant proportional to the product of the Henry's Law constant and the ratio of the surface diffusion coefficient to the gas phase diffusion coefficient. The effect of this surface flow on the permeability of a membrane with a pore radius of 8 A is shown in Fig. 10. The effect on the separation factor is shown relative to variation in pore radius in Fig. 11. The Henry's Law adsorption constants are approximate values based on measured adsorption data, and the surface flow constants are reasonable values used to approximate the measured flow data. The predictions from this model seem to represent the qualitative behavior of these gas measurements, particularly as indicated by comparing the calculations shown in Fig. 11 with the results shown in Figs. 5 and 6.

CONCLUSIONS

Work continues with good promise of fabricating membranes with mean pore radii of less than 5 A. Comparisons of calculations using the mathematical model as developed so far with experimentally measured flow data are very encouraging for use in guiding the development effort. The model suggests that the separation results can not be estimated very well from individual pure gas permeability measurements. Efforts are presently under way to make binary gas separation measurements as a function of pressure to provide better information for further development of the model. Gas permeability and separation measurements will be made at higher temperatures as soon as practical. In addition, further development of the model to predict the temperature dependence of permeability and separation factors will be continued.

207

WELDABILITY OF

S. A. David, T. Zach

Oak Ridge Nati
P.O. B

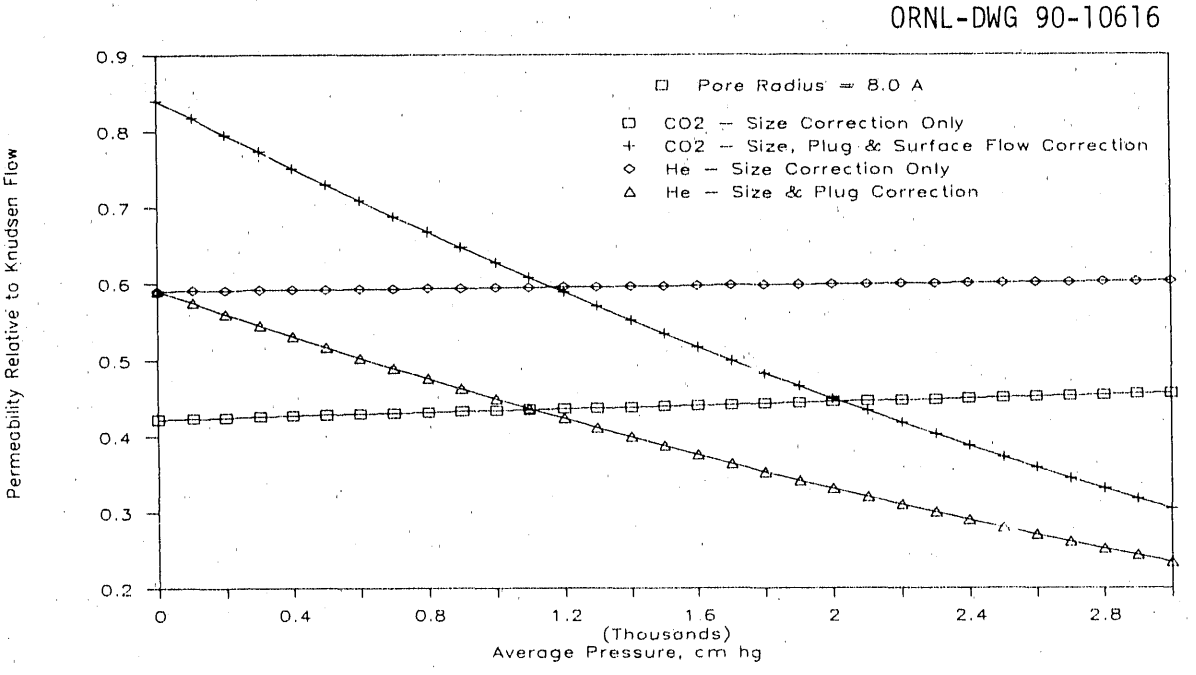

Fig. 10. Model calculation of He and CO_2 permeabilities relative to Knudsen permeability correcting for molecule size and with adsorption plugging and surface flow.

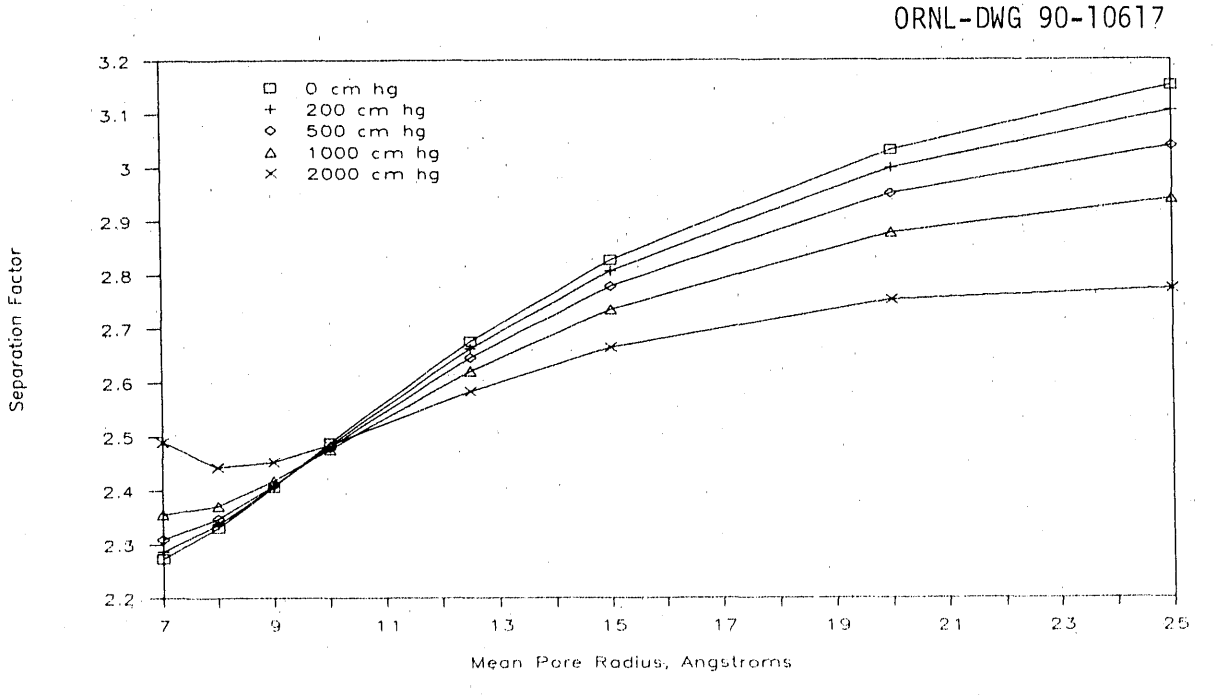

Fig. 11. Model calculation of He and CO_2 separation factors correcting for molecular size, adsorption plug, and surface flow.

SESSION II - NEW ALLOYS

DEVELOPMENT OF IRON ALUMINIDES

C. G. McKamey

Oak Ridge National Laboratory
P.O. Box 2008
Oak Ridge, TN 37831-6084

ABSTRACT

Iron aluminides based on Fe_3Al are of interest to the Fossil Energy Program because of their excellent oxidation and corrosion resistance, especially in sulfur-bearing atmospheres. The work at Oak Ridge National Laboratory (ORNL) has centered on developing Fe_3Al-based alloys with improved ambient temperature ductilities and increased strengths at temperatures of 600-700°C. We now believe that what in the past has been described as "inherent" brittleness in this system is actually caused by a dynamic environmental embrittlement involving atomic hydrogen. We have made great strides in understanding this embrittling phenomenon and are now producing, through composition modification and thermomechanical processing, alloys with room temperature ductilities of >10% and tensile yield strengths at 600°C of as high as 500 MPa. Creep rupture lifes of over 200 h at 593°C and 207 MPa can be produced through alloy modifications to induce precipitate strengthening. This paper summarizes our present efforts in improving the high temperature creep strength and the present status of our understanding of the role of composition, heat treatment, and microstructure on improving room temperature tensile properties by minimizing environmental embrittlement in this system.

INTRODUCTION

Iron aluminides based on Fe_3Al have excellent oxidation and corrosion resistance.[1] However, until recently their potential use as structural material was in doubt due to low room temperature ductility (<5%) and a drop in strength above 600°C. Development efforts at this laboratory have indicated that, by controlling alloy chemistry and thermomechanical processing, Fe_3Al-based alloys can be produced with ambient temperature tensile ductilities of 10-20% and yield strengths of as high as 500 MPa.[2] Similar efforts have improved the creep rupture life at 593°C (1100°F) and 207 MPa (30 ksi) from 2-5 h to over 200 h.[3] Recent studies indicate that the poor ambient temperature ductility observed in many aluminides is caused by dynamic hydrogen embrittlement resulting from the dissociation of water molecules in the environment by aluminum atoms on the surface

of the alloy.[4-6] This environmental embrittlement can be minimized through modification of alloy chemistry, microstructure, and surface condition.[2,6] This paper will summarize our studies of the high temperature creep properties of binary Fe_3Al and ternary alloys, and will report initial results from our efforts to understand the effects of chemistry, microstructure, and surface conditions on the hydrogen embrittlement phenomenon.

HIGH TEMPERATURE CREEP RUPTURE PROPERTIES AND MECHANISMS

Recently, a detailed study of the high temperature creep rupture properties of binary Fe_3Al and ternary alloys containing molybdenum or niobium was initiated. High temperature creep in ordered alloys is a complicated process, often controlled by diffusional processes, so that the activation energy for creep is the same as for self-diffusion.[7] Diffusional processes are restricted in ordered lattices by nearest and next-nearest neighbor interactions, resulting in a decrease in the creep rate upon ordering. Our study of the creep rupture of iron aluminides involved fitting their behavior to the standard creep equation,

$$\dot{\epsilon} = A \sigma^n (e^{-Q/RT})$$

where $\dot{\epsilon}$ is the secondary creep rate, A the pre-exponential term, σ the applied stress, n the creep exponent, Q the activation energy for secondary creep, R the gas constant, and T the absolute temperature. The possible mechanisms can be described in terms of being controlled by either diffusional creep ($n \approx 1$), dislocation glide ($n \approx 3$), dislocation climb ($n \approx 4$-5), or particle strengthening ($n \geq 6$).

Flat tensile specimens (0.76 × 3.18 × 12.7 mm), mechanically punched from the hot rolled sheet, were used for this study. After punching, the specimens were electro-polished to remove burrs, and heat treated to produce approximately the same initial grain size (80-90 μm) and DO_3 ordered structure. Table I lists the alloys tested, their heat treatments, comparative creep rupture data, and secondary creep rates. All tests were performed in air at temperatures of 550-750°C (0.47-0.57 T_m) and stresses of 35-276 MPa. The complete test apparatus, including specimen, was held at the test temperature for at least 30 min before testing.

Table I. Iron aluminides tested in creep rupture at 650°C and 138 MPa

Alloy Composition (at.)	DO_3-B2 Transition Temp. (°C)	Heat Treatment[a] (°C)	Rupture Life (h)	Ductility (%)	Secondary Creep Rate (s^{-1})
Fe-28Al	≈540	1h/750	0.6	37.0	8.5×10^{-3}
Fe-28Al-2Mo	≈600	1h/900	49.9	44.3	1.3×10^{-4}
Fe-28Al-1Nb	575-600	1h/1000	304.0	37.3	1.4×10^{-6}

[a]Plus 4d at 500°C for ordering.

Figure 1 compares the creep curves of the alloys tested at 650°C and 138 MPa. The binary alloy is very weak in creep, with a rupture life of only 0.6 h. Additions of molybdenum or niobium significantly increased the creep rupture life (to 50 and 304 h, respectively). In ternary alloys, niobium appears to be the best alloying agent. Other ternary additions, including Cr, Ti, and Mn, produced no dramatic improvements. Figure 2 shows a plot of the secondary creep rate versus temperature, the slope of which

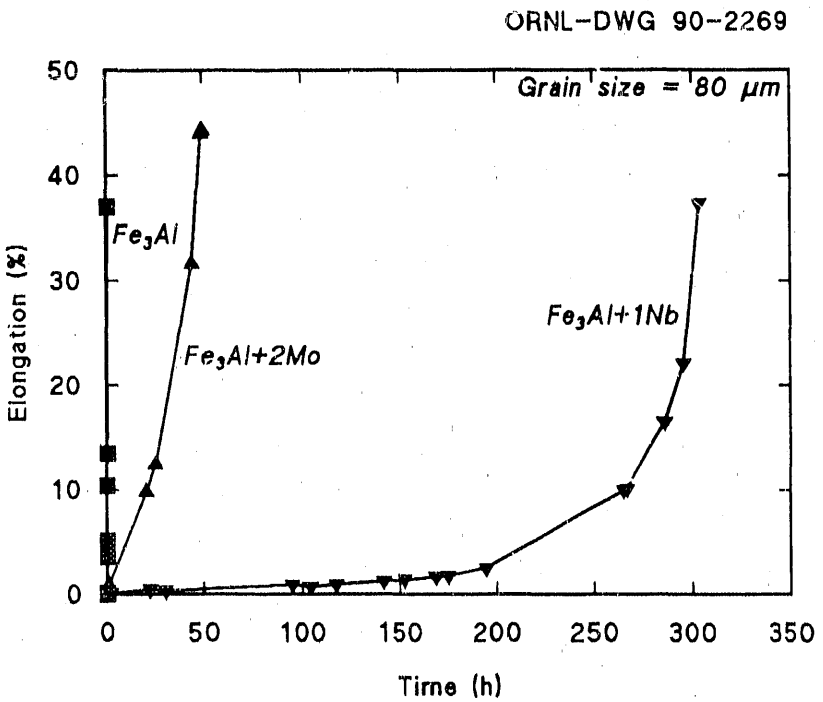

Fig. 1. Creep curves of Fe_3Al-based alloys at 650°C and 138 MPa.

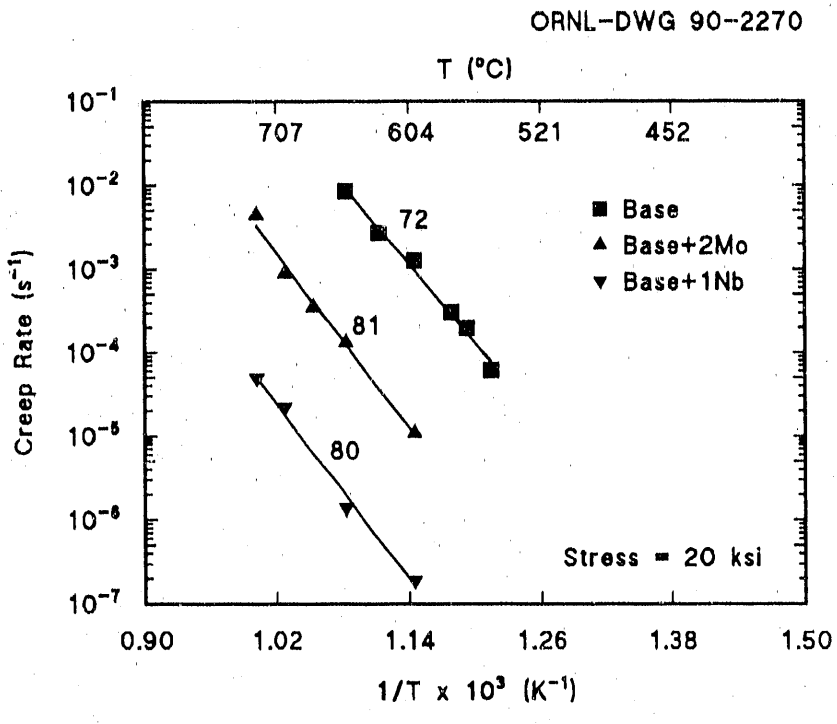

Fig. 2. Secondary creep rate versus temperature for the iron aluminide alloys tested. The slope equals the activation energy for creep in kcal/mole.

represents the activation energy for creep. No diffusion data for these specific alloys have been reported. However, reported activation energy values for self diffusion of iron and diffusion of aluminum in iron (for low amounts of Al) all range between 40 and 70 kcal/mole. Our study resulted in activation energies of approximately 70-80 kcal/mole for all three alloys, indicating that diffusional processes are the controlling mechanisms in creep. The slightly higher Q values of our study compared to the reported diffusion data can be attributed to the order in our system (the previously reported diffusion data are from disordered systems).

Determination of the exact creep mechanism in iron aluminides has proven to be more difficult. As indicated above, theory predicts that the value for the creep exponent n suggests the type of controlling mechanism. Figure 3 is a plot of creep rate versus creep stress, the slope of which is the value n. Assuming a straight-line fit, n for both the binary and ternary containing molybdenum was near 4, suggesting a dislocation climb type of mechanism for creep, while n for the ternary containing niobium was 6.2,

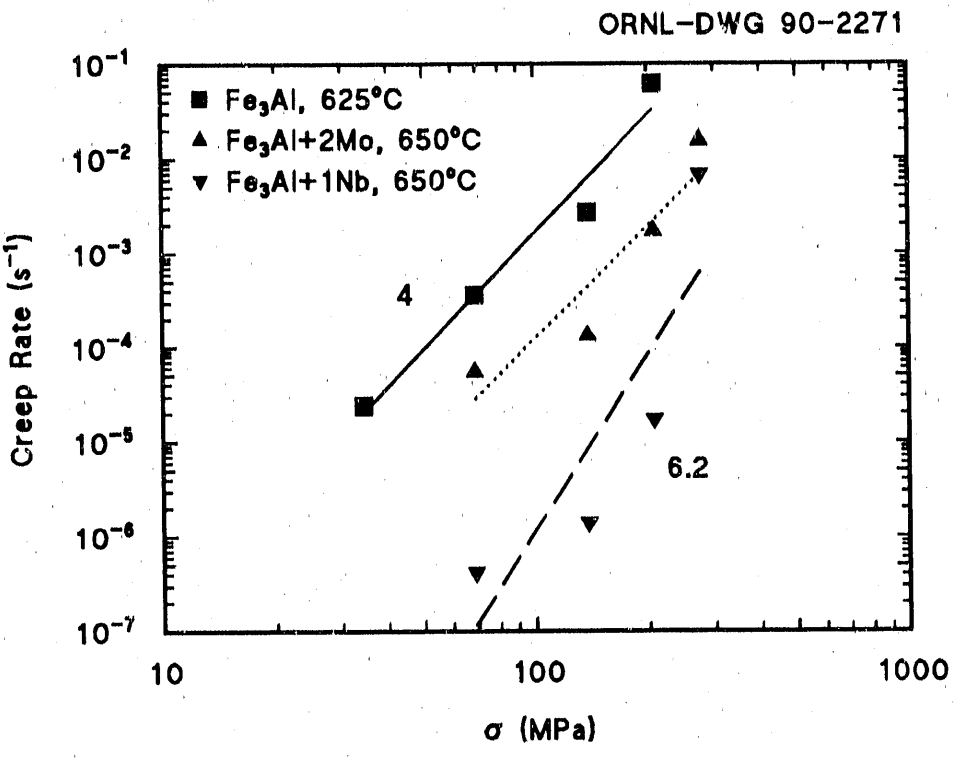

Fig. 3. Creep stress-strain rate behavior as a function of composition. The slope equals the creep exponent n.

suggesting a precipitation strengthening mechanism. This simplified analysis is consistent with the fact that the binary alloy and ternary aluminide with molybdenum both are single phase, while niobium does not go into solution but instead produces Fe-Nb precipitates.[8,9] Recent studies by Whittenberger[10] have suggested that creep in iron aluminides are much more complicated than this. The controlling mechanism may in fact change with other factors such as grain size and test conditions. If so, this may explain why our data points for determining Q (Fig. 2) fit straight lines, while our data points to determine n, taken from the same creep curves, did not.

Our study of the creep processes will be continued with more complicated compositions. Initial screening of our more advanced alloy compositions indicated that synergistic effects occur between molybdenum or niobium and the other additives. In general, other elements, when added to the molybdenum-containing ternary alloy, will increase the creep life, while additives to the niobium-containing ternary alloy will shorten the life. In some cases, we have been able to identify specific combinations which appear

to enhance creep resistance and others which degrade it; for example, zirconium together with molybdenum enhances, while carbon with zirconium and molybdenum reduces the life significantly. Although they improve the high temperature creep rupture properties of iron aluminides, large amounts of these elements have a detrimental effect on room temperature tensile ductility. Table II shows that by using small amounts of these three elements, along with chromium for increased room temperature ductility, we can produce alloy compositions which exhibit both good high temperature creep rupture properties and sufficient (>10%) room temperature ductility. Also included in this table is the tensile and creep rupture data for FA-122 (Fe-28Al-5Cr-0.1Zr-0.05B, at.%), a composition which has been optimized for room temperature tensile ductility but not for high temperature strength.

ENVIRONMENTAL EMBRITTLEMENT OF IRON ALUMINIDES

Recent studies have indicated that all iron aluminides are susceptible to environmental embrittlement at ambient temperatures in the presence of water vapor.[4-6] The suggested mechanism is similar to that observed in aluminum alloys: the reaction of water molecules with freshly exposed aluminum atoms at the crack tip results in the formation of atomic hydrogen that drives into the metal along cleavage planes and causes embrittlement. This phenomenon occurs only during stressing of the metal, when a crack is formed and fresh aluminum atoms are exposed, and is therefore a "dynamic" embrittling phenomenon. Several factors have been suggested as means of minimizing this effect, including compositional and microstructural changes and surface chemistry modifications. These changes are aimed at (1) preventing penetration of atomic hydrogen through the surface of the specimen, (2) trapping of the hydrogen by precipitates in the matrix, or (3) catalyzing the formation and dissipation of molecular hydrogen. Studies in each of these areas are underway at this laboratory, as are studies of the mechanisms of embrittlement and failure.

Compositional effects on the room temperature tensile properties of Fe_3Al have been the main emphasis of this program since its inception.[11,12] Our studies have indicated that, as a ternary addition, only chromium produces improved ductility, while additions of other elements such as niobium, molybdenum, and zirconium result in

Table II. Comparison of creep rupture and tensile properties for iron aluminide alloys

Alloy	Composition (at.%)	Creep rupture		RT tensile		600°C tensile	
		Life (h)	Elong. (%)	Yield (MPa)	Elong. (%)	Yield (MPa)	Elong. (%)
FA-91	Fe-28Al-2Mo-0.1Zr	208	55	698	5.7	567	20.9
FA-130	Fe-28Al-5Cr-0.5Nb-0.5Mo-0.1Zr-0.05B	202	61	554	12.6	527	31.2
FA-122	Fe-28Al-5Cr-0.1Zr-0.05B	13	49	480	16.4	474	31.9

improved strength. The reasons for improved ductility with addition of chromium was postulated in earlier reports as being related to effects on slip and dislocation character and antiphase boundary energies.[13,14] However, with the discovery of environmental embrittlement in these alloys, it now seems plausible that the most important effect of chromium may involve the surface oxide chemistry and its ability to block the movement of atomic hydrogen into the specimen. Studies are presently underway to further study chromium in the light of these new findings.

Our initial results of the effect of recrystallization on room temperature tensile properties (using FA-122 as our test composition) are plotted in Fig. 4, indicating that fully stress relieved specimens (annealed at 650-750°C) with elongated grains characteristic of the as-rolled condition produce both the highest strengths and ductilities. (The ductilities in these specimens are lower than previously reported for some of our other alloy compositions because the heat treatments used for this study were selected to eliminate other possible contributions to the properties; in other words, all the parameters for fabrication and heat treatment of these specimens were not optimized to produce maximum attainable ductilities.) In this particular composition, annealing at temperatures to 1100°C for up to 6 h has not produced grain sizes larger than 70 μm. As stated above, FA-122 contains some zirconium and boron resulting in precipitates which appear to be effective at pinning grain boundaries. The reason for the improved strength and ductility with stress-relieved, unrecrystallized microstructures is believed to be due to the

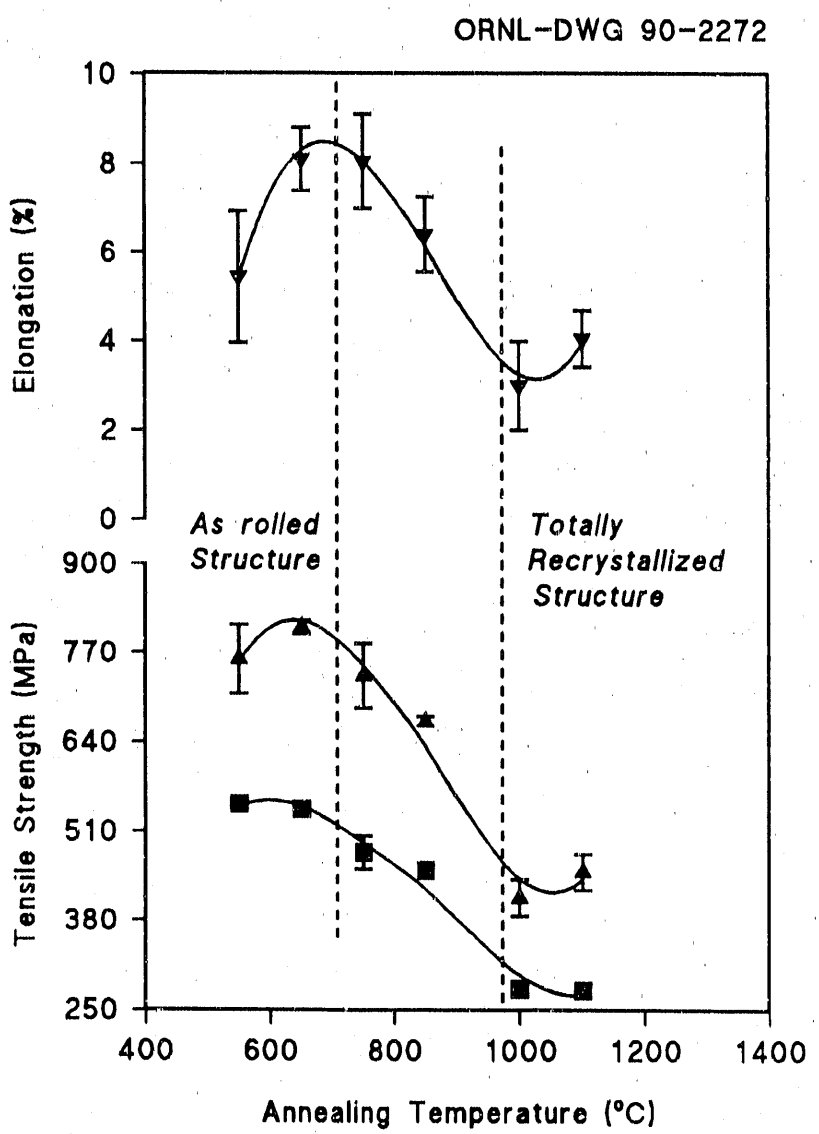

Fig. 4. Effect of annealing temperature on room temperature tensile properties of FA-122.

elongated grains, with essentially no transverse cleavage planes, which reduces the amount of hydrogen diffusion into the specimen.[2]

To summarize, it now appears that minimizing the effects of environmental embrittlement will involve a combination of techniques including adjusting composition through elemental additions and adjusting microstructure through thermomechanical processing and heat treatment.

CONCLUSIONS

Our research at ORNL has contributed to the identification of the embrittling mechanism in iron aluminides. This mechanism involves the dissociation of water molecules in the environment by aluminum atoms on the surface of the alloy, releasing atomic hydrogen which drives into the specimen along cleavage planes during stressing. We have made great strides in understanding this mechanism and in minimizing its effects through alloy composition modifications and thermomechanical processing. Room temperature ductilities of 10-20% can now be obtained from alloys which contain chromium as one of the alloying elements and which have been heat treated to relieve stress but minimize recrystallization.

Our efforts to produce alloy compositions with improved high temperature creep rupture properties have resulted in alloys with lives of over 200 h at 593°C and 207 MPa. Preliminary studies of the high temperature creep mechanisms indicated that precipitation strengthening, through addition of niobium and/or molybdenum, in combination with other elements to promote precipitate formation, is the most effective means for improving high temperature creep properties in this system.

REFERENCES

1. J. H. DeVan, H. S. Hsu, and M. Howell, "Sulfidation/Oxidation Properties of Iron-Based Alloys Containing Niobium and Aluminum," ORNL/TM-11176, May 1989.

2. V. K. Sikka, C. G. McKamey, C. R. Howell, and R. H. Baldwin, "Fabrication and Mechanical Properties of Fe_3Al-Based Aluminides," ORNL/TM-11465, March 1990.

3. C. G. McKamey, unpublished data.

4. C. T. Liu, E. H. Lee, and C. G. McKamey, "An Environmental Effect as the Major Cause for Room-Temperature Embrittlement in FeAl," Scripta Metal. 23, 875-880 (1989).

5. C. T. Liu, C. G. McKamey, and E. H. Lee, "Environmental Effects on Room-Temperature Ductility and Fracture in Fe_3Al," Scr. Metall. 24(2), 385 (1990).

6. C. T. Liu and C. G. McKamey, "Environmental Embrittlement--A Major Cause for Low Ductility of Ordered Intermetallics," to be published in Proc. TMS/ASM Symposium on High Temperature Aluminides, Oct. 1-4, 1989.

7. N. S. Stoloff and R. G. Davies, "The Mechanical Properties of Ordered Alloys," Prog. Mater. Sci. 13, 1 (1966).

8. M. G. Mendiratta, S. K. Ehlers, D. M. Dimiduk, W. R. Kerr, S. Mazdiyasni, and H. A. Lipsitt, "A Review of Recent Developments in Iron Aluminides," in Materials

Research Society Symposium Proceedings, Vol. 81, High-Temperature Ordered Intermetallic Alloys, II, eds. C. C. Koch, C. T. Liu, N. S. Stoloff, and O. Izumi, Materials Research Society, Pittsburgh, PA, 1987, pp. 393-404.

9. D. M. Dimiduk, M. G. Mendiratta, D. Banerjee, and H. A. Lipsitt, "A Structural Study of Ordered Precipitates in an Ordered Matrix within the Fe-Al-Nb System," Acta Metall. 36(11). 2947-2958 (1988).

10. J. D. Whittenberger, "The Influence of Grain Size and Composition on Slow Plastic Flow in FeAl between 1100 and 1400 K," Mater. Sci. & Eng. 77 (1986) 103.

11. C. G. McKamey, C. T. Liu, J. V. Cathcart, S. A. David, and E. H. Lee, "Evaluation of Mechanical and Metallurgical Properties of Fe_3Al-Based Aluminides," ORNL/TM-10125, Sept. 1986.

12. C. G. McKamey, C. T. Liu, S. A. David, J. A. Horton, D. H. Pierce, and J. J. Campbell, "Development of Iron Aluminides for Gasification Systems," ORNL/TM-10793, July 1988.

13. C. G. McKamey, J. A. Horton, and C. T. Liu, "Effect of Chromium on Room Temperature Ductility and Fracture Mode in Fe_3Al", Scripta Metall. 22(10), 1679-81 (1988).

14. C. G. McKamey, J. A. Horton, and C. T. Liu, "Effect of Chromium on Properties of Fe_3Al," J. Mater. Research 4(5), 1156-63 (1989).

WELDABILITY OF IRON ALUMINIDES

S. A. David, T. Zacharia, and R. W. Reed

Oak Ridge National Laboratory
P.O. Box 2008
Oak Ridge, TN 37831-6095

ABSTRACT

A preliminary investigation was carried out to determine the weldability of a class of advanced iron aluminides. Thin sheets of iron aluminides were gas tungsten arc (GTA) and electron beam (EB) welded at different travel speeds and power levels. The results indicate that the weldability of these alloys is very sensitive to the welding conditions and compositions, producing good welds sometimes and severely cracked welds at other times. Alloys containing TiB_2 additions for improved strength and ductility cracked severely upon welding. Alloys without boron and zirconium, in particular alloy FA-129, was found to show more promise for welding than most of the other iron aluminides.

INTRODUCTION

In recent years ordered intermetallic alloys have been receiving considerable attention.[1-2] An alloy of recent interest is the iron aluminide, Fe_3Al. Iron aluminide has attractive electrical, magnetic and corrosion-resistance properties. Other features such as the low cost of iron and aluminum, and low density and adequate strength at temperatures below 600°C, make iron aluminides an attractive candidate for structural applications.

One of the major issues in the development of this new class of material, including Fe_3Al, is welding because joining by conventional processes is an important means of fabricating engineering materials into structural components. This paper describes the behavior of Fe_3Al type alloys when subjected to weld thermal cycles.

EXPERIMENTAL PROCEDURE

Alloys used in this study are listed in Table 1. Both EB and GTA autogenous welds (melt runs) were made on 20 × 40 × 0.7 mm coupons. Further characterization of weldability under variable restraint conditions can be carried out using Sigmajig test.[3] Since crack-free weld was not obtained consistently during unrestrained autogenous welding, Sigmajig test was not performed on any of these alloys. The welding variables were adjusted to produce full-penetration welds at various welding speeds. Specimens for microstructural characterization were prepared by conventional metallographic techniques and etched with a solution containing 40 ml HNO_3, 60 ml CH_3CoOH, and 20 ml HCl. Microstructural characterization of the weldments was conducted by using light microscopy.

RESULTS AND DISCUSSION

Electron Beam Welding

Previous investigations on the weldability of ordered intermetallic alloys have shown that the high energy beam process, in general, can produce successful welds owing to the highly concentrated heat source and possible refinement in the fusion zone structure. Therefore, initial interest was focused on EB welding. The alloys were EB welded at speeds ranging from 2.1 to 20.8 mm/s. After welding, the specimens were carefully examined for cracks using a low-magnification microscope. The presence of cracks was further confirmed using metallographic techniques. Table 2 summarizes the results of EB welding. In general the results indicate that the alloys containing TiB_2 added for grain refinement showed a severe tendency to crack.[4] These cracks have been found to be hot cracks. Figure 1 shows the typical transverse hot cracks observed in the alloy FA-41 fusion zone. However, the higher order alloys FA-122 and FA-129 modified with chromium and niobium did not exhibit any tendency to crack. Figure 2 shows the typical crack-free microstructure of alloy FA-129. Because of the nearly circular puddle shape, the grain structure development in the fusion zone is much finer.

Table 1. Alloy composition

Heat	Al	Cr	Nb	Zr	B	C	TiB_2	Fe
FA-41	17.0						0.5	Bal.
FA-37	15.7						0.5	Bal.
FA-122	15.88	5.46		0.19	0.01			Bal.
FA-129	15.86	5.45	0.97			0.05		Bal.

Table 2. EB weldability

	Speed mm/s					
Heat	2.1	4.2	8.5	12.5	16.9	20.8
FA-41		•	o		o	
FA-37		•	o		o	
FA-122	•	•		•		•
FA-129	•	•		•		•

• = No cracks
o = Cracks

Y-205220

Fig. 1 Fusion zone microstructure of alloy FA-41.

Y-212756

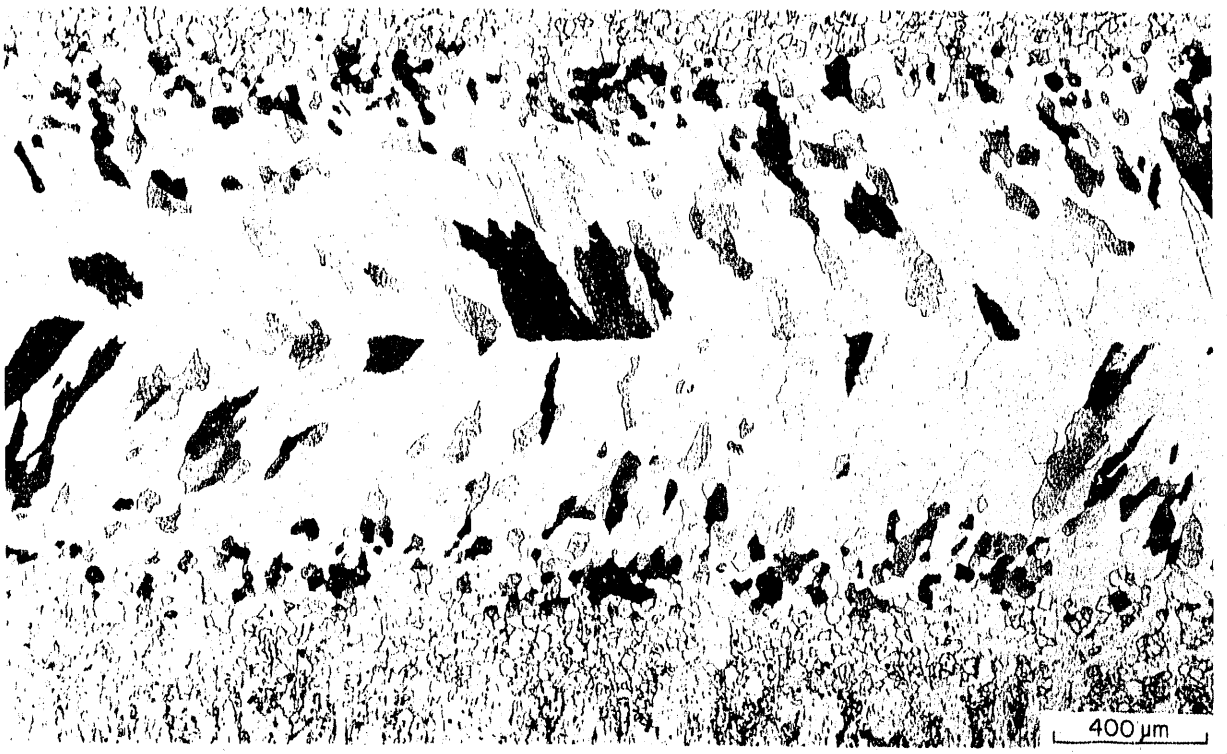

Y-212757

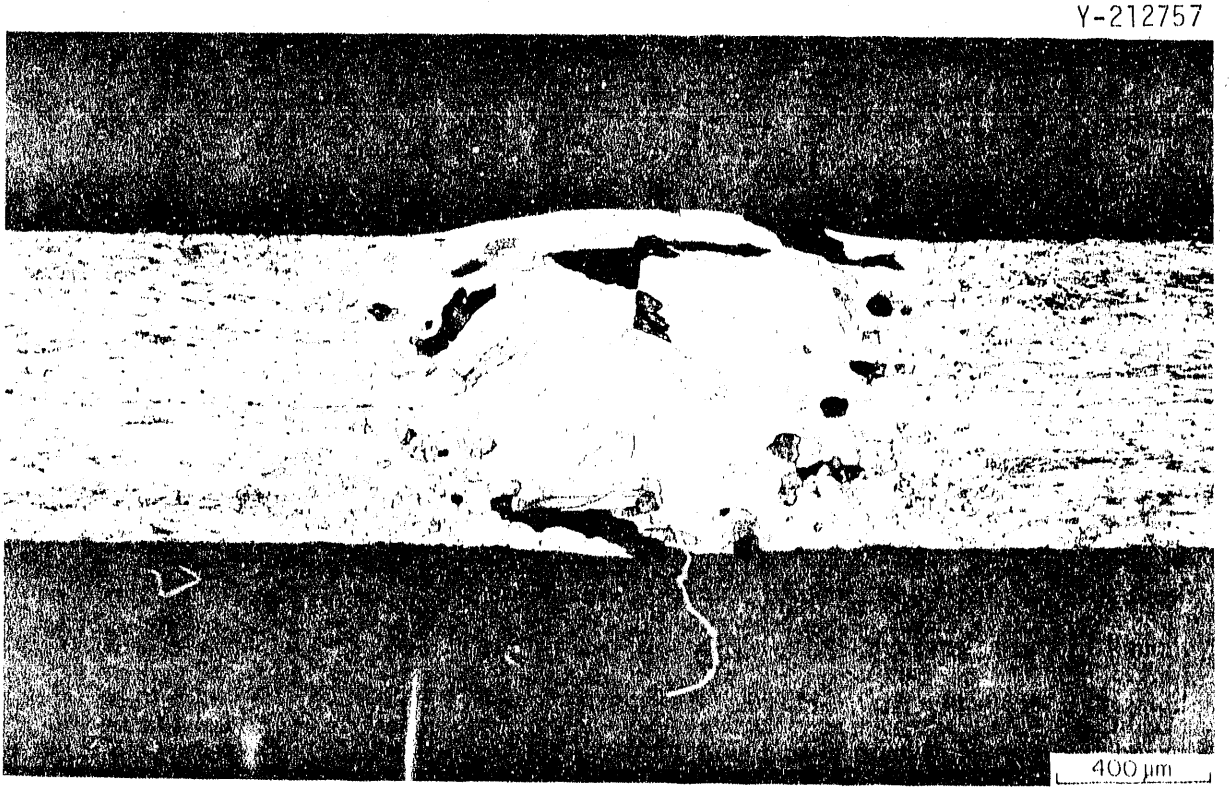

Fig. 2 Optical micrograph showing the longitudinal and the transverse section of the EB weld fusion zone of FA-129B alloy.

Gas Tungsten Arc Welding

Table 3 summarizes the results of the GTA welding of the various alloys investigated. Full penetration GTA welds were made at welding speeds ranging from 4.2 to 21.6 mm/s. The results indicate that some of the alloys can be successfully welded using GTA welding process at low welding speeds. The alloys containing TiB_2 (FA-41 and FA-37) and zirconium and boron (FA-122) cracked severely. Indeed, zirconium in combination with boron may be a bad activator for weldability. Of all the alloys investigated, the alloy FA-129 modified with niobium, chromium, and carbon has been found to exhibit some promise for weldability. Figure 3 shows a typical FTA weld made in alloy FA-129. In contrast to the fine fusion zone grain structure observed in the EB welds, the fusion zone structure is much coarser in the GTA welds.

Table 3. GTA weldability

	Speed mm/s				
Heat	4.2	8.5	12.5	16.9	21.6
FA-41	o	o			
FA-37	o	o			
FA-122	o	o	o		o
FA-129	•	•	•		o

• = No cracks
o = Cracks

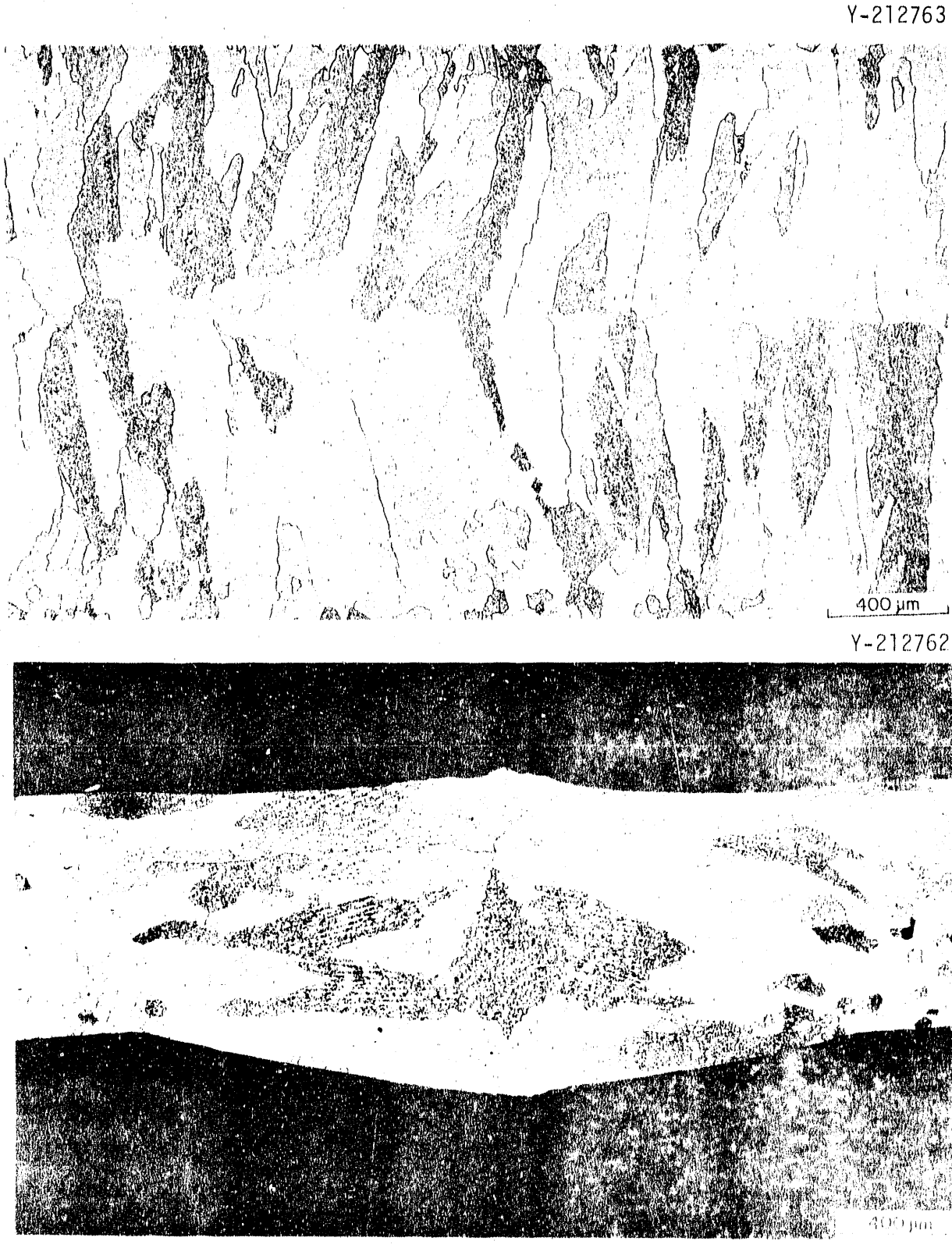

Fig. 3 Optical micrograph showing the longitudinal and the transverse section of the GTA weld fusion zone of FA-129B alloy.

SUMMARY

The preliminary weldability studies indicate promising results for one of the iron aluminides investigated i.e., alloy FA-129. Successful welds with minimum cracking were produced in this alloy. The results indicate that the weldability of iron aluminides is very sensitive to composition and welding parameters. Alloy compositions with zirconium in combination with boron and TiB_2 have been found to be bad activators for weldability of these alloys.

ACKNOWLEDGEMENTS

The author would like to thank D. N. Braski and J. F. King for reviewing the paper and K. W. Gardner for preparing the paper.

REFERENCES

1. C. T. Liu, *Int. Metall.* Rev. 29, 168, 1984.
2. N. S. Stoloff, *Int. Mater.* Rev. 34, 153, 1989.
3. G. M. Goodwin, *Weld. J.* 77(2), 33s-38s, 1987.
4. S. A. David, J. A. Horton, C. G. McKamey, T. Zacharia, and R. W. Reed, *Weld. J.* 68(9), 372s-381s, 1989.

MOISTURE-INDUCED EMBRITTLEMENT OF Fe_3Al

D. J. Alexander, J. H. DeVan, and V. K. Sikka

Oak Ridge National Laboratory
P.O. Box 2008
Oak Ridge, TN 37831-6151

ABSTRACT

Recent tests at ORNL indicate that the ductility of iron aluminides is very sensitive to the test environment. It is believed that the loss of ductility observed in moist air environments is associated with a hydrogen embrittlement phenomenon as a result of dissociation of water vapor and the intake of atomic hydrogen into the aluminide matrix. This possibility will be investigated in a series of tests under controlled environmental conditions. Compact specimens will be tested under controlled stress intensity conditions. Crack growth rates as a function of the applied stress intensity will be measured with the direct-current potential drop technique. Initial tests will be conducted in moist air and in vacuum at room temperature. In an additional series of tests the temperature of the moist air will be varied to permit the determination of an activation energy for the embrittlement process. Fractographic examination of the fracture surfaces will also be performed. It is anticipated that this series of tests will increase our understanding of the environmentally-induced embrittlement of iron aluminide alloys.

INTRODUCTION

Recent tests at ORNL indicate that iron aluminides are very sensitive to test environment.[1,2] These tests show that the ductility of both FeAl and Fe_3Al alloys is reduced to a minimum when specimens are tested in moist environments. Much higher ductilities are observed when testing is carried out in vacuum or dry gas environments. It is believed that this loss of ductility is due to the dissociation of water vapor at the crack tip and the generation of atomic hydrogen, which is absorbed by the matrix and results in embrittlement. A series of tests are planned to study this phenomenon and increase our understanding of the environmental effects on ductility in Fe_3Al alloys.

PLANNED TESTING

The iron aluminide alloy FA129 has been selected as the material for this investigation. The nominal composition of this alloy is Fe-28Al-5Cr-1Nb-0.2C (at. %). Initial tests of the fracture toughness will be made at room temperature. Charpy V-notch and J-integral resistance curve (J-R curve) tests will be conducted. The specimens will be fabricated in the TL and LT orientations (crack plane parallel and perpendicular to the rolling direction, respectively). Based on these tests, one orientation will be selected for further studies of crack growth.

The rate of crack growth vs time (da/dt) will be studied as a function of the applied stress intensity (K). The applied load will be controlled to alter the stress intensity, and the rate of crack growth will be monitored using the direct-current potential drop technique. The first series of tests will study the effect of test environment at room temperature on the crack growth rate. Moist air and vacuum will be used. A second series of tests will be conducted in air at several different temperatures (-25, 22, 50, and 100°C). This should permit an activation energy to be derived. Fractographic and metallographic examinations will also be conducted. These tests should provide information about the controlling processes and mechanism of environmentally induced embrittlement.

PRELIMINARY RESULTS

Some preliminary Charpy impact testing has been conducted. Specimens were taken from 12.5-mm-thick plate which was stress-relieved in air at 750°C for 1 h. These results are shown in Fig. 1. The data indicate that this alloy has a very high ductile-to-brittle transition temperature, and also shows an orientation effect. The transition temperatures, evaluated at the midpoint between the upper and lower shelves, are 251°C for the TL orientation and 325°C for the LT orientation, whereas the upper-shelf energies are 39 and 57 J, respectively. Thus, the LT orientation has both a higher transition temperature and a higher upper-shelf energy level than the TL orientation. This suggests that there is a significant texture in

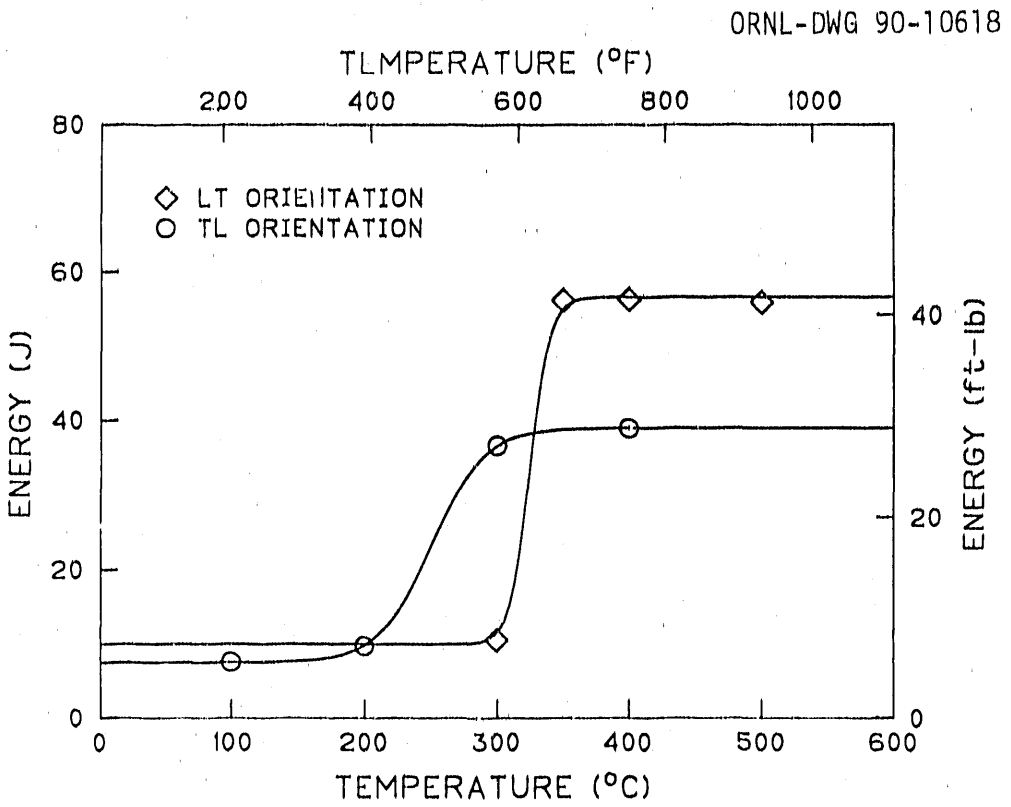

Fig. 1. Charpy impact energy vs temperature for iron aluminide alloy FA129, LT and TL orientations.

the rolled plate material. Metallographic examination revealed very large, highly elongated pancake grains. In addition, numerous small cracks were present along the edges of the Charpy specimens. It is believed that these cracks were produced during the machining of the specimens, perhaps by surface grinding.

DISCUSSION AND CONCLUSIONS

The metallography indicates that the working and stress relief produce large, textured grains. This is reflected in the very high transition temperatures. The thermomechanical treatment should be altered to produce a fine recrystallized grain size, which should reduce the transition temperature, and may also improve the upper-shelf energy level. The cracks observed on the Charpy specimen edges indicate that care is needed during specimen fabrication. Further work is planned to attempt to determine which operation produces such cracks.

ACKNOWLEDGMENTS

We would like to thank K. Farrell for several helpful discussions, J. J. Henry, Jr., who performed the Charpy testing, and J. L. Bishop who prepared the manuscript.

REFERENCES

1. C. T. Liu, E. H. Lee, and C. G. McKamey, "An Environmental Effect as the Major Cause for Room-Temperature Embrittlement in FeAl," *Scripta Metall.*, Vol. 23, pp. 875-80, 1990.

2. C. T. Liu, C. G. McKamey, and E. H. Lee, "Environmental Effects on Room-Temperature Ductility and Fracture in Fe_3Al," *Scripta Metall. Mater.*, Vol 24, pp. 385-89, 1990.

MELTING OF IRON-ALUMINIDE ALLOYS

V. K. Sikka

Oak Ridge National Laboratory
P.O. Box 2008
Oak Ridge, TN 37831-6083

ABSTRACT

The melting of Fe_3Al-based alloys at the Oak Ridge National Laboratory (ORNL) and commercial vendors is described. The melting processes evaluated includes arc melting, air-induction melting (AIM), vacuum-induction melting (VIM), and electroslag remelting (ESR). The quality of the ingots studied are based on internal soundness and the surface finish obtained. The ingots were analyzed for recovery of various elements during melting. The impurity levels observed in the alloys by various melting processes were compared. Recommendations are made for viable processes for commercial melting of these alloys.

INTRODUCTION

Recent improvements[1] in room-temperature ductility of Fe_3Al-based iron aluminides have initiated a strong potential for their use in many applications. However, prior to their commercial use, information regarding melting, processing, and properties of these alloys is required. This paper presents the status of melting of Fe_3Al-based iron-aluminide alloys. Specifically, the presentation will deal with results of AIM, VIM, and ESR. The recovery of various elements and the quality of ingots produced by various processes will be discussed. The melting process results will be described for work performed at ORNL and commercial vendors.

ALLOY NOMENCLATURE

There are three categories of alloys under investigation. The first is sulfidation resistance and is designated as FAS. The second is designed for maximum room-temperature tensile ductility and is designated as FAL. The third is designed for maximum high-temperature strength and is designated as FA-129. The final designation of this alloy will be FAH. Nominal compositions of the three alloys are given in Table 1.

Table 1. Nominal composition (wt %) of Fe_3Al-based alloys under investigation at ORNL

Element	Alloy		
	FAS	FAL	FA-129
Al	15.9	15.9	15.9
Cr	2.20	5.5	5.5
B	0.01	0.01	
Zr		0.15	
Nb			1.0
C			0.05
Fe	Balance	Balance	Balance

MELTING

Arc Melting

Alloy development was conducted on 500-g (1-lb) heats, which were arc melted in water-cooled copper crucibles in a chamber backfilled with argon. The alloys were prepared as buttons prior to casting. The buttons were melted six times for homogeneity and then drop cast through a copper crucible with a bottom hole into split copper molds to cast 25- × 12- × 125-mm (1- × 0.5- × 5-in.) ingots. The alloys were prepared from high-purity electrolytic iron, aluminum, and electrolytic chromium. The boron additions were made through a Fe-4 wt % B master alloy. Niobium, zirconium, and carbon were added as elemental materials. Each ingot was weighed after casting to check for any losses. Generally the change was negligible and alloy composition was assumed to be the same as target. The ingot surface quality by this method was excellent. Some solidification shrinkage was noted in the ingot center. A typical ingot by this process is shown in Fig. 1.

Air-Induction Melting

Initial scaleup at ORNL consisted of melting 7-kg (15-lb) heats using the AIM process, and ZrO_2 was used as the crucible material. This crucible material was somewhat attacked by the melt. A scaleup conducted at a commercial vendor suggested Al_2O_3 is a

YP6549

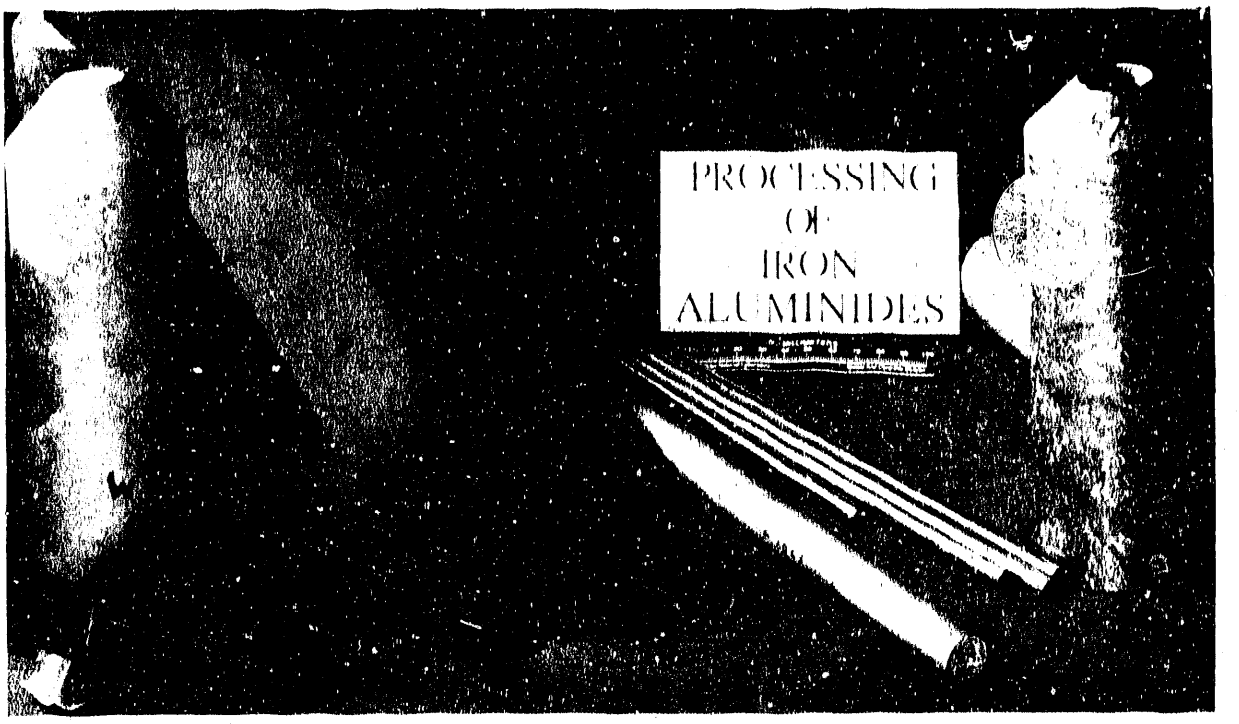

Fig. 1. Photograph showing the 500-g (1-lb) drop casting, the sheet produced from drop casting, the air-induction-melted ingots, and the extruded tubing fabricated from iron-aluminide alloys. The bar and rod produced by extruding and swaging processes are also shown.

better crucible material than ZrO_2. The melt stock for ORNL heats consisted of electrolytic iron that was hydrogen-gas fired at 1000°C and stored in desiccators. The hydrogen firing was done to reduce any oxide on iron chips and the storing in desiccators to prevent further oxidation. The aluminum was pure ingot stock that was forged and rolled to plate and then chopped into melt stock. The aluminum chips were cleaned in HCl solution, washed, dried, and stored in a desiccator until ready for melting. This type of storage prevented any adsorption of water on the surface of the chips or formation of surface oxide. When appropriate, elemental additions such as niobium, zirconium, boron, chromium, and carbon were made using high-purity stock. The melt was normally held at 1650°C for 2 to 5 min and top-poured into graphite molds to make 72-mm-diam (2.85-in.) ingots with an extrusion nose on one end. The graphite mold was preheated to 500°C, and a 100-mm-diam (4-in.) hot-top was used to minimize solidification shrinkage. No shrinkage in the ingot was found, even very close to the hot-top. Typical ingots produced by this method are shown in Fig. 1. Note that the surfaces were smooth and essentially no oxidation was

observed. One heat of iron aluminide was also cast into a slab, and no unusual problems were encountered. A graphite mold with a core rod of graphite was used to produce hollow ingots by casting. The graphite rod was drilled from the solid ingot, and the resulting hollow ingot is shown in Fig. 1.

The first scaleup of iron aluminide by a commercial vendor was conducted at Combustion Engineering, Chattanooga, Tennessee. Three alloys were prepared by the AIM process. The initial plan was to melt all 230-kg (500-lb) heats by AIM and cast them into 150-mm-diam (6-in.) ingots. However, the first cast ingot showed bulging of the hot-top rather than conventional shrinking. Once the hot-top was cut, the ingot also showed large voids. At this point, the vendor suggested that the ingots were trapping gas. After a discussion between the staff at ORNL and the vendor, it was suggested that the gas was possibly hydrogen and was resulting from the thermodynamically favored reaction of aluminum with water vapor in the air; for example,

$$2Al + 3H_2O \rightarrow Al_2O_3 + 6H.$$

The free energy for this reaction is -896.6 kJ/mol. Such a process could produce copious amounts of hydrogen. Once the hydrogen-gas entrapment was suspected, it was decided that the iron and aluminum for the melt stock should be baked to remove any moisture. This practice was tried in the induction furnace with an argon cover gas for 70-kg (150-lb) heats, and the problem was significantly reduced. At this stage, the vendor supplied one 230-kg (500-lb) heat and one each of the 70-kg (150-lb) heats for all of the compositions. Figure 2 is a photograph showing all of the ingots received by ORNL. All of the ingots were cast in sand molds and, thus, had rough surfaces.

The next scaleup was performed by The Timken Company, Canton, Ohio. The first trial involved performing AIM on a 230-kg (500-lb) heat. The entire heat was cast into a 200-mm^2 (8-$in.^2$) ingot. The ingot was found to be riddled with holes, similar to those observed for the 230-kg (500-lb) heat melted by Combustion Engineering. At this point, it was decided to melt these alloys by VIM. One 45-kg (100-lb) heat of FA-129 was VIM and cast into 100-mm-diam (4-in.) tapered molds. These ingots were of excellent quality and did not show any visible porosity. In vacuum melting, the elimination of porosity related to hydrogen was probably caused by a combination of two factors: (1) no moisture came in contact with the melt, and (2) any trapped gas that might have been produced by the reaction shown in the equation was pumped out as the melting proceeded. Thus, from

YP7104

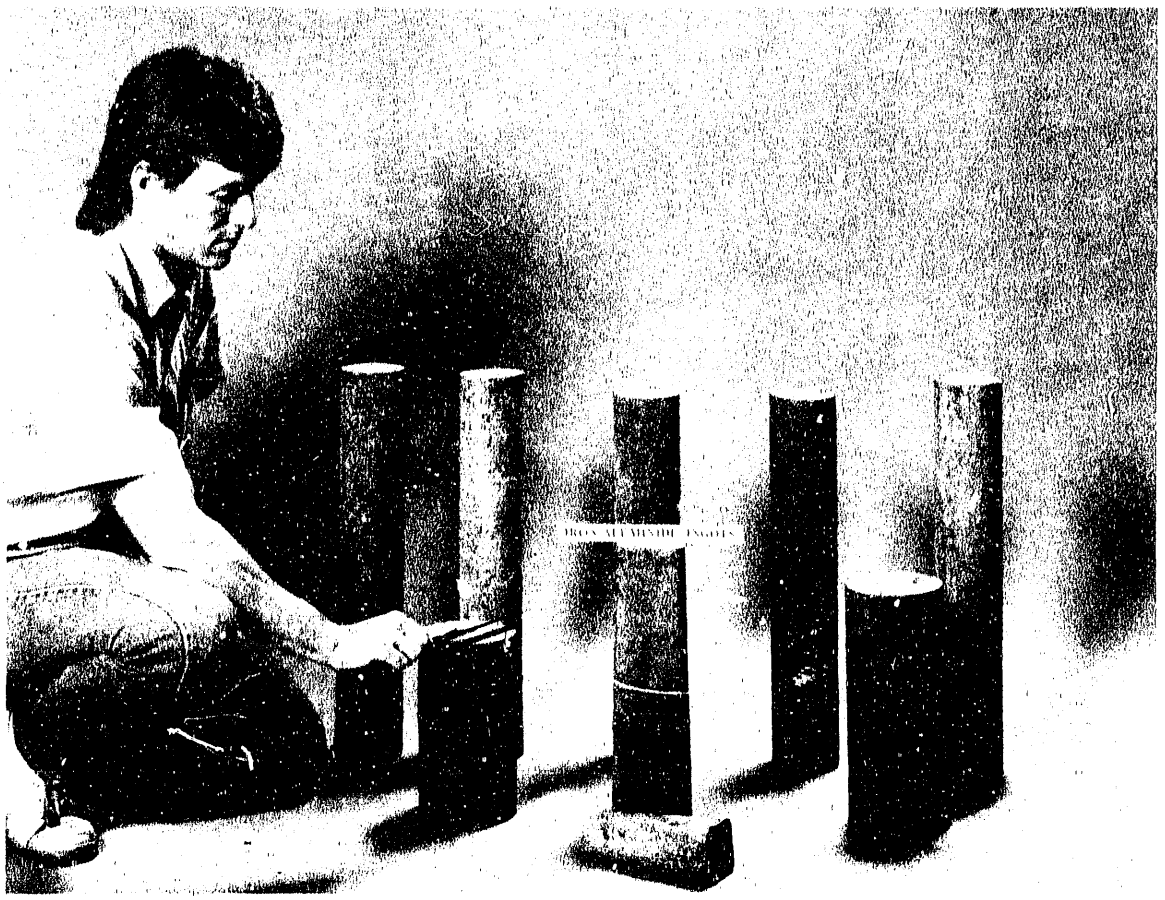

Fig. 2. Photograph of iron-aluminide ingots of 70 to 230 kg (150 to 500 lb) melted by air-induction melting at Combustion Engineering.

experience at both Combustion Engineering and The Timken Company, it is recommended that Fe_3Al-based iron aluminides be melted by VIM and, if desired, further refined by vacuum-arc remelting or by ESR.

Vacuum-Induction Melting and Electroslag Remelting

The next step of melting processes investigated were VIM and ESR. In addition to Timken, the process has also been utilized to prepare iron-aluminide heats at ORNL, Haynes International, and CarTech. The 7-kg (15-lb) heats from ORNL were cast into 72-mm-diam (2.85-in.) graphite molds with extrusion noses. The surface quality of these ingots was excellent and no porosity was observed. The VIM heats at Haynes International

were 38 kg (85 lb) in size. One heat was cast into 38-mm-diam (1.5-in.) bars, and the other two heats were cast into 76-mm-diam (3-in.) tapered bars. One set of 76-mm-diam (3-in.) bars were ESR into 100-mm-diam (4-in.) ingots at Haynes International. The VIM and ESR ingots from Haynes International are shown in Fig. 3. The VIM ingots had slightly oxidized surfaces indicating that the ingots might have been taken from the molds while they were still too hot. The ESR ingot surface was of excellent quality. No porosity was observed in either the VIM or the ESR ingots.

YP9508

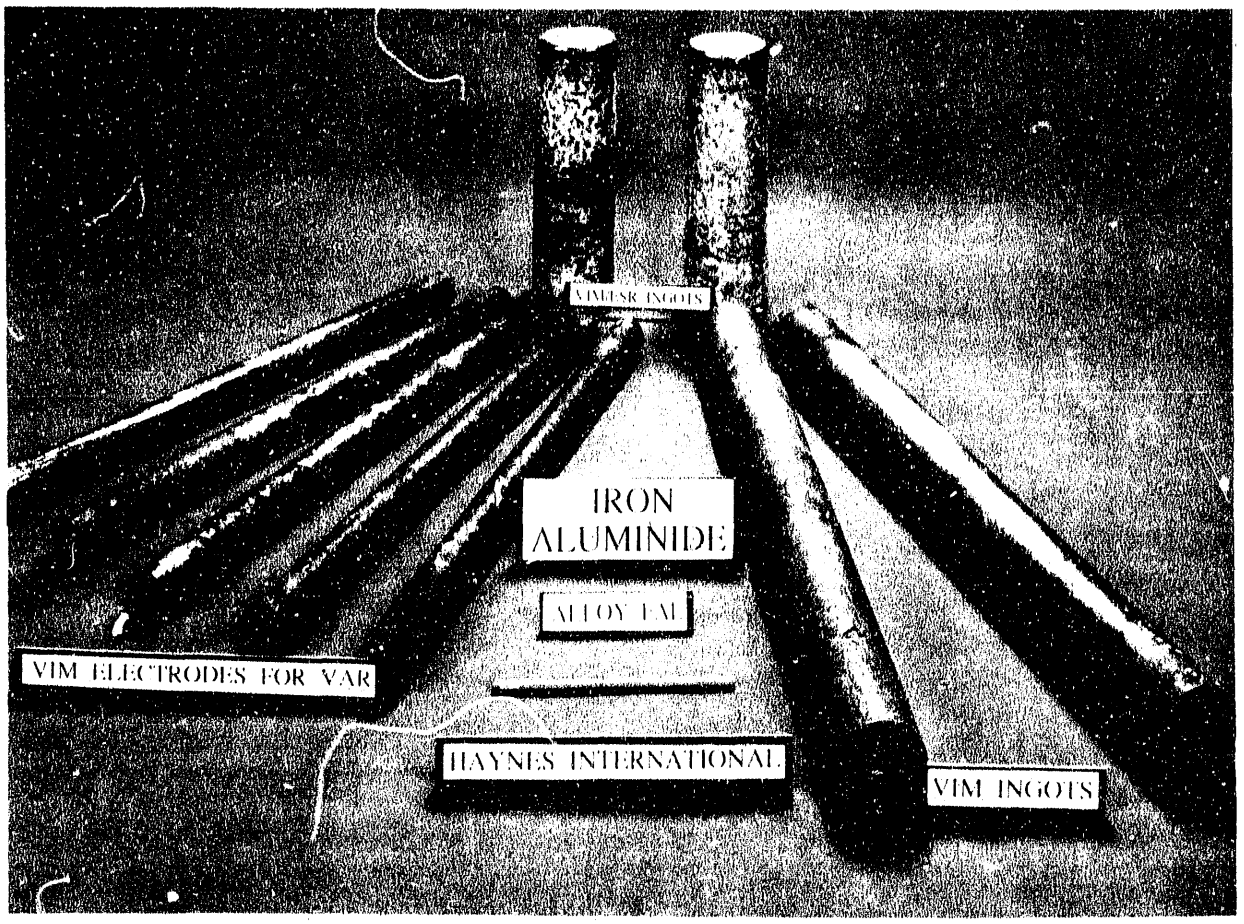

Fig. 3. Photograph showing vacuum-induction melted and electroslag-remelted ingots of iron-aluminide alloy FAL from Haynes International.

In the process of making ESR ingots, CarTech made a 182-kg (400-lb) VIM. electrode of iron-aluminide alloy FAL. The VIM electrode was 150-mm (6-in.) diam and is

shown in Fig. 4. The VIM electrode was electroslag remelted into a 200-mm-diam (8-in.) ingot. The ESR ingot is shown in Fig. 5. The ingot was covered with a film of the slag, which was removed mechanically prior to processing.

R&D #112-3

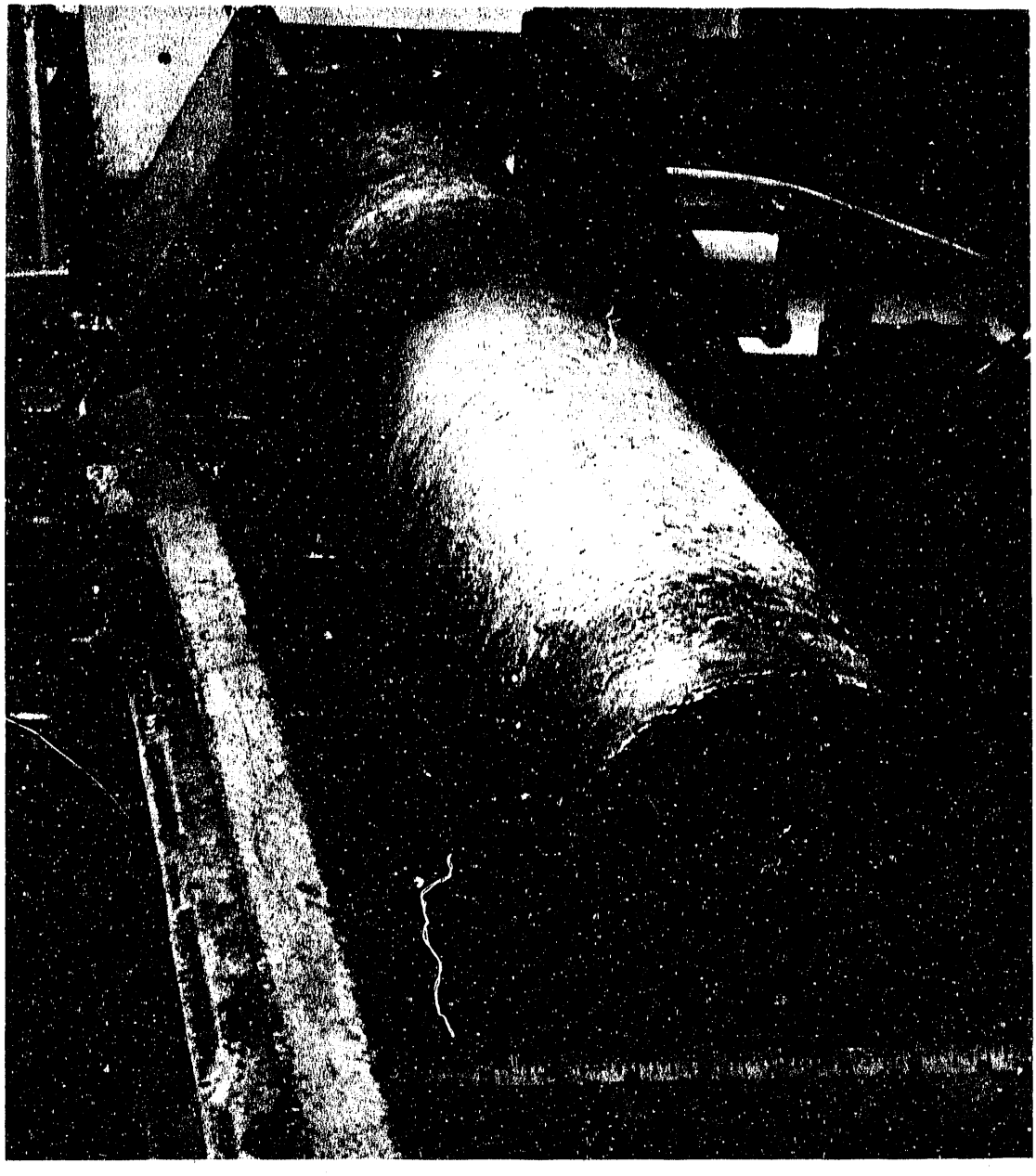

Fig. 4. Photograph of 150-mm-diam (6-in.) vacuum-induction-melted ingot of iron-aluminide alloy FAL prepared at CarTech.

R&D #112-6

Fig. 5. Photograph of 200-mm-diam (8-in.) electroslag-remelted ingot of iron-aluminide alloy FAL prepared at CarTech.

CHEMICAL ANALYSIS

Chemical analysis of iron-aluminide alloys produced by the arc melting, VIM, AIM, and ESR processes were completed. Based on these analyses, a summary is shown in Table 2 of the typical impurities observed in these alloys melted by the various methods and at different vendors. The following are specific observations:

1. Carbon is always picked up by the alloy irrespective of the melting process. The extent of carbon pickup depends on the melt stock. Carbon generally comes from its presence in chromium and can be reduced by selecting a low-carbon chromium. In commercial practice, an argon-oxygen-deoxidation (AOD) process can be used to control the carbon level.
2. The nitrogen content of ORNL and Haynes International material was the highest. It must come from the melt stock. If it came from air, the nitrogen content of air-melted stock would be the highest. However, it was the lowest. The nitrogen content can probably be controlled by proper selection of melt stock.
3. The oxygen content of Haynes International ingots was the highest. The oxygen can come from the melt stock or air. The air melting produced oxygen levels of 0.0025. Thus, the high levels of oxygen in ORNL and Haynes alloys must come from the melt stock. The oxygen level for the CarTech ingot was the lowest.

Table 2. Typical impurity levels (wt %) observed in Fe_3Al-based iron aluminide prepared by various melting methods and vendors

Element	ORNL		CE	Haynes International		CarTech	
	Arc melting	VIM	AIM	VIM	ESR	VIM	ESR
C		0.011	0.050	0.011	0.015	0.021	0.027
N_2	0.006	0.007	0.0006	0.013	0.007	<0.001	<0.001
O_2	0.006	0.006	0.0025	0.020	0.015	<0.001	<0.001
S	0.002	0.001	0.010	0.002	0.001	0.002	0.002
P	<0.001	0.003		0.002	0.001	0.002	0.004
Si	<0.01	<0.01		<0.01	0.04	0.03	0.06
Mg						0.0010	0.003

4. Sulfur was generally low in all material except air-melted ingots from Combustion Engineering. The sulfur pickup is expected from the melt stock.
5. The phosphorus content was low for materials from all sources.

6. The silicon content was low for all processes except ESR. The higher amount of silicon in the ESR ingot comes from the reduction of SiO_2 in the slag. However, the levels are still extremely low, and could be reduced further by proper selection of slag.
7. Magnesium was analyzed only for the CarTech material. The ESR ingot was found to contain three times the level amount of magnesium as the VIM ingot. The VIM process at CarTech used a MgO crucible. The crucible was attacked by the alloy and aluminium can reduce the MgO to magnesium in Fe_3Al compositions. The higher magnesium content in the ESR process came from the reduction of MgO in the slag by aluminum in the alloy. Even 0.003 wt % of magnesium was found to segregate to several percent levels in the center of the ingot. Such segregation caused alligatoring during the hot rolling process. Therefore, it is recommended that MgO not be used as a crucible material or in the slag for any future ESR operations.

The recovery of various elements during AIM on Fe_3Al-based iron-aluminide alloys is summarized in Table 3. Note that the recovery of aluminum in these alloys is nearly 97%. The alloy additions such as zirconium, molybdenum, and niobium have recoveries of 100%. Chromium recovery was typically 95% and boron had a recovery of about 80%. The element recovery data in Table 3 are extremely useful in scaleup of Fe_3Al-based alloys. The element recovery data need to be updated as additional heats of the alloys are melted.

Table 3. Recovery of various elements during air-induction melting of 7-kg (15-lb) iron-aluminide heats at ORNL

Element	Alloy 1		Alloy 2		Alloy 3		Alloy 4	
	Target (wt %)	Recovery (%)	Target (wt %)	Recovery (%)	Target (wt %)	Recovery (%)	Target (wt %)	Recovery (%)
C					0.04	250.00[a]		
Cr	2.157	98.75	5.46	91.03	5.46	95.24	2.194	95.72
Mo	0.995	100.00						
Nb	1.542	100.00			0.21	100.00		
Al	15.672	96.86	15.88	96.73	15.88	97.54	15.932	96.67
B	0.011	81.82	0.01	80.00			0.011	27.27
Zr	0.189	100.00	0.19	100.00				
Fe	Bal.[b]		Bal.[b]		Bal.[b]		Bal.[b]	

[a]Recovery of greater than 100% indicates pickup of carbon from external sources or as impurity in alloy addition such as chromium. For example, a graphite rod was used for stirring the liquid metal and a small fraction of the graphite was probably dissolved in the metal.

[b]Balance (100 minus total of all other elements).

DISCUSSION

Iron-aluminide alloys based on Fe_3Al can be melted by a range of processes for the laboratory-size heats. The laboratory heats have provided direction to the recovery of elements, impurity levels reached by various processes, internal soundness, and surface quality of ingots. The laboratory melting was generally carried out using high-purity elemental materials. The commercial melting will use the combination of steel scrap and pure materials. It is anticipated that the commercial melting will be carried out using the AOD process followed by refining by any one of the processes such as VAR or ESR. During the AOD process, the steel scrap will be deoxidized until desired levels of carbon and other impurities are achieved. At this stage, additions of aluminum will be made. The dissolution of aluminum in iron and the formation of Fe_3Al is an exothermic process, which is expected to provide sufficient energy to maintain the bath temperature. Once the aluminum addition and dissolution is completed and the bath temperature is maintained, alloying additions such as zirconium, niobium, and boron will be made. The alloy at this stage can be cast into ingots for processing or electrode molds for subsequent processing. The VAR process will be used to produce controlled melting and solidification under vacuum. The gas content of the alloy will be reduced by this process. In the ESR process, proper selection of slag will help to reduce impurities such as sulfur and silicon. The selection of slag and atmosphere over the slag are extremely important to avoid impurity pickup by the alloy. For example, MgO in the slag can introduce magnesium in the alloy. The moisture in air over the slag could transfer some hydrogen into the alloy. The ESR process allows controlled solidification and an ingot surface that requires no conditioning. Besides the melting techniques, the melt stock will introduce certain impurities into the alloy. These are expected to include carbon, manganese, silicon, phosphorus, sulfur, and copper. The influence of such elements on the properties of Fe_3Al-based iron-aluminide alloys needs to be evaluated systematically. Efforts are currently under way to prepare Fe_3Al-based iron-aluminide alloys commercially by various processes including AOD, VIM, and ESR.

SUMMARY AND CONCLUSIONS

The melting of Fe_3Al-based iron-aluminide alloys at ORNL and commercial vendors was described. The melting processes described included arc melting, AIM, VIM, and ESR. Data were presented on the recovery of various elements in these alloys, and impurity levels were observed by various processing methods. The internal soundness and

the surface quality of the ingots by various methods were also described. The specific conclusions include:

1. The Fe_3Al-based alloys can be melted in small heats by many processes including arc melting, AIM, VIM, and ESR.
2. Alloys were susceptible to gas porosity during AIM if the melt stock was not properly handled. Similar porosity was eliminated during VIM or ESR.
3. The commercial melt stock tended to intrude impurities in the alloy. The most common impurity was carbon, which might come from its presence in chromium.
4. The MgO in the slag could be reduced by aluminum during ESR to introduce magnesium in the alloy, which is detrimental. The MgO should be avoided in the slag for commercial melting.

ACKNOWLEDGMENTS

The author would like to thank G. E. Angel and J. D. Vought for the melting of the alloys, R. R. Judkins and C. G. McKamey for technical review, and M. L. Atchley for preparing the manuscript.

REFERENCE

1. V. K. Sikka, C. G. McKamey, C. R. Howell, and R. H. Baldwin, *Fabrication and Mechanical Properties of Fe_3Al-Based Iron Aluminides*, ORNL/TM-11465, March 1990.

THE INFLUENCE ON THERMOMECHANICAL PROCESSING ON MICROSTRUCTURE AND MECHANICAL PROPERTIES OF Fe_3Al ALLOYS

R. N. Wright

Idaho National Engineering Laboratory
EG&G Idaho, Inc.
P. O. Box 1625
Idaho Falls, ID 83415-2218

ABSTRACT

Alloys based on Fe_3Al have an equilibrium DO_3 structure at low temperatures and transform to a B2 structure above about 550°C. The influence of different rates of quenching from the B2 region to room temperature on the microstructure and mechanical properties of alloys with two different Cr contents has been examined. By optimizing the processing to maximize the amount of B2 order, room temperature ductility approaching 20% has been achieved although the fracture mode is primarily brittle cleavage. Increasing the Cr content from 2% to 5% has little effect on mechanical properties.

INTRODUCTION

In this study the effect of different quenching treatments on the microstructure of two chromium containing alloys is examined using x-ray diffraction as well as optical metallography. The mechanical properties resulting from the various structures have been determined by room temperature and elevated temperature tensile testing of extruded and hot rolled materials produced by powder metallurgy (P/M) processing.

Fe_3Al alloys exhibit good oxidation and sulfidation resistance as well as excellent resistance to abrasive wear and erosion, but until recently interest in these alloys has been limited because of their low room temperature ductility. Improved understanding of the effects of alloying and thermomechanical processing has resulted in higher strength alloys with improved ductility [1]. Warm working the material to create a high defect density at room temperature and appropriate heat treatments have increased the room temperature ductility significantly [2]. Cr is added principally to improve the room temperature ductility [1].

Compositions with stoichiometries of approximately 3 iron to 1 aluminum have three possible crystal structures. Above about 1100°C a solid solution of the two elements on a bcc lattice is the equilibrium structure. Two ordered phases exist at lower temperatures. The FeAl phase field is present above a critical temperature of about 550°C and has the B2 structure. Below the critical temperature DO_3 is the equilibrium structure. For both B2 and DO_3 order it is assumed that Cr occupies Fe and Al sites with equal probability [1].

B2 phase can easily be retained at room temperature be quenching from above the critical temperature, indicating that the B2 to DO_3 transformation is sluggish [4,5]. By quenching from different temperatures and into different quenching media, the relative volume fractions of the two ordered phases can be controlled. The amount of each type of order can be described by the Bragg-Williams long range order parameter. This parameter is determined by measuring the integrated intensity of the x-ray diffraction peaks and comparing the measured values to calculated values for perfect order.

PROCEDURE

Two batches of powder with stoichiometries designed to yield Fe_3Al and containing nominally 2% and 5% chromium by weight were produced by atomization with argon gas. The powders were canned in mild steel, evacuated, and hot extruded at 1000°C to an area reduction ratio of 9:1. The as-extruded structure was examined using standard optical metallography techniques. Round tensile bars were machined by centerless grinding from a portion of the extrusions. One specimen of each alloy was heat treated at 750°C for 1 h and quenched. Tensile bars were tested in both the as-extruded and heat treated conditions.

After removing the steel can, a second portion of each alloy extrusion was forged at 1000°C to a reduction of about 75% and then rolled at 800°C to sheet approximately 2.5 mm thick. The sheet was finish rolled at 650°C to a thickness of 0.75 mm. Tensile bars were punched from the sheet after a heat treatment of 700°C for 1 h followed by quenching. The specimens were heat treated for 1 h at temperatures of 700, 750, 800, or 850°C and either quenched or air cooled. Six 5% Cr

specimens treated at 750°C and quenched were tested at room temperature to check repeatability. Tensile testing of the sheet specimens was performed at a strain rate of 0.2/min. Additional specimens were cut from the 2% Cr sheet before heat treating and heat treated to produce varying amounts of the DO_3 ordered phase prior to tensile testing at room temperature at a strain rate of 0.04/min. These specimens were all heat treated at 700°C for 2 h; one was quenched from that temperature, another was furnace cooled to 400°C, held for 24 h and then quenched, and the final specimen was furnace cooled to 500°C, held for 24 h and then quenched. Additional sheet tensile specimens of each alloy were tested at a strain rate of 0.2/min. at temperatures of 100, 300, 500, 700, and 800°C. Prior to testing these samples were quenched from 750°C after 1h.

The fracture surfaces of some of the room temperature samples were examined using scanning electron microscopy (SEM). The grip sections of the tensile bars were examined using optical metallography techniques to measure the grain size by the line intercept method. X-ray diffraction was used to measure the order parameters in the as-atomized powders and some of the heat treated sheet specimens. Diffraction studies of the rolled specimens indicated that they had texture so (111) diffraction peaks were used for the order parameter measurements.

RESULTS AND DISCUSSION

The atomized powders of both compositions were generally spherical and had a mean particle size of approximately 0.4 mm. Chemical analyses of the two alloy powders are shown in Table 1.

TABLE 1. Chemical Analysis of Fe_3Al Powders by X-ray Fluorescence (wt%)

Powder	C	S	P	Si	Cr	Fe	Al
2% Cr	0.012	0.001	0.003	0.034	1.94	83.78	14.23
5% Cr	0.019	0.001	0.002	0.014	4.63	80.73	14.55

Figure 1 shows the microstructure of the as-extruded material in the longitudinal and transverse directions. The grains were elongated somewhat and there was no evidence of prior particle boundaries. The nearly isotropic nature of the microstructure indicates that partial recrystallization may occur during extrusion. Figure 2 shows an example of a typical microstructure from sheet that was hot rolled from the extrusions, taken in the plane of the sheet; the 5% Cr alloy has an average grain diameter of 0.028 mm. The 2% Cr alloy has a somewhat larger average grain diameter, approximately 0.035 mm.

The fracture surfaces of several of the sheet specimens tested at room temperature indicated primarily cleavage fracture. However, small areas of dimpled ductile fracture were found in two quenched specimens that had total elongations greater than 15%, shown in Figure 3. The appearance of the fracture surfaces suggests very little ductility; however, even the least ductile specimen had a total elongation of 10%.

The room temperature tensile data for the sheet tensile specimens are presented in Figures 4, 5, and 6. Duplicate tensile tests for the 5% Cr alloy exposed to one of the heat treatments indicate good repeatability. The room temperature yield and tensile strengths and the elongations for the 2% Cr alloy were generally about the same as those of the 5% Cr alloy. The quenced tensile bars generally had greater elongation than the air cooled specimens of the same alloy and heat treatment temperature. X-ray diffraction indicates that none of the DO_3 phase is present in the quenched specimens, while the air cooled specimens have DO_3 order parameters of about 0.3 (see Table 2).

Figure 7 shows the flow curves for the three specimens heat treated to result in varying amounts of DO_3 order. The sample quenched directly from 700°C exhibits only B2 order. This condition resulted in the least strength and most ductility of the three specimens. The specimen held at 400°C for 24 h before quenching has the highest strength and the lowest ductility, while the specimen held at 500°C has intermediate strength and ductility. Although both hold temperatures are below the critical temperature, the equilibrium degree of order decreases as the critical temperature is approached, [3] so that the specimen held at 400°C is expected to have the most DO_3 order. The order parameters measured by x-ray diffraction are presented in Table 2.

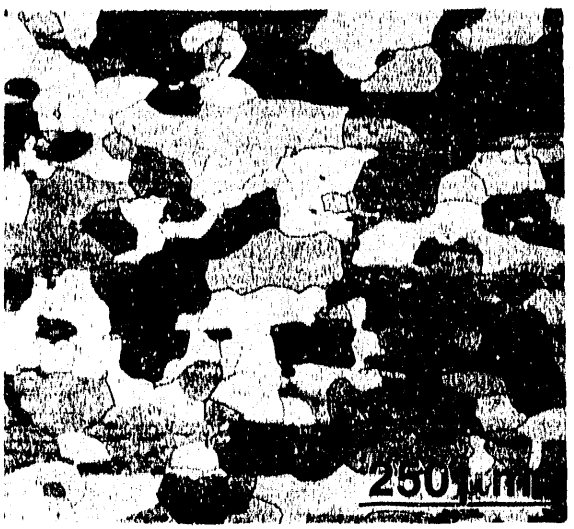

a. longitudinal direction

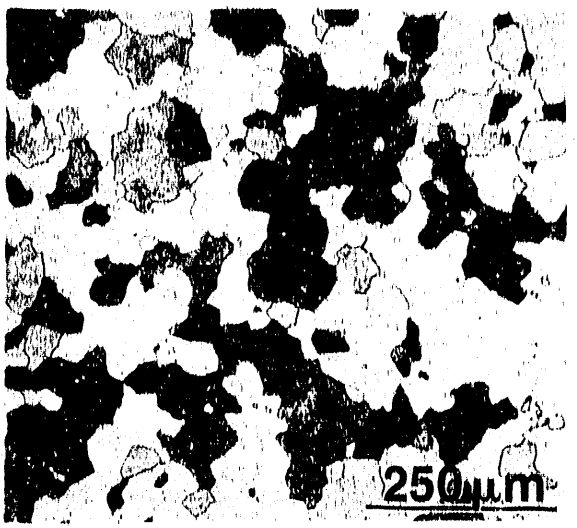

b. transverse direction

Fig. 1. Microstructure of extruded Fe_3Al with 5% Cr

Fig. 2. Microstructure of hot rolled Fe_3Al with 5% Cr.

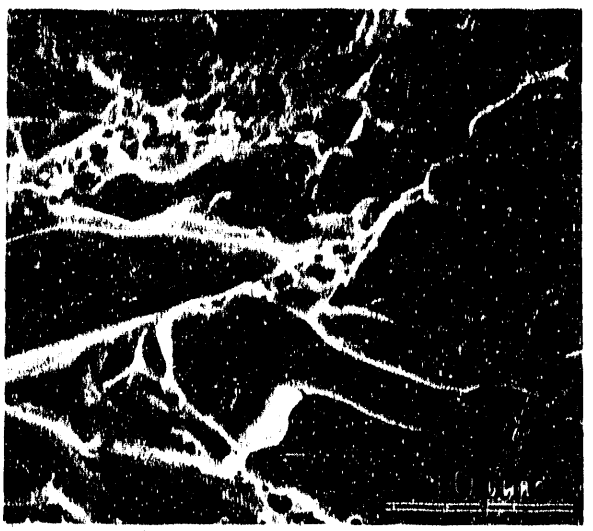

Fig. 3. Fracture surface of Ee_3Al 2% Cr tensile bar.

The elevated temperature tensile test results for quenched specimens are shown in Figures 8 and 9. As expected, ductility increases significantly with increasing test temperature. Elongations near 100% for the two specimens tested at 800°C indicate that these alloys may be superplastic. At testing temperatures up to 300°C ultimate tensile strengths are approximately constant and yield strengths decrease only slightly. However, at higher temperatures both the ultimate tensile and yield strengths drop dramatically and are virtually identical for a given test temperature, indicating little or no work hardening. The yield

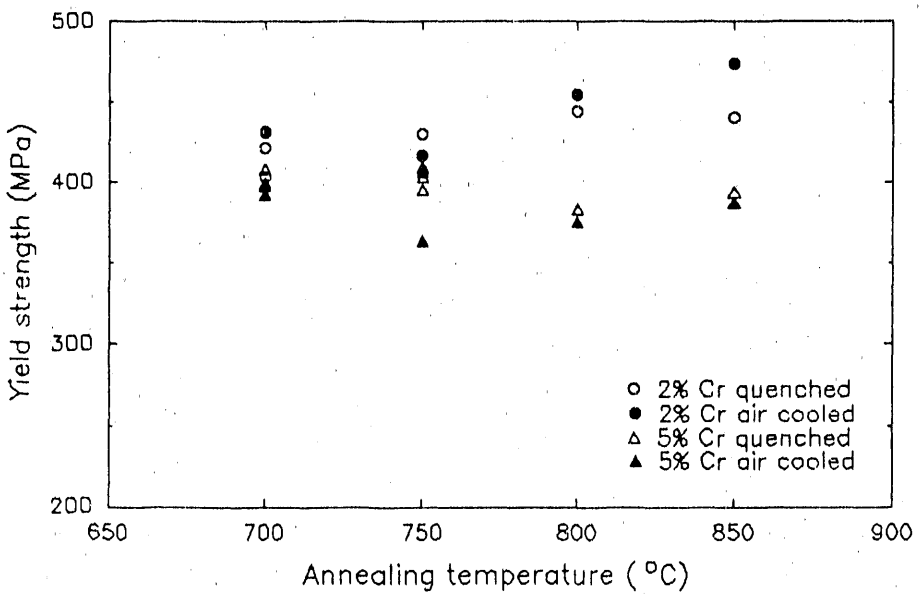

Fig. 4. Yield strength as a function of annealing temperature for 2% and 5% Cr sheet tensile specimens subjected to both quenching and air cooling.

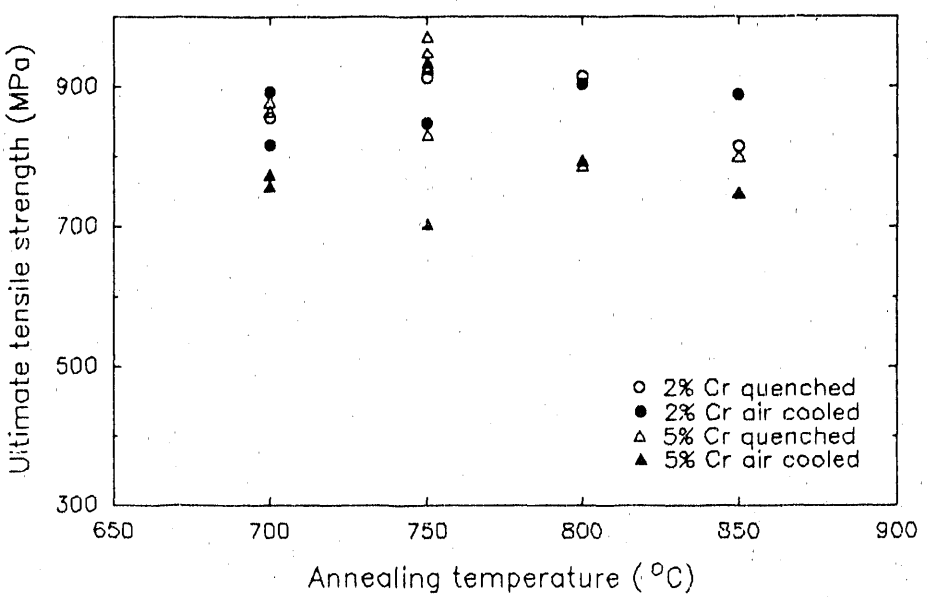

Fig. 5. Ultimate tensile strength as a function of annealing temperature for 2% and 5% Cr sheet tensile specimens subjected to both quenching and air cooling.

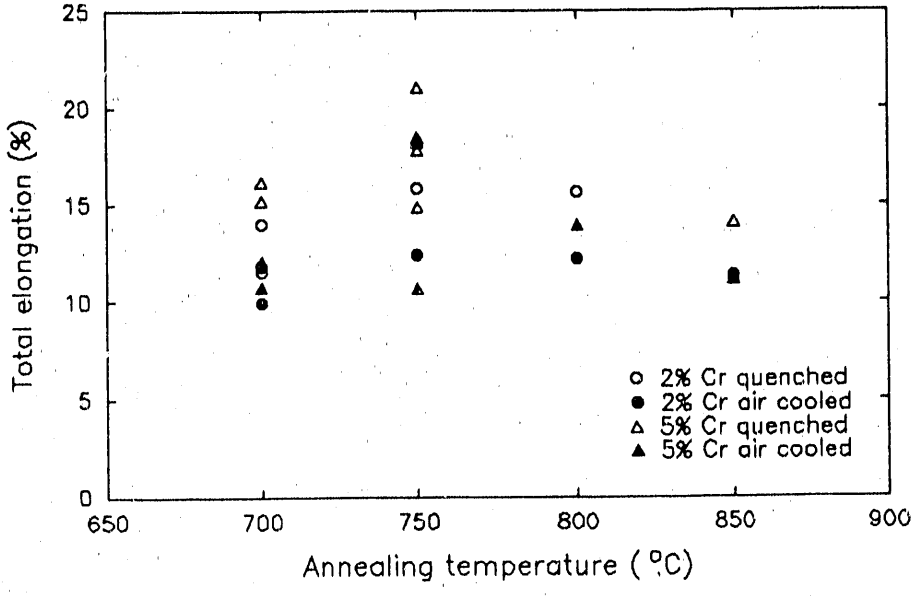

Fig 6. Total elongation as a function of annealing temperature for 2% and 5% Cr sheet tensile specimens subjected to both quenching and air cooling.

strength of the 5% Cr specimen tested at 500°C is slightly increased above that of the specimens tested at other temperatures. A maximum in the yield strength at temperatures near the critical temperature has been reported for Fe_3Al, particularly for specimens the DO_3 structure [6]. However, the quenched specimens used in the elevated temperature testing had primarily B2 order prior to testing. It is possible that the apparent maximum is the result of prolonged exposure to 500°C before load was applied that caused the specimen to partially transform to DO_3. In general, the behavior of the two alloys is very similar at all test temperatures.

The strength of the heat treated extruded specimens exceeded those of the rolled specimens; however, the ductilities were similar. For the 2% and 5% Cr alloys the heat treated extrusions had ductilities of 15.6% and 16.1%, respectively, which far exceeded the values of 12.4% and 6.2% for the as-extruded material. However, yield strengths of 616 and 503 MPa for the 2% and 5% Cr as-extruded specimens were slightly higher than the 549 and 490 MPa found for the heat treated condition. The ultimate tensile strength of 1182 MPa for the 2% Cr alloy was also slightly higher than 1131 MPa for the as-extruded condition. The ultimate tensile strength of 786 MPa for the 5% alloy is low because of premature failure as indicated by the low ductility.

TABLE 2. Order Parameters of Selected Samples

Description	S_{DO_3}	S_{B2-}
2% Cr As Atomized Powder	0.25	0.13
5% Cr As Atomized Powder	0.24	0.18
2% Cr rolled, 700°C 1h, quench, stamped, 700°C 1h, quench	0.00	0.23
2% Cr rolled, 700°C 1h, quench, stamped, 700°C 1h, air cool	0.29	0.29
2% Cr rolled, 700°C 1h, quench, stamped, 800°C 1h, quench	0.00	0.43
2% Cr rolled, 700°C 1h, quench, stamped, 800°C 1h, air cool	0.36	0.33
5% Cr rolled, 700°C 1h, quench, stamped, 700°C 1h, quench	0.00	0.20
5% Cr rolled, 700°C 1h, quench, stamped, 700°C 1h, air cool	0.20	0.21
2% Cr rolled, cut, 700°C 2h, furnace cool to 400°C and hold 24h, quench	0.43	0.23
2% Cr rolled, cut, 700°C 2h, furnace cool to 500°C and hold 24h, quench	0.37	0.25

CONCLUSIONS

Room temperature ductilities of 15-20% can be obtained for Fe_3Al alloys with 2 al 5% cr when given an appropriate heat treatment. The mechanical properties show little change between the two levels of Cr. Preliminary results from elevated temperature testing suggest that these materials may be superplastic. The B2 to DO_3 reaction is quite sluggish and can easily be suppressed to form only B2 order by quenching. The highest room temperature ductilities result from this type of order.

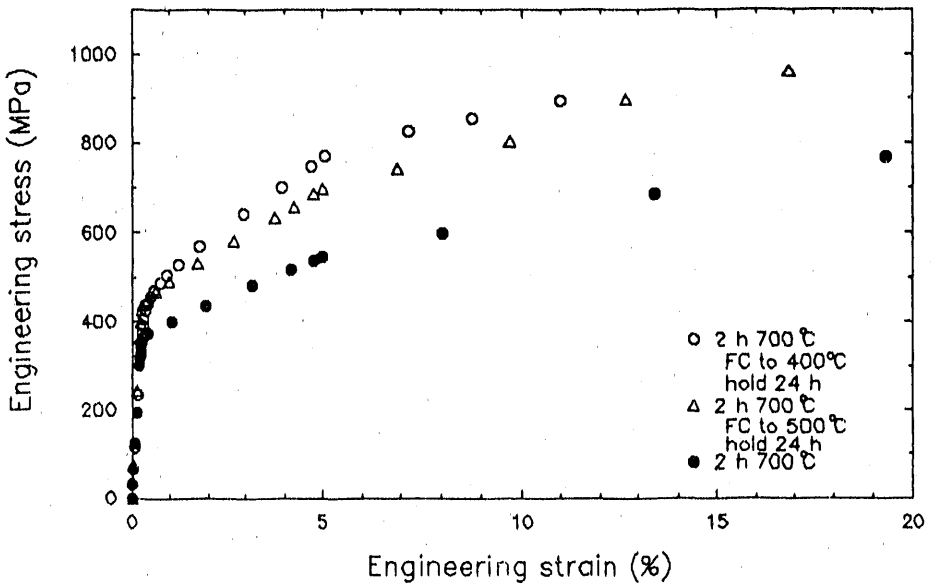

Fig. 7. Engineering stress strain curves for the 2% Cr alloy in B2 and DO_3 conditions.

REFERENCES

1. C. G. McKamey, J. A. Horton, and C. T. Liu, "Effect of Chromium on Properties of Fe_3Al," J. Mater. Res., 4, 1989, p. 1156.

2. R. S. Diehm, M. P. Kemppainen, and D. E. Mikkola, "Processing and Alloying of Modified Iron Aluminides," Mater. & Manufacturing Processes, 4, 1989, p. 61.

3. R. T. Fortnum and D. E. Mikkola, "Effects of Molybdenum, Titanium and Silicon Additions on the DO_3 ↓ B2 Transition Temperature for Alloys near Fe_3Al," Mater. Sci. Eng., 91, 1987, p. 223.

4. L. Anthony and B. Fultz, "Kinetic Paths of B2 and DO_3 Order Parameters: Experiment," J. Mater. Res., 4, 1989, p. 1140.

5. K. Oki, M. Hasaka and T. Eguchi, "Kinetics of Ordering in Fe-Al Alloys," Trans. JIM, 15, 1974, p. 143.

6. P. Morgand, P. Mouturat, G. Sainfort, "Structure et Properties de Fe-Al," Acta Met., 16, 1968, p. 867.

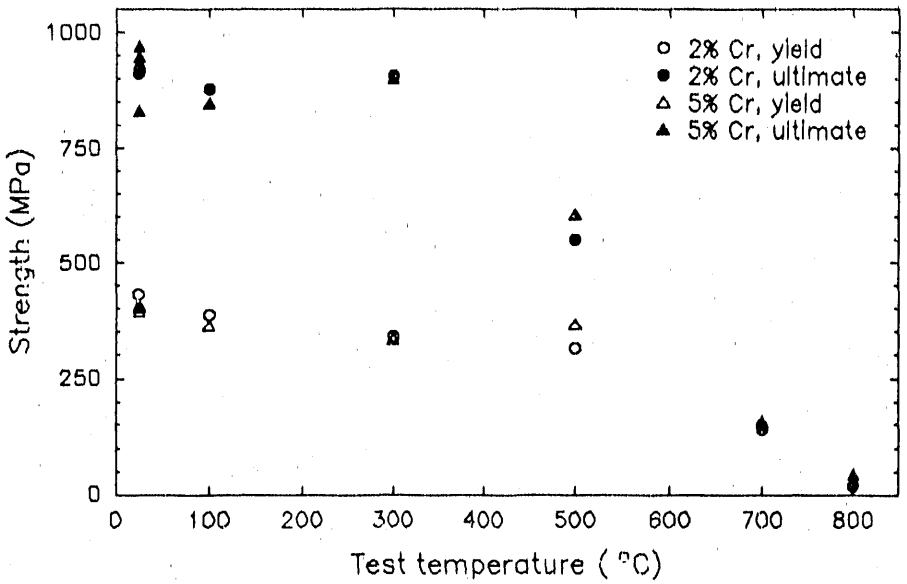

Fig. 8. Elevated temperature yield and ultimate tensile strength for 2% and 5% Cr sheet tensile specimens subjected to quenching.

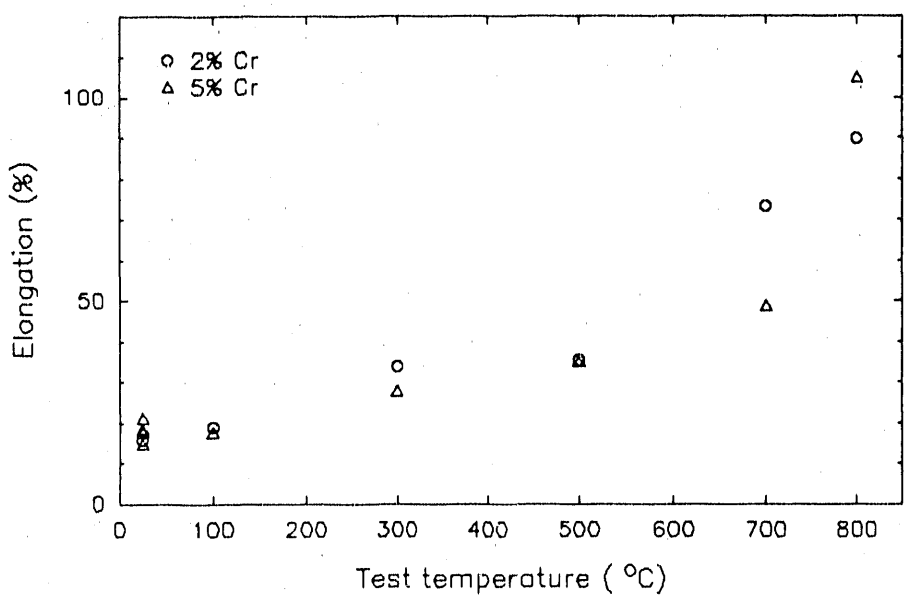

Fig. 9. Elevated temperature total elongation for 2% and 5% Cr sheet tensile specimens subjected to quenching.

INVESTIGATION OF THE WELDABILITY OF POLYCRYSTALLINE IRON ALUMINIDES

D.I. Ash*, G.R. Edwards*, and S.A. David†

*Center for Welding and Joining Research
Department of Metallurgical and Materials Engineering
Colorado School of Mines
Golden, Colorado 80401

†Metals and Ceramics Division
Materials Joining Group
Oak Ridge National Laboratory
Oak Ridge, Tennessee 37831-6095

ABSTRACT

Iron aluminide (Fe_3Al) weldments are susceptible to intergranular sub-solidus cracking. This cracking phenomenon is attributed to both excessive grain growth and environmental effects, and can be interpreted in terms of the brittle fracture criteria. Methods for improving cracking resistance are discussed in terms of refining slip path length and dispersing slip in these ordered materials.

INTRODUCTION

Sub-solidus heat-affected zone cracking in Ni_3Al alloys has been attributed to a minimum ductility regime at intermediate temperatures. However, the hot deformation behavior of Fe_3Al alloys contrasts the Ni_3Al deformation behavior, revealing no minimum ductility regime as seen in Fig. 1. Therefore, sub-solidus cracking in iron aluminides was not expected. However, David and co-workers[1] have shown that the chromium-bearing alloy FA-129 (28 Al-5 Cr-0.5 Nb-0.2 C atomic percent, bal. Fe), was susceptible to intergranular cracking transverse to the weld during gas-tungsten arc (GTA) welding. This cracking, which was brittle in nature, has been attributed to environmental effects. The goal of this research effort is to understand cracking susceptibility in Fe_3Al alloys while improving cracking resistance through application of metallurgical principles.

DISCUSSION OF CURRENT ACTIVITIES

Recently[2], it has been observed that binary Fe_3Al alloys are susceptible to embrittlement by water vapor at ambient temperatures, and the embrittlement has been shown to be independent of the B2 or DO_3 superlattice structure. Although room temperature fracture morphology was independent of environment, decreases in elongation and ultimate tensile strength were observed for both structures in water vapor-containing environments. Since water vapor is present in air, GTA weldments are susceptible to this embrittlement phenomenon. Also,

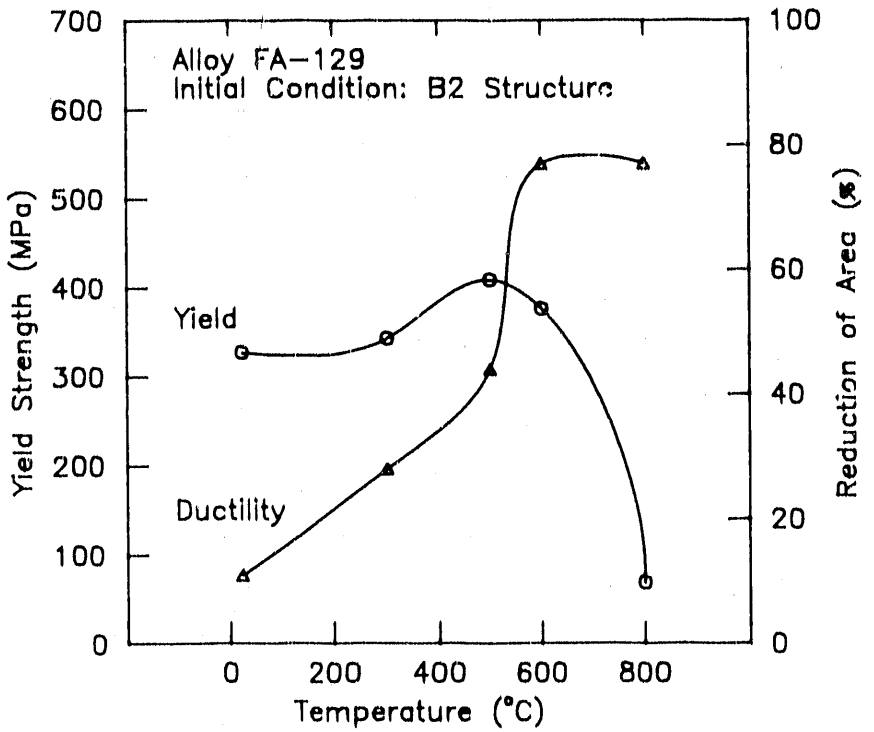

Figure 1. Hot Deformation Behavior of Alloy FA-129.

excessive grain growth in both the fusion and heat-affected zone which can decrease cracking resistance, has been observed for Fe_3Al weldments[1,3].

Since sub-solidus cracking in Fe_3Al weldments is brittle in nature[1], the idea of the brittle fracture criteria can be applied to

describe the cracking susceptibility.

Brittle fracture can be expected when:

$$\frac{\sigma_{app}}{\tau_{app}} \geq \frac{\sigma_F}{\tau_F}$$

where σ_{app} and τ_{app} are the maximum applied normal stress and shear stress, and σ_F and τ_F are the fracture stress and flow stress of the material. When the above criteria are satisfied, the material will fail in a brittle manner.

The sensitivity of both the fracture stress and flow stress to various factors is summarized in Table 1. Fracture stress is more sensitive to environment and slip path length (grain size or dislocation barrier spacing) compared to flow stress. In contrast to the fracture stress, flow stress is more sensitive to temperature and alloying. As seen in Fig. 2 for FeCo in either the B2 ordered or disordered condition, the fracture stress and flow stress reveal their sensitivity to grain size[4].

TABLE 1 Factors Affecting Fracture and Flow Stress

Fracture Stress (σ_F)	Flow Stress (τ_F)
Environment	Temperature
	Alloying
Slip Path Length ($d^{-1/2}$)	Slip Path Length ($d^{-1/2}$)
Grain Size	Grain Size
Domain Size	Domain Size

It has been shown previously[5] that the hot ductility of alloy FA-129 is sensitive to grain size. Fig. 3 graphically demonstrates the hot ductility differences between on-heating specimens (30μm grain size) and on-cooling specimens (100μm grain size) tested at 600°C in air. These differences also correlated with fracture surfaces as noted. Taking

these results into account, coarse slip path lengths and aggressive environments are expected to enhance cracking of these materials upon cooling from welding temperatures.

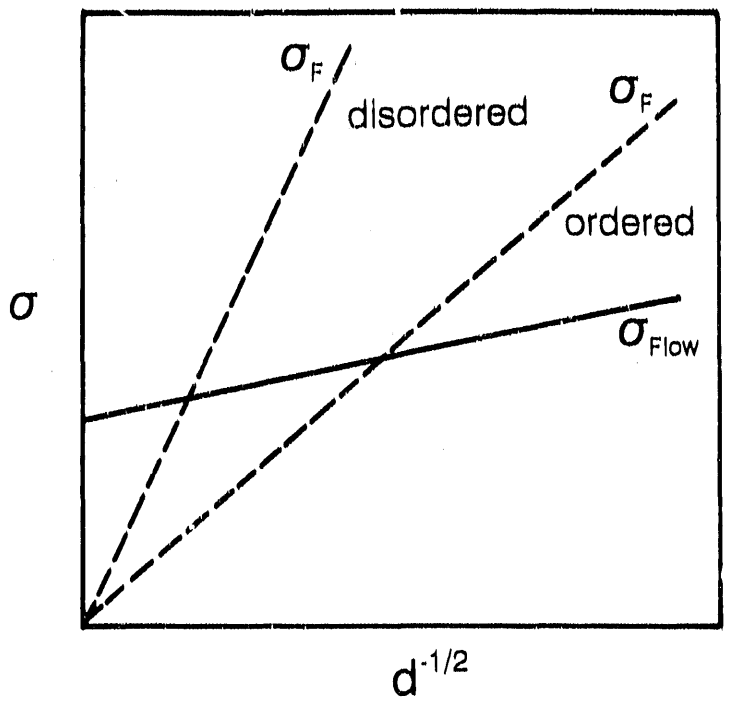

Figure 2. Effect of grain size on flow stress (solid line) and fracture stress (dashed line) for FeCo in either the B2 ordered condition or disordered condition. From Reference 4.

The sub-solidus cracking susceptibility of iron aluminides can be counteracted by any of these methods:

1) Remove hydrogen environment to increase σ_F.

2) Alloy to reduce τ_F, increase σ_F, and enhance cross-slip.

3) Refine microstructure, using grain size or domain structure.

The first method is not very realistic unless Fe_3Al is exclusively electron beam welded, since the more practical GTA welding process is difficult to make completely free of water vapor. Thus, to minimize weld cracking in these environments, slip must be further dispersed.

The second method has been accomplished partly by alloying with chromium[5,6]. Chromium is effective in increasing ambient temperature ductility and ultimate tensile strength (UTS) in air but also reduces the yield strength. However, the effects of chromium were diminished for tests performed at 600°C. Chromium effects on ambient temperature mechanical properties of Fe_3Al were attributed to decreased antiphase boundary (APB) energies. Lower APB energies result in further separation of the component dislocations which make up the Fe_3Al four-fold superlattice dislocations.

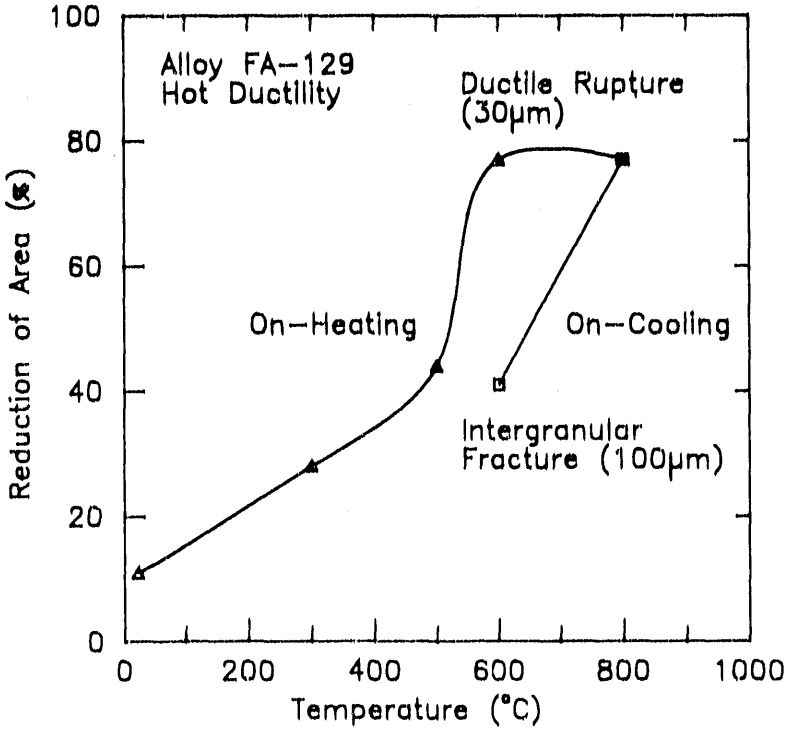

Figure 3. FA-129 hot ductility results for on-heating and on-cooling tests. Grain size and fracture morphology are also given.

Separation of component dislocations leads to enhanced cross-slip of either dislocation pairs or individual dislocations, rather than to planar slip, or motion of perfect superlattice dislocations. Thus increases in both ductility and UTS are expected for this behavior.

The third method, dispersing slip through microstructural

refinement, has been successful in improving the hot ductility and weldability of ordered Ni_3Al[8]. In this case, chromium additions were made to an alloy containing boron and hafnium to create antiphase domain (APD) structures. These structures refined the dislocation barrier spacing, effectively dispersing slip in the minimum ductility range, which decreased weld cracking.

In the case of Fe_3Al alloys, it has been shown that fine grain sizes (short slip path lengths) are beneficial to cracking resistance. However, the effects of fine APD structures on Fe_3Al deformation behavior have not been well documented. A study by Davies[9] suggests that a fine DO_3 APD structure would have significant effects on ductility. However, the temperature below which the DO_3 APD structure forms (~550°C) may be too low to realize any improved weld cracking resistance. On the other hand, B2 APD structures form at higher temperatures (~800°C) and their size is dependent upon cooling rate[10]. Although B2 APD structures are not thermally stable during annealing, they can affect strength if sufficiently fine when the load is applied[11].

If either a fine B2 APD structure or fine stabilized grain structure can be created, slip dispersal may be sufficiently enhanced to avoid weld cracking even in the presence of water vapor. The anticipated improved cracking resistance for finely spaced dislocation barriers in FA-129 at temperatures elevated by welding is shown in Fig. 4. This can also be interpreted in terms of improved hot ductility as seen in Fig. 5 for the condition of variation in B2 domain size. If high cooling rates are experienced by both the fusion zone and heat-affected zone, the material will retain a fine B2 APD structure which is anticipated to be more resistant to cracking.

The first step of this study was to develop a data base for the mechanical behavior of alloy FA-129 deformed at ambient temperature in air. An experimental matrix was developed to determine the effects of DO_3 structure and B2 structure on the room temperature deformation behavior of FA-129. Specimens were annealed at 500°C for 24, 48, or 96 hours to produce increasing levels of DO_3 long range order after stress relieving (690°C for one hour, water quench). The results of tensile

testing at room temperature in air are shown in Fig. 6. Also included is the DO_3 long range order as a function of time. For long times at 500°C and correspondingly large differences in long range order, minor differences in tensile properties were observed. The lack of any significant differences in ductility for the B2 or DO_3 structures may be attributed to coarse APD structures, which are not effective in dispersing slip.

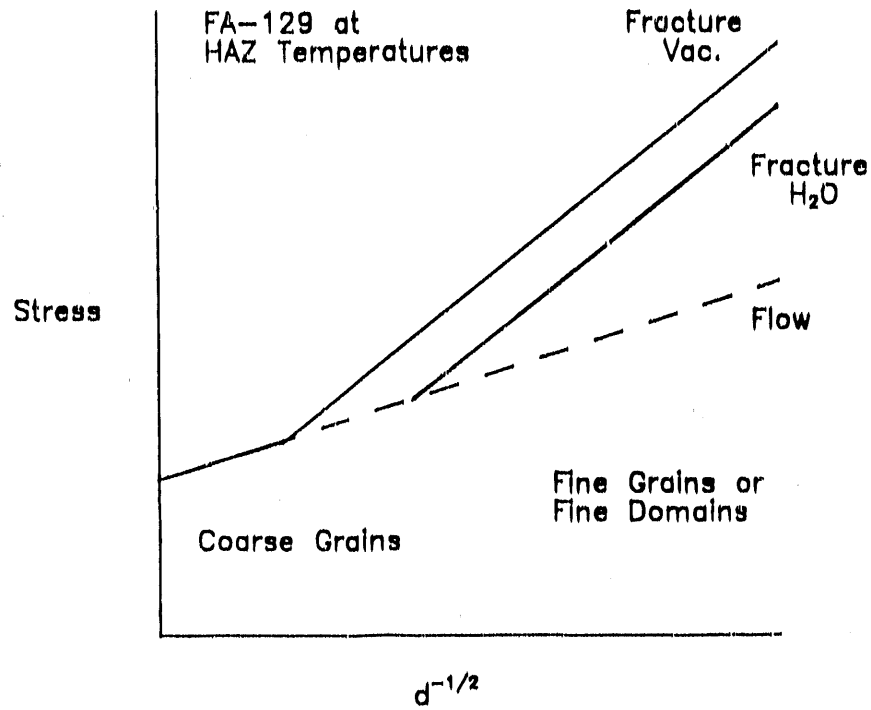

Figure 4. Anticipated improved cracking resistance for FA-129.

CONCLUSIONS

Sub-solidus cracking phenomena in Fe_3Al weldments can be interpreted in terms of the brittle fracture criteria. While chromium has been effective in improving ambient temperature ductility and fracture strength in air environments, further slip dispersal at welding temperatures is needed for improved weld cracking resistance. Since these materials show a strong grain size effect and are embrittled by

water vapor, it is anticipated that a either a fine B2 APD structure or a fine stabilized grain structure will reduce the cracking susceptibility of iron aluminide weldments through refinement of slip path length. The first baseline data for this study has shown that long-time anneals at 500°C caused significant change in the DO_3 long range order parameter, but only minor differences in the ambient temperature mechanical properties of specimens tested in an air environment.

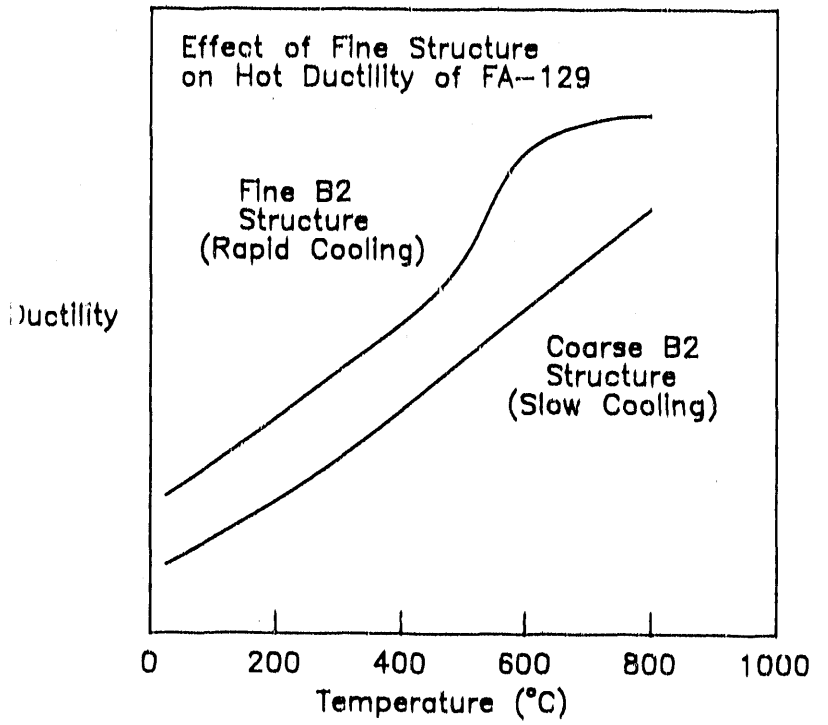

Figure 5. Anticipated hot ductility effect of fine structure.

FUTURE STUDY

The effects of a fine B2 APD structure, stabilized grain structure, and environment on hot deformation behavior of FA-129 will be examined, and any improvements will be correlated with improved weld cracking behavior.

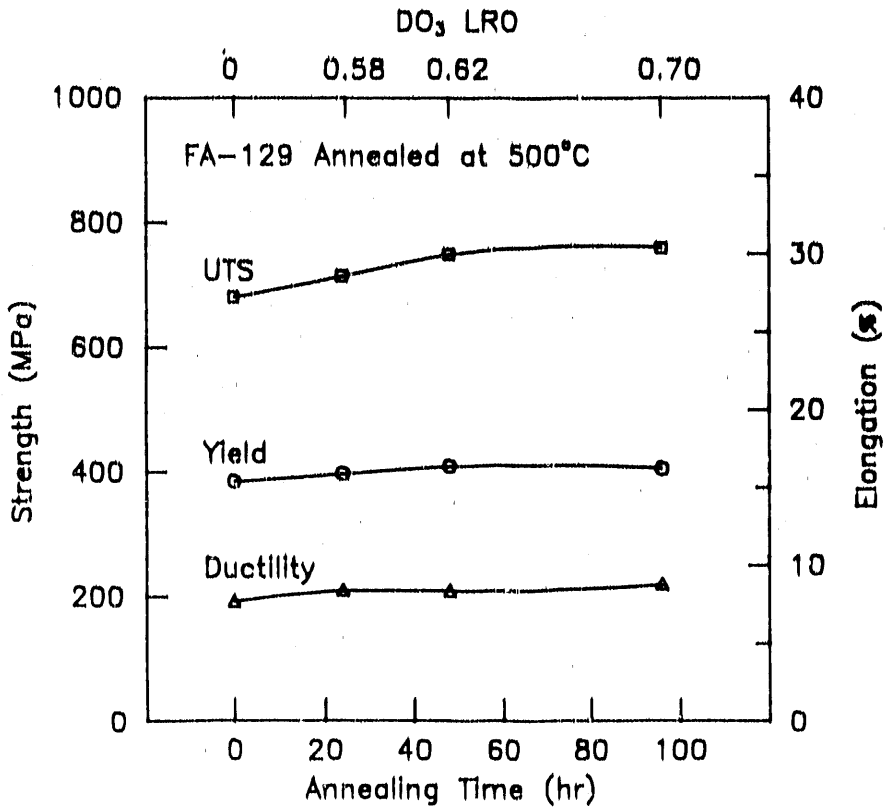

Figure 6. Ambient temperature material properties in air versus annealing time at 500°C. DO_3 long range order parameter is also included.

REFERENCES

1. S.A. David, T. Zacharia and R.W. Reed, Private Communication, Oak Ridge National Laboratory, Oak Ridge, Tennessee, 1988.

2. C.T. Liu, C.G. McKamey and E.H. Lee, "Environmental Effects on Room-Temperature Ductility and Fracture in Fe_3Al," *Scripta Met. et Mat.*, 24, 385-390 (1990).

3. S.A. David, J.A. Horton, C.G. McKamey, T. Zacharia and R.W. Reed,"Welding of Iron Aluminides," *Welding Journal* 68 ,no. 9, 372s-381s (1989).

4. M.J. Marcinkowski,"Strengthening of Alloys by Atomic Order," *Phys. Stat. Sol. (a)* 90, 621-630 (1985).

5. D.I. Ash, G.R. Edwards and S.A. David,"Investigation of the Weldability of Polycrystalline Iron Aluminides," ORNL/FMP-89/2, AR&TD Fossil Energy Materials Program Semiannual Report for the Period Ending September 30, 1989, Oak Ridge National Laboratory, Oak Ridge, Tennessee, 229-237.

6. C.G. McKamey, J.A. Horton and C.T. Liu,"Effect of Chromium on Properties of Fe_3Al," *J. Mater. Res.* 4, no. 5, 1156-1163 (1989).

7. C.G. McKamey, J.A. Horton and C.T. Liu,"Effect of Chromium on Room Temperature Ductility and Fracture Mode in Fe_3Al," *Scripta Met.* 22, 1679-1681 (1988).

8. M.C. Maguire, G.R. Edwards and S.A. David,"Investigation of the Weldability of Ductile Nickel Aluminides," ORNL/FMP-89/1, AR&TD Fossil Energy Materials Program Semiannual Report for the Period Ending March 31, 1989, Oak Ridge National Laboratory, Oak Ridge, Tennessee, 219-229.

9. R.G. Davies,"Kinetics of Ordering and Domain Hardening in Fe_3Al," *Trans. AIME* 230, 903-907 (1964).

10. M.J. Marcinkowski and N. Brown,"Direct Observation of Antiphase Boundaries in the Fe_3Al Superlattice," *J. Appl. Phys.* 33, no. 2, 537-552 (1962).

11. M.J. Marcinkowski and R.M. Fisher,"Theoretical Analysis of Plastic Deformation in Superlattices Based on the Body-Centered Cubic Structure," *J. Appl. Phys.* 34, no. 8, 2135-2145 (1963).

DEVELOPMENT AND EVALUATION OF ADVANCED AUSTENITIC ALLOYS

R. W. Swindeman, P. J. Maziasz,
J. F. King, and E. Bolling

Oak Ridge National Laboratory
P.O. Box 2008
Oak Ridge, TN 37831-6155

ABSTRACT

Research was performed on advanced austenitic alloys for tubing in heat recovery systems. Evaluations addressed the need to optimize strength, fabricability, and surface protection for specific environments and temperatures. Alloys studied included advanced lean austenitic stainless steels and higher chromium alloys to 760°C, nickel-chromium-iron aluminides at temperatures to 760°C, and Ni-Cr alloys with capability for service to 1000°C. Coordinated research was performed at a number of universities and industrial research facilities. Evaluation of the lean stainless steels focused on MC-forming alloys and a family of modified 316 stainless steels. Work nearing completion revealed that many of the alloy design criteria for the lean stainless steels could be met. With the judicious selection of thermal-mechanical processing, data indicated that high strength and ductility could be achieved in both base metal and weldments. Fabrication requirements needed to produce optimum performance called for high solution treating temperatures and small levels of cold or warm work. Evaluations of high chromium stainless steels and modifications of alloy 800H were encouraging, and good properties were observed for temperatures to 760°C. Work on the alloys and claddings for service to 1000°C was begun on two commercial alloys of interest in PBFC hot gas cleanup systems.

INTRODUCTION

The purpose of this task is to evaluate advanced austenitic alloys for the design, construction, and reliable operation of advanced heat recovery systems and hot gas cleanup systems.[1] Due to limitations in the high-temperature strength and corrosion resistance of iron-base alloys and the prohibitive cost of nickel-base superalloys, most fossil power plants produce steam around 550 °C and 32 MPa. However, advances in materials science relating composition and microstructure of steels to their high-temperature mechanical properties and stability have made it possible to develop austenitic alloys with significantly improved strength and ductility. Similar advances in the development of coating and cladding techniques of these high-strength alloys provides an opportunity to improve the reliability in regard to corrosion protection. Being new alloys, or modifications of commercial alloys, there is a great need for research on joining

methods, high-temperature design methodology, and life prediction methods.[2] These are subjects of great concern in all of the applications, even when old alloys are used for new applications; hence significant benefits will result from a generic approach to high-temperature alloy evaluation.

LEAN STAINLESS STEELS

The lean stainless steels are those that contain less than 20% chromium, and types 304, 316, 321, and 347 stainless steels are typical examples. However, to meet the demands for tubing in an advanced boiler, it was expected that a candidate alloy would need to possess nearly twice the creep strength of the best of the 300 series austenitic stainless steels.[2] To accomplish this, emphasis was placed on the evaluation of MC-forming alloys which are compared to type 316 stainless steel in Table 1. Typical MC-forming elements are titanium, niobium, and vanadium. The first two alloys listed (types 316 and 347 stainless steels) are used on a commercial basis in the United States and included in Section I of the American Society of Mechanical Engineers (ASME) Boiler and Pressure Vessel (BPV) Code. The chemistry provided for type 316 stainless steel is for a single heat (80432297) while the chemistry listed for type 347 stainless steel is representative of the chemistry of several heats of type 347 stainless steel tubing examined by Teranishi.[3] This fine-grained material was found to be much superior to standard 347 stainless steel and is a serious contender for tubing in an advanced steam cycle. A second group of alloys in Table 1 includes steels that have been used on a somewhat restricted basis within the United States, but some have experienced extensive use overseas. Esshete 1250 and 17-14CuMo stainless steel fall into this category. A third group of alloys are new materials that are in the research stage and includes the Sumitomo ST3Cu® stainless steel[4] and variations within an alloy family identified as HT-UTS (high-temperature ultrafine-precipitation strengthened) steels by Maziasz.[5] The chemistries of all alloys listed in Table 1 should be regarded as typical and do not provide the range specified for the specific alloy designation.

Table 1. Chemical compositions of several lean stainless steels (wt %)

Alloy	C	Si	Mn	Ni	Cr	Ti	Nb	V	Mo	P	B	S	N	Cu	Fe
316SS	0.057	0.58	1.86	13.50	17.2	0.02			2.34	0.024		0.019	0.030	0.10	bal
347SS	0.070	0.60	1.60	12.00	18.0		0.70								bal
17-14CuMo	0.098	0.95	0.83	13.80	16.5	0.21	0.45	0.07	1.96	0.014		0.005	0.025	3.34	bal
Esshete 1250	0.100	0.50	6.00	10.00	15.5		1.00	0.25	1.00	0.025	0.006	0.014			bal
ST3Cu	0.110	0.19	0.80	09.20	18.0		0.39			0.021		0.001	0.086	2.88	bal
HT-UTS CE3	0.086	0.21	1.75	16.20	14.5	0.27	0.12	0.56	2.41	0.071	0.005	0.008	0.012	1.96	bal
HT-UTS AX5	0.076	0.12	2.04	16.20	13.9	0.27	0.15	0.52	2.46	0.024	0.005	0.015	0.021		bal
HT-UTS AX8	0.074	0.12	2.05	15.90	13.9	0.24	0.08	0.15	2.48	0.043	0.005	0.015	0.022		bal
HT-UTS BWT4	0.088	0.10	1.79	15.04	13.7	0.10	0.17	0.44	2.19	0.016	0.004	0.002	0.008		bal

Fabricability

The lean stainless steels have been found to be readily fabricable, and several routes are available for producing tubing.[6] All of the alloys identified in Table 1 have been produced as tubing, and several have had many years in boiler exposure. The newer HT-UPS alloys have been produced as cold pilgered tubing by Combustion Engineering[7] and extruded tubing by Babcock & Wilcox.[8] It has been shown by Carolan and coworkers[9] that a solution treatment in excess of 1150 °C followed by approximately 5% cold work is required to produce the best strength. Techniques for introducing cold work have included cold sinking and rotary straightening, and the optimization of fabrication schedules are being finalized by Topolski.[10]

Weldability remains a key issue and is being examined in some detail by Lundin and coworkers.[11] Several of the MC-forming alloys have compositions that are known to cause problems with hot cracking. Specifically, the 17-14CuMo stainless steel, ST3Cu stainless steel, and the HT-UPS alloys have low chromium to nickel ratios, while the high levels of niobium in type 347 stainless steel and Esshete 1250 are causes for concern. The HT-UPS alloys are known to have hot cracking problems and cannot be autogenously welded. Filler metals that are being examined include Inconel 82®, 17-14CuMo stainless steel, CRE 16-8-2 stainless steel, Haynes alloy 556®, and Inconel 617®. Of these, the CRE 16-8-2 has been the best joining alloy.[7]

Metallurgical Stability

The time-temperature-transformation diagrams have been constructed for several of the MC-forming alloys, including type 347 stainless steel,[12] Esshete 1250,[13] 17-14CuMo stainless steel,[14] and the HT-UPS steels.[15] The first two steels precipitate sigma phase, while the second two precipitate Laves. Under the proper prior thermal-mechanical conditioning, all steels form a fine MC precipitate that contributes to creep strength. However, the amount of precipitate, its uniformity, and its stability are factors that influence the relative strength and ductility of the alloys. In the HT-UPS alloys, the precipitate coarsens very slowly and the kinetics of the coarsening has being examined by Todd and Ren.[15] The typical microstructure in a specimen that ruptured after 18,000 h at 700 °C and 170 MPa is shown in Fig. 1. Here, the grain microstructure was found to include fine MC carbides with a few phosphide needles (Fig. 1a), while the grain boundaries contained coarse $M_{23}C_6$ and a few Laves particles (Fig. 1b). Although there was little or no evidence of precipitate-free zones near the grain boundaries, recrystallized regions were present that were precipitate free. Possibly, the recrystallization is part of the rupture process.

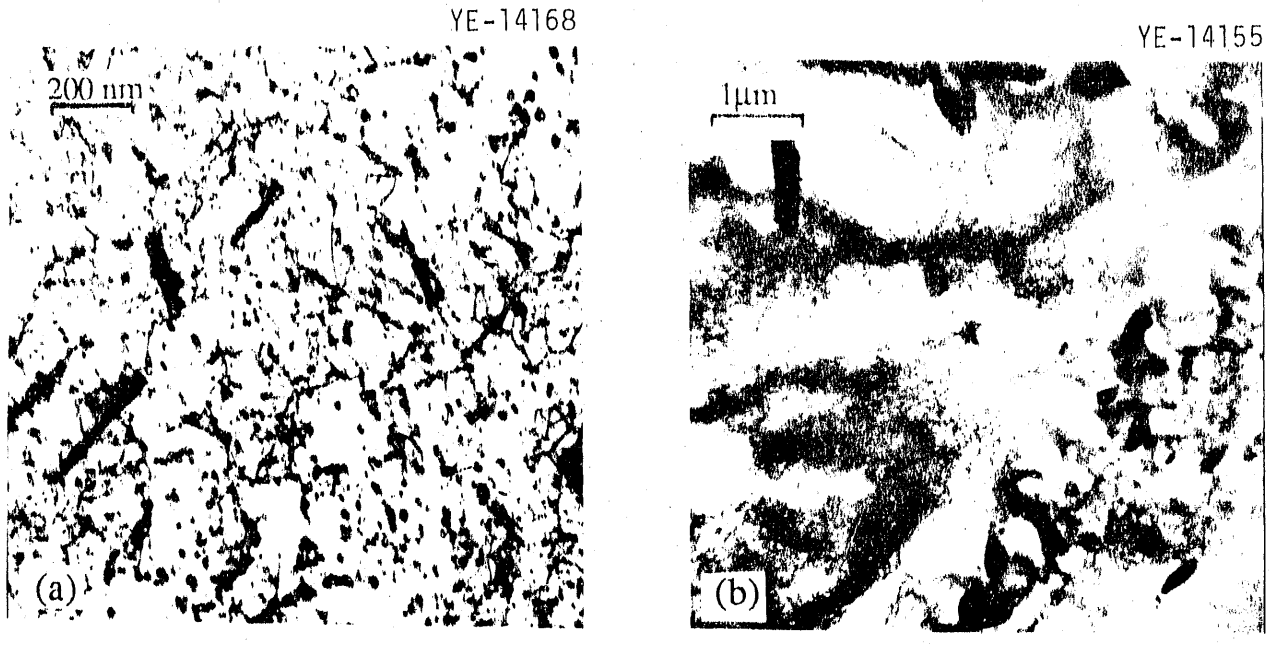

Fig. 1. Microstructure developed in a HT-UPS lean stainless steel after 18,750 h at 700 °C and 170 MPa: (a) matrix structure showing a fine MC precipitate and a few phosphide needles; (b) grain boundary region showing coarse carbides, a few Laves precipitates, and recrystallized regions emanating from the grain boundary.

Aging of the MC-forming steels has been studied by several investigators, and all steels showed loss of toughness as determined by impact testing (Izod, Charpy keyhole, and Charpy V-notch).[3, 4, 7, 13] Generally, the alloys retained impact energies equivalent to, or better than, type 316 stainless steel (>20 J). A few of the cold-worked HT-UPS alloys, however, produced energies closer to aged nickel base alloys (<10 J).

High Temperature Strength and Ductility

Larson-Miller parameter curves have been established to compare the relative strengths of the lean stainless steels. In the "annealed" condition, it was found that none of the alloys could meet the original alloy design criterion that called for an average rupture strength of 100 MPa for 100,000 h at 700 °C. Literature data suggested that small amounts of cold work could improve the strength of the FG347 stainless steel[3] and Esshete 1250.[13] Similar strength improvements were found in 17-14CuMo stainless steel tested at ORNL.[7] With small levels of warm or cold work the HT-UPS alloys were found to exceed the target strength level by a wide margin. Trends for the alloys are compared in Fig. 2a. The rupture ductilities of base metals were reported to be adequate for most of the base metals. The exception was 17-14CuMo stainless steel which was judged to be marginal with reduction of area values below 10% for some combinations of temperature and time.[7]

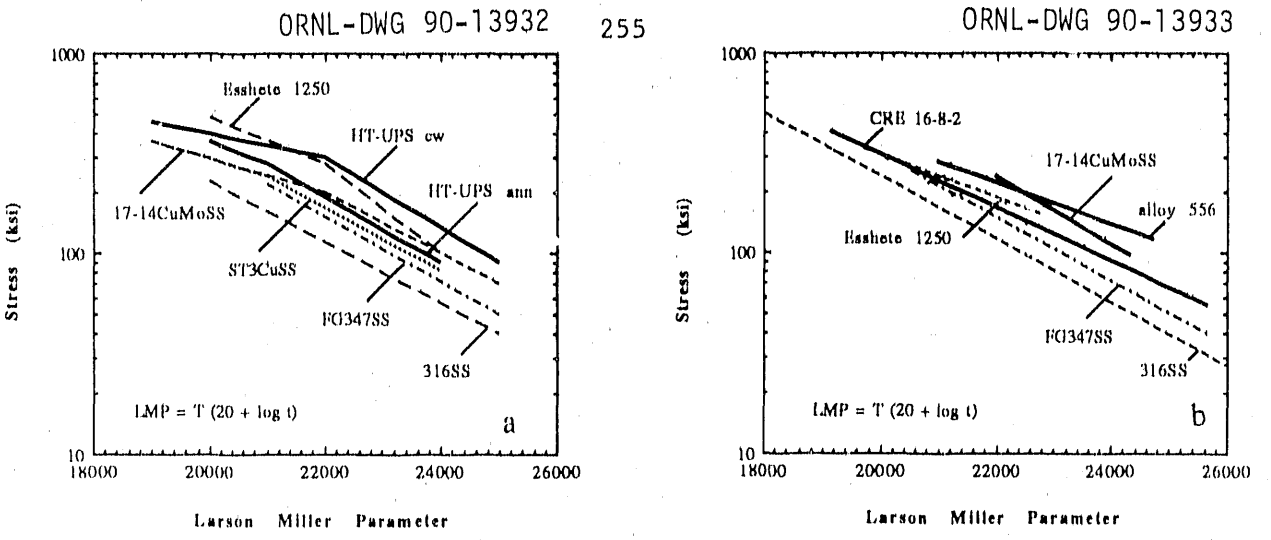

Fig. 2. Comparison of the rupture strength of lean austenitic stainless steels on the basis of log stress versus the Larson-Miller parameter: (a) base metal; (b) transverse weldments. Note that CRE 16-8-2, 17-14CuMoSS, and alloy 556 were filler metals in the HT-UPS weldments.

The performance of weldments in the lean stainless steels was examined under stress-rupture conditions. Literature data for FG347,[3] Esshete 1250,[16] and ST3Cu[4] stainless steels indicated that transverse weldments in these steels failed at strength levels within the scatterband for base metals. Since the filler metals for the HT-UPS were different than the base metal, however, a broad range of strengths was possible. Larson-Miller parameter curves were constructed from stress rupture tests on weldments of three filler metals, CRE 16-8-2 stainless steel, 17-14CuMo stainless steel, and alloy 556. In Fig. 2b these curves are compared to similar curves for type 316 stainless steel base metal, FG347 stainless steel weldments, ST3Cu stainless steel weldments, and Esshete 1250 weldments. Because of its good ductility compared to other filler metals, the CRE 16-8-2 stainless steel filler metal was selected for the HT-UPS steels. Tests on longitudinal weldments were also performed. Type 316 stainless steel plate specimens developed heat-affected zone (HAZ) cracks that propagated into both the weld metal and base metal. However, in HT-UPS AX8 no observable HAZ crack growth was detected. Efforts to grow HAZ cracks by fatigue testing of HT-UPS weldments at 650°C were also unsuccessful.

HIGH CHROMIUM ALLOYS

The high chromium austenitic alloys are those that contain 20 to 30% chromium, 20 to 35% nickel, and iron. Examples are 310 stainless steel and alloy 800H. There are many modifications to the alloys and new alloys of particular interest to the advanced austenitic alloy evaluation activity include Sumitomo HR3C®,[17] which is a modified type 310 stainless steel, and

Nippon Steel NF709®,[18] which is a modified 20Cr-25Ni steel. In addition, modifications to alloy 800H have been examined at ORNL[19] and Hitachi.[20] Typical compositions are identified in Table 2. Again, the new alloys contain MC formers, but some of the Japanese alloys also contain high nitrogen.

Table 2. Chemical compositions of several high chromium alloys (wt %)

Alloy	C	Si	Mn	Ni	Cr	Ti	Nb	V	Mo	P	B	S	N	Al	Fe
310SS	0.100	0.60	2.00	20.00	25.0										bal
HR3C	0.060	0.40	1.20	20.00	25.0		0.40			0.015		0.005	0.200		bal
NF709	0.070			25.22	20.1	0.06	0.27		1.56		0.004		0.180		bal
800H	0.080	0.24	0.90	31.90	19.5	0.42						0.003		0.43	bal
Hitachi m800H	0.065	0.50	1.00	34.20	23.2		0.39		1.24						bal
ORNL AX3 m800H	0.092	0.22	2.00	30.60	20.6	0.36	0.24	0.52	2.00	0.031	0.01	0.010	0.029		bal
ORNL BWT m800H	0.100	0.19	2.00	30.09	20.1	0.28	0.22	0.59	1.89	0.022		0.006			bal

Fabricability

All of the alloys have been produced as tubing, and the Japanese alloys have been placed in boilers. The ORNL-modified 800H alloys were produced by several fabrication routes including centrifugal casting and cold pilgering by Combustion Engineering and vacuum induction melting (VIM), hot extruding, and cold pilgering by Babcock & Wilcox.[10] Again, small amounts of cold or warm work were found to be beneficial in improving the strength of the modified alloy 800H.

Hot cracking has been a problem in the high chromium alloys, but successful procedures have been developed for the Japanese alloys.[17,18] Matching filler metal has been used with NF709 but the HR3C alloy has been welded with alloy 82 and alloy 625. In an effort to examine the characteristics of the HAZ, the filler metals selected for the ORNL-modified 800H included alloy 92, 17-14CuMo stainless steel, and alloy 556. Base metals that contained high phosphorous or high residuals exhibited extensive HAZ cracking but welds in VIM melted alloys were acceptable in regard to minimization of cracking. Extensive recrystallization and grain growth were observed in the HAZ, which suggested that significantly more work is needed in evaluating the weldability of the high chromium alloys.

Metallurgical Stability

Little is known about the metallurgical time-temperature-precipitation diagrams and phase stability of the high chromium alloys. Only $M_{23}C_6$ has been reported for the NF709 alloy[18] but the HR3C stainless steel contains MC as well as $M_{23}C_6$. The possibility of massive sigma formation is of concern at high temperatures, but sigma precipitation in the HR3C steel is suppressed by the high nitrogen content. The ORNL modified 800H is strengthened by the MC formation when hot or cold work has been introduced in the alloy.

Aging studies revealed that the high chromium alloys were embrittled at room temperature by the formation of $M_{23}C_6$ precipitates on the grain boundaries. Charpy impact values around 20 J were seen.

High-Temperature Strength and Ductility

Excellent strengths have been produced in the NF709 alloy and slightly cold-worked modified 800H alloys. Stress rupture test data to beyond 20,000 h have been summarized in Fig. 3 on the basis of log stress versus the Larson-Miller parameter. Here, it may be seen that all alloys have been strengthened relative to alloy 800H and that the slightly cold-worked ORNL modified 800H has a distinct strength advantage over all other alloys.

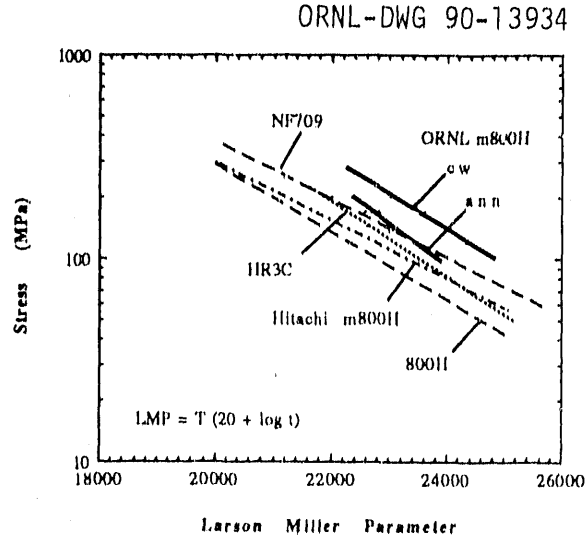

Fig. 3. Comparison of the rupture strength of high chromium alloys on the basis of log stress versus the Larson-Miller parameter.

More needs to be learned about the long-time creep ductility and room temperature embrittlement of the high chromium steels. To date the ORNL modified 800H alloys have shown excellent creep ductilities with reduction of area exceeding 40% for times beyond 20,000 h. The room-temperature impact energies are expected to be low, however, and values of about 20 J could be encountered after very long-time exposure.

The performance of weldments in stress rupture is another area of concern. The alloy 82 used for welding HR3C stainless steel is weak and embrittlement of alloy 625 filler metal is expected due to the formation of Ni_3Nb. Good rupture strength has been reported for the NF709 alloys, however.

NICKEL- BASE ALLOYS

For advanced steam cycle applications, nickel base alloys are of interest as claddings for the lean stainless steel and high chromium alloys. Typical claddings include Inconel 671® and Inconel 690®. All of the lean stainless steels have been clad by one process or another, and a full evaluation of cladding methods for the HT-UPS alloys is being undertaken by Topolski[10]. For hot gas cleanup systems the nickel base alloys of interest include RA333®, Haynes alloy 556®, and Inconel 617®. Since these are well developed commercial alloys, the research is being directed at producing the data needed for high temperature component design rather than optimization of chemistry or fabrication processes. Work being planned includes creep-fatigue, thermal-mechanical fatigue, and the development of parameters needed in design evaluations.

ALUMINUM-BEARING ALLOYS

Because of their low creep strength, the aluminum-bearing stainless steels such as RA85H® are of most interest as cladding, rather than tubing. The aluminides of most interest have been nickel base with chromium and iron additions. These have proven to be nonfabricable, nonweldable, and weak relative to the other alloy groups. Efforts on the nickel-base aluminides has been abandoned, and further work will be directed toward the iron-base alumindes. Research on the fabrication methods and performance of iron-aluminide clad products is in the planning stage.

SUMMARY

Research efforts are concluding on the evaluation of lean austenitic stainless steels for advanced steam cycle applications. It was found that excellent high-temperature strength can be produced when compositions and fabrication schedules are selected to promote the development of a fine stable MC precipitate. Progress has been made in understanding the limitations of the alloys in regard to weldability and long-time embrittlement. The assessment of the performance of this class of alloys in combustion environments and steam is an issue yet to be resolved.

Candidate high chromium alloys have been identified for advanced steam cycle service. The best strengths were found in niobium-bearing alloys such as NF709 and the ORNL modified alloy 800H. The evaluation of the long-time performance of weldments and the better understanding of potential embrittling mechanisms are yet to be accomplished.

REFERENCES

1. P. L. Rittenhouse, et al., *Assessment of Materials Needs for Advanced Steam Cycle Coal Fired Plants*, ORNL-6274, 1985.

2. R. W. Swindeman et al., *Alloy Design Criteria and Evaluation Methods for Advanced Austenitic Alloys in Steam Service*, ORNL-6274, May 1986.

3. H. Teranishi et al., "Fine Grained TP347H Steel Tubing with High Elevated Temperature Strength and Corosion Resistance for Boiler Applications," paper 33-1 in *Second International Conference on Improved Coal Fired Power Plants*, EPRI publication GS-6422, 1989.

4. Sumitomo Metal Industries, Ltd., *Properties of High Strength ST3Cu Austenitic Stainless Steel Tubing for Boiler Application*, document 808 F-No 1858, 1988.

5. P. J. Maziasz, "Developing an Austenitic Stainless Steel for Improved Performance in Fossil Power Facilities," *J. Met.* 41, 14-20 (1989).

6. H. A. Domian and S. E. LeBeau, *Literature Review of Workability and Phase Stability Relative to Advanced Austenitic Alloys in Steam Service*, Report No. ORNL/SUB/88-SB775/01, Babcock & Wilcox, Alliance, Ohio, 1989.

7. R. W. Swindeman et al., *Evaluation of Advanced Austenitic Alloys Relative to Alloy Design Criteria for Steam Service- Part 1- Lean Stainless Steels*, ORNL-6629, May 1990.

8. S. E. LeBeau, *Production of Small Heats of Austenitic Tubing- Final Report CRD#1191*, Babcock & Wilcox report RDD;89:4423-01-01:01, Alliance, Ohio, 1988.

9. R. A. Carolan et al., "Effect of Copper on the Strength of AISI 316 Stainless Steel," *Metall.Trans.* 20A, 421-29 (1989).

10. M. Topolski, Babcock and Wilcox Company letter report to R. W. Swindeman, Oak Ridge National Laboratory, May 1, 1990.

11. C. D. Lundin et al., *The Hot Ductility and Hot Cracking Behavior of Modified 316 Stainless Steels Designed for High Temperature Service*, University of Tennessee Report No. ORNL/Sub/88-07685/01, 1989.

12. Y. Minami, H. Kimura, and M. Tanimura, "Creep Rupture Properties of 18%Cr-8%Ni-Ti-Nb and Type 347H Austenitic Stainless Steels," pp. 231-40 in *New Developments in Stainless Steel Technology*, American Society for Metals, Metals Park, Ohio, 1986.

13. J. D. Murray, J. Hacon, and P. H. Wannell, "The High Temperature Properties of an Advanced Austenitic Steel: Esshete 1250," pp. 403-25 in *High Temperature Properties of Steels*, Publication 97, Iron and Steel Institute, London, 1967.

14. H. Kimura and Y. Minami, "The Effect of Cu Additions on the Creep Rupture Strength of 17Cr-14Ni-Cu-Mo Stainless Steel," pp. 221-28 in *Proceedings, International Conference on Creep*, Japan Society of Mechanical Engineers, Tokyo, Japan, 1986.

15. J. A. Todd and J-C. Ren, *Microstructural Studies of Advanced Austenitic Steels*, University of Southern California report number ORNL/Sub/19X-SA663C, 1989.

16. E. Lister, J. Micklerath, and A. Higgenbottom, "High Temperature Properties of Steampipe Welds," pp. 474-81 in *High Temperature Properties of Steels*, Publication 97, Iron and Steel Institute, London, 1967.

17. Sumitomo Metal Industries, *Characteristics of a New Steel Tube (HR3C) with High Elevated Temperature Strength and High Corrosion Resistance for Boiler*, December 1987.

18. T. Takahashi et al., "Development of a High Strength 25Ni-20Cr Steel for Tubes in Ultra Supercritical Power Boilers," paper 41-1 in *Second International Conference on Improved Coal Fired Power Plants*, EPRI publication GS-6422, 1989.

19. R. W. Swindeman et al., *Procurement and Screening Test Data for Advanced Austenitic Alloys for 650 °C Steam Service (Part 2, Final Report)*, ORNL/TM-10206/P2, April 1988.

20. H. Doi et al., "Effects of Nb and Mo on Creep Rupture Strength of 23Cr-34Ni Iron Base Alloy," pp. 227-32 in *Proceedings, International Conference on Creep*, Japan Society of Mechanical Engineers, Tokyo, Japan, 1986.

METALLURGICAL EFFECTS ON THE FLOW PROPERTIES OF MODIFIED AUSTENITIC ALLOYS

P.D. Ferro, R.D. Black, Che-Yu Li

Department of Materials Science and Engineering
Cornell University, Ithaca NY 14853

ABSTRACT

Creep and load relaxation data of Cu-modified type 316 alloys are reported. Cu content is found to affect creep hardening and work hardening properties of these alloys. Grain structure for plate and tube heats heats of modified alloy 800H is shown to be correlated with high-temperature flow strength.

INTRODUCTION

Refractory metals additions have been shown to be effective in improving the flow strength of austenitic alloys at elevated temperatures [1]. In the case of lean austenitic alloys such as AISI Type 316 stainless steel, the further modification by the addition of copper is found to exhibit a synergistic effect with the refractory metals addition to further improve the flow strengths of these alloys [2]. In general, it has been shown that the grain size plays an important role in governing the flow strength of austenitic alloys at strain rates in the creep range [3].

In this work, we have investigated the effect of copper content on the creep hardening and work hardening properties of modified type 316 alloys, CE3 and AX7. Creep hardening represents hardening which occurs during constant load creep. Work hardening, in this case, represents hardening which occurs during constant displacement rate tensile loading. Creep and load relaxation data for the two alloys, CE3 and AX7, are discussed in this paper.

Progress has been made in understanding the role of grain size on the high-temperature flow strength of modified 800H. Evidence of a grain growth rate difference between AX3 and X-3891 heats is shown.

EXPERIMENT

Specimen Preparation

Compositions of materials that were creep and load relaxation tested are listed in Table 1.

Alloy CE3, a modification of AISI 316 steel, was received from Oak Ridge National Laboratory in plate form in the mill-annealed condition. The plate was cold rolled, with intermediate anneals at 1100C until a sheet of 0.8mm final thickness was produced. Load relaxation specimens were machined from the rolled sheet such that the tensile axes of the specimens were parallel to the final rolling direction. Specimens had a nominal gage width of 3.6mm and a nominal gage length of 12.7mm.

Alloy AX7, a modification of AISI 316 steel, was received from Oak Ridge National Laboratory in the same form as that described above for CE3, and processed in the same manner to obtain load relaxation test specimens.

Alloy AX3, a modification of alloy 800H, was also received and processed in the same manner as that described for CE3 in order to obtain load relaxation test specimens.

Modified alloy 800H heat X-3891 was received in superheater tube form. The tube had a nominal 63mm outside diameter and a nominal 7.5mm wall thickness. A section of the tube was sliced, and hot rolled (1100C) in the axial direction to 0.8mm thickness. Load relaxation test specimens were machined from the rolled sheet such that the tensile axes of the specimens were parallel to the rolling direction of the sheet.

Mechanical Testing and Data Analysis

Creep testing was performed at Oak Ridge National Laboratory. Constant load creep tests were performed in air on specimens in the mill-annealed condition. Linear voltage displacement transducer (LVDT) gauges were used to measure strain. Tests were performed at 700C and at initial applied stresses of 140, 170 and 190/200MPa.

The details of the principles of the load relaxation test can be found in other papers [4,5]. Load relaxation testing was performed in a universal testing (Instron) machine by loading a specimen in tension at a constant displacement rate of 0.25mm/minute to a predetermined level of plastic strain, and then fixing the cross-head of the test machine. Load relaxation occurs by conversion of the elastic strain in the

test system, including the specimen, into plastic strain in the specimen. The tests were performed in air at 700C. The data are presented as log(stress) vs. log(inelastic strain rate), and are referred to as flow curves.

Grain Structure

The dependence of grain size on heat treatment time and temperature variables was investigated for AX3 and X-3891.

TABLE 1. Compositions of alloys (wt. pct.)

	AX3	X-3891	AX7	CE3
Cr	20.60	20.85	14.2	14.53
Ni	30.60	31.08	16.0	16.18
Al	0.00	0.02	---	0.03
Mo	2.00	1.99	2.48	2.41
Cu	0.00	0.03	1.50	1.96
P	0.03	0.003	0.073	0.071
B	0.01	0.007	0.005	0.007
N	0.03	0.010	0.024	0.0120
V	0.52	0.47	0.53	0.56
Ti	0.36	0.29	0.18	0.27
Mn	2.00	1.93	1.65	1.75
S	0.01	0.013	0.008	0.008
Si	0.22	0.24	0.21	0.21
Nb/Ta	0.24	0.20	0.15	0.11
C	0.09	0.095	0.073	0.086
Fe	bal.	bal.	bal.	bal.

Coupons of dimensions 1cm x 2cm were cut from the laboratory (AX3) and tube heat (X-3891) rolled materials, and subjected to a range of solution treatment times and temperatures. Table 2 gives, in matrix form, the solution treatment times and temperatures along with corresponding grain sizes for AX3 and X-3891. Polished coupons and load relaxation test specimens were immersion etched for 10 minutes in an etchant solution of 50ml HCl- 25ml HNO_3- 25ml H_2O, and water rinsed. Polaroid photomicrographs were obtained for grain structures at 50x. The lineal intercept method [6] was used to determine average grain size.

RESULTS AND DISCUSSION

Effect of Cu Content on Creep Hardening and Work Hardening Properties of Modified Type 316 Stainless Steel

Figures 1 through 3 compare 700C creep data of CE3 and AX7 at applied stress levels of 140, 170, and 190/200MPa. The data shows that AX7 has a lower secondary creep rate at 700C

than CE3, for a range of applied stresses. In the initial stage of creep (shown in figs. 1-3 inserts), AX7 shows a relatively high creep rate and creep hardens relatively quickly, resulting in a relatively low secondary creep rate. On the other hand, CE3 shows a relatively low initial creep rate, but does not creep harden as much as AX7.

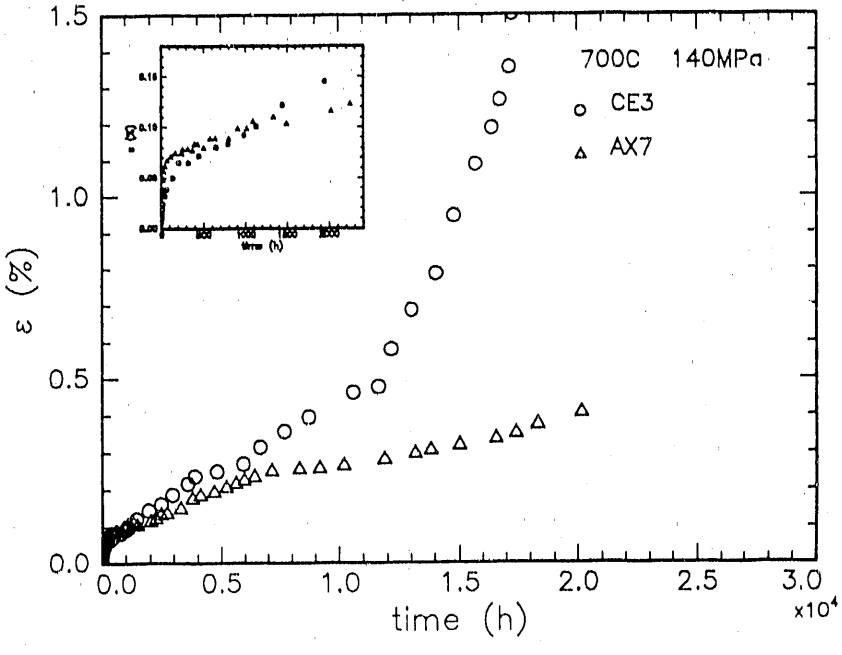

Figure 1. 700C creep data for CE3 and AX7 at an initial applied stress of 140MPa.

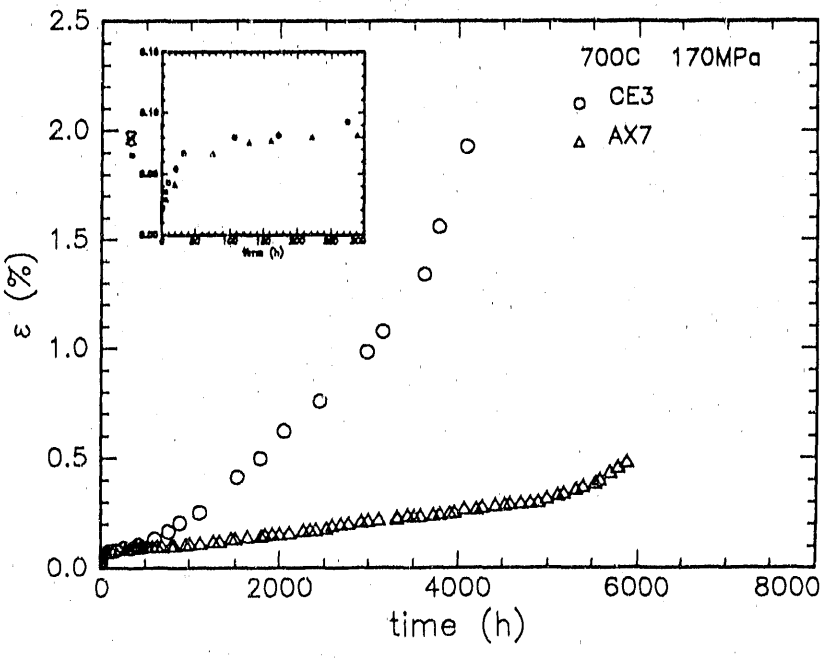

Figure 2. 700C creep data for CE3 and AX7 at an initial applied stress of 170MPa.

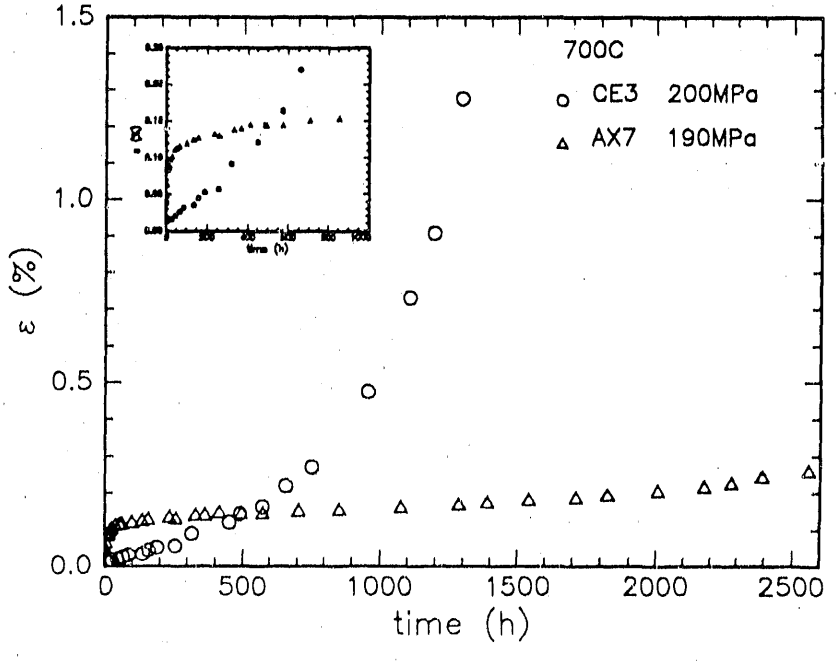

Figure 3. 700C creep data for CE3 and AX7 at initial applied stresses of 200 and 190MPa respectively.

Figures 4 and 5 show 700C load relaxation data of CE3 and AX7 respectively. Both specimens received a thermo-mechanical pre-treatment which consisted of one hour at 1150C, 5% cold work, and two days at 850C. Flow curves for plastic strain levels of 0.2, 2, and 5% are shown in figures 4 and 5. AX7 shows a wider stress level separation between flow curves obtained at different plastic strain levels than does CE3. The wider stress level separation between flow curves shown by AX7 is an example of evidence of a strong work hardening ability for this alloy.

In austenitic alloys, copper is believed to increase the stacking fault energy [2], with the resulting effect of decreasing the width of dislocations. The copper addition in austenitic alloys acts synergistically with refractory metals additions, to improve the flow strength through enhanced MC carbide precipitation. The difference in creep strength between CE3 and AX7 suggests that there is an optimum level of copper content. Apparently in the case of CE3 (relatively high Cu content) in the mill-annealed condition before creep testing, and in the cold worked and stabilization aged condition before load relaxation testing, the alloy is already quite strong as indicated by its decreased ability to creep harden (figures 1-3) and to work harden (figures 4 and 5) as compared with AX7.

For AX7, in the mill-annealed condition before creep testing, and in the cold worked and stabilization aged condition before load relaxation testing, the alloy is not as strong as CE3. During the initial stage of creep, a greater amount of dislocations (relative to CE3) are generated, which are pinned by MC carbides, resulting in significant creep hardening and in a relatively low secondary creep rate. The strong ability of AX7 to creep harden is consistent with its higher ability to work harden as shown by the data in figures 4 and 5.

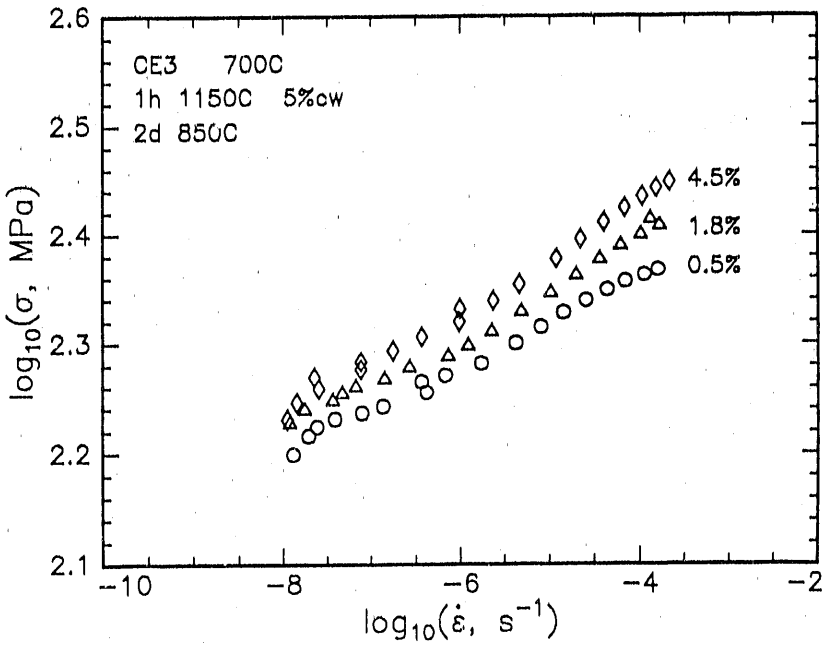

Figure 4. 700C load relaxation data for CE3.

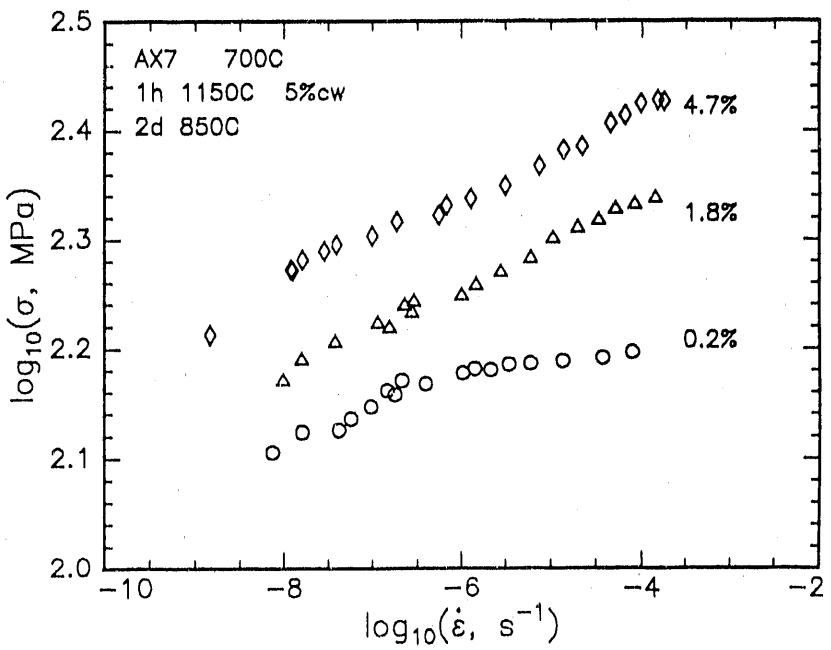

Figure 5. 700C load relaxation data for AX7.

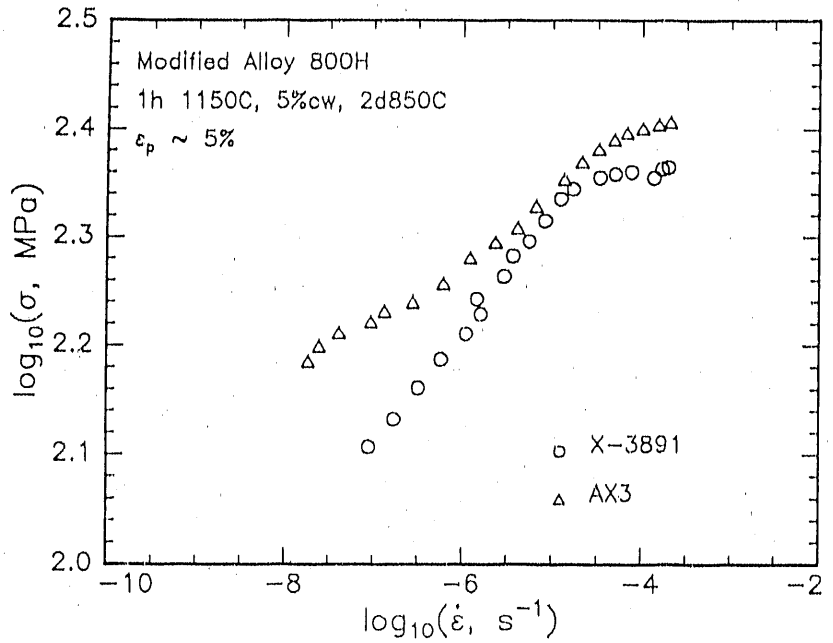

Figure 6. 700C load relaxation data for AX3 and X-3891 heats of modified alloy 800H. Plastic strain prior to relaxation was nominally 5%.

Grain Structure

Figure 6 shows typical 700C load relaxation results for the AX3 and X-3891 heats of modified alloy 800H. The load relaxation data in figure 6 are for AX3 and X-3891 specimens which were solution treated for one hour at 1150C, cold worked 5% in tension at a constant displacement rate of 0.25mm/minute, and stabilization aged for two days at 850C. Plastic strain prior to relaxation was nominally 5% for both specimens.

The average grain size for AX3 and X-3891 coupons in the 1h 1150C solution treated condition was 55 microns (ASTM 5.4) and 58 microns (ASTM 5.2) respectively. After load relaxation testing for approximately 72h at 700C, the average grain size of AX3 and X-3891 load relaxation test specimens was 71 microns (ASTM 4.7) and 57 microns (ASTM 4.9) respectively. Figures 7a and 7b show post-test photomicrographs of lab heat and tube heat specimens, taken at 50x. AX3 apparently has a faster grain growth rate, under stress at 700C, compared with X-3891.

Table 2. Grain growth data for AX3 and X-3891.

heat	sol'n.(°C)	time	avg g.s (μm)	ASTM
AX3	1100	1h	40	6.3
AX3	1125	1h	55	5.4
AX3	1150	1h	55	5.4
AX3	1175	1h	58	5.2
AX3	1200	1h	108	3.5
X-3891	1100	1h	55	5.4
X-3891	1125	1h	36	6.7
X-3891	1150	1h	58	5.2
X-3891	1175	1h	55	5.4
X-3891	1200	1h	data not available	
AX3	1100	4h	42	6.2
AX3	1125	4h	42	6.2
AX3	1150	4h	98	3.8
AX3	1175	4h	108	3.5
AX3	1200	4h	40	6.3
X-3891	1100	4h	70	4.7
X-3891	1125	4h	73	4.6
X-3891	1150	4h	79	4.4
X-3891	1175	4h	73	4.6
X-3891	1200	4h	70	4.7

The effect of large grain size in suppressing grain boundary sliding is indicated by the high flow strength at low strain rates during load relaxation testing, as shown by the load relaxation data for AX3 in figure 6. The S-shaped flow curve for AX3 is representative of plastic deformation involving grain boundary sliding [7]. It is believed that the grains in AX3 grow quickly during load relaxation testing to produce the grain structure shown in figure 7a, resulting in the flow strength behavior shown in figure 6.

Table 2 summarizes the thermo-mechanical treatment matrix used in the present investigation. The table includes solution treatment time and temperature information, and corresponding grain size for each of the two materials tested. Trends in the grain size data support the conclusion that AX3 has a faster grain growth rate than X-3891. The low grain growth rate of the tube material may be related to the cleanliness of the heat, and to the presence of minor tramp elements which are not controlled.

Figure 7a. Grain structure (50x) of an AX3 specimen after load relaxation testing for approximately 72h at 700C. Thermo-mechanical treatment prior to testing included 1h at 1150C, 5% cold work, and 2d at 850C.

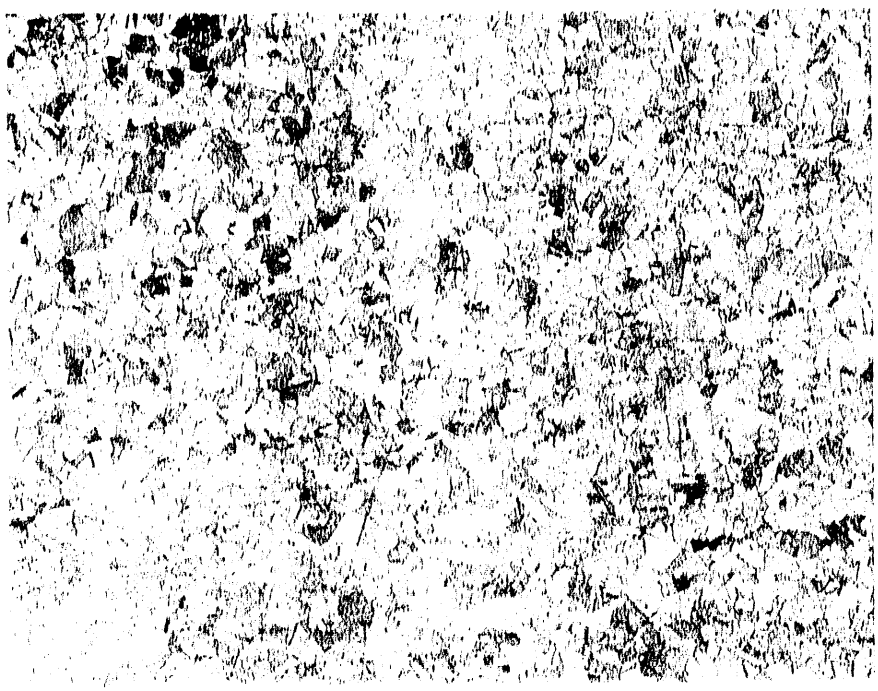

Figure 7b. Grain structure (50x) of an X-3891 specimen after load relaxation testing for approximately 72h at 700C. Thermo-mechanical treatment prior to testing included 1h at 1150C, 5% cold work, and 2d at 850C.

CONCLUSIONS

Copper content is found to strongly affect the creep hardening and work hardening ability of modified type 316 stainless steel, as evidenced by comparing creep and load relaxation data of alloys with different copper levels. Differences in grain size can cause large differences in flow strength at low strain rates at temperatures near $0.5T_m$. The grain growth rate of modified alloy 800H is observed to be affected by manufacturing processing schedule; the presence of (uncontrolled) tramp elements may be responsible for observed differences in grain growth rate found in laboratory heat (AX3) and tube heat (X-3891) materials.

REFERENCES

1. P. Marshall, Austenitic Stainless Steels; Microstructure and Mechanical Properties, Elsevier, London, England (1984), pp. 48-49.

2. R. Carolan, C.-Y. Li, P.J. Maziasz, R.W. Swindeman, J.A. Todd, J.-C. Ren, "Effect of Copper on the Strength of AISI 316 Stainless Steel", Met. Trans. 20a (1989), pp. 421-429.

3. P.D. Ferro, B.D. Coulombe, C.-Y. Li, "Mechanical Properties and Microstructural Stability of Advanced Austenitic Alloys", ORNL/FMP-89/2 (1989), p. 239.

4. D. Lee, E.W. Hart, Met. Trans. v. 2 (1971), p. 1245.

5. M.A. Korhonen, S.-P. Hannula, C.-Y. Li, "State Variable Theories Based on Hart's Formulation", Unified Constitutive Equations for Creep and Plasticity, A.K. Miller, ed., Elsevier Applied Science, London and New York (1987), p. 1559.

6. ASTM E112-85, Standard Methods for Determining Average Grain Size (1985), p. 138.

7. C.H. Wilson, "Grain Boundary Sliding Phenomena in Polycrystalline Solids", Cornell University, Ph.D. thesis (1989).

INVESTIGATION OF WELDING AND JOINING TECHNIQUES FOR ADVANCED AUSTENITIC ALLOYS

C.D. Lundin, C.Y.P. Qiao, Y. Kikuchi and C.C. Chen

Materials Joining Research
Materials Science and Engineering
The University of Tennessee, Knoxville, TN 37996-2200

ABSTRACT

The weldability of modified 316, modified 800H, Haynes HD556 and Inconel 617 alloys were evaluated using the Varestraint Hot Cracking Test and compared to that of nuclear grade 316 stainless steels. Generally, the modified 316 and modified 800H alloys showed appreciably lower hot cracking resistance than the nuclear grade austenitic stainless steels whereas the Haynes HD556 and Inconel 617 showed a similar level of the hot cracking resistance to the nuclear grade austenitic stainless steels. Microstructural examination and EDAX analysis were conducted in order to rigorously characterize the hot cracking behavior in these alloys and some typical test results are presented. The base metal HAZ liquation behavior was emphasized and the test results reveals that the base metal HAZ liquation cracking tendency in modified 316 and modified 800H materials was enhanced due to the alloying and impurity element segregation at the grain boundaries.

INTRODUCTION

Development of high-strength austenitic alloys to meet the requirements of modern power plant heater and reheater systems (650 ^{o}C, 35 MPa) has been aggressively promoted in Japan, Europe and The United States. Extensive research has been conducted by DOE, through the AR & TD Fossil Energy Program managed by ORNL in US recent years where several candidate alloy systems were developed. Evaluation of the mechanical properties, metallurgical stability at elevated temperature, corrosion resistance and fabricability are being conducted through this program.

The weldability and joining technique studies for candidate austenitic alloys are being conducted at The University of Tennessee as a part of the overall program. Weldability and heat-affected-zone sensitization of candidate materials have been evaluated and reported in

prior Fossil Energy Program reports. Recently, weldability evaluation of the newly provided modified 316 and 800H, Haynes HD556 and Inconel 617 heats was completed. Preliminary studies involving microstructural analysis of the fusion zone and heat-affected-zone were also completed. Quantitative studies on the relationship between minor alloy elements and heat-affected-zone hot cracking behavior have been initiated in order to precisely characterize and thus improve the weldability of candidate materials.

DISCUSSION OF CURRENT ACTIVITIES

The base metal weldability response, filler metal development, transition joint behavior and weld metal and HAZ corrosion behavior are four specific tasks in the weldability assessment for the alloys under study. Among them, extensive hot cracking resistance evaluations on the modified 316, Reference 316, 17-14 CuMo, modified 800H, Haynes HD556 and Inconel 617 have been conducted by means of the Varestraint Hot Cracking Test, Sigmajig Hot Cracking Test, Finger Hot Cracking Test and Gleeble Hot Ductility Test. The evaluation of the corrosion behavior of these alloys is completed, and the filler metal development and transition joint behavior studies are in progress. Multiple heats of modified 316 and modified 800H materials with various alloying element adjustments (mainly P, S, C, Nb and W) have been tested in the current period. The Varestraint test results and the comparative weldability studies are emphasized in this report.

The chemical composition of the materials evaluated are listed in Table 1. Generally, three groups of the modified 316 are; higher P+S, higher P+S plus added Cu, and lower P+S but with higher C. Two groups of the modified 800H differ with higher P+S and lower P+S plus higher C. A single heat of Haynes HD556 (developed by Haynes International Corporation) and Inconel 617 (developed by the Huntington Alloy Products Division of the International Nickel Company) for high temperature applications were used for hot cracking and comparative studies. In order to determine the exact chemical composition of the tested Varestraint specimens, chemical check samples were extracted from the

Table 1. Chemical Composition of the Materials studied

Materials and Heat No. / Element	Modified 316 A48*CE1890	Modified 316 L1168W	Reference 316	Modified 316 BWS470	Modified 316 BWS478	Modified 316 BWS479	Modified 800H A42*CE1891	Modified 800H BWS480	Modified 800H V888-1	Hastel. HOS56 B556571H5	Inconel 617 X4184A61H
C	0 079	0 085	0 057	0 077	0 098	0 087	0 097	0 10	0 10	0 11	0 06
Si	0 27	0 11	0 58	0 23	0 22	0 24	0 24	0 31	0 19	0 49	0 18
Mn	1 77	1 86	1 86	2 19	1 61	1 22	1 91	1 74	2 00	1 70	0 02
Ni	16 87	15 59	13 48	15 90	16 58	16 72	31 08	29 02	30 09	19 44	55 13
Cr	14 29	14 22	17 25	15 45	16 07	16 24	20 85	19 48	20 13	21 39	21 74
Ti	0 21	0 12	0 02	0 33	0 34	0 36	0 39	0 42	0 28	-	-
Nb	0 10	0 19	<0 01	0 16	0 14	0 14	0 20	0 19	0 22	0 76*	-
V	0 52	0 51	-	0 82	0 82	0 90	0 47	0 77	0 59	-	-
Mo	2 27	2 21	2 34	2 56	1 24	1 26	2 01	1 32	1 83	2 72	8 91
P	0 040	0 028	0 024	0 010	0 010	0 009	0 003	0 011	0 022	-	-
S	0 010	0 004	0 019	0 006	0 004	0 004	0 013	0 004	0 006	<0 005	0 002
N2	0 012	0 0082	0 03	0 0083	0 0022	0 0074	0 010	0 011	-	-	-
O2	-	-	-	0 0046	0 022	0 0033	-	0 004	-	-	-
Cu	0 02	<0 05	0 1	2 78	<0 05	<0 05	0 03	<0 05	-	-	-
B	0 006	0 005	0 005	0 008	0 007	0 007	0 007	-	-	-	-
Al	0 006	0 016	0 021	-	0 042	0 031	0 02	0 056	-	0 76	1 11
W	-	-	-	-	1 95	2 13	-	1 80	-	2 08	-
Co	<0 01	-	0 02	-	-	-	0 01	-	-	19 08	12 32
La	-	-	-	-	-	-	-	-	-	0 010	-
Fe	Bal	Bal	Bal	Bal	Bal	Bal	Bal	Bal	Bal	Bal	0 53

*Nb + Ta

actual Varestraint test specimens and duplicate analyses were conducted at B&W. These check analysis showed some differences in carbon content and these may be significant in the behavior of the experimental heats.

Hot Cracking

Varestraint hot cracking tests were conducted on a modified subscale moving torch Tig-A-Ma-Jig device.

Fusion Zone Hot Cracking Test Results

Fusion zone cracking is usually regarded as solidification cracking which is related to the solidification mode (Ferrite potential and primary solidification mode are considered as the most important factors which can affect the solidification cracking resistance in austenitic stainless steels). Usually, to obtain a higher fusion zone hot cracking resistant for austenitic stainless steels the existence of about 5% ferrite (5FN) is required. However, the existence of ferrite alone does not necessarily ensure good weldability. In particular, the location of ferrite and the sequence of ferrite and austenite formation appear to be the dominant factor in determining weldability. Since the ferrite

potential for the modified austenitic stainless steels is negative, it is expected that modified 316 and modified 800H will possess a tendency toward fusion zone hot cracking. A higher hot cracking tendency for the modified austenitic alloys is enhanced by the addition of alloy elements such as Nb, Ti and V, higher C and high P+S all of which are generally recognized to reduce the hot cracking resistance in austenitic stainless steels.

The fusion zone hot cracking tendency has been characterized in terms of total crack length and maximum crack length by the Varestraint test. The fusion zone hot cracking test results on modified 316 and modified 800H are shown in Figures 1 and 2. It is evident that higher carbon heats of modified 316 (BW5478 and BW5479) and modified 800H (BW5780) [even with a reduced P+S content as contrasted to the initial modified 316 heat (AX6/CE3890) and modified 800H heat (AX2/CE3891)] showed a hot cracking tendency similar to those with high P+S heats. Modified 316 with high Cu and low carbon (heat BW5470) falls at the lower bound of hot cracking in the modified materials. Thus an increase in Cu content to about 3% does not significantly affect hot cracking resistance for modified 316 materials but carbon apparently plays an important role in hot cracking resistance.

The Varestraint hot cracking evaluation on Haynes HD556 and Inconel 617 alloys has been completed. The purpose of the evaluation of these alloy was to compare with the modified 316 and modified 800H materials and to define an alloy for use as a filler metal which has an optimum combination of elevated temperature mechanical properties and weldability. The mechanical properties and high temperature aging stability including creep, tensile and aging, of these alloys were evaluated and reported by McCoy and King at Oak Ridge National Laboratory [1, 2]. The fusion zone hot cracking behavior of Haynes HD556 and Inconel 617 is shown in Figure 3. It should be noted that these materials are far less hot crack sensitive than the modified alloys.

To interpret the behavior of solidification hot cracking, several mechanisms have been proposed. In a study of the weldability of fully austenitic 310S stainless steels Matsuda et al. [3] pointed out that the

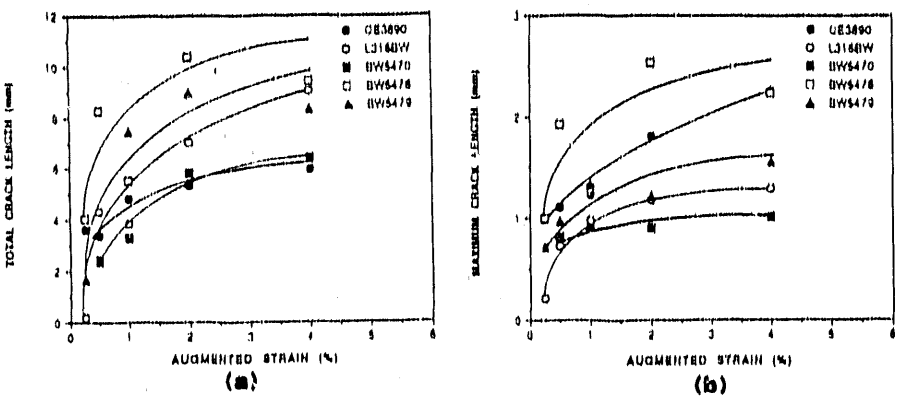

Figure 1. Fusion zone hot cracking behavior of the modified 316 stainless steels in the Varestraint test. (a) Total crack length as a function of augmented strain; (b) Maximum crack length as a function of augmented strain.

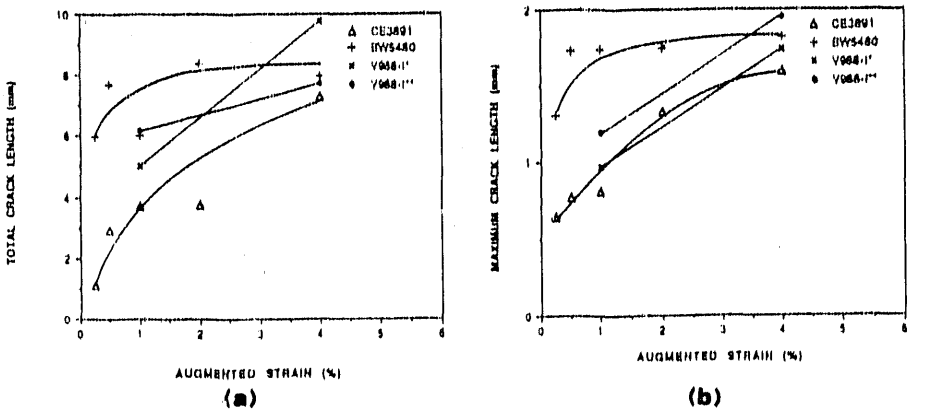

Figure 2. Fusion zone hot cracking behavior of the modified 800H materials in the Varestraint test. (a) Total crack length as a function of augmented strain; (b) Maximum crack length as a function of augmented strain.

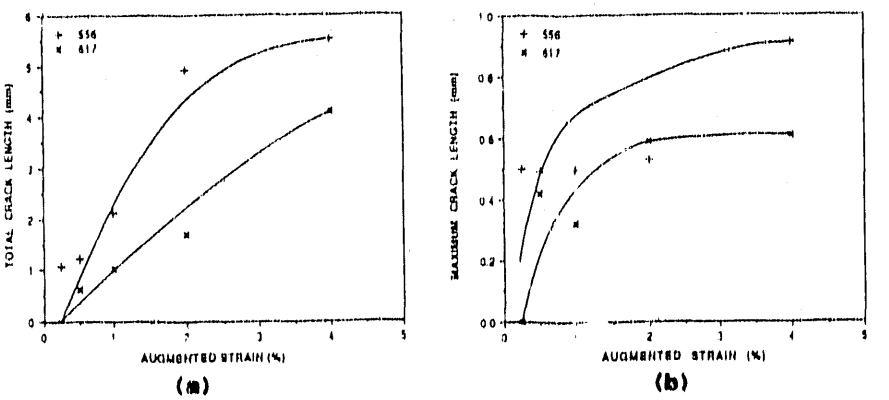

Figure 3. Fusion zone hot cracking behavior in the Haynes HD556 and Inconel 617 materials. (a) Total crack length as a function of the augmented strain; (b) Maximum crack length as a function of augmented strain.

rejection of alloying elements and impurities into the residual liquid adjacent to the solid-liquid interface for a primary austenitic solidification in stainless steels is greater than for a primary ferritic solidification. The enrichment in impurities and alloying elements in the residual liquid between the dendrites may significantly lower the residual liquid melting temperature. Therefore, residual liquid between the dendrites may be present to relatively low temperatures (just below bulk solidus). Moreover, the grain boundaries can remain pinned by the residual liquid, although grain boundary migration does occur in the regions where solid bridging has occurred. The length of the dendrites is dependent on many factors. The lower the segregation coefficient of the alloying elements and impurities in the iron-chromium-nickel stainless steel systems, the more segregation may occur. This will cause a decrease in the solidus temperature of residual liquid and, therefore, the length of the dendrites will increase. Based upon the above, the length of the dendrites, which co-exist with the residual liquid beyond the solid-liquid interface, is generally longer during fully austenitic solidification as contrasted to that during primary ferritic solidification. In addition, the occurrence of residual liquid at a pinned grain boundary during solidification in the fully austenitic stainless steels can enhance crack propagation.

SEM and EDAX were used to further characterize the influence of the solidification mode and alloy/impurities elements on hot cracking behavior. Figure 4 shows an SEM micrograph of the fusion zone structure in modified 316 (BW5470) (Varestraint test sample). Clear evidence of cracks which initiated at and propagated along the dendritic boundaries is indicated. It can be predicated that cracks will form during solidification if the residual liquid is not sufficient to fill the space between the dendrites caused by shrinkage during solidification. This region is enlarged by the augmented strain in the Varestraint test. The crack tip shown at A in Figure 4 (a) is more clearly seen in Figure 4 (b). The evidence shown by the discontinuous nature of the crack indicates that the liquid along the dendrites was not connected to the weld pool and liquid metal bridges between the crack surfaces prevent

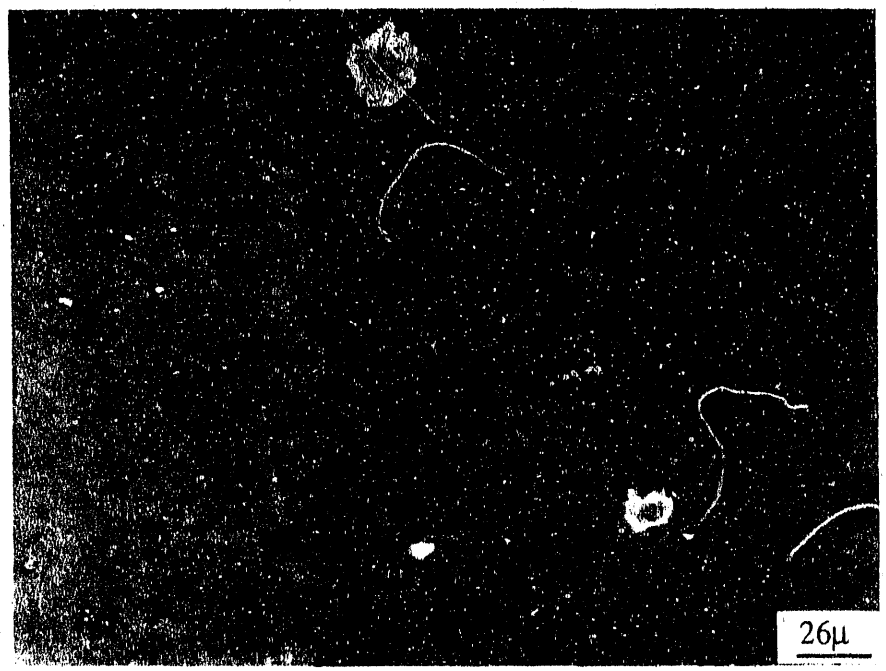

(a)

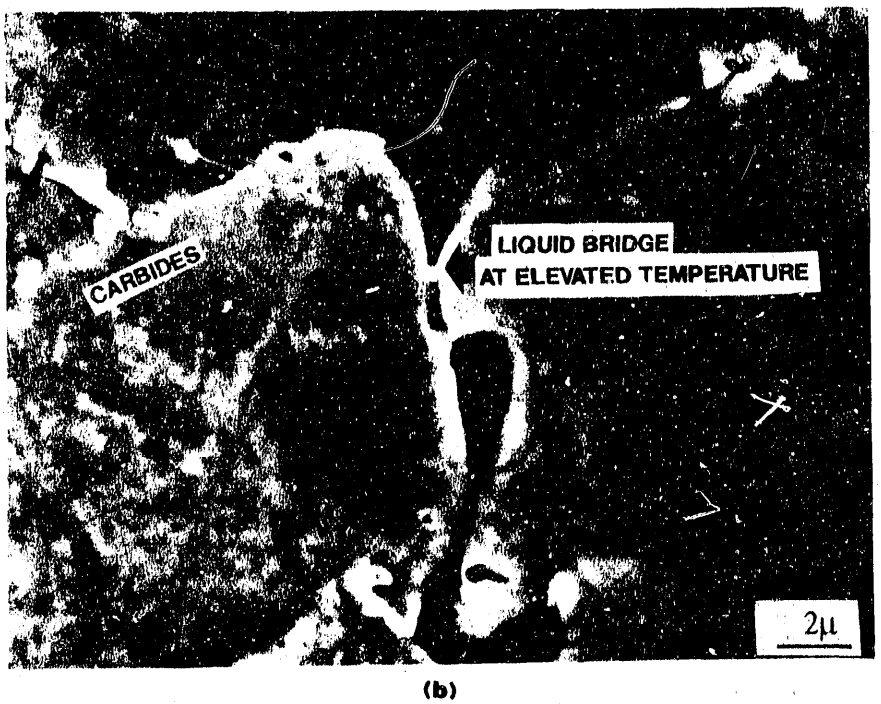

(b)

Figure 4. SEM photomicrograph of the fusion zone hot cracking in the modified 316 (BW5470) stainless steel. (a) Fusion zone hot cracking morphology; (b) Higher magnification from location A in Figure 4 (a)

liquid flow at the time of crack formation (see arrows in 4 (b)). The precipitates at crack tip are Mo, Nb, Ti and V rich. In this sample, the Cu content in the region near the grain boundary is slightly higher than in the matrix. However, evidence of a detrimental influence of Cu on fusion zone hot cracking behavior was not observed. No evidence of S and P segregation along the grain boundaries was detected in this sample. However, the EDAX results from modified 316 (AX6/CE3890) showed segregation of S and P in the cellular dendritic boundaries.

Base Metal HAZ Hot Cracking Behavior

Base metal HAZ cracking behavior is of concern in developing a new alloy since filler metal adjustments can significantly affect the base metal HAZ behavior. The Varestraint test criteria; maximum crack length (MCL), total crack length (TCL) and cracked HAZ length (CHL) are employed to evaluate and explain base metal HAZ hot cracking behavior. The base metal HAZ hot cracking behavior for the materials tested is shown in Figures 5 - 7.

It is clear that the higher carbon modified 316 (BW5478 and BW5479) and modified 800H (BW5480) showed the lowest base metal HAZ hot cracking resistance. Haynes HD556 and Inconel 617 showed the highest base metal HAZ hot cracking resistance. Modified 800H (V988-1) material showed intermediate base metal HAZ hot cracking resistance. However, only two Varestraint test specimens for modified 800H (V988-1) were available for each cold worked condition. Therefore, only two strain levels (1% and 4%) were used in Varestraint testing of this heat.

Liquation during thermal exposure in the HAZ is commonly used to explain HAZ hot cracking. Grain boundary liquation can be enhanced by the "sweep up" phenomenon related to grain boundary migration. [4] Liquation along grain boundaries at elevated temperature may cause grain boundary separation under the welding thermal strain and if there is insufficient liquid to heal the grain boundary separation, a crack will form. Any factors which cause chemical non-uniformity in the base metal HAZ increase the liquation tendency. S and P are detrimental elements, significantly decreasing the hot cracking resistance. Kujjanpa et al. [5] showed that the concentration of S+P in the grain boundaries is

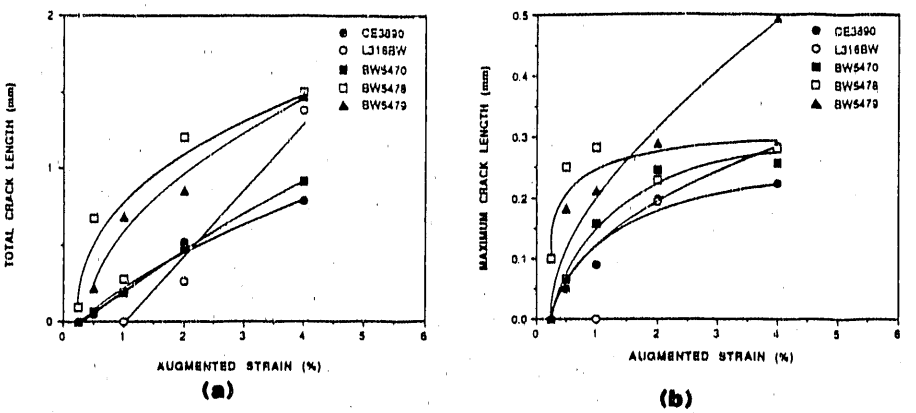

Figure 5. Base metal HAZ crack behavior of the modified 316 materials in Varestraint test. (a) Total crack length as a function of augmented strain; (b) Maximum crack length as a function of augmented strain.

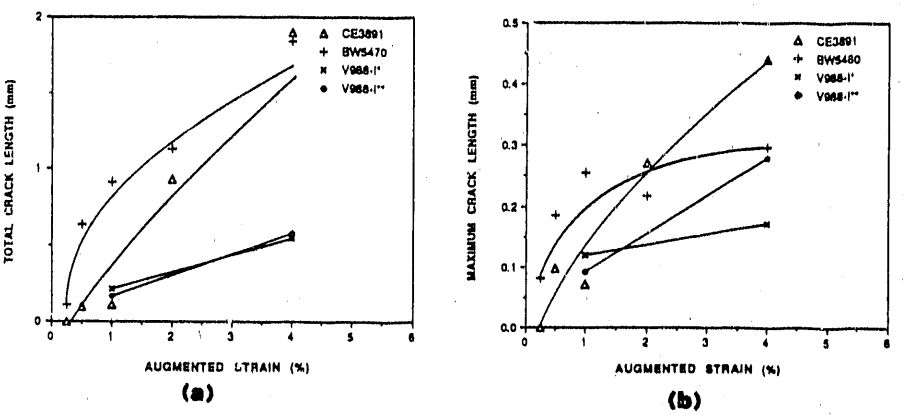

Figure 6. Base metal HAZ cracking behavior of the modified 800H materials in Varestraint test. (a) Total crack length as a function of augmented strain; (b) Maximum crack length as function of augmented strain.

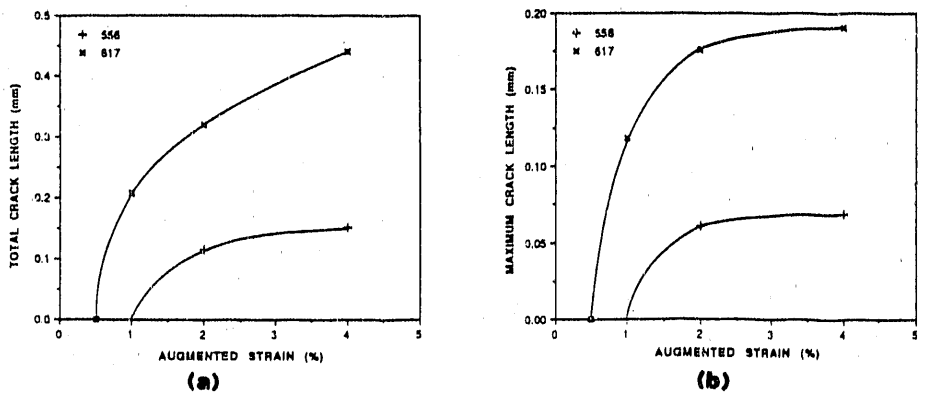

Figure 7. Base metal HAZ crack behavior of the Haynes HD556 and Inconel 617 in Varestraint test. (a) Total crack length as function augmented strain; (b) Maximum crack length as a function of augmented strain.

generally much higher than that in the matrix. For the modified 316 and 800H materials, relatively higher alloying element content and additional precipitation inducing alloying elements are present as compared to conventional 316 stainless steels and P had been intentionally added to alloys in the early modified heats (such as AX6/CE3890 and AX2/CE3891). Figure 8 shows base metal HAZ hot cracking morphology in a modified 316 stainless steel Varestraint coupon using SEM microscopy. A typical intergranular crack is exhibited and some evidence of the liquation on the crack edges can be observed. Location A in Figure 8 shows a liquated grain boundary (at elevated temperature) which is enriched in Nb, Ti and Mo whereas location B shows Ti and Nb rich carbides. The evidence of lack of sufficient liquid, at elevated temperature, to fill the opened space is also indicated in the figure by the ruptured liquid metal bridges.

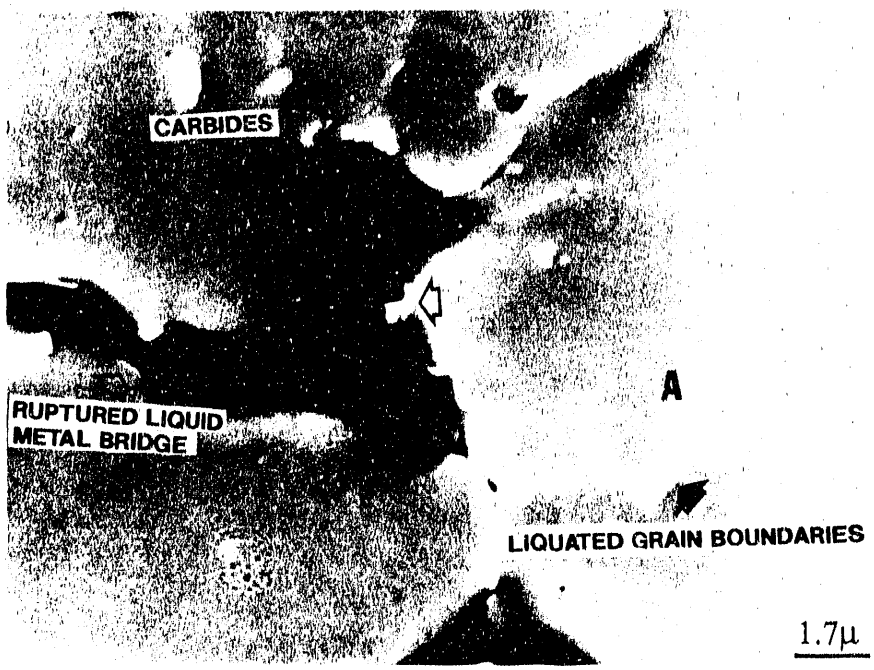

Figure 8. SEM micrograph of base metal HAZ crack in the modified 316 (BW5470) and EDAX analysis.

Weld Metal HAZ Hot Cracking Behavior

The hot cracking behavior in weld metal HAZ in the Varestraint tests is shown in Figures 9 - 11. The ranking of weld metal HAZ hot

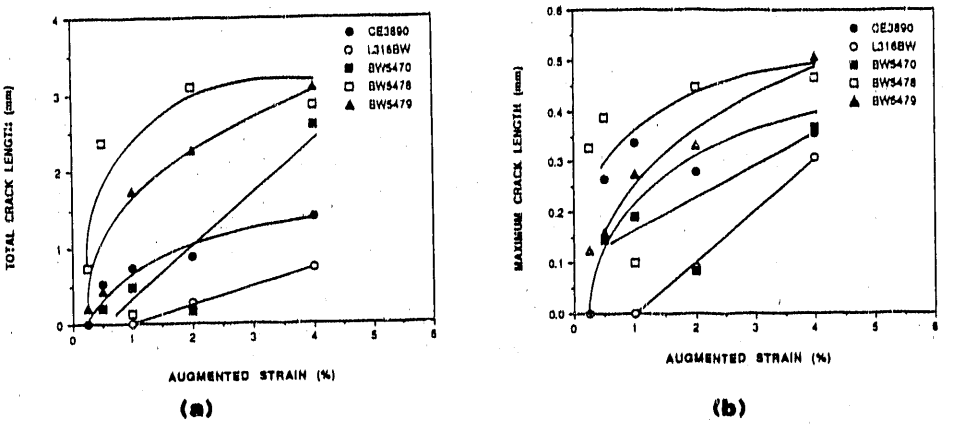

Figure 9. Weld metal HAZ hot cracking behavior in the modified 316 materials. (a) Total crack length as a function of the augmented strain; (b) Maximum crack length as function of augmented strain.

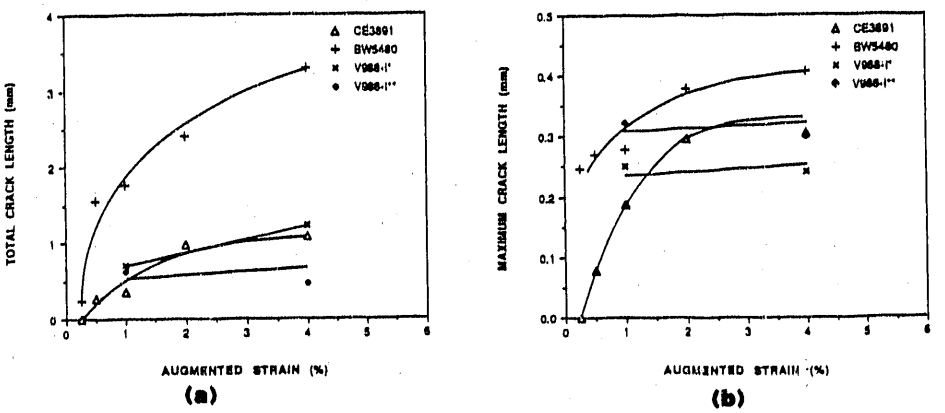

Figure 10. Weld metal HAZ hot cracking behavior in the modified 800H materials. (a) Total crack length as a function of the augmented strain; (b) Maximum crack length as function of augmented strain.

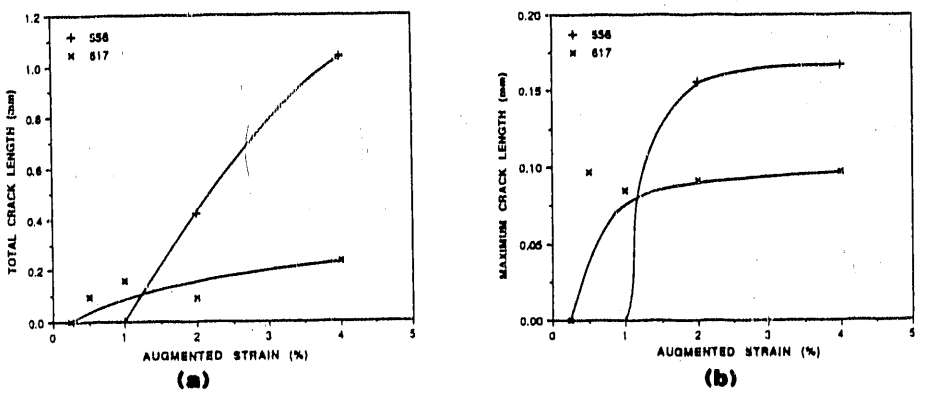

Figure 11. Base metal HAZ liquation crack in the modified 316 (L316BW) Varestraint test. (a) Optical photomicrograph of the base metal HAZ liquation crack; (b) SEM photomicrograph of a base metal HAZ liquation crack.

cracking resistance is similar to the ranking obtained for the fusion zone hot cracking resistance. However, the mechanism of weld metal HAZ hot cracking is not precisely the same as that of fusion zone hot cracking. In the weld metal HAZ, the cracking usually initiates and propagates along the solidification substructure boundaries (between the cellular dendrites). The concentration difference in alloying elements and impurity elements between the center and edge of dendritics, which formed during the former weld bead solidification, causes differences in the melting temperature between the bulk matrix and the inter-dendritic regions. During welding, the dendrite boundary will preferentially liquate.

Figure 12 shows the weld metal HAZ hot cracking morphology in the modified 316 (BW5470). The crack is located along a cellular dendrite boundary with a significant number of precipitates along the crack. EDAX examination of the precipitates shows that all of the precipitates can be defined as Nb, Mo, Ti and V enriched carbides.

Figure 12. Weld metal HAZ liquation cracking morphology in modified 316 (BW5470) Varestraint test specimen and EDAX analysis.

Figure 13 shows the comparison of the hot cracking behavior for the materials tested in terms of the maximum crack length as a function of augmented strain. The prior results on nuclear grade stainless steels,

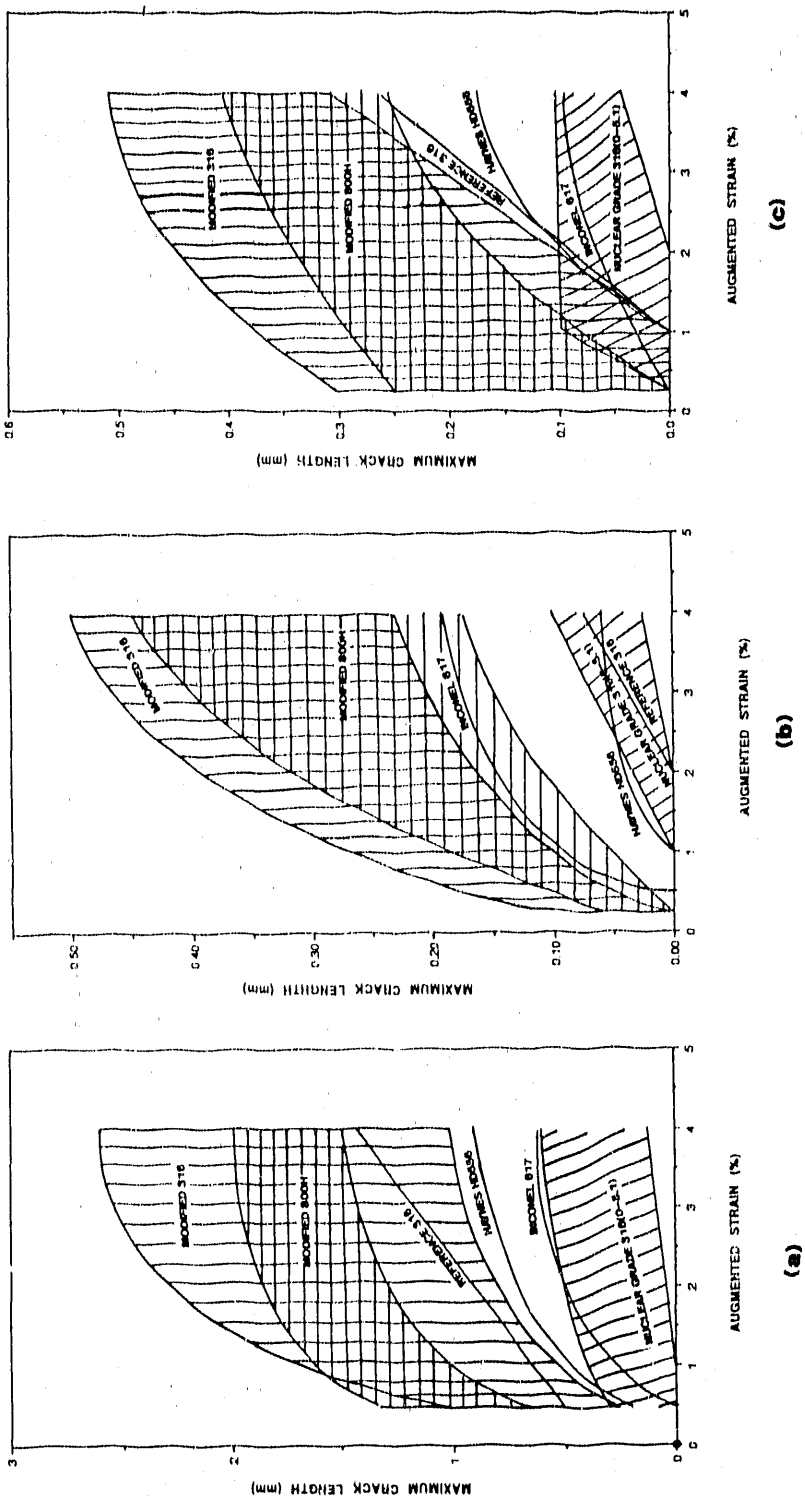

Figure 13. Comparison of hot cracking tendency between all the materials studied. (a) Comparison of fusion zone hot cracking tendency; (b) Comparison of base metal HAZ hot cracking tendency; (c) Comparison of weld metal HAZ hot cracking tendency.

which are generally considered to exhibit good weldability, are also shown in the figures for comparison. It is clear from these figures that the modified 316 and modified 800H showed appreciably lower hot cracking resistance in all three zones as compared to the nuclear grade stainless steels. However, adjustment of the alloying elements in these alloys may be able to improve the weldability. Haynes HD556 showed the best base metal HAZ liquation cracking resistance, relatively better fusion zone crack behavior and good weld metal HAZ hot cracking resistance equivalent to the nuclear grade 316 stainless steels. Inconel 617 also showed better hot cracking resistance than the modified 316 and modified 800H alloys. However, the base metal HAZ hot cracking resistance is lower than for Haynes HD556.

SUMMARY

1. The Varestraint hot cracking test revealed that the modified 316 and modified 800H austenitic alloys show a greater hot cracking tendency in all three weld zones as compared to conventional standard 316 stainless steels.

2. Haynes HD556 and Inconel 617 high temperature alloys show a high resistance to both solidification hot cracking and HAZ liquation cracking. The base metal HAZ liquation cracking resistance for Haynes HD556 is equivalent to Nuclear Grade 316 stainless steels.

3. The fully austenitic structure plus higher P+S, C and the precipitation alloying elements result in the higher hot cracking tendency of the modified 316 and modified 800H materials. To improve the weldability of the modified 316 and modified 800H, the P+S content should be reduced and the carbon content should be kept low.

4. Base metal HAZ hot cracking mechanisms in modified 316 and modified 800H have been defined. The alloying elements and impurity elements re-precipitation during the weld thermal cycling plus a "sweep up" phenomenon related to grain boundary migration appears to increase the segregation and, thus, increase the liquation cracking tendency.

ACKNOWLEDGEMENT

The authors acknowledge the financial support through Fossil Energy Materials Program, U.S. Department of Energy operated by Martin Marietta Energy System, Inc. at Oak Ridge National Laboratory.

REFERENCES

1. H.E. McCoy, J.F. King, "Evaluation of HD556 and Incoloy 802 for High-Temperature Gas-Cooled Reactor Application," Technical Report, ORNL/TM-9382, Oak Ridge National Laboratory.

2. H.E. McCoy, J.F. King, "Mechanical Properties of Inconel 617 and 618," Technical Report, ORNL/TM-9937, Oak Ridge National Laboratory.

3. F. Matsuda, H. Nakagawa, T. Uehara, S. Katayama and Y. Arata, "A new Explanation for role of Delta-Ferrite improving Weld Solidification crack Susceptibility in Austenitic Stainless Steels," P 105-112 Compilation of the Report Published on Solidification Crack Susceptibility and Its Improvement in Fully Austenitic Stainless Steels Weld Metals.

4. C.D. Lundin, C.Y.P. Qiao, T.P.S. Gill and G.M. Goodwin, "Hot Ductility and Hot Cracking Behavior of Modified 316 Stainless Steels Designed for High Temperature Service," Presented at the 71st AWS Annual Convention, April 1990.

5. V.P. Kujjanpa, S.A. David and C.L. White, "Characterization of Heat-Affected-Zone Cracking in Austenitic Stainless Steel Welds," Welding Journal, 66 (8) 221s to 228s, 1987.

EVALUATION OF THE FABRICABILITY OF ADVANCED AUSTENITIC TUBING

M. J. Topolski and H. A. Domian

Babcock & Wilcox Research
1562 Beeson Street
Alliance, OH 44601-2196

ABSTRACT

This program addresses the feasibility of fabricating commercial tubing from candidate alloys for advanced steam cycle superheaters and reheaters. The specific alloys being investigated were defined through an earlier alloy screening program that was concerned with the strength and metallurgical stability of the alloys at temperatures in the range of 650° to 760°C. Samples of the tubing produced under this task will be used in complimentary projects that examine the mechanical behavior, weldability, and fireside and steamside corrosion behavior of the tubing.

Clad tube hollows (800H/IN690, 800H/IN671, Lean Stainless/IN690, Lean Stainless/IN671) as well as monolithic hollows of both the modified 800H and Lean Stainless have been produced via powder metallurgy and hot extrusion methods. The clad and Lean Stainless alloy hollows have been tube reduced to finished dimensions of 2" OD x 0.35" wall (51mm OD x 8.9mm wall). The modified 800H monolithic hollows have been reduced to 2" OD x 0.5" wall (51mm OD x 12.7mm wall). After final anneal, the tubes were rotary straightened to induce cold work into the material.

INTRODUCTION

The scope of the current program consists of melting experimental alloys, conditioning, forging of ingots into extrusion billets, and production of seamless tubing. A portion of some of the sample tubing will be clad on the outside with high-chromium, high-nickel alloys (Alloy 671, 690) for corrosion protection. Specific details on each of the processing routines and results of chemical and metallurgical testing of tubing produced last year are presented in earlier reports issued to Martin Marietta Energy Systems.[1,2,3] Samples of the tube produced under this task will be used in complementary tasks to examine the mechanical behavior, weldability, and fireside and steamside corrosion of the tubing.

DISCUSSION OF CURRENT ACTIVITIES

The current contract calls for the production of seamless tubing via commercial methods of two development alloys: a modified type 316 stainless steel known as Lean Stainless and a modified 800H alloy. In addition to base alloy tubing, representative samples will be clad on their outer surface and coextruded and cold reduced into a metallurgically bonded bimetallic tube to provide enhanced fireside corrosion resistance for these alloys. Production of tubing on a commercial basis will assess the fabricability of these developmental alloys as well as provide test material for complementary tasks involving mechanical behavior, weldability and fireside and steamside corrosion testing.

TUBING PRODUCTION TRIALS

Seamless tubing has been successfully produced from both a Lean Stainless and a modified 800H alloy similar to alloys investigated in preliminary studies at ORNL.[4] In addition, two forged billets of the Lean Stainless alloy were also clad with Inconel 671 via a powder metallurgy (P/M) technique. Hot isostatic pressing (HIP) of canned powder to form a clad billet, followed by coextrusion into 2.500" OD (63.5mm) bimetallic tubing. The bulk of this bimetallic tubing displayed a uniform distribution of cladding and no apparent debonding. Metallographic evaluations revealed the presence of blocky carbide precipitates in the diffusion zone. It is believed that the elevated temperatures used during the HIP cycle may be responsible for extensive interdiffusion and subsequent precipitation of chromium carbides at the clad base metal interface.

Current trials have focused on an alternative manufacturing P/M process without the HIP cycle. The gas atomized metal powder that forms the clad layer around the solid core is consolidated using forces

present during the hot extrusion of the evacuated container. The extrusion forces consolidate the clad layer to 100% of theoretical density and forms a metallurgical bond between the clad and the wrought core. In this work the cladding is either IN671 or IN690, and the core is either Lean Stainless or a modified 800H. The chemical composition of the experimental materials are listed in Table 1. The extruded bimetallic hollows will then be cold finished to typical boiler tube dimensions. In addition, hollows of monolithic Lean Stainless and modified 800H have also been cold finished to final dimensions. The elimination of the lengthy HIP cycle from the process should minimize the formation of the carbide precipitates at the interface.

Table 1
Chemical Composition of Experimental Materials

Element	IN690	IN671	Lean Stainless	800H
C	0.035	0.026	0.085	0.10
Cr	29.5	49.8	14.2	20.1
Ni	59.7	Bal	15.6	30.09
Mo	0.06		2.21	1.89
Mn	0.16	0.06	1.86	2.00
Ti	0.26	0.49	0.12	0.28
P			0.017	0.022
V			0.51	0.59
Fe	9.16		Bal	Bal

Billet Production

The powder metal billets were produced by Crucible Compaction Metals by welding a stainless steel can around the core alloy of either Lean Stainless or modified 800H, filling the can by vibratory methods with either IN690 or IN671 powder to a 70% density, outgassing the powder, pulling a vacuum on the can, and finally sealing the can prior to extrusion.

Extrusion

The extrusion trial for the powder metal clad billets was performed at AMAX in Coldwater, Michigan. The entire powder/can/core hollow billets were forwarded extruded using conventional tooling. The billets were heated at 2050°F (1121°C) for 5 hours. They reduced from 8" OD x 2.69" wall to 4.53" OD x 103" wall (203mm OD x 68mm wall to 115mm OD x 26mm wall), which amounts to a 62% wall and a 75% area reduction, respectively. The visual inspection of the extruded hollows did not reveal any apparent defects. Metallurgical examination of the extrusion discards obtained from AMAX indicates a good metallurgical bond between the clad and core alloys on all four clad billets.

Conditioning and Ultrasonic Inspection of Extrusion

The extruded hollows were conditioned (OD can removed by machining and ID honed to improve surface finish) and inspected ultrasonically for clad thickness and bond quality at Crucible Compaction Metals. The extruded billets were found to have developed some eccentricity from the machining away the type 304 stainless steel can. Ultrasonic measurements showed wall thickness variations on the order of 0.05" to 0.22" (1.3mm to 5.7mm). Figure 1 graphically represents the ultrasonic measurements for the wall thickness of the extruded hollows after conditioning of the OD and ID.

composition and morphology of the regrown
validity of these latter suppositions.

British Coal Gasi

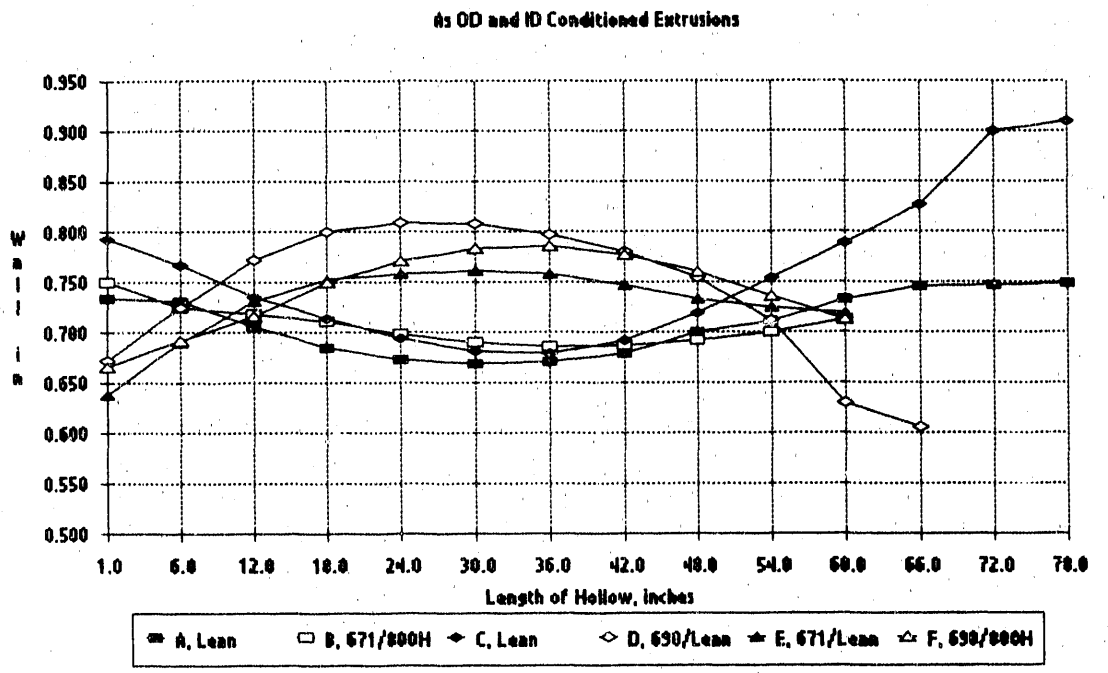

Fig. 1. Wall thickness measurements for OD and ID extruded hollows after conditioning.

First Cold Reduction Pass

The cold reduction trials were performed at the B&W tube mill in Koppel, PA. The first reduction pass was initiated on the 800H/IN690, 800H/IN671, Lean Stainless/IN690, and Lean Stainless/IN671 as well as on the monolithic hollows of Lean Stainless. The incoming hollows to this processing step were all approximately 4" OD x 0.75" wall (102mm OD x 19mm wall). They were to be reduced to 3" OD x 0.5" wall (76mm OD x 13mm wall). This is approximately a 33% wall reduction and a 49% area reduction. The 800H/IN671 and Lean Stainless/IN671 hollows were the only extrusions that did not survive this reduction. They experienced excessive delamination and extrusion of the base metal out from underneath the clad layer upon initiation of the first cold reduction pass. Figure 2 is a photograph of the end of the Lean Stainless/IN671 hollow.

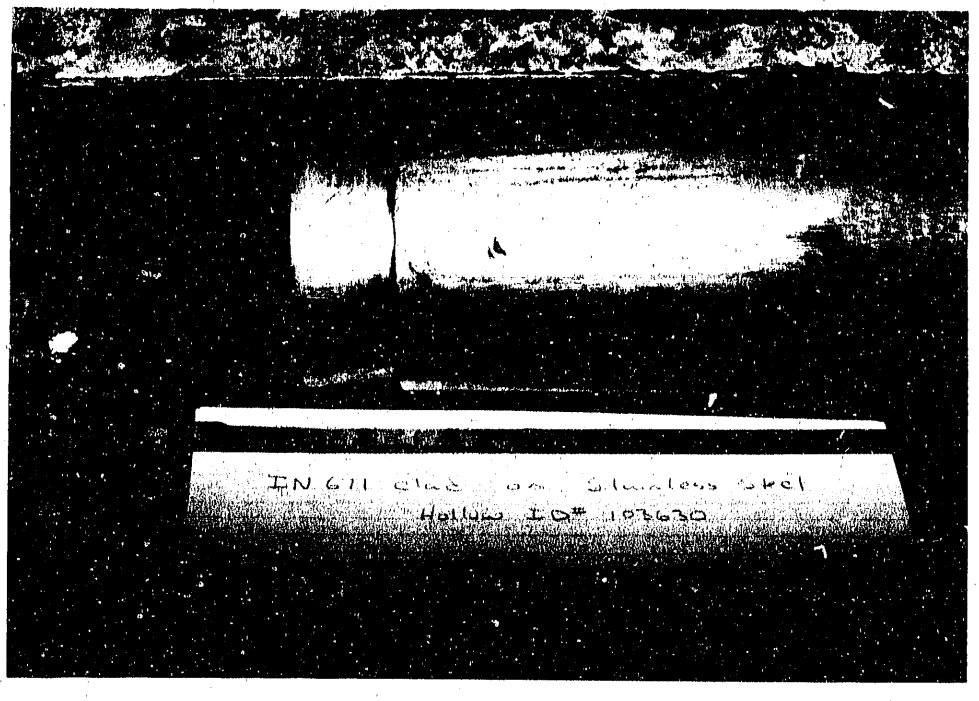

Fig. 2. The Lean Stainless core extruded out from underneath the IN671 cladding approximately 1-1/4" before the tube reduction pass was stopped.

It was found through metallographic examination that a discontinuous network of carbides exist at the clad layer interface of these two combinations. Figure 3 is a photomicrograph of the interface between the Lean Stainless base metal and the IN671 cladding.

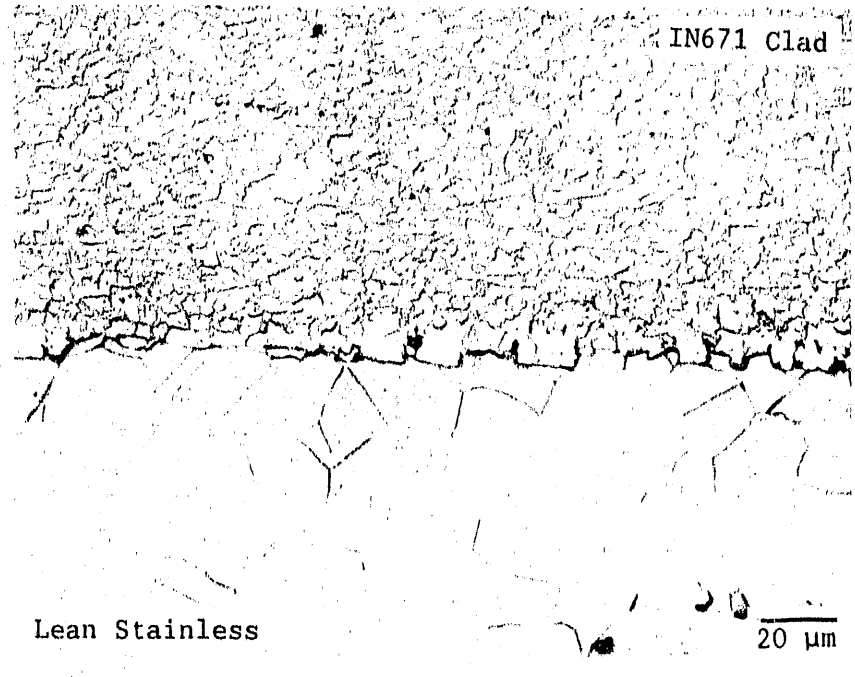

Fig. 3. As-hot extruded Lean Stainless/IN671 interface showing large fractured chromium carbides. The carbides are probably fractured, and the space between the segments filled in with matrix material during hot extrusion.

The 800H/IN690, Lean Stainless/IN690, and the monolithic hollows of Lean Stainless all were successfully converted to 3" OD x 0.5" wall (76mm OD x 13mm wall).

Ultrasonic Inspection

The hollows were reinspected ultrasonically for clad thickness and bond quality at Crucible Compaction Metals. Ultrasonic measurements showed that wall thickness variations were on the order of 1mm to 3mm. Some lack of bond was detected within 6" (152mm) of an end of the 800H/IN690. No lack of bond was detected on the Lean Stainless/IN690 hollow. Figure 4 graphically represents the ultrasonic measurements for the wall thickness of the reduced hollows.

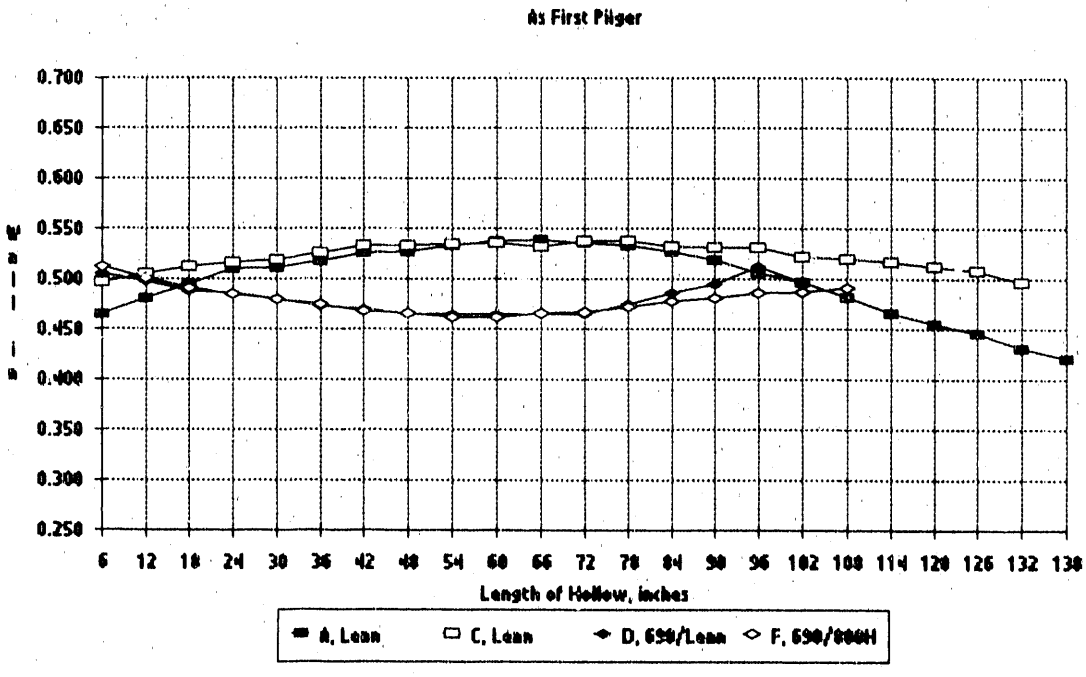

Fig. 4. Wall thickness measurements following the first cold reduction.

Intermediate Anneal

An intermediate anneal of 2050°F (1121°C) was performed between the first and second pass which is the standard anneal currently used by our mill in Koppel.

Second Reduction Pass

The 800H/IN690, Lean Stainless/IN690, and the monolithic hollows of Lean Stainless, all at 3" OD x 0.5" wall (76mm OD x 13mm wall), in this pass, are to be converted to a finished size of 2" OD x 0.35" wall (51mm OD x 9mm wall). This is approximately a 30% wall and a 54% area reduction, respectively, from the previous hollow. The hot extruded

modified 800H monoliths join the cold reduction campaign at this step at 3" OD x 0.63" wall (76mm OD x 16mm wall) to be converted to 2" OD x 0.5" wall (51mm OD x 13mm wall) tubing. This is approximately a 20% wall and a 49% area reduction, respectively.

Final Anneal

All monolithic and bimetallic tubes received a full anneal at 2050°F (1121°C). The hardness of the final annealed tubing, mid-wall, was about 80 Rb for the modified 800H and about 70 Rb for the Lean Stainless.

Cold Work (Rotary Straighten)

The tubes have been rotary straightened in an attempt to induce cold work into the material. This resulted only in an increase in hardness of the surface of the tubes. An increase in through wall hardness of approximately 90 to 94 Rb is the goal. Earlier work with small amounts of cold drawing will be investigated to see if this method will yield the desired through wall hardness.

Final Inspection

The final clad layer thickness has yet to be determined. The 800H/IN671 and Lean Stainless/IN671 hollows, having experienced excessive delamination of the clad layer and extrusion of the base metal at the start of the reduction pass, seem to have a discontinuous network of carbides at the clad layer interface that is probably responsible for the delamination. Representative samples from the finished tubes will be subjected to extensive metallographic and electron optical analysis. In addition, the tubing will be inspected and tested to confirm that it meets industry standard specifications for seamless pressure tubing.

In summation, the clad tube hollows 800H/IN690 and Lean Stainless/IN690, as well as the monolithic Lean Stainless and modified 800H, have been successfully hot extruded and cold reduced to 2.00" OD (50.8mm OD). Rotary straightening of the finished tubing did not induce an increase in through wall hardness to 90 to 94 Rb as was planned. Small amounts of cold drawing will be investigated. The Lean Stainless/IN671 and the 800H/IN671 hollows experienced excessive debonding due to carbides at the interface during the initiation of the first cold reduction. The Lean Stainless/IN671 combination was hot extruded successfully to 2.5" OD (63.5mm OD) in earlier work.

REFERENCES

1. S. E. LeBeau, "Production of Small Heats of Austenitic Tubing - Final Report", Babcock & Wilcox Letter Report RDD:89:4423-01-01:01, August 1988.

2. S. E. LeBeau, "Evaluation of the Fabricability of Advanced Austenitic Tubing Fossil Energy Materials Program", Semi-Annual Progress Report, March 1989, ORNL/FMP-89/1.

3. S. E. LeBeau, "Evaluation of the Fabricability of Advanced Austenitic Tubing Fossil Energy Materials Program", Semi-annual Progress Report, September 1989, ORNL/FMP-89/2.

4. R. W. Swindeman, et al., "Procurement and Screening Test Data for Advanced Austenitic Alloys for 650°C Steam Service", ORNL/TM-10206/P2, August 1988.

DEVELOPMENT OF SURFACE TREATMENTS AND ALLOY MODIFICATIONS FOR CORROSION-RESISTANT OXIDE SCALES

J. H. DeVan

Oak Ridge National Laboratory
P.O. Box 2008
Oak Ridge, TN 37831-6138

ABSTRACT

Alloys based on the long-range ordered system Fe_3Al are under development at Oak Ridge National Laboratory in support of coal conversion and combustion materials requirements. Of particular interest is the performance of these alloys in coal gasifiers involving product gases with relatively low oxygen activities ($\leq 10^{-20}$ atm) and high sulfur activities ($\geq 10^{-8}$ atm). Using H_2S-H_2-H_2O gas mixtures, several experimental iron-aluminum alloys have been tested to assess the effects of aluminum concentration on oxidation-sulfidation response at 700 to 800°C in a simulated gasifier environment. Metallographic and chemical analyses of the corrosion product scales and the underlying alloy were performed to determine the role of respective metallic elements on the sulfidation-oxidation processes. These results, together with thermogravimetric analyses, are discussed in terms of the apparent corrosion mechanisms and optimization of alloy composition for exposure to coal-derived environments.

More recently, the corrosion performance of an Fe-28% Al-2% Cr alloy has been evaluated in gases produced by an operating gasifier. The reaction products and scale morphologies under actual service conditions were generally similar to the laboratory test results except for the presence of an ash deposit on the gasifier specimens.

INTRODUCTION

Because of high temperatures and the presence of sulfur, chlorine, and other oxidants in coal-derived environments, metal components in coal combustion and conversion systems are subject to severe corrosion. Accordingly, the objective of the present work is to develop protective scales on iron-based alloys in mixed-oxidant (oxygen-sulfur) environments for coal-related applications at 500 to 800°C. The experimental approach involves (1) development of protective oxide scales by modifying oxide chemistry and/or microstructure to reduce the transport of sulfur through the scales; (2) formation of a sulfur-diffusional barrier under or above the protective scale to minimize the sulfur attack; and (3) study of the effects of alloy chemistry, oxide morphology, and temperature on the breakdown of protective scales. To this end, corrosion studies during the last two years have concerned the oxidation-sulfidation properties of Fe_3Al-based alloys being

developed at the Oak Ridge National Laboratory. Developmental alloys containing additions such as Cr, Nb, Mo, Zr, Y, and B were exposed to H_2S-H_2-H_2O gas mixtures at 700 and 800°C, respectively. These studies[1] have established that chromium must be limited to levels of about 2% in Fe_3Al-based alloys to perform acceptably in simulated gasifier environments. Additions of niobium and molybdenum appeared to be beneficial in reducing sulfidation attack in similar environments, but vanadium and manganese additions were detrimental. Additions of yttrium and zirconium also proved beneficial, apparently by blocking sulfur diffusion in the scale, since neither of these elements perceptibly affected scale adherence. Increasing the aluminum level from 28% (standard for Fe_3Al-based alloys) to 35% effectively masked any third-element effects, as all alloys tested with 35% Al performed as well or better in H_2S-H_2-H_2O than the binary Fe_3Al.

In the last year, comparative screening tests of developmental alloy modifications have been superceded by studies of the mechanisms of oxidation/sulfidation processes in the alloys with particular emphasis on the effects of chromium additions. Further insight into the kinetics of scale growth has been provided by thermal cycling tests of both as-surface-finished and preoxidized Fe_3Al alloys. In the past year, exposure of an Fe_3Al alloy containing 2% Cr to the product gas of an operating gasifier has provided a comparison of corrosion behavior under actual gasifier conditions with our laboratory test results.

LABORATORY TEST RESULTS

Preoxidation Studies

Three Fe_3Al-based alloys (PS28, -29, and -30 in Table 1) were preoxidized in dry air at 800°C for 7 h and then were exposed to a 5.35% H_2S, 79.23% H_2, 1.70% H_2O, 13.72% Ar mixture at 800°C for 100 to 200 h in a continuously recording microbalance system. Results were compared with tests of the same three alloys without the preoxidation treatment. Preoxidation lowered the weight gain of the 5% Cr alloys (PS28 and -29) by a factor of 4 over a 120-h period. However, the parabolic rate constant of the latter alloys did increase slightly after 75 h. Preoxidation of the 2% Cr alloy (PS30) reduced the weight gain to an imperceptible level with no change over a

Table 1. Compositions of test alloys

Alloy designation	Al	Cr	Nb	Zr	Other
PS28 (FAL)	28	5		0.1	0.05B, bal Fe
PS29 (FALM)	28	5	0.5		0.05C, bal Fe
PS30 (FAS 28-8)	28	2			0.05B, bal Fe
PS33 (FA135)	28	2	0.5		0.05B, bal Fe
FA117	28	2	0.8	0.1	0.5Mo, 0.03Y, 0.06B, bal Fe

175 h period. There was little change in the general appearance of preoxidized alloys that occurred during the H_2S exposure (i.e., the surfaces retained the bronze-colored oxide formed during preoxidation). However, in the case of a 5% Cr alloy (PS28), examination by SEM revealed the growth of flat needles and blades at the sharp corners formed by the intersecting sides of the specimens (Fig. 1). Energy-dispersive spectrographic analysis showed the growths to consist predominantly of iron sulfides with some aluminum also present. These growths are apparently responsible for the increase in the parabolic rate constant after 75 h and obviously reflect a mechanical breakdown of the preoxidized surface scale at points of disregistry (i.e., sharp corners).

The preoxidation results support our previous findings that the compatibility of Fe_3Al alloys with H_2S derive from the relatively fast kinetics of protective Al_2O_3 scale growth compared to the growth of nonprotective CrS and $Fe_{1-x}S$ scales.[1] Adding chromium to the alloys at concentrations above 2% accelerates the growth of chromium and iron sulfides, as minifested by much greater weight gains compared to alloys with lesser chromium levels and the coverage of exposed surfaces by an FeS outer scale. Based on the preoxidation test results, chromium in the alloy does not affect the stability (or growth rate) of a preformed Al_2O_3 scale in H_2S. However, if a mechanical breakdown in this scale occurs, the presence of chromium leads to preferential growth of FeS, as opposed to Al_2O_3, in the replacement scale. Thus, chromium acts to promote the growth of sulfides relative to Al_2O_3 but does not appear to affect the transport properties of the Al_2O_3 scale.

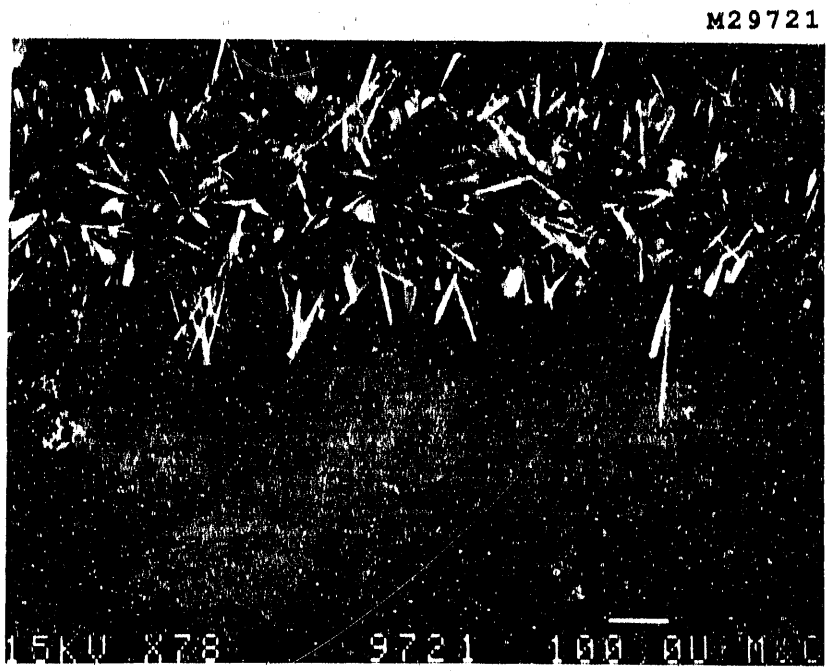

Fig. 1. Scale formed on preoxidized coupon of Fe-28% Al-5% Cr alloy (PS28) exposed to simulated gasifier atmosphere at 800°C.

Effects of Thermal Cycling

We have noted previously[1] that, despite the excellent resistance of Fe_3Al-based alloys to H_2S-H_2-H_2O mixtures, there is significant scale exfoliation on cooling to room temperature following exposure of the alloys at 700 to 800°C. Despite this spalling tendency, however, repeated thermal cycling of the binary alloy between room temperature and 800°C did not significantly increase the rate of metal oxidation because the scale is quickly re-established and grows very slowly.[1] Thermal cycling tests have now been completed on an alloy containing 2% Cr (PS33 in Table 1) cycled between 800°C and room temperature, as shown in Fig. 2. The cycles were imposed after accumulated exposures of 116, 182, 248, 271, 294, 317, 340, and 410 h, respectively. The sudden decrease in weight at the time of each thermal cycle and the relatively rapid gain in weight following each cycle reflect the detachment and spalling of corrosion product scale during each cooldown. Even with this repeated removal of scale, however, the loss of metal over the 410-h period was less than 0.44 mg/cm^2. This loss, averaged over 400 h, translates to a wastage rate of less than 1.5 μm/year.

The effect of thermal cycling on the weight change of an alloy containing 5% Cr (PS29 in Table 1) can be seen in Fig. 3. Three individual

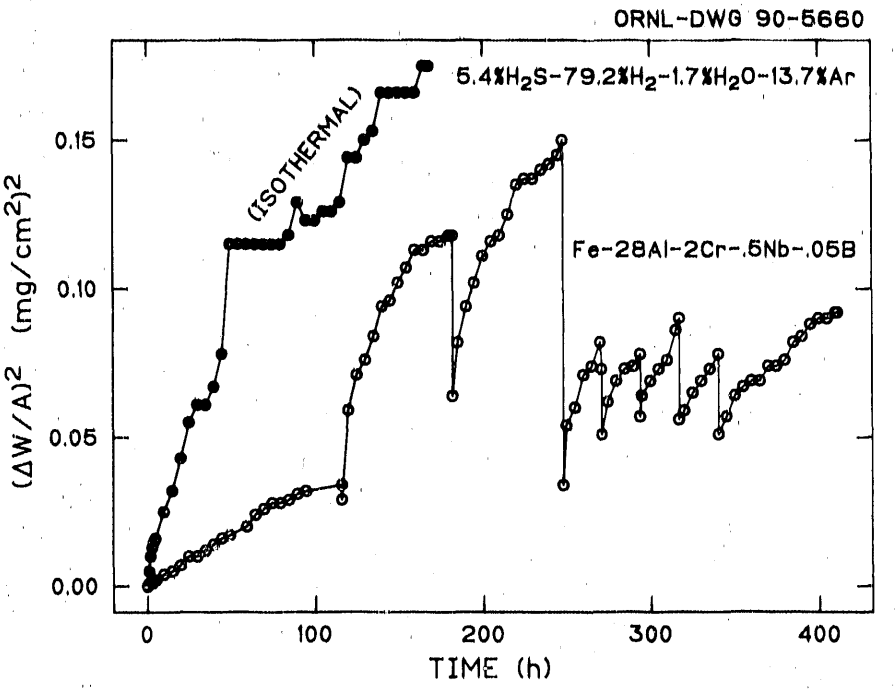

Fig. 2. Comparison of weight changes of Fe-28% Al-2% Cr alloy (PS33) under isothermal conditions and with intermittent thermal cycles to room temperature. Alloy was exposed to H_2S-H_2-H_2O gas mixture at 800°C.

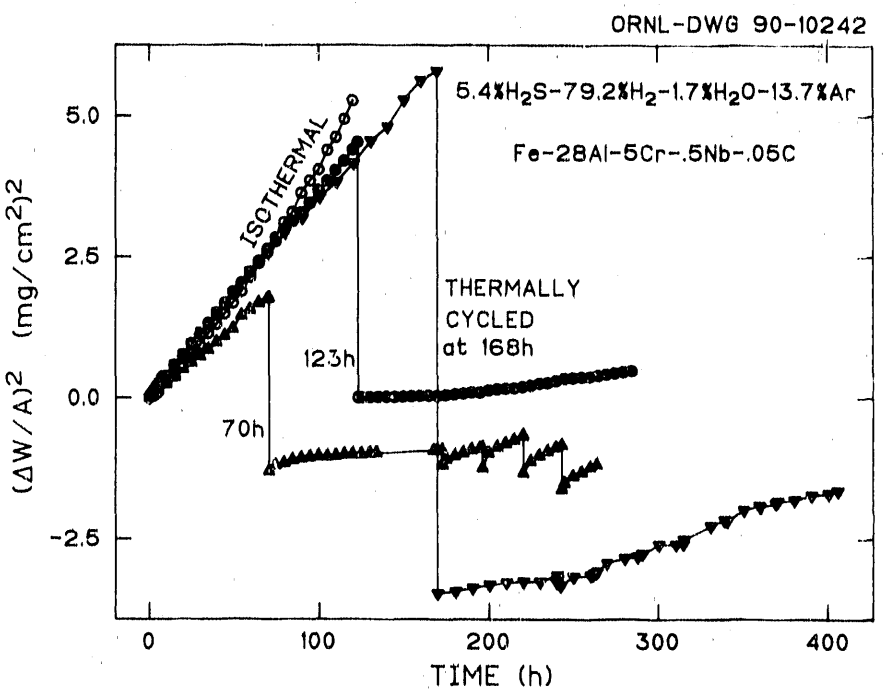

Fig. 3. Effect of thermal cycling on weight change of Fe-28% Al-5% Cr alloy (PS29).

tests were conducted on this alloy, the tests differing only in the duration of the initial isothermal exposure at 800°C prior to the first cooldown. These initial exposures were 70, 123, and 168 h, respectively. Note that the extent of scale lost during the first thermal cycle increased directly with the time of the isothermal exposure i.e., the greater the scale thickness, the greater the scale loss on the initial cycle. However, the kinetics of regrowth of the scale on re-exposure at 800°C were also affected by the duration of the initial isothermal exposure: the greater the initial scale loss (i.e., the longer the exposure), the slower the kinetics of weight gain following the loss. It is evident that the parabolic rate constant for the reaction process occurring on initially exposing the 5% Cr alloy to the H_2S-containing gas remains constant with exposure time (at least to 168 h) so long as the initially developed scale remains in contact with the alloy. Once the specimen is thermally cycled and some or all of the initial scale is lost, the succeeding reaction process is much slower. For initial isothermal exposures longer than 70 h, there was little effect of further thermal-cycling on the reaction rate constant, even when the cycling was extended for 200 h. However, in the case of the 70 h isothermal exposure, the slower kinetics following the first thermal cycle remained in effect for about 100 h, at which point scale was lost with each succeeding cycle and the rate of new scale growth increased after each cycle. The basic conclusion to be drawn from these results is that removal of the initially-formed corrosion product scale is extremely beneficial in reducing the corrosion rate. The degree of benefit increases with the length of the initial exposure, at least out to 123 h. One possible explanation is that iron and chromium sulfides, which are major constituents in the initially-formed scale, remain in place as long as the specimen is isothermal, and these sulfides limit the effectiveness of the underlying alumina as a sulfur/oxygen barrier. Once the sulfide products are removed, as a consequence of exfoliation of the scale on the first cooldown, alumina becomes the major constituent in the reformed scale, and corrosion rates correspond to those where preformed (preoxidized) alumina scales exist, as described in the previous section. The predominance of alumina in the regrowth process but not in the initially-formed scale can be attributed to the selective removal of chromium and/or enrichment of aluminum near the exposed surface that accompanies the growth of the initial scale. Metallographic examinations are being conducted to determine the chemical

composition and morphology of the regrown corrosion product to check the validity of these latter suppositions.

British Coal Gasifier Exposures

An Fe_3Al alloy containing 2% Cr (designated FA117 in Table 1) was supplied to the Coal Research Establishment (CRE) of British Coal Corporation for testing in their 12 ton/day gasifier at Stoke Orchard, Gloucester. The material was exposed in two successive runs (PP10 and -11) for times of 940 and 850 h, respectively. The samples (20 x 10 x 6 mm) were located in the gas cooler and were mounted on each of three uncooled corrosion probes alongside numerous other alloy compositions, all in the form of plate specimens. The probes were positioned at three different elevations along the gas cooler, the uppermost being exposed to uncooled product gas and the lower two to the same gas as it was being cooled by passage through a heat exchanger. Thermocouples were located on both sides of the specimen assembly and recorded the ranges of temperatures shown in Table 2.

Table 2. Temperatures of CRE sample probes

Test	Temperature range (°C)		
	Probe 1	Probe 2	Probe 3
PP10	870-910	680-720	560-610
PP11	800-870	600-700	460-600

Typical gas compositions and calculated equilibrium sulfur and oxygen fugacities are listed in Tables 3 and 4, respectively. The gas compositions contain a much lower concentration of H_2S than used in our laboratory tests ($\leq$0.25 vs 5.4%); however, they also contain a measurable concentration of chlorides (100-300 ppm HCl), a species not yet included in our laboratory tests. Using an 800°C reference temperature, our laboratory gas mixture is more reducing ($p_{O_2} = 10^{-22}$ atm) than the CRE gasifier product gas ($p_{O_2} \sim 10^{-20}$ atm) and a factor of 10 higher in sulfur activity (10^{-6} vs 10^{-7} atm).

Table 3. Typical composition of CRE product gas

Test	Gas composition (% by volume)						vppm	
	CO	CO_2	H_2O	H_2	CH_4	N_2	H_2S	HCl
PP10	14	10	12	12	0.6	52	2500	300
PP11	14	9	10	11	0.6	55	1300	112

Table 4. Equilibrium sulfur/oxygen potentials

Temperature (°C)	Test	P_{S_2} (atm)	P_{O_2} (atm)
900	PP10	6.8×10^{-7}	4.2×10^{-17}
	PP11	1.6×10^{-7}	3.3×10^{-17}
800	PP10	2.4×10^{-7}	8.6×10^{-19}
	PP11	6.0×10^{-8}	7.6×10^{-19}
700	PP10	1.0×10^{-7}	1.3×10^{-20}
	PP11	2.8×10^{-8}	1.2×10^{-20}
600	PP10	4.2×10^{-8}	7.2×10^{-23}
	PP11	1.1×10^{-8}	6.7×10^{-23}

Visual and metallographic examinations of the specimens after exposure were initially performed by CRE. (Weight changes were not reported.) CRE reported[2] that the specimens had shown no visual changes except for darkening, and metallographic examinations revealed little surface attack, with one exception. This exception was the specimen from the top probe in test PP10 which had been positioned in an area where the alloy 800 support probe had suffered catastrophic attack, apparently because of NiS/Ni formation. This Fe_3Al specimen showed isolated pits with average depths of 30 to 40 μm. Following the examinations by CRE, the metallographically mounted specimens were forwarded to ORNL for additional microscopic and chemical analyses. These analyses have confirmed the excellent resistance of the alloy to attack by the gasifier product gas even at temperatures greater than 800°C. Figure 4(a) shows the metallographic appearance of the specimen mounted on the highest temperature probe from run PP11 (see Table 2). Microprobe examination of the reaction product layer on this specimen shows a relatively thick outer

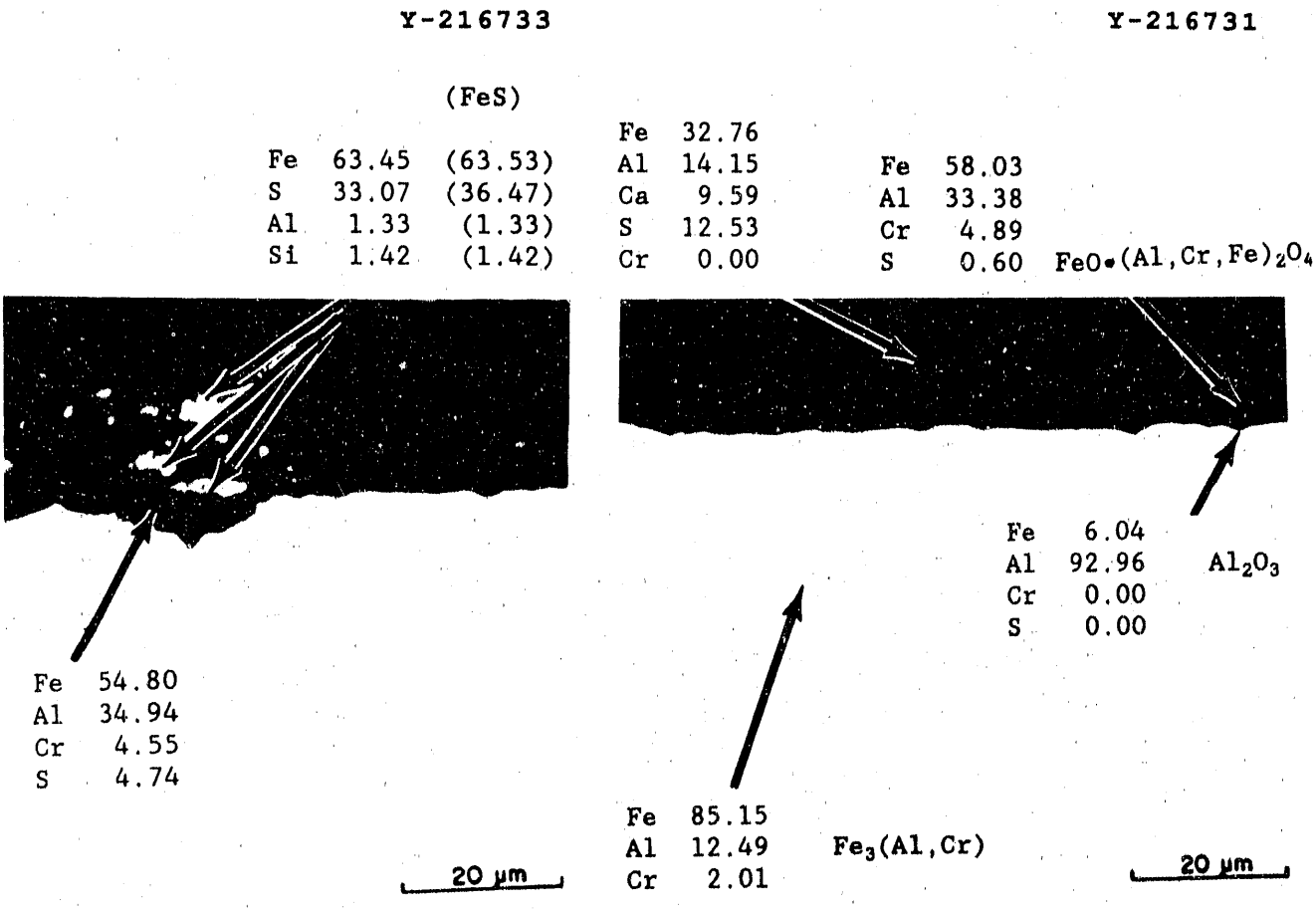

Fig. 4. Metallographic appearance of Fe_3Al + 2% Cr alloy (FA117) after exposure in run PP11 in CRE 12 tpd gasifier. (a) General appearance of surface. (b) Isolated pitted region under pyrrhotite particle. (1000X)

layer containing calcium and sulfur, a thinner oxide layer containing iron and aluminum, and an even thinner alumina layer at the oxide-metal interface. The morphology and chemistry of the outer layer shows it to be a very uniform and compact deposit containing ash constituents that possibly combined with calcium (≤10%). A portion of the total sulfur (≤35%) in the deposit can be attributed to the presence of CaS, which presumably relates to the fact the coal feed to the gasifier was mixed with limestone for part of run PP11.

The deposit contains a relatively high concentration of aluminum (≤20%) and essentially no oxygen, an implication that the aluminum is present as a sulfide. (The latter could occur only if the oxygen fugacity within the deposit were considerably below that of the gas.) The high aluminum and iron concentrations in the deposit appear to be indigenous to the ash, since there is no evidence of any solid-state reactions between the deposit and the

underlying metal. However, isolated shallow pits such as that shown in Fig. 4(b) were found in a few locations and were associated in all cases with iron sulfide particles incorporated in the deposit. The localized attack associated with these particles suggests that their sulfur acitivity was even higher than that of the surrounding deposit. Such a result could be explained if the particles had derived from pyrite (FeS_2) inclusions in the coal, given the fact that pyrite is unstable above 743°C and would decompose to yield pyrrhotite ($Fe_{1-x}S$) particles [observed in Fig. 4(b)] and free sulfur.

The corrosion behavior of the specimens exposed by CRE is in good agreement with that projected from the results of laboratory studies of Fe_3Al alloys containing ≤2% Cr. There was no evidence of any species associated with chlorine, and oxide reaction products that developed below the deposited layer were typical of those seen in our laboratory studies. It should be noted, however, that the heat load required to bring the gasifier from ambient to steady-state operating conditions is supplied by operating the gasifier as a coal combustor (i.e., with excess air). Accordingly, there is an effective preoxidation treatment which, as noted in a preceding section, significantly enhances the corrosion resistance of the reference alloy on subsequent exposure to H_2S.

SUMMARY AND CONCLUSIONS

1. The oxidation and sulfidation properties of Fe_3Al alloys were studied in gas mixtures of $H_2 + H_2S + H_2O$ at 800°C. The alloys contained 28% Al and 2 and 5% Cr, respectively. The sulfidation resistance of alloys containing 5% Cr was significantly improved by preoxidation in air at 800°C prior to exposure in the mixed gas. Preoxidation produced a relatively impervious alumina scale, although sulfide reaction products did gain precedence at the edges of specimens where mechanical breakdown of the scale occurred. Thermal cycling of the 5% Cr alloy between 800°C and room temperature in the H_2-H_2S-H_2O mixture resulted in a significant weight loss on the initial cooling cycle. However, the growth rate of scale thereafter was retarded compared to the rate after a comparable exposure under isothermal conditions. The beneficial effect on scale growth rate after thermal cycling appears to be associated with chromium depletion near the surface and overgrowth of alumina.

2. An Fe_3Al alloy containing 2% Cr was exposed to product gas in a British Coal Research Establishment gasifier at maximum temperatures from 800 to 900°C. After exposures of 940 and 850 h, respectively, metallographic examinations showed very little evidence of corrosion. A relatively thin two layered oxide [Al_2O_3 and $FeO \cdot (Al,Fe)_2O_3$] was observed under a thicker ash deposit containing Ca, Fe, Al, and S. Small widely separated pits were associated with microscopic pyrrhotite particles occluded in this latter layer.

3. The major difference between laboratory tests and the gasifier results is the presence of a sulfur-containing ash deposit on the gasifier specimens. The relatively high calcium concentration suggests that the deposit is associated in part with limestone additions made to the gasifier. Also contained in this deposit are isolated pyrrhotite particles that appear to be vestiges of pyrite impurities in the coal. There were no detectable corrosion effects associated with chlorine impurities in the coal.

REFERENCES

1. J. H. DeVan, "Oxidation Behavior of Fe_3Al and Derivative Alloys," *Oxidation of High Temperature Intermetallics*, pp. 107-116, The Minerals, Metals, and Materials Society, Warrendale, PA, 1988.

2. M. St. J. Arnold, British Coal Research Establishment, Cheltenham, United Kingdom, personal communication to R. R. Judkins, Oak Ridge National Laboratory, Oak Ridge, Tenn., September 1989.

CODEPOSITION OF CHROMIUM-SILICON AND CHROMIUM-ALUMINUM IN DIFFUSION COATINGS FOR IRON-BASE ALLOYS USING PACK CEMENTATION

Mark A. Harper, David M. Miller, and Robert A. Rapp

Department of Materials Science & Engineering
The Ohio State University
Columbus, OH 43210

ABSTRACT

The codeposition of chromium and silicon into low alloy steels has been achieved using the pack cementation process. Surface compositions of the coatings are 20-40wt% Cr and 2-4wt% Si. Cyclic oxidation tests of coated coupons show a dramatic decrease in the oxidation kinetics of the substrate materials. Likewise, chromium and aluminum have been codeposited by a two-step treatment into low-alloy steels. The coatings are expected to resist gaseous attack in mixed oxidants (oxygen+sulfur, oxygen+carbon, etc.) at intermediate temperature (500-750°C). The appropriate choices for the Cr-Si and Cr-Al masteralloy compositions, halide activator salts, and temperature for the coating process were guided by using a computer-assisted evaluation of pack thermodynamics.

INTRODUCTION

Pack cementation is a modified chemical vapor deposition process which consists of heating a closed/vented pack to an elevated temperature (e.g. 1050°C) for a given amount of time (e.g. 16 hours) during which a diffusional coating is produced. The pack consists of four components: the substrate(s) or part(s) to be coated, the elements(s) to be deposited (in the form of a powder masteralloy), a halide activator salt (e.g. NaF), and an inert powder filler (e.g. Al_2O_3 or SiO_2). An inert gas (e.g. argon) surrounds the pack. Upon heating to the elevated temperature, the activator salt reacts with the elements of the masteralloy to form metallic halide vapors which diffuse to the substrate surface through the gas phase in the porous pack[1].

Alloys involving an interactive use of two corrosion-resistant components generally are more effective than a simple binary alloy. Upon exposing an Fe-30wt%Cr-3Si alloy, or Fe-20Cr-4Al alloy to an oxidizing environment, a Cr_2O_3 scale forms initially, preventing: 1) the rapid oxidation of Fe, and 2) the internal oxidation of the Si or else Al. By its formation, the Cr_2O_3 scale reduces the oxygen activity at the scale-metal interface, thus allowing the thermodynamically more stable and very slow growing SiO_2 or else Al_2O_3 films to form beneath the Cr_2O_3 at steady state[2]. However, excessively higher alloy contents would lead to inadequate ductility and a propensity to form an embrittling sigma phase in service.

Currently, most commercial pack cementation coating processes involve the deposition of single elements (Al, Cr, or Si), and although coating processes involving two elements (e.g. Cr-Al or Al-Si) have been advertised, usually complex two-step procedures are used to incorporate the elements sequentially into the substrate surface[3,4]. Furthermore, the introduction of Cr during the coating of carbon-containing alloys usually results in the formation of a chromium carbide surface layer ($Cr_{23}C_6$), which subsequently blocks the inward diffusion of Cr. However, the introduction of Si or Al during the coating process acts to push the carbon into the substrate due to a strong repulsive thermodynamic interaction between Si or Al and C. Thus the usual surface carbide layer can be avoided for certain processing conditions.

The current studies have been carried out in an attempt to deposit corrosion- and oxidation-resistant coatings onto Fe-base alloys, thus enhancing their use and service lives in high-temperature severe environments: combustion product gases, mixed O_2/S_2, O_2/C and more complex multioxidant gases, and corrosive fused salts. Such Fe-Cr-Si coatings may also resist acidic oxidizing aqueous environments.

THERMODYNAMICS

The refractory enclosure containing the substrate(s), powdered masteralloy, activator salt(s), and the inert filler is treated as a closed

system in thermodynamic equilibrium. The fused or volatile halide salt reacts with the elements in the source alloy to form metallic halide vapors which diffuse through the porous pack to the substrate. As the simplest condition, two metallic elements may be codeposited if their vapor species have comparable vapor pressures. If the halide vapor pressure of one component greatly exceeds that of the other, then the deposition of one element dominates (i.e., either chromizing or siliconizing or aluminizing).

In the present work, the calculation of the equilibrium partial pressures was performed using a computer program which is a modification of SOLGASMIX. The program calculates the equilibrium partial pressures for a given temperature in a multicomponent system, and is based on the minimization of the Gibbs energy of the system and the conservation of mass for each element.

Four Cr-Si compositions (90Cr-10Si, 80Cr-10Si, 70Cr-20Si, and 60Cr-40Si) representing four two-phase fields (A,B,C,D) in the Cr-Si system, and four activators (NaCl, NaF, $FeCl_2$, and $CrCl_2$) were investigated. Calculations were performed for pack compositions consisting of:

1) 73.0% inert filler (Al_2O_3 or SiO_2)
2) 23.0% masteralloy
3) 2.0% halide activator salt.

Figure 1 shows the equilibrium condition for a pack using Cr-Si masteralloys and a NaCl activator at 1323 K. Stable values can only be achieved for compositions in the two-phase fields of the Cr-Si diagram indicated by the points A, B, C, and D. Such analyses for the Cr-Al system have been previously reported in this research. The mutual suitability of an activator salt and a masteralloy composition in the Cr-Si system depends on the partial pressures of the Cr and Si halides being of comparable magnitude for any given two-phase region. According to Fig. 1, codeposition of Cr and Si in some ratio using a NaCl activator should be possible for masteralloys corresponding to regions B, C, and D.

In Fig. 2, the vapor pressures are plotted for a pack containing a NaF activator at 1323 K. The possibility for codeposition in this case would only exist for masteralloys corresponding to region A, where the partial pressures of CrF_2 and SiF_2 are within two orders of magnitude of each other.

EXPERIMENTAL PROCEDURE

The surfaces of Fe-2.25Cr-1.0Mo-0.15C coupons were ground smooth and flat with 600 grit paper and then the coupons were weighed and placed into the crucible pack. This crucible was placed within a ceramic tube in the uniform heating zone of an electric resistance furnace and heated to the coating temperature (usually 1000 to 1050°C) for a time ranging from 16 to 24 hours. Argon was passed through the tube to provide an inert surrounding atmosphere which prevented oxidation of the coupon or masteralloy. Following the diffusion coating process, the specimens were prepared for optical metallography. Energy dispersive spectroscopy (EDS) was used to measure the composition profiles in the coated substrate. The success of a given treatment was evaluated in terms of composition, coating morphology, and coating thickness. Based on conclusions drawn from such an analysis, variations were made to the pack composition and/or temperature for the succeeding experimental runs. Usually after a few iterations using this procedure. a pack composition and temperature were established that produced a desired coating.

RESULTS AND DISCUSSION

Coating Results

Two methods were developed to codeposit Cr and Si into carbon-containing iron-base alloys resulting in a surface composition of approximately 30Cr-3Si (wt%).

By the first method, a masteralloy of 90wt%Cr-10Si (two-phase field A), a SiO_2 filler and a "double activator" consisting of a fused solution of NaCl and NaF were used. For an Fe-2.25Cr-1.0Mo-0 steel coated using a 90Cr-10Si masteralloy and a NaCl activator, the substrate was essentially chromized with insufficient Si present. For the same steel using a 90Cr-10Si masteralloy and a NaF activator, the codeposition of Cr and Si was achieved but the Cr content is less than desired. Thus, for this masteralloy, the NaCl activator predominantly deposits Cr while the NaF activator deposits the desired amount of Si. For the given fixed activities of Cr and Si in the two-phase field,

codeposition was made possible by adjusting the activities of NaCl and NaF through the use of molten activator solutions of various concentrations. Figure 3 shows the microstructure and compositional profiles for an Fe-2.25Cr-1.0Mo-0.15C steel coated using a 90Cr-10Si masteralloy and an activator consisting of 95at%NaF-5%NaCl. This combination of masteralloy, filler, and activator produced a dense coating with the desired surface composition of approximately 35Cr-3.5Si (wt%).

By the second method, an 85Cr-15Si masteralloy (single-phase Cr_3Si), a filler of 95wt% Al_2O_3-5% SiO_2 and a mechanical mixture of NaCl and NaF were used. Figure 4 shows the microstructure and compositional profile for a coated Fe-2.25Cr-1.0Mo-0.15C steel. The use of a mixed inert filler was necessary to increase the partial pressures such that the fluxes of the halides of both Cr and Si to the substrate surface were large enough to produce appreciable codeposition.

Some previous reports have identified successful coating procedures for chromizing-aluminizing austenitic steels, ferritic stainless steels, and low-alloy (carbon-containing) steels. Further progress has been made in the most difficult task of coating the low alloy steels. In that case, a 92Cr-8Al masteralloy with a mixed activator of NaBr+$AlCl_3$(1:1) was used to coat the Fe-2.25Cr-1.0Mo-0.15C alloy in two steps (900°C for 16 h. followed by 8 h. at 850°C).

Oxidation Resistance

A coated coupon with a surface composition of 34Cr-3Si has been cyclically oxidized in air at 700°C for four months (47 cycles) with an almost negligible weight-gain (< 0.2 mg/cm^2) and no detectable scale spalling, as shown in Fig. 6. The slow growth of an SiO_2 layer underneath an initial transient outer thin chromium oxide scale can only account for the slow kinetics. Thus coatings with concentration profiles as shown in Figs. 3 or 4 exhibit excellent oxidation resistance, even at relatively low temperatures (700°C). Such excellent scaling resistance is likely to be achieved also for complex oxidizing atmospheres, e.g. those involved with hot corrosion, coal gasification, refuse incineration, combustion product gases, petrochemical

gases, etc. Corrosion testing in these environments and in oxidizing acidic aqueous solutions is planned.

CONCLUSIONS

Diffusion coatings on an Fe-2.25Cr-1.0Mo-0.15C steel with surface concentrations of approximately Fe-30wt%Cr-3%Si have been produced using the pack cementation method. The codeposition of Cr and Si requires the use of a "double activator" (fused salt mixture of NaF and NaCl). Cyclic oxidation of a coated coupon with a surface concentration of 34Cr-3Si at 700°C in air has shown excellent oxidation resistance and should show similar behavior in more complex oxidizing atmospheres.

ACKNOWLEDGMENTS

The authors acknowledge the financial support from Oak Ridge National Laboratory (R. R. Judkins) under contract FWP-FEAA028.

REFERENCES

1. S.R. Levine and R.M. Caves, J. Electrochem. Soc., 121, 1974, 1051.

2. C. Wagner, Corros. Sci., 5, 1965, p. 751.

3. E. Godiewska and K. Godiewski, Oxid. Metals, 22, 1984, p. 117.

4. J.E. Restall, U. S. Patent No. 4,687,684, 1987.

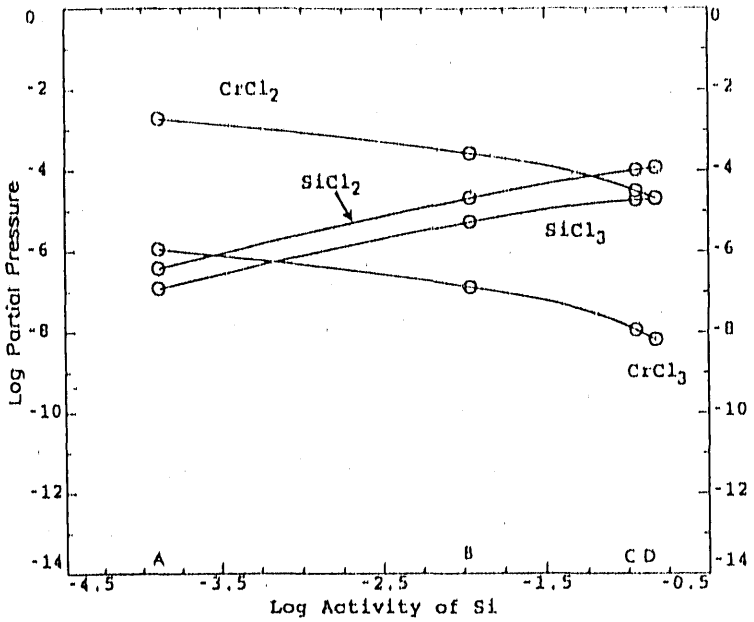

Fig. 1: Equilibrium partial pressures of metallic halides in NaCl activated packs containing Cr-Si masteralloys at 1323 K. Equilibrium in the pack (SiO_2 filler).

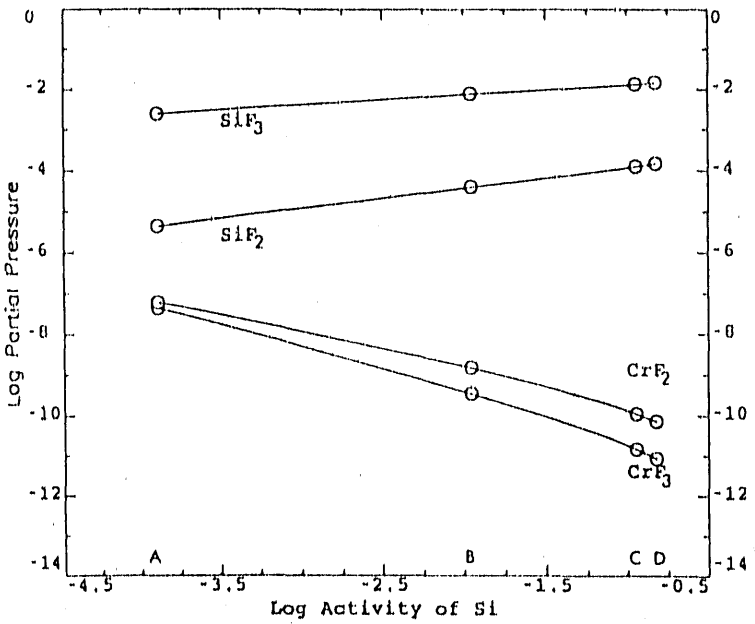

Fig. 2: Equilibrium partial pressures of metallic halides in NaF activated packs containing Cr-Si masteralloys at 1323 K. Equilibrium in the pack (SiO_2 filler).

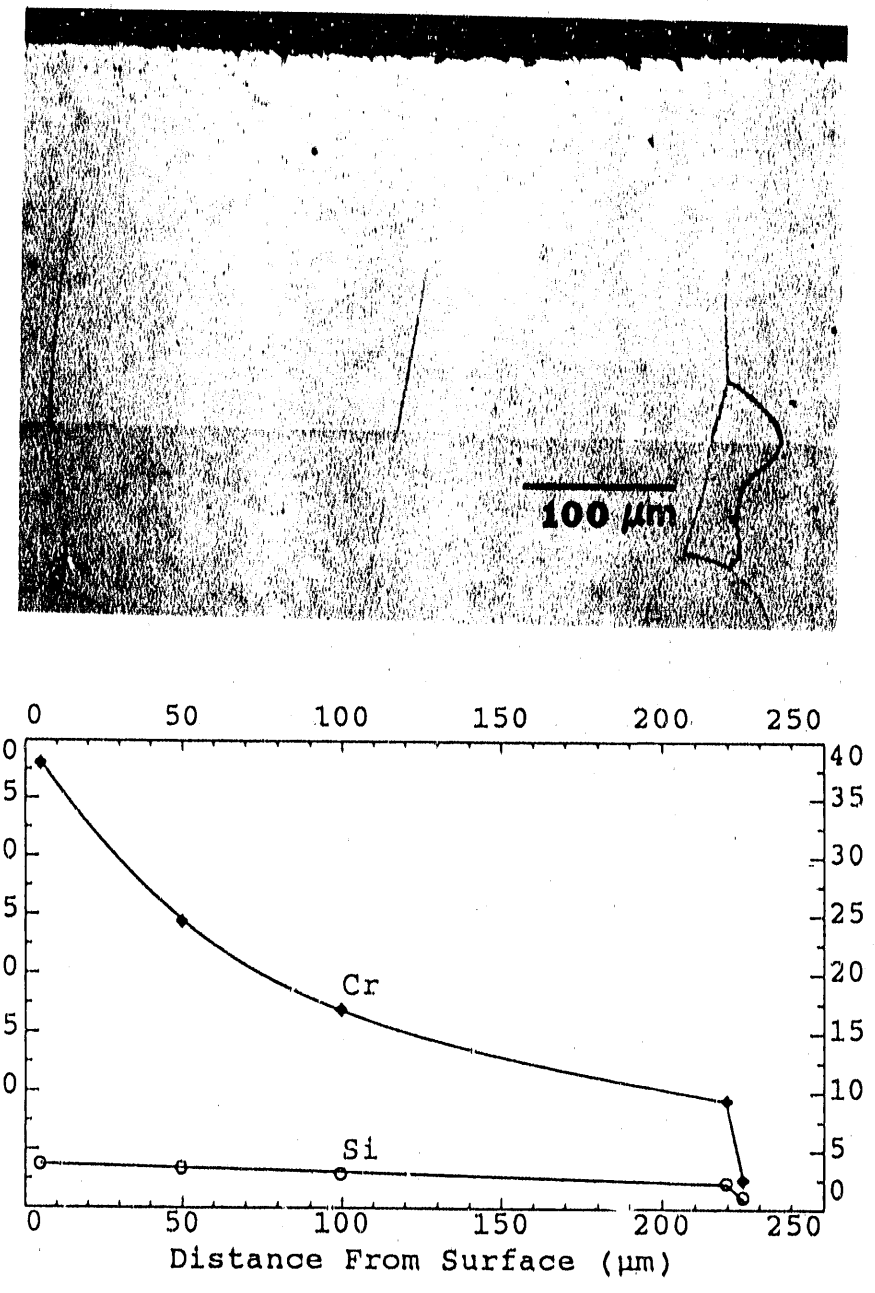

Fig. 3: Microstructure of coating and concentration profiles for Fe-2.25Cr-1.0Mo-0.15C steel using 90Cr-10Si masteralloy and 95at%NaF-5%NaCl (melt) activator diffused at 1050°C for 16 hours (SiO_2 filler)

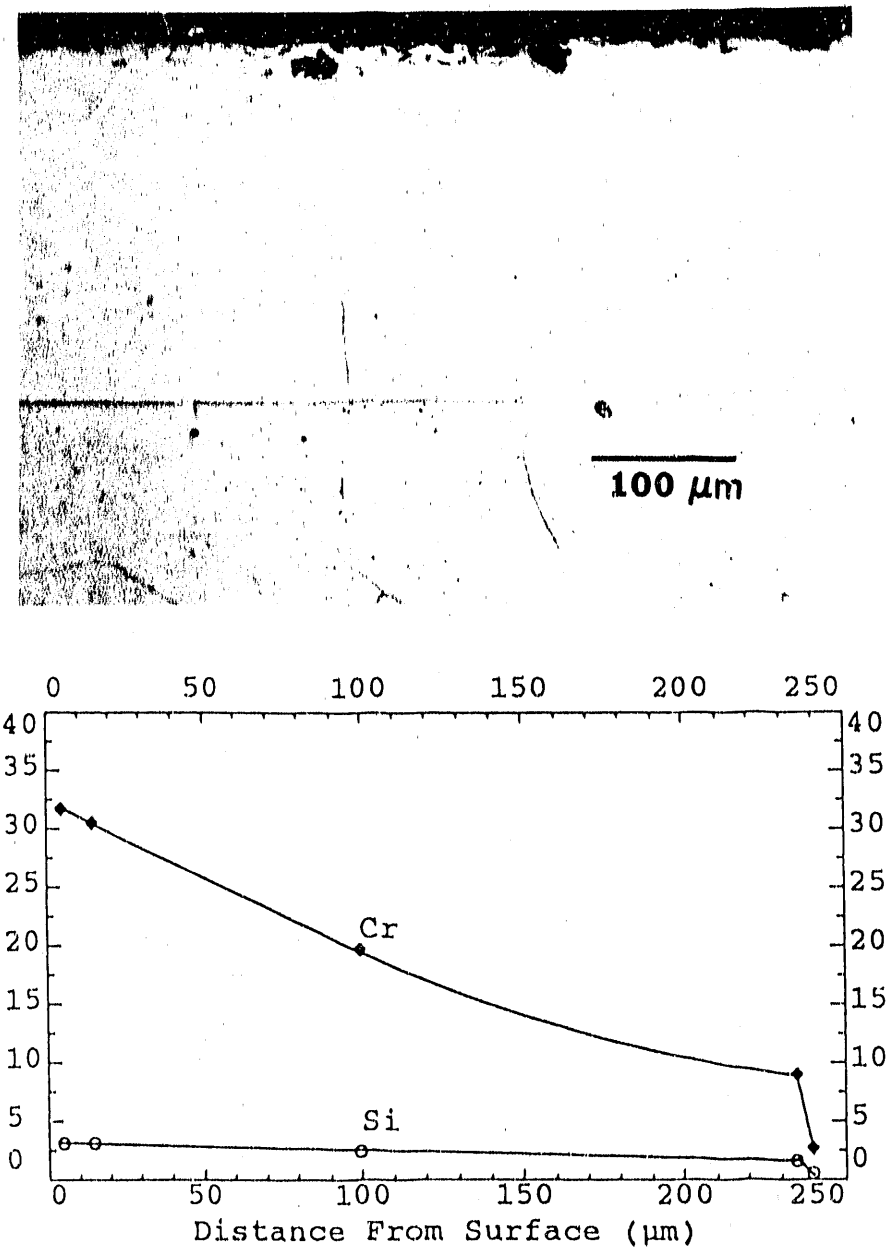

Fig. 4: Coating and concentration profile achieved on Fe-2.25Cr-1.0Mo-0.15C steel using 85Cr-15Si masteralloy and 50wt%NaF-50%NaCl (mechanical mixture) activators diffused at 1070°C for 19 hours (95wt% Al_2O_3 -5% SiO_2 filler).

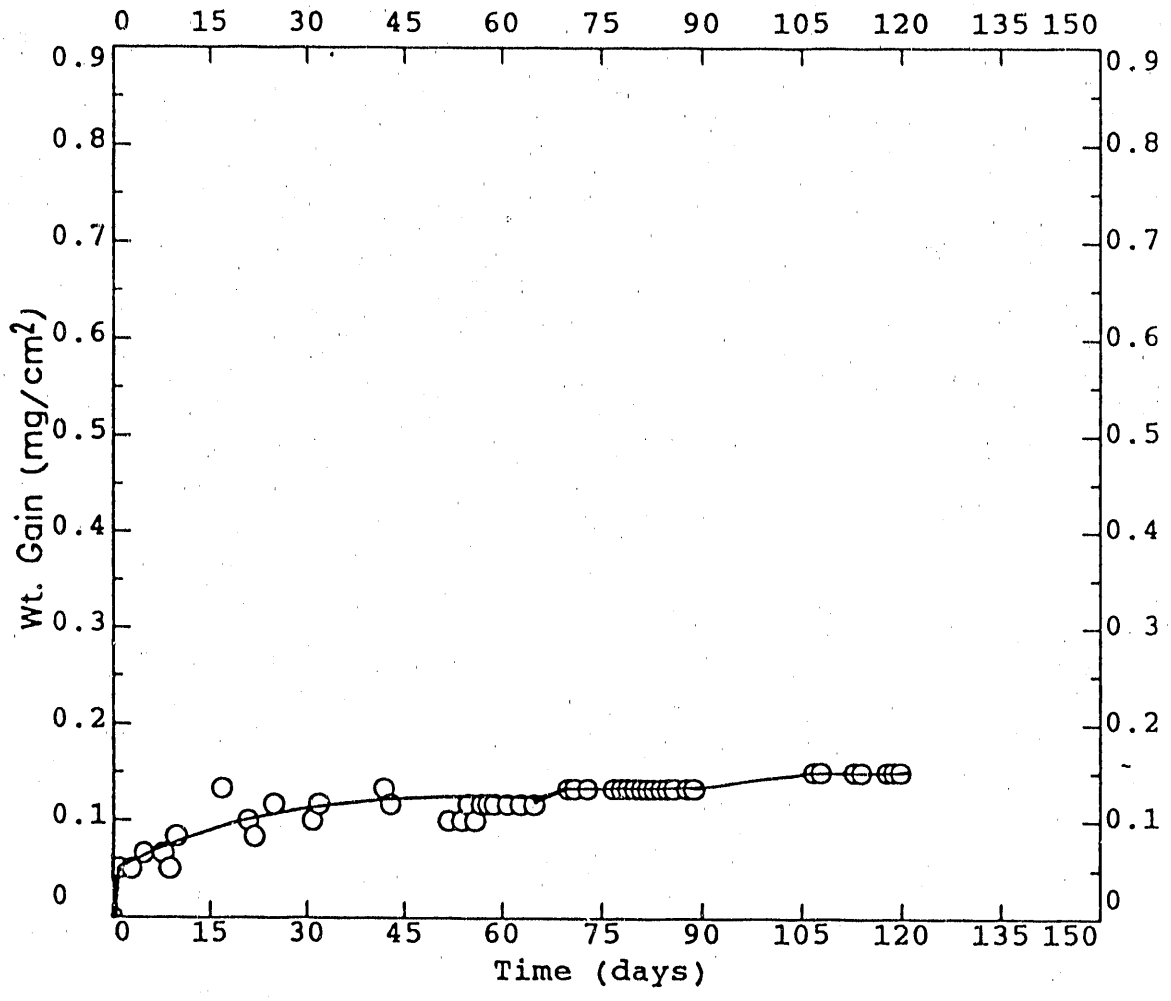

Fig. 5: Plot of weight-gain versus time for the cyclic oxidation in air of coated sample with surface composition of 34Cr-3Si. Each indicated point represents the weight-gain measured after a cool down from 700°C to room temperature

ELECTRO-SPARK DEPOSITED COATINGS FOR PROTECTION OF MATERIALS IN SULFIDIZING ATMOSPHERES

R. N. Johnson

Westinghouse Hanford Company
P.O. Box 1970, L6-39
Richland, WA 99352

ABSTRACT

A wide variety of commercially available hardsurfacing or corrosion-resistant materials have been applied by electro-spark deposition (ESD) for evaluation in fossil energy environments. One of the better performing coatings first identified was chromium carbide, which exhibited nearly four times better sulfidation resistance at 875°C than type 310 stainless steel. A modification of this coating involving the ESD addition of aluminum alloyed into the surface is showing further improvement in sulfidation resistance.

One of the most promising advances in ESD coatings for fossil energy applications has been the successful development of Fe_3Al as a coating material. The ESD parameters have been developed to the point that consistent, defect-free coatings over 100 μm thick can be applied relatively rapidly with good transfer efficiency. The Fe_3Al appears to produce some of the best coatings of all the materials evaluated for ESD application.

Preliminary results from corrosion tests in progress at Argonne National Laboratory show that all the ESD coating candidates provided improved corrosion resistance relative to the untreated 2¼Cr-1Mo substrates, and the coatings that performed best were those highest in aluminum or aluminum + chromium content. The results provide excellent direction indicators for further development of Fe_3Al-based coatings. Developments in progress include the further alloying of aluminum to the Fe_3Al surface by ESD to produce FeAl. Candidate coatings of Fe_3Al + chromium and aluminum, and Fe_3Al + chromium and silicon have been produced and are being evaluated. Similarly, additions of niobium, platinum, and palladium are being developed as possible corrosion inhibitors or protective scale stabilizers.

INTRODUCTION

The objective of this program is to develop candidate coatings, using the electro-spark deposition (ESD) process, for the protection of

materials in sulfidizing atmospheres typical of fossil energy applications.

The ESD process contributes a new dimension to materials for fossil energy applications by allowing the investigation of surface compositions that are difficult or impractical to achieve by other processes. A wide range of both stable and meta-stable surface alloys and structures can be produced by the ESD alloying and by the rapid solidification inherent in the process. Not only can the standard corrosion-resistant alloys be formed or deposited, for example, but it is also possible to apply refractory metal alloy diffusion barriers on the surface or between the substrate and primary corrosion protection coatings.

Coatings of interest include single or multi-layer deposits of commercially available hardfacing alloys, as well as custom formulations of metal aluminides, chromium alloys, refractory metals, carbides, silicides, and borides. Materials to be protected include low alloy steels, alloy 800, type 310 stainless steel, and modified ("lean") stainless steels.

BACKGROUND

Electro-spark deposition is a pulsed-arc micro-welding process that uses short-duration, high-current electrical pulses to weld a consumable electrode material to a metallic substrate. The short duration of the electrical pulse allows an extremely rapid solidification of the deposited material and results in an extremely fine-grained, homogeneous coating that may be amorphous for some materials. The microstructures produced by ESD can provide exceptional corrosion-resistance and wear-resistance for many materials.

The ESD process is one of the few methods available by which a fused, metallurgically-bonded coating can be applied with such a low total heat input that the bulk substrate material remains at or near ambient temperatures. This eliminates thermal distortions or changes in metallurgical structure of the substrate. Since the coating is

metallurgically bonded, it is inherently more resistant to damage and spalling than the mechanically-bonded coatings produced by most other low-heat-input processes such as detonation gun, plasma spray, electrochemical plating, etc. Nearly any electrically-conductive metal, alloy, or cermet can be applied by ESD to metallic substrates.

Further background information on the ESD process is provided in Reference 1.

DISCUSSION OF PRIOR ACTIVITIES

Data collected so far indicate that ESD coatings tend to show lower corrosion rates in most environments than the same material would in either bulk form or as a coating applied by other processes. For example, ESD-applied coatings of chromium carbide-15% nickel exhibit significantly lower corrosion rates in aqueous and liquid metal environments than similar detonation-gun applied coatings.[2] The superior performance of the former is attributed to the extremely fine-grained, nearly amorphous structure inherent to the ESD coatings compared to the larger-grained, more heterogeneous detonation-gun coatings.

In tests at Argonne National Laboratory (ANL), this same ESD coating (chromium carbide-15% nickel) showed four times better sulfidation resistance than Type 310 stainless steel at 875°C.[3] Normally, this composition would not be expected to perform that well because of the strong susceptibility of a nickel matrix to sulfidation attack. Again, the fine-grain structure is believed to be a major factor in the corrosion resistance. This observation is in agreement with other Fossil Energy Materials Program work that indicates one mechanism of improving lifetimes of protective oxide films and scales is to maintain as fine a grain structure as possible.[4]

One of the most significant advances in ESD coatings for use in sulfidation environments has been the successful development of Fe_3Al as a coating material. Oak Ridge National Laboratory (ORNL) has demonstrated the exceptional corrosion properties of Fe_3Al in bulk form,

but alloying the Fe_3Al to achieve acceptable mechanical properties so far appears to compromise the corrosion performance. As one alternate approach, ORNL-supplied electrode materials to Westinghouse Hanford Company (WHC) for use in ESD coating development. (Using Fe_3Al as a coating material allows the selection of the substrate material for optimum mechanical properties and economy while retaining the corrosion resistance offered by the coating.) The coating results to date have been outstanding. The ESD parameters have been developed to the point that consistent, defect-free coatings over 100 μm thick can be applied relatively rapidly with good transfer efficiency. The Fe_3Al appears to produce some of the best coatings of all the materials evaluated for ESD application.

DISCUSSION OF CURRENT ACTIVITIES

Corrosion Tests

Materials

Three ESD coatings were applied to the outside diameter of tubular specimens of 2¼Cr-1Mo steel and were returned to ANL for corrosion testing. The ESD coatings were:

1. Fe_3Al
2. Fe_3Al over an ESD coating of Nb-1Zr
3. Chromium carbide-15% nickel with a further ESD treatment with aluminum to produce chromium carbide + NiAl

The coatings were 20 to 40 μm thick.

Argonne National Laboratory also included in the tests three additional ESD coatings developed in earlier investigations. These were experimental iron-base hardfacings developed by Climax Metals Company as follows:

4. XF2020 (Fe-20Mo-20Cr-10Ni)
5. XF2020 over an ESD coating of Ta-10W
6. XF2020 over an ESD coating of Ta-38Nb-2W-2Mo

The refractory metal alloys are applied as intermediate diffusion barrier coatings to prevent the long-term migration of less resistant constituents from the base metal to the surface and, likewise, to inhibit the diffusion of corroding elements into the base metal. (The ESD process is one of the few practical processes available by which a refractory metal diffusion-barrier coating can be applied to a metal surface.)

Aluminum diffusion coatings are also known to be resistant to sulfidation attack in many sulfur-containing environments. Argonne National Laboratory included aluminized 2¼Cr-1Mo steel specimens in the tests. The principal surface composition of this coating was FeAl, which allowed a comparison with a coating of significantly higher aluminum content than the Fe_3Al ESD coatings. Argonne National Laboratory also included a chromium diffusion coating and an aluminum + chromium diffusion coating in the tests.

Test Conditions

The tests at ANL were designed to simulate heat exchanger tubes exposed in a coal gasification environment. Ring specimens of coated and uncoated 2¼Cr-1Mo steel were assembled to form an internally air-cooled tube with various coatings exposed to the hot, corrosive gas on the exterior. The exterior gas temperature was held constant at 871°C. The exterior metal temperature was held at 500°C or 650°C by adjusting the flow rate of the coolant gas through the tube. The corrodant gas mixtures (room-temperature inlet composition and calculated compositions at elevated temperatures) are provided in Table 1.

The tests (in progress) have so far accumulated exposure times of 500 to 2000 hours. Additional test details are provided in Reference 5.

Summary of Results

Corrosion results, shown in Table 2, are only available for 500-hour exposures on the three ESD coatings of principal interest, compared to 2000-hour exposures on other materials. Therefore, comparisons of corrosion rates are preliminary until comparable test exposures can be

obtained or at least until data can show whether corrosion is progressing at a linear or parabolic rate. However, some conclusions can be drawn from the observations and data available.

Table 1. Gas Compositions (in vol.%) and Oxygen and Sulfur Partial Pressures (in atm) Used in the Test Program.

Gas Species	Gas Mixture Temperature (°C)			
	20	500	650	871
CO	21.8	4.5	31.0	43.9
CO_2	43.7	49.2	30.7	19.7
CH_4	7.3	3.8	1.4	<0.1
H_2	26.2	13.1	24.3	23.4
H_2O	--	28.2	11.7	12.2
H_2S	1.02	1.22	0.94	0.85
pO_2	--	9.2×10^{-28}	1.2×10^{-23}	3.8×10^{-18}
pS_2	--	7.7×10^{-8}	1.0×10^{-6}	1.4×10^{-5}

Table 2. Corrosion Loss, μm, for 2¼Cr-1Mo Steel, With or Without Various Coatings, After Exposure to the Sulfidation Environment.

Material	Temperature		Exposure Hours
	500°C	650°C	
2¼Cr-1Mo Steel	755	>2700 (destroyed)	2000
Cr Carbide + Al	38	125	500
Fe_3Al on Nb-1Zr	95	580	500
Fe_3Al	216	700	500
XF2020	545	1520	2000
XF2020 on Ta-10W	430	1300	2000
XF2020 on Ta-38Nb	500	1800	2000
Al Diffusion Coating (FeAl)	128	90	2000
Cr Diffusion Coating	35	20	2000
Cr + Al Diffusion Coating	35	50	2000

1. For the corrodant gas composition and conditions used in these tests, the diffusion coatings of aluminum, or chromium, or mixed aluminum-chromium produce a thinner scale and show lower corrosion rates than the ESD coatings. This provides valuable direction for the continued optimization of ESD coating compositions. In particular, the Fe_3Al coating still appears to be an excellent base coating with potential for substantial improvement through ESD additions of aluminum, chromium, or other corrosion inhibitors. The aluminum diffusion coating, for example, has a surface composition of primarily FeAl, compared to the Fe_3Al used in the ESD coating. The ESD process can be used to either alloy additional aluminum into the Fe_3Al surface to produce FeAl or to directly apply FeAl with appropriate electrodes.
2. The addition of aluminum to a chromium carbide-15Ni coating by ESD improved the corrosion performance, presumably by the better corrosion resistance of the resulting NiAl. However, FeAl is a more sulfidation resistant material than NiAl in most environments. Therefore, the next chromium carbide coating to be developed will attempt to replace the nickel with iron or FeAl to further improve the corrosion resistance while retaining the good wear and erosion resistance.
3. The XF2020 coating, with or without a refractory metal diffusion barrier, exhibited lower corrosion rates than the base metal, but not as low as desirable to be a candidate for further development. The 10% nickel content probably limits the alloy's performance in the sulfidizing environments.
4. The addition of an intermediate layer of Nb-1Zr as a diffusion barrier coating appeared to be beneficial to the corrosion performance of the Fe_3Al coating. Scanning electron microscopy is being performed to determine the composition gradient of niobium in the coating and to aid in evaluating the role of niobium as a corrosion inhibitor in Fe_3Al.

5. Other oxidation/sulfidation conditions could have a strong influence on the relative performances of the coatings and on the optimum compositions required.

Additional details of the corrosion tests conducted at ANL are provided in Reference 5.

NEW COATINGS IN DEVELOPMENT

Two advanced Fe_3Al candidate coatings were developed and are being characterized while awaiting corrosion tests. One consists of Fe_3Al with ESD additions of chromium and aluminum, and the other of Fe_3Al with ESD additions of chromium and silicon. Other additions being evaluated are niobium, palladium, and platinum. We are also planning to evaluate FeAl as a coating alloy when electrode materials are received from Oak Ridge National Laboratory.

ESD EQUIPMENT DEVELOPMENT

An advanced applicator head has been developed and is being evaluated. The new applicator uses an oscillating electrode motion to prevent welding of the electrode to the substrate during coating, in contrast to the rotating electrode used in our standard system. Preliminary results show that each type of applicator appears to have advantages in specific situations. The new applicator has produced marked improvements in application rates, improved coating finishes, and less sensitivity to electrode geometry variations when used to apply refractory metal diffusion barrier coatings, such as niobium. But Fe_3Al coatings appear better and are applied nearly five times faster using the standard rotating electrode applicator, at least within the range of parameters so far evaluated. The advantages and limitations of each are still being investigated.

REFERENCES

1. R. N. Johnson, "Principles and Applications of Electro-Spark Deposition", *Surface Modification Technologies*, T. S. Sudarshan and D. G. Bhat, eds., The Metallurgical Society, January 1988, p. 189-213.

2. R. N. Johnson, "Coatings for Fast Breeder Reactors", in *Metallurgical Coatings*, Elsevier Sequoia, S. A., New York, 1984, p. 31-47.

3. K. Natesan and R. N. Johnson, "Corrosion Resistance of Chromium Carbide Coatings in Oxygen-Sulfur Environments", *Surface and Coatings Technology*, Vol. 33, 1987, p. 341-351.

4. I. G. Wright and J. A. Colwell, "A Review of the Effects of Micro-Alloying Constituents on the Formation and Breakdown of Protective Oxide Scales on High Temperature Alloys at Temperatures Below 700°C", ORNL/Sub/86-57444/01, September 1989.

5. K. Natesan and R. N. Johnson, "Development of Coatings with Improved Corrosion Resistance in Sulfur-Containing Environments", presented at the International Conference on Metallurgical Coatings, San Diego, April 1990, to be published in *Surface and Coatings Technology*.

SESSION III - CORROSION AND EROSION

CORROSION BEHAVIOR OF MATERIALS IN FBC ENVIRONMENTS

K. Natesan

Materials and Components Technology Division
Argonne National Laboratory
Argonne, IL 60439

ABSTRACT

Oxidation–sulfidation interactions that lead to accelerated metal wastage of components can occur in fluidized-bed combustion (FBC) systems, owing to the presence of sorbent deposits on metal surfaces and/or the low oxygen partial pressures in the exposure environment. Laboratory tests were conducted to examine the influence of deposit and gas chemistry and alloy pretreatment on corrosion of high–chromium alloys such as Incoloy 800 and Type 310 stainless steel. Detailed chemical and physical analyses that were conducted on spent–bed materials were correlated with the observed corrosion behavior of the alloys. The influence of bubbling– and circulating–bed deposits on the corrosion of several candidate alloys was comparatively analyzed.

INTRODUCTION

Combustion of coal in a fluidized bed is widely considered a viable process for producing electric power and generating industrial–process steam. In power–generating applications, tubes carry a working fluid, either steam or air, that eventually drives a turbine. In steam cycles, the fireside surfaces of superheater tubes operate at temperatures of 550–700°C, whereas the temperatures of air tubes can be as high as the bed temperature in the range of 850–900°C. In addition, two types of fluidized–bed combustion (FBC) concepts, namely, Bubbling– and Circulating–fluid bed are popular today. Heat exchanger tubes in the bubbling–bed are immersed in the bed and in the convective sections of the system, whereas in a circulating bed, the heat exchanger tubes are generally situated outside the fluid bed. The operating temperature of the fluid bed directly affects sulfidation of calcined limestone (CaO) or dolomite (CaO,MgO), NO_x formation from fuel–bound nitrogen, combustion of the coal feed and char recycle, and heat transfer to the in–bed surface. The design temperature of the in–bed tube materials can range from 500 to 870°C, depending on the concept and objective of the system. Therefore, the alloys selected for heat exchange should exhibit adequate erosion/corrosion resistance and sufficient mechanical properties at the service temperature. Corrosion and erosion of FBC materials are of practical concern because several AFBC and PFBC bubbling units have experienced substantial metal wastage of their in–bed and above–bed components [1,2].

The purpose of this paper is to present the mechanisms of corrosion in environments that are characteristic of FBC systems and establish the role(s) of major variables in the corrosion degradation of materials. Laboratory test data and corrosion/erosion information obtained from exposures in large FBC test facilities were used to assess the long-term performance of materials in FBC environments.

MECHANISMS OF MATERIAL DEGRADATION

The environment experienced by materials exposed in a fluidized-bed atmosphere is both mechanically and chemically hostile to metals, and the concern over the corrosion/erosion potential for in-bed metal parts has resulted in several test programs in laboratory and pilot-plant scale. The corrosion and erosion data obtained from all these studies have shown considerable variation in the extent of degradation among specimens exposed in different locations within the same bed as well as among specimens exposed in different beds of nominally similar environments. To rationalize this varying behavior of materials in FBC systems, attempts have been and are being made to understand the chemical and physical nature of the in-bed environment and its effect on materials.

Effect of In-bed Gas Environment

The FBC of coal produces a gas that contains principally O_2, CO_2, H_2O, SO_2, and N_2, with minor amounts of SO_3, nitrogen oxides, chlorides, and other volatilized salts. The

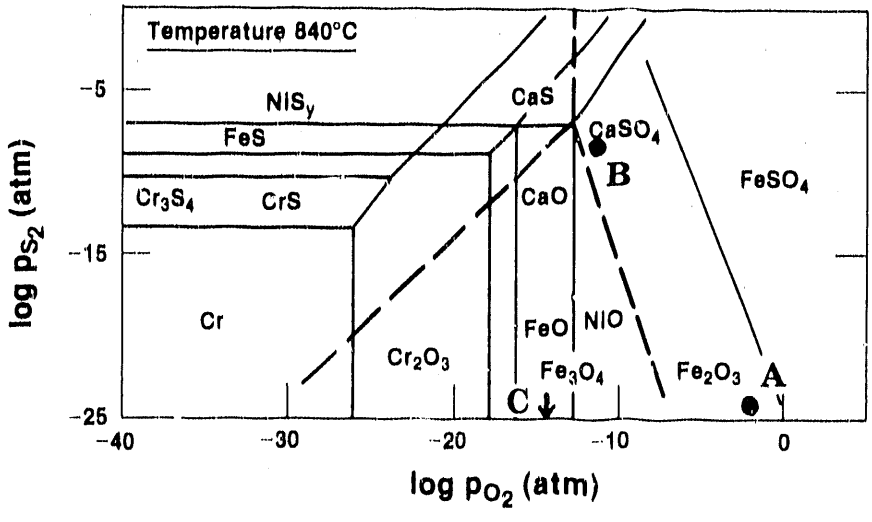

Fig. 1. Diagram of oxygen-sulfur thermochemistry at 840°C, depicting regions of stability of various oxide and sulfide phases. The phase fields for the CaO–CaS–$CaSO_4$ system (dashed lines) are also shown.

composition of the gas depends significantly on the air/coal stoichiometric ratio. In addition, the SO_2 concentration in the gas phase will be determined by the type and amount of sulfur sorbent and the sulfur content of the coal used in the combustion process. Figure 1 shows the calculated thermochemical diagram for iron, chromium, and nickel at 840°C, indicating the thermodynamic stability of various oxide and sulfide phases [3]. From this diagram and from the oxygen partial pressures measured in various FBC systems, it is evident that $CaSO_4$ should be the thermodynamically stable phase in the deposit. The extent of interaction between the deposit and the substrate or the deposit and the scale depends on three factors: the porosity of the deposit layer and the transport of gaseous molecules containing sulfur, the dissociation of $CaSO_4$, to establish a sulfur pressure at the underside of the deposit; and the rate of reaction between the underlying alloy elements and the reactants, such as oxygen and sulfur, to form oxide/sulfide scales and enable internal penetration of oxygen/sulfur into the substrate.

At metal temperatures below 600°C (at which alloys such as low chromium–molybdenum and carbon steels are used), the alloys predominantly develop external scales of iron oxide and internal layers of either iron sulfide or a mixture of iron sulfide and chromium sulfide. In alloys with intermediate chromium levels (e.g., Fe–9Cr–1Mo steel), an internal layer of chromium oxide and/or chromium sulfide forms. At higher chromium levels, e.g., alloys such as 310 stainless steel and Incoloy 800, the scales consist of thin chromium–rich oxides, but the scale thicknesses and depth of sulfur penetration increase with an increase in metal temperature. The oxide scales are porous, however, and generally contain a sulfide phase that results from the reaction between the base metal constituents and the sulfur released from the reaction of chromium or aluminum (in Cr_2O_3–forming or Al_2O_3–forming alloys, respectively) with SO_2. The porosity of the scale enables SO_2 gas molecules to permeate to the scale/substrate interface and cause internal sulfidation. For a given in–bed test condition, an increase in metal exposure temperature leads to only a small increase in scale thickness, but the depth of internal penetration in the substrate material can increase significantly. Even though the gas environment alone can affect the corrosion behavior of materials, the components in FBC systems are always covered by a deposit of bed material. Therefore, an understanding of the corrosion behavior of materials in the presence of a combination of deposit and gas atmosphere is essential.

Effects of Deposits and Gas Chemistry

Deposits in FBC systems are typically a mixture of CaO, $CaSO_4$ (also Mg compounds in the case of PFBCs), ash constituents, and carbon particles. How these constituents are deposited on the metallic surfaces is not well established; however, a typical deposit, which has been reported to consist of particles less than 1 μm in diameter, has a density of >99%. However, such a high density could have resulted from chemical reactions that can occur

within the deposit and physical sintering of deposit constituents over long periods of time at elevated in–bed temperatures. Laboratory studies [3] have shown that (a) a $CaSO_4$ deposit alone can initiate sulfidation in iron– and nickel–base alloys at temperatures of 593°C and higher, and (b) sulfidation of these alloys does not require the presence of sulfur in the gas phase.

Experiments were conducted to examine the combined effect of sorbent/gas chemistry on the corrosion of structural alloys over a wide range of metal temperatures, gas chemistries, gas cycling conditions, and deposit types [3,5]. Figure 2 shows scanning electron microscopy (SEM) photographs of corrosion product layers that developed on Incoloy 800 specimens, coated with deposit mixtures (defined by lines 1–3 and a point 4 in the pO_2-pS_2 diagram in), after exposure at 840°C to a gas mixture with oxygen and sulfur partial pressures of 5.4×10^{-12} and

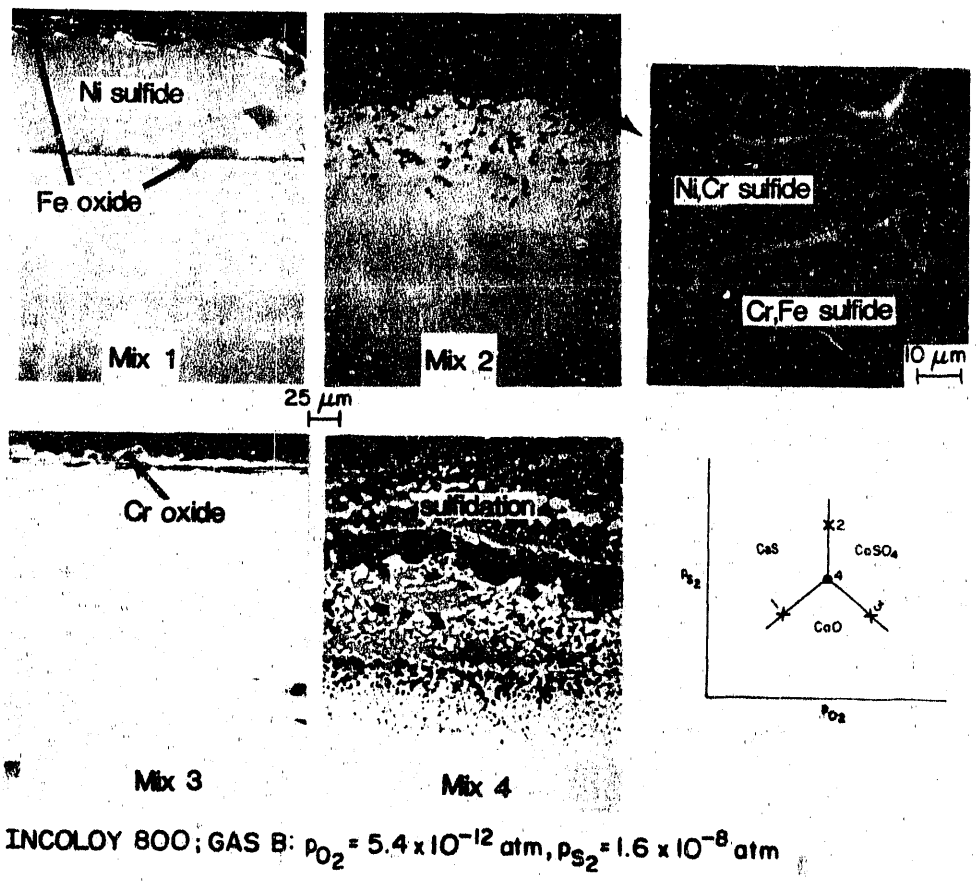

Fig. 2. Morphologies of scale layers that developed on Incoloy 800 specimens coated with different deposit mixtures (defined by lines 1–3 and point 4 of the pO2–pS2 diagram) and exposed to a gas mixture with oxygen and sulfur partial pressures of 5.4×10^{-12} and 1.6×10^{-8} atm, respectively.

1.6×10^{-8} atm, respectively. Specimens coated with mixtures 1, 2, and 4 exhibited sulfidation attack in these experiments, whereas the specimen coated with mixture 3 still developed a thin chromium oxide scale. The implication of these tests is that, when mixtures 2 and 4 are in the presence of SO_2 in the gas phase, a fairly high pS_2 and low pO_2 can be established in the pores of the deposit material and in the deposit/alloy interface region. Consequently, the alloy has a tendency to undergo sulfidation attack in these two tests. In the presence of mixture 1 and SO_2 in the gas phase, the dominant reaction in the deposit will be sulfation of CaO, which will result in an increase in pO_2 and pS_2 in the pores of the deposit; however, the pO_2 will still be below that dictated by the $CaO/CaS/CaSO_4$ triple point. As a result, the alloy will undergo sulfidation attack, and nickel sulfide and iron oxide will be the reaction product phases. In the presence of mixture 3 and SO_2 in the gas phase, the dominant reaction in the deposit will be sulfation of CaO to $CaSO_4$ (which can decrease the pS_2 in the pores of the deposit material) and the alloy will have a tendency to undergo oxidation. On the other hand similar experiments conducted with Type 310 stainless steel showed (Fig. 3) only an oxidation mode of attack in the presence of any of the four deposit mixtures. However, these specimens were exposed at an

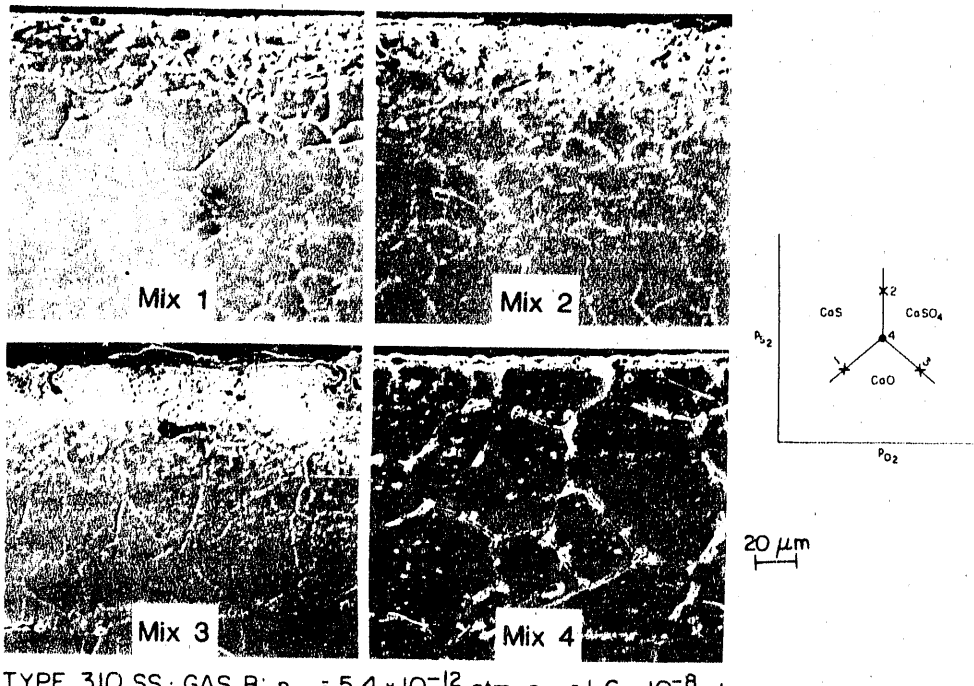

Fig. 3. Morphologies of scale layers that developed on Type 310 stainless steel specimens coated with different deposit mixtures (defined by lines 1–3 and point 4 of the pO2–pS2 diagram) and exposed to a gas mixture with oxygen and sulfur partial pressures of 5.4×10^{-12} and 1.6×10^{-8} atm, respectively.

elevated temperature for only ~100 h. In earlier 3000–h tests [5], it was shown that the presence of a $CaSO_4$ deposit and a low pO_2/moderate pS_2 gas mixture can trigger sulfidation of the underlying base alloy, even in Type 310 stainless steel, but the extent of attack is much less than that in Incoloy 800.

The role of two pretreatments (namely, preoxidation and precarburization) of alloy specimens in the subsequent corrosion of alloys in the presence of different deposit mixtures and gas environments was examined. In the preoxidation treatment, the alloys were oxidized for ~80 h at 840°C in a sulfur-free gas atmosphere with a pO_2 of 3.6×10^{-14} atm. Preoxidation of the specimens in a low-pO_2 environment produced thin, chromium-rich oxide scales on the specimens. Subsequent exposure of the specimens to any of the four deposit mixtures in the presence of a SO_2-containing gas mixture had no deleterious effect on the preformed oxide scales, indicating that sulfidation of Cr_2O_3 scale (once developed) is extremely slow and of no concern from the standpoint of corrosion.

In the precarburization treatment, the specimens were carburized at 840°C in a 5 vol.% CH_4-H_2 gas mixture for 64 h. In such an environment, carburization of the alloy specimens simulates carbon pickup in the alloy because of the deposition of unburnt carbon (i.e.,in the vicinity of coal feed ports or due to incomplete combustion) on the alloy components. The precarburization resulted in extensive precipitation of (Cr,Fe) carbides in the alloy. As a result, the effective chromium concentration and activity in the alloy decreased and caused the alloy to behave (from scaling standpoint) as a medium-chromium alloy. At a carbon activity of ~0.3, up to which $M_{23}C_6$ carbide is stable, the precipitation of carbides can lower the chromium content in the matrix phase to less than 15 wt.%. Figure 4 shows SEM photographs of initially carburized Incoloy 800 specimens that were coated with deposit mixtures 1–4 and exposed at 840°C to a gas mixture with oxygen and sulfur partial pressures of 5.4×10^{-12} and 1.6×10^{-8} atm, respectively. Exposure of the precarburized specimens led to the formation of nonprotective surface scales in the presence of all the deposit mixtures investigated. A comparison of photographs in Figs. 2 and 4 shows that precarburization has little effect on the morphology of the scale layers and that the layers are somewhat thicker in the precarburized specimens. Sulfidation is the mode of attack in this alloy either with or without precarburization treatment. The SEM photographs in Fig 5 show the scale layers that developed on Type 310 stainless steel after exposure to oxygen-sulfur environments in the presence of different deposit mixtures. The photographs show a substantial amount of carbide precipitation, but the thickness of the scale layers is much less than in Incoloy 800, confirming a superior corrosion resistance of the Type 310 stainless steel, even with carburization pretreatment. These results also indicate that carburization is not essential to subsequent sulfidation, and that the alloy scaling behavior of the carburized alloys is determined by the effective chromium concentration in the austenite matrix.

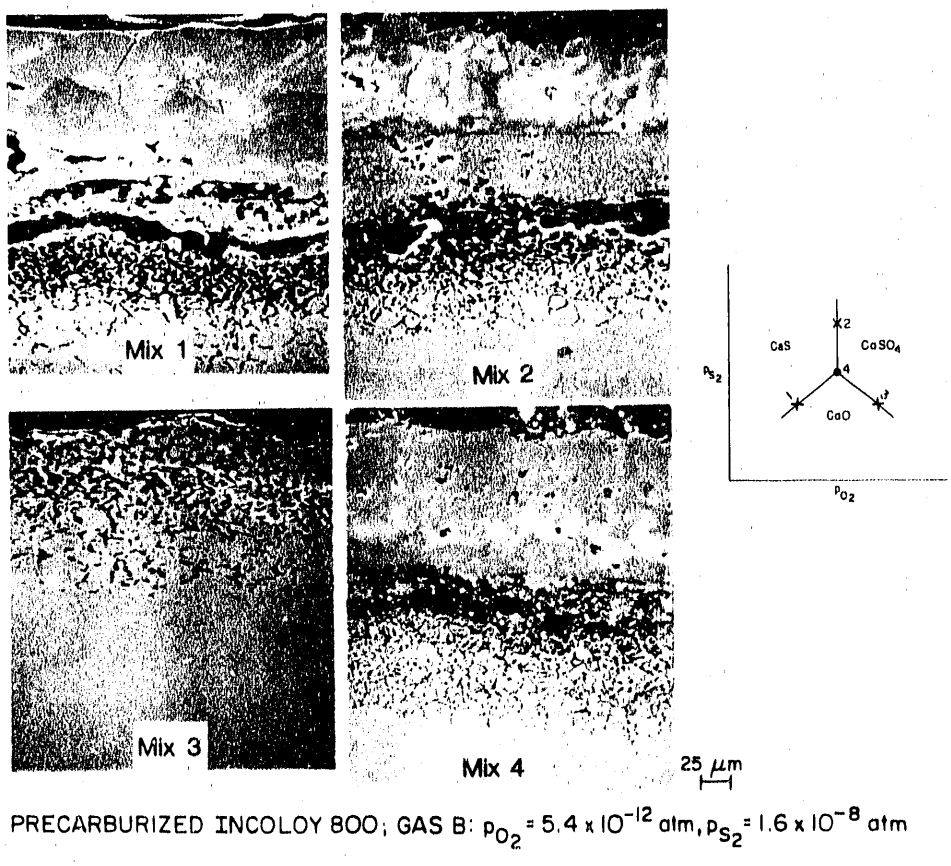

PRECARBURIZED INCOLOY 800; GAS B: $p_{O_2} = 5.4 \times 10^{-12}$ atm, $p_{S_2} = 1.6 \times 10^{-8}$ atm

Fig. 4. Morphologies of scale layers that developed on initially carburized Incoloy 800 specimens coated with different deposit mixtures (defined by lines 1–3 and point 4 of the pO_2–pS_2 diagram) and exposed to a gas mixture with oxygen and sulfur partial pressures of 5.4×10^{-12} and 1.6×10^{-8} atm, respectively.

Effect of Spent-bed Materials

Spent-bed materials were obtained from four different test facilities, namely, TVA 20–MW, IEA/Grimethorpe, Nova Scotia/Point Tupper, and CE/Lurgi. Materials from the first three sources were from bubbling–type beds, whereas the CE/Lurgi material was from a circulating–type bed. In addition, the IEA/Grimethorpe facility is a pressurized unit, whereas the others are atmospheric combustors. Spent–bed materials from the TVA facility were obtained for two different time periods, when either Reed or Fredonia limestones were used as a sulfur sorbent. The particle size distribution for the four spent–bed materials indicated that ~40 wt.% of the material was ~1690 μm in diameter and was essentially the same for the three different FBC materials. To determine chemical differences (if any) between different mesh–size fractions, we analyzed samples (from the various sources) in mesh–size ranges of –8 to +18 and –40 to +60 (average particle sizes of ~1690 and 335 μm, respectively), as well as a sample of ash from a circulating–fluid bed system [6]. Several inferences were drawn from

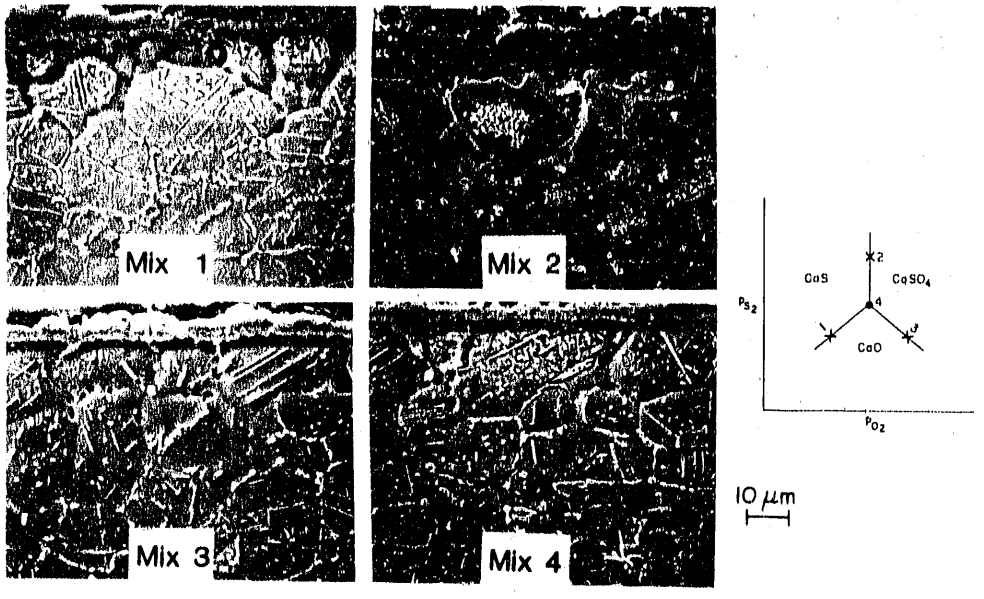

PRECARBURIZED 310 SS; GAS B: $p_{O_2} = 5.4 \times 10^{-12}$ atm, $p_{S_2} = 1.6 \times 10^{-8}$ atm

Fig. 5. Morphologies of scale layers that developed on initially carburized Type 310 stainless steel specimens coated with different deposit mixtures (defined by lines 1–3 and point 4 of the pO_2–pS_2 diagram) and exposed to a gas mixture with oxygen and sulfur partial pressures of 5.4×10^{-12} and 1.6×10^{-8} atm, respectively.

these results: (a) The K_2SO_4 content of the TVA–bed material is approximately the same when either the Fredonia or Reed limestone was used, but is much greater than that of the material from the other sources (this indicates that K_2SO_4 content is probably related to coal and not sulfur sorbent); (b) The ash from the circulating–fluid bed has a low alkali sulfate content compared to that of ash from bubbling beds; (c) The $CaSO_4$ content of the circulating–fluid bed ash was also extremely low compared to that of bubbling beds; (d) A wide variation in SiO_2 and Al_2O_3 content was observed in the materials from the various bubbling beds; (e) The calculated values for the free silica (probably quartz) in the materials range between 0.5 and 38.0 wt.%, if one assumes that all the alumina in the spent–bed material is present as dehydrated kaolinite (with a composition of $Al_2O_3.2SiO_2$). The highest value was obtained for the Grimethorpe material, which had an average particle size of ~1690 μm; and (f) The calculated value for the free silica amount in the CFB ash is ~27.6 wt.%.

Effect of bubbling-bed deposits

To evaluate the effect of spent-bed materials on the corrosion of candidate materials, three gas environments (identified as A, B, and C in Fig. 1) were selected. Gas mixture A has pO_2 and pS_2 values of 7×10^{-3} and 2.6×10^{-28} atm, respectively, which typify a flue-gas environment. Gas mixture B has pO_2 and pS_2 values of 5.4×10^{-12} and 1.6×10^{-8} atm,

respectively, which represent a reducing environment during gas cycling. Gas C has a pO_2 value of 3.6×10^{-14} atm and has no sulfur, representing a reducing atmosphere without sulfur. It has been shown earlier [3,5], that sustained exposure (500 to 2000 h) of structural materials to gas mixture B in the presence of a $CaSO_4$ or $CaSO_4/CaO$ deposit can lead to internal sulfidation of the alloys. As a result, gas mixtures A and C were used along with the spent-bed materials from the different FBC systems to evaluate corrosion susceptibility of candidate materials.

Figure 6 contains SEM photographs of scale layers that developed on Incoloy 800 and Type 310 stainless steel specimens that were coated with a reagent–grade $CaSO_4/CaO$ mixture and spent-bed materials from the TVA AFBC and Grimethorpe PFBC facilities. The top row of photographs, which shows the morphologies that developed when Incoloy 800 specimens with the deposits were exposed to gas mixture A (typical flue-gas atmosphere) reveals that the specimens developed thin chromium oxide scales in the presence of all three deposits. The middle row of photographs shows that deposit–coated Incoloy 800 was exposed to a gas mixture of low-pO_2 and no sulfur, the scales that developed were predominantly Fe and (Fe,Cr) oxide and (Fe,Ni) sulfide. Such scales are nonprotective. Scale layer thicknesses ranged from 0.30 to 1.2 mm; the thicker layers in the presence of spent-bed materials are indicative of the more aggressive nature of the bed material toward Incoloy 800 than that of the reagent grade material. Further, the source of sulfur for sulfidation of these specimens is the deposit material because the gas phase included no sulfur-containing species. Also, in the absence of deposits (i.e., absence of a sulfur source), Incoloy 800 specimens would have developed thin chromium-oxide scales when exposed to the low-pO_2 atmosphere used in these tests. Bottom row of photographs shows that developed when Type 310 stainless steel specimens with the deposits were exposed to the sulfur–free low pO_2 atmosphere, the scales that formed were thin and composed of oxide and sulfide phases, with some intergranular precipitation of sulfides in the substrate alloy. These results conclusively indicate that the composition of the deposit material, the local gas phase environment, and alloy chemistry must be considered in an evaluation of oxidation–sulfidation behavior of candidate heat exchanger materials for FBC applications.

CORROSION IN BUBBLING–BED VS. IN CIRCULATING–FLUID BED ENVIRONMENTS

A comparative study of materials performance in environments that simulate both bubbling– and circulating–fluid bed (CFB) atmospheres was conducted at Argonne National Laboratory [5]. In these experiments, specimen surfaces were coated with either reagent–grade $CaSO_4$ (simulating a bubbling–bed deposit) or CFB ash. The specimens were exposed for 3000 h at a metal temperature of 871°C while the gas phase was maintained at ~900°C. The corrosion test probes were cooled to room temperature after every 500 h of exposure at the test temperature. During the cooldown period, the specimens were recoated with the deposit

material to ensure that there was no lack of reactant for continuation of the corrosion process. Gas mixture B and compressed air were used to simulate the bubbling-bed and CFB conditions, respectively.

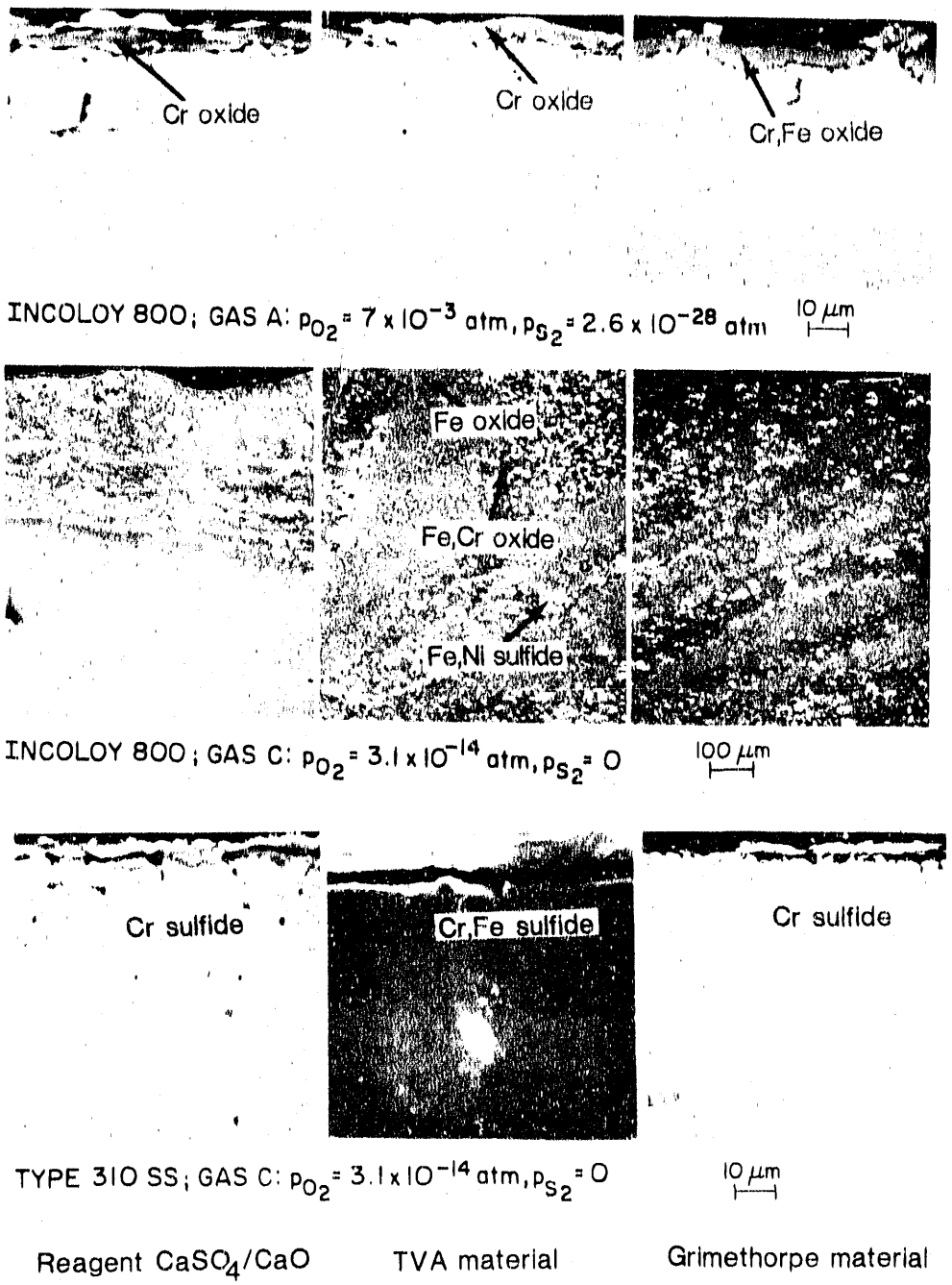

Fig. 6. Corrosion scale morphologies that developed on Incoloy 800 and Type 310 stainless steel coated with a reagent grade CaO-$CaSO_4$ mixture or spent-bed materials from TVA and Grimethorpe and exposed to different gas mixtures.

Figure 7 shows the corrosion–product morphologies observed on the deposit side of Types 304 and 310 stainless steel and Incoloy 800 specimens after 3000–h exposures in the two test environments. The figure shows that Type 304 stainless steel with a chromium content of ~18 wt.% predominantly developed (Cr,Fe) oxide scales in the presence of either deposit. The scale thicknesses were fairly small, and the substrate exhibited a significant amount of carbide precipitation at the grain boundaries. $CaSO_4$–coated Type 310 stainless steel, even though it contained 25 wt.% Cr, developed a ragged oxide scale with substantial internal penetration of sulfur. On the other hand, CFB–ash coated Type 310 stainless steel developed chromium oxide

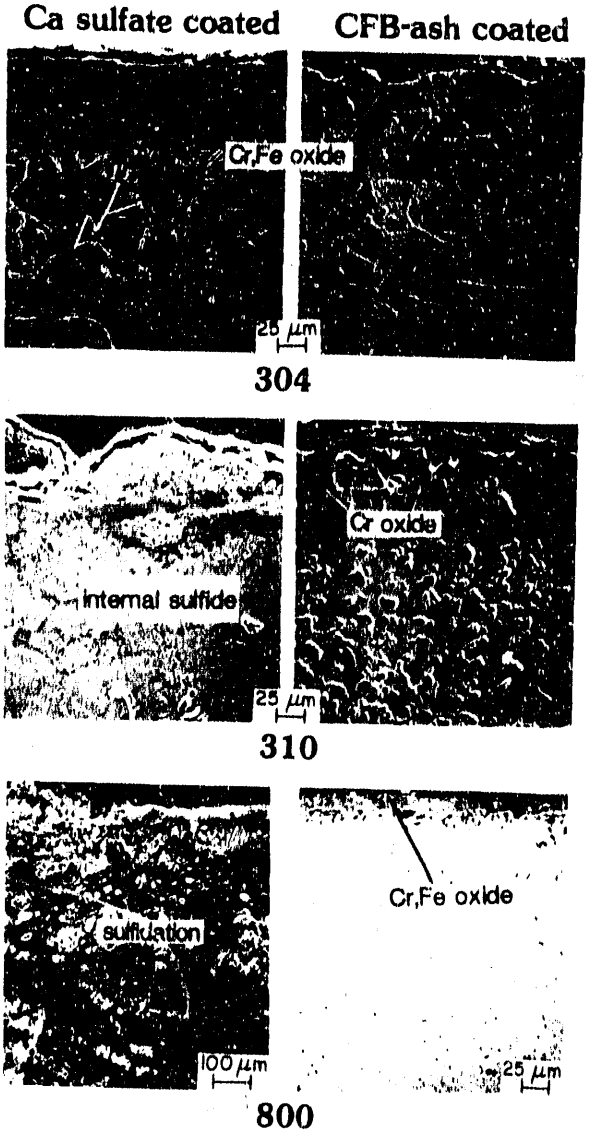

Fig. 7. Microstructures of Types 304 and 310 stainless steel and Incoloy 800 with either $CaSO_4$ or CFB ash deposit after 3000–h exposure at 871°C.

scale, and virtually no sulfur was detected in either the scale or the substrate alloy. In general, Type 310 stainless steel was susceptible to formation of (Fe,Cr) sigma phase during thermal exposure. An Incoloy 800 specimen coated with reagent-grade $CaSO_4$ underwent severe sulfidation indicating susceptibility of an alloy with higher nickel content (32.5 wt.%) to sulfur attack. On the other hand, the same alloy coated with CFB ash developed a (Cr,Fe) oxide scale (with no trace of sulfur), indicating that negligible sulfur pressure was established via dissociation of sulfur-containing ash components in the deposit layer. Similar corrosion information has been developed for alloys exposed to simulated FBC environments [5].

IN-BED MATERIALS DATA

In the preceding section, we showed that materials (especially high-chromium alloys exposed to an FBC environment) can undergo corrosion by oxidation-sulfidation and that life expectancy of components would be strongly influenced by the internal sulfidation penetration of the substrate materials. To be a viable candidate for use in FBC system, an alloy must exhibit acceptable corrosion rates, even under the most extreme in-bed reducing conditions ($pO_2 = 10^{-12}$ to 10^{-14} atm). In general, metallic heat-exchanger tubes are coated with a dense and sometimes thick deposit, the composition of which depends on gas chemistry, exposure time, and temperature. In-bed wastage data, developed over the years, in general, indicate that the erosion contribution will not be significant for components that operate between 650 and 900°C; however, the erosion processes in FBCs are not well understood, and a few instances of unanticipated catastrophic erosion of in-bed cooling tubes have been reported. Thus, the interpretation of metal wastage data calls for caution. These difficulties not withstanding, the materials data base was reviewed earlier [1,2] to evaluate the time and temperature dependence of the wastage, scale thickness plus internal penetration, and corrosion rates for several alloys or classes of alloys tested in FBC systems. The data for a few of the alloys are summarized below.

Figure 8 shows plots of corrosion rate for Type 310 stainless steel and Incoloy 800 versus in-bed exposure temperature obtained over a wide range of conditions and exposure times in several FBC test facilities. Corrosion rates were calculated on the assumption of parabolic kinetics (i.e., the amount of degradation proportional to the square root of the duration of exposure) for both scale thickness and penetration depth. In some instances, where scale thickness and penetration data are not reported, the metal loss information was used to calculate corrosion rates. A comparison of the laboratory and in-bed data shows that the former is higher by a factor of two; however, the laboratory data were obtained in a much more reducing environment (i.e., pS_2 and pO_2 in the vicinity of the CaO–CaS–$CaSO_4$ triple point) and can be considered as an upper bound rate for the material from the standpoint of corrosion. Over the entire temperature range, the corrosion rate for Incoloy 800 is approximately twice

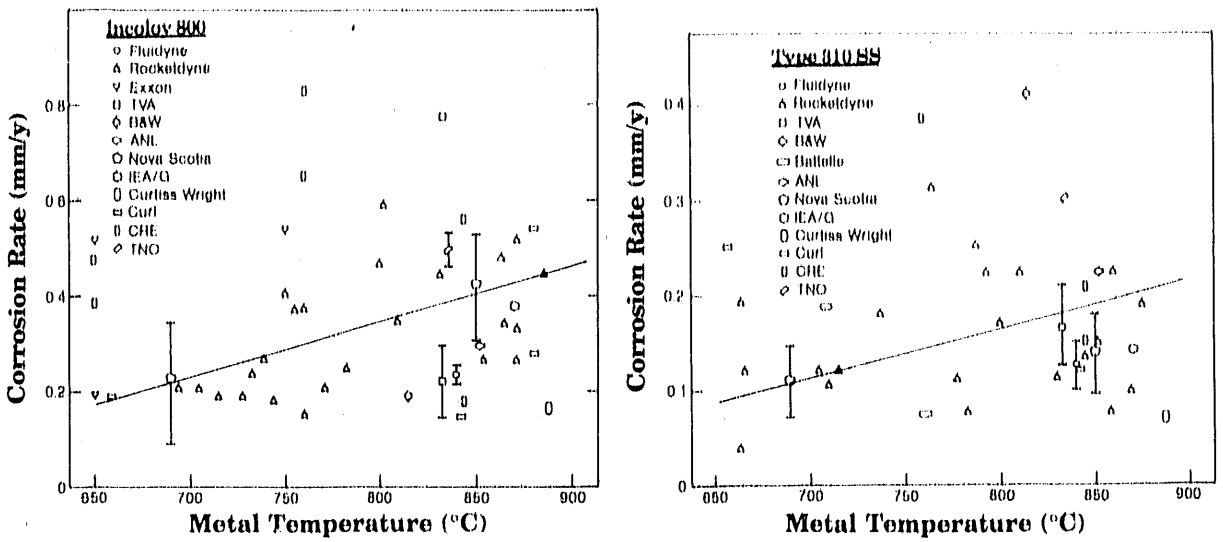

Fig. 8. Variation of corrosion rate with temperature for Incoloy 800 and Type 310 stainless steel.

that for Type 310 stainless steel. Furthermore, the long-time performance of the Incoloy 800 is not promising, because the life-limiting parameter, namely, the internal penetration depth, increases significantly with exposure time. In addition, the alloy is susceptible to catastrophic oxidation-sulfidation corrosion when exposed to low-pO_2 environments, as evidenced by the laboratory test results discussed in earlier sections of this paper.

The information presented in this paper establishes the role of several key variables in the corrosion of candidate structural materials for FBC application and also aids in understanding the mechanism of corrosion in the dynamic environment of the FBC system. Materials degradation depends on local conditions that are prevalent near the area of attack, and these can fluctuate significantly over small intervals of distance and time. If we could establish quantitative relationships among operating parameters and measurements of process conditions (as independent, controllable variables), and local bed conditions in the vicinity of in-bed component materials and the corrosion/erosion behavior of those components (as dependent variables), we would significantly speed the development of FBC technology.

CONCLUSIONS

This paper addresses the role of several key variables such as deposit chemistry, gas chemistry, and alloy pretreatment in the oxidation-sulfidation behavior of candidate structural alloys. Several deposit mixtures involving combinations of reagent-grade CaO, CaS, and $CaSO_4$, and spent-bed materials from the TVA 20-MW, IEA/Grimethorpe, Nova

Scotia/Point Tupper, and CE/Lurgi CFB facilities, were used in the study to evaluate the effect of deposit chemistry on the corrosion process.

The laboratory test results established the gas chemistry and deposit compositions that can lead to accelerated oxidation–sulfidation corrosion of materials. The results also showed that the scale thickness and internal penetration in the presence of circulating-fluid bed (CFB) ash were much lower than those obtained with $CaSO_4$ or spent-bed materials from bubbling-bed units. From the corrosion standpoint, several commercial/engineering alloys can be expected to perform acceptably over a long period of time in CFB units, primarily because the sulfur pressure established by the CFB ash is negligible. Based on the test results, a similar conclusion cannot be reached for materials performance in bubbling-bed systems. A comparison of laboratory test data— developed in a low-pO_2 environment— with the in-bed corrosion data showed that the corrosion rates determined in the laboratory are higher by a factor of ~2 and that these rates can be treated as an upper bound value if the alloys are not susceptible to breakaway corrosion.

ACKNOWLEDGMENTS

This work was supported by the U.S. Department of Energy, Office of Fossil Energy, Advanced Research and Technology Development Materials Program, Work Breakdown Structure Element ANL–3, under Contract W–31–109–Eng–38. D. L. Rink assisted with the experimental program and the microstructural analyses of exposed specimens.

REFERENCES

1. K. Natesan, S. A. Miller, and W. F. Podolski, *An assessment of the performance of heat exchanger materials in fluidized bed combustors*, Argonne National Laboratory Report ANL–86–42 (Feb. 1987).

2. K. Natesan, S. A. Miller, and W. F. Podolski, *J. Mater. Eng.*, *9* (1987) 269.

3. K. Natesan, *High Temp. Technol.*, *4* (1986) 193.

4. A. J. Minchener, P. T. Sutcliffe, I. S. Scott, R. S. Courtney, D. M. Lloyd, D. C. Read, T. Golesworthy, and J. E. Oakey, *Materials evaluation for fluidized-bed combustion systems*, Report CS–3511, Electric Power Research Institute, Palo Alto, CA, 1984.

5. K. Natesan and W. F. Podolski, *Laboratory Tests in Support of Atmospheric Fluidized-Bed Cogeneration Air Heater Experiment: Summary Report*, Argonne National Laboratory Report ANL-88–36 (July 1988).

6. K. Natesan, *Assessment of Corrosion in FBC Systems*, Proc. Fourth Berkeley Conf. on Corrosion–Erosion–Wear of Materials at Elevated Temperatures, January 31–February 2, 1990, Berkeley, CA, to be published.

FIRESIDE CORROSION TESTING OF CANDIDATE SUPERHEATER TUBE ALLOYS, COATINGS AND CLADDINGS

S. Van Weele

J. L. Blough

Foster Wheeler Development Corporation
12 Peach Tree Hill Road
Livingston, New Jersey 07039

INTRODUCTION

Coal-ash corrosion continues to be a problem affecting the reliability and life of a coal-fired power plant, especially at utilities where impurities in the coal are not monitored. The higher metal temperatures experienced by reheaters during start-up and by superheater and reheater tubes as a unit is overfired also accelerate the coal-ash corrosion.

Coal-ash is caused by the formation of alkali-iron trisulfate on the tube surfaces (1,2). The corrosion occurs at the ash and gas interface. The alkali and sulfur come from the coal and the iron from either the coal or the tubewall surface. The aggressiveness of the alkali-iron is most severe if the tubewall temperature is between 538 and 704°C (1000 and 1300°F). Recent work by Rehn (3) and Kihara (4) has refined the bell-shaped curve to higher temperatures and has shown shape and temperature variation with alloy composition. The resultant corrosion rate is affected by the alkali content of the deposited ash and by the SO_2 content in the combustion gas (4-8). The actual means of trisulfate formation and whether it will occur are very complex subjects, and all the variables affecting the formation are not fully understood. The literature infers that the corrosion depends on coal quality (3). As a result a number of investigators have prepared corrosivity indices are functions of the impurities in the coal (9,10).

The "Boiler R&D for Improved Coal-Fired Power Plants" project, sponsored by the Electric Power Research Institute; Foster Wheeler Development Corporation; and Ishikawajima-Harima Heavy Industries Company, ltd,. is being conducted to investigate the variables affecting the coal-ash corrosion mechanism (11). This program includes laboratory and field corrosion testing to determine the corrosion resistance of boiler material as a function of coal impurities concentration. The coals and their deposits, which are formed on the tube surfaces, are being analyzed to provide a data bank and possibly an index for predicting corrosivity under various combustion conditions.

Laboratory and field testing are being combined (12). The laboratory tests (13) include material exposures in corrosion retorts, coal and deposit characterization, and combustion testing. The field tests comprise corrosion probe testing, loop testing, and deposit analysis. This work is being performed not only to obtain corrosion rates on various materials, but also to provide a good characterization of the chemistry and mechanism of deposit formation. The combined effort will result in a methodology for the selection of replacement alloys and the prediction of corrosion rates with alternative coals.

This paper describes the exposure and evaluation of a group of new alloys and claddings techniques proposed by Oak Ridge National Laboratories for the advanced coal fired power plant. The work is divided into tasks. Task 1, a literature search updating the previous work by Rehn, has been completed and is being finalized for publication. Task 2, the laboratory corrosion testing, was started and has completed 100 hours of the 1000 hours test for two of the four test conditions being evaluated.

DISCUSSION OF CURRENT ACTIVITIES

Experimental Procedure

The experimental test retort and test methods used in this project are nearly identical to work conducted in the past by Rehn 3,7,8 and will not be described here in detail. The retorts have fifteen test chambers each containing three sets of coupons for each of the materials listed in Table 1. The coupons to be tested were coated with synthetic coal ash, placed in a sealed retort, and exposed to a simulated flue gas at either 650°C or 700°C for 1000 hours. After the first 100 hour exposure, one set of coupons was removed from testing and destructively examined. Another set of coupons was steam cleaned to simulate sootblowing, recoated with fresh ash and replaced in the retort. The third set of coupons was recoated with fresh ash and replaced in the retort. Both sets of coupons will continue to be exposed and recoated in 100 hour increments until 1000 hour of exposure is achieved. The lean stainless steel specimens and one set of alloy 800H specimens were coated with synthetic ash consisting of 90 wt% Fe_2O_3, 5 wt% K_2SO_4, and 5 wt% Na_2SO_4. All other specimens were coated with an ash of 25 wt% Fe_2O_3, 37.5 wt% K_2SO_4, and 37.5 wt% wt% Na_2SO_4. The 90-5-5 ash is comparable in composition to deposits found on superheater tubes from a boiler burning a moderately aggressive coal. The 25-37.5-37.5 ash is a much more aggressive ash than is found in a typical boiler but provides an accelerated test and an environment where there is a large data base of coal ash corrosion data for comparison. It was established in previous work (3,4) that approximately 30 mg/cm^2 is sufficient to provide an aggressive non-diluted ash in 100 hour exposures. To insure that an active ash is present the coupons were coated with approximately 170 mg of synthetic ash per cm^2. The simulated flue gas was composed of 14.0%CO_2, 10.0%H_2O, 4.0%O_2, and 0.25%SO_2 with a balance of N2. The exposures with 1.0%SO_2 at 650° & 700°C are scheduled for later retort test.

Examination of Specimens

Macroscopic Examination of Specimens

The specimens exposed to the synthetic ashes and synthetic combustion gas containing 0.25%SO_2 at 650°C and 700°C for 100 hours are currently being examined to determine both the mode and severity of attack. The condition of the fused ash on the coupon surface was observed and the ash/corrosion products were removed by a three step process of caustic, inhibited acid bath and mechanical abrasion with pumice. The method of attack on all specimens was pitting attack from narrow isolated to broad profuse pitting in some covering the complete specimen surface. On several specimens corrosion occurred nonuniformly with patches of deep corrosion and completely unaffected areas side by side. Scales formed on the iron and nickel based alloys possessed a lamellar structure, gunmetal gray in color. Both aluminides displayed a scale morphology different from the other alloys: Dark, hard nodules formed on both coated and uncoated backside areas of the aluminide specimens. The scale that formed showed angular, crystalline facets quality, and proved to be quite dense and tenacious.

Microscopic and Chemical Analysis of the Scale and Metal

An EXEC autoscan with a EDAX energy dispersive x-ray analysis unit was used for microscopic analysis and determination of the chemical composition for the scale and metal surface. Examination of the bottom and sides of pits on the attacked surface in many cases showed sulfidation and surface enrichment of chromium. This examination is ongoing and further analysis will be forth coming.

Weight Loss and Wastage Determination

Weight losses per a unit area for specimens exposed at 650°C and 700°C are shown in figures one. The weight loss data indicate that the temperature for the maximum wastage varies with different alloys. The LSS with the less aggressive ash and the 17-14CuMo, and aluminides with the most aggressive ash indicate high wastage rates as expected by the low chromium levels in these alloys. The 347 at 700°C has an unusual higher than 17-14CuMo wastage rate. This behavior will be clarified with further evaluation. The ash with the higher levels of alkali sulfates is 3-4 times more aggressive than the ash containing the lower level as shown by comparing the data for alloy 800 and alloy 800*.

Specimen thickness reductions, both in the form of general wastage and pitting attack for specimens exposed at 650°C and 700°C are shown in figures two and three respectively. Pitting attack was evident on the majority of specimens except for modified 800H coated with the (90-5-5) less reactive ash.

Alloy RA-85H, 671/LSS and 671 experienced almost no pitting at 700°C but did experience pitting at 650°C. While the LSS and alloy 800 with the less aggressive (90-5-5) ash showed minimal pitting at 650°C but experienced pitting at 700°C. This further indicates the bell shape curve of corrosion vs temperature varies with different alloys. The pitting results do not indicate the same beneficial effect of chromium as the weight loss data in Figure 1. The trend is, as previously found by Rehn(8), that alloys containing nickel levels above 30 percent are not beneficial and negate the benefit of chromium. If the nickel is above 30 percent then the chromium level must be increased. Also the beneficial effect of Aluminum and Silicon have been reconfirmed as shown by the lower corrosion of RA-85H.

CONCLUSIONS

The retort testing with a synthetic coal ash containing 37.5 percent Na_2O_3, 37.5 percent K_2SO_4 and 25 percent Fe_2O_3 in combination with a synthetic combustion gas containing 0.25 percent SO_2 provides very aggressive exposure for all the alloys. The reduction to 90 percent Fe_2O_3, 5 percent Na_2SO_4 and 5 percent K_2SO_4 results in a 3-4 fold decrease in the weight loss and an even greater reduction in the pitting depths. Alloy 671 experienced the lowest weight loss of $32mg/cm^2$ which is 130 mils/year extrapolated at a linear rate.

The temperature for the maximum corrosion, in the classic bell shaped coal ash corrosion vs temperature curve, varies with different alloys.

Preliminary analysis indicates a beneficial effect of Chromium, Aluminum, and Silicon in reducing the coal ash corrosion. Additional microstructural and EDAX analysis will be performed to correlate various effects and to evaluate the attack mechanism with the various alloys.

REFERENCES

1. W. Nelson and C. Cain, Jr. "Corrosion of Superheaters and Reheaters of Pulverized-Coal-Fired Boilers." Transaction of the ASME, Series A. Journal of Engineering for Power. Vol. 82, 1960, pp. 194-204.

2. C. Cain, Jr. and W. Nelson. "Corrosion of Superheaters and Reheaters of Pulverized-Coal Fired Boilers, II. " Transaction of the ASME. Journal of Engineering for Power. vol. 83. 1961, pp. 468-474.

3. I. M. Rehn. "Fireside Corrosion of Superheater/Reheater Alloys for Advanced Cycle Steam Plants." EPRI CS-5195, May 1987.

4. S. Kihara, et al. "High Temperature Corrosion in Energy System." TMS/AIME, M.F. Rothman (ed.). 1984, pp. 361-376.

5. K. Nakagawa, et al. "Electrochemical Evaluation of Superheater Materials in Coal Ash Corrosion Atmosphere." ASME 83-JPGC-Pwr-38, 1983.

6. K. Nakagawa, et al. "Coatings and Bimetallics for Aggressive Environments." Conference Proceedings. ASM. R.D. Sisson, Jr. (ed.). 1984, pp. 77-88.

7. I. M. Rehn. "Laboratory Fire-Side Corrosion Evaluation of Improved Superheater Tube Alloys and Coatings." EPRI CS-3134. Project 644-1, June 1983.

8. I. M. Rehn. "Fireside Corrosion in Coal-Fired Boilers." EPRI CS-1653. Project 644-1, November 1980.

9. R. W. Borio and R. P. Hensel. "Coal-Ash Composition as Related to High-Temperature Fireside Corrosion and Sulfur-Oxides Emission Control." Transactions of the ASME. Journal of Engineering for Power. Vol. 94, 1972, pp. 142-148.

10. J. Shigeta, et al. "Development of a Coal Ash Corrosivity Index for High Temperature Corrosion." ASME 86-JPGC-FACT-3, 1986.

11. W. Wolowodiuk, et al. "Coal-Ash Corrosion Investigations." Proceedings of the First International Conference on Improved Coal-Fired Power Plants. Palo Alto, California, November 1986.

12. J. L. Blough, S. Kihara. "Coal-Ash corrosion in Superheaters and Reheaters. "Corrosion/88, Paper 129. Nation Association of Corrosion Engineers, St. Louis, Missouri March 1988.

13. W. Wolowodiuk, S. Kihara, K. Nahagaua. "Laboratory Coal Ash Corrosion Tests. "EPRI. GS-66449, July 1989.

TABLE 1

TEST ALLOYS

	Cr	Ni	Fe	Mo	Nb	Al	Ti	Mn	Si	Other
Fe_3Al+Cr	2		82			16				
$(Ni,Fe)_3Al$+Cr	7	70	13			9				
LSS 14	16	65		2.1	0.15			0.3	1.9	B, V
17-14CuMo	16	15	61	2.5	0.4		0.2	0.8	0.63	Cu
347 18	12	67		0.7				1.6	0.6	
RA85H	18	15	61			1		0.5	3.9	Cu, N
800MOD	21	31	43	2	0.2		0.3	1.9	0.24	B, V
NF709	20	25	51	1.5	0.3			1.0	0.6	B, N
690 30	58	10								
690/LSS	31	57	9					0.17	0.26	
690/800	31	57	9					0.17	0.26	
CR35A	35	45	19		0.59		0.11			
671 48	52									
72/800	43	55	0.55							
671/LSS	48	51						0.11		

Typical Compositions

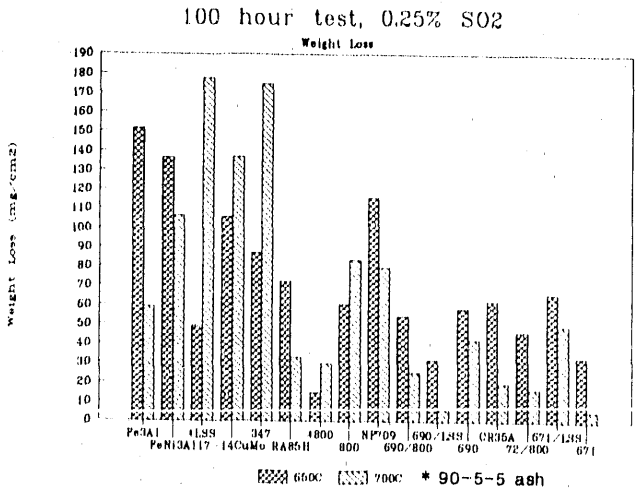

FIGURE 1

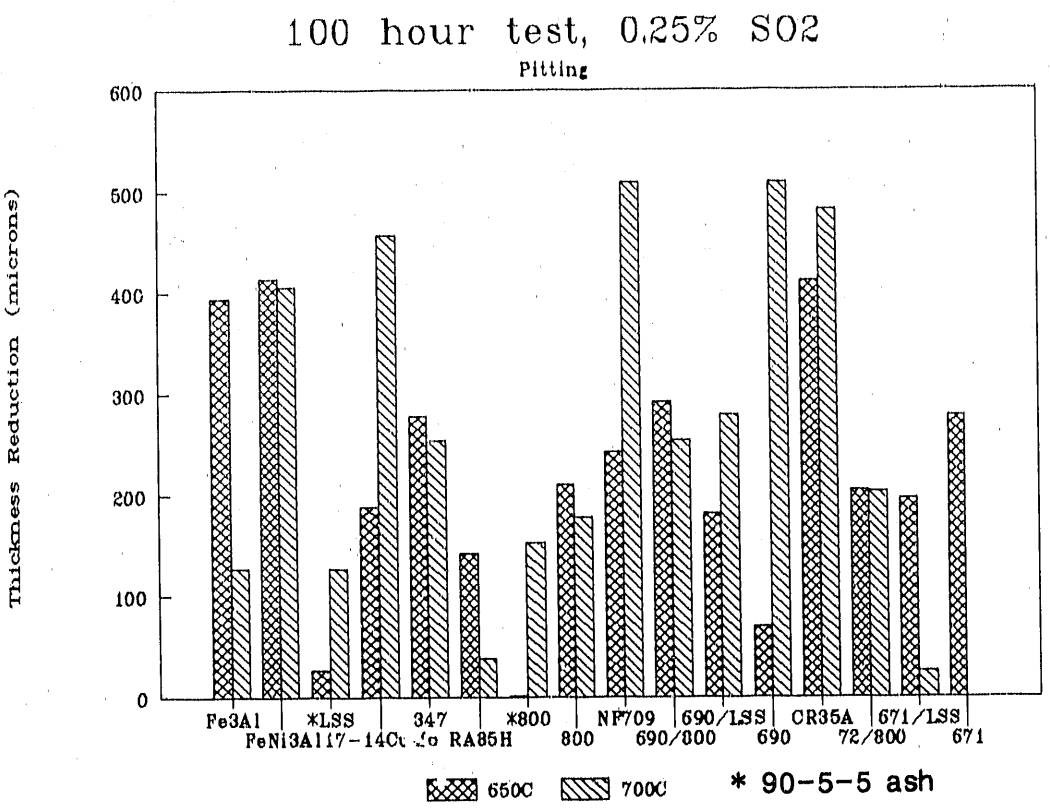

FIGURE 2

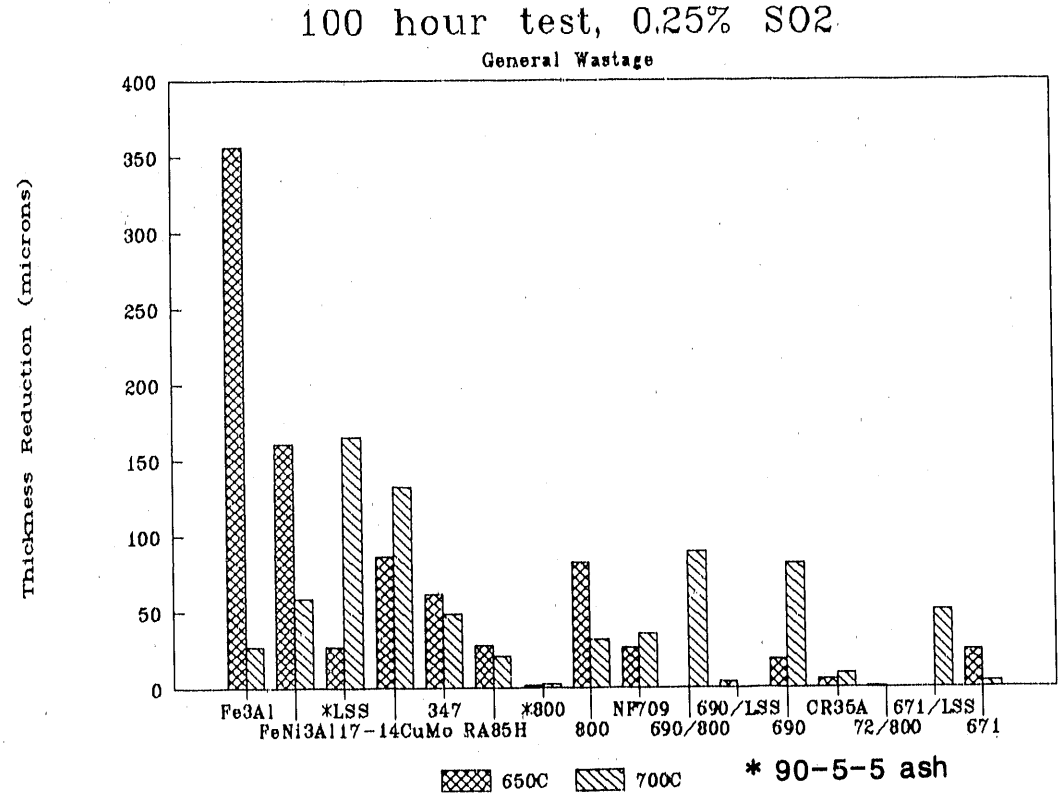

FIGURE 3

THE EFFECTS OF ALLOYING CONSTITUENTS AND CONTROL OF THE GROWTH OF PROTECTIVE OXIDE SCALES

I. G. Wright*, J. A. Colwell*, D. R. Baer** and L. H. Schoenlein**

Battelle Columbus(*) and Pacific Northwest Laboratories(**)

ABSTRACT

Results are presented for the effects of minor alloying additions on the breakdown of chromia scales on Fe-Cr-Ni-based alloys at 700°C in an environment simulating those in coal combustion or conversion processes. Under isothermal conditions the scales formed by FeCrNi-based alloys were inferior in protection to those on similar FeCr-based alloys, except where additions of Si or Y/Y_2O_3 were made by powder metallurgical (PM) techniques. No large difference in S segregation at the alloy-scale interface was found between the PM Y_2O_3-containing alloy, and the PM or cast FeCrNi base alloy. The chromia scales degraded via the formation of Fe-rich sulfides external to the main scale, with eventual overgrowth by these sulfides and undermining of the original chromia scale. Alloys that were preoxidized in a S-free environment exhibited the same mode of degradation. No S penetration of the chromia scales was observed as a precursor to external sulfide formation.

INTRODUCTION

The intended operating conditions of the alloys studied in this program are the temperature range of 500 to 700°C, in environments representing those in coal combustion or gasification processing. The objectives of this program are to understand the effects of minor alloying constituents on the development and mode of breakdown of protective oxide scales, with a view to achieving improvements in high-temperature corrosion resistance of heat exchanger and heat recovery materials. The main focus of this paper will be the scales formed on alloys based on Fe-25Cr-20Ni, although reference is also made to the observations made for the other alloy classes studied.

EXPERIMENTAL PROCEDURES

The base alloy compositions studied were Fe-25Cr (compositions in weight percent), and Fe-25Cr-20Ni. These were made by vacuum arc remelting and hot forging, and exhibited a total impurity content of <0.05% (0.002-0.003% S). Small additions of single alloying elements (Al, Si, Y, Hf, Mn, Nb) were made by remelting and casting or, to the FeCrNi base only, by rapid solidification (RS) or high-energy milling (HEM) followed by consolidation by hot isostatic pressing. By analogy with results from higher temperature studies, the major intended effects of the microalloying additions were

modification of the type of protective scale formed via, for instance, changes in the sequences of events occurring in the initial stages of scale development, and improvement of the adherence of the scale to the alloy, especially during thermal cycling.

The gas composition chosen simulated that resulting from substoichiometric combustion of a high-S coal; the equilibrium O and S partial pressures of this gas at the metal temperature of interest, i.e., 700°C, were 10^{-20} and 10^{-8} atm, respectively. The expected corrosion product formed by the FeCrNi and FeCr alloys in this environment, judged from Ellingham-Pourbaix phase stability diagrams, is a protective Cr_2O_3 scale, although if the alloy becomes sufficiently depleted in Cr, Fe (or Ni on FeCrNi) sulfides (MPt. of Ni-NiS is 645°C) may form. In addition, any Fe- or Ni-base oxide formed on the alloy would be converted to the respective sulfide on contact with this gas mixture.

Limited studies of the early stages of oxidation were made, and an Auger electron spectroscopy (AES) high vacuum chamber was used to characterize segregation behavior on the surfaces of the three master alloys during the early stages of scale growth(1).

RESULTS

The weight gain-time data for the Fe-25Cr and Fe-25Cr-20Ni-base alloys exposed in the simulated substoichiometric gas mixture at 700°C were not very reproducible, but in general the alloys based on Fe-25Cr exhibited smaller weight gains than those based on Fe-25Cr-20Ni(2). Additions to the ferritic alloy base that exhibited lower weight gains than the master alloy were 1 and 3% Si, and 1% Y. Additions of 0.1 and 1% Hf and 0.1% Y appeared to have little effect on the weight gains, whereas 1 and 2% Al and 2% Mn led to larger weight gains. Of the additions made to the cast Fe-25Cr-20Ni alloy, 1 and 3% Si and 1% Hf led to consistently lower weight gains, whereas additions of Y, Si, or Y_2O_3 made by PM routes led to lower weight gains than the cast base alloy, with the additions of Si and Y_2O_3 being the most effective.

The initially formed scales were degraded by a process that was manifested by the appearance on the outer surface of the scale of small nodules (or crystals) of Fe-rich sulfide, the time at which such nodules appeared, their number, and rate of growth being dependent on the type of alloying addition, ar d on some experimental variables the most critical of which was the approach of the gas composition to the CrS/Cr_2O_3 phase boundary. On some alloys, these external Fe-sulfide nodules grew and eventually impinged on each other so that a semi-continuous external sulfide layer was formed; as the nodules grew they also developed morphologies suggestive of their having been molten, which may have been a consequence of an increasing Ni content. The original protective scale typically remained unchanged in appearance until the external Fe-rich sulfides had grown into a layer, at which point it was transformed into a thickened, mixed Cr-oxide/sulfide which apparently

allowed S transport into the alloy.

A question of particular interest is the way in which the initial Fe-rich sulfides form on the outside of an apparently protective scale, since their morphology suggests that a continuous source of Fe is available at the outside of the scale. As a means of trying to follow the sequence of events involved in breakdown of these scales, alloy samples were first preoxidized under S-free conditions, and then were exposed to the $H_2/H_2O/H_2S$ environment without any intermediate cooling or handling. The weight change data for the alloys based on Fe-25Cr-20Ni in these exposures are illustrated in Fig. 1. The cast alloys exhibited a rapid weight gain in the first 75 h of exposure to the $H_2/H_2O/H_2S$ gas mixture and essentially all showed evidence of change on the external surface of the oxide scale. The two cast alloys that were subsequently exposed for longer times (2% Al or 3% Si) exhibited similar weight gains to the unalloyed base alloy after 75 h, although observations of the scales in plan at this point did not reveal any signs of distress. With increased exposure, these alloys experienced a decrease in the rate of weight gain such that the slopes of the weight gain-time curve after the longer times approximated that of the binary Fe-25Cr ferritic alloy. Of the alloys produced by PM, RS alloys containing 0.1 and 1.0% Y, and 1.5% NbC exhibited weight gains over the first 75 or 125 h of exposure similar to those of the cast alloys, whereas RS alloys containing 2 or 6% Si, and the HEM alloy containing 2% Y_2O_3 exhibited low rates of weight gain out to 550 h exposure which were of the same order as that for the binary Fe-25Cr material.

The general morphologies of the scales formed on alloys that were removed after 75 h exposure to the $H_2/H_2O/H_2S$ gas mixture are illustrated in Fig. 2. The scales comprised essentially a thin basal layer of oxide, on the outer surface of which had grown nodules of Fe-Ni sulfide. In no case was any obvious breaching of the basal scale observed and there were no obvious internal sulfide particles connected to the outer nodules. The cast alloy containing 1% Al which exhibited the largest weight gain formed a scale which in places consisted of a semi-continuous outer sulfide layer on top of a basal layer which had locally thickened.

Figure 3 shows an area on unalloyed Fe-25Cr-20Ni after 75 h exposure and illustrates the chemistry associated with areas of external sulfide nodules. The X-ray maps indicate that the nodules are Fe-sulfides containing some Ni but essentially no Cr, and that the basal layer contains Cr with a small amount of Fe but no S or Ni. There appears to be no S penetration into or beneath the basal layer. In the area shown, one of the external nodules is growing on top of a 4 to 5 μm-thick basal layer, whereas the other nodule is growing on an area where the basal layer is much thinner, on the order of 1 μm or so. Quantitative spot analyses indicated that the alloy beneath the latter nodule was depleted in Cr to about 4% and enriched in Ni to about 43%, some 2.5 μm beneath the nodule. Essentially no Cr depletion was observed immediately beneath areas of thicker basal scale. At a depth of 4 μm into the alloy, some 5 μm from the centerline of the external nodule, the alloy composition was essentially nominal with a Cr content of 25%.

An electron probe line scan through an external nodule formed on the cast Fe-25Cr-20Ni-1Si

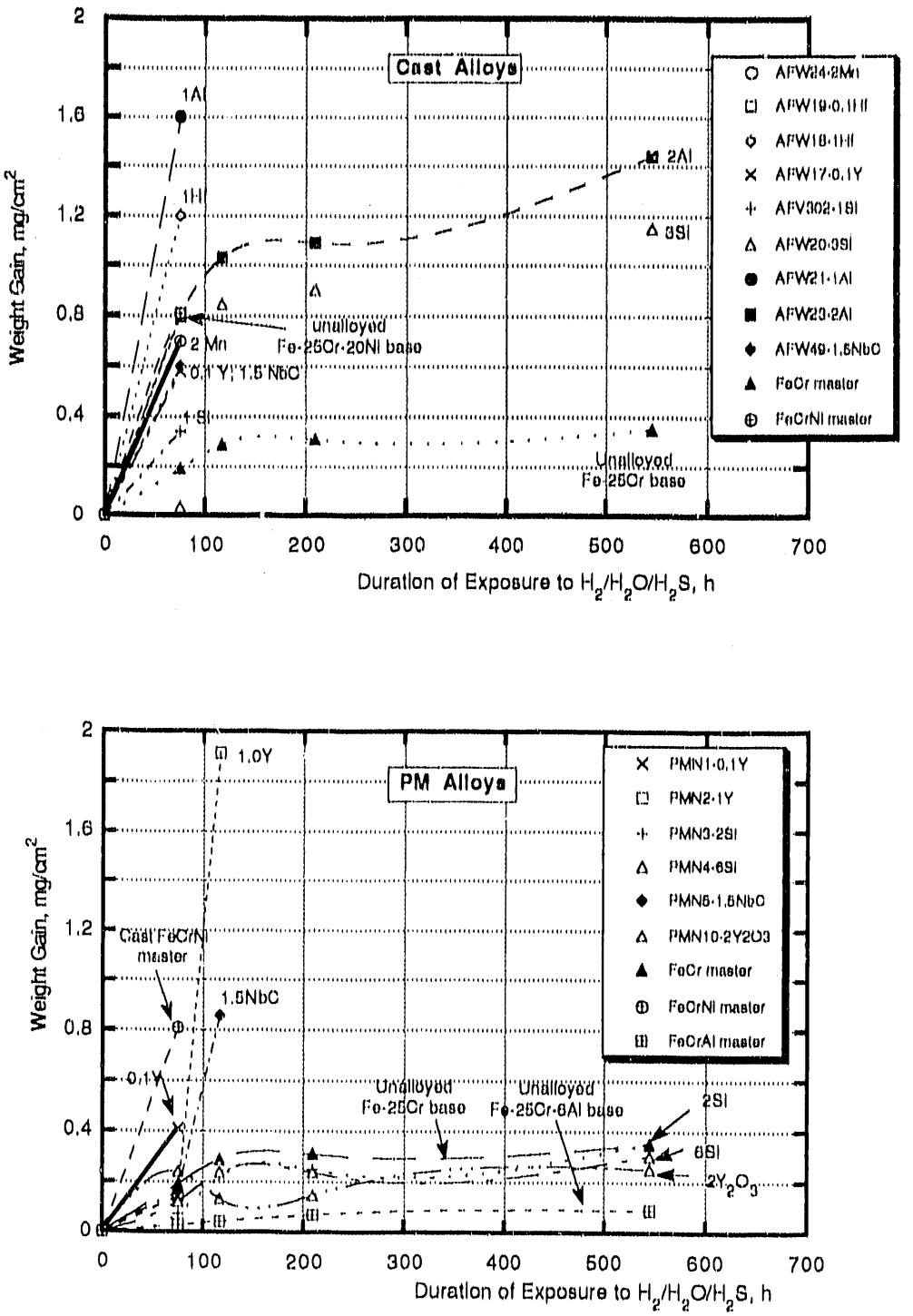

Fig. 1. Weight gain-time data for preoxidized Fe-25Cr-20Ni-based alloys exposed to a simulated substoichiometric gas mixture at 700°C.

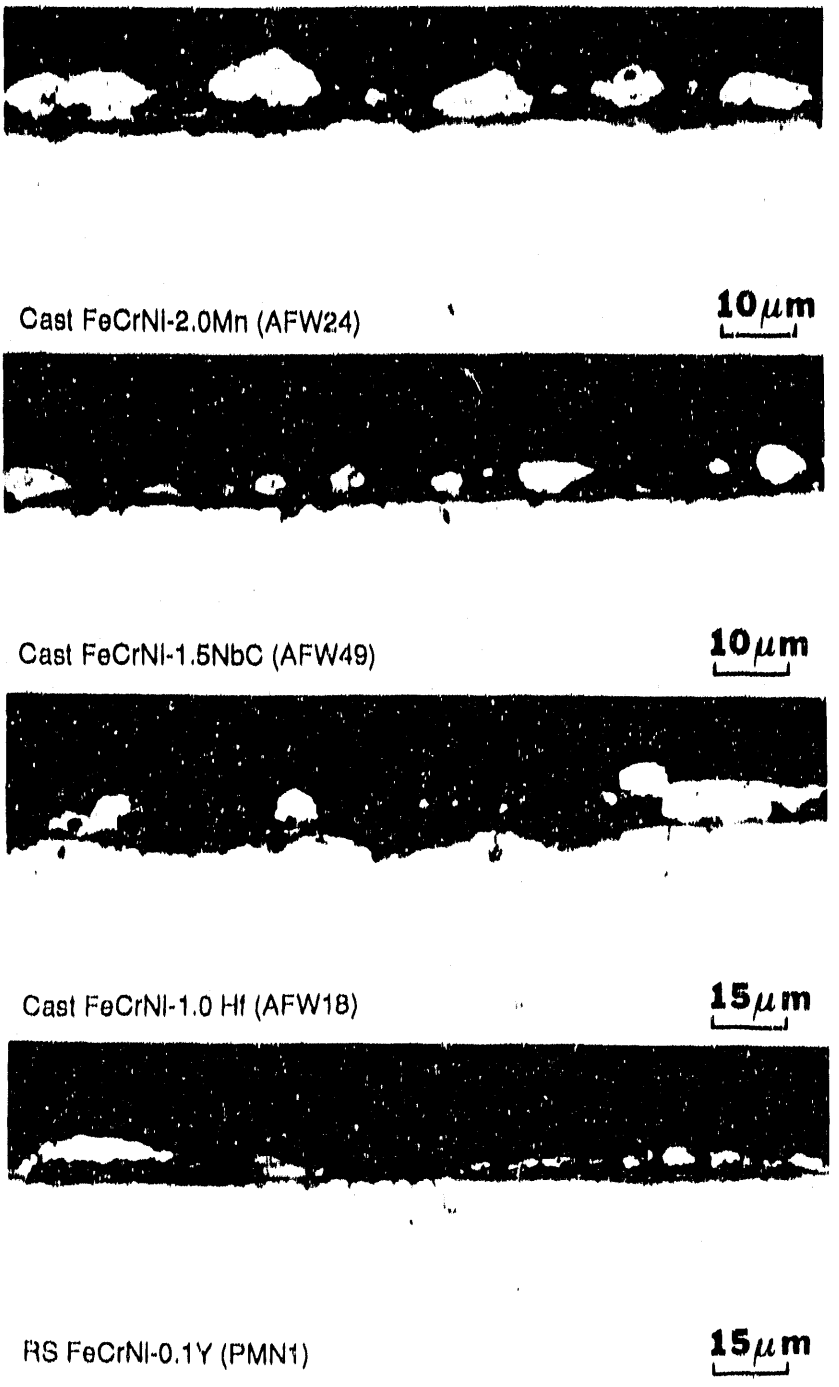

Fig. 2. Cross sections of scales formed on preoxidized alloys after 75h exposure to a simulated substoichiometric gas mixture at 700°C.

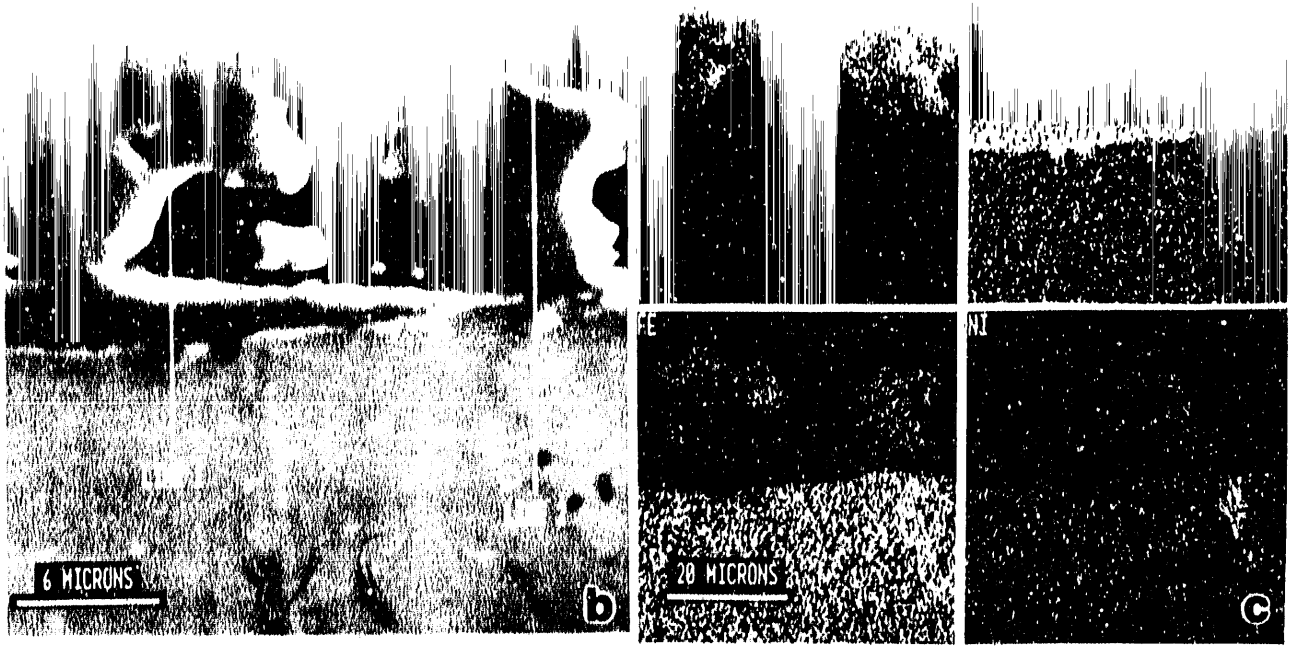

Fig. 3. Cross sections of scale formed on preoxidized, unalloyed Fe-25Cr-20Ni after 75h exposure to a simulated substoichiometric gas mixture at 700°C.
(a) optical micrograph; (b) secondary electron image of scale with external sulfide nodules;
(c) characteristic X-ray maps

alloy showed a notable difference from the unalloyed base alloy in that the external sulfide formed on the Si-alloy contained significantly less Ni (5 vs 18%), and possibly a higher level of Cr. X-ray maps and quantitative point analyses also suggested that the basal scale contained a lower level of Fe than on the unalloyed base composition (11 vs 15%), and a slight enrichment in Si. The alloy immediately beneath the basal scale layer was enriched in Cr at the expense of Fe, while there was no appreciable enrichment of Si at the base of the external scale.

A line scan through an external nodule on the cast Fe-25Cr-20Ni-2Mn alloy after 75 h showed the inner part of the sulfide nodule to have a composition similar to those formed on the unalloyed base alloy, with the S content increasing and the Fe:Ni ratio decreasing as the nodule was traversed towards the gas interface. This nodule contained significantly lower levels of Mn than the nominal alloy content. Also the S level dropped to essentially background level toward the basal scale-alloy interface. There was essentially no depletion of Cr beneath the external scale, whereas the Mn content was only about half the measured bulk alloy content.

In all these cases, the external sulfides appeared to have grown on the outside of the scale through transport of Fe and Ni outward through the scale. There was no evidence of the operation of an alternative mechanism observed under substoichiometric conditions at higher temperatures[3], which involved penetration of the scale by S to form internal sulfides, with eventual disruption of the external scale by extrusion of molten sulfides through it to form external sulfide nodules. There was also little evidence of changes in chemistry of the external scale or subjacent alloy in the immediate vicinity of the external nodules despite the large amounts of Fe and Ni that had been transported out.

Three alloys (cast unalloyed Fe-25Cr-20Ni, RS Fe-25Cr-20Ni-2Si , and PM Fe-25Cr-20Ni-2Y_2O_3) were exposed for 21 h at 700°C to the preoxidation conditions (H_2/H_2O mixture, $P_{O2} = 10^{-20}$ atm), and to the $H_2/H_2O/H_2S$ mixed gas ($P_{O2} = 10^{-20}$, $P_{S2} = 10^{-8}$ atm), and the resulting scales were examined by scanning electron microscopy (SEM), X-ray photoelectron spectroscopy (XPS), AES, and secondary ion spectroscopy (SIMS). For the unalloyed cast alloy, most of the scale formed in either environment was rich in Cr, but contained some Fe as indicated by energy dispersive X-ray (EDS) spectra shown in Fig. 4. The SIMS profiles for the scales formed under the two conditions, shown in Fig. 5, indicated quite different Fe distributions: while the scales formed in both environments were enriched in Fe near the outer surface, this enrichment was significantly increased in the sample exposed in the mixed gas. No differences were observed in the mass 32 peak in these profiles, which was attributed to O_2^+.

Figure 6 shows the SIMS profiles of the scales formed on the Si-containing alloy. The scale formed in the oxidizing gas was relatively non-uniform in thickness and contained darker (Fe-rich) areas of various sizes ranging up to about 1 to 2 mm in diameter. A considerable amount of Si was incorporated into the scale; semi-quantitative analysis from an AES spectrum indicated the level of Si to be roughly 7%. Transmission and scanning electron microscopy of the scale formed after 0.25 h exposure to the mixed gas indicated that the scale was a mixture of Fe-Cr sesquioxide and Fe-Cr

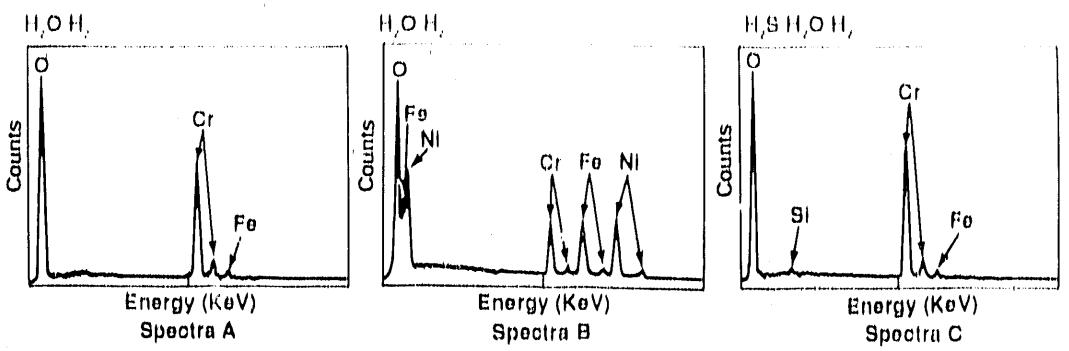

Fig. 4. Energy dispersive X-ray spectra from scales formed on cast Fe-25Cr-20Ni alloy after exposure at 700°C for 24h in: (a) and (b) H_2/H_2O, and (c) $H_2/H_2O/H_2S$. Spectrum (b) shows a Ni-rich particle on the scale surface.

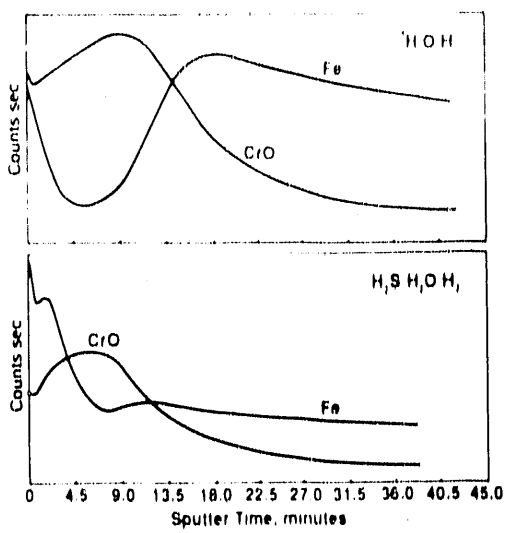

Fig. 5. SIMS depth profiles of scales formed on cast Fe-25Cr-20Ni alloy after exposure at 700°C for 24h in: (a) H_2/H_2O, and (b) $H_2/H_2O/H_2S$.

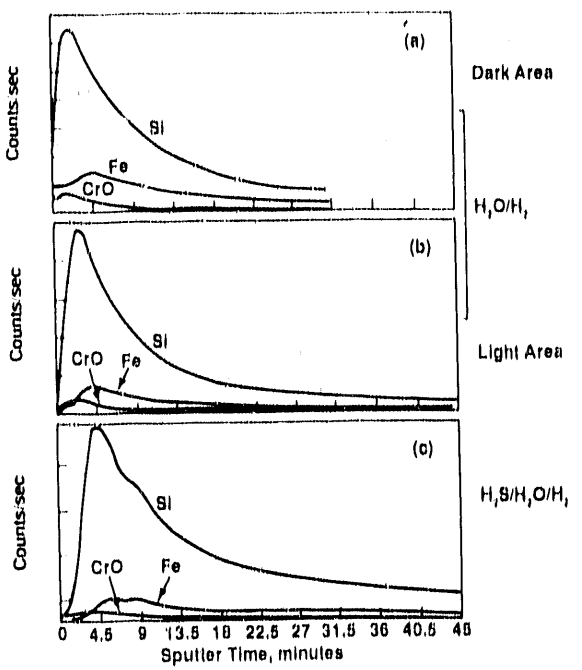

Fig. 6. SIMS depth profiles of scales formed on cast Fe-25Cr-20Ni-1Si alloy after exposure at 700°C for 24h in: (a) and (b) H_2/H_2O, and (c) $H_2/H_2O/H_2S$. Profile (a) is from an Fe-rich (dark) area, while (b) is from a light-appearing areas with less Fe.

spinel, while Si was detected throughout the scale and was present as SiO_2 at the oxide and spinel grain boundaries. Large amounts of Si were also detected in the metal grain boundaries near the metal-oxide interface.

The scales formed on the Y_2O_3-containing alloy were similar in general appearance in both environments, with more rapid scale growth occurring at the alloy grain boundaries. The SIMS profiles shown in Fig. 7 indicate that no Y was observed in the scale, except possibly at the scale-metal interface, and that the concentration of Fe in the outer part of the scale was greater in the specimen exposed in the mixed gas environment. This scale was the most Cr-rich of the alloys; the scale on the specimen exposed to the mixed gas environment for 0.25 h was almost entirely 100 nm diameter grains of Fe-Cr sesquioxide containing only about 4% Fe. A few areas of blade-shaped grains of Fe-Cr spinel were observed, as were $YCrO_3$ particles at the scale metal interface.

Efforts were also made to follow the oxidation behavior of both the unalloyed cast Fe-25Cr-20Ni base alloy and the Y_2O_3-containing PM alloy in a Perkin-Elmer 545 scanning Auger system[4]. Initial examination of the unalloyed cast alloy started with sputter cleaning of the surface, after which the specimen was heated to 700°C and exposed to the H_2O/H_2 oxidizing gas mixture ($P_{O2} = 10^{-20}$ atm). After this heating, the specimen exhibited a high surface concentration of S. Extended exposure of this alloy to this environment, sputter cleaning of the S layer, or increasing the O activity failed to produce significant oxidation [O/(Fe + Cr) ratio varied from 0.2 to 0.25]. Examination of the specimen at room temperature indicated that small areas of the surface that had not been sputter cleaned had in fact oxidized, whereas the sputter-cleaned area showed no oxidation.

Next, the surface segregation of S on both alloys was examined as a function of temperature. Each alloy was sputter cleaned, heated to a specific temperature, and the surface composition measured at each temperature as a function of time. After 0.5 to 0.67 h at temperature, the temperature was raised. The results of two such sputter-clean-and-heat cycles are shown in Fig. 8 and show little difference between the alloys. After exposure to similar conditions, both the rate and extent of S segregation appeared to be greater for the cast, unalloyed composition than for the Y_2O_3-containing alloy as shown in Fig. 9. These results demonstrate that there may be differences in the total amount of S that will readily segregate to the surface of the two alloys but that the Y_2O_3 addition did not prevent S segregation. It should also be noted that the grain size of the Y_2O_3-containing alloy is considerably smaller than the cast base composition, so that the former alloy probably contains significantly greater internal surface over which S segregation could occur.

Figure 10 shows the O/(Fe+Cr) signal ratios for the two alloys as a function of time. The surface O concentration on the unalloyed base composition never increased, whereas the Y_2O_3-containing alloy readily oxidized. Comparison of the rate of S segregation on the cast alloy with the rate of oxide formation on the Y_2O_3-containing alloy suggested that the rate of oxidation on the Y_2O_3-containing alloy is somewhat faster than the rate at which S segregates on the cast composition.

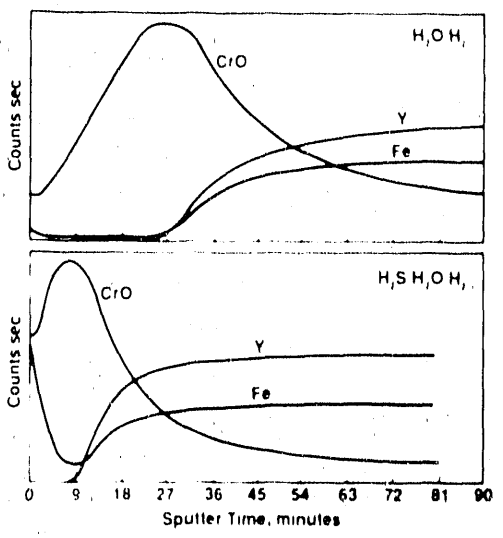

Fig. 7. SIMS depth profiles of scales formed on powder metallurgy Fe-25Cr-20Ni-2Y_2O_3 alloy after exposure at 700°C for 24h in: (a) H_2/H_2O, and (b) $H_2/H_2O/H_2S$.

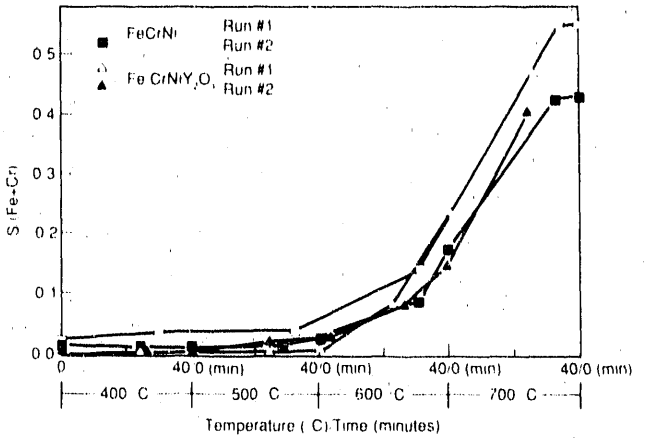

Fig. 8. Variation with time and temperature of the S/(Fe+Cr) atom ratios on the surfaces of cast Fe-25Cr-20Ni and PM Fe-25Cr-20Ni-2Y_2O_3. Specimens were heated in H_2/H_2O to the specified temperatures and held for ≈0.67h before the temperature was increased further.

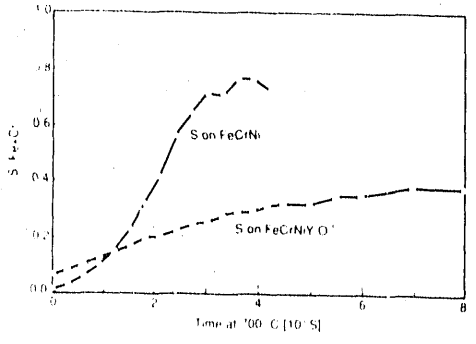

Fig. 9. Variation of S/(Fe+Cr) atom ratio with time at 700°C for cast Fe-25Cr-20Ni and powder metallurgy Fe-25Cr-20Ni-2Y_2O_3. Each specimen had been heated and sputter-cleaned prior to these runs.

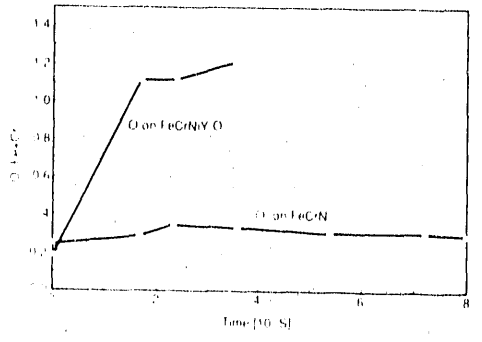

Fig. 10. Variation of O/(Fe+Cr) atom ratio with time for cast Fe-25Cr-20Ni and powder metallurgy Fe-25Cr-20Ni-2Y_2O_3 during oxidation at 700°C in H_2/H_2O.

DISCUSSION

Preoxidation in an S-free environment followed by exposure to the simulated substoichiometric gas mixture resulted in an improvement in the protective behavior of most of the Fe-Cr-based cast alloys, while the cast alloys based on Fe-Cr-Ni still showed relatively rapid initial weight gains when exposed to the S-containing gas, although the apparent oxidation rate of some of these alloys (notably those containing 2% Al or 3% Si) slowed down markedly with increasing exposure time. Other alloys based on Fe-Cr-Ni composition but made by PM routes and containing 2 or 6% Si or 2% Y_2O_3 exhibited low rates of weight gain when exposed to the S-containing gas after preoxidation, these rates being similar to or slower than that exhibited by the unalloyed, cast Fe-25Cr alloy. All of the preoxidized alloys that exhibited rapid weight gains when exposed to the S-containing gas appeared to degrade by the same mechanism that operated for non-preoxidized alloys, that is, by the formation of Fe-Ni-rich sulfides external to the pre-oxidized scale. In none of these cases did there appear to have been any obvious penetration of the preoxidized scale by S from the environment, no obvious sulfides were observed beneath the scale or in the alloy surface, and yet quite significant transport of Fe and Ni through the pre-oxidized scale had occurred to form the external sulfide nodules.

Detailed comparisons among scales formed in a S-free atmosphere and scales formed in an atmosphere having the same O partial pressure but also containing S, indicated that the addition of S to the environment did not lead to significant quantities of S in the scale, but changed the chemical profile of the scales formed. For both the cast Fe-Cr-Ni base alloy and the PM Fe-Cr-Ni-2% Y_2O_3 alloy the scales formed in the S-containing gas exhibited increased levels of Fe near the outer parts of the scale. In addition, the scales formed in the S-containing gas had a more uniform, smooth appearance than those formed in the S-free gas mixture. In situ oxidation experiments indicated that considerable segregation of S can occur at the surface of the cast Fe-Cr-Ni alloy, and that the extent of S segregation on the PM Fe-Cr-Ni-2% Y_2O_3 alloy was significantly less.

Apparently, in the S-containing gaseous environment, transport of Fe and Ni through a nominally protective, Cr_2O_3-based scale is enhanced. This phenomenon is usually explained by invoking the presence of channels or pathways for cation or anion diffusion through the scale that are thought to be associated with S incorporated into the oxide scale during the initial stages of oxidation. The fact that the same mode of degradation is observed on alloys directly exposed to the S-containing gas or first pre-oxidized in a S-free environment suggests that, at least for the Fe-Cr-Ni-based alloys, a mechanism involving incorporation of S from the gaseous environment into the scale to form short-circuit paths may not be applicable. Instead, the observed rapid S segregation from the alloy itself may be the source of S incorporated into the initial oxide scales, in which case preoxidation would not be expected to significantly change the sulfidation behavior of the alloy.

Some implications of these observations for alloy design are that elements capable of preventing S segregation in the initial stages of oxidation may significantly influence the protective nature of Cr_2O_3-based oxide scales. However, the level and availability of these elements should be sufficient to ensure a uniform distribution at the oxidizing surface. Further, additions that can act to block the outward diffusion of cations other than Cr through the Cr_2O_3-based scale, by either being incorporated into the scale to modify its structure, or to form a rate-controlling basal layer would also be expected to be effective in improving the performance of Cr_2O_3-based scales. It appears that Si falls into this category, apparently by becoming incorporated into the scale structure, and there are indications that small additions of Al (2%) may also be effective, possibly by forming an oxide sublayer. Previous work [5] has indicated that Nb additions can also act to form an oxide sublayer which is effective in the same manner.

Comparison between the scales formed on the ferritic Fe-Cr base alloys and the austenitic Fe-Cr-Ni base alloys has shown that the scales on the former alloys are typically of the M_2O_3-type which, as initially formed, contained low levels (about 4%) of Fe which decreased rapidly with time, whereas the scales on the latter alloys are typically of the M_3O_4-type or a mixture of M_2O_3 and M_3O_4, and contain substantial levels of Fe with some Ni which tend to increase rather than decrease with time. The fact that one noticeable effect of S in the gas mixture is to promote an increase in the Fe level towards the outer surface of nominally Cr_2O_3 scales, and the fact that the initial mode of breakdown is the formation of external Fe sulfide nodules, suggests that any alloy modifications that can promote the exclusive formation of M_2O_3-type scales on the austenitic alloys should also enhance their sulfidation resistance. Of the alloying additions studied in this program, Y_2O_3 added by a PM route appears to perform this function.

REFERENCES

1. D. R. Baer, L. H. Schoenlein and I. G. Wright, in Corrosion and Particle Erosion at High Temperatures, V. Srinivasan and K. Vedula, eds., The Metallurgical Soc., Warrendale, PA (1989), pp. 109-125.

2. I. G. Wright, J. A. Colwell, J. T. Prater and D. R. Baer, in Corrosion and Particle Erosion at High Temperatures, V. Srinivasan and K. Vedula, eds., The Metallurgical Soc., Warrendale, PA (1989), pp. 65-107.

3. V. Nagarajan, M. A. Rocazella, I. G. Wright and R. D. Smith, in Corrosion-Resistant Materials for Coal Conversion Systems, D. B. Meadowcroft and M. I. Manning, eds., Applied Sci. Pub., London (1983), pp. 371-388.

4. D. R. Baer, I. G. Wright and T. R. Jervis, Surface and Interface Analysis, 15, 143-149 (1990).

5. D. J. Baxter and K. Natesan, in Proc. 3rd Berkeley Conf. on Corrosion-Erosion-Wear of Materials at Elevated Temperatures, A. V. Levy, ed., NACE, Houston (1987), pp. 309-323.

EFFECTS OF SEVERAL VARIABLES ON THE GROWTH AND BREAKDOWN OF PROTECTIVE ALUMINA OR CHROMIA SCALES IN MIXED GAS ENVIRONMENTS

V. Srinivasan

Universal Energy Systems, Inc.
4401 Dayton-Xenia Road
Dayton, OH 45432

ABSTRACT

During the period under review (October 1989 - March 1990), the effect of addition of Si and inert alumina particles on the formation and breakdown of protective oxide scale was investigated in the case of Fe-25Cr and Fe-25Cr-20Ni alloys in low oxygen activity substoichiometric gas mixtures. SEM/EDS, AES (SAM), XPS (ESCA) and Nanoindentor were used to characterize the scales. Both additions significantly improved the sulfidation resistance of Fe-25Cr-20Ni in simulated coal derived atmospheres.

INTRODUCTION

Mixed gas corrosion is a major concern in coal combustion and gasification environments. Alloys and coatings to be used in these environments require the formation and retention of protective alumina or chromia scales to resist the corrosion attack. The relatively high activity of S and low partial pressure of O encountered in coal-derived atmospheres not only make the formation and maintenance of protective oxide scales difficult, but very often cause the early breakdown of initially formed protective scales.

Minor additions of oxygen active elements, their oxides or other alloying elements improve considerably the overall oxidation resistance of high temperature alloys and coatings. However, their efficacy in resisting sulfidation at intermediate temperatures, 500-700°C is not yet established. The objective of this program is to understand the effect of several variables such as alloying additions, ion-implantation and oxidizing conditions on the growth and breakdown of protective scales in simulated substoichiometric gas mixtures and to provide basic information on alloying and processing for the development of

ferrous alloys/coatings with long term sulfidation resistance in coal derived atmospheres. This report contains the study performed during the last six months (October 1989 - March 1990) on Si and Al_2O_3 containing Fe-25Cr and Fe-25Cr-20Ni. Both additions are found highly beneficial.

EXPERIMENTAL MATERIALS AND METHODS

Fe-25Cr, Fe-25Cr-3Si, Fe-25Cr-1.5Al_2O_3, Fe-25Cr-20Ni, Fe-25Cr-20Ni-3Si and Fe-25Cr-20Ni-1.5Al_2O_3 are the experimental alloys. The alloys with alumina dispersions were made through P/M route and others through I/M procedure. The alloys were exposed to various gas mixtures as described in Table 1. The cyclic test consisted of exposing the samples to H_2-H_2O-H_2S-Ar at 700°C (P_{O_2} = 1.17×10^{-20} and P_{S_2} = 1.22×10^{-8} atm) periodically. A block of thermal cycles, Figure 1 was repeated four times. The scales and the substrates were characterized using SEM/EDS, AES(SAM), XPS(ESCA) and Nanoindentor.

Table 1. Test Matrix at 700°C

Alloy	(1)	(2)	(3)	(4)	(5)	(6)
Fe-25Cr	YES	NO	NO	NO	YES	YES
Fe-25Cr-3Si	YES	YES	YES	YES	YES	YES
Fe-25Cr-1.5Al_2O_3	YES	YES	YES	YES	YES	YES
Fe-25Cr-20Ni	YES	NO	NO	NO	YES	YES
Fe-25Cr-20Ni	YES	YES	YES	YES	YES	YES
Fe-25Cr-20Ni-1.5Al_2O_3	YES	YES	YES	YES	YES	YES
Fe-25Cr-6Al	YES	YES	YES	YES	YES	YES

(1) P_{O_2} = 1.17×10^{-20}; P_{S_2} = 1.22×10^{-8} atm, Iso. 96 h
(2) P_{O_2} = 1.17×10^{-20}; P_{S_2} = 1.22×10^{-8} atm, Cyc. 96 h
(3) P_{O_2} = 1.3×10^{-21}; P_{S_2} = 1.19×10^{-8} atm, 96 h
(4) P_{O_2} = 1.18×10^{-22}; P_{S_2} = 1.19×10^{-8} atm, 96 h
(5) P_{O_2} = 1.13×10^{-20} (Preoxidation, 96 h)
(6) P_{O_2} = 1.13×10^{-20} (Preoxidation, 96 h)
P_{O_2} = 1.17×10^{-20}; P_{S_2} = 1.22×10^{-8} atm (Oxidation/Sulfidation, 48 h)

RESULTS AND DISCUSSION

Oxidation in Pure O_2

Isothermal and cyclic oxidation behavior of P/M and other alloys was studied at temperatures, 700-900°C. Figures 2a and b

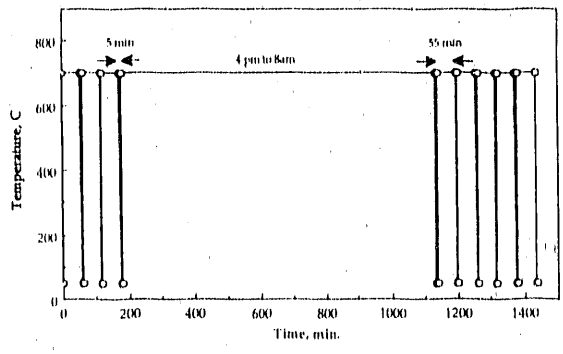

Fig. 1. One Block of Thermal Cycles.

show the weight gain kinetics for the base and oxide dispersed (OD) alloys. The activation energy for thermal oxidation estimated from the Arrhenius plots (not shown here) is about 40 kcal/mole. The scales on Fe-25Cr, Fe-25Cr-1.5Al_2O_3 and Fe-25Cr-20Ni-1.5Al_2O_3 are rich in Cr. Fe-rich scale with Ni and Cr is observed on Fe-25Cr-20Ni.

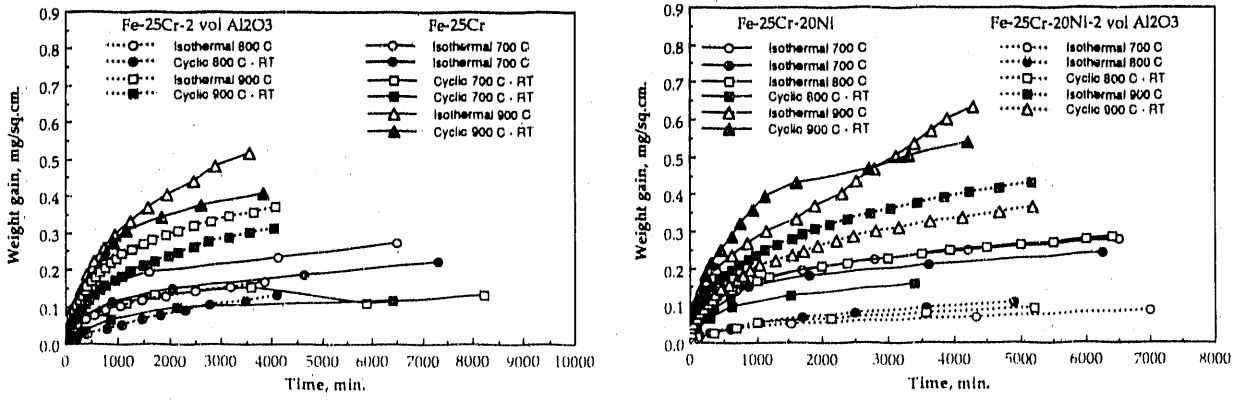

a b

Fig. 2. Specific Weight Gain vs Time in Oxygen.

Scaling kinetics of P/M and I/M Alloys in Simulated Substoichiometric Gas mixtures

The weight gains were monitored in a TGA apparatus during isothermal exposure of the base alloy, Fe-25Cr-20Ni-3Si, and P/M Fe-25Cr-20Ni-1.5Al_2O_3 to a substoichiometric gas mixture of H_2-H_2O-H_2-H_2S-Ar at 700°C. The kinetics curves are shown in Figure 3. The oxygen and sulfur activities were 1.17×10^{-20} and 1.22×10^{-8} atm, respectively. Considerably lower kinetics are observed in the case of I/M Fe-25Cr-20Ni-3Si and P/M Fe-25Cr-20Ni-1.5Al_2O_3 alloys under the reported experimental conditions.

The scales observed on samples exposed to 700°C, $P_{O_2} = 1.17 \times 10^{-20}$ and $P_{S_2} = 1.22 \times 10^{-8}$ atm isothermally and

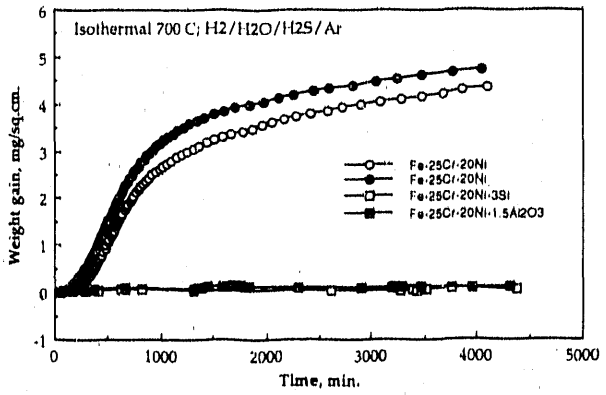

Fig. 3. Specific Weight Gain vs Time. $P_{O_2} = 1.17\times10^{-20}$ and $P_{S_2} = 1.22\times10^{-28}$ atm.

cyclically are shown in Figures 4 and 5. Their compositions determined by EDS are also given in the figures. The scales are thin in most cases, and hence the EDS analysis of scales in X-sections is not reliable in those cases. The scales on isothermally exposed base alloys are considerably thicker (not shown here) and their compositions are: 68Cr-24Fe 8S(Fe-25Cr) and (21-0.5)Cr-(47-62)Fe-(6-37)Ni-(15-20)S(Fe-25Cr-20Ni). Scanning Auger microscopy was used to characterize the scales on Fe-25Cr-20Ni-3Si and Fe-25Cr-20Ni-1.5Al_2O_3 at different depths up to 2000 Å. Ar sputtering at an estimated rate of 160 Å/min was used. S and C were detected at the unsputtered surface as impurities due to exposure to lab air during transfer. Both disappeared after a brief sputtering. The Auger spectra of scales on Fe-25Cr-20Ni-3Si and Fe-25Cr-20Ni-1.5Al_2O_3 suggest that the scales are essentially Cr-rich oxide at the gas/scale interface and below.

Scales were intact and no cracking and spallation was observed in thermally cycled samples. Further, no sulfidation was noticed especially in Fe-25Cr-20Ni-Si and Fe-25Cr-20Ni-1.5Al_2O_3. The observation of Cr-rich oxide (Cr_2O_3) scale on Fe-25Cr-20Ni-3Si and Fe-25Cr-20Ni-1.5Al_2O_3 is in contrast to that of sulfides on the base alloy Fe-25Cr-20Ni just after 5 min of exposure. Scale breakdown was observed in cyclically exposed Fe-25Cr-1.5Al_2O_3.

Sequential Preoxidation and Sulfidation

Preformed oxide scales on Fe-25Cr-3Si, Fe-25Cr-1.5Al_2O_3, Fe-25Cr-20-20Ni-3Si and Fe-25Cr-20Ni-1.5Al_2O_3 at 700°C/96 h, $P_{O_2} = 1.13\times10^{-20}$ atm are shown in Figure 6.

10μm

a Fe-25Cr-1.5Al_2O_3 (98Cr-2Fe)*

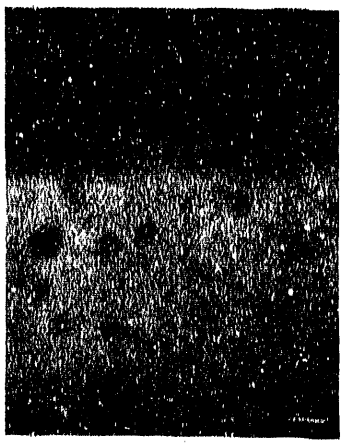

1μm

b Fe-25Cr-1.5Al_2O_3 (Thin Scale)

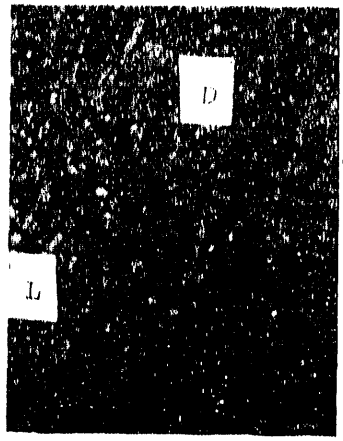

10μm

c Fe-25Cr-3Si (L: 90Cr-9Fe-1Si-0.12S D: 78Cr-17Fe-5Si)*

10μm

d Fe-25Cr-20Ni-1.5Al_2O_3 (92Cr-6Fe-2Ni)*

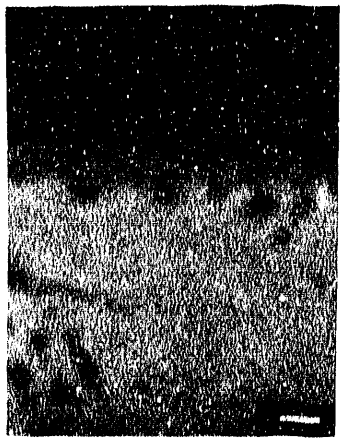

1μm

e Fe-25Cr-20Ni-1.5Al_2O_3 (Thin Scale)

10μm

f Fe-25Cr-20Ni-3Si (42Cr-42Fe-12Ni-4Si)*

*Scale composition in wt.%

Fig. 4.SEM (Planar) and BEI (X-section) of Scales. Isothermal Exposure: 700°C/96 h, P_{O_2} = 1.17×10^{-20} and P_{S_2} = 1.22×10^{-8} atm.

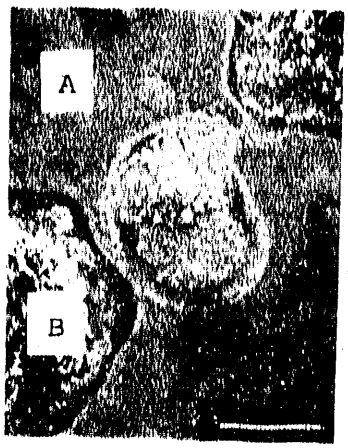

100μm

a Fe-25Cr-1.5Al_2O_3 (A: 88Cr-12Fe B: 27Cr-56Fe-17S)*

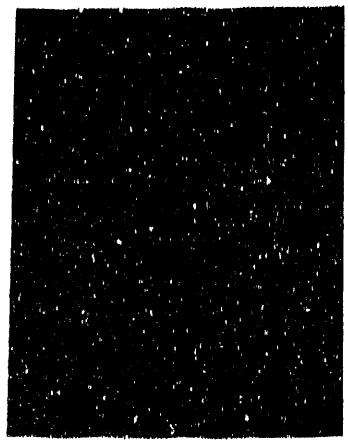

1μm

b Fe-25Cr-1.5Al_2O_3 (Thin Scale)

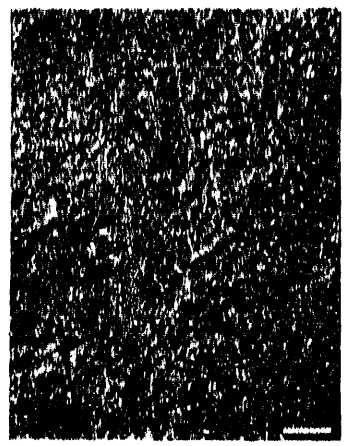

10μm

c Fe-25Cr-20Ni-1.5Al_2O_3 (92Cr-6Fe-2Ni)*

10μm

d Fe-25Cr-20Ni-3Si (51Cr-34Fe-11Ni-4Si)*

*Scale composition in wt.%

Fig. 5. SEM (Planar) and BEI (X-section) of Scales. Thermally Cycled: 700°C/96 h, $P_{O_2} = 1.17 \times 10^{-20}$ and $P_{S_2} = 1.22 \times 10^{-8}$ atm.

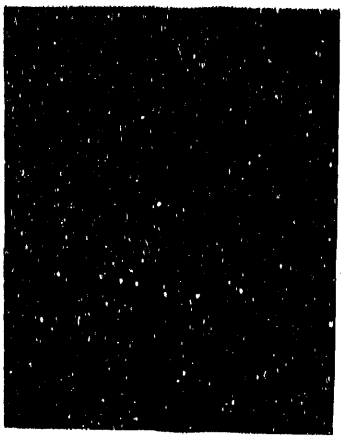

10μm

a Fe-25Cr-3Si (52Cr-28Fe-20Si)*

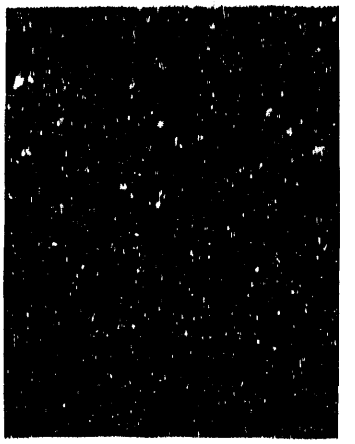

10μm

b Fe-25Cr-1.5Al_2O_3 (71Cr-29Fe)*

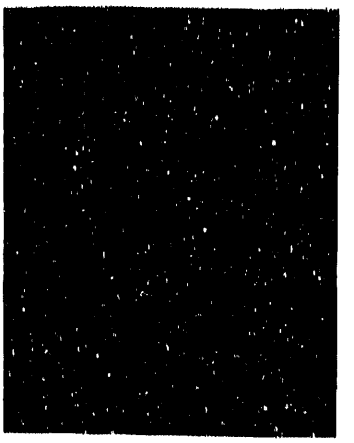

1μm

c Fe-25Cr-1.5Al_2O_3 (Thin Scale)

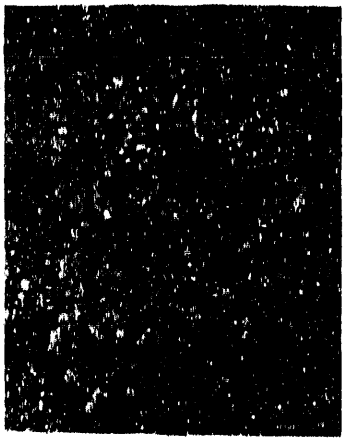

10μm

d Fe-25Cr-20Ni-3Si [(31-50)Cr-(37-46)Fe-(13-15)Ni-(1-9)Si]*

10μm

e Fe-25Cr-20Ni-1.5Al_2O_3 (96Cr-4Fe)*

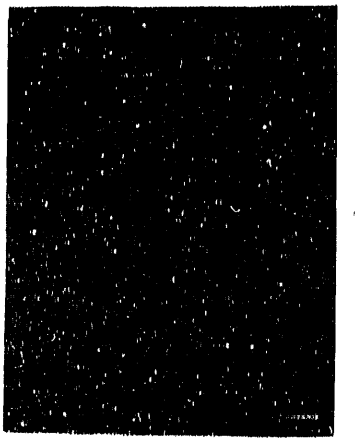

1μm

f Fe-25Cr-20Ni-1.5Al_2O_3 (Thin Scale)*

*Scale composition in wt.%

Fig. 6. SEM (Planar) and BEI (X-section) of Scales. Preoxidized 700°C/96 h, $P_{O_2} = 1.13 \times 10^{-20}$ atm.

Concentration depth profiles by SIMS of the preformed scale on Fe-25Cr-20Ni-3Si show the presence of Cr, Fe, Ni, Si and O across the scale.

Scanning Auger maps of Cr and Si at the gas/scale interface show that the scale is essentially Cr-rich (Cr_2O_3) oxide with a small amount of Si. C was present at the unsputtered surface as an impurity. The scale is thin ($\sim$2500 Å).

Quick survey runs and extended multiplexing procedure were used to characterize the performed oxide scales of Fe-25Cr-20Ni and Fe-25Cr-20Ni-1.5Al_2O_3 in x-ray photo electron spectrometer (XPS). The scale is uniform depth-wise without any abrupt changes in the chemistry. The nature of oxides and the presence of unreacted metals are identified by the peak positions and separations in the binding energy spectra. C and Si were detected on the surface as impurities. The preformed scale on Fe-25Cr-20Ni is rich in Fe, most likely to be Fe_3O_4 (P_{O_2} = 1.13×10^{-20} atm) and little Cr_2O_3, 87 and 13%, respectively. After sputtering for about 60 min, the presence of metallic Fe and FeO was detected besides Fe_3O_4 (74%). Ni was not present. In contract, the unsputtered preformed scale on Fe-25Cr-20Ni-1.5Al_2O_3 is rich in Cr_2O_3 (79.34%). The other constituent of the scale is iron oxide, (Fe_3O_4, 20.66%). After sputtering for about 60 min only Cr_2O_3 is found along with metallic Fe, Cr and Ni. Thus there is a distinct difference in the nature of the scale formed at P_{O_2} = 1.13×10^{-20} atm on the base alloy Fe-25Cr-20Ni and the P/M Fe-25Cr-20Ni-1.5Al_2O_3, and this difference appears to be responsible for their difference in their resistance to sulfidation as described earlier. The addition of inert submicron-size Al_2O_3 has resulted in the formation of oxide scale with Cr_2O_3 as the major constituent in the low oxygen activity environment.

Scale breakdown mechanism was studied by subjecting the preoxidized (700°C/96 h) coupons to substoichiometric S-containing gas mixture (700°C/48 h). Figure 7 shows the scales in planar and cross-sectional views. The only alloy that was attacked by sulfur is the Fe-25Cr-20Ni (not shown), and in this case sulfidation starts from the gas/scale interface. In the case of Si-containing alloys and Fe-25Cr-6Al, the scales are thin

10μm

a Fe-25Cr-3Si (46Cr-48Fe-6Si)*

10μm

b Fe-25Cr-1.5Al_2O_3 (81Cr-19Fe)

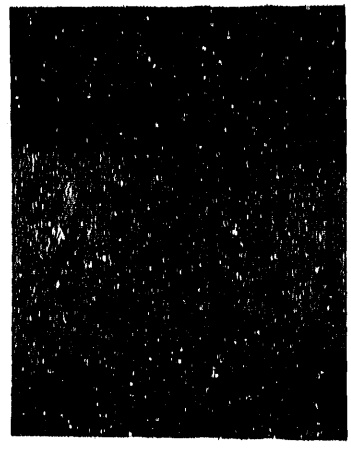

1μm

c Fe-25Cr-1.5Al_2O_3 (Thin Scale)

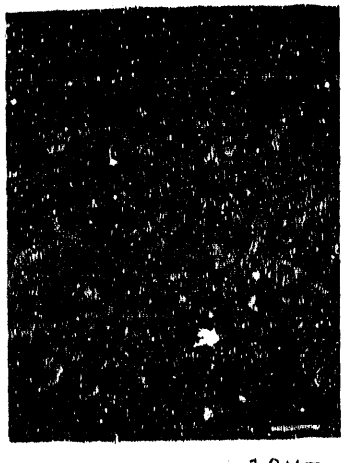

10μm

d Fe-25Cr-20Ni-3Si (46Cr-45Fe-9Si)*

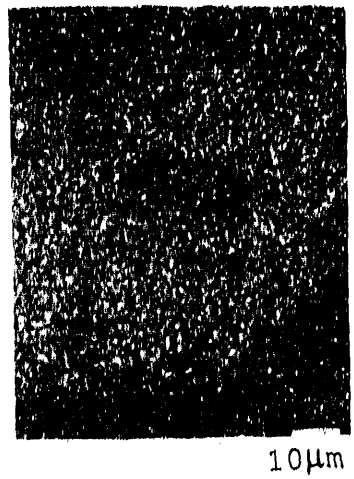

10μm

e Fe-25Cr-20Ni-1.5Al_2O_3 (98Cr-2Fe)*

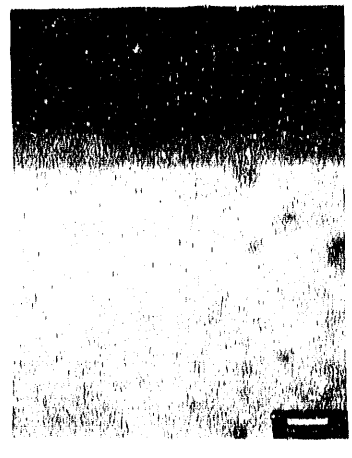

1μm

f Fe-25Cr-20Ni-1.5Al_2O_3 (97Cr-3Fe)*

*Scale composition in wt.%

Fig. 7. SEM (Planar) and BEI (X-section) of Scales. Preoxidized 96 h, $P_{O_2} = 1.13 \times 10^{-20}$ atm and Sulfidized 48 h $P_{O_2} = 1.17 \times 10^{-20}$ and $P_{S_2} = 1.22 \times 10^{-8}$ atm at 700°C.

as the tarnished substrates are visible to the naked eye, and no cross sections were made.

Auger spectra of corrosion scales on Fe-25Cr-20Ni-3Si and Fe-25Cr-20Ni-1.5Al_2O_3 were obtained from different depths up to 2000 Å. S was detected only at the gas/scale interface and disappeared after a brief sputtering. Only Cr and O were present in the scale up to the depth investigated. SIMS analysis was done. The mass resolution required to distinguish between $^{32}S^-$ and $^{32}O_2^-$ is 17.8×10^{-3} amu, but quadrapole mass resolution available is 1 amu. An alternate procedure is to use the target bias offset method. However, the target bias range currently available is not adequate to accomplish this.

Effect of Oxidizing Conditions

Alloys that resisted sulfidation at 700°C, $P_{O_2} = 1.17\times10^{-20}$ and $P_{S_2} = 1.22\times10^{-8}$ atm were exposed to substoichiometric gas mixtures at 700°C with different oxygen activities, $P_{O_2} = 1.13\times10^{-20}$ and $1.18\times^{-22}$ at a constant $P_{S_2} = 1.19\times10^{-8}$ atm to study the effect of oxidizing conditions. The scanning electron micrographs of scales observed at the lowest oxygen activity are shown in Figure 8.

Fe-25Cr-6Al, Fe-25Cr-1.5Al_2O_3, Fe-25Cr-3Si, and Fe-25Cr-20Ni-3Si resist sulfidation at low oxygen activities, 10^{-21} and 10^{-22} except Fe-25Cr-20Ni-1.5Al_2O_3 which was attacked significantly at $P_{O_2} = 1.18\times10^{-22}$.

Mechanical Properties of the Scale

The protective scales that formed under the reported conditions were more often relatively thin and therefore the nondestructive Nanoindentor was used to evaluate the mechanical properties of the scales for comparative study. In cases of scales that had a distinct morphology or chemistry locally or along the substrate grain boundaries, attempts were made to get hardness and compliance data for these regions.

a Fe-25Cr-3Si (24Cr-73Fe-3Si)*

b Fe-25Cr-1.5Al_2O_3 (97Cr-3Fe)*

c Fe-25Cr-1.5Al_2O_3 (Thin Scale)

d Fe-25Cr-20Ni-3Si (50Cr-35Fe-13Ni-2Si)*

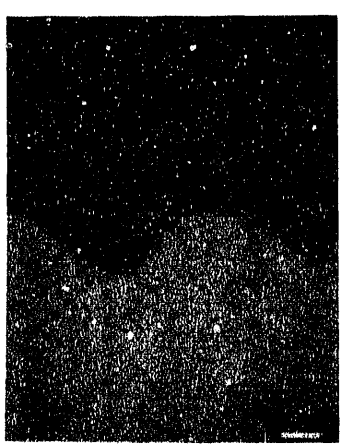

e Fe-25Cr 20Ni-3Si (Thin Scale)

f Fe-25Cr-20Ni-1.5Al_2O_3 (41Cr-37Fe-16Ni-6S)*

*Scale composition in wt.%

Fig. 8. SEM (Planar) and BEI (X-section) of Scales. Exposed to 700°C/96 h, $P_{O_2} = 1.18 \times 10^{-22}$ and $P_{S_2} = 1.19 \times 10^{-8}$ atm.

Compliance variations with the reciprocal of scale depth are shown in Figure 9 for Fe-25Cr-20Ni, Fe-25Cr-20Ni-3Si and Fe-25Cr-20Ni-1.5Al_2O_3 exposed to pure oxidation (oxn 1 atm O_2, 700°C/120 h), preoxidation (PO, 700°C/96 h, P_{O_2} = 1.13×10^{-20} atm) and preoxidation-sulfidation (PO + SO; preoxidation 700°C/96 h, P_{O_2} = 1.13×10^{-20} atm + sulfidation 700°C/48 h, P_{O_2} = 1.17×10^{-20} and P_{S_2} = 1.22×10^{-8} atm). The reciprocal of the slopes of these lines is a measure of Young's modulus of the medium indented. The modulus of the scales on Fe-25Cr-20Ni-3Si seems to be higher than that of scales on Si-free alloy suggesting a correlation between Young's modulus of the scale and the ability to resist sulfidation.

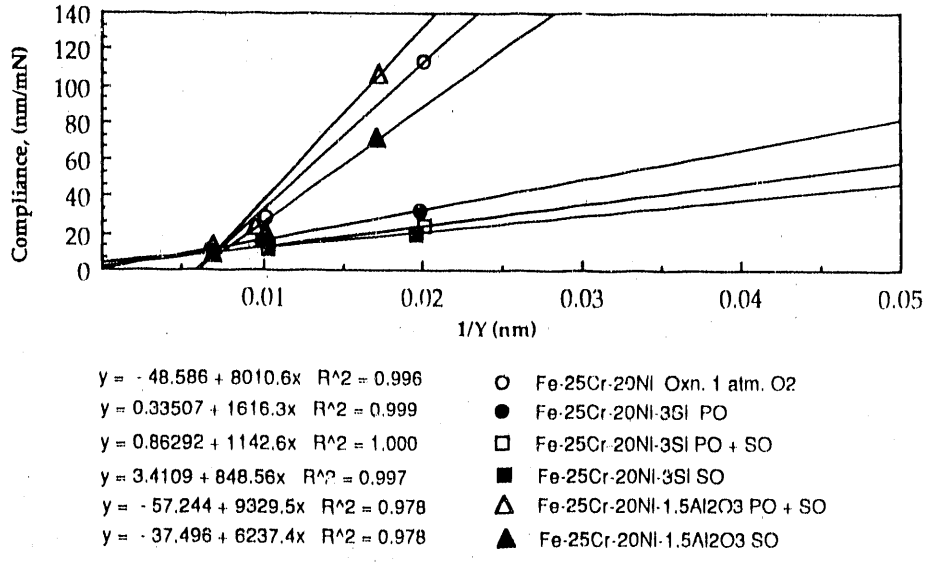

Fig. 9. Compliance vs the Reciprocal of Depth.

SUMMARY

The addition of Si or Al_2O_3 considerably improves the sulfidation resistance of the base alloy Fe-25Cr-20Ni (>96 h against <10 min in similar condition). The effect of Al_2O_3 addition to Fe-25Cr is marginal.

ACKNOWLEDGMENT

The SIMS, SAM and XPS study and the mechanical property evaluation were performed at the Materials Analysis User Center of HTML, ORNL, Oak Ridge, TN. The participation of Dr. M. Ferber, Dr. John Cathcart, Dr. A. Choudhury, Mr. R. A. Padgett and Mr. L. A. Harris of the above Center is appreciated.

STRESS CORROSION CRACKING SUSCEPTIBILITIES OF IRON ALUMINIDES

R. A. Buchanan and J. C. Kim

Department of Materials Science and Engineering
University of Tennessee, Knoxville
Knoxville, TN 37996-2200

ABSTRACT

U-bend stress-corrosion-cracking (SCC) tests were performed on two iron-aluminide compositions based on Fe_3Al and containing 2 and 5 a/o Cr, respectively. Under freely-corroding conditions, cracking failures were produced within 200h for both compositions in thiosulfate and tetrathionate solutions, but not in an acid-chloride solution. U-bend SCC tests were also performed at applied anodic and cathodic potentials in the acid-chloride solution. Cracking failures were produced within 200h only at the more severe hydrogen-generating cathodic potentials and only for the lower Cr composition. It is concluded that the iron aluminide compositions evaluated are highly susceptible to SCC in thiosulfate and tetrathionate solutions. It is also concluded that the iron aluminides are susceptible to SCC in acid-chloride solution if the corrosion potential is sufficiently active to generate hydrogen, that the mechanism is related to hydrogen embrittlement rather than anodic dissolution, and that increased Cr levels are beneficial in minimizing the SCC susceptibility.

INTRODUCTION

A current research program within the Metals and Ceramics Division at Oak Ridge National Laboratory involves development of low-cost, low-density intermetallic alloys based on Fe_3Al with optimum combinations of strength, ductility, and corrosion resistance for use in advanced fossil-energy conversion systems.[1,2] The overall purpose of the present project is to study the ambient-temperature aqueous corrosion characteristics of the experimental iron aluminides, and when appropriate, to make recommendations on alloying-element changes to enhance aqueous-corrosion resistance. Previous reports have described results of earlier work, which has focused on the corrosion properties without

stress application over a range of electrolytes. [3,4] Among other results, this earlier work has revealed the beneficial effects of increased Cr levels (up to 6 atomic percent (a/o)), and the addition of Mo (up to 2 a/o), for improving the resistance of iron aluminides to chloride-induced localized corrosion. This current report summarizes activities over the past six months, which have primarily dealt with the stress-corrosion-cracking (SCC) tendencies of the iron aluminides, and whether the cracking is related to anodic-dissolution effects (i.e. corrosion per se) or to hydrogen-embrittlement effects.

PROCEDURES AND RESULTS

U-bend SCC tests were performed on two iron-aluminide compositions, designated as FA-84 and FA-129, and containing 2 and 5 a/o Cr, respectively. The complete compositions are given in Table 1. In all cases, the final heat treatment

Table 1. Chemical compositions of iron aluminides (atomic percent).

Material	Fe	Al	Cr	C	Nb	B
FA-84	69.95	28	2	--	--	0.05
FA-129	65.8	28	5	0.2	1	--

consisted of 1 hour at 750 C (air) followed by an oil quench, which is believed to result in the B2 superlattice at room temperature. U-bend specimens were formed from strips measuring 119 x 10 x 0.76 mm. The specimens were first ground in the longitudinal direction through 600-grit SiC paper, and then deformed into the U shape with a fixture designed specifically for this purpose. The bend radius was 15.9 mm, resulting in a total strain of 0.024 (ASTM G 30), which exceeded the yield strengths of the iron aluminides. The legs of the U-bend specimens were secured with polyvinyl chloride bolts to avoid galvanic-corrosion effects.

The U-bend tests were conducted for a maximum time of 200 hours (when failure did not occur) in three electrolytes: acid-chloride (pH=4 (H_2SO_4), 200 ppm

Cl^- (NaCl)), 0.1M sodium thiosulfate ($Na_2S_2O_3$), and 0.1M sodium tetrathionate ($Na_2S_4O_6$). The pH values of the latter two solutions were measured to be 5 and 4, respectively. Justifications for selection of these electrolytes were presented in a previous report.[4]

Results of the first series of 200-hour U-bend SCC tests are given in Table 2. In this series, the specimens were allowed to remain at their natural, freely-corroding, open-circuit corrosion potentials (E_{corr} values). It is seen that cracking did not occur in the acid-chloride solution within 200h for either the 2 or 5 a/o Cr iron aluminides. Furthermore, whereas localized corrosion was not evident for the 5 a/o Cr material (the entire surface remained bright and shiny), localized corrosion was readily apparent on the 2 a/o Cr material (although no cracks were initiated). The sulfur-compound solutions proved to be highly damaging to both iron-aluminide compositions, with severe corrosion and cracking failures occurring in both thiosulfate and tetrathionate solutions within 200 hours. Scanning-electron-microscopy analyses of the fracture surfaces indicated that the dominant cracking modes were transgranular for FA-84 (2a/o Cr) and intergranular for FA-129 (5 a/o Cr).

Table 2. U-bend results at open-circuit corrosion potentials (E_{corr}).

Material	Electrolyte	E_{corr}, Avg. (mV (SHE))	Results
FA-84 2 a/o Cr	Acid Chloride	(-200) ➤ (-315)	No Cracking Localized Corrosion
	Thiosulfate	(-372) ➤ (-315)	Cracking Failure, Transgranular
	Tetrathionate	(-410) ➤ (-355)	Cracking Failure, Mode Unidentified Due to Severe Corrosion Products
FA-129 5 a/o Cr	Acid Chloride	(-40) ➤ (+290)	No Cracking No Localized Corrosion
	Thiosulfate	(-390) ➤ (-300)	Cracking Failure, Intergranular
	Tetrathionate	(-415) ➤ (-395)	Cracking Failure, Intergranular

A second series of U-bend SCC tests were performed under identical experimental conditions, except that the specimen-potentials (E) were potentiostatically controlled. In terms of background information, it is helpful to describe the conditons that exist as a function of electrochemical potential. Under freely-corroding conditions ($E = E_{corr}$) the corrosion rate (or metal-oxidation rate) is equal to the cathodic-reactant reduction rate. At anodic potentials ($E>E_{corr}$), the corrosion rate is higher than the reduction rate; and at cathodic potentials ($E<E_{corr}$), the reduction rate is higher than the corrosion rate. Furthermore, the degree of imbalance increases as E is forced further away from E_{corr}. Thus, higher anodic potentials progessively accelerate the corrosion reaction, and lower (more-negative) cathodic potentials progressively accelerate the reduction reaction(s). In addition to the E_{corr} values, the following applied potentials were investigated: (a) anodic,+300 mV (SHE); and (b) cathodic, -900,-1000, and -1500 mV (SHE). The locations of these potentials are illustrated in Figure 1 with reference to the anodic and cathodic polarization curves of FA-129 in the acid-chloride solution. At the cathodic potentials, it must be recognized that different reduction reactions occur over different potential ranges. The possible reduction reactions are identified as: (A) $O_2 + 4H^+ + 4e \rightarrow 2H_2O$, (B) $2H^+ + 2e \rightarrow 2H$, and (C) $2H_2O + 2e \rightarrow 2H + 2(OH)^-$. Only reaction A will occur at potentials greater than -236 mV(SHE); whereas below this value, all three reactions will occur. Thus, atomic hydrogen is generated at the specimen surfaces only at potentials less than -236 mV (SHE). (A corollary to this statement is that if E_{corr}, the freely corroding potential, is greater than -236 mV(SHE), which it has been for all iron aluminides tested without stress application in the acid-chloride solution, no hydrogen is generated at the surface.) Kinetically, based on the shape of the typical cathodic polarization curve in Figure 1 for the acid-chloride solution (pH = 4), it was observed that reaction A dominated the cathodic reactions down to a potential of approximately -550 mV (SHE), with the oxygen diffusion limit occurring at approximately 30 $\mu A/cm^2$. Within this range, reactions B and C occurred below -236 mV (SHE), but at slower rates than reaction A. Below -550 mV(SHE), reaction C dominated the cathodic reactions. At the applied cathodic potentials of -900, -1000, and -1500 mV(SHE), hydrogen gas-bubble generation at the specimen surfaces was observed to occur at progressively higher rates.

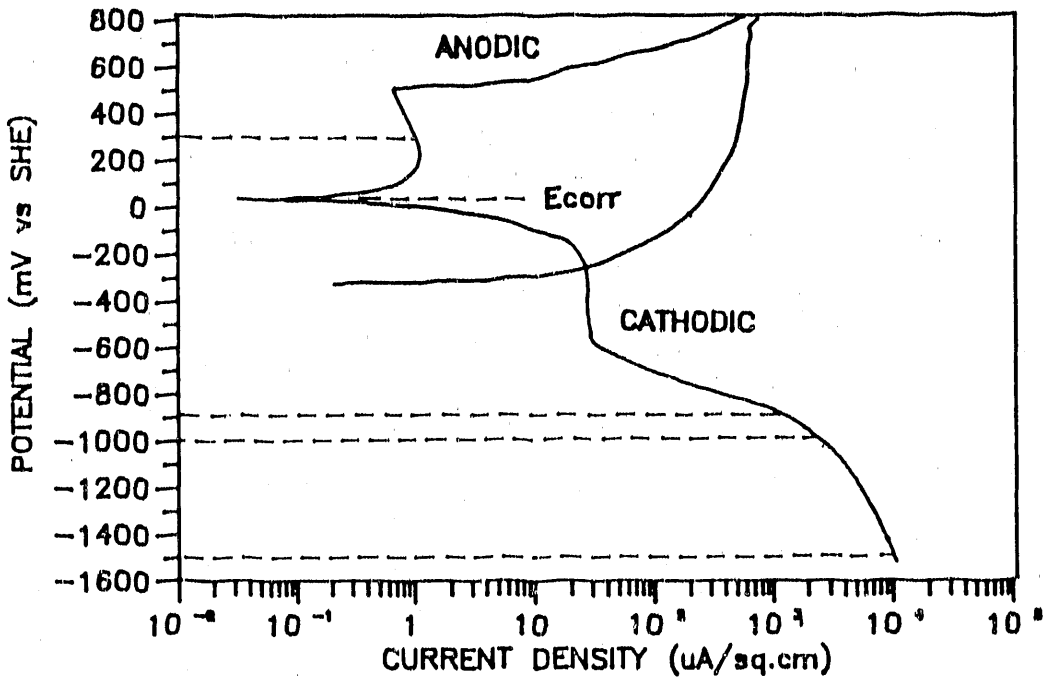

Fig. 1. Anodic and cathodic polarization curves for FA-129 iron aluminide in acid-chloride solution. Applied anodic and cathodic potentials are identified by dashed lines.

Results of the series of U-bend SCC tests with potentiostatically-controlled potentials are presented in Table 3. At the anodic potential of +300 mV(SHE), localized corrosion initiated on both the 2 and 5 a/o Cr iron aluminides. However, cracking failures did not occur for either material. Indeed, localized corrosion was so severe for the 2 a/o Cr material that through-thickness penetrations were evident at several sites; yet the U-bend specimens did not crack and mechanically fail. At the applied cathodic potentials, for the 2 a/o Cr iron aluminide, cracking did not occur within 200h at -900 mV (SHE), but did occur in 45h (average) at -1000 mV(SHE), and 17h (average) at -1500 mV(SHE). For the 5 a/o Cr iron aluminide, cracking did not occur within 200h at any of the applied cathodic potentials.

Table 3. U-bend test results in acid-chloride solution over a range of applied potentials.

Material	E(Applied) (mV (SHE))	Results	No. of Tests
FA-84 2 a/o Cr	+ 300	No Cracking Localized Corrosion	3
	(-200) → (-315) E_{corr}	No Cracking Localized Corrosion	2
	-900	No Cracking	2
	-1000	Cracking Failure, Transgranular (45 h, avg.)	2
	-1500	Cracking Failure (17 h, avg.)	2
FA-129 5 a/o Cr	+ 300	No Cracking Localized Corrosion	2
	(-40) → (+ 290) E_{corr}	No Cracking No Localized Corrosion	2
	-900	No Cracking	2
	-1000	No Cracking	2
	-1500	No Cracking	1

DISCUSSION AND CONCLUSIONS

200h U-bend stress-corrosion-cracking (SCC) tests of two iron-aluminide compositions (2 and 5 a/o Cr) under freely-corroding conditions, i.e. at open-circuit corrosion potentials (E_{corr} values), produced cracking failures in thiosulfate and tetrathionate solutions, but not in an acid-chloride solution. Additional tests in the acid-chloride solution at an applied anodic potential (corrosion acceleration) did not produce cracking failures for either the 2 or 5 a/o Cr iron aluminides. Further testing at applied cathodic potentials sufficiently

active to generate hydrogen at the specimen surfaces (while simultaneously decreasing the corrosion rate) produced cracking failures in the 2 a/o Cr iron aluminide at the more severe cathodic potentials, but did not produce cracking failures in the 5 a/o Cr iron aluminide.

The results indicated that the iron aluminides evaluated in this study are highly susceptible to SCC in thiosulfate and tetrathionate solutions under freely-corroding conditions.

The results also indicated that the iron aluminides are susceptible to SCC in an acid-chloride solution, that the mechanism is related to hydrogen-embrittlement effects rather than anodic-dissolution effects (i.e. corrosion per se), and that higher Cr levels are beneficial in minimizing this form of SCC.

A critical question at this point is whether the iron aluminides would ever undergo SCC under the freely-corroding condition (E_{corr}) during U-bend-type testing (constant strain, approximately constant stress) in the acid-chloride solution. Recall that the time duration in the present study was 200h. Also recall from previous discussion that E_{corr} must be less than -236 mV(SHE) at pH = 4 in order for the cathodic reaction to produce hydrogen during the corrosion process. Based on the E_{corr} values in Table 3 and the nature of the cracking mechanism revealed in this study, one must reasonably conclude that SCC could occur under freely-corroding conditions during a U-bend-type test (and by implication, during a constant-stress-type situation) for the 2 a/o Cr iron aluminide at a time period greater than 200h, but would never occur for the 5 a/o Cr iron aluminide.

Consistent with the above arguments, it is noted in Table 2 that the E_{corr} values during U-bend SCC testing in thiosulfate and tetrathionate solutions were always less than -236 mV(SHE), meaning that hydrogen was being generated at the surfaces during the corrosion process. Also, as previously described, cracking failures occurred within 200h in all cases. Previous work has shown that the iron aluminides do not passivate in these solutions, [4] an effect which not only leads to high corrosion rates, but also causes a low E_{corr}, hydrogen generation, and cracking.

With regard to the promising SCC responses of the iron aluminides, especially the 5 a/o Cr material, in the acid-chloride solution under U-bend-test conditons, a note of caution must be expressed. A different situation could exist during a constant-extension-rate SCC test. Under these conditions, fresh, nonpassivated

(nonprotected) surfaces are continuously being exposed to the electrolyte as a consequence of dislocation movement to the surface during plastic deformation. For short periods of time, until the fresh surfaces self-passivate, E_{corr} could be quite active--sufficiently active to produce hydrogen locally, which in turn could lead to hydrogen-embrittlement cracking and loss of ductility. Because of these possibilities and concerns, constant-extension-rate SCC tests have now been initiated as part of this overall program.

ACKNOWLEDGMENT

The authors wish to acknowledge the many helpful discussions in this topic area with Dr. E. E. Stansbury, Professor Emeritus, University of Tennessee.

REFERENCES

1. C.G. McKamey, V. K. Sikka, S. A. David, J. A. Horton, and C. T. Liu, "Development of Iron Aluminides," Fossil Energy Materials Program, Semiannual Progress Report for Peroid Ending March 31, 1989, pp. 267-272, Oak Ridge National Laboratory, ORNL/FMP-89/1.

2. C. G. McKamey, V. K. Sikka, and C. T. Liu, "Development of Iron Aluminides," Fossil Energy Advanced Research and Technology Development Materials Program, Semiannual Progress Report for Period Ending September 30, 1989, pp. 271-282, Oak Ridge National Laboratory, ORNL/FMP-89/2.

3. R. A Buchanan and J. G. Kim, "Aqueous Corrosion of Iron Aluminides," Fossil Energy Materials Program, Semiannual Progress Report for period ending March 31, 1989, pp. 553-564, Oak Ridge National Laboratory, ORNL/FMP-89/1.

4. R. A. Buchanan and J. G. Kim, "Aqueous Corrosion of Iron Aluminides," Fossil Energy Advanced Research and Technology Development Materials Program, Semiannual Progress Report for Period Ending September 30, 1989, pp. 593f, Oak Ridge National Laboratory, ORNL/FMP-89/2.

MATERIAL BEHAVIOR DURING SOLID PARTICLE EROSION OF ANNEALED 1100 ALUMINUM

J. R. Keiser, M. Rao,* and D. F. Wilson
Oak Ridge National Laboratory
P.O. Box 2008
Oak Ridge, Tennessee 37831-6156

ABSTRACT

Studies were conducted to evaluate the response of annealed 1100 aluminum to single and multiple erosive particle impacts. The 30° incidence angle multiple particle impact conditions ranged from that necessary to produce damage characteristic of the incubation period through that required to develop the steady state condition. Single impacts on samples were done at room temperature by spherical particles with an incidence angle of 30°. A mechanical properties microprobe was used to measure the hardness at the bottom of the craters formed by single impacts and in the material below the craters. A characteristic ripple structure developed on the surface with increasing dose. For the incubation period samples, the increase of deformation of the subsurface layers was studied using taper-sectioning techniques in conjuction with a mechanical properties microprobe while normal sectioning was used for the steady state samples. Distinct differences were observed in the hardness profiles beneath crests and valleys which form the ripple structure.

INTRODUCTION

Knowledge of how materials respond to erosive particle impacts and what properties control that response is essential to understanding erosion. Past studies of solid particle erosion of metals and alloys have established that the rate of erosion goes through several regimes (see, for example, ref. 1). An initial threshold period with little or no mass loss (or even a mass gain due to particle embedment) is typically seen, followed by an incubation period during which there is a steadily increasing rate of material loss. Ultimately, a steady state erosion rate is reached when the rate of mass loss achieves a constant value with respect to the amount of erodent impacting the surface.

Several other characteristics related to material removal mechanisms are well known. For ductile materials, erosion rates are maximum at grazing angles (≈20°) of incidence and decrease towards normal incidence.

---

*Department of Materials Science and Engineering, University of Notre Dame, Notre Dame, IN 46556.

Models of erosion incorporate material loss due to micromachining action of the erodent particles or removal of plate-like debris formed by straining the material beyond the fracture limit. These mechanisms are strongly influenced by erodent size and shape, and details have been published in several review articles/volumes.[2-4] Material properties which have been correlated to erosion behavior with varying degrees of success include hardness,[5] general mechanical properties,[6] bond energies,[7] melting points,[8] and other thermal properties.[9-11] Reported material responses range from melting,[12,13] to softening of the surface layers,[14,15] to failure by brittle fracture in the surface layers.[16]

Eroding surfaces develop characteristic topographies for both normal and glancing impacts. For normal impact a rough surface consisting of hills and valleys tends to develop during incubation.[15,17,18] For oblique impact, characteristic ripples (similar in appearance to a wavy surface) develop on the surface through incubation.[16,19-23] The ripples are presumed to strongly influence loss processes as material is removed from breaking waves and replenished onto wave crests from the valley bottoms.[16,20,21]

The present study focused on the work hardening caused by erosive particle impacts to increase knowledge and understanding of fundamental material behavior under erosive conditions. In addition, some information obtained can provide insights into ripple formation and propagation.

EXPERIMENTAL DETAILS

This report describes a series of erosion studies conducted at Oak Ridge National Laboratory (ORNL). First, the effects of single impacts on annealed 1100 aluminum were studied, followed by an evaluation of the changes in samples of the same material eroded to steady state conditions. As a bridge between these studies, the effect of erodent doses less than that required to reach steady state conditions was studied.

The single particle impact studies utilized a particle gun that is incorporated into a specially modified scanning electron microscope (SEM).[24] Prior to test, samples of annealed 1100 aluminum were polished to a 0.5-μm diamond finish followed by etching for a few seconds in an HF solution to remove most of the work-hardened surface created by mechanical polishing. Each sample was subjected to a single 30° impact made at room temperature with a particle velocity of 28.5 ± 1.0 m/s. Following each impact, mechanical property microprobe (MPM) hardness measurements were made on the bottom of each crater and in the material directly beneath the impact craters, by impacting a sample obtained by cross-sectioning through a crater and then polishing and lightly etching.

For the multiple particle impact studies, ORNL-prepared samples were exposed to a stream of erosive particles in the room temperature erosion tester at Lawrence Berkeley Laboratory.[25] Spherical steel shot 600 to 700 μm in diameter, traveling 45 m/s at 25°C, and impacting at 30° incidence angle, were used. For steady state evaluation, samples were exposed to at least 400 g of erodent. The same test system was used to expose samples to either 5, 10, 20, 40, 80, or 120 g of erodent, which covered the incubation period. Following exposure, the samples were returned to ORNL, where they were cut along the longer axis of the oval erosion crater, and then metallographically mounted, polished and lightly etched to prepare them for examination. The rippled surface structure reported by other researchers was observed on these samples.[20,24]

Characterization of the hardness immediately below the surface of these samples was done with an MPM, an ultralow load indentation instrument that allows force and displacement to be measured with resolutions of 0.3 μN and 0.16 nm, respectively.[26] A three sided pyramidal Berkovitch diamond indenter with the same depth-area relationship as a Vickers indenter is used. A coil and magnet assembly controls the indenter movement and applies the load, while the position of the indenter is measured by a capacitive displacement gauge. For these studies, the load was applied by moving the indenter at a constant velocity of 5 nm/s to a depth of 300 nm. The MPM measures load and displacement continuously during the load application cycle, so hardness can be calculated throughout the depth of the indentation. However, only those hardness values obtained at a depth of 200 nm below the polished cross sectional surface are reported in this paper. Because the accuracy of MPM hardness values depends on having a rigorous, but difficult, mathematical description of the indenter tip and because the MPM hardness values have not been correlated with traditional microindentation hardness, the hardnesses reported here are normalized with respect to the hardness of an unimpacted area of the sample.

RESULTS

The results shown in Fig. 1 of the hardness measurements on the singly impacted annealed 1100 aluminum samples indicate that the material was hardened to a depth of about 120 μm, and the surface hardness increased by 10 to 20%. Samples eroded by multiple impacts to a steady state condition developed a rippled surface, and hardnesses were measured below a selected, characteristic wave valley and below a wave crest. Figure 2 shows the relative hardness vs depth below the wave valleys.

COMPUTER MODELS

Spherical Particle Mode

The spherical particle impact model, previo

ORNL-DWG 90-13923

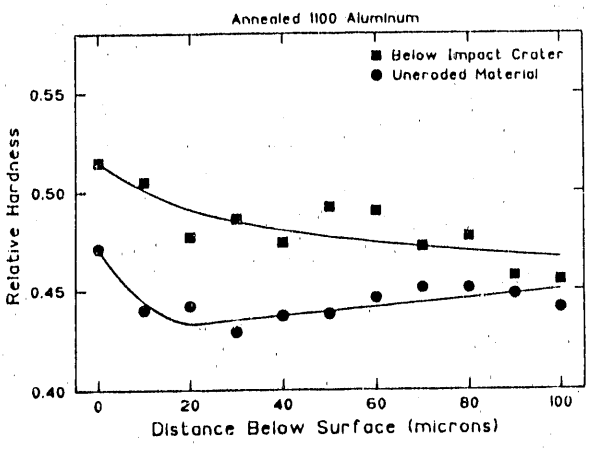

Fig. 1. Relative hardness vs depth for MPM hardness studies made below a single impact crater on annealed 1100 aluminum.

ORNL-DWG 90-13924

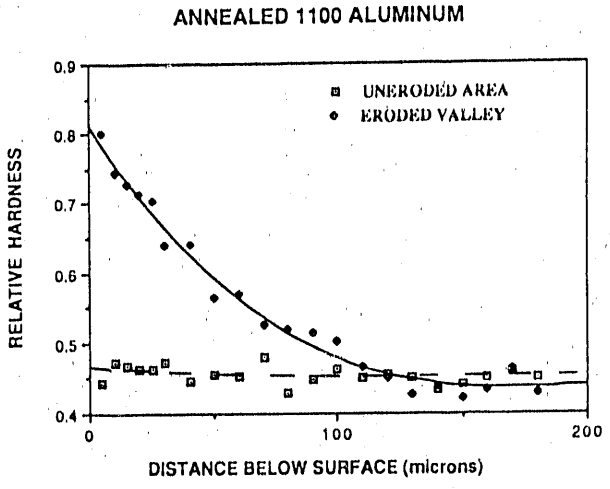

Fig. 2. Relative hardness vs depth for MPM hardness studies made below the wave valley of annealed 1100 aluminum.

Despite the fact that single impacts were made under somewhat different conditions (smaller, more dense particles traveling at lower velocity), the shapes of the hardness curves are remarkably similar. In the 10 μm just below the impacted surface, hardness was considerably greater for the samples subjected to multiple impacts than for the singly impacted samples, but, within the limits of our estimates, the depth of hardening in the valleys was about the same as that for the singly impacted samples. Figure 3 shows the relative hardness vs depth below the wave crest of the steady state annealed 1100 aluminum sample and indicates that hardening occurred to a depth of about 600 μm, a distance about equal to the height of the wave plus the depth to which hardening occurred below the valley.

Examination of the eroded surfaces of samples subjected to multiple impacts that left the samples in the incubation stage showed the development of the ripple structure with increasing dose. A comparison of the ripple structure made by tracing surface contours from micrographs of the taper sections is shown in Fig. 4. The 5-g sample shows only minor surface undulations associated with initial impacts, but the start of a regular ripple structure can be seen by the 20-g dose. The hills and valleys seen in the contours agree well with the shapes reported in the literature for obliquely eroded ductile metals.[16,19-23] Lips of material apparently on the verge of being removed can be seen on the peaks (except for the 5-g sample). The lips are located on the sides of the peaks

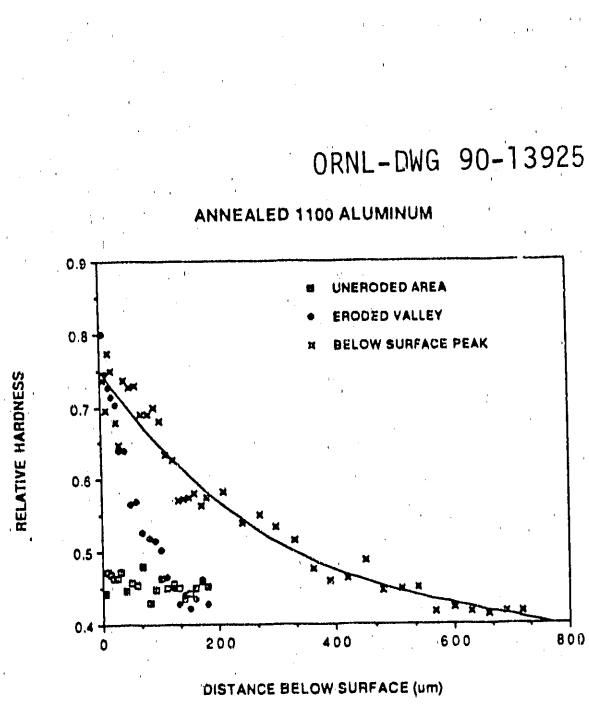

Fig. 3. Relative hardness vs depth for MPM hardness studies made below the wave crest of annealed 1100 aluminum. Hardness data taken below a wave valley and an uneroded surface are shown for comparison.

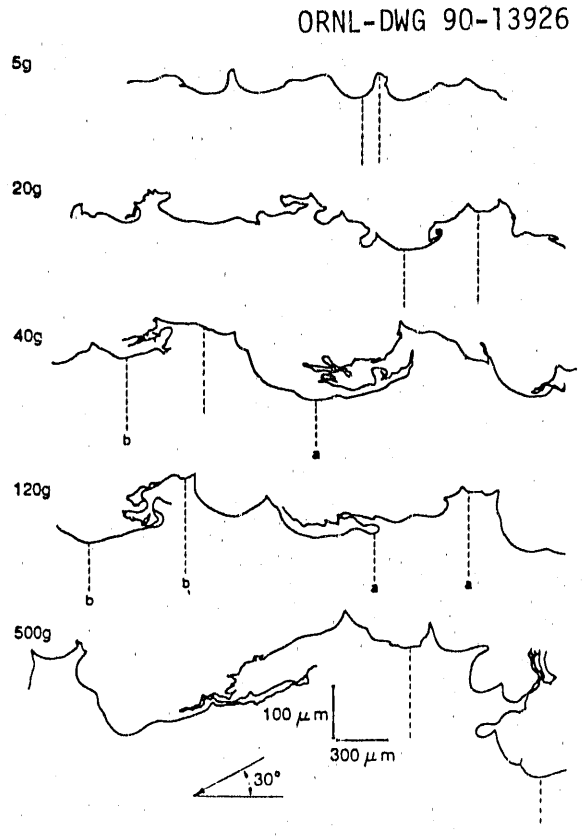

Fig. 4. Tracings of surface contours from taper sections of samples. Dotted vertical lines indicate where hardness profiles were made using the MPM. The arrow indicates the erodent direction.

facing away from the impact direction which also agrees well with literature observations. The ripple structure is already well developed in the incubation period (less than 120-g erodent dose) although peak heights and spacings are larger during steady state. Exact crest heights are difficult to estimate because small differences in the taper angles magnify errors in the vertical direction.

A number of the samples were extensively surveyed using the MPM. The dotted vertical lines in Fig. 4 represent areas where a series of regularly spaced indents was made from the surface down to levels where the hardness reached values equal to that of the annealed material. In addition, MPM measurements were made at other strategic locations, such as along the surface and on lips of material apparently about to be detached.

Figures 5 through 8 are plots of hardness versus distance below the surface for various crest and valley pairs indicated in Fig. 4. Each hardness value represented is an average of data from several indentations

ORNL-DWG 90-13927

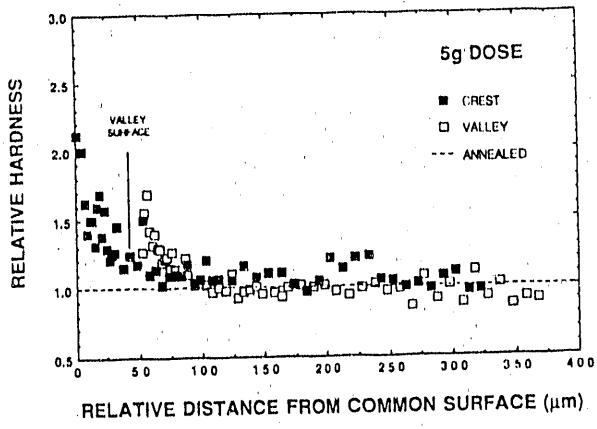

Fig. 5. Relative hardness vs depth below eroded surface for the 5-g dose sample. The depth has been corrected for the taper in this and subsequent plots.

ORNL-DWG 90-13928

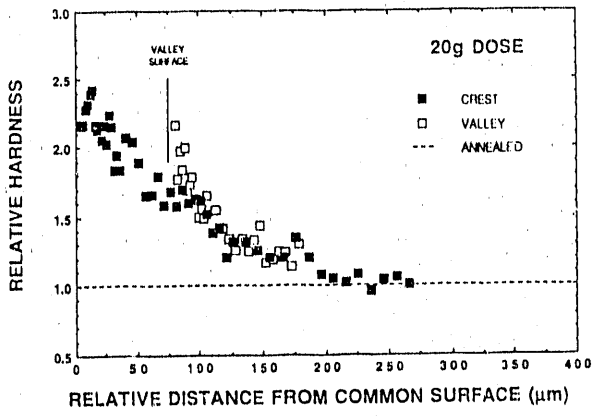

Fig. 6. Relative hardness vs depth below eroded surface for the 20-g dose sample.

ORNL-DWG 90-13929

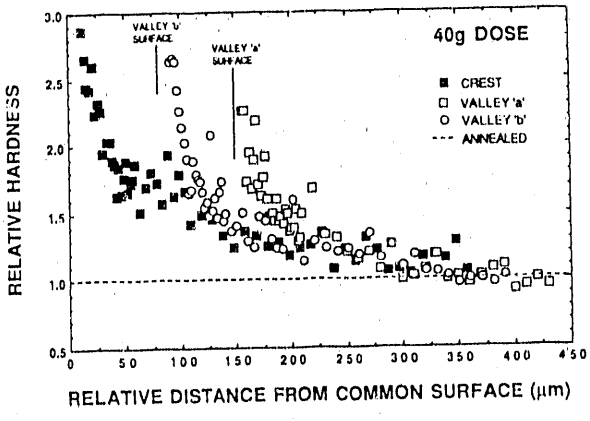

Fig. 7. Relative hardness vs depth below eroded surface for the 40-g dose sample. Data are from the crests and valleys indicated in Fig. 4.

ORNL-DWG 90-13930

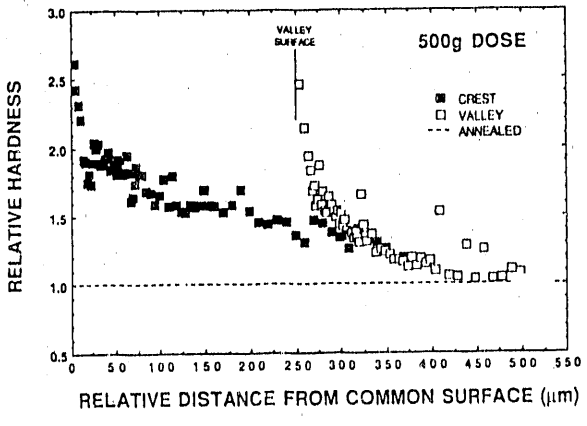

Fig. 8. Relative hardness vs depth below eroded surface for the 500-g dose sample.

at the same depth. For ease of comparison, the depths have been referenced to a common surface, thus correcting for the different heights and depths of the features. The common reference has been arbitrarily taken as the tip of the highest crest. For example, with reference to the 5-g sample in Fig. 4, the top of the crest containing the dotted line was taken as the reference surface. The surface of the adjoining valley lies about 50 μm below this peak. Consequently, the hardness versus depth plot for the valley starts from a distance 50 μm below the common reference, as seen in Fig. 5. Also shown in Figs. 5 through 8 are vertical dotted lines representing the position of the local surface for the particular feature. These show that hardness indentations were not made at equally close surface locations in all cases: Figures 5 and 7 show examples where, because of edge rounding introduced during metallographic polishing, indentations could not be made within 10 μm of the local surface.

Figure 5 shows the crest and valley hardness profiles for the 5-g dose sample. Significant hardening can be seen even at this low dose; the surface layers are about twice as hard as the underlying annealed material. Material near the surface of the valley area appears to have hardened to a lesser extent than the crest. Although the thickness of the hardened layer is less under the valley, both hardness profiles merge into a common profile at a depth of about 100 μm.

Hardness profiles for the 20-g samples are shown in Fig. 6. The extent of peak hardening increased over the 5-g sample, but the other trends are similar. The profiles under a crest and the valleys on either side are shown in Fig. 7 for the 40-g sample. There was a further increase in peak hardness, and, in addition, the shallower valley (valley "b" in Fig. 4) appears to have hardened to a larger extent than the deeper valley. However, this effect may be magnified somewhat by the lack of near surface indentations for the deeper valley (valley "a"). There was little or no further increase in peak hardness for samples subjected to higher erodent doses.

Hardening after different erodent doses is represented graphically in Fig. 9 which includes data from the 80-g sample. Maximum hardnesses are shown as a function of erodent dose. These measurements indicate how deformation accumulates during erosion. Both parameters appear to saturate around a 40-g erodent dose (part-way through the incubation period). Maximum hardness is around 2.5 to 3 times the hardness of annealed material, and the maximum work hardened layer under valleys extends to around 150 μm.

From the hardness profiles and the hardness traverses along the surface and other locations on crests and valleys, a hardness contour map can

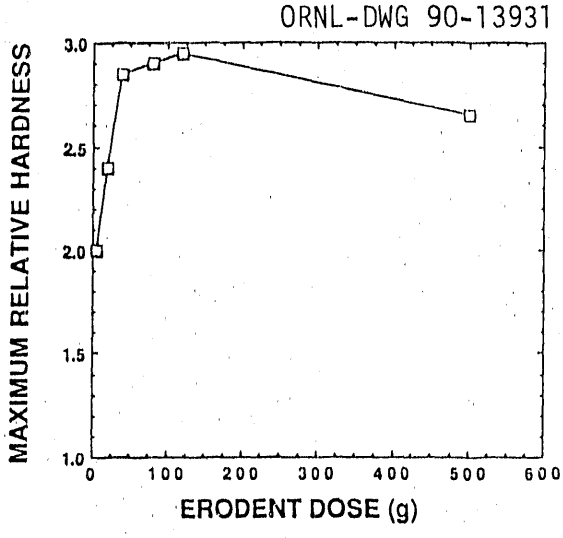

Fig. 9. Graph summarizing information from the hardness profiles as a function of erodent dose. The maximum relative hardness is the value measured on the tips of the crests.

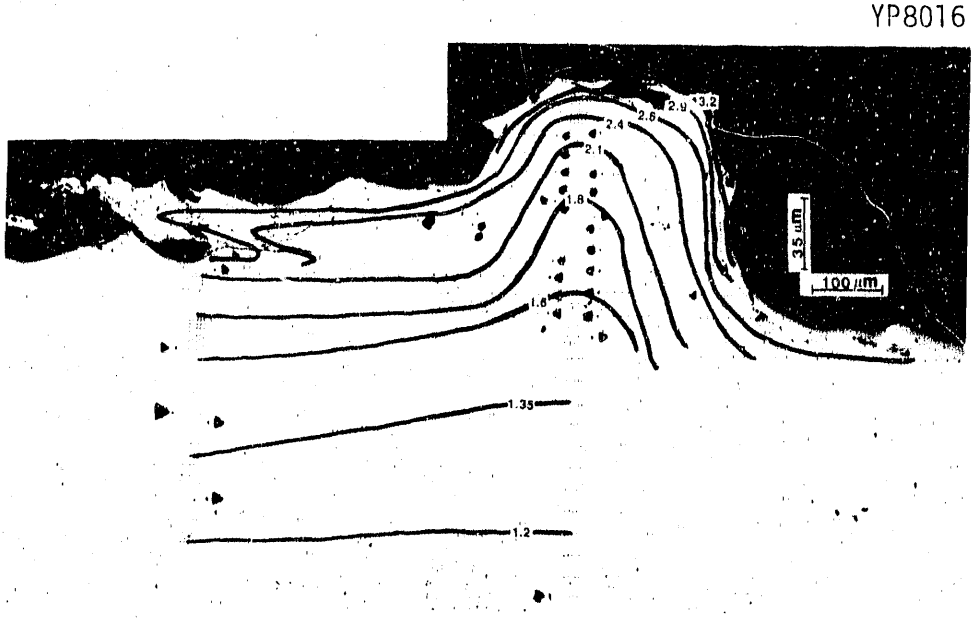

Fig. 10. Relative hardness contours drawn on a tapered section micrograph from an area of the specimen exposed to 120 g of erodent. Erodent direction is from the upper right.

be drawn. One such map is shown in Fig. 10 for the sample eroded with 120-g of steel shot. The crest-valley pair shown is the one marked "a" in Fig. 4 and the same relative hardness scale has been used. A skin of high hardness develops in the surface regions and eventually the hardness blends into that of the annealed material. Note that slightly higher hardness levels were measured in a narrow region directly facing the impinging particles.

Hardness measurements were made across a lip of material apparently on the verge of removal as indicated by a crack running almost all the way through it. The hardness values measured from the MPM indentations showed no additional hardening or softening associated with the crack. The observed values were typical of those measured at similar depths, as presented in the hardness profiles.

DISCUSSION

Before comparing the results from the various studies, it is important to note a few important differences in erosion test parameters. For the single impact studies, 343 μm diameter tungsten carbide balls were impacted on the target at about 28.5 m/s, while the multiple particle studies used 600-700 μm steel balls at 45 m/s. The kinetic energy of the steel balls was about eight times that of the tungsten carbide balls; however, the area of impact over which this energy was deposited was somewhat greater for the steel balls. Since the erosive particle rebound velocity is not known for either the single or multiple particle tests, the amount of energy transferred to the target material during an impact cannot be calculated. Therefore, even though the conditions of these two tests were not identical, the fact that both tests used spherical particles impacting at a 30° incidence angle at room temperature makes some limited comparison of these studies reasonable.

For oblique, single impacts, annealed 1100 aluminum showed appreciable surface hardening. Other studies have shown that when different aluminum alloys are impacted, the weaker, more ductile alloy hardens to a much greater depth, but the surface hardness increase is less.[24]

Under conditions of oblique impact, the 1100 aluminum used in the incubation stage portion of this study quickly developed a wavy surface structure. As shown in Fig. 4, surface undulations indicating plastic flow from exit edges of craters can be seen even at the low 5-g dose, where significant portions of the craters were not overlapping. The ripple structure can be identified at the 20-g dose at a stage where material loss is still insignificant. Appearance of a wavy structure

early in the incubation period agrees very well with literature observations.[20]

Although the surface layers reached a saturation hardness early in the erosion process, there was some indication that the surface layers at the valleys may not achieve as high a hardness as the tops of the crests. Figures 5 through 8 show that the maximum hardnesses measured under valleys were 10 to 25% lower than the peak hardnesses under corresponding crests. Some of this may be attributed to the lack of near-surface measurements for many valleys. However, extrapolation of the hardness profiles to the surface still leaves the local surface at valleys consistently softer than the local surfaces at crests. Nevertheless, the difference is not as great as that measured by Carter et al.[16] who reported surface microhardness values on valleys to be about half that on wave crests.

Figure 8 appears to indicate that hardnesses were comparable across both valleys and crests for the incubation stage sample that reached steady state condition. This approximate equivalence agrees with hardness measurements of crests and valleys for the sample intentionally taken to steady state conditions shown in Fig. 3. This may indicate that the hardness distribution does continue to change during later incubation and early steady state erosion, leading to an equi-hardness skin on crests and valleys. However, it is difficult to conclude this based on our data; it may well be that a certain amount of heterogeneity exists in the hardness of the surface layers on valleys.

Previous reports[24,27] also noted that the absence of any indication of softening directly contradicts reported results for similar materials and erosion conditions.[14] The confirmation provided by the extensive results presented here can be attributed to the greater sensitivity of the MPM.

The hardness data measured on the fracturing lip indicate that crack propagation and material fracture occurs at the maximum flow stress, perhaps on reaching a critical fracture strain. This is also supported by Fig. 9, which shows that maximum hardness (and thus the flow stress) levels are reached early in the erosion process. Also, Fig. 9 shows that the extent of hardening, represented by the hardened depth beneath valleys, quickly reaches a limit. This is not surprising if one considers that the deepest extent of plastic deformation would occur from initial impacts on annealed material. As the material work hardens, subsequent impacts would plastically deform a smaller volume. Thus, the depth of hardening should quickly reach a steady state value while near surface layers continue to harden to higher levels. It is significant that the

hardening depth for the single impact sample is quite comparable to the "saturation" hardening depth in Fig. 9. The "saturation" depth would be restricted to the depth of hardening by a single particle on the annealed surface as discussed above. Peak hardness under single impacts was significantly less than under multiple impacts, indicating that several impacts are needed to reach peak hardnesses. This is very clearly seen in the results presented here, with a steady increase in peak hardnesses shown from the 5-g to the 40-g samples. Obviously, several overlapping impacts are necessary to achieve maximum strain hardening.

The hardness profiles also show that the hardness under a valley decreases much more rapidly than under a crest. Thus, even though the higher elevations (peaks) on the sample are slightly harder than valleys, the hardening extends to a greater depth than it does in the low lying areas (valleys). Apart from deviations in the near surface regions, the data approximate a reasonably smooth curve. The rapid decrease of hardness in the valleys is independent of their relative depths from the original surface; in both Figs. 7 and 8 the hardness profiles of the valleys merge with the general curve within 80 to 100 μm. On the other hand, the extent of hardening under a crest increases with the height of the crest. Typically, the entire crest is hardened to levels found only in the top 10 to 20 μm of the valleys (see Fig. 10). Impacting particles would appear to affect the material differently depending on whether the impacts occur in the valleys or crests. The observations presented here support the view that wave crests are formed by ridges on impact craters or by material pushed up from the valleys.[16,19,21] This would leave the wave valleys as the area from which material was most recently removed, and thus, an area with the steepest hardness profiles. Material being pushed out would be highly strain hardened as observed for wave crests. Furthermore, upon subsequent impacts, the material under wave crests would tend to deform less because of higher flow stresses over larger volumes. Thus, a ripple structure once formed would tend to persist. The hardness contours in Fig. 10 show that overall hardening seems to be greater on the side of the crest facing the erodent (the contours are not centrally symmetric with respect to the wave crest).

The fact that maximum hardness levels are reached during incubation when erosion rates are still increasing indicates that the material continues to strain with no further hardening. Under high-strain rate conditions, a saturation flow stress is achieved while the material continues to accommodate further deformation. This effect is thought to be due to dynamic recovery processes.[28] In this sense, a strain distribution would be more informative than the flow stress distribution represented here,

and may indicate higher strains developing on the wave crests and on the fracturing lips seen on the leeward side of the wave crests. This material would eventually embrittle and fail, as suggested by Carter et al.[16] Material removal may also occur in the valleys as material is being pushed up due to breaking of ridges from overlapping craters or similar mechanisms. However, the present study does not provide any information on these latter hypotheses.

Indentations made in semi-detached wave crest material did not indicate any significantly different hardness than adjoining "bulk" material or wave valleys; no softening was observed in areas directly beside observed cracks, in front of crack paths, or in areas of heavy deformation (where adiabatic conditions might have existed and caused thermal softening). The similarity in maximum hardnesses, and the fact that these hardnesses are reached before steady-state conditions are achieved,[27] suggest that the fracture (material loss) criterion cannot be a critical flow stress. It appears more likely that material fails when some critical strain is exceeded, as noted above.

SUMMARY AND CONCLUSIONS

A comparison was made of the extent of subsurface hardening for aluminum samples subjected to single erosive particle impacts, to multiple impact conditions resulting in steady state erosion rates, and to multiple impact conditions resulting in pre-steady state conditions. Results indicate the following:

1. Work hardening occurs on all samples with no evidence of softening or melting. Surface hardening is greater after multiple particle impacts.

2. A wavy ripple structure develops on the surface early in the erosion process. Only a few overlapping impacts are necessary to form the initial ridges which form the wave crests.

3. Several overlapping impacts are necessary to achieve maximum strain hardening on the surface. The ripple structure is observable before this occurs.

4. The depth of hardening under wave valleys after multiple impacts is roughly equal to that provided by a single impact. Strain hardening limits the depth to which hardening can increase under subsequent impacts.

5. Hardening extends to much greater depths under wave crests; the depth of hardened material below the wave crest surface is about equal to the height of the wave plus the depth of hardening below the valley. This

supports the assertion[16,19] that strain hardened material is pushed up from the wave valleys into the crests.

6. Wave crests persist under subsequent impacts because the impact energy is distributed over smaller volumes in the highly strain hardened material. Impacts on wave valleys cause greater deformation because of the shallower hardened depths.

7. Material removal is controlled by the attainment of a critical fracture strain since erosion rates continue to increase even after peak hardnesses are achieved. Fracturing lips of material on wave crests indicate no further hardening.

ACKNOWLEDGMENT

Alan V. Levy of Lawrence Berkeley Laboratory conducted the multiple particle erosion tests on the samples, and we gratefully recognize his contribution. One of the authors (MR) was supported by an appointment to the U.S. Department of Energy Laboratory Cooperative Postgraduate Research Training Program administered by Oak Ridge Associated Universities.

REFERENCES

1. G.P. Tilly, *Wear* **14**, 63 (1969).

2. C.M. Preece, ed., *Treatise on Materials Science and Technology, Vol. 16, Erosion*, Academic Press, New York (1979).

3. W.F. Adler, ed., *Erosion: Prevention and Useful Applications*, ASTM Spec. Tech. Pub. 664, Amer. Soc. Test. Mater., Philadelphia (1979).

4. J.E. Field and I.M. Hutchings, *Materials at High Strain Rates*, T.Z. Blazynski, ed., (1987), p. 243.

5. I. Finnie, J. Wolak, and Y. Kabil, *J. Mater.* **2**, 682 (1967).

6. D.G. Rickerby, *Wear* **84**, 393 (1983).

7. A.K. Vijh, *Wear* **39**, 173 (1976).

8. C.E. Smeltzer, M.E. Gulden, and W.A. Compton, *J. Basic Eng.* **92**, 639 (1970).

9. P. Ascarelli, *Relation Between the Erosion by Solid Particles and the Physical Properties of Metals*, U.S. Army Materials and Mechanics Research Center Technical Report, 71-47, 1971.

10. I.M. Hutchings, *Wear* **35**, 371 (1975).

11. S. Malkin, *Wear* **68**, 391 (1981).

12. T. Christman and P.G. Shewmon, *Wear* **54**, 145 (1979).

13. B. Brown and J.W. Edington, *Wear* **70**, 347 (1982).

14. R. Bellman, Jr. and A.V. Levy, "Platelet Mechanism of Erosion of Ductile Metals" in *Wear of Materials-1981*, S.K. Rhee, A.W. Ruff, and K.C. Ludema, eds., The American Society of Mechanical Engineers, 1981, p. 564.

15. A.V. Levy, *Wear* **108**, 1 (1986).

16. G. Carter, M.J. Nobes, and K.I. Arshak, *Wear* **65**, 151 (1980).

17. R. Brown and J.W. Edington, *Wear* **69**, 369 (1981).

18. A.K. Cousens and I.M. Hutchings, *Wear* **88**, 335 (1983).

19. I. Finnie and Y.H. Kabil, *Wear* **8**, 60 (1965).

20. R. Brown, E.J. Jun, and J.W. Edington, *Wear* **70**, 347 (1981).

21. R. Brown and J.W. Edington, *Wear* **79**, 335 (1982).

22. I.G. Wright and V. Nagarajan, *Proc. of U.K. Corro ·on 1984*, Int, Conf. and Exhibition, p. 55, Institute of Corrosion Science and Technology.

23. John Stringer and Ian G. Wright, "Some Views on the Formation of Ripples on Eroded Surfaces," *Proceedings of 7th International Conference on Erosion by Liquid and Solid Impact*, John L. Field, ed., Univ. of Cambridge, paper No. 47 (1987).

24. J.R. Keiser, R.S. Heidersbach, D.L. Dobbs, Jr., and W.C. Oliver, *Wear* **124**, 105 (1988).

25. L. Lapidas and A. Levy, *Wear* **58**, 301 (1980).

26. J.B. Pethica, R. Hutchings, and W.C. Oliver, *Phil. Mag. A* **48**, 593 (1983).

27. Mukund Rao, James Keiser and Dane Wilson, *Script. Met.* **23**(9), 1475 (1989).

28. U.S. Lindholm and G.R. Johnson, *Materials Behavior Under High Stress and Ultrahigh Loading Rates*, J. Mescall and V. Weiss, eds., Plenum Press, New York, p. 61 (1982).

A STUDY OF EROSIVE PARTICLE REBOUND

T.H. Kosel and K. Anand

Department of Materials Science and Engineering
University of Notre Dame
Notre Dame, IN 46556

ABSTRACT

Predictions of computer models for the impact of spherical and angular particles are compared with experimental data for the magnitudes and directions of particle rebound velocity during both single- and multiple-particle impact. Experimental systems have been developed to measure dynamic hardness, and rebound velocities for either single or multiple particles.

Single impacts of angular particles give a much wider range of magnitudes and directions of rebound velocities, and the mean velocity is lower than that for spheres at low but not at high angles of incidence. The range of values is attributed to differing particle orientations, leading to differing energy losses due to plastic deformation of the target and to rotational energy imparted to the particle, as suggested by the computer model. Multiple-particle rebound data are in general agreement with single-particle data, except that the mean rebound velocity is lower for multiple- than for single-particle rebound at low angles of incidence. This is attributed to surface roughening during multiple-particle erosion. Multiple-particle rebound velocities are nearly the same for 6061-T6 Al and quenched 1080 steel at both 15° and 75° incidence, in disagreement with the models for 75°. However, the angular particle model agrees well with data for rebound velocity for 6061-T6 Al.

INTRODUCTION

This work examines the use of computer models of the impact process to predict the magnitude and direction of particle rebound velocity V_r during erosive impact. The project includes development of computer models and experiments to test the model predictions.

Previous studies of the impact process have included models for impact of either spherical or angular particles. The present work examines the fit of new experimental data to a previous spherical particle impact model,[1] and to a newer model for angular particle impact. A more complete discussion of many results in the present paper has been published elsewhere.[2]

COMPUTER MODELS

Spherical Particle Model

The spherical particle impact model, previously described by Sriram and Kosel,[1] is a modification of a model presented by Hutchings, Winter and Field[3] and later improved upon by Rickerby and Macmillan.[4,5] The model assumes a uniform contact pressure equal to the dynamic hardness H_d over the area of contact, producing forces which alter the direction and magnitude of the velocity vector during successive time increments in the model.

Angular Particle Model

The angular particle impact model assumes a two-dimensional particle. As with the sphere model, the general approach is to integrate the equations of motion of the particle by evaluating the contact area during successive time increments, using H_d to find the forces on the particle, and calculating the change of position and velocity vector during each time increment.

The contribution of stored elastic energy is incorporated in a manner similar to the sphere model,[1] and the loss of kinetic energy when the particle acquires rotational energy as a result of moments exerted on it by the material is also accounted for. The model is designed to permit the study of particles of arbitrary regular or irregular polygonal shape.

EXPERIMENTAL TECHNIQUES AND MATERIALS

Dynamic Hardness

The dynamic hardness of each material investigated, which serves as the primary material input parameter for the models, was determined by measuring the 90° incident and rebound velocities of a 635 μm sphere. Further details are given elsewhere.[2,6]

Single-Particle Rebound Apparatus

The single-impact rebound system[2,7] measures the magnitude and direction of V_r for a single spherical or angular particle impacting a flat, uneroded planar surface. This system directly simulates the conditions assumed in the computer models, which ignore surface roughening and hardening. A single particle is propelled by a gas pulse through a tube at a known angle of incidence α_i, intercepting a pair of flat laser beams parallel to the specimen surface before impact. The incident velocity V_i is determined from the time of flight measurement knowing the preset α_i. As the particle rebounds, it passes through one pair of flat laser beams parallel and one pair perpendicular to the sample, giving the components of V_r tangential and normal to the surface, V_{rx} and V_{ry} respectively, from time of flight measurements. The tangent of the rebound angle α_r is given by V_{ry}/V_{rx}; the α_r measurement is accurate to about $\pm 1°$.[2,7]

There is generally a small component of rebound velocity V_{rz} in the z direction, normal to the x-y plane of incidence. To limit the magnitude of this unmeasured velocity component, the laser beams are only 1 cm wide in the z direction, and only particles passing through all four beams during rebound are measured. This can introduce errors of up to 3.1% in V_r for $\alpha_r = 45°$, due to neglect of V_{rz}.

Multiple Particle Rebound Apparatus

Multiple particle impact experiments were performed to test the angular particle model under steady-state erosion conditions, and to evaluate the effects of surface roughening and hardening which are absent in single-impact tests. The experiments were done in a rotating arm erosion system which accelerates particles mechanically in vacuum. V_r is measured optoelectronically[8] as the particles rebound through a pair of light beams set at a particular α_r, and both the particle flux and V_r distribution at this α_r are determined. α_r is then incremented and the measurements repeated, until V_r and flux are characterized for the appropriate range of α_r for a particular α_i and V_i.

Specimen Materials

The spherical particle model was tested earlier[2] for four metals having a range of H_d from 0.117 to 6.61 GPa. In the present work, we discuss results from precipitation-hardened 6061-T6 Al (H_d = 0.861 GPa) and water-quenched (martensitic) 1080 steel (H_d = 6.61 GPa).

RESULTS

Single Impact Experiments

The variation of the magnitude of V_r with V_i for the single-particle rebound experiments with spherical particles has been given previously for all four materials.[2] The results were in good general agreement with the spherical particle impact model with regard to the variation of V_r with V_i, α_r with α_i, and V_r with H_d. The model fits the results most accurately at 90° and at an α_i which varies somewhat with material but is near 45°.

The single-particle rebound data for angular Al_2O_3 particles on 6061-T6 Al will be compared with the spherical particle model and data to examine the effects of particle shape. Figures 1 and 2 show plots of V_r vs. V_i for spherical and angular particles for 30° and 60° incidence, together with the sphere model predictions. The spherical particle data for each α_i have been adjusted slightly for differences in particle density and elastic modulus, using the model. There is much more scatter for angular than spherical particles, and at low α_i the mean V_r is significantly lower for angular than spherical particles. As α_i increases, the angular particle data gradually shift upwards relative to the sphere data, until at 60° and 75° incidence the two sets of data share nearly the same mean.

Multiple Particle Rebound Experiments

In agreement with single-particle tests, V_r distributions were significantly wider than the V_i distribution, typically varying between

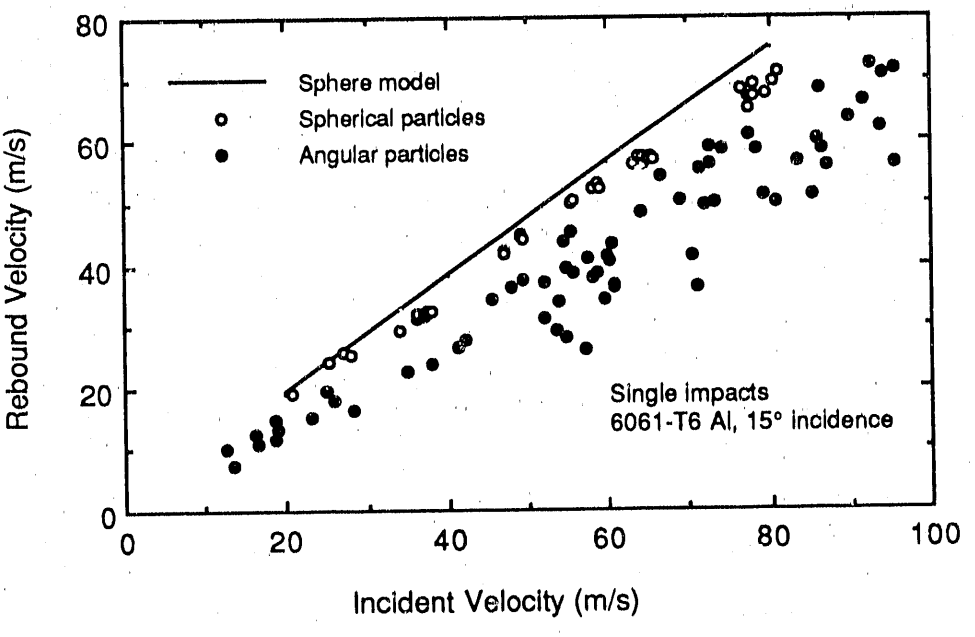

Figure 1. Comparison of dependence of V_r on V_i for 1 mm dia. 440C stainless steel spheres, 700 μm Al_2O_3 particles, and the sphere model predictions for 15° incidence on 6061-T6 Al.

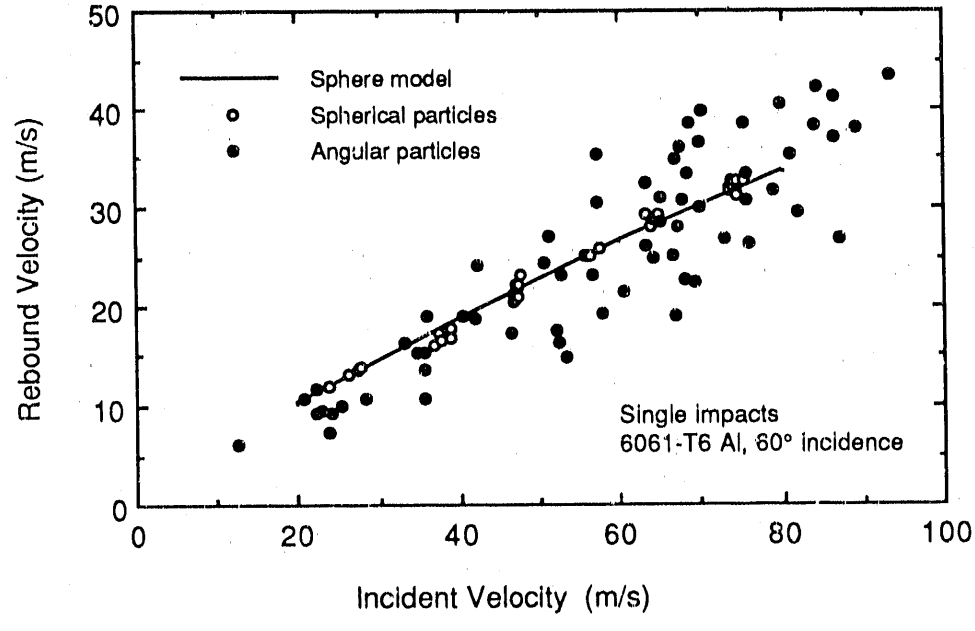

Figure 2. Comparison of dependence of V_r on V_i for 1 mm dia. 440C stainless steel spheres, 700 μm Al_2O_3 particles, and the sphere model predictions for 60° incidence on 6061-T6 Al.

about 28 and 43% of the mean, compared to 4% for V_i.

It was observed that the mean V_r depends fairly strongly on α_r for lower α_i, with this dependence decreasing at higher α_i, as illustrated in Figure 3 for 44.6 m/s impacts of 138 μm quartz on 6061-T6 Al and quenched 1080 steel. A similar trend also exists for single-impact tests with angular Al_2O_3 particles.[2]

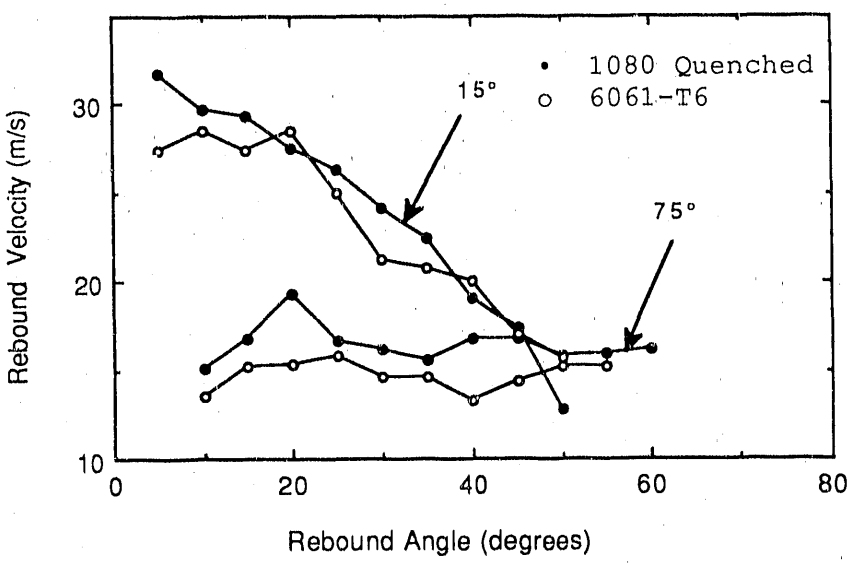

Figure 3. Dependence of V_r on α_r for multiple-particle impact of 138 μm crushed quartz particles on 6061-T6 Al and quenched 1080 steel at 15° and 75° incidence.

As may be seen from Figure 4, the mean ratio V_r/V_i was consistently lower for multiple- than for single-particle experiments on 6061-T6 Al, especially at lower α_i. The multiple-particle rebound results have been calculated by multiplying the mean V_r at each α_r by the flux value at that α_r, giving a weighted average V_r. The angular particle model predictions for pentagonal or hexagonal shapes are also shown.

The dependence of average α_r on α_i was quite similar for single- and multiple-impact angular particle experiments on 6061-T6 Al (Figure 5), and α_r was much less sensitive to α_i for angular than for spherical

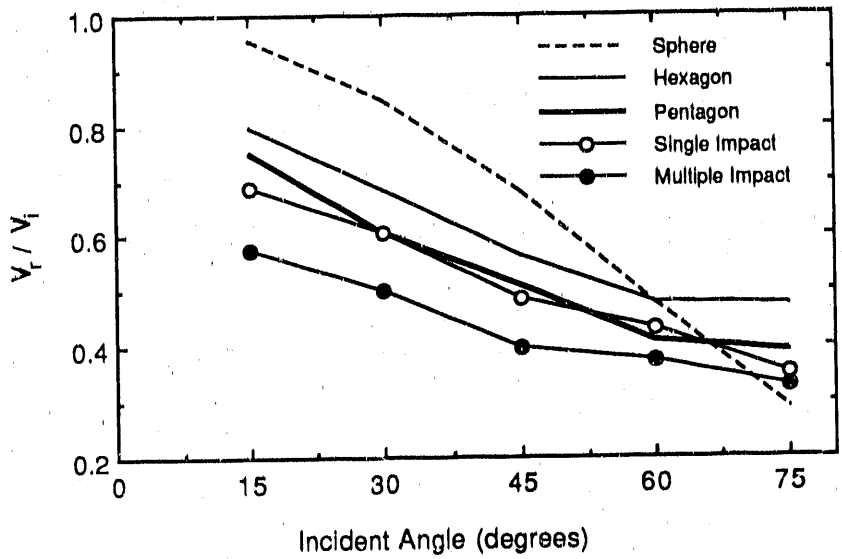

Figure 4. Comparison of angular particle results for dependence of normalized V_r on α_i from single- and multiple-particle tests with predictions of spherical and angular particle models.

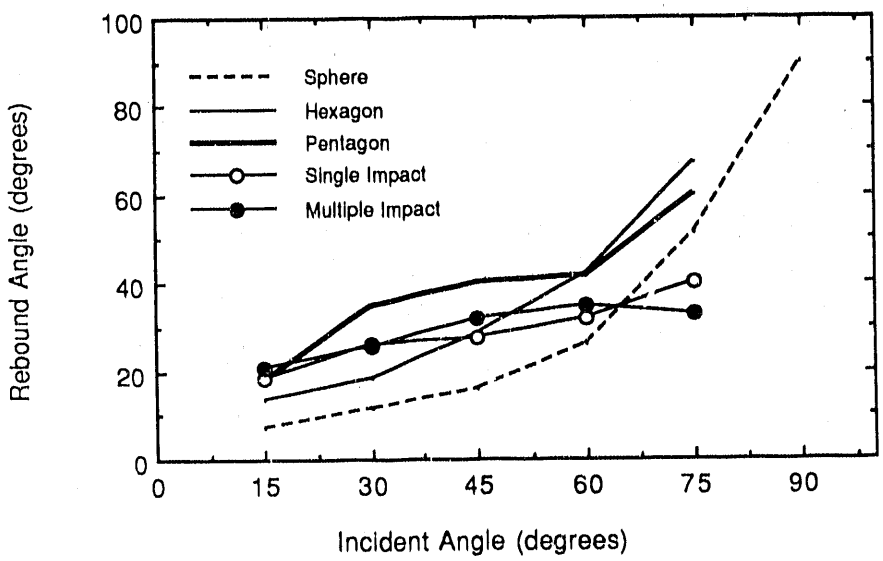

Figure 5. Comparison of angular particle results for dependence of normalized α_r on α_i from single- and multiple-particle tests with predictions of spherical and angular particle models.

particles. The angular particle model predictions for a regular hexagon or pentagon are also included, and these fit the data better than the spherical particle model at lower α_i.

DISCUSSION

Single-Particle Rebound

The much greater range of V_r for angular than spherical particles can be explained by the effect of differing incident particle orientations. If the attack angle between the surface and the leading face of the particle is small, we would expect a plowing interaction with the surface, with a small crater volume and depth of penetration. Since penetration is shallow, the moment exerted on the particle by the material is small, and the resulting rotational energy imparted to the particle (and subtracted from its original kinetic energy) would be small. In contrast, a high attack angle should lead to deeper penetration and greater energy losses due to both plastic deformation and rotational energy. The angular particle computer model confirms these qualitative expectations.[2]

Multiple-Particle Rebound

The multiple-particle experiments confirm the large range of α_r and V_r observed in single-impact experiments with angular particles. The angular particle model suggests that the decrease of mean V_r with increasing α_r at lower α_i (Figure 3) can also be attributed to the effect of attack angle, with higher attack angles giving lower V_r as explained above, and also resulting in higher α_r.

The observation (Figure 4) that the mean V_r is lower for multiple- than single-particle tests on the same material (6061-T6 Al) could be influenced by several factors. Erosion severely work hardens the surface of most metals,[9] which would increase the dynamic hardness of the steady-state eroded surface. Since this should increase V_r for multiple-particle tests, some other factor must be more important.

Model predictions show that the effect of differences in density and elastic constants of the Al_2O_3 and crushed quartz used for single- and multiple-particle tests respectively should be much smaller than observed. The particles used in multiple-particle tests appeared to be somewhat more rounded than those in the single-particle tests, but this would tend to increase V_r for multiple-particle tests at low α_i. We therefore believe that the difference is caused primarily by the surface roughening present in multiple-particle tests. Incident particles striking the exit ends of impact craters should encounter a higher local α_i than the macroscopic angle and lose more energy by plastic deformation because V_r decreases with increasing α_i. Particles striking parallel to the entrance slope of a previous crater would initially lose less energy, but would eventually come to the end of the previous impact crater and lose more energy.

The angular particle model predictions of V_r/V_i vs. α_i for pentagonal or hexagonal shapes shown in Figure 4 are in much better agreement with the single-particle results than the spherical particle model predictions are. The fact that the angular particle model agrees less favorably with the multiple-particle results is probably due to the effects of surface roughening just discussed.

The mean V_r for multiple-impact tests of quenched 1080 steel is essentially the same as that for 6061-T6 Al for both 15° and 75° incidence (Figure 3). This is in agreement with the model for 15°, since the predicted dependence of V_r on H_d is very weak. However, the spherical particle model predicts that V_r should be about three times higher for the much harder quenched 1080 steel, while the data show an almost negligibly higher value. This could be due to energy losses due to deformation of the quartz particles by the steel target, which is of the order of 70% of the quartz hardness before the work hardening introduced by erosion. Other possible factors might be particle fragmentation, or greater work hardening of the 6061-T6 alloy than the steel. Further study will be necessary to understand this very recent result.

The smaller dependence of α_r on α_i for angular than spherical particles (Figure 5) is most pronounced at higher α_i. Since angular

particles would rarely impact in a symmetrical orientation at 90° incidence, asymmetrical forces would cause them to rebound to the side, while a sphere should rebound at 90° unless it has a large initial rotational speed. We thus expect α_r to remain less than 90° as α_i approaches 90° for angular particles, as observed. At low α_i, the angular particle model predicts a larger mean α_r than for spheres, as observed.

CONCLUSIONS

1. The experimental systems provide accurate data for both single- and multiple-particle rebound.
2. Single angular particles have a lower mean V_r than spheres at low α_i, but a comparable mean at high α_i.
3. Angular particles have a much larger range of V_r and α_r. Qualitative arguments and the angular particle model indicate that this can be attributed to greater energy losses due to variations of plastic deformation of the target and particle rotational energy with initial particle orientation.
4. Single- and multiple-particle rebound data for angular particles have similar trends of V_r with α_r, and of α_r with α_i, and are reasonably accounted for by the angular particle model.
5. The similar values of V_r for multiple-particle experiments on quenched 1080 steel and 6061-T6 Al is in reasonable agreement with the models for $\alpha_i = 15°$, but not for $\alpha_i = 90°$.
6. The observation that the mean V_r is lower for multiple- than single-particle rebound of angular particles is attributed to surface roughening.

ACKNOWLEDGEMENTS

This work was supported by the Fossil Energy Materials Program of the U.S. Department of Energy under Martin Marietta subcontract #19X-91346C, and the authors are grateful for this support.

REFERENCES

1. T.S. Sriram and T.H. Kosel, "Computer Modeling of the Rebound Characteristics of Spherical Erodent Particles," Proc. 7th Int. Conf. on Erosion by Liquid and Solid Impact, Cambridge, England, Sept. 7-10, 1987, pp. 67-1 to 67-8.

2. T.H. Kosel, K. Anand, V. Sundararaman, T.S. Sriram, M. Kotteyil and P.J. Nailos, "Rebound of Erodent Particles from Metal Surfaces," Proc. 4th Berkeley Conf. Corrosion-Erosion-Wear of Materials at Elevated Temperatures, Berkeley, California, Jan. 31-Feb. 2, 1990, NACE, ed. A.V. Levy (submitted for review)

3. I.M. Hutchings, R.E. Winter and J.E. Field, "Solid Particle Erosion of Metals: The Removal of Surface Material by Spherical Projectiles," Proc. Roy. Soc. London A 348 (1976) 379-392.

4. D.G. Rickerby and N.H. Macmillan, "Erosion of Aluminum and Magnesium Oxide by Spherical Particles," Proc. Int'l. Conf. on Wear of Materials - 1981, ASME, San Francisco,CA, March 30-April 1, 1981, pp. 548-563.

5. D.G. Rickerby and N.H. Macmillan, "On the Oblique Impact of a Rigid Sphere Against a Rigid-Plastic Solid," Int. J. Mech. Sci. 22 (1980) 491-494.

6. T.H. Kosel, U.S. Dept. of Energy, Fossil Energy Materials Program Semiannual Progress Report for the Period Ending March 31, 1989, ORNL/FMP-89/1, pp. 517-552

7. V. Sundararaman, M.S. thesis, " A Single-Impact Study of the Rebound of Erodent Particles," University of Notre Dame, August, 1990

8. T.H. Kosel and K. Anand, "An Optoelectronic Particle Velocimeter," Proc. Symp. Corrosion & Particle Erosion at High Temperatures, Las Vegas, Nevada, Feb. 27 - March 3, 1989, Ed. V. Srinivasan and K. Vedula, TMS-AIME, 1989, 349-368

9. J.R. Keiser and M.C. Rao, "Deformation of Eroding Surfaces," Proc. 4th Berkeley Conf. Corrosion-Erosion-Wear of Materials at Elevated Temperatures, Berkeley, California, Jan. 31-Feb. 2, 1990, NACE, ed. A.V. Levy

MECHANISMS OF GALLING AND ABRASIVE WEAR

L. K. Ives and W. W. Duvall

Ceramics Division
National Institute of Standards and Technology
Gaithersburg, MD 20899

ABSTRACT

Piston ring and cylinder wear is a serious problem encountered in diesel engines operated on pulverized coal-fuels. Materials with much greater wear resistance than those used in conventional oil-fueled engines will be required for these engines. To assist in seeking solutions to this problem, a program is being conducted at the National Institute of Standards and Technology which is aimed at developing a fundamental understanding of wear processes that occur when a lubricant contains abrasive particles. In this report we present results and analyses concerned with the effect of particle hardness and particle concentration in oil on wear rate.

INTRODUCTION

The successful commercial development of direct coal-fueled diesel engines depends on solving severe wear problems that are not encountered with present day oil-fueled engines. The purpose of this program is to develop a fundamental understanding of the processes and mechanisms that are responsible for wear at the critical piston ring/cylinder wall contact. Particulate matter both from the raw fuel and from combustion products enters the piston ring/cylinder wall contact region and causes rapid wear as a result of direct abrasion of the ring and cylinder wall materials and/or by interfering with the normal lubrication process. In this program, analyses and tests are carried out on raw fuel materials and combustion particulates to determine their abrasion characteristics. Laboratory wear tests are conducted under carefully controlled conditions that are consistent with those occurring at the piston ring/cylinder liner contact in the diesel engine. The effects of test conditions, different types of

particulate materials, different lubricants and lubricant additives, and various specimen materials are studied.

DISCUSSION OF CURRENT ACTIVITIES

In this report we will first present some results of an analysis of the effect of particle hardness on the wear rate of 52100 steel. It is found that wear rate increases with increasing particle hardness greater than that of 52100 steel. This is contrary to the usual observation that wear rate remains constant once the particle hardness exceeds that of the wearing surface. Then, in the remainder of the report, we will present some interesting findings on the influence of particle concentration on wear rate. In particular, the results show that combining soft (coal) particles with hard (quartz) particles results in a much higher wear rate than would be expected on the basis of direct superposition of the separate wear rates of the two particle types.

Effect of Particle Hardness

Previously[1], wear rate data for several different types of particles were reported without a detailed analysis of the results. Wear rate data were obtained by means of rotating pin-on-disk tests.[2] Although several different pin and disk specimen materials have been studied, results cited in this report refer only to 52100 steel. The pins were 9.525 mm diameter bearing balls having a nominal hardness of 800 kg/mm^2. The disks were machined from annealed rod stock and heat treated to a hardness of approximately 760 kg/mm^2. Only pin wear was measured. With the low wear volumes involved, it was not, in general, feasible to measure disk wear in the rotating pin-on-disk test. A summary of the test conditions is given in Table 1. The tests were conducted under boundary lubrication conditions. Particles were added to the oil at selected concentrations to determine their effect on wear rate. Properties and wear rate data for three well characterized

Table 1. Wear test conditions

Load -- 15 N
Speed -- 63-64 cm/s
Atmosphere -- Air, Relative Humidity ~20 - 65%
Temperature -- 23±2°C
Oil -- Paraffinic mineral oil (335-365 SUS @ 37.8°C)
Oil+Particle charge per test -- 1.77g

hard abrasive particle types studied are listed in Table 2. Coal which is comparatively quite soft is also included. The hardness value for coal does not reflect the fact that the coal-fuel particles employed in the wear tests contained ~1%* mineral particles. A small

Table 2. Particles (2 μm) and wear rates at 5% concentration

Particle Type	Hardness (kg/mm^2)	Wear rate ($\mu m^3/m$)
MgO	700	470
SiO_2	1000	1420
Al_2O_3	2100	70210
Coal	34	~90

fraction of the mineral particles were relatively hard quartz and iron pyrite; the remainder were softer clay, calcite, anhydrite, and ferric sulfate.[3] The presence of the mineral particles is probably responsible for a large part of the increase in wear rate observed with coal-fuel particles. Here, the wear rate value for coal is an estimate based on results for higher concentrations. The estimated value represents an increase of about 30% above the wear rate obtained without particles added to the oil.

The wear rate value for 2μm quartz also was not measured directly but was determined by interpolation of results obtained for 1, 3, and 10μm quartz particles.[1] In this size range, wear rate was found to

*All concentrations are in weight percent

increase exponentially with increasing particle size according to the relationship,

$$\text{Wear Rate } (\mu m^3/m) = 587\ e^{0.44d} \qquad (1)$$

where d is the particle size in μm.

Employing the data in Table 2, wear rate vs. hardness is presented in the semi-log graph in Fig. 1. The curve in Fig 1. is a least squares fit to the data, excluding coal-fuel. The fit is quite good for these abrasives, all of which are approximately equal to or greater in hardness than the 52100 steel pin surface (800 HV @ 500g) being worn. The fitted curve is described by the relation,

$$\text{Wear Rate } (\mu m^3/m) = 39.3\ e^{0.00357h} \qquad (2)$$

where h is the particle hardness in kg/mm^2.

The wear rate with the coal-fuel particles, despite their low hardness compared to 52100 steel, is higher than predicted by Eq. (2). This is at least partly due to the presence of hard mineral particles in the coal. In any case, there is no reason to expect that the soft particle response should be the same as that for hard particles. Additional studies will be required to examine the soft particle regime.

The above results can be compared with those reported in the literature. In general it is found that wear rate decreases rapidly when the hardness of the abrasive particles is less than about 0.8 times the hardness of the surface being worn.[4-6] On the other hand, when the hardness of the abrasive exceeds that of the surface being worn by more than a factor of about 1.2, wear rate is relatively high and remains constant independent of abrasive hardness.[4,6] It is the latter observation that is of particular interest here.

In addition to this investigation, two other studies were noted where it was reported that wear rate did not remain constant but increased with increasing particle hardness. In both of those investigations wear behavior was studied at lubricated contacts with

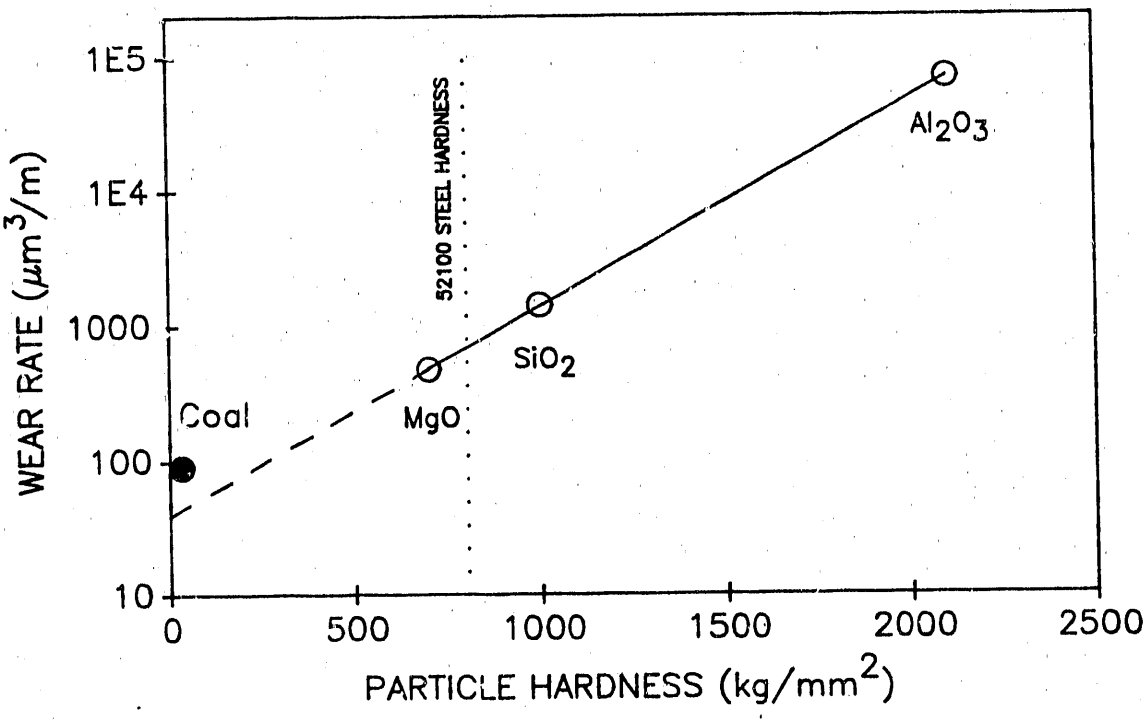

Fig. 1. Effect of particle hardness on wear rate of 52100 steel. Particles at 5wt.% concentration in mineral oil.

hard particles in the lubricant. One investigation[7] dealt with hydrodynamic lubrication and the other[8] with boundary lubrication conditions. No explanation was given for the fact that the observed wear behavior differed from that generally reported in the literature.

It appears that the difference in behavior is related to the nature of abrasive wear tests employed. When the wear rate remains constant with abrasives that are more than 1.2 times than the surface being abraded, so called low stress abrasive wear tests were employed. In a low stress test the abrasive particles are not subject to appreciable crushing in the contact. This is a consequence of the particles being supported by a relatively soft counterface material, for example, when the particles are bonded to paper or cloth. Under this condition, abrasion by a given particle is determined by the depth of penetration of that particle into the surface, and, of course, by geometry and other factors that are not related to

hardness. High stress abrasion refers to a condition under which the particles are likely to be crushed when they enter or pass through the contact. This is the condition that probably exists at lubricated contacts comprising relatively hard metal and ceramic bearing elements. The strength of a particle, with some exceptions where, for example, easy cleavage may occur, is directly proportional to its hardness. Thus, the greater the hardness, the more resistant the particle is to crushing and the more effective it is in producing abrasion.

Effect of Particle Concentration

Previously[1,9], we reported that wear rate increased with increasing particle concentration for concentrations as high as 20%. This relationship, the increase in wear rate with particle concentration, was found to hold for a variety of different particle types including those listed in Table 2 and for coal-fuel combustion particles[1], as well. Although the particle concentration that may be present at the piston ring / cylinder wall contact of a diesel engine operating on coal-fuel is not known, it is likely to be quite high. The high observed wear rates alone would lead to this conclusion. Thus, it is important to have an understanding of the effect of large particle concentrations. A significant fraction of the particles which settle on the cylinder wall surface are likely to be unburned coal-fuel. Since only about 1% of the coal-fuel consists of ash, even 99% combustion efficiency would lead to approximately 50% coal particles. In fact, samples of diesel exhaust particulates that we have examined have contained a large proportion of coal particles.

A series of wear tests was conducted with a range of concentrations of coal-fuel particles in mineral oil to which 5% of 1 μm size quartz particles was added. The results are shown in Fig. 2. The tests were conducted at several different levels of relative humidity. In previous experiments we found that relative humidity could have a marked influence on wear rate, with wear rates being significantly higher at low relative humidities. The effect of

relative humidity appeared to diminished at high particle concentrations; this observation is confirmed here.

In Fig. 2 it is seen that wear rate increases only slightly at combined total particle concentrations below 20%. Above 20%, wear rate increases markedly. At 35% (30% coal-fuel + 5% quartz), the wear rate is from 10 to 35 times greater than at 5% quartz particles, depending on relative humidity. At a concentration of 20% the mineral oil-particle mixture was noticeably more viscous. At 35% the mixture

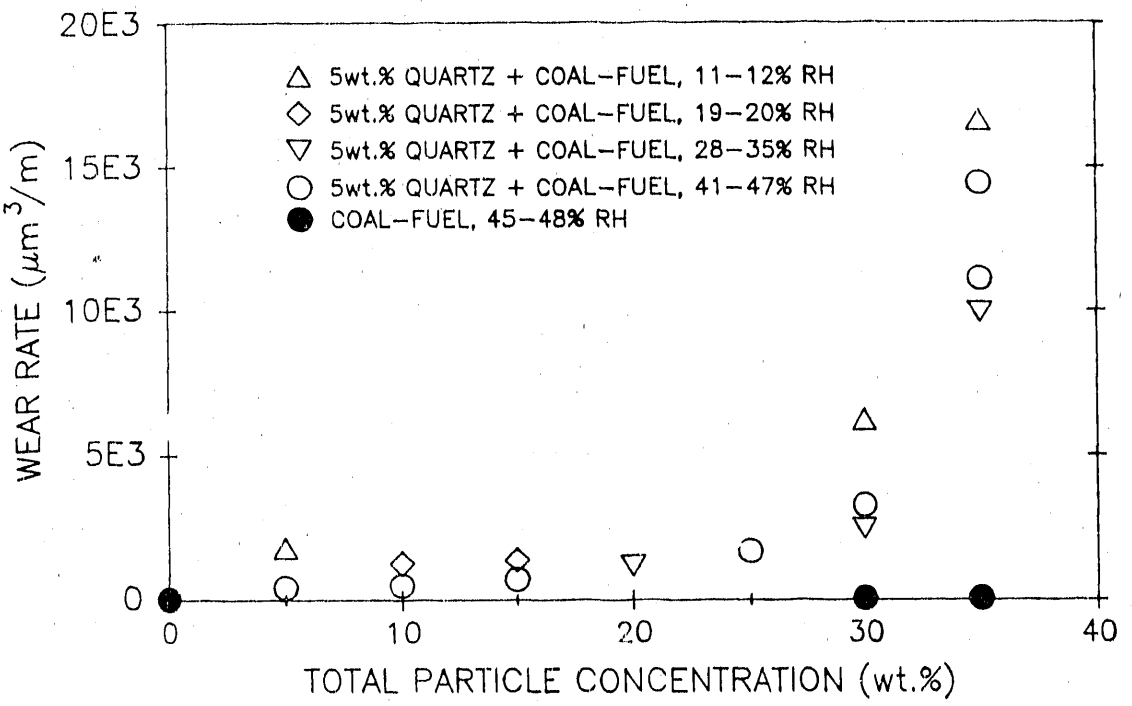

Fig. 2. Effect of coal-fuel particle concentration on wear rate by 5%, 1μm quartz particles in mineral oil.

was almost a paste and did not flow back immediately into the track on the disk following passage of the pin. This suggests that inadequate lubrication might be responsible for much of the increase in wear rate.

To determine if inadequate lubrication might contribute to the increased wear rate, tests were conducted with an addition of 35%

coal-fuel particles and no quartz particles. In this way the viscosity was increased without contributing the large abrasion component associated with the quartz particles. A small increase in wear rate was obtained, consistent with effect of additions of coal-fuel particles at lower concentrations.[1] Apparently, the high viscosity did not interfere substantially with lubrication. That sufficient lubricant was still available at the contact, even though the flow rate of the oil-particle mixture was greatly diminished at high particle concentrations, is probably due to the crisscrossing pattern traversed by the pin on the disk. As a result of this pattern, the oil-particle mixture once pushed aside is intersected later in the cycle.

For further comparison, tests were conducted with the same quantities of oil and quartz particles which were used in the 5% quartz-30% coal-65% oil mixture but without the coal. The assumption here is that the only function of the coal particles was to increase the effective concentration of quartz particles in the oil. With the resulting 7.15% quartz particle content and smaller oil-particle charge, the wear rate increased by less than a factor of 3, a relatively small change compared to the 10-34 fold increase resulting from the addition of 30% coal particles.

In summary, the source of the marked increase in wear rate which occurs when more than 20% coal-fuel particles are added to mineral oil containing 5% quartz particles is not explained by poor lubrication. Nor is it the result of an effective increase in the concentration of quartz particles. The most likely explanation appears to be that the change in rheology of the fluid brought about by high concentrations of coal-fuel particles causes more quartz particles to enter the contact. That is, the quartz particles are held in a viscous fluid film which is present at the contact. This results in the observed increase in wear rate.

CONCLUSIONS

The following conclusions can be drawn based on results obtained by means of rotating pin-on-disk tests employing 52100 steel specimen materials. Paraffinic mineral oil without additives was the lubricant.

1. Wear rate increases exponentially with increasing particle hardness for particles of hardness approximately equal to or greater than the surface being worn. The effect can be explained by the increasing resistance of harder particles to crushing.

2. With a constant 5% concentration of 1μm quartz particles, increasing the concentration of coal particles above approximately 20% results in a marked increase in wear rate. The effect can not be attributed to the abrasivity of the coal particles. It appears to result from an increase in the effective number of quartz particles that enter the contact as a consequence of the increase in fluid viscosity which is associated with the increasing particle concentration.

REFERENCES

1. L. K. Ives, M. B. Peterson and E. P. Whitenton, "Mechanisms of Galling and Abrasive Wear," in AR&TD Fossil Energy Materials Program Quarterly Progress Report for the Period Ending September 30, 1989, ONRL/FMP-89/2, Oak Ridge National Laboratory, Oak Ridge, TN, January, 1990, pp. 447-465.

2. L. K. Ives and M. B. Peterson "Effect of Solid Additives on Wear by Greases Containing Abrasive Particles", Wear of Materials - 1985, K. C. Ludema, ed., ASME, NY (1985) pp. 355-363.

3. R. C. Streeter, "Evaluation of the Effect of Coal Cleaning on Fugitive Elements--Phase IV Identification of Mineral Forms in Coal," BCR Report L-1551, (1986), Available from NTIS Springfield, VA.

4. M. M. Khruschov, "Principles of Abrasive Wear," Wear 28 (1974) pp. 69-88.

5. R. C. D. Richardson, "The Wear of Metals by Relatively Soft Abrasives," Wear 11 (1968) pp. 245-275.

6. A. Misra and I. Finnie, "An Experimental Study of Three-Body Abrasive Wear," Wear of Materials - 1981, S. K. Rhee, A. W. Ruff and K. C. Ludema, eds., ASME, NY (1981) pp. 426-431.

7. J. L. Xuan, I. T. Hong and E. C. Fitch, "Hardness Effect on Three-Body Abrasive Wear Under Fluid Film Lubrication," ASME Journal of Tribology 111 (1989) pp. 35-40.

8. F. Hirano and S. Yamamoto, "Four-Ball Test on Lubricating Oils Containing Solid Particles," Wear 2 (1958/59) pp. 349-363.

9. L. K. Ives, M. B. Peterson and E. P. Whitenton, "Mechanisms of Galling and Abrasive Wear," in AR&TD Fossil Energy Materials Program Quarterly Progress Report for the Period Ending March 31, 1989, ONRL/FMP-89/1, Oak Ridge National Laboratory, Oak Ridge, TN, July, 1989, pp. 455-469.

THE WASTAGE OF STEELS IN THE EROSION-CORROSION OF FLUIDIZED BED COMBUSTORS

Alan V. Levy, BuQian Wang, Gangqiang Geng
Lawrence Berkeley Laboratory
University of California
Berkeley, California 94720

ABSTRACT

The behavior of alloy steel surfaces in the erosion-corrosion (E-C) environments of the convection pass of fluidized bed combustors (FBC) has been studied in both in-service and laboratory test exposures. A good correlation was obtained in both metal wastage rates and the composition and morphological characteristics of the E-C surfaces. Flat sheet specimens were exposed in operating FBC's as well as tube shaped specimens. The effects of environmental variables, including temperature and particle velocity, impact angle and solids loading on E-C by FBC bed material particles were determined.

The effects of the composition of bed materials, particularly the amounts of silica and calcium compounds in them, were studied to determine how FBC feedstock constituents affect the erosivity of the resultant bed materials. It was determined that larger quantities of calcium compounds such as CaO and $CaSO_4$, compared to the silica content, promoted the formation of protective layers that markedly reduced the amount of metal wastage over a range of particle velocities at 450°C.

Several types of protective coatings including plasma sprayed carbide composites and multi-element hardened alloys were tested to determine the nature of their erosion and erosion-corrosion behavior. Coatings with continuous carbide networks had considerable erosion resistance.

INTRODUCTION

The metal wastage of heat exchanger tube surfaces in fluidized bed combustors (CFBC)[1,2] continued to be the main thrust of the research

effort at the Lawrence Berkeley Laboratory (LBL) to better understand the degradation of materials from impacts by small, solid particles. This year's work has concentrated on three areas: the erosivity of particles from operating FBCs, the erosivity of various sand limestone and sand calcined limestone mixtures and the elevated temperature erosion of protective coatings. Through the understanding of the basic loss mechanisms that has been gained in the past years has evolved an ability to modify both the basic steels and their surfaces (by way of applied coatings) to markedly increase their resistance to erosion-corrosion metal wastage.

EROSIVITY OF PARTICLES FROM OPERATING FLUIDIZED BED COMBUSTORS

A series of laboratory erosion-corrosion tests was carried out at conditions which nearly simulated those in the convection pass of CFBCs.[3] A total of sixteen different FBC bed material particles from ten different combustors, including bubbling (BFBC), circulating (CFBC), and pressurized (PFBC) types, as well as several sand and limestone particles were tested. The laboratory tests used the different particles as a means to obtain variations of composition, shape, size and strength of the erodents to determine the effects of these variables on their erosivity in laboratory tests where every other variable, i.e., target metal, temperature, particle velocity and impact angle, solids loading, test time was held constant. The single set of test conditions most nearly simulated those experienced by CFBC convection pass superheater tubes. They did not simulate the lower temperature, lower particle velocity, higher solids loading that BFBC in-bed tubes are subjected to.

Test Conditions

The tests were carried out in the elevated temperature blast nozzle type of tester described in reference 4. Air was utilized as the carrier fluid for the particles, creating a generally oxidizing

atmosphere. The target material for the erosion-corrosion tests was 1018, plain carbon steel which is commonly used in both BFBC in-bed evaporator tubes and CFBC convection pass primary superheater tubes. The particles from the CFBCs were taken at a location in the convection pass below the superheater tube banks. It is not known where the particles from the BFBCs and PFBCs were taken, but it is assumed that they were taken from bed drains.

The particles have a wide range of particle sizes. The particle sizes from the BFBCs had a much wider range than those from the CFBCs, including particles considerably over 1 mm in diameter. To be able to compare the erosivity of different bed material particles, an average particle size of 250μm was screened out and used as a standard test size. By screening the actual bed material to obtain one size of particles, an unknown degree of particle selection occurred as the characteristics of larger and smaller particles in a total bed material can differ somewhat. To account for this, the actual, as-received, particle sizes of the different bed materials were also used as erodent particles.

The test conditions nearly simulated the E-C environment in the convection pass, superheater region of a circulating fluidized bed combustor. Particle velocity was determined using a computer program.[5] The particle loading resulted in a steady state metal loss condition.[6] The metal wastage of the specimens was determined by microscopic dimensional measurements of cross sections through the area of greatest metal loss to determine the thickness of the remaining sound metal.

Results

The metal wastage of specimens E-C by the different erodent particles in order of erosivity ranking are listed in Table 1. The particles that caused the greatest metal loss in the 5 hour tests had the most angular shape, the highest amount of SiO_2 and the lowest amount of CaO or $CaSO_4$. When the as-received size particles were used as erodents, generally the larger size particles were more erosive than the smaller

TABLE 1

RANKING OF EROSIVITY OF BED MATERIAL PARTICLES

Bed Material Particle No.	Unit	Type	Metal Loss, μm 250μm Particle Size	Metal Loss, μm Other Particle Size	Erosivity Ranking
1	A	CFBC	7.9		1
2	A	CFBC	6.6		2
4	B	CFBC	5.4		3
3	C	CFBC	4.8	5.1(1)	4
8	A	CFBC	4.0		5
16	A	CFBC	3.95	4.7(2)	6
10	G	CFBC	3.9		7
5	D	BFBC	3.2		8
7	E	BFBC	3.1		9
9	F	CFBC	2.8		10
12	I	PFBC	2.5	6.7(3)	11
6	D	BFBC	2.3		12
14	J	BFBC	2.3	5.8(4)	12
13	J	BFBC	1.9	3.4(5)	13
15	D	BFBC	---	2.6(6)	14
11	H	BFBC	1.9,	2.1(7)	15
Angular Sand	A			12.5(8)	
Round Sand	A			3.3(9)	
Angular Sand	B			5.5(10)	
Limestone	A			5.8(11)	
Limestone	B			4.5(12)	

Test Conditions:

Material = 1018 steel

T = 450°C
  = 30°
V = 20 m/s
t = 5 hrs. (375 g loading)
air
Particle size = 250μm
Other particle sizes:

(1)	365μm	(7)	770μm
(2)	370μm	(8)	450μm
(3)	670μm	(9)	400μm
(4)	720μm	(10)	230μm
(5)	570μm	(11)	800μm
(6)	800μm	(12)	300μm

ones. However, this effect varied considerably, as can be seen in Table 1. The smaller size CFBC particles were generally more erosive than the larger size BFBC particles. The largest size particle, No. 15, at 800μm dia., had a lower erosivity than several of the 250μm dia. bed material particles because of its other characteristics. Where the same type of particles was tested at two different sizes, for example, particle Nos. 13 and 14, the larger size particles were more erosive, although other characteristics also contributed to the differences. On the other hand, an increase in particle No. 11's size from 250μm to 770μm caused almost no change in erosivity. Also, the same size particle from the same FBC,, particle Nos. 1 and 2, had different erosivities because of their other characteristics. In Table 1, it can be seen that round sand was much less erosive than the angular sand at nearly the same particle size because of the difference in their shapes.

Table 1 shows that, with one exception, CFBC bed material particles had higher erosivity than BFBC or PFBC bed material particles. This difference was primarily due to the fact that the CFBC bed materials had a higher SiO_2 content as the result of purposeful sand additions to the feedstock of the combustor. The BFBC and PFBCs only contained SiO_2 from the coal fuel. The reason for the one exception (CFBC particle No. 9) is related to particle shape and composition.

In Table 1 it can also be seen that among the different CFBC bed materials, particle Nos. 1 and 2 had the highest erosivity. Particle Nos. 8 and 16 had much lower erosivity than particle Nos. 1 and 2 even though they were all from the same unit A. BFBC bed material particles Nos. 13, 15 and 11 had the lowest erosivity of all of the particles tested.

In-Service Exposure of Tubing Alloys

Flat specimens of four steel alloys were tack welded to tube shields at several locations in the convection pass, superheater region of an operating circulating fluidized bed combustor and exposed at two different times for different durations to somewhat different erodent

particle flows. The resulting thickness losses are listed in Table 2. The behavior of the specimens related to such factors as their composition, location, operating conditions, and the difference in the bed material particles in each of the two exposures. Their behavior under the in-service conditions correlated quite well with the morphology of their surfaces and to laboratory test results. However, there were anamolies, some explainable, some not.

Generally, the metal wastage decreased with increasing chromium content. There was no significance difference in thickness loss at the two impact angles in the 950 hr. test. At the highest test temperature, the two lower chromium content steels could not develop a protective scale and failed rapidly. Only the 18%Cr, 304H SS had a low enough oxidation rate at 785°C to have a relatively low metal wastage rate.

An apparent anamoly, the much higher loss rates on the near wall of the primary superheater in the 1855 hr test, compared to the same location in the 950 hr. test can be explained. The reason is an indication of how sensitive metal wastage of superheater tubes can be to subtle differences in operating conditions. The sand constituent in the bed material of the 1855 hr. run was known to have almost 2 times the amount of larger size particles,> 425 microns dia., of the 950hr. run. The larger particles, having greater momentum than the smaller ones, were carried across the convection pass to the rear wall in greater numbers than the smaller particles in the shorter run and resulted in considerably more metal wastage occurring, see Table 2.

EROSIVITY OF VARIOUS SAND-LIMESTONE AND SAND-CALCINED LIMESTONE MIXTURES

In previous work it was reported that fluidized bed combustor (FBC bed materials with higher percentages of stronger/harder particles, such as SiO_2, were more erosive.[6] The greater was the amount of weaker/softer limestone in the charge and the larger the resultant CaO content of the bed material, the lower was the bed material's erosivity. It appears that CaO promotes the formation of a layer of mixed bed material-iron oxide on the metal surface that protects it from metal

TABLE 2

METAL WASTAGE OF FLAT SPECIMENS ON SUPERHEATER
TUBE SHIELDS OF CIRCULATING FLUIDIZED BED COMBUSTORS

Location in Convection Pass Superheaters	Impact Angle	Temp °C (°F)	Exposure Time Hours	Thickness Loss in Mils/1000 hrs A1	T22	T91	304H
Primary; Front Wall	90°	530 (1000)	950	5.2	4.0	2.5	1.1
			1855	5.0	4.4	3.0	2.5
Primary; Rear Wall	90°	530 (1000)	950	4.5	3.9	1.8	1.1
			1855	9.8	22.5	16.2	8.7
Primary; Rear Wall	30°	530 (1000)	950	4.1	3.0	2.5	1.5
			1855	5.6	4.6	3.5	2.7
Secondary; Inlet Header	90°	560 (1044)	950	3.9	2.7	2.6	1.2
			1855	2.5	2.0	1.7	0.7
Secondary; Rear Wall	90°	785 (1448)	950	Total	Total	25.6	3.5
			1855	Total	Total	38.4	4.4

Alloy:
A1 - mild steel
T22 - 2 1/4Cr1Mo Steel
T91 - 9Cr1Mo Steel
304H - 18Cr8Ni Stainless steel

Specimen Size: 1.0 x 2.0 x 0.25 in.

wastage.

In order to determine the effect of the ratio of sand (SiO_2) to calcined limestone (CaO) on the formation of the protective layer and the resultant amount of metal wastage that occurred on 1018 steel, a series of erosion-corrosion tests was carried out at conditions that nearly simulated those in the convection pass region of FBCs.[7] Various laboratory prepared sand-limestone and sand-calcined limestone mixtures were used as the erodents in the investigation.

Figure 1 shows curves of the metal thickness loss v.s. the proportion of sand/calcined limestone at three particle velocities. A transition ratio occurred, on both sides of which the metal losses were linear. Moreover, as Figure 1 shows, at the transition ratio the metal loss was essentially the same, 2.3um at all three particle velocities. However, more CaO was required as the particle velocity increased. This is due to the greater force of the impacting particles at the higher velocities requiring more calcium compound to overcome that erosive force to initiate the formation of a protective layer. For a given CaO content, metal loss increased with particle velocity. Beyond the transition ratio, at higher CaO contents, the increase was quite small and the metal loss became a function of the erosivity of the particles rather than the particle velocity. Prior to the transition ratio, at higher SiO_2 contents, the metal wastage had a strong dependency on particle velocity.

The difference in the effect of particle velocity on metal wastage strongly relates to the formation of the protective layer. At the higher, angular shaped SiO_2 contents, the metal itself was participating in an elevated temperature erosion process that occurred at a high rate. When the CaO content exceeded that of the transition ratio, a protective layer formed that prevented direct participation by the base metal in the metal loss process. Rather, the protective layer was being eroded and the metal wastage rates decreased. The loss of the layer was a function of the erosivity of the erodent, which slowly decreased with increasing CaO content.

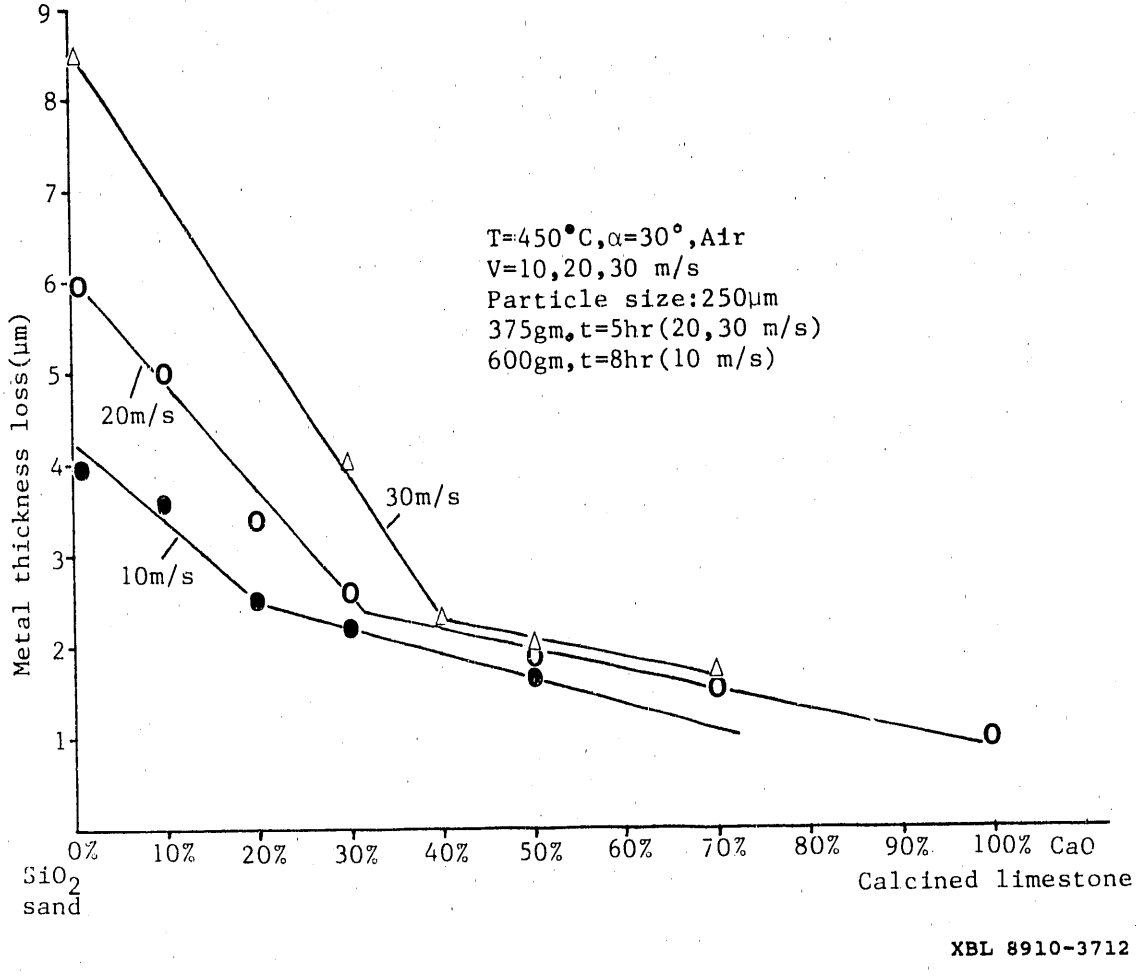

Figure 1. Metal thickness loss v.s. sand/calcined limestone mixtures at V = 10, 20, 30 m/s.

ELEVATED TEMPERATURE EROSION OF PROTECTIVE COATINGS

A number of metallic and hard material coatings designed to protect metal surfaces against erosion-corrosion were applied to 1018 steel by thermal spraying and the coatings' erosion behavior was determined at the standard test conditions used to determine the E-C behavior of heat exchanger tubing steels.[8] Two different erodents were used; FBC bed material No. 2 and SiO_2 fused quartz. All of the coatings were commercially available coatings applied by industrial thermal spray companies. The coatings and their erosion behavior are listed in Table 3.

Several comparisons of the coatings can be made from Table 3. Among them are:

- All of the coatings tested, using both erodents, had lower material wastage rates than bare 1018 steel.
- Generally the SiO_2 fused quartz was more erosive than the FBC bed material.
- When the FBC bed material was the erodent, the hardness of the coatings had no direct relationship to material wastage.
- When the SiO_2 fused quartz was the erodent, the hardness of the coatings had an inverse relationship to material wastage.
- When the FBC bed material was used, the much softer metal spray coating had approximately the same material wastage as the twice as hard WC-Co coatings.
- The WC-Cr, Ni, Co coating had the lowest metal wastage when FBC bed material was the erodent.
- The ratio of coating hardness/erodent hardness had a consistent inverse relationship to material wastage, above 0.56, when SiO_2 fused quartz was the erodent.
- The coatings had different relative material thickness losses with each of the two erodents used.
- The harder MCrAl coating had the lower metal wastage.

TABLE 3

MATERIAL WASTAGE OF THERMAL SPRAY COATINGS

Coating Designation	Coating Process	Coating Material	Eroded by Bed Material No. 2				Eroded by SiO_2 (Fused Quartz)			
			Coating Thick, mm (After Polish)	Surface Hardness Hv_{100}	Hv Coating / Hv Erodent	Thick Loss, µm	Coating Thick, mm (After Polish)	Surface Hardness Hv_{100}	Hv Coating / Hv Erodent	Thick Loss, µm
405 + 420	Wire bonding & wire thermal spray	420SS	0.57	443	0.63	3.2	0.44	425	0.32	5.7
Jk420	Hypersonic spray	420SS	0.21	455	0.65	4.0	0.07	439	0.33	5.3
JK112	Hypersonic spray	WC + 12% Co	0.34	948	1.36	3.7	0.18	944	0.71	3.3
Metco 74SF	Plasma spray	WC + 12% Co	0.10	780	1.12	3.5	0.06	739	0.56	3.9
Metco 76F-NS, No. 1	Plasma Spray	WC + 18% Co	0.15	997	1.43	5.1*	0.10	992	0.75	2.7
Metco 76F-NS, No. 2	Plasma Spray	WC + 18% Co	---	---	---	---	0.17	1335	1.00	2.5
SMI-28	Thermal Spray	WC + Cr-Ni-Co	1.0	1011	1.45	1.8	0.50	936	0.70	3.4
Metco 465	Plasma Spray	FeCrAlMo	---	---	---	---	0.37	408	0.31	6.8
Metco 468-	Plasma	NiCoCrAl	0.82	360	0.51	4.5	0.44	354	0.27	7.8
1018 steel						6.6				12.3

TEST CONDITIONS

T = 450°C
V = 20 m/s
α = 30°
t = 5 hrs
Loading 375g

SiO_2-1329HV
Bed Material No. 2:
Sand (76%) 881 Hv
CaO 92%) 117 Hv

*After test, coating broke away

- The presence of porosity in the hypersonic sprayed materials made the material thickness losses of the 420SS and the WC+12%Co materials similar even though the carbide was twice as hard as the steel.

REFERENCES

1. J. Stringer, J. F. Stallings, J. M. Wheeldon, "Wastage in Bubbling Fluidized Bed Combustors: an Update,: Proceedings of ASME 1989 International Conference on Fluidized Bed Combustion, pp. 857 - 862, San Francisco, CA, May 1989.

2. C. E. Witherell and R. G. Meisenheimer, "Tubing Wastage in Fluidized-Bed Coal Combustors," Livermore National Laboratory Report No. UCRL-21039, January 1988.

3. B. Q. Wang, G. Q. Geng, A. V. Levy, "Erosivity of Particles from Operating Fluidized Bed Combustors," Paper No. 288, NACE Corrosion 90, Las Vegas, Nev, April 1990.

4. A. V. Levy, J. Yan, J. Patterson, "Elevated Temperature Erosion of Steels," WEAR 108 No. 1, pp. 43 - 60, 1986.

5. D. M. Kleist, "One Dimensional, Two Phase Particulate Flow," Report LBL-6967, 1977, Lawrence Berkeley Laboratory, University of California, Berkeley, CA 94720, Masters Thesis.

6. B. Q. Wang, G. Q. Geng, A. V. Levy, "Fluidized Bed Combustor Particles Effects on the Erosion-corrosion of Steel," Proceedings of EPRI-ANL Workshop on Materials Issues in Circulating Fluidized Bed Combustors, Argonne, Ill, June 1989.

7. G. Q. Geng, B. Q. Wang, A. V. Levy, "The Effect of Fluidized Bed Combustor Bed Materials Compositions on the Erosion-Corrosion of Carbon Steel," Paper No. 290, NACE Corrosion 90, Las Vegas, Nevada, April 1990.

8. B. Q. Wang, G. Q. Geng, A. V. Levy, "Erosion-Corrosion of Thermal Spray Coatings," Proceedings of 17th International Conference on Metallurgical Coatings: ICMC-17, San Diego, CA, April 1990.

STUDY OF PARTICLE REBOUND CHARACTERISTICS AND MATERIAL EROSION AT HIGH TEMPERATURES

W. Tabakoff, A. Hamed and M. Metwally

Department of Aerospace Engineering and Engineering Mechanics
University of Cincinnati
Cincinnati, Ohio 45221

ABSTRACT

The results of an experimental investigation are presented for coal ash particles impact and rebound characteristics and the associated metal erosion. This data has been used in an analytical study of the dynamics of the particulate flow throughout a two stage gas turbine. For the typical ash aprticle size distribution considered, the results demonstrate that the size distribution has a significant influence on the blade erosion intensity and pattern.

INTRODUCTION

The objective of this research work is to investigate the basic erosion processes and fluid mechanics associated with material degradation in the components of various coal conversion and utilization systems. The understanding of erosion patterns and rates will be enhanced through a study of the rebound characteristics of particles impinging various surfaces and through the measurement of erosion rates of materials and coatings exposed to high temperatures. The overall goal is to develop a quantitative model, which will facilitate the prediction of erosion in systems operating in particulated environments.

THE USE OF SUPERALLOYS AND PROTECTIVE COATINGS IN TURBOMACHINERY

The major problem confronting developers of coal-burning boilers and turbines is the serious erosion of the system components by the suspension of fly ash in the hot combustion gases. A permanent loss of performance

is associated with the surface erosion, which is caused by particle surface impacts. The performance loss depends upon the location and the condition of the deteriorated surfaces. These are critical to the aerodynamic performance of turbine blades which are particularly sensitive to the blade leading and trailing edge configuration and the condition of the blade suction surface. Computer codes are used to model the particle dynamics in turbomachinery flow fields through the various blade rows, and to determine the particle impact conditions with the various surfaces which affect their erosion. The codes however require empirical equations for particle restitution characteristics [1, 2] to represent the effects of particle surface interactions on the particle trajectories and the resulting surface erosion.

Nickel and cobalt base superalloy blades and vanes are widely used in hot section of gas turbine. To enhance superalloy resistance to hot erosion-corrosion, protective coatings have been used. The most widely used coatings are those based on the NiAl (on nickel base superalloys) and CoAl (on cobalt base superalloys) formed by interaction of superalloy surfaces with aluminum. To improve resistance to hot erosion-corrosion, aluminide coatings are modified to contain elements such as chromium, platinum, rhodium and silicon. In this study an experimental investigation was conducted to investigate the particle rebound characteristics and the erosion behavior of superalloys and aluminide coatings at elevated temperatures. The presented results show the variation of the erosion rate (weight loss per unit weight of particles) and particle restitution ratio with the impingement angle for the coated and uncoated superalloys and coatings. The particle mass effect on both weight losses and erosion rates are shown. Based on the experimental results, the coating lifes have been estimated.

EXPERIMENTAL SET-UP

The experimental set-up consists of the erosion wind tunnel, the LDV system, the data acquisition system and the particle feeder. A detailed description of the wind tunnel and the particle feeder is given in Ref. [3]. The two-component LDV system used in the measurement of the

restitution characteristics at different impact angles is described in references [1] and [2].

TEST CONDITIONS

It is well known that particle velocity, particle impingement angle, aerodynamic effects and material sample temperature strongly influence the erosion rate. These parameters were varied in the present test program for the different tested materials listed in Table 1. The experimental measurements were obtained for fly ash particles with impact velocities ranging between 600 and 1200 ft/sec at temperatures from ambient to 1500°F. Figure 1 shows the tested fly ash particle size distribution, while Table 2 lists its chemical composition. The particle velocity was controlled by varying the tunnel air flow. The particle impingement angle was set by rotating the sample relative to the flow stream direction. The aerodynamic effects are preserved by the design of the tunnel test section to simulate the flow aerodynamics around the blade sample. The sample temperature was varied by heating the flow stream which heated the material sample to the desired temperature.

Test data was accumulated by setting the particle impingement angle at 15, 30, 45, 60 and 90 degrees for each of the different test temperatures and particle velocities.

TABLE 1. THE TESTED COATINGS

Coating	Treatment	Substrate	Coating Thickness (mils)
C	Aluminized	X40*	--
N	Aluminized	M246**	--
RT22	Platinum Aluminized	M246	5
RT228	Rhodium/Platinum Aluminized	M246	3
RT44	Low Rhodium/Platinum Aluminized	X40	3
RT44B	Rhodium/Platinum Aluminized	X40	3
NiCoCrALY	Chromized	M246	--

* X40: Cobalt based X40 Superalloy.

** M246: Nickel based MAR-M246 superalloy.

TABLE 2. ANALYSIS OF FLY ASH

CHEMICAL ANALYSIS

Chemical	Percentage
Silicon Dioxide (SiO_2)	48.08
Iron Oxide (Fe_2O_3)	20.05
Aluminum Oxide (Al_2O_3)	21.16
Magnesium Oxide (MgO)	0.93
Sulphur Trioxide (SO_3)	1.20
Moisture Content	0.13
Loss of Ignition	0.73
Available Alkalies as Na_2O	0.64
Undetermined	7.08

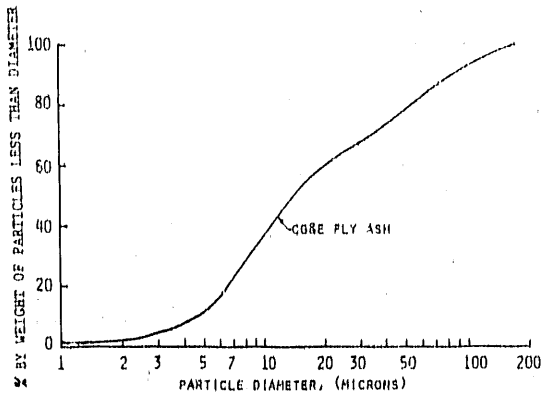

Fig. 1 Fly Ash Particle Size Distribution

RESTITUTION PARAMETERS

The experimental measurements of the particle rebound conditions after surface impacts are obtained using laser Doppler velocimetry for particle laden flows over the sample materials listed in Table 1. The measurements at various incidence angles and flow velocities indicate that these ratios are mainly dependent upon the impingement angle for a given particle material combination. The restitution parameters are a measure of the kinetic energy exchange between two objects upon impact.

Figures 2 and 3 present the results for M246 alloy with and without "N" coating, while Figures 4 and 5 present similar results for X40 alloy with and without "C" coating. The figures show the variation of the velocity restitution ratio V_2/V_1, and the directional coefficients β_2/β_1 with the impact angle over the 0 to 90° range. The curves in the figures represent the mean value of the experimentally measured restitution parameter density distribution function at each impact angle. To facilitate the use of these experimental data in particle trajectory and erosion computation, emprical equations were obtained using a least squares polynomial curve fit of the mean value of the restitution parameters, leading to the following equations·

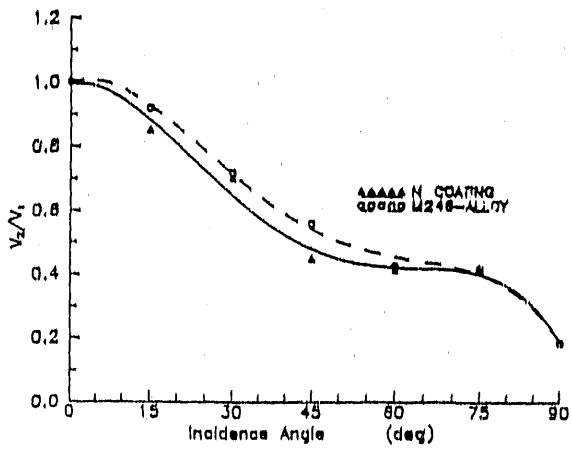

FIG. 2 TOTAL VELOCITY RESTITUTION RATIO VERSUS INCIDENCE ANGLE β_1 AT U_p= 320 ft/sec , 15 MICRON FLY ASH

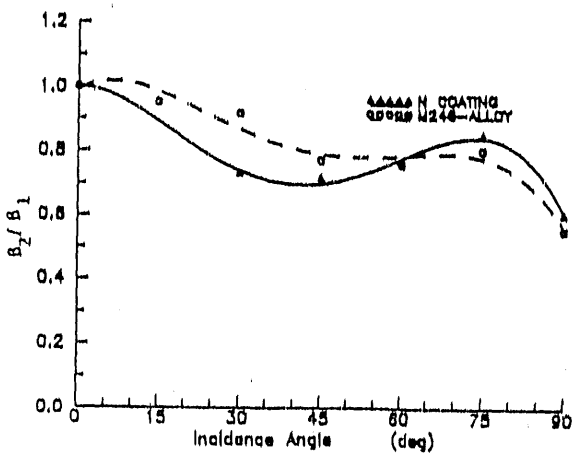

FIG. 3 DIRECTIONAL COEFFICIENT (β_2/β_1) VERSUS INCIDENCE ANGLE β_1 AT U_p= 320 ft/sec , 15 MICRON FLY ASH

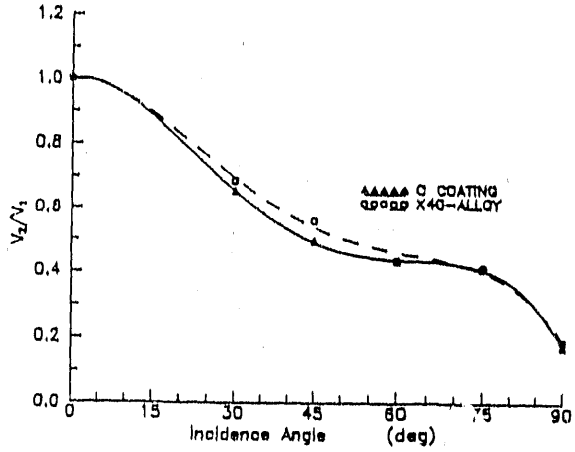

FIG. 4 TOTAL VELOCITY RESTITUTION RATIO VERSUS INCIDENCE ANGLE β_1 AT U_p= 320 ft/sec , 15 MICRON FLY ASH

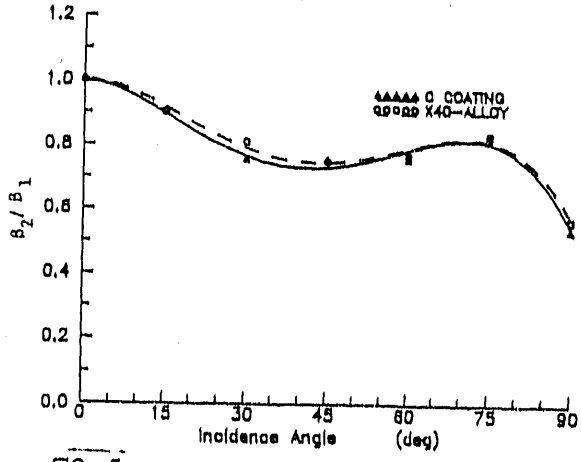

FIG. 5 DIRECTIONAL COEFFICIENT (β_2/β_1) VERSUS INCIDENCE ANGLE β_1 AT U_p= 320 ft/sec , 15 MICRON FLY ASH

For M-246 Alloy

$$\frac{V_2}{V_1} = e_V = 1.00 - 0.00601123 \times \beta_1 - 0.000957896 \times \beta_1^2 + 1.77426 \times 10^{-5} \times \beta_1^3 - 9.94 \times 10^{-8} \times \beta_1^4$$

$$\frac{\beta_2}{\beta_1} = e_\beta = 1.00 - 0.00872424 \times \beta_1 - 0.000834276 \times \beta_1^2 + 1.63771 \times 10^{-5} \times \beta_1^3 - 9.75683 \times 10^{-8} \times \beta_1^4$$

X-40 Alloy

$$\frac{V_2}{V_1} = e_V = 1.00 + 0.000951 \times \beta_1 - 0.000725 \times \beta_1^2 + 1.43015 \times 10^{-5} \times \beta_1^3 - 8.34 \times 10^{-8} \times \beta_1^4$$

$$\frac{\beta_2}{\beta_1} = e_\beta = 1.00 + 0.001295 \times \beta_1 - 0.000645 \times \beta_1^2 + 1.55053 \times 10^{-5} \times \beta_1^3 - 1.008 \times 10^{-7} \times \beta_1^4$$

"N"-Coating

$$\frac{V_2}{V_1} = e_V = 1.00 + 0.00337812 \times \beta_1 - 0.000977626 \times \beta_1^2 + 1.94275 \times 10^{-5} \times \beta_1^3 - 1.12 \times 10^{-7} \times \beta_1^4$$

$$\frac{\beta_2}{\beta_1} = e_\beta = 1.00 + 0.000159243 \times \beta_1 - 0.000723929 \times \beta_1^2 + 1.81865 \times 10^{-5} \times \beta_1^3 - 1.185 \times 10^{-7} \times \beta_1^4$$

"C"-Coating

$$\frac{V_2}{V_1} = e_V = 1.00 - 0.0024071 \times \beta_1 - 0.000934 \times \beta_1^2 + 1.89526 \times 10^{-5} \times \beta_1^3 - 1.11169 \times 10^{-7} \times \beta_1^4$$

$$\frac{\beta_2}{\beta_1} = e_\beta = 1.00 - 0.001127 \times \beta - 0.0005889 \times \beta_1^2 + 1.53245 \times 10^{-5} \times \beta_1^3 - 1.03 \times 10^{-7} \times \beta_1^4$$

where V_1 and β_1 represent the particle impact velocity and impingement angle (degrees) while V_2 and β_2 are the rebound velocity and rebound angle, measured from the impact surface.

Erosion of Protective Coatings

Figures 6 through 15 present two types of erosion test results. The erosion rate and the cumulative mass loss. The erosion rate is defined as the ratio between the change in the sample mass and the mass of the impacting particles. The erosion rate tests were carried out in one cycle using 100 gm of particles impacting the sample surface. In the cumulative mass loss tests, the fractional change in the specimens weight were determined after fractionally increasing the particle amount to the time when all the coating was removed by erosion. The cumulative mass erosion tests were conducted only at the impact angles corresponding to maximum erosion. The reported erosion test results were obtained at 1500° test temperatures and 1200 ft/sec impact velocity.

RESULTS AND DISCUSSION

Erosion Tests for "N"-Coatings

The "N"-coating is a nickel base aluminide that was applied to nickel base M-246 superalloy. The erosion rate variation with the impingement angle for nickel base superalloy MAR-M246 with and without N-coating are shown in Fig. 6. Inspection of this figure shows that this material exhibits a ductile erosion pattern with maximum erosion at 45°. The incremental erosion test results for the same materials at 45° impingement angle are shown in Fig. 7. The coating deteriorated completely after impacts of 140 grams as shown in Fig. 8. Figures 9 and 10 present the incremental erosion test results using "Allison Co." particle, obtained at the scale combustion chamaber research project for DOE. The chemical composition and particle size distribution of "Allison" particles are not published. These tests were conducted at conditions similar to those with the other particles at the maximum erosion angle. Figure 9 shows that the sample gained weight (deposition) in the first two test runs due to particle impediment. Therefore, the erosion rate shown in Fig. 10 is negative at low Allison particle mass.

Erosion Tests for "C"-Coatings

The "C"-coating is a cobalt based aluminide that was applied to the cobalt based X-40 superalloy. The erosion characteristics are shown in Figs. 11 through 13 for the X-40 superalloy with and without "C"-coating. The erosion rate versus the impingement angle shows a ductile erosion

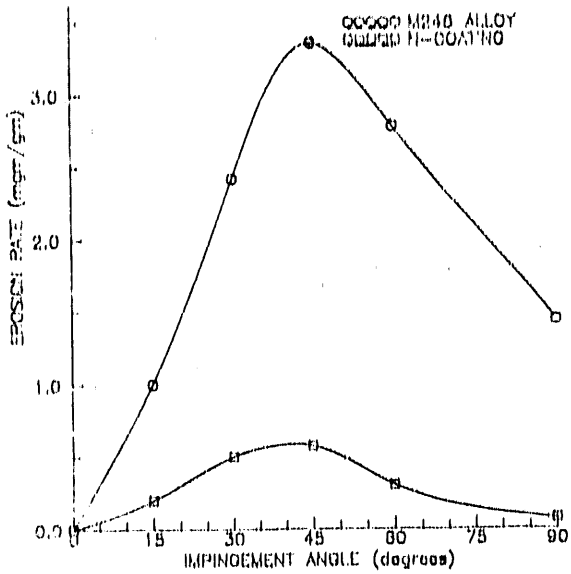

FIG. 6 M246 ALLOY AND N--COATING EROSION RATE AT T=1500 F, U=1200 fps, FLY ASH

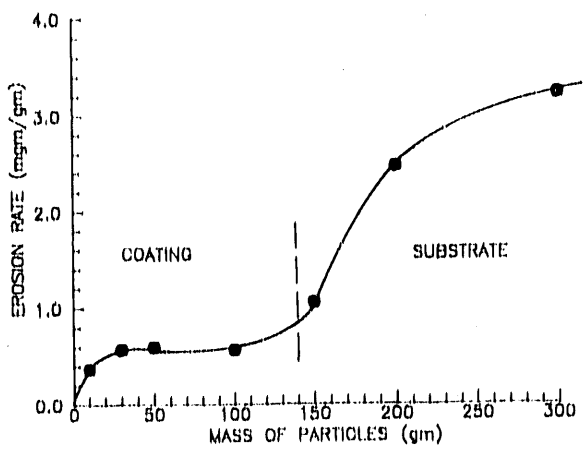

FIG. 8 VARIATION OF N--COATING EROSION RATE WITH MASS OF PARTICLES AT 45 IMPINGEMENT ANGLE, T=1500 F, U=1200 fps FLY ASH

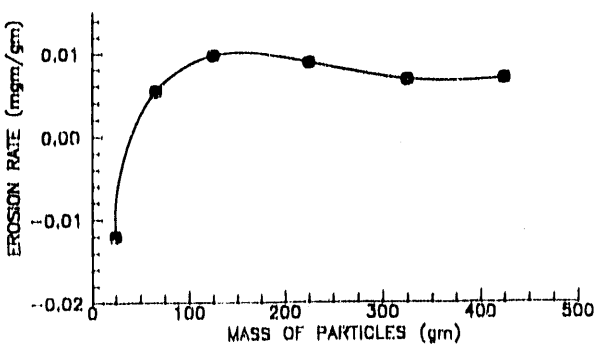

FIG. 10 VARIATION OF N--COATING EROSION RATE WITH MASS OF PARTICLES AT 45 IMPINGEMENT ANGLE, T=1500 F, U=1200 fps, ALLISON PARTICLES

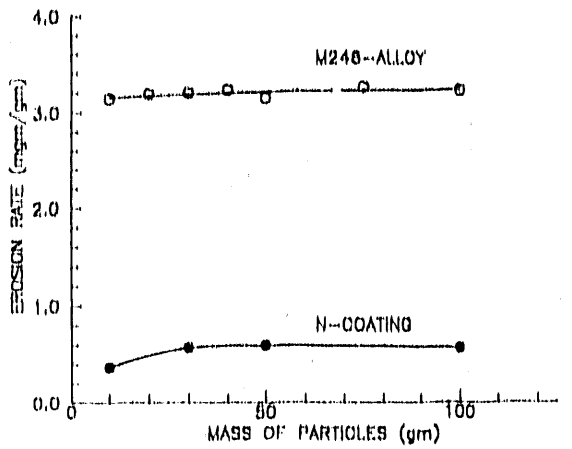

FIG. 7 EROSION RATE VS MASS OF PARTICLES FOR N--COATING AND M246--ALLOY AT MAXIMUM EROSION IMPINGEMENT ANGLE, T=1500 F, U=1200 fps, FLY ASH

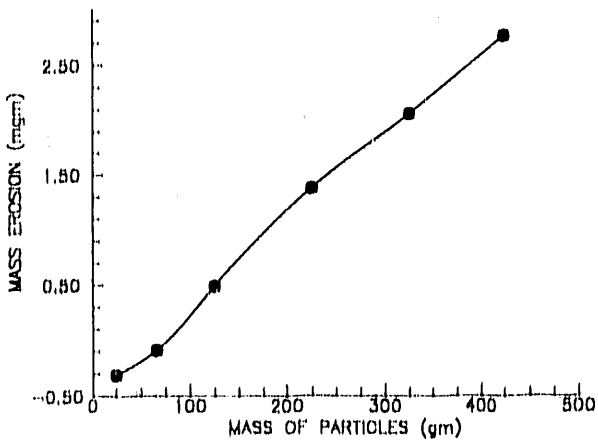

FIG. 9 N--COATING EROSION VERSUS MASS OF PARTICLES AT 45 IMPINGEMENT ANGLE, T=1500 F, U=1200 fps, ALLISON PARTICLES

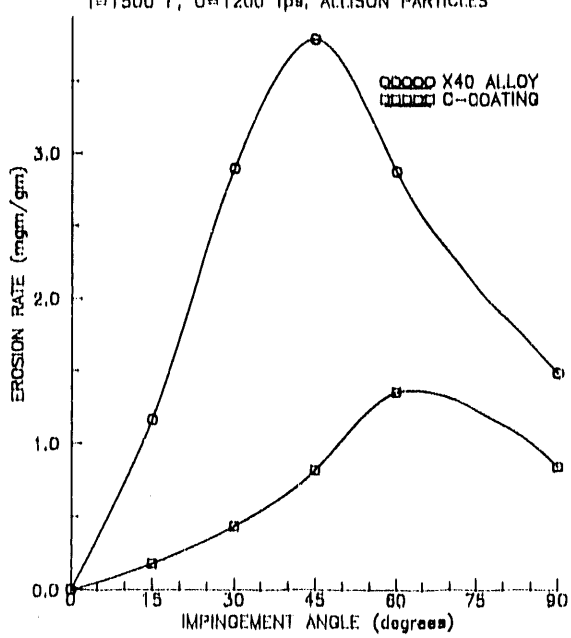

FIG. 11 X40 ALLOY AND C--COATING EROSION RATE AT T=1500 F, U=1200 fps, FLY ASH

pattern with maximum erosion at 60° impingement for the coated samples and 45° for the uncoated samples. The erosion rate results of Fig. 11 indicates that this coating provides a significant erosion protection, compared to the substrate. Figure 12 shows the incremental erosion test results for the "C"-coating and the substrate at the maximum erosion angle for each. Figure 13 shows that for the coated samples, the erosion rate increases, then reaching a steady state at impacting particle mass of 70 gm, afterwards the rate starts to increase rapidly at the particle mass of 135 gm when the coated surface is completely eroded. The complete erosion of the coating has been confirmed by visual and microscopic inspection. The particle mass data at which the coating is completely eroded can be used to calculate the coating life.

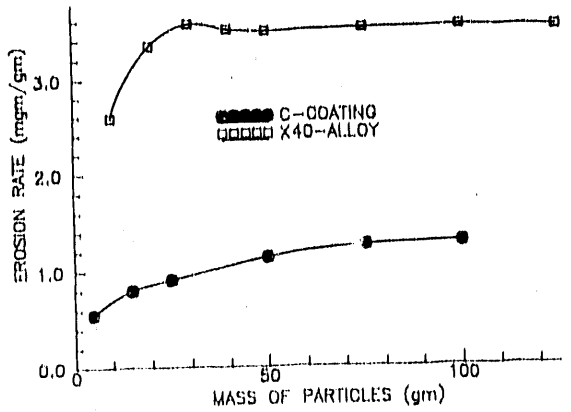

FIG. 12 VARIATION OF EROSION RATE VS MASS OF PARTICLES FOR C-COATING AND X40-ALLOY AT MAXIMUM EROSION IMPINGEMENT ANGLE AND T=1500 F, U=1200 fps FLY ASH

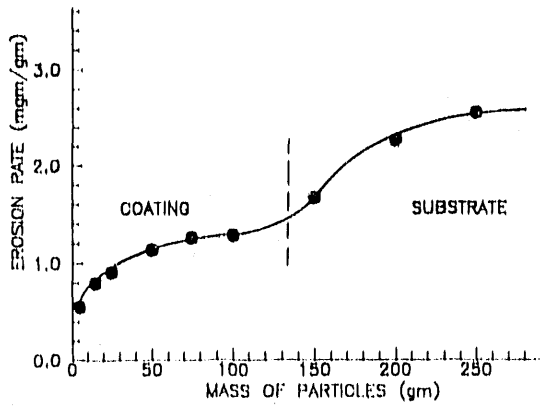

FIG. 13 VARIATION OF C-COATING EROSION RATE WITH MASS OF PARTICLES AT 60 IMPINGEMENT ANGLE, T=1500 F, U=1200 fps FLY ASH

Erosion Tests for RT22 Coating

This coating is a platinum aluminide that was applied to nickel based MAR-M-246 superalloy. Figure 14 shows that the erosion rate curve follows the familiar form of ductile erosion with a peak at 30°. Comparing Figs. 14 and 6, one can conclude that the platinum content in the aluminide coating enhances the erosion resistance. The erosion rate is seen to be reduced to less than half the erosion rate of the aluminide coating, while the maximum erosion angle has been decreased to 30°. Comparing Figs. 14 and 6, one can see that the erosion rate of the base material (MAR-M-246) is more than an order of magnitude greater than the erosion rate of the platinum aluminide coating. Figure 15 shows that the coating is completely eroded after being impacted by 825 gm gas particles. The RT22 coating has high initial erosion rate, which decreases rapidly to the lower steady state erosion rate as shown in Fig. 15.

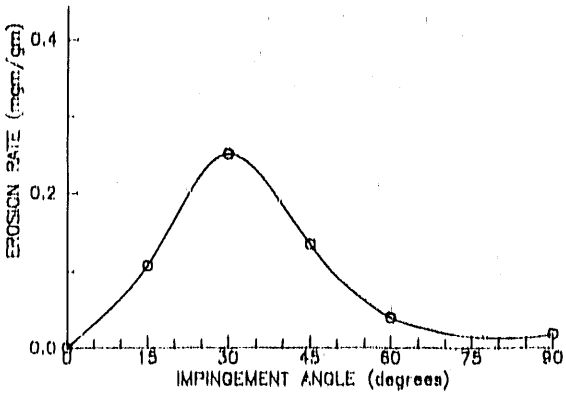

FIG. 14 R122--COATING EROSION RATE AT T=1500 F, U=1200 fps FLY ASH

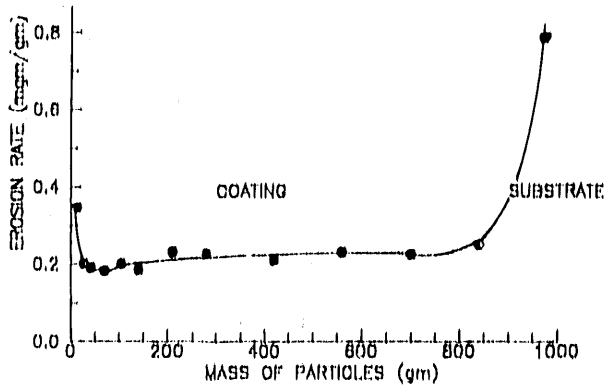

FIG. 15 VARIATION OF R122--COATING EROSION RATE WITH MASS OF PARTICLES AT 30° IMPINGEMENT ANGLE, T=1500 F, U=1200 fps FLY ASH

Particle Dynamics and Blade Erosion in Axial Flow Turbine

The particle trajectory and blade erosion analysis were carried out through a two stage axial flow turbine. The presented blade erosion results, were obtained from the trajectories corresponding to 75,000 ingested particles or 22×10^{-5} grams of ash in the gas turbine for standard inlet air equivalent conditions at 1893 rpm and 7.071 lb/sec weight flow.

Figures 16 and 17 show sample projections of the particle trajectories through the blade rows in z-θ plane and z-r plane for four typical particle diameters of 2.5, 15, 40 and 135 microns. The effect of particle size on the trajectories can be clearly seen in these figures. Figure 16 shows that the deviation of the particle trajectories from the streamlines increases with the particle size. Consequently, large particles have more impacts with the blade surfaces. The projection of particle trajectories in r-z plane (Fig. 17) demonstrate the strong influence of blade impacts on the particle radial motion. The larger particles centrifuge faster after they impact the rotor blade suction surface near the leading edge.

The computed particle impact locations over the blade pressure surface in the two stage turbine are presented in Figs. 18 and 19 for nonuniform and uniform particle size distribution, respectively. The results indicate that the particle centrifugion is more pronounced in the case of uniform particles as evidenced by the absence of impacts near the hub. This effect is less noticeable in the impacts of the actual nonuniform particle size. This is due to the negligible effect of blade impacts on the radial motion of the smaller particles which continue to impact the entire blade pressure surface as shown in Fig. 20. The blade

erosion prediction is based on the particle computed impact data as determined from the particle trajectory calculations, and erosion empirical equation. Further results are presented in the ASME Paper 90-GT-114 which will be presented in June this year in Brussels, Belgium and published in the ASME Journal of Turbomachinery. The results provide a detailed description of the blade surface erosion pattern and intensity through two stage gas turbine engine for both nonuniform and uniform solid particles.

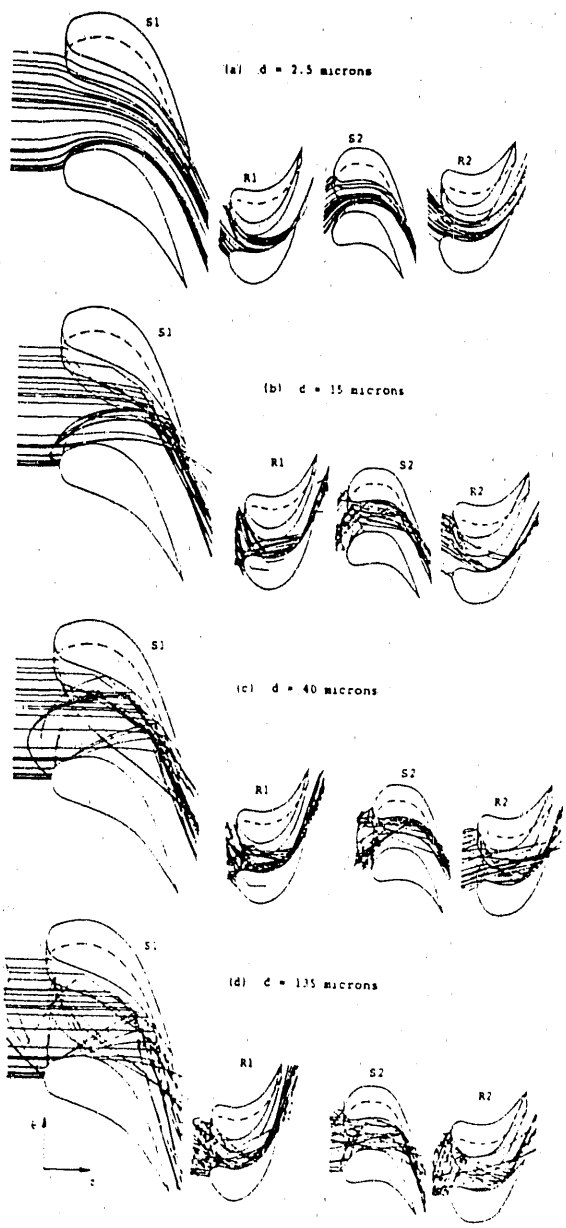

Fig. 16. Particle Trajectories in θ -z Plane.

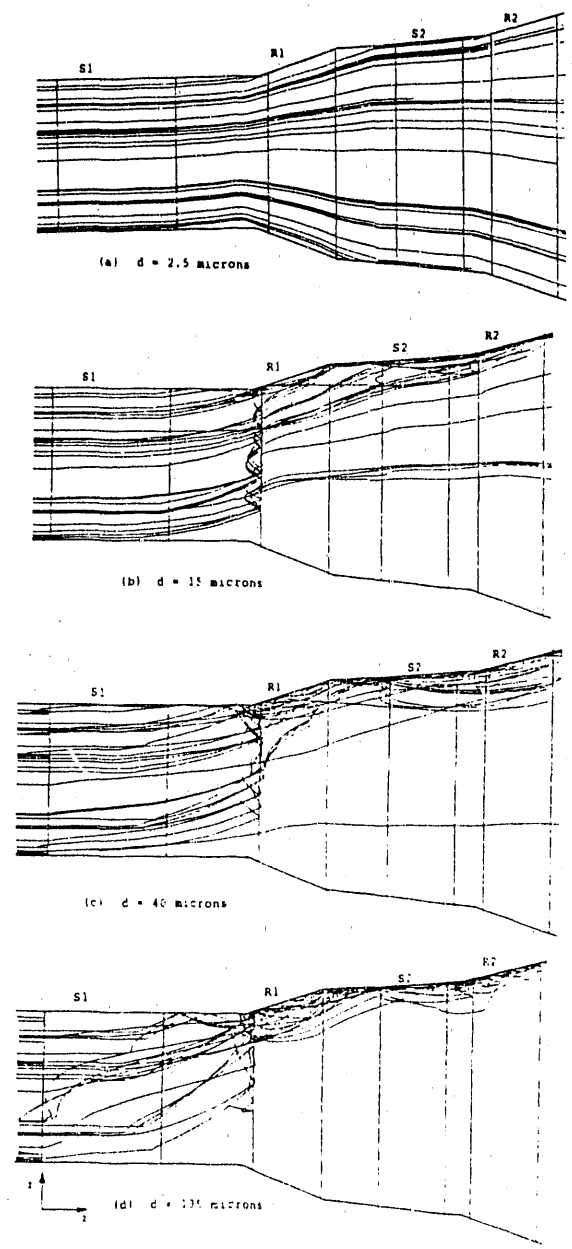

Fig. 17. Particle Trajectories in r-z Plane.

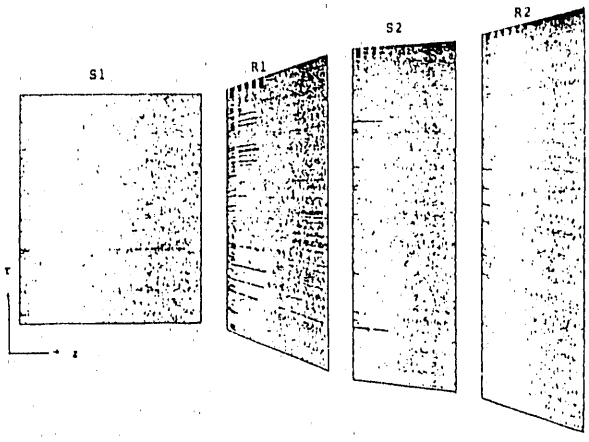

Fig. 18. Impact Location for the Nonuniform Particles.

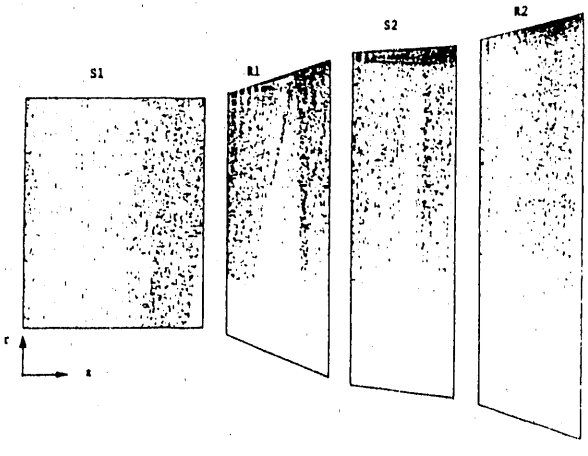

Fig. 19. Impact Location for the Uniform Particles

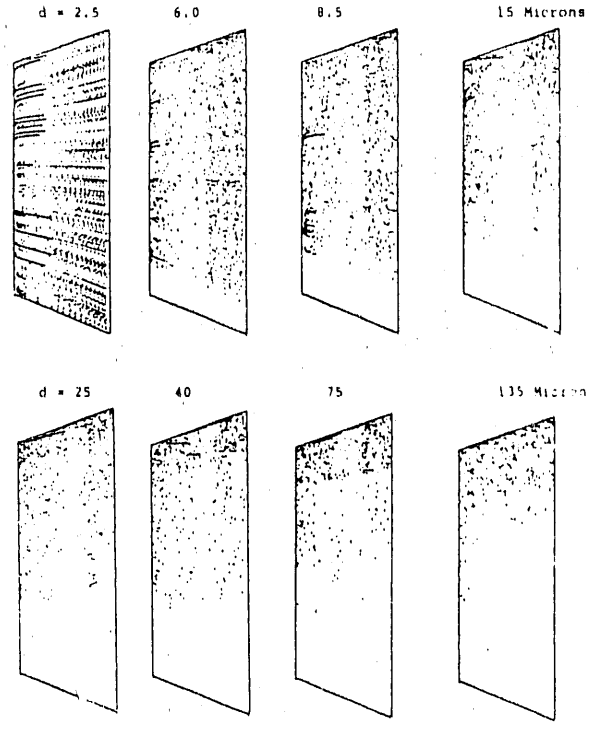

Fig. 20. Impact Locations for the Individual Particle Sets, First Rotor.

REFERENCES

1. Tabakoff, W., Hamed, A. and Eroglu, H., "Study of Particle Rebound Characteristics and Material Erosion at High Temperature," Final Technical Report, Fossil Energy Materials Program, U.S. Department of Energy, ORNL/Sub/84-89628/01, December 1986.

2. Tabakoff, W. and Hamed, A., "Laser Measurements of Solid Particles Rebound Parameters Impacting on 2024 Aluminum and 6Al-4V Titanium Alloys," AIAA Journal of Aeronautics and Astronautics, Vol. 25, May 1987, pp. 721-726.

3. Tabakoff, W. and Wakeman, T., "Test Facility for Material Erosion at High Temperature," ASTM Special Publication 664, 1979, pp. 123-135.

A THEORECTICAL MODEL OF A SOLID PARTICLE IMPACT ON THE TARGET OF DUCTILE MATERIALS

Jian J. Yeuan and Widen Tabakoff

Department of Aerospace Engineering and Engineering Mechanics
University of Cincinnati
Cincinnati, OH 45221

Abstract

The objective of this research work is to simulate single solid particle impact on the solid target using the elastic-plastic theory. The governing equations for the two dimensional elastic-plastic flow are formulated in Lagrange coordinates. The equation of state in the elastic region is the time rate change of Hooke's law. The experimental Hugoniot equation of state and the yield condition of R. von Mises are used in the plastic region. The effect of strain rate on the material strength is considered using an empirical formulation. The entire impact process involves the adhesion, deformation and rebound process interacting between the solid particle and the target. A computer program that is second order accuracy in time is developed to simulate the particle impact phenomena. This program employes the finite volume numerical technique and two step explicit MacCormack scheme to resolve the transient phenomena of impact. The results are presented for the hard tool steel particle impacting on the mild steel target at 90 degree impact angle. The computational results are compared with the

experimental data for a range of impacting velocities up to 350 m/sec.

Introduction

The problem of describing solid particle impacts which cause erosion is very complex one and has not yet been solved completely. A simple theoretical approach in which a constant plastic identation pressure is assumed to allow the impact to be modelled with fair accuracy (Rickerby and Hutchings) [1,2]. This model can not predict the condition at 90. degree impact angle. The reason for this as the author indicated is lack of elastic energy prediction in this model [2]. A similar theoretical approach, with the elastic energy added, is reported by Sriram and Kosel [3] to be able to predict the normal solid particle impact. His model has improved the predictions of the rebound characteristics at low impact angle, nevertheless the result of volume loss is not indicated. His results of particle rebound velocity at high impact angle show poor predictions comparing with the experimental data. Therefore we have used different theoretical approach by employing the elastic-plastic mechanics to study this problem. The strain rate affecting the solid particle impact mechanism has been proposed by (Hutchings) [4], however the validation of this idea has not been made quantitatively.

The Theoretical Particle Rebound Model

A theoretical model of single solid particle impact on the target of ductile materials is conducted. This model is based on the

elastic-plastic theory and Rankine-Hugoniot relation for pressure correlations in the plastic region. The effect of strain rate on the strength of material is also included in this model. The assumption is that the impacted target and particle behave like the time varied elastic-plastic bodies under the influence of strain rate. The fracture mechanism is not included in this model. The constitutive equations independent of the equations of motion are used. The Lagrangian formulations of conservation of mass, momentum and energy [5] can provide the geometrical distortions of target and particle associated with the stresses and velocities.. The yield condition, which depends on the strain rate and strain energy, is used to define the interface of elastic and plastic flows in the materials.

Equations of motion are written in two dimensional Cartesian coordinates as:

$$\rho \frac{\partial \dot{x}}{\partial t} = \frac{\partial \Sigma_{xx}}{\partial x} + \frac{\partial T_{xy}}{\partial y} \quad , \quad \rho \frac{\partial \dot{y}}{\partial t} = \frac{\partial \Sigma_{yy}}{\partial y} + \frac{\partial T_{xy}}{\partial x}$$

$$\text{and} \quad \Sigma_{xx} = S_{xx} - (P + q) \quad , \quad \Sigma_{yy} = S_{yy} - (P + q)$$

Equation of continuity:

$$\frac{\dot{V}}{V} = \frac{\partial \dot{x}}{\partial x} + \frac{\partial \dot{y}}{\partial y}$$

Energy equation:

$$\dot{E} = - (P + q) \dot{V} + V (S_{xx}\dot{\epsilon}_{xx} + S_{yy}\dot{\epsilon}_{yy} + T_{xy}\dot{\epsilon}_{xy})$$

Artificial viscosity

$$q = C_0^2 \rho_0 \left(\frac{\dot{V}}{V} \right)^2 \frac{A}{V} \quad , \text{ where } C_0 = 2.$$

Equations of state:

$$\dot{S}_{ii} = 2 \mu \left(\dot{\epsilon}_{ii} - \frac{1}{3} \frac{\dot{V}}{V} \right) + \delta_{ii} , \qquad \dot{T}_{xy} = \mu \left(\dot{\epsilon}_{xy} \right) + \delta_{xy}$$

Where subscript ii can be xx, yy or zz

Velocity strains:

$$\dot{\epsilon}_{xx} = \frac{\partial \dot{x}}{\partial x} \quad , \quad \dot{\epsilon}_{yy} = \frac{\partial \dot{y}}{\partial y} \quad , \quad \dot{\epsilon}_{zz} = 0. \quad , \quad \dot{\epsilon}_{xy} = \frac{\partial \dot{x}}{\partial y} + \frac{\partial \dot{y}}{\partial x}$$

The expressions of hydrostatic pressure are as follows:

In the elastic limit

$$P = - (\lambda + \mu) \ln V \ , \qquad \lambda \text{ and } \mu \text{ are Lamé constants}$$

For the points beyond elastic limit, the pressure is represented by empirical Hugoniot formulation.

The hydrostatic pressure is:

$$P = a (\eta - 1) + b (\eta - 1)^2 + c (\eta - 1)^3 , \qquad \eta = \frac{1}{V} = \frac{\rho}{\rho_0}$$

which a, b and c are constants.

Von Mises yield condition:

$$S_1^2 + S_2^2 + S_3^2 - \frac{2}{3} Y_0^2 \leq 0 \qquad , Y_0 \text{ is yield strength.}$$

The symbols used in previous equations are as follows:

x, y is space coordinates

$\dot{x}$ and $\dot{y}$ are the velocities in x and y direction.

Σ_{xx}, Σ_{yy} are the total stresses, T_{xy} is the shear stress

S_{xx}, S_{yy}, S_{zz} are the deviatoric stresses.

S_1, S_2, S_3 are the deviatoric stresses in principal direction.

$\dot{\epsilon}_{xx}$, $\dot{\epsilon}_{yy}$, $\dot{\epsilon}_{xy}$, $\dot{\epsilon}_{zz}$ are the strain rates.

δ_{xx}, δ_{yy}, δ_{xy} are corrections for body rotation.

P is the hydrostatic pressure. V is the relative volume.

ρ is the density. A is the surface area.

E is the internal energy per original volume

The dot sign represents the time derivative of the variables. When tension occurs in the material, the pressure is cut off at $P = -\frac{1}{3} Y_0$ to be consistent with a simple tension test. The expression for deviatoric stresses are modified to include a small correction term for body rotation.

The yield strength determines the amount of energy conserved in the impacted target and of energy losses due to plastic deformation. The yield strength is function of temperature and strain rate. The semi-empirical formulation [6] of yield strength for steel is applied in the numerical calculations of single particle impact phenomena.

The Numerical Method

The numerical scheme is derived by the finite volume method with arbitrary mesh configuration. This scheme is consistent, second order accurate in time and first order accurate in space. For a better unsteady resolution, the two step explicit MacCormack algorithm is applied to the governing equations.

Predictor:

$$U^{*n+1}_{i,j} = U^{n}_{i,j} - \Delta t\, A^{n}$$

Corrector:

$$U^{n+1}_{i,j} = U^{n}_{i,j} - \Delta t\, (A^{n+1} + A^{n}), \quad A^{n+1} \text{ is calculated from } U^{*n+1}$$

U can be x or y which are horizontal and normal velocities respectively. The operator A is derived from finite volume method integrating around a quadrilateral or triangular mesh.

Results and Discussions

The material of the circular particle is hard tool steel. The diameter of the particle is 9.5 mm. The target is a 5 cm long, 3 cm width rectangular mild steel piece. The fixed boundary is applied on the target base while the free boundary conditions are applied on the other three sides of the target except for the contact surface of the solid particle and the target. The contact surface can proceed during the process of adhesion, deformation, and rebound depending on the transient stress condition. The results of 350 m/s impact velocity and 90 Deg. impact angle are presented. The target has 151 x 31 mesh points,

and the particle has 39 x 8 mesh points. Fig (1) shows the deformation of the particle and the target at the moment of the particle leaving the target. The crater around the contact surface is enlarged and presented in fig (2).

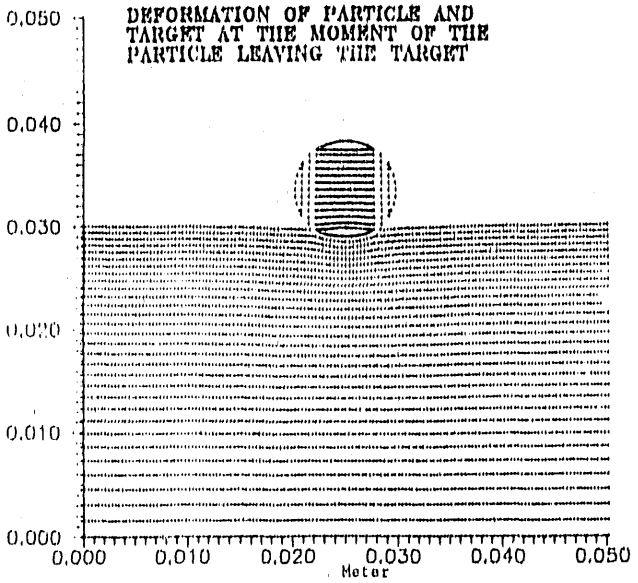

Fig 1. The distortions of particle and target.

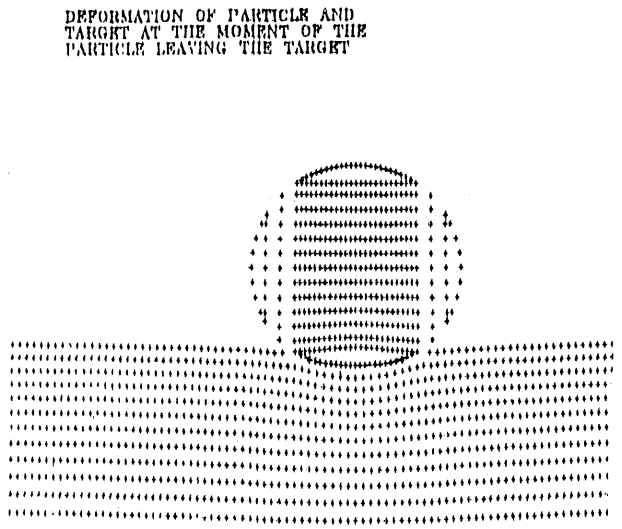

Fig 2. The enlarged configuration for distortions around the crater.

The normal stress distributions for two different time periods are presented. Fig(3a,3b) are the normal stress distributions at 1000 time steps caused by particle impact. The time period is 5.5807 μ sec after particle impact, and the impact velocity at this moment is reduced to 76.96 m/s downward to the target. In these figures the negative sign means the compressive stress. The maximum compressive stress occurs under the contact surface and the normal stress wave propagating in the impact direction is faster than that propagating in the lateral direction. The high normal stress gradient occurs under the edge of the crater of target. The same phenomena is found in the particle.

Fig 3a. The normal stress contour for particle at 1000 time steps.

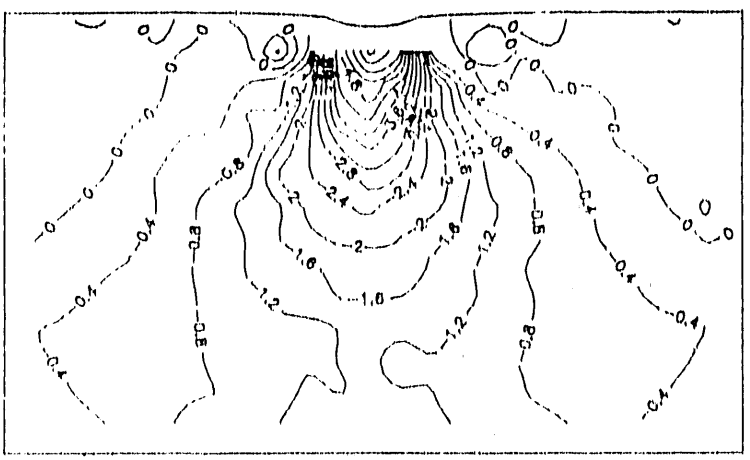

Fig 3b. The normal stress contour for target at 1000 time steps.

Fig(4a,4b) are the normal stress distributions when the particle is about to leave the target. The maximum compressive stress is located on both sides under the crater of the target. The interior of the particle is under the tension stress condition (+), while the particle around the edge is under the small compressive stress (-).

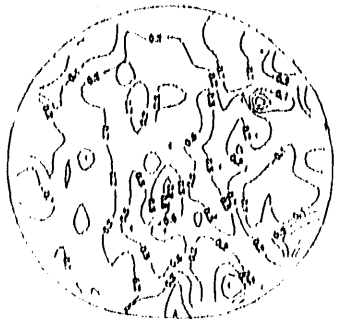

Fig 4b. The normal stress contour for target at the moment of particle leaving the target.

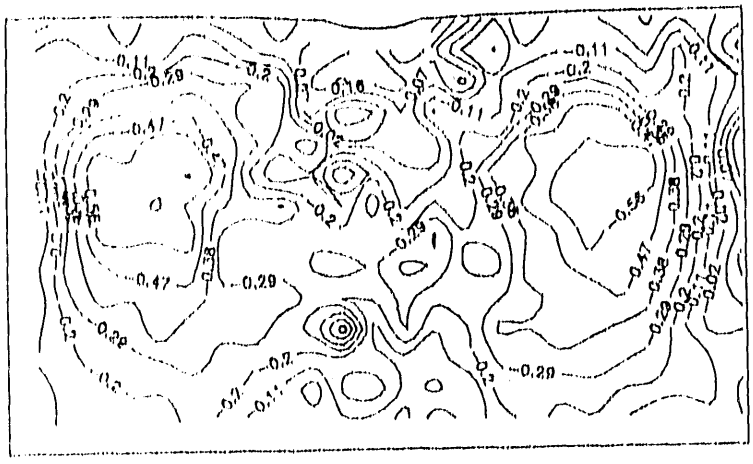

Fig 4a. The normal stress contour for particle at the moment of particle leaving the target.

Fig (5) presents the result of rebound velocities at different impact velocities for 90 Deg. impact angle. Fig (6) shows the loss of kinetic energy of the particle at different impact velocities. The last two figures show good agreement with the

experimental data obtained by Hutchins [2]. Fig (7) presents the crater volume loss at different impact velocities. However, there is not enough experimental data to compare the crater volume loss.

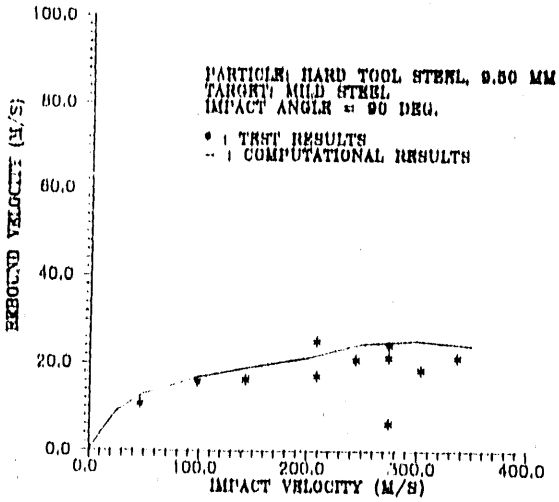

Fig 5. The rebound velocities versus impact velocities at 90. degree impact angle.

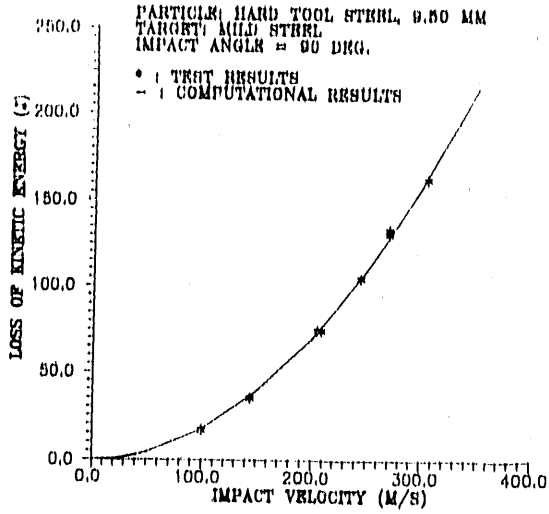

Fig 6. The loss of kinetic energy versus impact velocities at 90. degree impact angle.

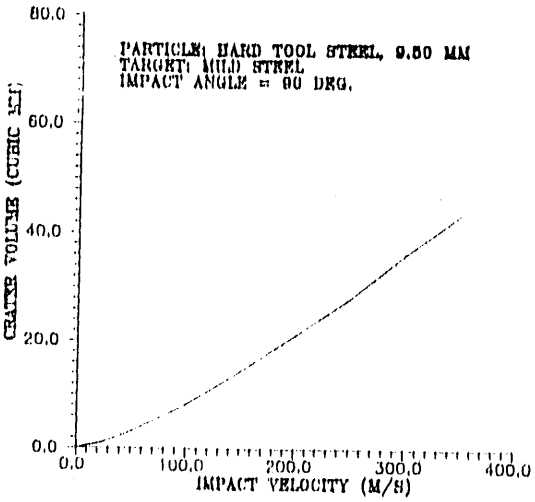

Fig 7. The calculated crater volume versus impact velocities at 90. degree impact angle.

Conclusion

The present model can successfully simulate the solid particle impact process. The computational results of stress

distributions and crater volume loss can be used to determine the strength of the material erosion resistance. The calculated rebound velocities can be used for calculations of the particle trajectories in particulate flow. The computational results show good agreement with the experimental data. Further investigations will be proceeded in the particle angular impact.

References

1. Rickerby, D.G. and Macmillan, N.H., "On The Oblique Impact of A Rigid Sphere Against A Rigid-Plastic Solid" Int. J. Mech. Sci. Vol. 22, 1980, pp 491-494.

2. Hutchings, I.M., D.G. Rickerby and N.H. Macmillan, "Further Studies of the Oblique Impact of a Hard Sphere Against a Ductile Solid," Int. J. Mech. Sci. 23, 1981, pp 639-646.

3. T.S. Sriram and T.H. Kosel, "Computer Modeling of The Rebound Characteristics of Spherical Erodent Particles," The Proceeding of the 7th international Conference on Erosion by Liquid and Solid Impact, Cambrige, England, Sept 6-10, 1987.

4. Hutchings, I.M., Winter, R.E. and Field, J.E. "Solid Particle Erosion of Metals: The Removal Of Surface material By Spherical Projectiles" Proc. R. Soc. Lond. A. 348, 1976, pp 379-392.

5. Mark L. Wilkins, "Calculation of Elastic-Plastic Flow" Method in Computational Physics, Vol. 3, PP 211-263, 1964.

6. A.R. Rosefield and G.T. Hahn, "Numerical Descriptions of The Ambient Low-Temperature and High-Strain Rate Flow and Fracture Behavior of Plain Carbon Steel" Tran. of The ASME, Vol. 59, PP 962-982, 1966

INITIAL DETERMINATION OF THE MICROMECHANICAL PROPERTIES OF OXIDE SCALES

P. F. Tortorelli, J. R. Keiser, K. R. Willson,* and W. C. Oliver

Oak Ridge National Laboratory
P.O. Box 2008
Oak Ridge, TN 37831-6084

*Geneva College
Beaver Falls, PA 15010

ABSTRACT

A depth-sensing submicron indentation technique is being used to characterize the mechanical response of oxide scales. The method has been applied to studies of chromia-rich and alumina scales grown on a stainless steel and an iron aluminide, respectively. Results on room temperature micromechanical properties (elastic modulus, hardness, etc.) are presented to provide data for determining scale fracture criteria and to evaluate models that propose reactive element additions to alloys modify the mechanical behavior of oxide scales and thereby improve scale adherence. Average values of elastic moduli for thin chromia-rich scales formed on 20-25-Nb steels were in good agreement with that for the bulk chromia. However, the elastic modulus of the alumina scale grown on an Fe-21.4 wt. % Al alloy differed significantly from that reported for bulk Al_2O_3. The addition of 0.13% Ce to the 20-25-Nb steel, which significantly improves scale adherence, did not affect the elastic modulus, hardness, strength, or plasticity of the oxide scale. Therefore, these findings did not support the subject models of scale adherence for cerium. Nevertheless, the technique of depth-sensing submicron indentation testing appears to offer promise as a method of characterizing oxide scales and their ability to protect alloys from high temperature corrosion and environmental degradation.

INTRODUCTION

The high-temperature corrosion resistance of metals and alloys is directly related to the presence of a protective surface oxide scale that is either inert to, or slowly reactive with, the environment. Accordingly, the mechanical integrity and properties of the oxide are of considerable importance in understanding and controlling oxidation, scale adhesion, and the interaction between chemical and deformation effects.[1-7] To this end, initial measurements of certain mechanical properties of oxide scales by a submicron indentation technique are presented for stainless steels and iron aluminide. Such results can be used in calculations of fracture energies and toughness of oxide scales and in the determination of the limits to scale adherence.[3-8] Furthermore, such information can ultimately be used in the design of high-temperature, corrosion resistant materials using both the chemical and mechanical properties of the scale as a basis for compositional and other modifications to a particular alloy system. Indeed, such results can also influence alloy

development as a result of forming scales that protect the bulk metallic material from environmental degradation by blocking the uptake of deleterious species (for example, hydrogen).

As discussed in recent overviews,[9-11] the presence of relatively small amounts of rare earth (and other) oxide dispersoids or reactive elements in certain alloys can promote the formation of more adherent oxide scales. While there is no doubt that these reactive element/dispersoid additions (hereafter referred to as "REs") do generally improve scale adherence in many circumstances, there is considerable debate regarding the mechanism(s) by which they do so. Some of the proposed mechanisms suggest that REs decrease the propensity for scale cracking and spallation by modifying growth stresses, scale plasticity, or fracture toughness.[4,11-13] Indeed, a recent review cited the need for new or improved techniques for measuring the mechanical properties of oxide scales to differentiate between various proposed RE models.[11] Therefore, the present paper also attempts to evaluate possible effects of a RE addition on the micromechanical characteristics of chromia scales using the unique approach of submicron load-displacement measurements.

EXPERIMENTAL PROCEDURES

The elastic and plastic properties of chromia-rich and alumina scales were measured with a mechanical properties microprobe (MPM), which utilizes a depth-sensing submicron indentation technique[14] that has recently been successfully applied to mechanical characterization of thin films[15] and oxide scales.[16] The MPM is a modified version of a commercial instrument known as a Nanoindenter.[17] It is a load-controlled device in which the force on the indenter is applied via magnetic coupling and the resulting displacement is measured by a capacitance gage. The smallest load increment is approximately 0.3 μN (with a maximum load of 120 μN) and the displacement resolution is about 0.2 nm. A light microscope is used to position the indenter on the specimen surface, but subsequent movements in all three dimensions are controlled by a computer, which also is used for data acquisition and analysis. A Berkovitch type of diamond indenter was used; it produces the same relationship between area and penetration depth as a Vickers indentation.

A typical MPM indentation load-displacement curve is shown in Fig. 1. Normally, both elastic and plastic deformation occur during indentation.[14,15] Hardness is determined by the indentation load and the contact area of the indenter and thus can be calculated as a function of displacement depth. The elastic modulus of the material can be obtained from the slope of the unloading curve when the indenter is pushed back by the elastic restoring forces. Alternatively, as is done with the present MPM system, a small superimposed AC signal causes a brief, limited load reduction at a prescribed frequency during the entire loading phase of the indentation event (Fig. 1). This procedure allows the modulus to also be measured as a function of displacement. Extrapolation of the initial slope of the final unloading curve to zero load yields the plastic depth,

h_{plas}, as shown in Fig. 1. (This value also includes any friction contribution) While the presence of a substrate can affect the hardness and modulus measurements of thin layers, it has been shown that such an influence is minor if the total depth of the indenter penetration is a small fraction of the thickness of the film.[15] All indentations were made on normal or tapered polished cross sections so that substrate influence was minimal in most cases.

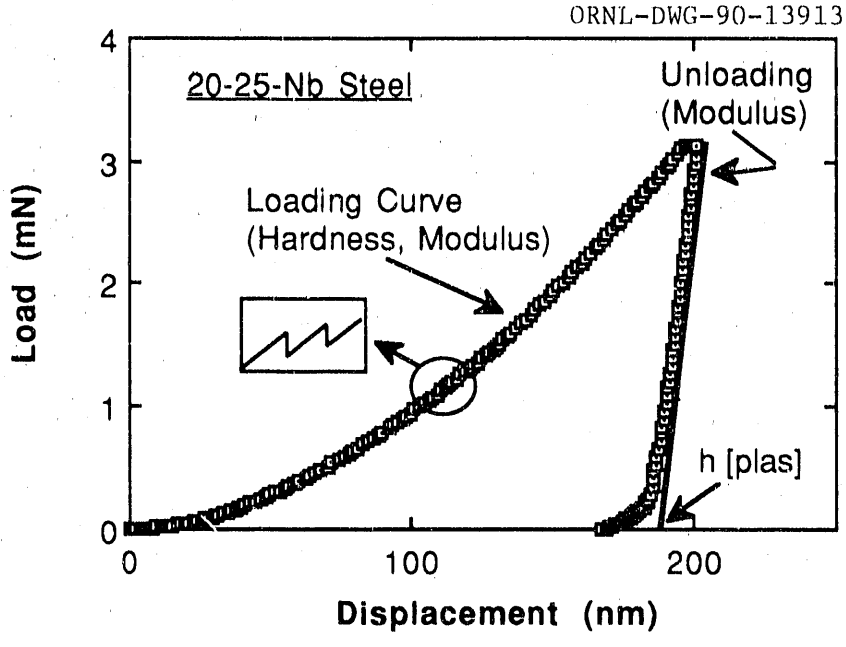

Fig. 1. Typical load-displacement curve from indentation test on 20-25-Nb steel.

Niobium-stabilized steels composed of Fe-20Cr-25Ni-0.7Mn-0.7Si-0.6Nb-0.04C and a model binary FeAl, FA-324, (Fe-21.4Al) were used in this study. (Concentrations are in wt %.) One of these steels (designated 20-25-Nb) was of the composition indicated, while the second (20-25-Nb+Ce) differed only in that it also contained 0.13 wt % Ce. Both steels were obtained from Harwell Laboratory. The oxidation behavior of these steels and the positive influence of Ce on scale spallation have been well documented.[2,3,18-20] The steel specimens were oxidized in air at 930 to 950°C to grow scales (composed principally of Cr_2O_3) for subsequent indentation testing. Because the addition of cerium results in slower scale growth, oxidation times were varied (24-96 h) to obtain scales of approximately the same thickness (1-2 μm). The iron aluminide was oxidized in air at 1050°C for 90 h. A thin (approximately 1.5 μm) Al_2O_3 scale was formed. After oxidation, the specimens were sectioned, metallographically polished, and examined. Some specimens were polished with a tapered cross section in order to have a thicker effective scale for indentation testing. After an appropriate section of adherent scale was located, a matrix of indentation positions covering both metal and oxide was selected and a MPM run was initiated. Under computer control, the series of steps shown in Table 1 was automatically performed at each indentation position. A typical indentation array is shown in Fig. 2.

Table 1. Typical indent sequence

Step	Description
1	Indenter approaches surface at >10 nm/s
2	Loading at 2 nm/s to depth of 200 nm
3	Hold at load, record 60 displacements at 1/s
4	Unloading at 100 μN/s to 10% maximum load
5	Hold at 10% load, record 50 displacements at 1/2 s
6	Unloading at 10 μN/s to zero load

M30270

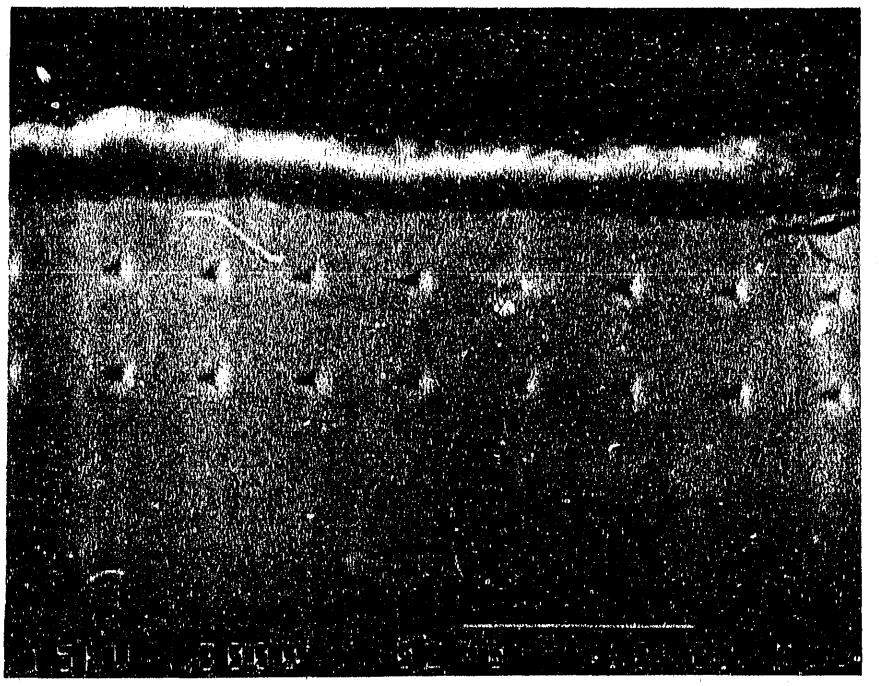

Fig. 2. Example of a programmed array of indentations in scale and substrate (20-25-Nb+Ce steel).

RESULTS

The application of the MPM to the characterization of the micromechanical properties of oxide scales was straightforward in principle, but somewhat difficult in practice. The relative thinness of the adhering scales and the thermal drift of the specimen and instrument hindered the placement of the indenter squarely in the scale. Furthermore, if the indenter location coincided with that of a preexisting scale defect, an atypical load-displacement curve was obtained and was subsequently neglected in the data compilation. (It is actually an advantage of this indentation technique that spurious results can often be detected and discarded, because this improves the precision in

determining the mechanical properties of the scales.) Therefore, only those indentations that yielded curves like that of Fig. 1, could be (usually) verified by scanning electron microscopy to be in the surface oxide, and were not distorted by defects were used in the determination of the scale properties. The micrograph in Fig. 3 is an example of an indentation in the oxide scale that was acceptable for analysis. As shown in Figs. 4 and 5, the difference between load-displacement curves for the alloy substrate and the respective scale was readily apparent. The load at a given displacement (indenter contact area) was substantially greater for indentations in the scale, thereby indicating a higher hardness for the oxides relative to the steel or the aluminide. The scales also showed a much greater elastic recovery, as evident from the respective shapes of the load-displacement curves in Figs. 4 and 5 and their correspondingly lower values of plastic depth (h_{plas}). Scanning electron microscope observations were consistent with these differences in hardness and plastic depth: for example, indentations in the steel were much larger than those in the chromia scales (see Fig. 6).

Fig. 3. Indentation in cross section of scale formed on 20-25-Nb steel.

ORNL-DWG 90-13914

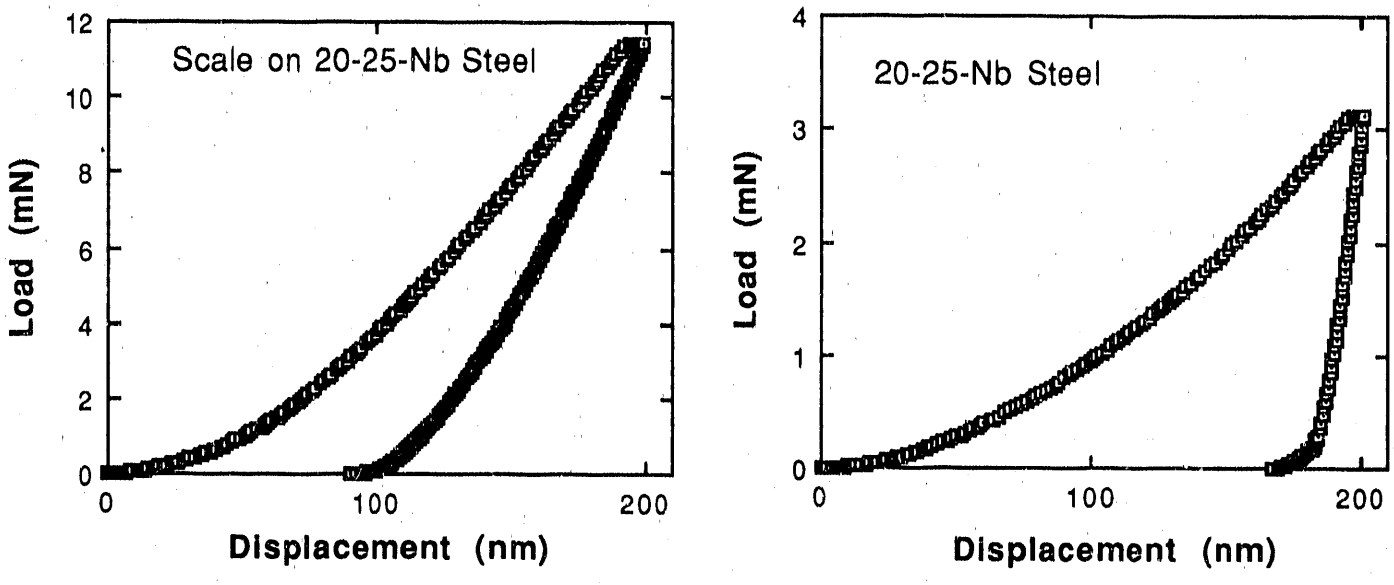

Fig. 4. Load-displacement curves for 20-25-Nb steel. (a) In scale. (b) In underlying scale.

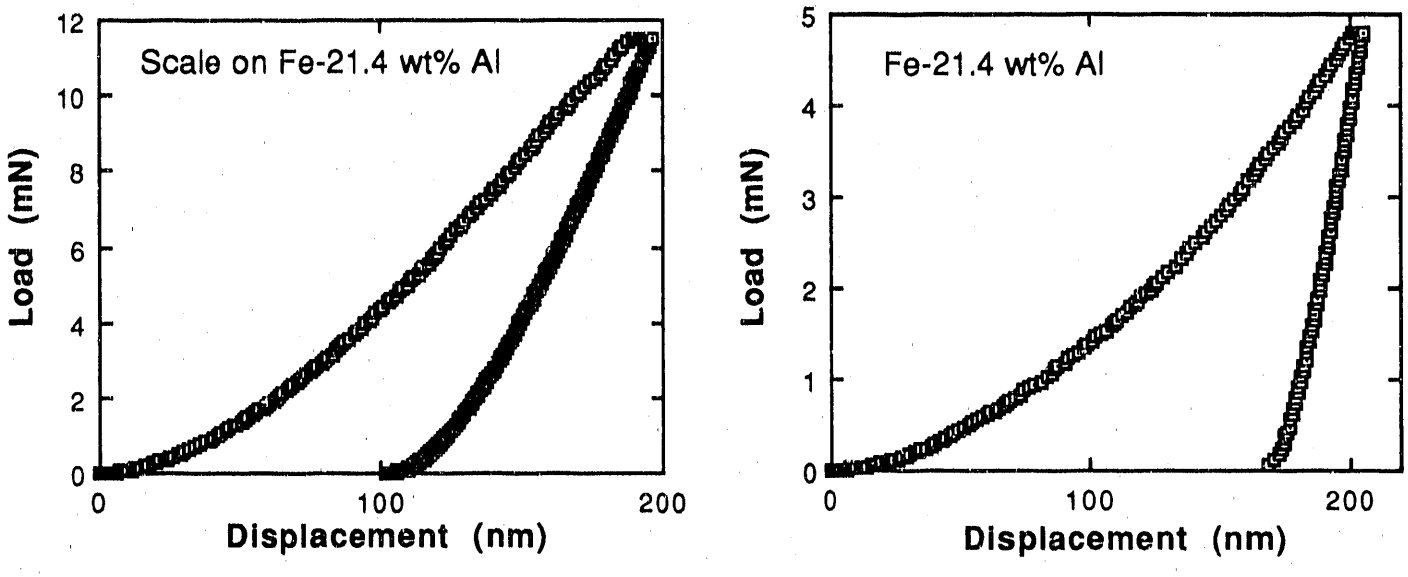

Fig. 5. Load-displacement curves for FA-324 (iron aluminide). (a) In scale. (b) In underlying alloy.

As described in the Experimental Procedures section, the MPM can yield hardness and modulus data as a function of indenter penetration depth. (In the present case, this depth is the distance below the polished cross section and is normal to the scale growth direction.) Therefore, the hardness and modulus from an individual indentation experiment were taken as averages of values determined at four depths between 140 and 170 nm, inclusively. In general, the hardness and modulus approached asymptotic values for indenter depths greater than about 80 nm. Table 2 presents the averages and standard deviations of the hardness, elastic modulus, and plastic depth

(h_{plas}) as determined from multiple indents in chromia-rich scales grown on both 20-25-Nb and 20-25-Nb+Ce steels and in an alumina scale on FA-324. Similar averages and standard deviations for the respective alloy substrates are also shown. No significant effect of Ce in 20-25-Nb steel on the hardness, modulus, or h_{plas} of the chromia-rich scale (or the steel) was found. The hardness of the alumina scale grown on the iron aluminide was greater (by about 20%) than the scales on the steels, while its elastic modulus was slightly less.

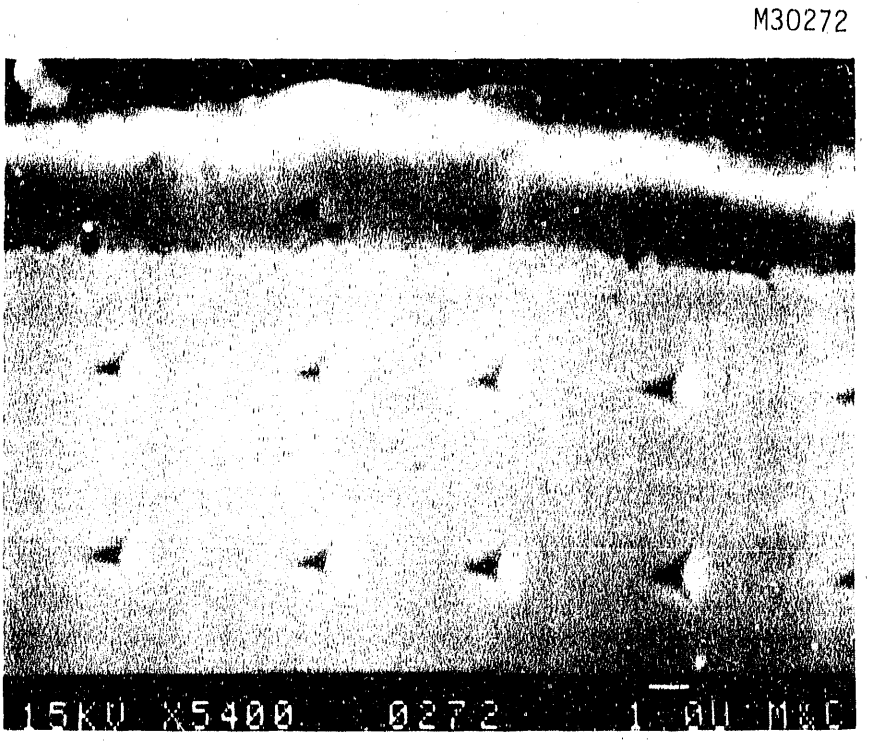

Fig. 6. Array of indentations made in scale and substrate (20-25-Nb+Ce steel).

Table 2. Mechanical properties microprobe results from analyses of polished cross sections of oxidized 20-25-Nb steels and FA-324

Steel	Material	Hardness (GPa)	Modulus (GPa)	h_{plas} (nm)
20-25-Nb	Oxide	23.4 ± 2.0	273 ± 18	132 ± 7
	Alloy	2.9 ± 0.2	229 ± 5	194 ± 4
20-25-Nb+Ce	Oxide	25.3 ± 1.3	296 ± 26	134 ± 6
	Alloy	3.1 ± 0.1	236 ± 12	194 ± 2
FA-324	Oxide	29.0 ± 2.5	261 ± 35	123 ± 5
	Alloy	5.4 ± 0.2	183 ± 7	177 ± 2

DISCUSSION

Knowledge of the mechanical characteristics of oxide scales is important for calculations and predictions of scale cracking and such properties have been measured and applied to oxidation phenomena for many years.[1-8] Therefore, the present results are not "new"; many of these scale properties have been measured previously. Rather, it is the measurement method and the application of the resulting mechanical properties data to evaluation of RE effects and to other aspects of alloy design that are unique to this investigation.

Elastic moduli of certain oxide scales measured by vibrational techniques have been previously reported (see, for example, refs. 1, 7, 21, and 22). However, a recent study of the limiting conditions for scale adherence[7] used elastic moduli determined for bulk oxides in the appropriate calculations because of concern with the accuracy of at least some of the reported measurements on scales. It is therefore significant that the present measurements of the elastic modulus for chromia scales resulted in values (273 ± 18 and 296 ± 26 GPa, see Table 2) that agree quite well with that used for bulk Cr_2O_3 (280 GPa) in the aforementioned work.[7] In actuality, the elastic moduli measured in this study for chromia-rich scales are within a factor of about 1.3 of many of those measured for scales grown on Ni- and Fe-based alloys.[21,22] The reasonably good precision of the MPM measurements (see Table 2) is due in part to the ability, mentioned above, to discriminate between normal and atypical indents based on the load-displacement behavior of each event and associated scanning electron microscopy.

In contrast to the results for the stainless steels, the measured elastic modulus for alumina grown on FA-324 differs from that of bulk Al_2O_3 (400 GPa) by about 50%. This difference does not seem to be due to a mixed (Fe,Al) oxide rather than an Al_2O_3 scale since energy dispersive x-ray analysis of the polished cross section showed that the metallic element composition of indented scale was normally greater than 95% Al. Therefore, in contrast with what would be concluded from the modulus data for the chromia-rich scales alone,[16] the present results cannot generally support the argument that elastic moduli for scales should be similar to those for bulk oxides of the same type.[7] As shown in Table 2, the average hardness of the alumina scale was about 20% higher than those measured for the scales on the stainless steels. This trend has also been observed for bulk oxides where the hardness of Al_2O_3 has been reported to be 33% greater than that of Cr_2O_3.[7] Again, there is some indication that bulk alumina may have different mechanical properties than Al_2O_3 scales (which have some incorporated iron), but it must be emphasized that these data (particularly for the scale grown on the iron aluminide) are preliminary. A more valid comparison between bulk and surface alumina will be possible as more extensive microstructural analysis of such scales are completed and as additional MPM data are obtained during the course of investigation of the influence of compositional modifications on the micromechanical properties of the scale formed on Fe_3Al.

A direct comparison of the hardnesses measured with the MPM and those determined by other techniques cannot be made with confidence due to the difficulty in determining the exact contact area of the MPM indenter and the lack of any extensive correlation with traditional microhardness values. Nevertheless, it is interesting to note that the MPM values of hardness for the steels (23.4 and 25.3 GPa) and FeAl (29.0 GPa) are within a factor of 1.5 of those reported for bulk chromia (15 GPa) and alumina (20 GPa).[7] Given this difficulty in comparison, the agreement between bulk and scale values is probably as good as can be expected, particularly in view of the reported scatter in hardness values for oxides[7] and of any inherent differences between the hardness of a thin oxide grown on a metallic substrates and that of the same oxide as a bulk solid.

Although the accuracy of this MPM technique for measurement of scale properties has not yet been quantitatively demonstrated, the finding that scale moduli and hardness determined from these measurements are within the expected range of values (suggested by previous measurements on scales and bulk oxides[1,7,21,22]) is most important. It certainly contributes to validation of the use of submicron indentation testing for obtaining mechanical characteristics of thin oxide scales grown on metallic materials and the precision that has been demonstrated increases the confidence in the technique as a way to evaluate relative changes in selected mechanical properties as a function of compositional changes (such as RE additions). In this regard, while the results in Table 2 may appear to suggest that the scale on the 20-25-Nb+Ce steel has a higher modulus than the scale on the 20-25-Nb steel, the standard deviations indicate that a real difference cannot be supported on the basis of these data. A variation in elastic modulus should not be expected since small changes in compositions or microstructure do not usually affect this property.[23] On the other hand, such small compositional modifications often affect properties such as hardness and strength. However, the results shown in Table 2 indicate that, as with the modulus, the difference in hardness between the scales formed on the two steels was within the overlap of the standard deviations of the respective measurements. Furthermore, the amount of room temperature plasticity (as measured by h_{plas}, see Fig. 1) was the same for both scales (see Table 2). It thus appears from these initial results that the presence of cerium, while significantly improving scale adherence, does not affect room temperature micromechanical properties in a way that influences spallation. Therefore, the present results do not support models in which RE additions modify the mechanical response of oxide scales to the extent that such models depend on changes in room temperature elastic modulus, hardness, strength, or plasticity.

These initial MPM results are encouraging with respect to the potential of depth-sensing submicron indentation testing for characterizing thin oxide scales on metallic substrates and for evaluating certain models of improved scale adherence. However, there are two important caveats with respect to these measurements. First, only parts of scales that remained attached to the substrate after an oxidation treatment and metallographic preparation were used for the measurements. Scale material that spalled was not characterized and it may be just such scales that

are most interesting for comparison and for understanding failure mechanisms. Second, the measurements were made at room temperature and they may not be characteristic of the scales at service temperatures, particularly with respect to plastic deformation. The present technique is useful for examining RE effects on high-temperature corrosion resistance only to the extent that any relative changes in room temperature mechanical properties of the scales are also operative at elevated temperatures in an oxidizing environment. A new type of MPM, designed for measurements at elevated temperature, is currently under development at Oak Ridge National Laboratory. When available and applied to the characterization of oxide scales, it will be possible to overcome these two limitations to the present approach by allowing measurements of the micromechanical properties of oxide scales at temperatures of interest and at which most protective scales are completely adherent. However, room temperature mechanical properties of scales may continue to be of interest in cases where a thin oxide surface layer serves as a barrier to hydrogen uptake and thereby helps to alleviate embrittlement of iron aluminides.[24]

SUMMARY AND CONCLUSIONS

Depth sensing submicron indentation testing was used to measure room temperature elastic and plastic properties of thin chromia and alumina scales formed on 20-25-Nb steels and a model binary FeAl, respectively. The elastic moduli for the chromia-rich scales were in good agreement with that for bulk Cr_2O_3, but there was a significant difference in the measured modulus for as-grown Al_2O_3 on iron aluminide and that reported for bulk alumina. As expected from data on bulk ceramics, the Al_2O_3 scales had higher hardness values than those that were chromia-rich.

The addition of 0.13% Ce to the 20-25-Nb steel, which significantly improves scale adherence, did not affect the room temperature elastic modulus, hardness, strength, or plasticity of the oxide scale. Therefore, on the assumption that relative changes in room temperature mechanical properties induced by compositional modifications are maintained at elevated temperatures in an oxygen environment, these findings do not support, for this alloy system, certain models of scale adherence in which RE additions modify the mechanical response of oxide scales

The MPM appears to offer promise as a method to measure the micromechanical properties of oxide scales, to test models of scale growth and adherence based on their mechanical response, and to develop better approaches to design of high-temperature corrosion- (and, possibly, hydrogen-) resistant alloys.

ACKNOWLEDGEMENT

Research sponsored by the Fossil Energy AR&TD Materials Program, U S. Department of Energy under contract DE-AC05-84OR21400 with Martin Marietta Energy Systems, Inc.

REFERENCES

1. P. Hancock, *Werkst. Korros.* **21** (1970) 1002-1006.

2. H. E. Evans and R. C. Lobb, *Corros. Sci.* **24** (1984) 209-222.

3. H. E. Evans, *Mater. Sci. Eng.* **A120** (1989) 139-146.

4. F. H. Stott, *Mater. Sci. and Technol.* **4** (1988) 431-438.

5. M. Schütze, *Mater. Sci. and Technol.* **4** (1988) 407-414.

6. M. Schütze, *Mater. Sci. Eng.* **A121** (1989) 563-569.

7. J. Robertson and M. I. Manning, *Mater. Sci. and Technol.* **6** (1990) 81-91.

8. P. Hancock and J. R. Nicholls, *Mater. Sci. and Technol.* **4** (1988) 398-406.

9. H. S. Hsu, *Oxid. Met.* **28** (1987) 213-235.

10. J. Stringer and P. Y. Hou, pp. 383-401 in *Corrosion and Particle Erosion at High Temperatures*, eds. V. Srinivasan and K. Vedula, TMS, 1989.

11. D. P. Moon, *Mater. Sci. and Technol.* **5** (1989) 754-764.

12. G. C. Wood and F. H. Stott, p. 227-250 in *High Temperature Corrosion*, ed. R. A. Rapp, National Association of Corrosion Engineers, Houston, TX, 1983.

13. T. A. Ramanarayanan, R. Ayer, R. Petkovic-Luton, and D. P. Leta, *Oxid. Met.* **29** (1988) 445-472.

14. J. B. Pethica, R. Hutchings, and W. C. Oliver, *Phil. Mag. A* **48** (1983) 593-606.

15. W. D. Nix, *Metall. Trans. A* **20A** (1989) 2217-2245.

16. P. F. Tortorelli, J. R. Keiser, K. R. Willson, and W. C. Oliver, "Effects of Reactive Elements on Oxide Scale Deformation and Cracking Based on Submicron Indentation Testing," to be published in *Microscopy of Oxidation*, eds. M. J. Bennett and G. W. Lorimer, The Institute of Metals, London, United Kingdom, 1990.

17. Nano Instruments, Inc., P. O. Box 14211, Knoxville, TN 37914.

18. M. J. Bennett, G. W. Horsley, and M. R. Houlton, pp. 282-291 in *Fundamental Aspects of Corrosion Protection by Surface Modification*, eds. E. McCafferty, C. R. Clayton, and J. Oudar, The Electrochemical Society, Princeton, NJ, 1984, 84-3.

19. M. J. Bennett et al., *Mater. Sci. and Eng.* **69** (1985) 359-373.

20. M. J. Bennett et al., *Mater. Sci. and Eng.* **A120** (1989) 199-206.

21. D. Bruce and P. Hancock, *J. Inst. Met.* **97** (1969) 148-155.

22. R. C. Hurst and P. Hancock, *Werkst. Korros.* **23** (1972) 773-776.

23. A. G. Guy, *Introduction to Materials Science*, McGraw-Hill, New York, 1972.

24. C. G. McKamey, "Development of Iron Aluminides," these proceedings.

MOLTEN SALT-INDUCED HOT CORROSION OF IRON ALUMINIDES

W. H. Lee and R. Y. Lin

Department of Materials Science
and Engineering
M. L. #12
University of Cincinnati
Cincinnati, OH 45221-0012

ABSTRACT

Molten Salt-induced high temperature corrosion of iron aluminides in air containing 1% SO_2 has been studied with a thermogravimetric analysis (TGA) technique at temperatures between 605 and 1000 C. The salt-induced corrosion rate is at least an order of magnitude higher than that of oxidation without the presence of salt. It is interesting to observe that while Al_2O_3 is the only reaction product on the corroded sample surface of normal oxidation, Fe_2O_3 and sulfides were detected in the reaction product layers of aluminide samples corroded in the presence of salt. It appears that the localized sulfur potential beneath the salt film during the process of hot corrosion increases significantly near the area where metal and oxide are in contact. Examinations with a scanning electron microscope (SEM) and energy dispersing spectroscope (EDS) suggest that the progressing of sulfides is through the grain of iron aluminide instead of the intergranular penetration. Such penetrations of sulfides through aluminide grains occur along certain preferential planes and results in parallel lines of sulfides on the cross section of the corroded samples. Results from this study show that the higher the chromium content, the smaller the extent of hot corrosion. Comparing with stainless steel 310 and 321, the two types of iron aluminide tested in this study behave poorly in the hot corrosion environment. This program was partially sponsored by ORNL through Martin Mariatta Energy Systems.

INTRODUCTION

Intermetallic compounds developed at Oak Ridge National Laboratory are being considered for applications in fossil energy systems such as fluidized-bed combustors, gas turbines and coal gasifiers.[1] In the development of beta iron aluminum, Fe_3Al, chromium is added to increase the phase transformation temperature[2] from DO_3 to B_2 for the purpose of increasing the high temperature strength. The addition of chromium can also alter the high temperature oxidation characteristics of iron aluminide. Even though the effects of alloying additions on the mechanical properties of these intermetallic compounds have been determined over a wide temperature range, very limited work was performed to evaluate the oxidation, sulfidation and hot corrosion resistance of these materials.

The operating conditions in fluidized-bed combustion (FBC) systems, gas turbines, coal gasification and oil-refining processes have been evaluated by some researchers.[3,4] In coal combustion and gas turbine systems, the oxygen partial pressure in the gas phase is fairly high, and the sulfur partial pressure (present as SO_2) is generally low. The gas along would attack the material under these conditions. Meanwhile, the environments have potential of forming solid sulfates ($CaSO_4$ in FBC systems) or liquid alkali sulfates and chlorides in turbine systems, which may deposit on the metallic components and lead to severe material degradation in service. The fly ash composition in coal combustion varies depending on the source of coal.[5] For example, Dakota Lignite contains 7.38% Na_2O, 0.70% K_2O, 8.48% Fe_2O_3, 23.11% SiO_2, 17 69% SO_3 and many others. During combustion, these oxides will combine with sulfur and oxygen to form sulfate salts and deposit on the surface of cool heater or reheater tubes. Severe environmental attack of heater and reheater tubes around the salt deposit have been the major concern of many researchers. In a DOE sponsored program at MIT, the characteristics of molten sodium sulfate and mixed sulfates have been investigated in the '70 for about 10 years. The MIT study[6] mostly provided basic thermochemistry of molten salt in the attempt to address the tendency and kinetics of salt-induced high temperature material degradation. Based on those studies, it is believed that oxygen and sulfur in molten media play the key roles in the accelerated and even catastrophic oxidation of hot corrosion.

The examination of the oxidation or mixed oxidation-sulfidation or hot corrosion behavior of these intermetallic compounds under above mentioned environmental corrosive media is, hence, critical to the further development of alloys and operation of the energy conversion units. It is therefore the objectives of this research work 1). to investigate high temperature degradation phenomena of aluminides in fossil fuel energy conversion environments, 2). to understand the mechanism of aluminide corrosion at high temperatures, 3). to provide scientific know-how in high temperature corrosion for the development of corrosion resisting aluminides.

EXPERIMENTAL TECHNIQUE

Sample Preparation

Iron aluminides, Fe3Al-2Cr and Fe3Al-5Cr, used in this study were supplied by Dr. Vinod Sikka of Oak Ridge National Laboratory. The compositions of these alloys are,

69.87% Fe, 28.01% Al, 2% Cr, 0.07% Zr, 0.05% B for Fe_3Al-2Cr, and 66.87% Fe, 28.01% Al, 5% Cr, 0.07% Zr, 0.05% B for Fe_3Al-5Cr, all in at.%. Before the experiment, these alloys were rolled to 1.5 mm thick and annealed at 1050 C for 1 hour in a vacuum of 10^{-5} atm. For the experiment, the annealed sheet were sheared into small coupons of 20 x 10 mm, polished with silicon carbide paper down to 600 grit and cleaned ultrasonically in distilled water and acetone. The rectangular specimen with a surface area of approximately 4 cm^2 and a thickness of 1 mm was exposed to air or 1% SO_2 and air gas mixture, with a flow rate of 150 ml/min, at 605, 800 and 1000 C for 1, 5 and 24 hours, respectively. For the hot corrosion study, specimens were coated with 1 ± 0.1 mg/cm^2 of Na_2SO_4-Li_2SO_4 eutectic mixture with a technique developed in this laboratory prior to the TGA experiment. The chemistry of the salt coating has been verified with a wet-chemistry analysis. The selection of this salt mixture is because that (a) Na_2SO_4 has been observed in the coal combustion power plant boilers; (b) the simple eutectic salt allow us to examine the hot corrosion phenomena at temperature as low as 600 C, which is the upper temperature limit of aluminide applications. Since previous results in the literature have shown that sulfur and oxygen are two key components in the hot corrosion reaction and it is known that the behavior of Li is similar to that of Na, the effect of Li_2SO_4 addition in salt on hot corrosion is primarily to reduce the melting point of the salt.

Experimental

The Thermogravimetric analysis (TGA) system used in this study is similar to that used in other oxidation work by the authors. Detailed description of the equipment have been reported elsewhere[7]. Roughly, it consists a Cahn 1000 Thermobalance, a reactor, a temperature control system and a atmosphere control system. In the reactor, the prepared specimen was suspended with a quartz wire to the beam of the thermobalance. The temperature of the specimen was continuously monitored with a Pt/Pt 13% Rh thermocouple and recorded on a strip chart recorder along with the weight of the specimen. Although Cahn 1000 has a sensitivity of ± 1 μg, with the flowing gas environment, the accuracy of experiments in this study has been observed to be about $\pm$ 0.05 mg. In order to minimized the thermal fluctuation in the reactor, the gas flow rate has been maintained at about 150 ml/min. Gas mixtures (analytical grade) were supplied by Union Carbide Corporation (Linde division). The reaction gas composition in the mixed oxidation-sulfidation and hot corrosion experiments was selected to be 1% SO_2 in air. This mixture simulates the partial pressure of SO_2 in combustion gases at 1 atm (0.10 MPa). This

environment resembles one in a gas turbine from a fuel containing 1 wt.% sulfur using an air/fuel ratio of about 6. The gases were passed over a platinum catalyst at the test temperature to ensure that the equilibrium partial pressure of SO_3 was attained.

For the reaction temperature control, a Marshall furnace was mounted on pulleys so that it could be quickly moved up or down to provide rapid heating or cooling of the specimens. Before starting the test, the furnace, which was kept at a position below the reactor, was preheated to a pre-set reaction temperature. Meanwhile, argon was flushed through the reactor for about 30 min and then the desired gas mixture was introduced. To start an experiment, the furnace was raised up to a pre-determined position to heat up the reactor and the specimen to the desired temperature. This brought the specimen to the experimental temperature in less than 10 minutes and minimized the extend of pre-mature reaction at temperatures below the pre-set experimental temperature. Weight changes of the sample as a result of oxygen pick-up during the corrosion reaction were recorded every second during the test. At the end of the experiment, which ran for 1 to 24 hours, the specimen was quenched by lowering down the furnace. It has been observed that in about 5 min, the specimen temperature can be cooled down to about 200 C and the reaction has been completely stopped as observed from the recorder. During the cooling down period, the test atmosphere was maintained in the reactor.

Tested Sample Analysis

After each experiment, the reaction products surface morphology was inspected with a scanning electron microscope (SEM, Stereoscan 600, Cambridge Instruments) and energy dispersing analysis of x-ray (EDS, International 707A) on every specimen. Phases of the corrosion products were determined using a x-ray diffractometer (Philips PW 1729 Generator) with nickel filtered CuKa radiation with the wavelength of 1.54 A. The polished cross sections were examined by an optical microscope (MeF Universal Camera Microscope), SEM and EDS for the distribution of oxide scales and elements.

RESULTS AND DISCUSSION

The TGA results of this study is shown in Figure 1. The top two diagrams are results of high temperature corrosion under 1% SO_2 in air with no salt in the system. The bottom two diagrams are high temperature corrosion results under the same environment but with salt coating on the specimen surface (hot corrosion). These diagrams clearly show

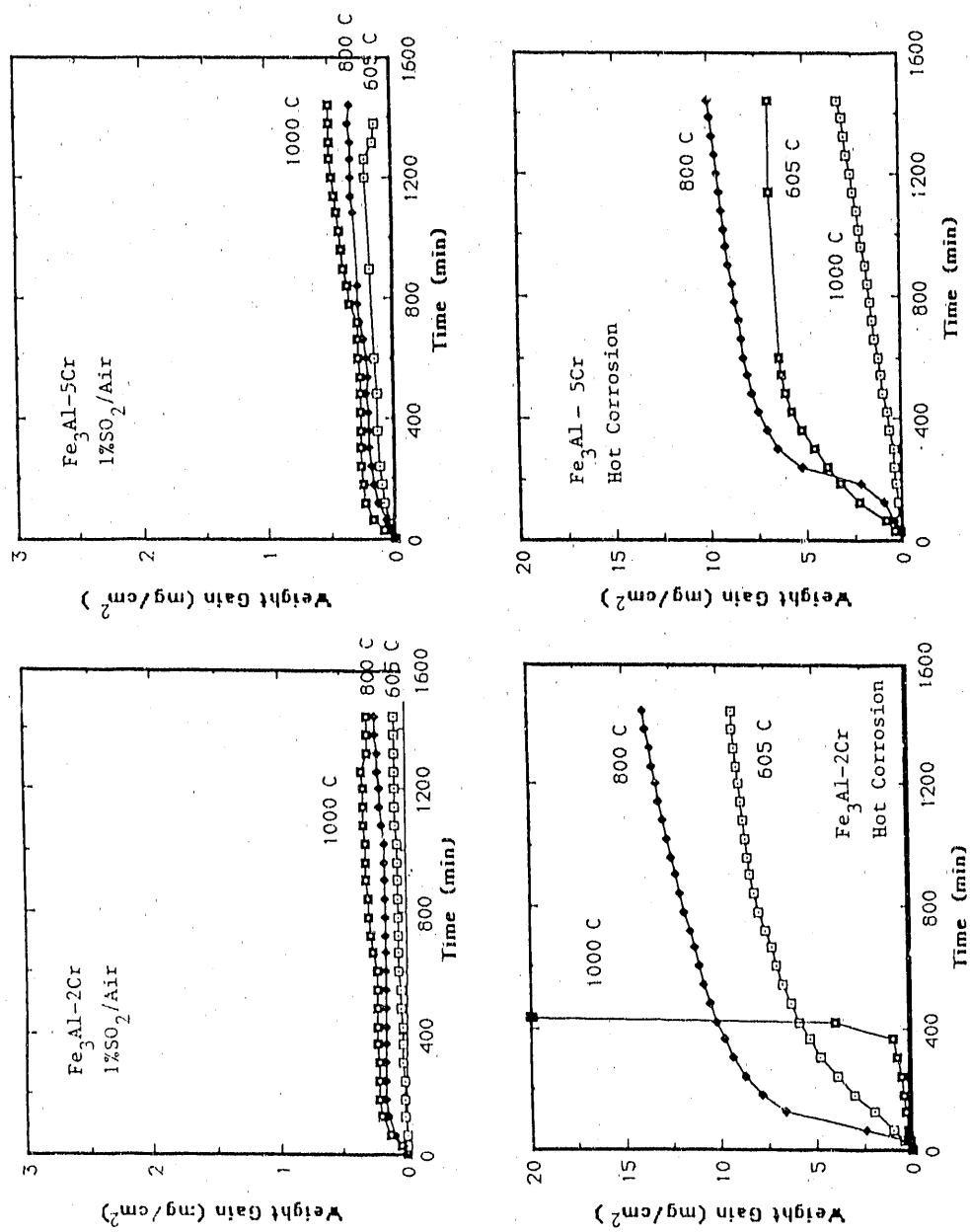

Figure 1. TGA kinetic results of high temperature corrosion in 1% SO2 with and without salt coatings.

that with a thin layer of salt coating on the specimen, the corrosion rate and total weight gain of both iron aluminides increase by more than one order of magnitude. For both aluminides, the x-ray diffraction analysis of the reaction product on the surface of samples tested without salt shows only Al_2O_3 at 1000 C and only base material at both 605 and 800 C. No oxide could be identified on specimens tested at 605 and 800 C due to that only a small amount of the corrosion product presented on the sample surface as observed from the SEM surface morphology of tested samples. On the other hand, the reaction product on hot corroded samples was identified to be Fe_2O_3 at both 605 and 800 C and Al_2O_3 at 1000 C. Comparing the TGA curves and the x-ray diffraction results, it appears that while the low corrosion rate is associated with Al_2O_3 being the reaction product, when Fe_2O_3 preferentially forms on the surface of iron aluminide, the reaction rate is high. Therefore, for the Fe3Al-5Cr specimen, the hot corrosion sample at 1000 C shows less corrosion than those at 605 and 800 C. For Fe3Al-2Cr, sample tested at 1000 C also shows the least weight gain initially among the three tested temperatures.

However, after about 7 hour hot corrosion at 1000 C, a catastrophic failure phenomenon was observed for Fe3Al-2Cr samples and resulted in a complete degradation of the entire specimen. Such catastrophic failure has been repeatedly observed at 1000 C. Further experiments have shown that there is a threshold temperature of about 960 C, below which no catastrophic failure phenomenon was observed. SEM surface morphology examinations have shown that, right after the catastrophic failure phenomenon starts, severe cracking occurs at edges and corners of the Al_2O_3 surface scale. Similar examinations on the Fe3Al-5Cr specimens tested under identical conditions show no cracks. It appears that the relatively dense Al_2O_3 layer grown on the Fe3Al-5Cr sample can withstand residual stresses which are resulted from the molar volume increase when aluminum is oxidized to alumina. It is known that the Pilling-Bedworth ratio of aluminum is 1.28.[8] The effect of Cr may be that, during oxidation, Cr oxidizes along with Al and dissolves in the Al2O3 lattice. Since the ionic size of Cr^{+3} is 0.69 A and that of Al^{+3} is 0.50 A, with Cr^{+3} occupying Al^{+3} sites, the lattice structure of Al_2O_3 will be slightly crowded. The oxide layer strength is likely increased and, thus, less likely to be cracked. Understanding the role of chromium in the oxidation resistance of iron aluminide will provide valuable information for the development of new materials suitable for uses in coal combustion or gasification environments. To verify the role of chromium as described above, further studies are recommended: A. Testing with Varying Chromium Contents to

Determine the Threshold Cr Concentration for Catastrophic Degradation; and B. Microprobe Analysis of the Chromium Distribution in Oxide Scales.

The high rate of hot corrosion comparing with the rate of normal oxidation without salt coating on the specimen surface is associated with two interesting scale characteristics: porous oxide layer and sulfide formation underneath the oxide layer. These characteristics have been observed on all hot corroded samples in this study. Figure 2 shows the SEM cross section microstructure of Fe3Al-5Cr tested at 800 C for 5 hour together with the EDS analysis for a few representative area on the cross section. It is to be noted that, on top of the layers shown in Figure 2, a layer of Fe_2O_3 had spalled off the sample upon cooling during the experiment. This figure illustrates that, from outside in, there are a layer of isolated iron oxide particles, a layer of aluminum oxide, an aluminum and chromium sulfide layer and the base metal. The formation of sulfide underneath the porous oxide layer is because of the localized high sulfur potential. At locations where oxide is in contact with the base metal, the oxygen potential is fixed to a very small value by the equilibrium between the oxide and metal. In the presence of molten salt, this will cause a significant increase in the sulfur potential and attack the base metal. Sulfide penetrated into the base metal and exhibited as parallel lines on the cross section. The hot corrosion of iron aluminide, thus, involves inward diffusion of sulfur in the Fe3Al phase.

Careful examinations of a number of cross sections suggested that the domain of a parallel line group on the cross section is about the size of a grain in the original material. Parallel lines on the cross section suggest that the sulfide penetration during hot corrosion followed parallel planes in the crystal structure of the Fe3Al high temperature structure. Outside the finger-like sulfide region is an area, G in the photo, rich in aluminum, chromium and sulfur with a little iron. It appears that the sulfur attack on the Fe3Al grain eventually convert the entire Fe3Al grain into sulfide. Due to probably fast outward diffusion of iron, these sulfide grains were defficient in iron and rich in aluminum. As oxygen migrate to the sulfide grain, sulfides will be oxidized to oxides. The oxygen potential required to convert sulfide into oxide can be determined with available thermochemical data in the literature. The fact that the spalled off layer is essential only Fe_2O_3 suggested that the outward diffusion of iron during oxidation is faster than the inward diffusion of oxygen and the outward diffusion of aluminum.

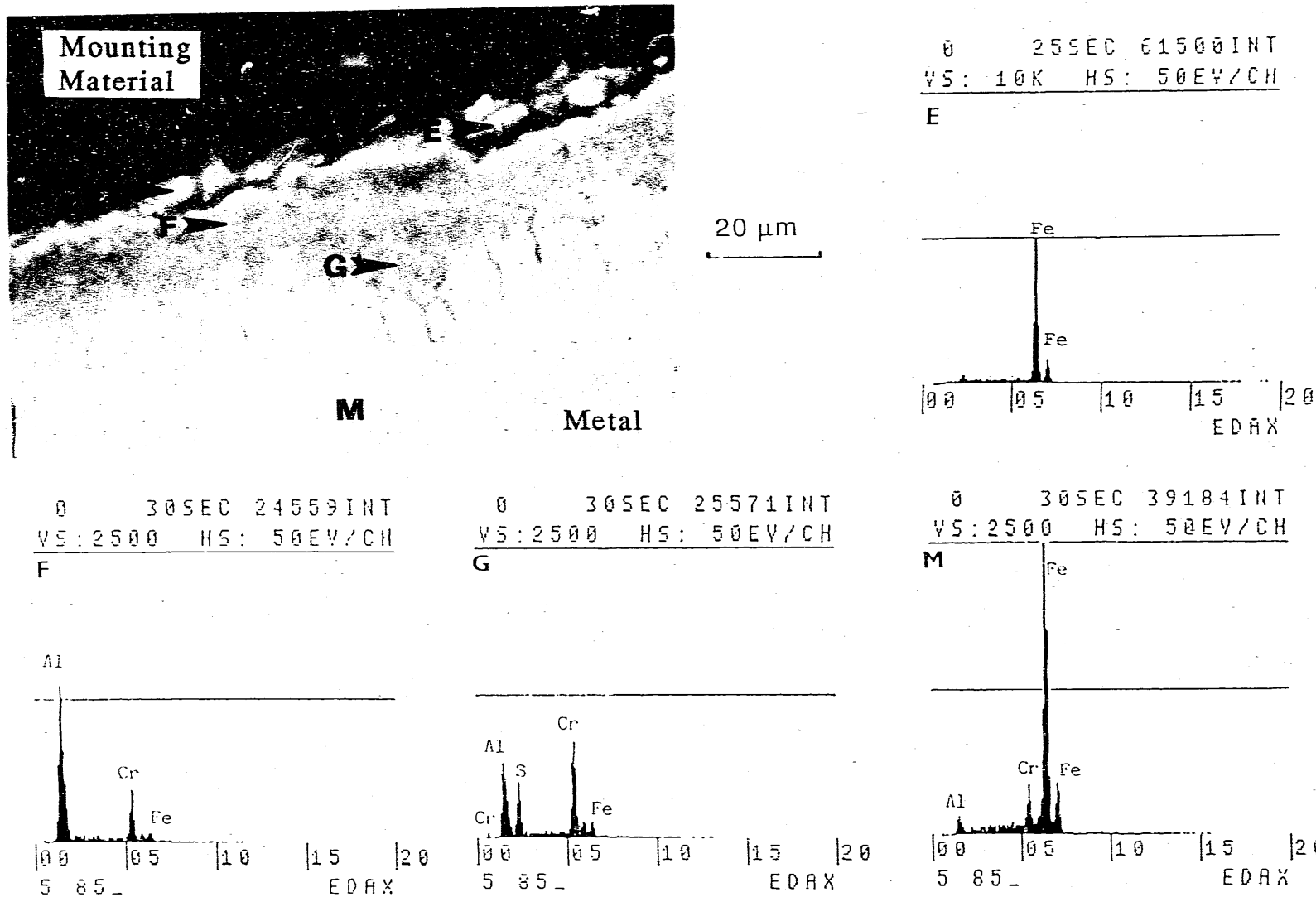

Fig. 2. The cross section and X-ray analysis of an iron aluminide with 5% Cr specimen hot corroded at 800°C for 5 hours.

From these observations, a mechanism can be presented to explain the porous oxide formation and the presence of sulfide compounds in the hot corroded iron aluminides.

a. Initially, metallic elements react with the molten salt to form metal ions and free electrons. Due to the concentration gradient, metal ions diffuse through the molten salt film toward the salt-gas interface. Meanwhile, at the salt-gas interface, oxygen is adsorbed on the salt surface, receive electrons from the salt, dissolve in salt as oxygen ions and diffuse inward through the molten salt film. As the concentration product of metal ion and oxygen ion exceeds the equilibrium solubility product of certain oxides, the nucleation and precipitation of oxide will occur in the molten salt. Since numerous nucleation sites can occur simultaneously, these oxide precipitates will coaleat to form a porous oxide layer. Thermodynamically, it is obtained that single oxides of all elements in the aluminide compound as well as mixed oxides can all be formed but are competing with each other. Oxides which nucleate easiest will form first. Factors determining the nucleation of oxides in the molten salt may include the free energy of formation of oxide, the interfacial energy between oxide and molten salt, base metal composition which controls the metal ion concentration in molten salt, and temperature.
b. At locations where oxide and metal are in contact, the oxygen potential as determined by the equilibrium between oxide and metal is relatively low and as a result, the sulfur potential is increased drastically. Such a localized high sulfur potential can quickly attack the metal and penetrate the base material either through the grain boundaries (in the case of nickel aluminide and nickel iron aluminide) or through specific crystal planes in the grains (in the case of iron aluminide). The sulfide formation, in the meantime, gradually reduce the sulfur potential.
c. As oxygen migrates inward through the porous mixed oxide-salt layer and reaches sulfides, oxygen will replace sulfur to convert sulfide into oxide and release sulfur. Again, the released sulfur causes the sulfur potential to increase and further establish the sulfur potential gradient, which allows sulfur to migrate further inward.
d. Depending on the type of oxide formed in the early stage, the porosity of the oxide layer varies significantly. A relatively dense oxide layer, such Al_2O_3, may slow down the oxygen migration through the oxide layer and thus reduce the rate of hot corrosion.

Comparison with Literature Results

Very little work has been done on the high temperature degradation of iron aluminides. J. DeVan[9] of ORNL has studied the air oxidation of a series of Fe_3Al with

various Cr content. Figure 3 shows the comparison of DeVan's oxidation results on Fe3Al-4Cr with results from this study at 800 C. Similar to DeVan's observation, results from this study indicate that the oxidation of Fe3Al in air is very slow. It is to be noted that the Fe3Al-4Cr sample used by DeVan contains no zirconium addition whereas the Fe3Al-2Cr and Fe3Al-5Cr samples used in this study contain 0.07% Zr. Doping of ZrO_2 in Al_2O_3 oxide layer creates a large number of cation defects and can facilitate the cation diffusion during oxidation. This is probably the reason that DeVan's oxidation results on Fe3Al-4Cr are smaller than the oxidation of Fe3Al-2Cr and Fe3Al-5Cr in air from this study.

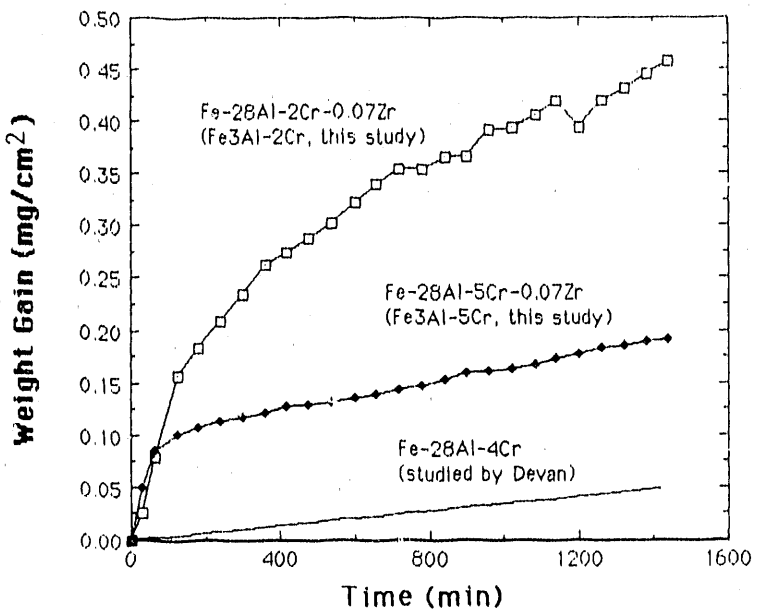

Fig. 3. The comparison of kinetic curves of alloys Fe-28-2Cr-0.07Zr, Fe-28Al-5Cr-0.07Zr, and Fe-28Al-4Cr exposed to air at 800°C.

For comparison, stainless steel 321 (S.S. 321) and 310 (S.S. 310), with about 23 and 18 at.% Cr, respectively, were also hot corroded in 1%SO_2/air atmosphere at 800 C for 24 hr along with iron aluminide without Cr addition and with higher Al content. The kinetic behavior of these materials are plotted in Fig. 4. Without a Cr addition, the Fe3Al intermetallic compound is catastrophically corroded. On the other hand, Fe3Al with the same amount of 5 at.%Cr additions but 36 at.%Al concentration revealed a better hot corrosion resistance than that with 28 at.%Al iron aluminide. Similarly, with high Cr contents, S.S. 310 and S.S. 321 also show good hot corrosion resistance. These results agree with those on the beneficial effect of Cr addition to superalloys on hot corrosion resistance studied by previous investigators.[10-12]

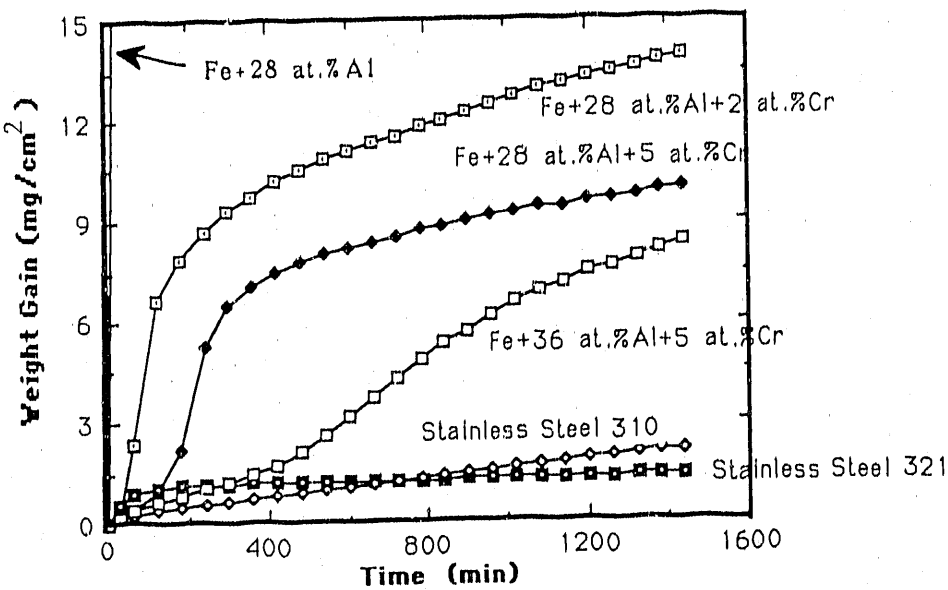

Fig. 4. The comparison of kinetic curves of iron aluminide, Fe+28 at.%Al, Fe+28 at.%Al+2%Cr, Fe+28 at.%Al+5%Cr and Fe+36 at.%Al+5 at.%Cr with that of stainless steel specimens hot corroded at 800°C for 24 hours.

CONCLUSIONS

Under the hot corrosion condition, all tested aluminides show at least a ten fold increase in the degradation rate. All oxide scales formed on the specimen surface are porous. At 1000 C, the Fe3Al-2Cr specimen was completely oxidized in about 7 hours although the Fe3Al-5Cr specimen shows the least attack among all aluminides tested. Since in coal combustion or gasification environments, alkaline oxides exist as impurities in coal. Together with sulfur in coal and oxygen in the environment, it is inevitable that alkaline sulfate salt will be deposit on power plant engine components and result in severe environmental attacks. Results from this study suggest that aluminides as developed to-date are not suitable for use in the environment with potential salt depositions due to the possible severe degradation of aluminide parts from hot corrosion.

SEM and EDS examinations of the cross section of all hot corroded aluminide specimens show the presence of sulfur-rich aluminum and nickel compounds believed to be

sulfides below the outer porous oxide scale and extended into the unattacked metallic portion of the sample. The sulfide formation is due to the localized high sulfur potential in molten salts as a result of the low oxygen potential near the oxide-metal interface. Although these sulfides were converted to oxides when oxygen migrates to the region, the rate of sulfide formation along with the rate of oxygen inward migration play critical roles in the kinetics of hot corrosion.

REFERENCES

1. R.C. Crawford, I.L. Ray, and D.J.H. Cockayne,"The Weak-Beam Technique Applied to Superlattice Dislocations in Iron-Aluminium Alloys, II. Fourfold Dissociation in DO_3-Type Order", Phil. Mag., Vol. 27, pp.1-7, 1973.

2. M. G. Mendiratta and H. A. Lipsitt, in Materials Research Soc. Symp. Proc., vol.39, pp.155-162, 1985.

3. R.A. Perkins, and S.J. Vonk, Materials Problems in Fluidized-bed Combustion System, EPR2-FP-12801, 1979.

4. K. Natesan,"High Temperature Corrosion in Coal Gasification Systems", Corros., Vol. 41, pp. 646-655, 1985.

5. D. N. French, "Metallurgical Failures in Fossil Fired Boilers," John Wiley & Sons, 1983.

6. J. F. Elliott, "Corrosion of Ceramics and Metals at High Temperature," Proc. 100th Ann. Meeting of Amer. Chem. Soc., 1976.

7. J. M. Ting and R. Y. Lin, "Molten Carbonate-Induced Hot Corrosion of Nickel," Oxid. Met., Vol. 32, No. 3/4, 1989, pp. 225-240.

8. M. G. Fontana, "Corrosion Engineering, 3rd Ed.," McGraw-Hill, N. Y., 1986, pp. 505-506.

9. J. H. DeVan, Oxidation Behavior of Fe3Al and Derivative Alloys," in Oxid. High Temp. Intermetallics, Ed. T. Grobstein and J. Doychak, TMS Pub. pp. 107-115, 1988.

10. P.A. Bergman,"Hot Corrosion of Gas Turbine Alloys", Corrosion, Vol. 23, pp. 72-81, 1967.

11. J.A. Goebel, F.S. Pettit, and G.W. Goward,"Mechanisms for the Hot Corrosion of Nickel-Base Alloys", Metall. Trans., Vol. 4, pp. 261-278, 1973.

12. A.U. Seybolt,"Contribution to the Study of Hot Corrosion", Tans. TMS-AIME, Vol. 242, pp. 1955-1961,1968.

APPENDIX A

AGENDA FOR FOURTH ANNUAL CONFERENCE ON FOSSIL ENERGY MATERIALS

FINAL PROGRAM
FOSSIL ENERGY MATERIALS CONFERENCE

Tuesday, May 15, 1990

7:00	Registration Desk opens Coffee and Rolls	
8:00	Welcome and Introductory Remarks	DOE and ORNL Program Managers

Session IA - Ceramics
T. L. Starr, Chairman

8:30	Characterization of Fiber-Reinforced SiC-Matrix Composites Fabricated by Chemical Vapor Infiltration	D. P. Stinton ORNL
9:00	Reaction-Sintered Silicon Nitride Composites with Cloth Lay-up Reinforcement	T. L. Starr Georgia Institute of Technology
9:30	High-Temperature Filtration Using Ceramic Filters	L. R. White 3M Company
10:00	Break	
10:20	Microwave Sintering of Ceramics for Fuel Cells	M. A. Janney ORNL
10:50	Investigation of Properties and Performance of Ceramic Composite Components	K. L. Reifsnider Virginia Polytechnic Institute and State University
11:20	Mechanical Properties and Testing of Ceramic Fiber-Ceramic Matrix Composites	J. Sankar North Carolina A&T State University
11:50	Lunch	

Tuesday, May 15, 1990

Session IB - Ceramics
W. A. Ellingson, Chairman

2:30	Nondestructive Evaluation of Advanced Ceramic Composite Materials	L. A. Lott Idaho National Engineering Laboratory
3:00	Measurement of Fiber-Matrix Interfacial Properties and Their Relation to Ceramic Composite Toughening	E. R. Fuller National Institute of Standards and Technology
3:30	Advanced Materials for High-Temperature Solid Electrolyte Applications	J. L. Bates Pacific Northwest Laboratory
4:00	Break	
4:20	Ceramic Catalyst Materials: Hydrous Metal Oxide Ion Exchange Supports for Direct Coal Liquefaction	D. H. Doughty Sandia National Laboratories
4:50	Development of Ceramic Membranes for Gas Separation	D. E. Fain ORDGP
5:20	Adjourn	
6:00 10:00	Social Event	

Wednesday, May 16, 1990

7:30	Registration Desk opens Coffee and Rolls	
	Session IIA - New Alloys R. R. Judkins, Chairman	
8:00	Introductory Remarks	
8:10	Development of Iron Aluminides	C. G. McKamey ORNL
8:30	Weldability of Iron Aluminides	S. A. David ORNL
8:45	Moisture-Induced Embrittlement of Fe_3Al	D. J. Alexander ORNL
9:00	Fabrication and Properties of Iron-Aluminide Alloys	V. K. Sikka ORNL
9:30	The Influence of Processing on Structure and Properties of Iron Aluminides	R. Wright Idaho National Engineering Laboratory
10:00	Break	
10:20	Weldability of Polycrystalline Iron Aluminides	G. R. Edwards Colorado School of Mines
10:50	Development and Evaluation of Advanced Austenitic Alloys	R. W. Swindeman ORNL
11:20	Metallurgical Effects on the Mechanical Properties of Copper-Modified Austenitic Alloys	C. Y. Li Cornell University
11:50	Lunch	

Wednesday, May 16, 1990

Session IIB - New Alloys
D. N. Braski, Chairman

1:30	Investigation of Joining Techniques for Advanced Austenitic Alloys	C. D. Lundin University of Tennessee
2:00	Fabricability of Advanced Austenitic Alloy Superheater Tubing	M. Topolski Babcock & Wilcox
2:30	Development of Surface Treatments and Alloy Modifications for Corrosion-Resistant Oxide Scales	J. H. DeVan ORNL
3:00	Break	
3:20	Fundamental Study of Aluminizing and Chromizing Processes	R. A. Rapp Ohio State University
3:50	Electro-Spark Deposited Coatings for Protection of Materials in Sulfidizing Atmospheres	R. N. Johnson Westinghouse Hanford Company
4:20	Adjourn	

Thursday, May 17, 1990

7:30	Registration Desk opens Coffee and Rolls	
	Session IIIA - Corrosion and Erosion **K. Natesan, Chairman**	
8:15	Introductory Remarks	
8:30	Corrosion Behavior of Materials in FBC Environments	K. Natesan Argonne National Laboratory
9:00	Fireside Corrosion Testing of Candidate Superheater Tube Alloys, Coatings, and Claddings	J. L. Blough Foster Wheeler Development Corporation
9:30	Effects of Alloying Constituents on the Growth of Protective Scales	I. G. Wright Battelle Columbus Laboratories
10:00	Break	
10:20	Effects of Several Variables on the Growth and Breakdown of Protective Alumina or Chromia Scales in Mixed-Gas Environments	V. Srinivasan Universal Energy Systems
10:50	Aqueous Corrosion and Stress Corrosion Cracking of Iron Aluminides	R. A. Buchanan University of Tennessee
11:20	Material Behavior During the Incubation Period of Solid Particle Erosion of 1100 Aluminum	J. R. Keiser ORNL
11:50	Lunch	

Thursday, May 17, 1990

Session IIIB - Corrosion and Erosion
A. V. Levy, Chairman

1:00	Comparisons of Observed and Predicted Rebound Velocities of Erodent Particles	T. H. Kosel University of Notre Dame
1:30	Wear by Coal-Fueled Diesel Combustion Particulates	L. K. Ives National Institute of Standards and Technology
2:00	The Wastage of Steels in the Erosion-Corrosion Environments of Fluidized Bed Combustors	A. V. Levy Lawrence Berkeley Laboratory
2:30	Break	
2:50	Study of Particle Rebound Characteristics and Materials Erosion at High Temperatures	W. Tabakoff University of Cincinnati
3:20	A Theoretical Model of a Solid particle Impact on the Target of Ductile Materials	Jian J. Yeuan University of Cincinnati
3:40	Effects of Reactive Elements on Oxide Scale Deformation and Cracking	P. F. Tortorelli ORNL
4:10	Molten Salt-Induced Corrosion of Iron Aluminides	R. Y. Lin University of Cincinnati
4:40	Adjourn	

APPENDIX B

LIST OF ATTENDEES AT FOURTH ANNUAL CONFERENCE ON FOSSIL ENERGY MATERIALS

FOURTH ANNUAL CONFERENCE ON FOSSIL ENERGY MATERIALS
MAY 15-17, 1990

LIST OF ATTENDEES

D. J. Alexander
Oak Ridge National Laboratory
P.O. Box 2008, 4500S, 6151
Oak Ridge, TN 37831-6151
(615) 574-4467

J. Lambert Bates
Pacific Northwest Laboratory
P.O. Box 999, MS K2-45
Richland, WA 99352
(509) 375-2579

James Bennett
U.S. Bureau of Mines
Tuscaloosa, AL 35405

Theodore M. Besmann
Oak Ridge National Laboratory
P.O. Box 2008, Bldg. 4515, MS-6063
Oak Ridge, TN 37831-6063
(615) 574-6852

P. J. Blau
Oak Ridge National Laboratory
P.O. Box 2008, Bldg. 4515, MS-6063
Oak Ridge, TN 37831-6063
(615) 574-4559

Jeffrey L. Blough
Foster Wheeler Development Corp.
12 Peach Tree Hill Road
Livingston, NJ 07039
(201) 535-2355

Joseph. A. M. Boulet
University of Tennessee
Engineering Science & Mechanics
310 Perkins Hall
Knoxville, TN 37996-2030

R. A. Bradley
Oak Ridge National Laboratory
P.O. Box 2008, 4515, MS-6067
Oak Ridge, TN 37831-6067
(615) 574-6094

David N. Braski
Oak Ridge National Laboratory
P.O. Box 2008, Bldg. 4508, MS-6084
Oak Ridge, TN 37831-6084
(615) 574-5092

Jeffrey D. Bright
Ceramatec
2425 South 900 West
Salt Lake City, UT 84119
(801) 972-2455

John B. Brooks
Tennessee Valley Authority
3N66A Missionary Ridge Place
Chatanooga, TN 37402-2801
(615) 751-5118

Ray A. Buchanan
University of Tennessee
Materials Science & Eng. Dept.
Knoxville, TN 37996
(615) 974-4858

Oral Buyukozturk
Massachusetts Inst. of Tech.
Dept. of Civil Engineering
Cambridge, MA 02139
(617) 253-7186

Paul T. Carlson
Oak Ridge National Laboratory
P.O. Box 2008, 4500S, MS-6153
Oak Ridge, TN 37831-6153
(615) 574-5135

J. P. Carr
U.S. DOE, Office of Fossil Energy
FE-14, B127 GTN
Washington, DC 20585
(301) 353-6519

Chi-Chang Chen
Univ. of Tennessee
Materials Science & Eng. Dept.
Knoxville, TN 37996
(615) 974-0880

Tim Clancy
U.S. Bureau of Mines
Tuscaloosa, AL 35405

C. E. Clark
Oak Ridge National Laboratory
P.O. Box 2008, Bldg. 4515, MS-6063
Oak Ridge, TN 37831-6063
(615) 574-4559

Kenneth V. Cook
Oak Ridge National Laboratory
P.O. Box 2008, Bldg. 4500S, 6158
Oak Ridge, TN 37831-6158
(615) 574-4422

John F. Dace
Univ. of Tenn. Space Institute
Design Engineering
Tullahoma, TN 37388
(615) 455-0631

Phillip L. Daniel
Babcock & Wilcox
1562 Beeson Street
Alliance, OH 44601

Sandy J. Dapkunas
Nat. Institute of Standards & Tech.
U.S. Dept. of Comm., Bldg. 223,
Rm. 256 Gaithersburg, MD 20899
(301) 975-6119

Stan A. David
Oak Ridge National Laboratory
P.O. Box 2008, 4508, 6095
Oak Ridge, TN 37831-6095
(615) 574-4804

John J. DeBarbadillo
INCO Alloys International
P.O. Box 1958, Riverside Drive
Huntington, WV 25720
(304) 526-5634

J. H. DeVan
Oak Ridge National Laboratory
P.O. Box 2008, Bldg. 4500S, MS-6138
Oak Ridge, TN 37831-6138
(615) 574-4551

C. E. DeVore
Oak Ridge National Laboratory
P.O. Box 2008, Bldg. 4515, MS-6063
Oak Ridge, TN 37831-6063
(615) 574-4559

David J. Alexander
Oak Ridge National Laboratory
P.O. Box 2008, 4500S, MS-6151
Oak Ridge, TN 37831-6151
(615) 574-4467

Peter A. Doty
Dow Chemical Company
Midland, MI 48674
(517) 636-3545

Dan Doughty
Sandia National Laboratory
P.O. Box 5800, Division 1846
Alburqerque, NM 87185

Thomas J. Dunyak
Virginia Tech.
Eng. Science & Mechanics
Blacksburg, VA 24061
(703) 231-5316

Glen R. Edwards
Colorado School of Mines
Ctr. for Welding & Joining Research
Golden, CO 80401
(303) 273-3773

B. Zane Egan
Oak Ridge National Laboratory
P.O. Box 2008, Bldg. 4501, MS-6223
Oak Ridge, TN 37831-5223
(615) 574-6968

Doug E. Fain
Oak Ridge National Laboratory
P.O. Box 2003, Bldg. 1004-L, MS-7271
Oak Ridge, TN 37831-7271
(615) 574-9932

Ed R. Fuller
Nat. Institute of Standards & Tech.
U.S. Dept. of Comm., Bldg. 223,
Rm. 256
Gaithersburg, MD 20899
(301) 975-5795

Rick Gleixner
Babcock & Wilcox Company
1562 Beeson Street, P.O. Box 835
Alliance, OH 44601
(216) 829-7332

Rolando E. Gonzalez
Center for Applied Research
3572 Iron Works Pike
Lexington, KY 40511
(606) 257-0266

James Hickerson
U.S. Department of Energy
Pittsburgh Energy Technology Center
MS-922-H, Rm. 122
P.O. Box 10940
Pittsburgh, PA 15236-0940

Don L. Hindman
Babcock & Wilcox
Box 11165, NNFD-RL
Lynchburg, VA 24506-1165
(804) 522-5825

E. E. Hoffman
DOE Oak Ridge Operations
P.O. Box 2001
Oak Ridge, TN 37831

Rollin E. Hook
ARMCO Inc.
705 Curtis Street
Middletown, OH 45043
(513) 425-2409

Caulton L. Irwin
West Virginia Univ.
617 Spruce Street, P.O. Box 6064
Morgantown, WV 26506-6064
(304) 293-7318

Lewis K. Ives
National Inst. of Stand. & Tech.
U.S. Dept. of Comm., Bldg. 220,
Rm.215
Gaithersburg, MD 20899
(301) 975-6013

Mark A. Janney
Oak Ridge National Laboratory
P.O. Box 2008, Bldg. 4508, MS-6087
Oak Ridge, TN 37831-6087
(615) 574-4281

Roger N. Johnson
Westinghouse Hanford Company
P.O. Box 1970, L6-39
Richland, WA 99352
(509) 376-3582

Roddie R. Judkins
Oak Ridge National Laboratory
P.O. Box 2008, Bldg. 4508, MS-6084
Oak Ridge, TN 37831-6084
(615) 574-4572

Don W. Keefer
EG&G Idaho, Inc.
P.O. Box 1625
Idaho Falls, ID 83415-2025
(208) 526-8003

J. R. Keiser
Oak Ridge National Laboratory
P.O. Box 2008, Bldg. 4500S, MS-6156
Oak Ridge, TN 37831-6156
(615) 574-4453

A. D. Kelkar
N.C. A&T University
Dept. of Mech. Eng.
Greensboro, NC 27411
(919) 334-7620

Yasushi Kikuchi
Univ. of Tennessee
Mat. Science & Engineering Dept.
Knoxville, TN 37996
(615) 974-5299

Jung-Gu Kim
Department of Materials Science
and Engineering
University of Tennessee
Knoxville, TN 37996

T. H. Kosel
Univ. of Notre Dame
Dept. of Met. Eng. & Mat. Sci.
Notre Dame, IN 46556
(219) 239-5642

Alan V. Levy
Lawrence Berkeley Laboratory
1 Cyclotron Road, MS 62-203
Berkeley, CA 94720
(415) 486-5822

Che-Yu Li
Cornell University
Mat. Science and Eng. Dept.
Ithaca, NY 14853
(607) 255-4349

Ray Y. Lin
Univ. of Cincinnati
Aerospace Eng. & Eng. Mech.
Cincinnati, OH 45221
(513) 556-3116

Larry M. Long
Tennessee Eastman
Kingsport, TN

Dick Loop
U.S. Department of Energy
785 DOE Place
Idaho Falls, ID 83402

Layman A. Lott
Idaho National Engineering Lab.
P.O. Box 1625
Idaho Falls, ID 83415-2218
(208) 626-6436

Richard A. Lowden
Oak Ridge National Laboratory
P.O. Box 2008, 4515, MS-6063
Oak Ridge, TN 37831-6063
(615) 574-7714

Carl D. Lundin
Univ. of Tennessee
Mat. Science & Engineering Dept.
Knoxville, TN 37996
(615) 974-5310

Daniel J. McGuire
Oak Ridge National Laboaratory
P.O. Box 2008, Bldg. 4500S, 6158
Oak Ridge, TN 37831-6158
(615) 574-4421

Claudette G. McKamey
Oak Ridge National Laboratory
P.O. Box 2008, 4500S, MS-6116
Oak Ridge, TN 37831-6116
(615) 574-6917

J. C. McLaughlin
Oak Ridge National Laboratory
P.O. Box 2008, Bldg. 4515, MS-6063
Oak Ridge, TN 37831-6063
(615) 574-4559

Ken Natesan
Argonne National Laboratory
9700 South Cass Avenue
Argonne, IL 60439
(708) 972-5103

Charles Peden
Sandia National Laboratory
P.O. Box 5800
Albuquerque, NM 87185

Cong Yue Qiao
Univ. of Tennessee
Mat. Science & Engineering Dept.
Knoxville, TN 37996
(615) 974-5299

Barry H. Rabin
Idaho National Engineering Lab.
P.O. Box 1625
Idaho Falls, ID 83415-2218
(208) 626-0058

T. C. Ramaraz
Tenn. Tech. Univ.
Manufacturing Center, P.O. Box 5077
Cookeville, TN 38505
(615) 372-3016/3362

Robert A. Rapp
Ohio State Univ.
116 West 19th Avenue
Columbus, OH 43210
(614) 292-6178

Kenneth L. Reifsnider
Virginia Polytechnic Inst. and
State University
Eng. Science and Mechanics
Blacksburg, VA 24061
(703) 231-5316

Laura Reister
Oak Ridge National Laboratory
P.O. Box 2008, Bldg. 4515, MS-6063
Oak Ridge, TN 37831-6063
(615) 574-4559

Dr. Remick
IGT
Chicago, IL

George Roettger
Martin Marietta Energy Systems, Inc.
P.O. Box 2007
Oak Ridge, TN 37831

Yvette G. Roman
Oak Ridge National Laboratory
P.O. Box 2008, 4515, 6063
Oak Ridge, TN 37831-6063
(615) 574-4556

J. Sankar
N.C. A&T University
Dept. of Mech. Eng.
Greensboro, NC 27411
(919) 334-7620

George Shier
Dow Chemic .l Company
Midland, MI 48674

Vinod K. Sikka
Oak Ridge National Laboratory
P.O. Box 2008, Bldg. 4508, MS-6083
Oak Ridge, TN 37831-6083
(615) 574-5112

William A. Simpson
Oak Ridge National Laboaratory
P.O. Box 2008, Bldg. 4500S, 6158
Oak Ridge, TN 37831-6158
(615) 574-4421

Jitendra P. Singh
Argonne National Laboratory
9700 South Cass Avenue
Argonne, IL 60439
(708) 972-5123

Gerald M. Slaughter
Oak Ridge National Laboratory
P.O. Box 2008, 4500S, MS-6152
Oak Ridge, TN 37831-6152
(615) 574-4267

Vasudevan Srinivasan
Universal Energy Systems, Inc.
4401 Dayton-Xenia Road
Dayton, OH 45432
(513) 426-6900

Thomas L. Starr
Georgia Tech. Research Inst.
GTRI/EMSL/MSD, Rm. 113 Baker Bldg.,
Atlanta, GA 30332
(404) 894-3678

Wayne W. Stinchcomb
Virginia Polytechnic Institute
Eng. Science and Mechanics Dept.
Blacksburg, VA 24061
(703) 231-5316

D. P. Stinton
Oak Ridge National Laboratory
P.O. Box 2008, Bldg. 4515, MS-6063
Oak Ridge, TN 37831-6063
(615) 574-4556

R. W. Swindeman
Oak Ridge National Laboratory
P.O. Box 2008, Bldg. 4500S, MS- 6155
Oak Ridge, TN 37831-6155
(615) 574-5108

Widen Tabakoff
Univ. of Cincinnati
Dept. of Aerospace Eng.& App. Mechanics
Cincinnati, OH 45221
(513) 556-3226

Steve Tassen
INCO Alloys International Inc.
P.O. Box 1958
Hunnington, WV 25720
(304) 526-5737

Scot D. Thompson
Allied-Signal Aerospace Company
7550 Lucerne Drive, Suite 203
Middleburg Hts., OH 44130
(216) 826-0330

Terry N. Tiegs
Oak Ridge National Laboratory
P.O. Box 2008, 4515, MS-6069
Oak Ridge, TN 37831-6069
(615) 574-5173

Judith A. Todd Copley
Illinois Inst. of Tech.
METM Dept., Perlstein Hall
Chicago, IL 60616
(312) 567-8867

Mark J. Topolski
Babcock & Wilcox Company
1562 Beeson Street, P.O. Box 835
Alliance, OH 44601
(216) 829-7301

P. F. Tortorelli
Oak Ridge National Laboratory
P.O. Box 2008, Bldg. 4500S, MS-6156
Oak Ridge, TN 37831-6156
(615) 574-5119

C. Vahlas
Oak Ridge National Laboratory
P.O. Box 2008, Bldg. 4515, MS-6063
Oak Ridge, TN 37831-6063
(615) 574-4559

Krishnan R. Vaidyanathan
N.C. A&T University
Dept. of Mech. Eng.
Greensboro, NC 27411
(919) 334-7620

James R. Weir Jr.
Oak Ridge National Laboratory
P.O. Box 2008, 4500S, MS 6134
Oak Ridge, TN 37831-6134
(615) 574-4064

Lloyd R. White
3M Company
3M Center/218-3S-03
St. Paul, MN 55144
(818) 767-4888

Marvis K. White
Un. of Tennessee Space Institute
Energy Conversion Programs
Tullahoma, TN 37388
(615) 455-0631

D. E. White
Martin Marietta Energy Systems, Inc.
P.O. Box 2007
Oak Ridge, TN 37831

Dr. Lane Wilson
Department of Physics
West Virginia University

Ian G. Wright
Battelle
505 King Avenue
Columbus, OH 43201-2693
(614) 424-4377

Richard N. Wright
Idaho National Engineering Lab.
P.O. Box 1625
Idaho Falls, ID 83415-2218
(208) 626-2218

Jian Yeuan
Univ. of Cincinnati
Aerospace Eng. & Eng. Mech.
Cincinnati, OH 45221
(513) 556-3360

C. S. Yust
Oak Ridge National Laboratory
P.O. Box 2008, Bldg. 4515, MS-6063
Oak Ridge, TN 37831-6063
(615) 574-4559

END

DATE FILMED

11 / 1 / 90